

edited by
LEONARD GREINER

UNDERWATER MISSILE PROPULSION

A Selection of Authoritative Technical and Descriptive Papers

COMPASS PUBLICATIONS, INC.,
ARLINGTON, VIRGINIA, U.S.A.



Preface

ENGINEERING LIBR.

Copyright © 1967

COMPASS PUBLICATIONS, INC.

Printed in United States of America

All Rights Reserved. This book, or any part thereof may not be reproduced in any form without written permission of the copyright owner, except brief quotations for inclusion in a review.

Library of Congress Catalog Card Number 67—31690



COMPASS PUBLICATIONS, INC.

Sum 1000, 1117 N. 19TH ST., ARLINGTON, VIRGINIA 22209

The ocean depths have evoked wonder and fear ever since their expansive, mobile surface was viewed by an ancestor millennia ago. These emotions actually have magnified with time and with growing sophistication in exploring and exploiting the deep ocean. Thus our probes—instrument, sampling, and man-carrying—have found unbelievable life forms existing, apparently contentedly, in an ever-changing, high-pressure liquid environment, and sufficient scientific, technological and economic challenges to keep whole populations gainfully and happily engaged for many more millennia. And replacing (almost completely) the imaginary monsters of the deep are well-authenticated ones, casually and ceaselessly crisscrossing and equipped with powers great enough to destroy any surface ship and, indeed, whole cities and nations hundreds of miles away.

Man has reacted strongly to such stimuli. Survival elicited the more vigorous response, and underwater-missile weapons, called torpedoes, are being readied to destroy the current monsters, called submarines, by an explosive charge carried to their sides. A similar missile with instruments instead of explosives can also explore the depths and so man's fear may be mitigated and his curiosity satisfied by a single technology: that of underwater guided missiles.

In contrast to space, where new propulsion methods were required to perform first-generation tasks, state-of-the-art techniques could be adapted to propel the first underwater missiles. But as underwater performance requirements increase, more specialized propulsion will be demanded, first in torpedoes and then in probes. This volume provides a technical and descriptive background on the propulsion of unmanned underwater missiles.

Because the lion's share of underwater missile propulsion technology has been developed for a weapon and therefore lies in a defense-sensitive area, this book did not move to press quickly: the quasi-legal process of appropriate "sanitization" required well over two years. Although, necessarily, information on actual torpedoes is excluded, basic technology on underwater missile propulsion, including examples, is contained in the book.

The book comprises thirty-one articles prepared by experts. Most are from papers originally presented at classified meetings of the American Institute of Aeronautics and Astronautics, a few from previous AIAA publications, and a number newly prepared. Virtually all were extensively modified for the book. They are grouped in the order next discussed.

The initial section of the book is an "Introduction to Underwater Missile Propulsion." It discusses objectives of torpedo propulsion and some objec-

tives of instrumented missiles, the latter based on selected examples. A theoretical comparison of rocket, heat, and fuel cell engines for underwater missiles is included. Since the purposes of various missiles differ, optimum powerplants also differ; fortunately, there are enough potential engine types to fit virtually any missile need. Certain powerplant adaptations are very efficient in the underwater environment, and even some rockets have propulsive performances at great depths that far exceed their capabilities in air, despite the greater back pressure underwater.

As indicated in the section on "Underwater Missile Propulsors," rotating propellers are generally used, since they are efficient at the relative low speeds that are common underwater. Shrouding the propeller to produce a pumpjet often provides means to better match the thruster and powerplant, and fundamental-empirical methods used in designing pumpjets is covered. Despite relative inefficiency underwater, rocket thrusters may have their place, if specialized new propellants are used, together in some instances with missile staging.

"Underwater Missile Drag," some three orders of magnitude greater than in sea-level air, is the obstacle to underwater movements. Methods of estimating the drag of missiles are described; these are not simple exercises for the uninitiated. Specialized shapes reduce drag by delaying turbulence, and certain materials introduced into the boundary layer reduce drag of normal body shapes by mechanisms as yet unknown.

Batteries are commonly used to power "Electrical Engines for Underwater Missile Propulsion." However, their performance potential would improve if they better fitted the available space in the missile, if only primary types were used, and if more potent electrochemical couples were developed. Alternatively, electricity can be supplied to the missile engines by a thin wire from a generator located at the launch platform. Whatever electrical system is used, the energy source-engine-propulsor combination must be optimized as a unit. A wild-blue-yonder electrical propulsion possibility, also discussed, is an MHD-powered water pump that may be entirely silent.

The state of the art of reciprocating and turbine "Heat Engines for Underwater Missiles" is well advanced. They require specialized propellants and compatible thermodynamic cycles. In the usual open-cycle system, the engine gases exhaust directly to the environment, and performance decreases with depth. The most energetic underwater propellant combinations are metal fuels that react with sea water. If used at great depth in an open-cycle system, these propellants should be burned at very great internal pressures—15,000 psi is one suggestion—to provide a high pressure ratio—for the engine. Closed cycles in which the propellant products exchange their heat to the engine working fluid are also suitable for underwater missiles. Nuclear energy, used in this same manner, can provide virtually unlimited range.

Whether the purpose of the underwater missile is to destroy or to observe, internally produced noises are distracting in an environment where sound is a primary means of external perception. Impacts of meshing gear teeth are a major source of noise at a spectrum of frequencies. The background of gear noise reduction, some of its theory, and means to effect its minimization are discussed in the section on "Gear Noise of Underwater Missiles."

Initial testing of new underwater missiles and components is best performed out of the ocean. As a result, a testing regime has evolved: from static to tethered to free-flight. Examples are described in the section on "Propulsion Test Facilities for Underwater Missiles." All such facilities are very specialized, including the final one described whose purpose is to elucidate torpedo gear noises.

As is probably true of all such compilations of papers, this one does not completely cover its subject. Nevertheless, it provides the best available modern coverage of underwater missile propulsion. It is the Editor's hope that it will whet appetites of its readers for further information on this growing discipline and provide an awareness of what can be done.

The Editor has many a "thank you" to make. These are to CETEC Corporation, Mountain View, Calif.; United Technology Center, Sunnyvale, Calif.; and to Texaco Experiment, Inc., Richmond, Va.; all organizations who have furnished direct assistance to him in preparing the book. Thanks also go to the American Institute of Aeronautics and Astronautics, who graciously made many papers available, and most important, to the numerous authors and to their organizations, half Naval and half industrial, who labored so long and hard on manuscripts; to them I also say, "well done!"

December 1967

Leonard Greiner, Volume Editor

CETEC Corporation
Mountain View, California

Contents

INTRODUCTION TO TORPEDO PROPULSION

Leonard Grciner, Scientist, Research and Development, Calif.

DESIGN OF UNDERSEA INSTRUMENTED MISSILES

J. M. Allison, Senior Technical Specialist, Missiles Engineering, North American Aviation, Inc., Columbus, Ohio.

THEORETICAL PERFORMANCES WITH HYDROGEN-OXYGEN AS PROPELLANT OF PERFECT ROCKET, HEAT, AND FUEL-CELL ENGINES IN UNDERWATER MISSILES

Leonard Greiner, Technical Assistant to Manager, Research and Advanced Technology Department, United Technology Center, Sunnyvale, Calif.

UNDERWATER MISSILE PROPULSORS

A METHOD TO DESIGN PUMPJETS

R. E. Henderson, Assistant Professor of Engineering Research, Ordnance Research Laboratory, Pennsylvania State University, University Park, Pa.

J. F. McMahon, Research Assistant, Ordnance Research Laboratory, Pennsylvania State University, University Park, Pa.

G. F. Wislicenus, Head, Department of Aerospace Engineering and Director, Garfield Thomas Water Tunnel, Ordnance Research Laboratory, Pennsylvania State University, University Park, Pa.

APPLICATIONS OF NEW SOLID PROPELLANTS TO UNDERWATER ROCKETS

Donald E. Tryk, Chief, Technology Projects Section, United Technology Center, Sunnyvale, Calif.

EFFECT OF STAGING ON THE RANGE OF UNDERWATER ROCKETS

William C. Ragsdale, Aerospace Engineer, Applied Aerodynamics Division, U. S. Naval Ordnance Laboratory, White Oak, Silver Spring, Md.

UNDERWATER MISSILE DRAG

SIMPLIFIED METHODS FOR ESTIMATING TORPEDO DRAG

John D. Brooks, Physicist, Underwater Ordnance Dept., Naval Undersea Warfare Center, Pasadena, Calif.

Thomas G. Lang, Research Mechanical Engineer, Underwater Ordnance Dept., Naval Undersea Warfare Center, Pasadena, Calif.

UNDERWATER DRAG REDUCTION THROUGH OPTIMUM SHAPE

Bruce H. Carmichael, Senior Technical Specialist, Research and Engineering, Autonetics Div., North American Rockwell Corp., Anaheim, Calif.

EFFECT OF POLYMER ADDITIVES ON FLUID FRICTION

J. W. Hoyt, Head, Propulsion Div., Underwater Ordnance Dept., Naval Undersea Warfare Center, Pasadena, Calif.

A. G. Fabula, Staff Scientist, Applied Science Div., Naval Undersea Warfare Center, Pasadena, Calif.

EXPERIMENTAL MODEL STUDIES OF NON-NEWTONIAN SOLUBLE COATINGS FOR DRAG REDUCTION

S. Thurston, Chief, Advanced Underwater Systems Group, Norair Div., Northrop Corporation, Hawthorne, Calif.

R. D. Jones, Senior Engineer, Nortronics Div., Northrop Corp., Hawthorne, Calif.

ELECTRICAL ENGINES FOR UNDERWATER MISSILES

BATTERIES FOR TORPEDOES

Francis G. Murphy, Head of the Electrical Engineering Div., Research Dept., Naval Underwater Weapons Research and Engineering Station, Newport, R. I.

WIRE TRANSMITTED ELECTRICAL POWER FOR TORPEDO PROPULSION

R. M. Dunlap, Associate Director for Research, Naval Underwater Weapons Research and Engineering Station, Newport, R. I.

W. R. Cox, Head, Power Branch, Electrical Engineering Div., Research Dept., Naval Underwater Weapons Research and Engineering Station, Newport, R. I.

ANALYSIS OF HIGH-PERFORMANCE ELECTRIC TORPEDO POWERPLANTS

M. L. Henderson, Staff Engineer, Electromechanical Systems, General Electric Co., Pittsfield, Mass.

APPLICATION OF A SPECIAL MAGNETOHYDRODYNAMIC INDUCTION COMPRESSOR TO UNDERSEA PROPULSION

249

Eugene Migotsky, Senior Consulting Scientist, Applied Physics Section, AVCO Corporation, Wilmington, Mass.

Joseph L. Neuringer, Senior Consulting Scientist, Applied Physics Section, AVCO Corporation, Wilmington, Mass.

HEAT ENGINES FOR UNDERWATER MISSILES

TORPEDO PROPELLANTS

Leonard Greiner, Technical Assistant to Manager, Research and Advanced Technology Dept., United Technology Center, Sunnyvale, Calif.

269

LITHIUM AND SODIUM AS WATER-REACTIVE FUELS FOR TORPEDO PROPULSION

281

William D. White, Thermodynamics Branch, Naval Undersea Warfare Center, Pasadena, Calif.

A SEA-WATER-ALUMINUM TORPEDO PROPULSION SYSTEM

289

Leonard Greiner, Research Associate, Texaco Experiment, Inc., Richmond, Va.

F. A. Hansen Jr., Project Engineer, Texaco Experiment Inc., Richmond, Va.

A CLOSED-CYCLE PROPULSION SYSTEM FOR DEEP SUBMERGENCE

301

K. E. Smith, Head, Torpedo Design Branch, Torpedo Development Div., Underwater Ordnance Dept., Naval Undersea Warfare Center, Pasadena, Calif.

L. C. Hidde, Turbachinery Branch, Propulsion Div., Underwater Ordnance Dept., Naval Undersea Warfare Center, Pasadena, Calif.

INVESTIGATION OF A ONCE-THROUGH STEAM GENERATOR

317

H. E. Karig, Consultant, Underwater Ordnance Dept., Naval Undersea Warfare Center, Pasadena, Calif.

D. N. Jackley, Mechanical Engineer, Underwater Ordnance Dept., Naval Undersea Warfare Center, Pasadena, Calif.

L. G. Hidde, Mechanical Engineer, Underwater Ordnance Dept., Naval Undersea Warfare Center, Pasadena, Calif.

RADIOISOTOPE AND REACTOR NUCLEAR POWER FOR UNDERSEA MISSILE PROPULSION

333

K. E. Buck, Principal Nuclear Engineer, Nuclear Engineering and Manufacturing Operations, Aerojet-General Corp., San Ramon, Calif.

H. K. McCluer, Senior Mechanical Engineer, Nuclear Engineering and Manufacturing Operations, Aerojet-General Corp., San Ramon, Calif.

GEAR NOISES OF UNDERWATER MISSILES

INTRODUCTION TO ACOUSTICAL ENGINEERING OF GEAR TRANSMISSIONS

349

Darle W. Dudley, General Electric Company, Lynn, Mass.

ACOUSTIC STUDIES ON POWER TRANSMISSIONS

357

Moe William Rosen, Senior Propulsion Research Engineer and Scientist, Propulsion Div., Naval Undersea Warfare Center, Pasadena, Calif.

GEAR NOISE CONTROL BY MANIPULATING TOOTH COMPRESSIVE STRESSES

379

John Maddock, Consulting Engineer, Lomita, Calif.

PROPELLION TEST FACILITIES FOR UNDERWATER MISSILES

TORPEDO PROPULSION TEST FACILITY

391

G. E. Anderson, Project Engineer, Experimental Test, Rescnrch Dept., U. S. Naval Underwatrr Ordnance Station, Newport, R. I.

THE GARFIELD THOMAS WATER TUNNEL

401

August F. Lehman, Head, Water Tunnel Division, Oceanies Inc.: formerly Associate Professor of Engineering Research Pennsylvania State University, University Park, Pa.

Thomas I. Peirce, Project Leader, Drag Reduction Program, Ordnance Rescnrch Laboratory, Pennsylvania State University, University Park, Pa.

THE HIGH SPEED BASIN AND INSTRUMENTATION OF THE NAVAL SHIP RESEARCH AND DEVELOPMENT CENTER

42

K. E. Schoenherr, Past Technical Director, Hydromechanics Laboratory, Naval Ship Research and Development Center, Washington, D. C.

W. F. Brownell, Assistant Head, Hydromechanics Laboratory, Naval Ship Research and Development Center, Washington. D. C.



THE AEROJET RING CHANNEL

439

Joscpb Levy, Manager, Hydrodynamics Staff, Aerojct-General Corp., Azusa, Calif.

THE UNDERWATER CABLEWAY

457

J. W. Hoyt, Head, Applied Science Div., Ocean Technology Dept., Naval Undersea Warfare Center, Pasadena, Calif.

A TORPEDO TEST FACILITY SUSPENDED UNDER WATER

Eric D. Swanson, Mechanical Engineer, Turbomachinery Branch, Propulsion Div., Underwater Ordnance Dept., Naval Undersea Warfare Center, Pasadena, Calif.

James H. Green, Head, Turbomachinery Branch, Propulsion Div., Underwater Ordnance Dept., Naval Undersea Warfare Center, Pasadena, Calif.

AN OPERATIONAL UNDERWATER THREE-DIMENSIONAL ACOUSTIC TRACKING SYSTEM

479

W. M. Sandstrom, Deputy Director, Applied Physics Laboratory, University of Washington, Seattle, Wash.

QUIET HIGH SPEED TRANSMISSION DRIVE FACILITY

495

Moe William Rosen, Senior Propulsion Research Engineer and Scientist, Prop&ion Div., Naval Undersea Warfare Center,

INTRODUCTION

INTRODUCTION TO TORPEDO PROPULSION*

Leonard Greiner[†]

CETEC Corporation, Mountain View, California

Abstract

The subsystems of a torpedo powerplant are optimized to accomplish the task of the weapon-to destroy a surface ship or a submarine. Since these targets can outdistance a prematurely detected torpedo and sonar is used for detection, noise from the torpedo propulsion mechanism must be low. Methods to reduce underwater drag can improve torpedo performance if the associated mechanisms do not replace a disproportionately large portion of the powerplant. Propeller-type thrusters are always used in torpedoes, and shrouded propellers (pumpjets) often permit a better match between thruster and engine. Since the propulsion-energy source is the greatest volume of any torpedo subsystem, batteries for electrical torpedoes and propellants for heat engines are sought with greater energy densities, as are more efficient electrical motors and heat engines. Heat engines, including their propellants, cycles, and mechanical parts, must be optimized as a unit, and specialized heat engines can operate independently of depth.

Introduction

Torpedoes have evolved from immobile hidden underwater bomb (resembling mines) to explosives attached by spar or cable to moving ships or freely floating on water and guided by expect currents, through several generations with crude internal propulsion and guidance, and finally to today's sophisticated self-propelled and guided underwater missile. Present torpedoes attack moving targets at great distances, so their powerplants are important. This paper is a qualitative introduction to the subject of modern torpedo propulsion. While torpedoes former

*Largely taken from references 1 through 16. Further details are in papers within this book.

[†] Scientist - Research and Development

attacked only surface ships, submarines at great underwater depths are also current targets: a guided torpedo with an explosive charge may be the only practical means of neutralizing such an enemy.

Future capabilities of enemy submarines, and hence requirements for a successful antisubmarine torpedo, are largely predicted from the planned capabilities of our own submarines. This dictates that newer torpedoes be capable of higher speeds, greater depths, and tighter maneuvers in three dimensions, and operable with lower radiated noise. Self noise is tremendously undesirable, since it can alert a target in time for it to escape. Limiting goals for torpedo noise are set, again on predictions of our own future sonar. The subsystems of a torpedo are selected, developed, and then integrated in a manner that achieves the highest kill probability for the total weapon consistent with cost, and propulsive performances and (resultant) radiated noise are traded against one another.

Noise and Speed

Intelligence underwater is largely conveyed by sound, which is used to detect and to avoid a foe. Noise generally increases with the velocity of an underwater body because of correspondingly increased rates of movement of internal mechanisms and increased hydrodynamically induced fluctuations external to the hull.

To show the importance of noise to a torpedo, consider that a torpedo has been launched and properly directed and is now approaching an enemy submarine. A final underwater run to intercept is involved, during which the submarine will be, as always, monitoring external sounds and will take evasive action when its suspicions are aroused. The instant the approaching torpedo can be detected depends on many things, including its distance from the target and the level and frequency distributions of the torpedo's noise. Since torpedo noise increases with its velocity, velocity is (hopefully) programmed to prevent detection at distances where the submarine can run from its pursuer until the torpedo exhausts its lesser reserve of fuel. On the other hand, too slow a torpedo speed permits the submarine to leisurely escape on recognizing an attack.

At any rate, the maximum speed of a torpedo must be greater than that of the submarine, and it will usually be employed during the final attack when the submarine will probably be aware of its close pursuer. Even here, torpedo speed must be adjusted so that (1) self noise does not mask sonar return

from the target, (2) the missile can accomplish necessary maneuvers, and (3) its fuel supply is not prematurely exhausted.

The speed and range of a torpedo is limited by the energy stored in it for propulsion, and this is well below the levels available to its targets--whether these are nuclear or chemical fueled. Thus, torpedo energy must be used sparingly. Propulsive power requirements increase with the cube of missile velocity, so range decreases greatly with speed. It can be shown that a moving target attacked from the stern will be intercepted at the greatest range when the pursuer's speed is 50% greater than the target's. If the latter may approach 40 knots (reference 17), then the torpedo should be capable of 60 knots. This is a respectable velocity underwater: a large torpedo may require 800 hp to go this fast.

Noise Reduction

Since noise limits its effectiveness as a weapon, torpedo noise reduction is a continuing study activity. It has been approached both theoretically and pragmatically--a vibration-isolating device placed between an offending noise maker and the torpedo hull often has proved a satisfactory "fix."

A major noise source, though not the only one, is the speed reduction machinery between powerplant and rotating propulsor. Gear pairs do not rotate in perfect mesh. As a result, momentary relative accelerations lead to impacts and/or discontinuous motions, both of which produce sonic disturbances. These are accentuated when their frequencies correspond to natural vibration modes of adjacent or internal parts of the mechanism. To minimize such noise sources, dimensional tolerances of torpedo gears are very small and only fine bearings are used. Gear teeth are not proportioned solely for maximum load-carrying capacity, since this results in variable stiffness in height and leads to flexures and resultant noise. Spur teeth, unless very specially designed, are avoided in favor of helical types which have several teeth in simultaneous mesh. Noise is also produced when displacement of air between meshing gear teeth occurs at sonic velocity. Noise is not entirely eliminated even when gears are replaced by smooth rollers, in intimate contact or separated by a liquid transfer medium, although this approach is promising.

Drag Reduction

Bodies moving within water are resisted by drag forces almost three orders of magnitude greater than in sea level air at the same velocity, due to the proportionately greater density

of water. This provides a great incentive to lower underwater drag.

The time-honored method to reduce drag is with specialized shapes. It is well known that certain pear-shaped body contours experience lower drag than rounded-end, right circular cylinders of equal volume. The former shape, however, is not satisfactory for torpedoes, since it is less efficiently stored aboard Naval ships, does not fit within standard torpedo tubes, and does not efficiently enclose normal torpedo subsystems. Very smooth body exteriors also have less drag, since protuberances trip turbulence at low Reynold's numbers. However, this is difficult to maintain during the storage and the repetitive practice firings of a torpedo. Generally speaking, the familiar rounded nose, cylindrical midsection, and tapered afterbody of a torpedo with reasonably smooth exterior has proved a satisfactory compromise for reasonably low form drag, accommodation to storage needs, handling, etc.

Drag is also reduced by surrounding the underwater missile with a gas so that energy transfer is not directly to water. To be practical, the means to produce and maintain the gaseous layer must be less bulky than the portion of the powerplant it replaces due to the now-lowered thrust requirement, but this has not been achieved. Drag is also reduced by drawing off the boundary layer before it develops maximum thickness, but competitively sized mechanisms for doing so have not been developed. Certain additives, which also induce non-Newtonian flow in water, reduce drag when present in the boundary layer of a moving body and this approach may yet prove satisfactory for use by a torpedo.

Underwater Thruster

Simple rocket thrusters are not suitable for torpedoes, since rocket-jet velocities are very high compared to the nominal 60 knots of a high-speed torpedo which results in very low propulsive efficiency. Instead, rotating propellers are used. These provide thrust at high propulsive efficiency by accelerating the ambient fluid rearward at an absolute velocity whose magnitude is the same as that of the missile. Such thrusters require torque-producing machinery, which is discussed in a later section.

Rotating thrusters have a distinguished history. Originally they resembled large wood screws. Now they are more or less canted blades revolving about their center and used either alone or in counter-rotating pairs. They can be designed for effective operation when only noncavitating or when always cavitating,

and gas may be injected from the blade tip. They may be located in a shroud to become a pumpjet. A definitive understanding of the working of propellers is not at hand and fundamental studies are continuing. The excellent current design procedures comprise a mixture of fundamentals, empiricism, and art, and final perfection of a new design involves testing.

There is a trend to consider pumpjets for torpedoes since they often provide a more optimum fit with other torpedo requirements. For example, the shroud on a pumpjet decreases cavitation tendencies at high propeller speeds, and this lowers the speed reduction required between powerplant and thruster (a cavitating propeller is another solution). They can be more efficient within a smaller overall diameter than can an open propeller, therefore fitting better within size limitations of certain torpedoes. Finally, if case diameter is not limiting, a pumpjet can be cavitation-free over a wider range of missile speed than an open propeller.

Energy Source

Torpedoes are considered too small to utilize nuclear energy. Instead, chemical energy is always used after conversion to heat or electricity. Present torpedoes are restricted to a maximum of 21 in. in diameter and 246 in. in length with roughly half the internal space, about 10 ft^3 , for energy storage. Such a large torpedo needs up to 800 hp to sustain at 60 knots, as already mentioned, and, to be capable of a 7-min high speed run, over $9 \text{ hp}\cdot\text{hr}/\text{ft}^3$ is required. If 35% of the theoretical available chemical energy is utilized by the powerplant (approximate efficiency of either batteries or heat engines), then the minimum theoretical energy potential of the stored chemicals must be about $26 \text{ hp}\cdot\text{hr}/\text{ft}^3$. This appreciable energy requirement is somewhat reduced in practice because a torpedo will not travel an entire run at full speed. However, a greater than 7-min duration may be needed and projected developments of both submarine and surface ships call for increased performances of future torpedoes. Thus, $26 \text{ hp}\cdot\text{hr}/\text{ft}^3$ remains a good goal.

Electrical Energy

Batteries are well established as energy sources for torpedoes. They quiescently produce electrical energy which is readily conducted to an electric motor to provide torque. Moreover, batteries do not suffer from the intrinsic Carnot-cycle inefficiency of heat engines. The competing electrical energy source, a fuel cell, has received less consideration because, at the power levels required, it does not fit within a torpedo hull.

The common lead-acid battery has too low an energy density for today's high performance torpedoes and the trend is to use zinc-silver or magnesium-silver chloride sea water batteries. These have potential performance improvements over the lead-acid battery of 5- and g-fold, respectively. Lesser attention is also given to more **exotic** cell couples with greater energy potentials. **However**, theoretical output of a cell couple does not tell the whole story--even the well established silver cell provides only 30% of its theoretical energy under many torpedo conditions, and this does not take into account packaging inefficiencies. Problems to be solved include (1) developing small contrivances to keep the battery chemicals in the spatial relationships necessary for effective reaction, (2) means to prevent the products of the main battery reaction from inhibiting later reaction and means of preventing side reactions from wasting the chemicals, and (3) designing the battery to better fit the space in the torpedo for energy storage.

Currently, pile-type battery constructions are being developed in which the anode of one cell directly contacts the cathode of the next, without intercellular spaces and connections, and with the complete battery in the form of a right circular cylinder. For best performance, a primary cell, which is not rechargeable, should be used since it is less bulky than a secondary cell, which is rechargeable. However, the inability to recharge the battery of a recovered torpedo is not a trivial disadvantage since torpedoes are regularly exercised.

Electric Motor

Batteries supply electricity for motors and the pair must be optimized together. The battery constitutes by far the greater bulk of the two, so more attention is paid to its development and preference is given to its needs in optimizing the combination.

The dc motors normally used with batteries are intrinsically less efficient than ac types. The latter can be used with batteries if their current is first rectified to ac, and solid state devices can be used to do so. The performance of an ac motor plus rectifier can be in the same hp/lb range as a dc motor alone, and so these combinations are being examined.

Heat Engine Propellants

Heat engines for torpedoes have received considerable attention recently. They are energized by chemical propellants which are reacted in a rocket-type combustor to produce high temperature products.

Drawing from space activities, a rocket-type solid propellant is now used to energize a torpedo reciprocating engine. The powerplant drives a small torpedo at satisfactory speeds to useful ranges because it exploits the high density and relative simplicity of a solid propellant.

A problem faced by this and similar powerplants, which expel gases from the engine and directly into the ocean, is that engine pressure-ratio, and therefore performance, decreases with depth. This degradation is made tolerable in this case by operating at a relatively high internal pressure. The problem of varying, on demand, the flow rate of the solid propellant in order to modulate the speed of the missile, proved **intrinsically** more difficult and a liquid monopropellant is being groomed as a replacement. This liquid is metered to a decomposition chamber where it produces hot gases.

Theoretically the most potent propellants are those in which the fuel is a metal, as aluminum, magnesium or lithium, since their combustion releases the most energy on a volume basis. In general, these fuels will react with an oxidizer carried within the torpedo, but higher performance is provided when "free" water from the environment is used as oxidizer--for the same reason that air-breathing missiles that react "free" air with carried-fuels have a higher performance than rockets which carry their oxidizer. The reaction products of metal fuels include solid oxides, which are not readily compatible with an engine. Storing and pumping metals into a combustion chamber and then achieving efficient chemical reaction are also difficult problem areas. These have received preliminary attention using molten metals or suspensions of finely divided metal particles in a liquid; however, no metal-fueled system has been qualified for a torpedo.

Whether or not all the reaction products of the propellant can condense to nongases on cooling in sea water is also important. If some permanent gases leave the engine exhaust and pass directly into the ocean, then the high pressure underwater lowers the engine pressure-ratio and performance, as previously mentioned. On the other hand, if all products can be condensed in an engine-exhaust chamber, the effluent can be pumped overboard with little power and the back pressure felt by the engine may be as low as the vapor pressure of the cooled and condensed products. Thus, development of specially formulated propellants whose products can be condensed in this manner holds considerable promise.

Heat Engines

Specialized heat-engine cycles have been suggested, and some developed, whose performances are largely unaffected by the high pressures underwater. Some depend on the properties of the propellant products, as indicated above, while others exchange the energy from the propellant products to the working medium of a closed thermodynamic-cycle engine. The latter procedure, in addition to being independent of depth, eliminates any incompatability problems between the powerplant and the propellant products, but it involves an extra pair of heat exchangers.

The characteristics of the mechanical powerplant also affect cost, efficiency, and usefulness. Studies are continuing to develop turbine wheels that are inexpensive and satisfactorily efficient under the low partial admission and changing pressure ratio conditions that often characterize torpedo powerplants. Turbines are generally more applicable to large torpedoes and reciprocating engines to small ones. In general, reciprocating engines can tolerate higher temperature working gases than can a turbine, but a turbine can accept slightly dirtier working gases. Very small reciprocating engines of the wobble plate or barrel type have been developed that put out the power necessary to propel a torpedo and still fit within the limited volume available.

Miscellaneous

The usefulness of a torpedo can be degraded by the properties of the chemicals it employs as energy source. For example, if the battery or propellant chemicals under accidental conditions can liberate toxic gases or explode, they will not be permitted aboard submarines or some surface ships. If the chemicals produce quantities of permanent gases that find their way into the torpedo's wake, the resultant bubbles can interfere with the torpedo's guidance and can leave a well-defined path for an enemy to follow back to the launch ship: these conditions may be **intolerable**. Finally, if **corrosive or abrasive** material must be removed from the torpedo powerplant between successive exercise runs, the added inconvenience and cost of doing so could eliminate the propulsion system.

Conclusions

The propulsion system of a torpedo comprises (1) a large volume for energy storage, (2) mechanical means to convert this energy to torque, and (3) a propeller-type thruster. Chemical energy is always used, whose theoretical minimum energy capacity

should be about $26 \text{ hp-hr}/\text{ft}^3$ for future torpedoes. The components of the propulsion system are integrated to provide highest kill probability of the weapon against surface ships and/or submarines. Here the effect of torpedo self noise is important and speeds are often programmed to prevent detection at sufficient range for the target to escape. The use of torpedoes to destroy enemy submarines is of increasing importance and certain heat engines can operate at great depth without loss of efficiency. Neither electrical or heat-engine powerplants have a clear-cut advantage. Better propellants for heat engines and batteries for electrical motors can provide improved performance. Heat engines and electrical motors, optimized for particular batteries and propellants, respectively, can be developed.

References

- ¹Bethell, P., "The Development of the Torpedo," Engineering, 403 (May 25, 1945); 442 (June 8, 1945); 4 (July 6, 1945); -- 41 (July 20, 1945); 301 (October 19, 1945); 365 (November 9, 1945); 529 (December 28, 1945); 73 (January 25, 1946); 121 (February 8, 1946); 169 (February 22, 1946); 242 (March 15, 1946)
- ²Norlin, F. E., "Evolution of the Torpedo," T. S. Consecutive No. 99, **Naval** Torpedo Station, Newport, **R. I.** (30 September 1946)
- ³Maxfield, F. A., "Torpedo Propulsion System," JARS, 166 (September 1949)
- ⁴Cohen, P., "The Automobile Torpedo," Sperry Engineering Review, 1 (September-October 1952)
- ⁵Brady, J. F., "Significant Environmental Differences Between Powerplants for Aerospace and Underwater Missiles," SAE paper 3496 (1961)
- ⁶Green, J. H., "Thermal Underwater Powerplants," NOTS TP 2870, Naval Ordnance Test Station, Pasadena, Calif. (November 1962)
- ⁷Greiner, L., "Selection of High Performing Propellants for Torpedoes," JARS 30, 1,161 (1960)
- ⁸Greiner, L., "Underwater Propulsion, State of the Art--1962," Astronautics 7, 126 (1962)
- ⁹Greiner, L., "Torpedo Propulsion-State of the Art," Undersea Technology (February 1965)

¹⁰Greiner, L., "Powerplants for Underwater Propulsion of Small Bodies," AIAA Symposium on Modern Developments in Marine Sciences, 55 (AIAA Los Angeles Section, 1966)

¹¹Adams, C. L., "New Navy Monopropellant Simplifies Torpedo Propulsion," SAE J, 61 (May 1967)

¹²White, W. D., "Torpedo Propellants and Powerplants," The Indian and Eastern Engineer (Bombay, India) 106, 137

¹³Sheets, H. E., "Underwater Propulsion," Astronautics, 71 (December 1961)

¹⁴Brady, J. F., "Underwater Propulsion," Proceedings of Symposium on Deep Submergence Propulsion and Marine Systems, 204 (AIAA Chicago Section, 1966)

¹⁵Brady, J. F., "Torpedo Propulsion--1964," Astronautics and Aeronautics, 50 (March 1965)

¹⁶Hoyt, W. J., "Hydrodynamic Drag Reduction," AIAA Symposium on Modern Developments in Marine Sciences, 37 (AIAA Los Angeles Section, 1966)

¹⁷Leary, F., "The **Antisub** Submarine," Space/Aeronautics, 52 (July 1966)

DESIGN OF UNDERSEA INSTRUMENTED MISSILES

J. M. Allison*-

North American Aviation, Inc.,

Columbus, Ohio

Abstract

Underwater instrumented missiles, either with present guidance or directly controlled from the launch ship, have been designed and used to collect oceanographic data. They are similar in size and weight to torpedoes and airborne missiles. Their subsystems may be designed from well-known principles in structures, guidance and control, aerodynamics and hydrodynamics, and propulsion of airborne and underwater vehicles. However, whether the underwater missile is to be used for military or for pure research purposes substantially affects both subsystem and system design. The selection of its propulsion subsystem can be made only after careful consideration of speed, depth, hull space available, and duration of run. Because of the small weight and volume of the payload (instruments), the hull is also so small that several kinds of propulsion--systems that have proved effective in larger manned underwater vehicles are of lesser usefulness in underwater missiles. A lithium hydride, stored-heat engine appears satisfactory for a military mission requiring high speed but short duration, and it is described. On the other hand, a battery-driven electrical motor was found satisfactory for a research mission operating at lower speeds for a longer duration, and it is also described.

Introduction

Design of underwater instrumented missiles has profited from related techniques developed for underwater manned vehicles and for torpedoes and aeronautical vehicles. This paper presents an analysis of design requirements and systems engineering procedures for military and nonmilitary unmanned underwater missiles, with special emphasis on propulsion

The author is indebted to the Applied Physics Laboratory, University of Washington, Seattle, Wash., for Figs. 7 and 8 and for description of the SPURV.

*Senior Technical Specialist, Missiles Engineering.

subsystems and their interfaces with other subsystems and with over-all performance.

Devices towed from surface vessels have proven satisfactory when used to collect, record, and/or transmit oceanographic data. Under some conditions, however, greater simplicity, ease of operations, and low cost can be achieved by the use of self-propelled, instrumented missiles. Much less development has been accomplished on such missiles than on manned underseas vehicles, and the two are often competitive with respect to acquisition of oceanographic data. However, the instrumented missile is much more economical to build and operate, because of reduced size of its hull and the absence of man as part of the payload.

Design Requirements

To be useful, an underwater instrumented missile must be able to collect oceanographic data and to record it internally and/or transmit it to a control point. At the end of its mission, it must be recovered by the launch ship, which also may control its trajectory.

Military Mission

As an example of a military, oceanographic mission, a combatant Naval ship may be required to obtain oceanographic data near the Task Force of which it is a part, without interfering with its primary assignment or increasing its vulnerability to submarine attack due to decreased speed. In such an application, the instrumented missile **must** be capable of launch and *recovery* while the mother (launch) ship maintains speed and heading.

Nonmilitary Mission

In a nonmilitary underwater mission, research data such as temperature, pressure, velocity of sound, and bottom relief measurements may be obtained. The missile is launched, recovered, and controlled by the mother ship. Comparison of nonmilitary with military design requirements follows:

- 1) The operating depth may be greater.
- 2) The trajectory may be less constrained, since the mother ship is not subject to attack and therefore can adapt its speed and course for optimum utilization of the missile's capabilities.

3) Duration of the mission will usually be Greater, but speeds may be slower.

4) The amount and kinds of data to be collected may be greater.

5) The desired precision **may** be greater.

6) Data processing may be more elaborate because the mother ship, presumably an oceanographic type, will be equipped for such operations.

7) Operation during heavy seas may not be mandatory, thus facilitating launch and recovery operations.

Design Procedures

Arrangement of Subsystems

The size and shape of an underwater, self-propelled, instrumented hull is determined by the volume, shape, and weight of its subsystems. If these are light but bulky, the inside dimensions of the hull must be made large to house them. If they are heavy and small, the outside dimensions of the hull must still be large enough to supply the required displacement. Nevertheless, ideally the size of the missile should be kept small. Thus, the internal and external volumes of the pressure hull should be just large enough to house the subsystems physically and still provide the desired small positive buoyancy for a given maximum depth.

All subsystems, including propulsion, must have shapes and weights that permit positioning each of them longitudinally and vertically within the vehicle so that the center of gravity (c.g.) of the vehicle is under and perhaps slightly abaft the center of buoyancy (c.b.). The locations of the c.g. and the c.b. determine the static longitudinal trim and the righting moment in roll of the missile. The line of propeller thrust, with respect to its moment about the c.g., should be located so as to reduce elevator trim drag for the predominant attitudes that the missile must assume in its planned trajectory. Expendable engine fuel should be located near the longitudinal c.g. so that the static trim will change as little as possible during a mission.

Design Disciplines:

--- The design of unmanned, underwater vehicles requires attention to **structures**, hydrodynamics, guidance and control,

and propulsion, all of which involve practices that may be taken from the better-developed, aeronautical fields, taking into account special considerations resulting from the water environment which affect design. Selection of an underwater propulsion system is especially restricted: as examples, the exhaust of open-cycle heat engines is opposed by the very great static pressure underwater, and underwater missile speeds are comparatively slow which makes high-speed jets less efficient than in space or air, where the speeds of jet and missile may be well matched.

Propulsion Interfaces

Propulsion is one of the bulkier and heavier subsystems, and it interfaces broadly with the other subsystems and with the assembled missile.

One propulsion design consideration is whether or not it is placed within the pressure hull. Structural weight can often be saved by installing it outside in a streamlined, faired, flooded section, particularly if its design already calls for heavy walls to resist other loads. Ideally, propulsion should have high performance for its weight and volume. It should contribute minimum drag, both internal (if ducts are used) and external (form drag). None of its components should present protuberances projecting beyond the hull contour line upon which recovery handling procedures may impose failure-producing loads. The performance of the propulsion system should not be appreciably affected by design depth.

Both the assembled missile and the propulsion subsystem must be compatible with shipboard operations with respect to equipment, skill level of personnel, and materials ordinarily carried in the ship's inventory. For example, replacing fast-burning, volatile, or corrosive fuels while the missile is aboard ship creates hazards that are unacceptable even in Naval ships, and avoiding these hazards is more important in nonmilitary vessels, where experience with such propellants is likely to be more limited.

Propulsion Types

The propulsion systems^{4,5} considered for underwater missiles are as follows:

1) Mechanical energy ('fly wheels, springs, weights). These are primarily applicable to low thrust or both low-thrust and short duration.

2) Stored thermal energy (molten salt or metals) used with a heat engine. These are easily serviced aboard ship, economical to operate, but have limited duration.

3) Chemical energy (combustible propellants). These are capable of high performance but are not applicable to low speeds and long durations; in addition, their servicing may be difficult.

4) Electrical energy (batteries). This is the most widely used propulsion system, and it will remain competitive as batteries are improved.

5) Electrical energy (wires from the mother ship to the vehicle). With more development, this may compete with more conventional methods.

6) Buoyancy changes^{1,2} (weighted vehicle launched downward which changes weight at depth and is then propelled upward by excess buoyancy). Considerable range can be achieved by sophisticated designs that use wings to glide and climb while expelling and taking on water as ballast.³

Examples of a Military and a Nonmilitary Missile Design

Designs of instrumented missiles for a military and a nonmilitary application may require somewhat different approaches, as illustrated below by specific examples.

Military

Requirements. Requirements for the mission used in the military example are the following:

1) The oceanographic data must be obtained without reducing the cruising speed of the mother ship, which launches and recovers the missile.

2) Pressure, temperature, and salinity in the local area at depths up to 5090 ft are required to be measured by the missile for use in accurately determining the local velocity of sound.

3) The missile system must be simple to operate, moderate in cost, and compatible with Naval shipboard operations.

Configuration. Tradeoffs of significant design parameters resulted in the configuration shown in Fig. 1.⁶ The 6061-aluminum-alloy, weldable hull is 19 in. in diameter and

114 in. long (6 diameters) with a cylindrical central section. Approximate volumes and weights are given in Table 1.

Table 1. Volumes and weights

Item	Volume, ft ³	Weight, lb
Body, ailerons, and tail	11.7 (external)	280
Subsystems		
Engine	3.3	200
Guidance and control	2.0	80
Detection-recovery	0.7	30
Instrumentation	1.5	50
Miscellaneous	0.5	10
Total		650

Positive buoyancy is about 15%, to aid detection of the vehicle at the end of its run and to permit it to rise in the event of propulsion malfunction. The length/diameter ratio of Ref. 6 is a good compromise for low friction and form drag. The hydrodynamic drag coefficient, C_D , based upon the maximum cross-sectional area of the hull, was estimated to be as small as 0.1130. This value was used in determining propulsion thrust required.

A tail shroud of 11-in. chord, and outer diameter the same as the hull diameter, was chosen to provide effective pitch and yaw control with small surface areas and a configuration with no part protruding beyond the central hull mold-line contour; the latter makes the vehicle less vulnerable to damage during recovery.

Instrumentation. Placement of the sensors is shown in Fig. 1. Water is forced by dynamic pressure through a duct whose inlet is at the stagnation point on the nose of the hull and whose dual outlets, located well back on the hull surface, provide symmetrical external flow. Salinity and thermistor sensors are mounted on the duct. This arrangement results in lower body drag, compared with probes mounted external to the hull. A pressure sensor attached to an internally closed

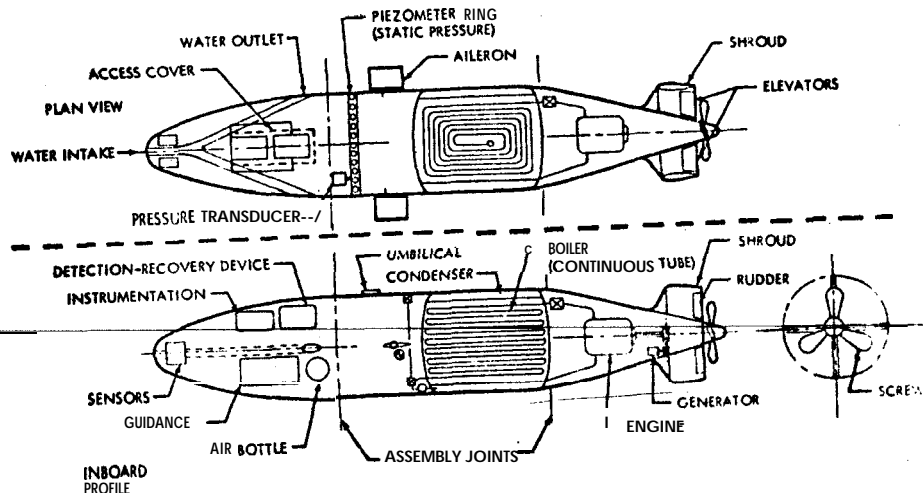


Fig. 1 Vehicle configuration of military missile.

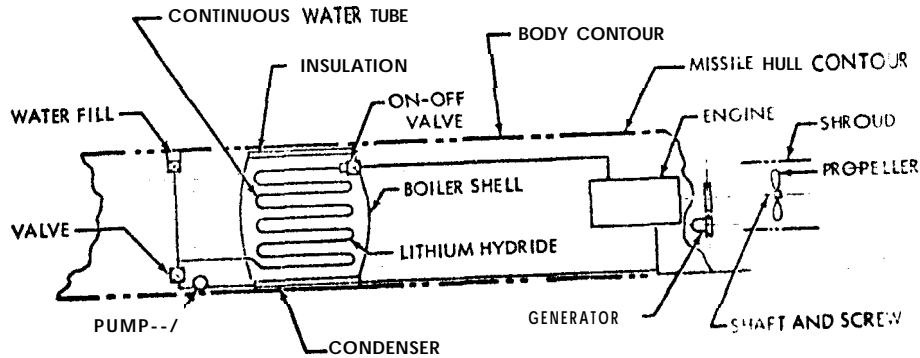


Fig. 2 Schematic diagram of Lithium Hydride stored-heat engine for military missile.

piezometer ring is located well aft, where interference with external flow is minimum. The sensing-recording system consists of expanded scale units and an oscillograph. Oscillograph records are removed through an access in the missile and processed aboard ship.

Propulsion. A closed heat-engine cycle propulsion system, unaffected by depth, was selected after considering fuel cells and batteries as alternatives. Fuel cells are too large for the short-duration mission, and batteries used in current torpedoes are too heavy.

The selected engine comprises a lithium hydride, stored-heat system that meets the requirements of horsepower and weight and has received sufficient design stud... A schematic is shown in Fig. 2. Lithium hydride, heated to the molten condition by the ship's electrical power before launch, provides enough stored heat for the duration of the mission. Cooling the melt from an initial temperature of about 1600°F , through its melting point of 1276°F , and then to 1000°F makes available about 2200 Btu/lb of fuel with a volume change from solid to liquid of $\frac{1}{3}$. A water-tube boiler located in the lithium hydride supplies steam to a Rankine-cycle engine, which converts linear piston motion into rotating shaft motion by a Wobble-plate drive. Six pounds of LiH per shaft horsepower (SHP) per hour are required, and a given charge should last for a number of heat cycles.

Figure 1 shows the longitudinal positioning of engine components within the hull. The boiler and condenser are just abaft midship, and the engine (the only other heavy item) is near the stern to keep the propeller shaft short. The weights of these components are offset by the moments produced by the instrumentation and recovery subsystems, which are well forward so that the c.g. of the assembled vehicle is near its midpoint. The propulsion subsystem occupies 3.3 ft^3 (about 30%) of the total internal volume of the hull. The underwater mission requires a 32 SHP engine for about 19 min, assuming 70% propeller efficiency. Based upon the reported data for developmental engines in the performance range, the engine will weigh about 220 lb. This includes 180 lb for the boiler, condenser, and lithium hydride, and 40 lb for the engine.

A single, continuous water tube boiler is supported from the boiler shell. A steam header is built in. An annular condenser surrounds this boiler, with insulation between the two. Heat rejection and condensation is accomplished by conduction to the sea water surrounding the hull. Approximately

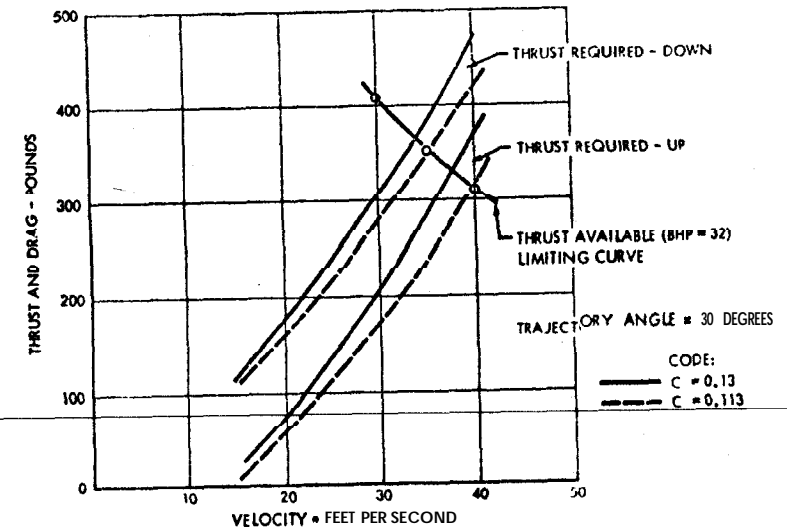


Fig. 3 Available thrust and drag vs velocity at two drag coefficients for military missile.

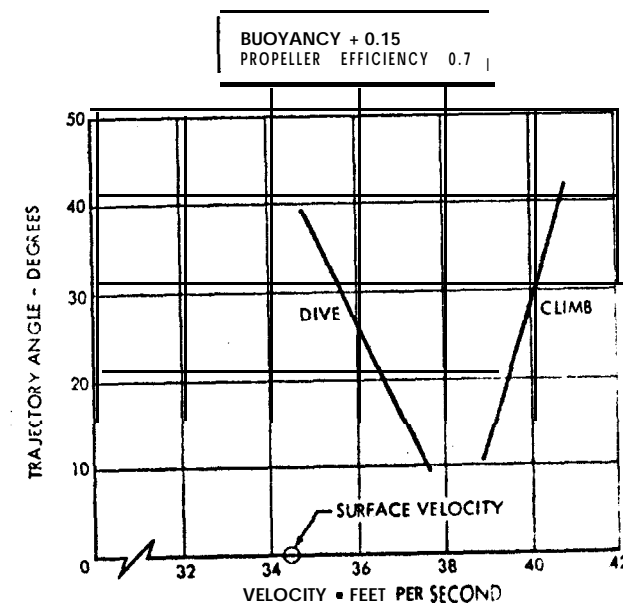


Fig. 4 Variation of velocities with dive and climb angles for military missile.

two pints of water are used in the engine. An electrically driven boiler feed pump is used, and the speed of the engine is regulated by a valve on its output side. A generator for instrumentation power may be driven off the propeller shaft.

Trajectory. To simplify the missile, a V-shaped, up-and-down trajectory was chosen. Various factors affect the capability of the missile to complete such a trajectory to the assumed maximum depth of 5000 ft and then surface ahead of the moving mother ship. The maximum down speed is affected by the decreased net thrust due to the positive buoyancy, and this effect increases with the trajectory angle measured from the horizontal. In Fig. 3, thrust and drag are plotted against velocity for a trajectory angle of 30° . Any point on the thrust-required curves above and to the right of the thrust-available curves is beyond the capability of the 32-SHP engine. Figure 4 shows, on an expanded scale, how velocity varies with up and down trajectory paths, assuming 15% positive buoyancy, constant 32 brake horsepower, 18.8 min run duration, and 70% propeller efficiency. At 20° angle, the velocity down is 26.5 fps, and velocity up is 39.4 fps.

Figure 5 shows the total down-range dispersion of the missile about its no-error point of surfacing. Shown on the curve is the 400-ft clearance point, which is approximately the minimum distance ahead of the ship necessary for recovery. The following guidance errors were assumed in this analysis: trajectory angle (down and up), $\pm 1^\circ$; vehicle speed (along trajectory), ± 0.5 knots; and depth error (at bottom of trajectory), ± 150 ft.

The trajectory angle errors include gyro processing, programming, and initial reference errors. When the maximum down-range dispersion is toward the oncoming ship, the clearance is the required minimum of 400 ft from the emergence point, which is 24,800 ft from the launch point.

The trajectory angle, both down and up, for surfacing ahead of a fast launch ship was 20° . As shown in Fig. 6, this is the greatest angle that would permit the vehicle to attain 5000-ft depth and still surface ahead of the ship.

Launch and Recovery. The missile is rail launched on the same heading as the mother ship from a cage on a structure that is retracted back to the deck of the ship after launch. 6 The launcher holds the missile in a ready position slightly below the surface of the water until the propulsion system is activated by remotely opening the steam valve to the engine through electrical control cables.

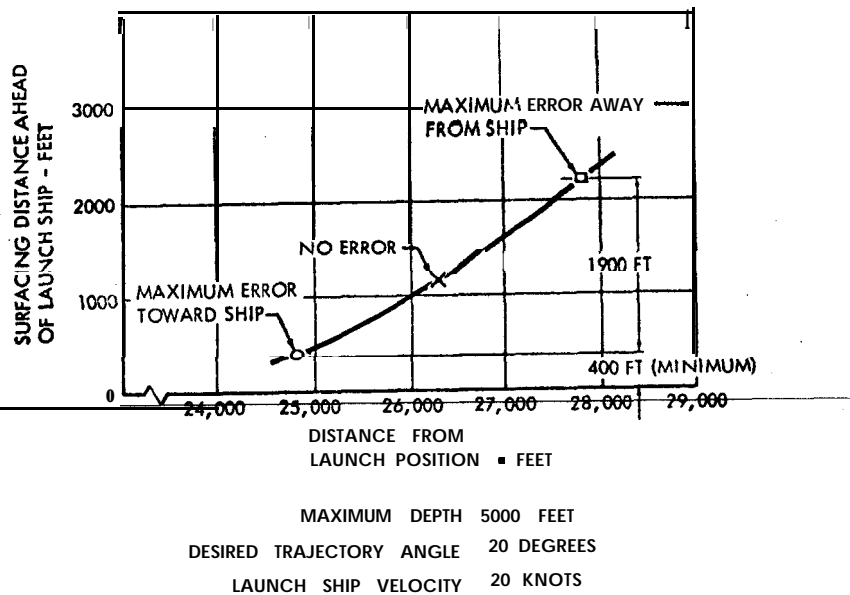


Fig. 5

Surfacing dispersion of military missile ahead of the moving launch-ship.

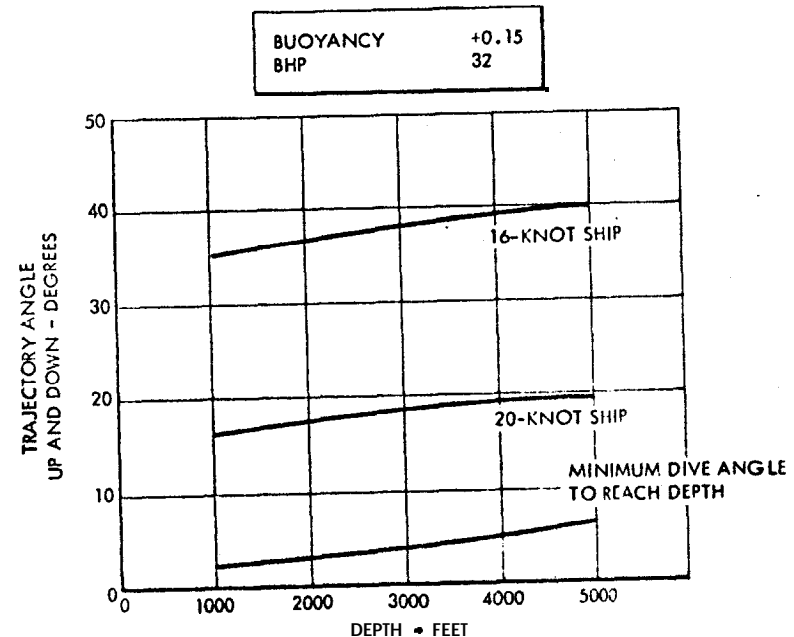


Fig. 6

Trajectory angles for military missile require: to surface ahead of 16- and 20- knot ships.

An empty folded balloon, packed in a water-tight compartment, is inflated with helium after a depth sensor triggers a valve when the missile surfaces. The inflated balloon is 5 ft in diameter and suspends a nylon cable attached to it by finger patches and a bridle cable. The balloon is easily detected by optical or radar means.

Recovery, the most difficult operation, particularly when the sea state is high, is beyond the scope of this paper. It appears feasible, using the launch structure equipped with a special arresting and capture device.

Nonmilitary

Requirements. Requirements for the mission used in the nonmilitary example are as follows:

- 1) The trajectory and attitude of the missile at depths to 12,000 ft and long durations must be controlled from the ship.
- 2) Pressure, temperature (using thermistors), sound velocity, turbulent velocity, and bottom topography data are required.
- 3) The missile system must be simple to operate, moderate in cost, and compatible with nonmilitary shipboard operations.

Configuration. A good example of an unmanned, underseas missile for oceanographic research is the SPURV (Self-Propelled Underwater Research Vehicle), developed by the Applied Physics Laboratory, University of Washington.⁷ Its performance is as follows: maximum operating depth, 12,000 ft; displacement, 1060 lb; net buoyancy, + 20 lb; and speed, 6 knots.

Figure 7 is a cutaway view of SPURV. Several instrumentation probes are mounted externally ahead of the nose and are protected against recovery damage by a shroud and a break-away, fail-safe device that allows the entire assembly to separate from the hull if excessive loads are encountered.

Approximate weights of components are shown in Table 2.

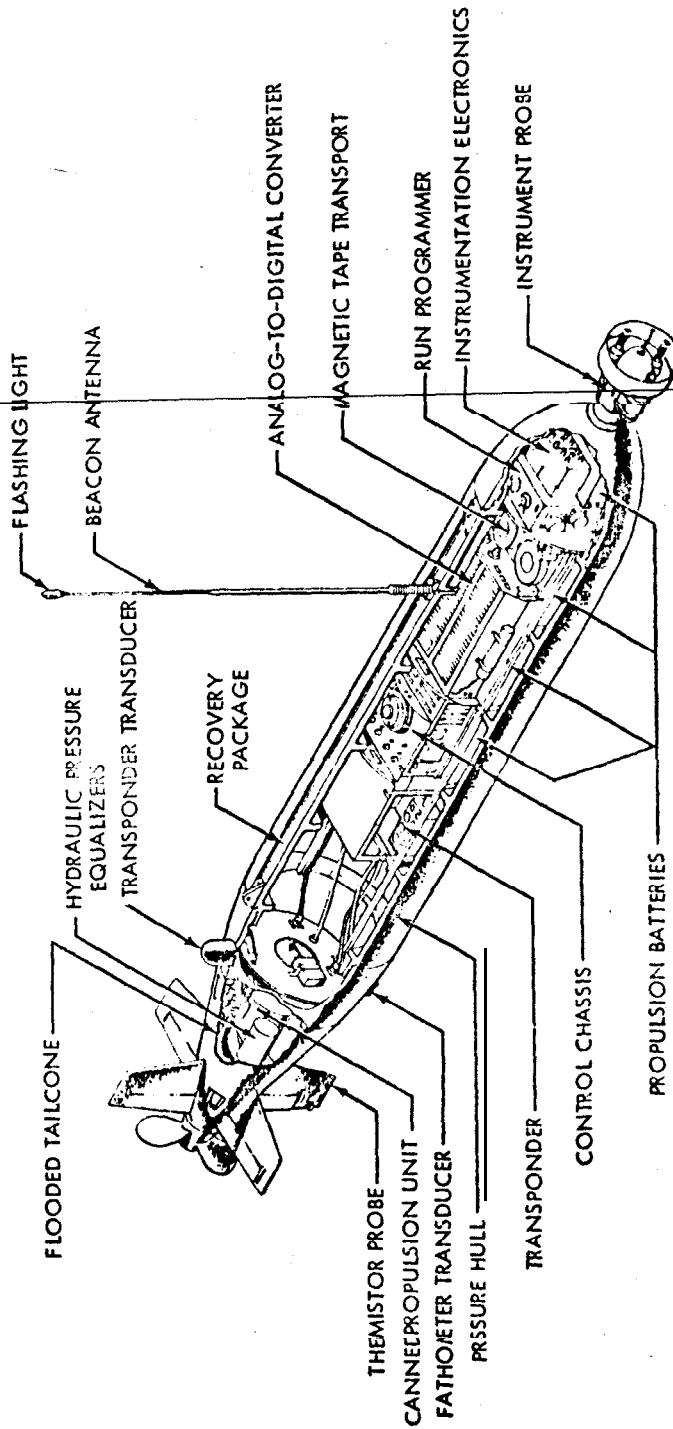


Fig. 7 Vehicle configuration of SPURV.

Table 2. Weights of components

Item	Weight (lb)
Hull	
Propulsion battery	
Instrumentation	
Auxiliary battery	15
Azimuth control	25
Depth control	15
Internal control	10
Acoustic track and command	15
Tail cone and control surfaces	20
Recovery system	10
Fathometer	5
Ballast	15
Miscellaneous	10
Total	1040

Instrumentation. The instrument payload of 40 lb includes, or will include, sensors for measuring temperatures, pressures, velocity of sound, conductivity, and velocity turbulence. Data are recorded internally, on tape, to the following precision: thermistors, 0.001° C; Gulton thermometer, 0.0005° C; sound velocity, 0.1 m/sec; and pressure, 0.1% of full scale.

Propulsion. Since duration is more important than high speed for this vehicle's mission, a battery-powered system is satisfactory for propulsion. It includes a 24-v d.c. motor modified from aircraft electrical systems, gear reduction unit, drive shaft, housing, propeller, motor enclosure can, and pressure equalization, all located outside the pressure hull in a flooded, faired tail cone. The motor delivers 1 HP at approximately 2000 rpm. Both motor and reduction gear are

exposed to the ambient water pressure and run in a fluid bath of Stoddard's cleaning solvent, whereas the drive shaft and shaft bearings operate in hydraulic oil. Equalization of pressure within the propulsion system is achieved by a flexible diaphragm as a fluid barrier and a compression spring that keep the internal pressure within about 2 psi above the ambient. Operation of the motor and drive train in a pressure-equalized system permits the use of low-pressure rotating propeller shaft seals that have low friction losses.

Trajectory. For trajectory control, an acoustic impulse is propagated from the ship, and three coplanar hydrophones on the ship receive the pulse returning from the missile. The three transit-time differences are used to compute the projection of the missile position on the plane of the hydrophones.

This position information is displayed and used primarily for navigation of the ship. A digital command link allows changes of the internal program of the missile during actual operations. This may change yaw (direction) and pitch (depth) to direct the missile on any trajectory within its limitations.

Launch and Recovery. Figure 8 shows the missile launcher, with vehicle attached, supported by a boom on the ship. Release is accomplished by pulling on the lanyard "J," in much the same way that a missile is launched from an aircraft bomb rack. The engine is started after launch by radio command from the ship.

Recovery consists of throwing a grappling hook at distances up to 40 ft across the vehicle, aft of the antenna, and catching the recovery guideline. The hook slides down the recovery line to engage a lifting sling on the vehicle. Acoustic tracking and command at ranges up to 15,000 ft enable the launch ship to control the surfacing distance from the ship just prior to recovery.

Development and Growth

Additional future applications of self-propelled unmanned vehicles include the following:

Military

1) Collection of oceanographic data over a given area in support of the ASWESPS (Anti-Submarine Warfare Entertainment Prediction System) program.

2) Surveying the floor of enemy harbors.

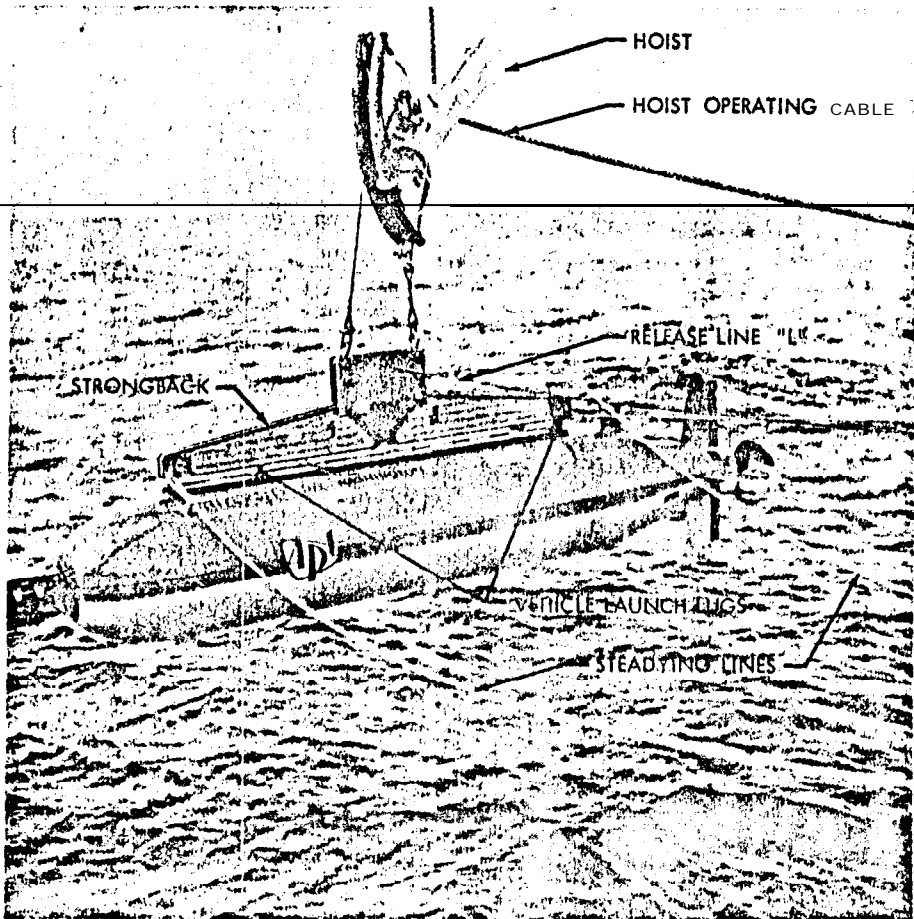


Fig. 8 Method of launching SPURV.

3) Simulation of submarines.

Nonmilitary

1) Recording of ambient **noise** and acoustic transmission signals.

2) Detection of salvagable sunken vessels.

3) Long-range exploration under ice shelves such as the Ross Ice Shelf in Antarctica.

Improvements in the precision of instruments will be made with further development, and eventually the **acoustic link** may have a **improved** to allow transmission of data between the vehicle and the ship.

Conclusions

1) The design of a propulsion **system** for an underwater instrumented **missile** must be carefully tailored to the mission. The selection of a propulsion type is controlled by the a) speed, depth, and duration of the trajectory; b) type of fuel and servicing required between runs; and c) amount of space **available** in the hull.

2) The effect upon efficiency of the water environment at depth makes "open" propulsion cycles relatively unattractive for the **missile** sizes considered.

3) The requirement for large ratios of horsepower and duration, per cubic foot of internal hull space, has limited the applicability of many types of propulsion **systems** which have proven satisfactory for other applications.

4) Hazards in servicing tend to make propulsion **systems** with exotic propellant fuels impracticable for underwater instrumented missiles.

5) Two types of propulsion, battery-driven electrical motor and **stored** heat, have proven satisfactory for specific designs.

6) Underwater instrumented **missiles** are suitable for missions that are competitive with those of towed devices and of **manned** underwater vehicles. Their **original** and operating costs are intermediate.

References

¹Marbury, F., Jr., "The vertical mobility of deep diving submarines," Ocean Sci. Ocean Eng. 2, 842-857 (1965).

²Leiss, W. J., Whitemarsh, D.C., and Wellington, T. C., "DIVEAR-An unmanned acoustic oceanographic research vehicle," Ocean Sci. Ocean Eng. 2, 864-875 (1965).

³Cannon, W. L., "Development of a self-propelled underwater vehicle for oceanographic data gathering," Marine Sciences Conference, Woods Hole, Mass. (September 11 - 15, 1961).

⁴Greiner, L., "Power plants for propulsion of small bodies underwater," AIAA Symposium on Modern Development in Marine Sciences (April 1966), pp. 55 - 84.

⁵Greiner, L., "State-of-the-art in torpedo propulsion," Underseas Technol. (February 1965).

⁶Allison, J. M., "Design and estimated performance of a self-propelled underwater vehicle for obtaining oceanographic data," AIAA Paper 64-303 (June 29 - July 3 1964).

⁷Murphy, S. R. and Nodland, W. E., "An unmanned research vehicle for use down to midocean depths," Ocean Sci. Ocean Eng. 2, 898-913 (1965).

⁸Henderson, J. E. and Murphy, S. R., "Operational experiences in the use of an unmanned vehicle in oceanographic research," AIAA Symposium on Modern Development in Marine Sciences (April 1966), pp. 153 - 168.

THEORETICAL PERFORMANCES WITH HYDROGEN-OXYGEN AS PROPELLANT OF PERFECT ROCKET, HEAT, AND FUEL-CELL ENGINES IN UNDERWATER MISSILES

Leonard Greiner*

United Technology Center, Sunnyvale, Calif.

Abstract

Theoretical specific impulse values are reported for stoichiometric hydrogen-oxygen when used in perfect rocket, heat, and fuel cell engines in underwater missiles traveling at 50 knots at sea level and 1,000-ft depths. Because completely efficient processes are assumed, ultimate performances of the engines are compared. Ordinary rockets are inefficient under water. However, when propellants such as hydrogen-oxygen are used, whose products condense to nongases on contacting water, specific impulse increases by a magnitude at great depth by passing the rocket exhaust through a jet ejector that educts sea water and exhausts a hot water jet rearward. Performance, then, improves with depth and the amount of water educted and is initially increased by introducing sea water into the combustion chamber, where it peaks at a ratio of water to propellant that condenses all gases to hot water in the chamber. Hydrogen-oxygen in perfect heat engine-propeller combinations has theoretical performances that are unaffected by depth and are a second magnitude greater than a sea-level rocket. These performances vary with the actual cycle, and it is necessary to condense the engine exhaust. Certain cyclic-continuous flow combinations of heat engines have the highest performance. Perfect fuel cell engines have the greatest potential performance at lowest internal temperatures of the engines considered.

Nomenclature

H-O = stoichiometric hydrogen-oxygen propellant, $H_2(g) + \frac{1}{2} O_2(g)$
Is = specific impulse per pound of fuel, lbf·sec/lbm

The writer wishes to acknowledge many useful discussions with Roger Dunlap of United Technology Center.

*Technical Assistant to Manager, Research and Advanced Technology Dept., presently with CETEC Corp., Mountain View, Calif.

h	= available energy from propellants, Btu/lb
F	= thrust, lbf
D	= drag, lbf
CD	= drag coefficient based on frontal area
A	= frontal area, ft ²
v	= velocity, f/s
?m	= density, lbm/ft ³
m	= flow rate, lbm/sec
p	= absolute pressure, psf
t	= temperature, °F
B	= $2g(p_3 - p_1)/\rho$
β	= m_o/m_r
s	= change in entropy over process, Btu/lb-°R
T	= absolute temperature, °R
q	= heat transferred at T_c to cyclic process per pound of fuel, Btu/lb
η_C	= Carnot efficiency, $(T_c - T_e)/T_c$
f	= change in free energy over process, Btu/lb

Subscripts

r298	= chemical reaction at room temperature
w	= water
a	= air
r	= rocket
c, o, 1, 2, 3, ∞	= see Fig. 1
F	= continuous flow process
c	= combustor or maximum
e	= engine exit
C	= Carnot cycle process
s	= sensible heat

Introduction

Unmanned missiles are likely to be used increasingly to supplement other means of underwater exploration,¹ and torpedoes with an explosive warhead are likely to remain the best means of combating enemy submarines.^{2,3} All such underwater missiles preferably should be capable of fairly great speeds, and their powerplants should evolve from a systematic optimization of all internal components of the missile in accomplishing the overall tasks. This paper, however, discusses only the performance theoretically achievable by selected "perfect" powerplants within high-speed underwater missiles when powered by a "universal" chemical propellant.

The capacity of a propellant to propel a missile depends on the propellant chemistry, the environment being traversed, the powerplant used to develop thrust, the speed of the missile, and the efficiencies within the powerplant. In this paper,

theoretical specific impulse values are determined for the universal propellant combination of stoichiometric hydrogen-oxygen in perfectly efficient rocket, heat, and fuel cell engines. Neglected are internal inefficiencies, component complexities, transient conditions, costs, sizes, etc. Trave 1 only at 50 knots and sea level and 100-ft depths is examined. The results directly compare only the ultimate performances of the powerplants, and ignore practical considerations.

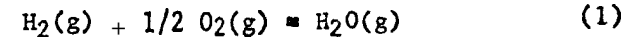
Study Conditions

Only a single fuel combination, a single missile velocity, and (where important) two operational depths are examined. The choices made and some of their rationale and consequences are discussed.

Propellant

Although this study does not assess the relative effectivenesses of propellants in underwater missiles,^{4,5} propellant properties and powerplant characteristics, including thermodynamic cycles, must be compatible. For example, certain heat engines require propellants whose products become nongases on contacting water in order to prevent performance degradation at depth. Also, the natures of rocket, heat, and fuel cell engines impose special requirements on the chemicals that can be used as energy sources. Because the familiar combination of hydrogen and oxygen in proportions that react to produce only water vapor fulfills all such requirements and its thermodynamic properties are well documented, it was selected for this analysis. Although other propellants will have different performances, their relative performances in the various powerplants should approximate that of stoichiometric hydrogen-oxygen, as long as they are similarly compatible with the engines.

The sole product of stoichiometric hydrogen-oxygen (hereafter designated H₂O) is water vapor, which is condensable to liquid water on contacting cold sea water. The propellant is assumed to be stored as gases, and the chemical change is



With products and reactants at standard conditions (1-atm pressure and 298°K or 77°F), 57.8 kcal of heat is liberated by each gram-mole of H₂O(g) formed, or $h_{r298} = 5770 \text{ Btu/lbm}$ of propellant. If this energy were completely converted to thrust in a missile traveling at 50 knots, the fuel specific impulse would be

$$I_s = \left(\frac{h_r 298}{50 \text{ knots}} \right) \left(\frac{777.6 \text{ ft-lbf}}{\text{Btu}} \right) \left(\frac{\text{knots}}{1.688 \text{ fps}} \right) = 9.21 \text{ hr}298$$

$$= (9.21)(5770) = 53,200 \text{ lbf-sec/lbm}$$
(2)

This ultimate performance is, of course, impossible.

Velocity

The thrust that pushes a missile is regulated by the velocity of the missile and of the **ejecta** that gives rise to thrust. The efficiency of the conversion of energy to thrust is **unity** when the absolute values of these two velocities are equal. Thrustors, as propeller types, that accelerate and then eject ambient fluid rearward can adapt to the latter's velocity to the missile's and so improve propulsive efficiency, whereas thrustors that accelerate expendable propellant mass, as rocket types, can adapt either not at all or only slightly. Moreover, the specific impulse of propeller-type thrustors [see Eq. (2)] is **inversely** proportional to missile velocity. For these reasons, the choice of representative missile velocity is important.

Underwater missiles include torpedoes and instrumented, unmanned, and self-propelled test bodies. Both should be capable of high speed. Torpedoes, for example must travel at a greater speed than their targets for a part of their mission. Instrumented missiles should be capable of rapidly examining a fairly extensive underwater volume, should quickly approach a search area (and then loiter, if necessary), and often must return to a moving ship. These circumstances call for high speeds; however, drag severely limits underwater speed.

The missile velocity used in this analysis was chosen to be comparable under water to that of a high-performance missile of the same dimensions in air, when identical thrusts are provided in both media. For a sustaining missile in either water or air,

$$F = D = C_D A v^2 \rho \quad (3)$$

and

$$v_w = v_a (C_D a \rho_a F_w / C_D w \rho_w A_w F_a) \quad (4)$$

Under assumed conditions, $A_a \equiv A_w$ and $F_w \equiv F_a$. Although drag coefficients in air and water are similar at equal velocities, the missile propelled by the same thrust in air will travel much faster, and $C_D a$ will be the greater. A simple iteration, using information from Ref. 3, shows $C_D a \approx 2C_D w$ at the

velocities involved. Substituting the previous information and **densities** into (4),

$$v_w = v_a (2)(0.075)/(64.0) = 0.0484 v_a \quad (5)$$

For $v_a = 1176$ knots (Mach 2) in sea-level air, the corresponding water velocity is 57 knots. This may represent a practical limit and the underwater missile will not always travel at maximum velocity; therefore, a compromise value of 50 knots is used.

A velocity of 50 knots is so low that it severely diminishes the propulsion efficiency of rocket-type thrustors because their exhaust velocities are much faster. Contrariwise, it has no effect on the **propulsive** efficiency of the perfect propeller-type thrustors considered in this analysis,

Operational Depth

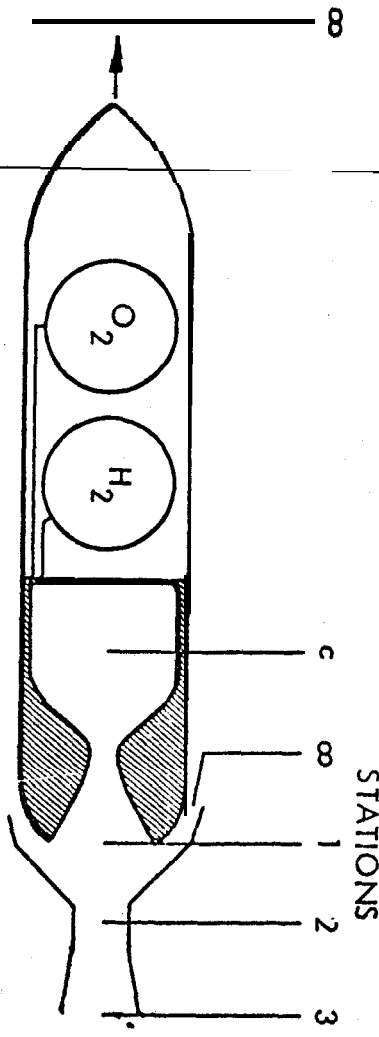
Depth underwater degrades performances of those heat engines which are affected by pressure ratio and which exhaust gases directly from the engine into the ocean. Such simple open-cycle systems, however, probably will not be used in missiles that operate at great depth, where other cycles are more appropriate, and are not considered here. On the other hand, the performances of simple rockets are badly degraded by external pressure, and specialized propellant formulations in water-augmented rockets actually have improved performances with depth. Thus, operational depth primarily affects the rocket thrustors of this study.

The probable initial need for instrumented underwater missiles will be in exploring the continental shelf to 100 fathoms, and torpedoes probably will not be required to descend much below 250 fathoms for some time to come. For these reasons, in those instances where depth affects performances values of sea level and 1,000 ft are taken.

Analysis

Theoretical fuel specific impulse values are examined for stoichiometric H-2O as the propellant in hypothetical rocket, heat, and fuel cell engines operating in underwater missiles whose velocity is 50 knots and whose depths are sea level and (where necessary) 1,000 ft. All internal efficiencies are taken as **unity**. The propulsive efficiency of the thruster, however, intrinsically depends on the relative velocities of the thrust-producing effluent and of the missile. Because these values are entirely set by operational conditions when a rocket-type powerplant is used, actual thrusts of rockets

Fig. 1 Schematic of hydrogen-oxygen underwater rocket with jet ejector.



are computed. On the other hand, the velocity of the thrust-producing effluent of propeller-type propulsors theoretically can be essentially matched to that of the missile. This results in unity propulsive efficiencies at very large water flow rates, which is assumed for such propulsors. In such an ideal case, all of the usable energy supplied by the propellant is converted to thrust, as shown in Appendix A.

Rocket

The specific impulse of H-O¹ in a simple rocket expanding from 1,000 psia to sea-level pressure is 370 lbf-sec/lbm. This value is independent of vehicle velocity and is reduced when the rocket operates under water against a greater ambient pressure, as is well known.

Because the H-O reaction products condense to liquid water on extreme cooling, its rocket performance under water can be improved and caused to increase with depth by passing its exhaust jet into an ejector that educts sea water and expels a water jet rearward⁹. Such a rocket system is indicated in Fig. 1. Referring to the figure, the rocket jet enters station 1, where it meets with a jet of sea water that has expanded from the high ambient pressure through the duct provided, which process converts the external pressure head largely to velocity. Water and rocket jet mix at constant pressure between stations 1 and 2, where the cool water condenses all the H-O water-vapor products to liquid water, and momenta addition of the two jets occurs. The pressure at stations 1 and 2 equals the vapor pressure of the thermally equilibrated water stream at station 2. This heated water stream diffuses from the low pressure at station 2 through the nozzle and exists at the pressure of the environment ($p_3 = p_\infty$). On doing so, a decrease in the water-steam velocity occurs, but it remains sufficient to provide thrust.

The specific impulse under water of the rocket of Fig. 1 is increased by the nozzle ejector for three reasons. First, the addition of the rocket-gas momentum to that of the educted water at stations 1 and 2 takes place with less loss of energy than had it occurred at stations 1 and ∞ (as with a simple rocket) because the water jet at station 1 has a velocity greater than at station ∞ because of acceleration on passing through the entry duct. Second, greater propulsive efficiency is achieved because the lower velocity of the water jet at station 3, compared to the rocket jet at station 1, better matches the missile velocity. And third, the rocket nozzle expansion process is more efficient and is unaffected by the ambient pressure because the pressure its nozzle "sees" is the

relatively low vapor pressure of the heated water at station 2 instead of the higher ambient pressure at station ∞ .

This technique can be used only when all of the rocket products become **nongases** on contacting water in the ejector. Otherwise, compression of gas between stations 2 and 3 would appreciably lower the velocity of the **stream**. Under most conditions, the exit momentum at station 3 would then be insufficient to counter the external pressure, and the ambient pressure would be felt in the duct so that the pressure at stations 1 and 2 would exceed the vapor pressure of the heated water. All of this would lower the velocity of the exit stream and little or no thrust would be produced. Because **only a hot water jet should exit the ejector (a slurry or a liquid solution is also satisfactory)**, the proper amount of sea water must be educted so that all of the rocket exhaust vapors are condensed and no sea water is vaporized.

The specific impulse for the *water augmented* rocket is computed as follows :

$$I_s = \frac{F}{gm_r} = \frac{\dot{m}_3 v_3 - \dot{m}_o v_o}{gm_r} \quad (6)$$

$$v_{rl} = I_{sr} g \quad (7)$$

for rocket expansion from P_c to P_1 , where P_1 is the vapor pressure of water at t_2 ,

$$V_{wl} = \left[2g(P_3 - P_1)/\rho_w + v_o^2 \right]^{\frac{1}{2}} = (B + v_o^2)^{\frac{1}{2}} \quad (8)$$

$$v_2 = \frac{v_{rl} \dot{m}_r + v_{wl} \dot{m}_o}{\dot{m}_r + \dot{m}_o} \quad (9)$$

and

$$v_3 = (v_2^2 - B)^{\frac{1}{2}} \quad (10)$$

Gathering (6-10) and noting $\beta = \dot{m}_c/\dot{m}_r$,

$$I_s = 1/g \left[(1+\beta) \left\{ \left[\frac{v_{rl} + \beta(v_o^2 + B)}{1+\beta} \right]^{\frac{1}{2}} - B \right\} - \beta v_o \right] \quad (11)$$

Also, as shown in Appendix B,

$$\lim_{\beta \rightarrow \infty} I_s = \frac{v_{rl} v_{wl} - B}{g v_o} \quad (12)$$

"Free" sea water can also be introduced into the combustion chamber of the H-O rocket. Doing so lowers the combustion temperature and increases the amount of working fluid; as a result, specific impulse peaks at an optimum ratio of water to fuel. Introduction of water may be accomplished¹⁰ by a

second ejector, called an injector, incorporated in a loop that leads from the combustor and then back to it, which is located so that sea water is educted into its interior. Injectors are commonly used to introduce feed water into commercial steam boilers, using steam from the boilers themselves to energize the process.¹¹ This pumping method is well suited to a rocket because it does not use rotating machinery. Moreover, theoretically it does not lower the enthalpy content of the rocket propellant because the enthalpy decrease in the motive steam is exactly matched by the enthalpy increase (in temperature and pressure) of the ingested water.

Table 1 includes theoretical specific impulse and internal information for augmented H-O rockets at 50 knots and at sea level and 1000-ft depth, with "free" water at 77°F (298°F) educted into the rocket exhaust and, in some cases, injected into the combustion chamber. Theoretical rocket-jet velocities, v_r , for use in Eqs. (11) and (12), were determined by established methods.^{6,8,12} When only gases are present, the pressure of the combustion chamber is taken as 1000 psia; however, when sufficient sea water is introduced to condense all vapors to water, the pressure then taken is the vapor pressure of water at the equilibrated temperature. The rocket:back pressure p_1 is the vapor pressure of the equilibrated water in the duct.

Results in the top section of Table 1 are for various amounts of water educted into the jet and none into the combustor. The I_s increases continuously as the sea water/fuel ratio goes to infinity, and it also increases with depth; at a 1000-ft depth and infinite ratio, an approximately four-fold increase in I_s is obtained over the simple rocket at sea level. Results in the lower sections of Table 1 are with water also injected into the combustor. At a water/fuel ratio of 12.76 and a 1000 psia pressure, all vapors in the combustor condense to water with this vapor pressure. At greater ratios, the vapor pressures of water in the combustor are the lower values given. Under these conditions, hot water, instead of water vapor, expands isentropically through the combustor nozzle to the lower pressure in the ejector. This is accompanied by partial vaporization of the water and a drop in enthalpy content, which give rise to high jet velocities, as with a normal rocket. As shown, the specific impulse, always a maximum at infinite water in the ejector, goes to a peak value as the ratio of water to fuel in the combustor increases, and it then decreases. This peak occurs with the rocket expanding hot water, and provides an I_s at a 1000-ft depth which is almost a magnitude greater than for the simple rocket at sea level.

Heat Engine

Underwater propulsion heat engines provide torque to drive propellers. In this paper, all processes in the powerplant, including the propeller thruster (see appendix A), are perfectly efficient; as a result, all of the thermodynamically available energy supplied by the propellant is converted to thrust. Performances of such engines are handicapped by the impossibility of converting heat completely to work and by limitations of the selected power cycle. Consequences of this are discussed next.

In a normal open-cycle powerplant, the propellant reaction products pass directly through the engine and are then exhausted;

the latter includes both mass and unused heat. In a normal closed-cycle powerplant, the propellant reaction products transfer heat energy at high temperature to the working medium of the engine which is in an enclosed loop. The reaction products are then exhausted directly to the environment, and the unusable energy of the cycle is rejected by heat exchange. Combinations of closed and open cycles are feasible, as are cycles that exploit special properties of the propellants. In all cases, the energy content and properties of the propellant products affect performance, as do the temperature, pressure, and other characteristics of the environment. The ocean provides an excellent sump for rejection of unusable heat at a low temperature, which predisposes high potential efficiency, but its high pressure degrades performance unless its effects are countered. Where possible, underwater powerplants exploit the good and avoid the bad characteristics of the environment.

Open or Modified-Open Cycle

Engine cycles resembling Rankine types are adaptable to underwater missile propulsion. In the simplest case, the propellant products pass (expand) through the engine and then go directly overboard. When such heat engines use propellants whose products are unalterably gaseous, a performance degradation occurs with depth, as with simple rockets, because of the decrease in pressure ratio. When the products are not permanent gases, as with H-O, the ocean water can be used to cool and condense them to nongases, which are then pumped overboard with minor power loss. The condensed products provide the pressure, as vapor pressure, which is felt by the engine, and this can be very low. Only those open cycles which exhaust into a condenser are considered in this paper.

Power cycles are first examined in which the exhaust gases from adiabatic combustion of H-O are isentropically expanded

Sea-water/propellant ratio		Combustor properties	Ejector properties	Specific impulse, 1bf-sec/lbm				
Over-all	In combustor	In eductor	Temp., °F	Press., psia	Temp., °F	Press., psia	At Sea Level	At 1000-ft depth
473.0	0	473. ^a	gas	6170	1000	212	14.7	370
66.0	0	49	gas	6170	1000	178	7.4	405
121.4	0	66	gas	6170	1000	133	2.5	439
280.0	0	121.8	gas	6170	1000	101	1.0	485
473.0	0	28	gas	6170	1000	91	0.7	500
8	0	473.	gas	6170	1000	77	0.5	529
280.0	2	278.0	gas	1392	1000	101	1.0	811
473.0	2	471	gas	1392	1000	91	0.7	832
8	2	8	gas	1392	1000	77	0.5	882*
280.0	12.8	267.0	liquid	544	1000	101	1.0	1121
473.0	12.8	460.0	liquid	544	1000	91	0.7	1135
1000	12.8	987.0	liquid	544	1000	77	0.5	1242
2000	12.8	1987.0	liquid	544	1000	77	0.5	2456
5000	12.8	4987.0	liquid	544	1000	77	0.5	n.c.
8	12.8	8	liquid	544	1000	77	0.5	3011
15.9	8	15.9	liquid	467	500	77	0.5	3077
17.0	8	17.0	liquid	445	400	77	0.5	3221
18.6	8	18.6	liquid	432	300	77	0.5	3421
21.0	8	21.0	liquid	382	200	77	0.5	3432
26.0	8	26.0	liquid	328	100	77	0.5	3448
32.3	8	32.3	liquid	281	50	77	0.5	3444
40.9	8	40.9	liquid	240	25	77	0.5	3410
49.6	8	49.6	liquid	14-	77	0.5	n.c.	3400
8	8	8	8	8	8	8	8	3221
n.c.	n.c.	n.c.	n.c.	n.c.	n.c.	n.c.	n.c.	3034

from 1000 psia to external pressures of 14.7 and 0.7 psia. The latter are obtainable at any underwater depth by cooling the engine exhaust products (with a contact ejector, often called a condensuctor, or a surface heat exchanger, etc.) to 212° and 91°F , respectively, where the products condense to liquid water with vapor pressures that are the values previously mentioned. The theoretically available^a energy can be conveniently determined from literature data⁴ on theoretical rocket specific impulse for the propellant under the same conditions, using the relation

$$h = 0.2067 I_{sr}^2 \quad (13)$$

together with Eq (2). Because sea water can be readily introduced into the combustion chamber of these engines (commonly)

by a mechanical pump geared to the output shaft) cycles are also examined with "free" water at 77°F added in this manner. This diluent water may also be the heated water of the exhaust condenser, instead of ocean water, and systems are examined using condenser water at 2120F . In either case, combustion temperatures are reduced and working gases augmented.

Neglecting the slight momenta of the incomin water perform-
ances are readily mputed from steam-table" data.'

Theoretical performances and other information on such systems are gathered in Table 2. They show that specific impulse values with simple heat engines can be a magnitude greater than those of the water-augmented rocket at depth, or about two magnitudes greater than the simple rocket at sea level. Highest performance is obtained when expansion is to very low pressures by extensively cooling the exhaust. The addition of water diluent to the combustor decreases specific impulse, and this decrement is not entirely regained by using the heated water from the condenser instead of cold sea water.

As indicated previously, operating the engine under conditions where the back pressure approaches the lowest value obtainable under environmental conditions greatly improves performance. Although doing so also lowers the temperature of the gas at the exit outlet (which is greater, of course, than that of the condenser water), this temperature theoretically can be lowered further. To utilize the total available energy-of the propellant, both temperature and pressure at the engine exhaust should be the minimum values possible.

The total available energy from a continuous flow process is¹³

$$h_F = (h_c - h_e) - T_e (s_c - s_e) \quad (14)$$

Table 2 Theoretical specific impulse and internal parameters of H₂-O₂ Rankine-type heat engines with condenser at engine exhaust in an underwater missile at 50 knots, at selected ratios of sea-water/propellant in the combustor

Ratio, Power dilant	Engine inlet condition Pressure, psia	Temp., °F	Pressure, psia	Engine outlet condition		Water temp. ^b , °F	Specific impulse, lb _f -sec/lb _m
				1 [∞]	0.7		
2	Open	1000	2363	14.7	0.7	212	25,180
3	Open	1000	1410	14.7	0.7	212	39,430
"Closed"	"Closed"	1000	2507	14.7	0.7	212	26,490
"Closed"	"Closed"	1000	1584	14.7	0.7	212	21,000
"Closed"	"Closed"	1000	1410	14.7	0.7	212	32,800
"Closed"	"Closed"	1000	1584	14.7	0.7	212	22,820

a Open cycle: diluent water of 77°F from ocean; "closed" cycle: diluent water at 212°F from condensor.

b After cooling in condensor.

Achieving h_f requires a more complex engine than a simple open-cycle type, such as suggested in Ref. 13. To compute h_f , obtainable low-energy properties of the gases at the engine exit must be assumed. The pressure here, as already shown, may be below the environment's; moreover, expansions can also occur to exit temperatures below the environment's: witness a carbon dioxide fire extinguisher. The exit conditions assumed for this analysis are 1-atm pressure and 212°F . These appear practical, although they are not minimum values, and they permit direct comparison with other powerplants with similar exit conditions, such as those in Table 2 with the same exit pressure and others to be discussed.

Results of calculations on the foregoing bases are listed in Table 3 at various ratios of diluent water to fuel. Comparing these with corresponding data from Table 2, a significant improvement is obtained when more of the temperature-enthalpy is utilized, but this improvement decreases with the water/fuel ratio.

Table 3 Theoretical specific impulse of $\text{H}_2\text{-O}_2$ continuous-flow engine with products entering at 1000 psia and exiting at 212°F and 1-1.7 psia in an underwater missile at 50 knots, at selected ratios of sea-water/propellant in the combustor

Ratio, water/fuel	Specific impulse, <u>1bf-sec/1bm</u>
0	45,200
2	35,600
3	32,600

Closed and Closed-Continuous-Flow Cycles

In the open-cycle process considered previously, the propellant products directly power the engine. By contrast, in a normal cyclic process, heat from the propellant products is transferred through an exchange surface to the working medium at the highest temperature of the cycle. By well-known events, this energy is then partially converted to work, the working medium made to return to the conditions at which it first received heat, and in between the unavailable heat is dumped to the environment. Also lost to the environment is the energy that heats the products of the chemical reaction from storage conditions to the highest cycle temperature,

because these products are normally discharged after exchanging their excess heat to the cycle medium. The latter loss increases with the maximum temperature of the cycle and opposes the increase in cycle efficiency with temperature. Thus, the maximum usable work is

$$h_C = q \left(\frac{T_c - T_e}{T_c} \right) = (h_{r298} - h_s) \left(\frac{T_c - T_e}{T_c} \right) \quad (15)$$

where h_s heats the products from storage temperature to T_c . A portion of h_s can be converted to work if the propellant gases are not immediately exhausted but instead used to energize a separate continuous-flow engine. This energy gain is given by (3), noting, however, that the discharge conditions for the ~~cyclic and the flow engines need not be the same~~.

Such theoretical performances are listed in Table 4 as a function of maximum temperature for a perfect cyclic process with propellant stored at 77°F , energy rejected at 77°F , and heat-source gases discharged at T_c , and then for a compound engine consisting of the same cycle plus a continuous-flow engine energized by the gases rejected by the cyclic process at T_c and with constant pressure of 14.7 psia and exit temperature of 212°F . As shown, the specific impulse of the simple cyclic process peaks when its maximum temperature is about 2000°F . Here, specific impulse values are comparable to those in Table 3 and exceed those, under similar conditions, in Table 2. The further addition of the continuous-flow powerplant provides even greater performances, which now increase continuously with temperature.

Fuel Cell

In a perfect underwater fuel cell powerplant, all of the electrical energy that can be produced by reaction of the propellants is used to power a no-loss electric motor that supplies all of its torque to a perfectly efficient propeller. Under such conditions, all of the electrical energy is converted to thrust. The latter is the free energy change of the isothermal chemical reaction (1) at T , where

$$f_T = h_T - T s_T \quad (16)$$

Equation (16) differs from (14) in that the changes involved in the former are for an isothermal chemical reaction, whereas those for the latter are for the products of the chemical reaction between entry and exit temperatures and pressures for the powerplant. Also, T_e of (14) is the sump temperature, which is low and constant; whereas T of (16) is the reaction temperature, which is variable. Primarily as a result of the

latter, f_T decreases with temperature. The product T_{ST} is energy that is not available to the electrical process and appears as heat. In the case of H₂-O₂, it is more than sufficient to warm the reactants from storage temperature to T .

Performance values and internal energies computed at various temperatures for the fuel cell with data from Ref. 8 are assembled in Table 5. For comparison with previous computations, reaction is at a constant 14.7 psia. Apparently, these electrical systems provide the highest theoretical specific impulse of the systems examined and do so at the lowest temperatures.

Table 4 Theoretical specific impulse and internal energies of H₂-O₂ Carnot-cycle engine (C) and Carnot-cycle plus continuous-flow engine (F) in an underwater missile at 50 knots at various maximum temperatures^a

T_c , °C, °F	n_s ,	q_1 ,	η_C ,	h_C ,	h_F' ,	h_{C+F} ,	I_s 1bf-sec/1bm
	Btu/lb	Btu/b		Btu/lb	Btu/lb	Btu/lb	
441	165	5610	0.400	2250	12	2260	20,700 20,800
621	251	5530	0.500	2770	40	2810	25,500 25,800
801	339	5440	0.571	3110	77	3180	28,600 29,300
999	430	5350	0.625	3340	123	3460	30,800 31,900
1161	524	5260	0.667	3500	176	3680	32,300 33,900
1340	621	5160	0.700	3610	246	3860	33,200 35,500
1521	721	5060	0.729	3690	299	3990	34,000 36,700
1701	724	4960	0.750	3720	369	4090	34,200 37,600
1881	930	4850	0.767	3720	443	4160	34,300 38,300
2061	1040	4740	0.786	3730	525	4260	34,300 39,200
2205	1150	4630	0.800	3700	604	4300	34,100 39,700
2421	1260	4520	0.812	3660	686	4350	33,700 40,000
2601	1380	4400	0.823	3620	780	4400	33,400 40,500

Carnot cycle: sump temperature = 77°F; continuous flow: pressure constant at 14.7 psia, gas exits at 212°F.

Table 5 Theoretical specific impulse and internal energy of H₂-O₂ fuel-cell engine in an underwater missile at 50 knots, at various constant temperatures

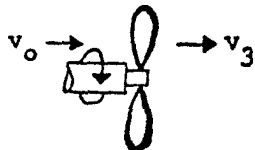
T_c , °C, °F	f_T , Btu/lb	I_s , 1bf-sec/1bm
259	5350	49,300
441	5240	48,200
621	5120	47,100
801	4990	46,000
999	4860	44,800
1161	4740	43,600
1341	4600	42,400
1521	4470	41,200
1701	4340	39,900
1881	4260	38,700
2061	4070	37,400
2205	3930	36,200
2421	3790	34,900
2601	3650	33,700

Concluding Remarks

Underwater missiles can be effectively propelled by rocket, heat, and fuel cell engines energized by chemical **propellants** whose exhaust products are **condensable** to **nongases** on cooling with sea water. Then, rocket systems can develop specific impulse values that improve with depth and approach a magnitude increase in performance over a simple rocket at sea level, if the rocket jet energizes a jet ejector that **educts** sea water and emits a stream of water rearward. The same propellant in a heat or a fuel cell engine which provides torque to a propeller can produce more than a second magnitude increase in performance over a simple sea level rocket. The fuel cell system has the best performance at low temperatures, but not dramatically better than the best heat engine at moderate temperature.

The preceding conclusions are based on theoretical analyses of perfectly efficient powerplants and do not consider practical problems that could change the relative ratings in actual situations. Moreover, the few types of powerplants in each class which were analyzed do not include all that are conceivable: a real possibility exists that ingenious new concepts will make all the system types approach one another in theoretical performance.

Appendix A: Conversion of propellant **energy** to thrust in perfect propeller type powerplant with infinite propeller flow



$$gT = \dot{m}_w (v_3 - v_o)$$

In perfect powerplants (neglecting conversion factors):

$$v_3 = \left[v_o^2 + (2h/\dot{m}_w) \right]^{\frac{1}{2}}$$

$$gT = \dot{m}_w \left\{ \left[v_o^2 + (2h/\dot{m}_w) \right]^{\frac{1}{2}} - v_o \right\} = \dot{m}_w v_o \left\{ [1 + (2h/\dot{m}_w v_o^2)]^{\frac{1}{2}} - 1 \right\}$$

Now,

$$(1 + 2h/\dot{m}_w v_o^2)^{\frac{1}{2}} = 1 + h/\dot{m}_w v_o^2 + \text{terms in } 1/\dot{m}_w^n, n > 1$$

Therefore,

$$\lim_{\dot{m}_w \rightarrow \infty} gT = \dot{m}_w v_o \left[1 + h/\dot{m}_w v_o^2 - 1 \right] = h/v_o$$

Appendix B: Limit of Is of water augmented rocket when β approaches ∞

$$\begin{aligned} gI_s &= (1 + \beta) \left\{ \left[\frac{v_{r1} + \beta (v_o^2 + B)^{\frac{1}{2}}}{1 + \beta} \right]^2 - B \right\}^{\frac{1}{2}} - \beta v_o \\ &= \left\{ \left[v_{r1} + \beta (v_o^2 + B)^{\frac{1}{2}} \right]^2 - (1 + \beta)^2 B \right\}^{\frac{1}{2}} - \beta v_o \\ &= \frac{v_{r1}^2 + 2v_{r1}\beta(v_o^2 + B)^{\frac{1}{2}} + \beta^2(v_o^2 + B)}{1 + \beta} - (1 + 2\beta + \beta^2)v_o \\ &\quad - \beta v_o \\ &= \left[v_{r1}^2 + 2v_{r1}\beta(v_o^2 + B)^{\frac{1}{2}} + \beta^2 v_o^2 + \beta^2 B - B - 2\beta^2 - \right. \\ &\quad \left. \beta^2 B^{\frac{1}{2}} \right] - \beta v_o \end{aligned} \quad (B1)$$

Cancelling terms and eliminating terms not containing β , which become relatively small as $\beta \rightarrow \infty$,

$$\begin{aligned} \lim_{\beta \rightarrow \infty} gI_s &= \left[2v_{r1}\beta(v_o^2 + B)^{\frac{1}{2}} + \beta^2 v_o^2 - 2\beta B \right]^{\frac{1}{2}} - \beta v_o \\ &= \left\{ \beta^2 v_o^2 + 2\beta \left[v_{r1}(v_o^2 + B)^{\frac{1}{2}} - B \right] \right\}^{\frac{1}{2}} - \beta v_o \\ &= \beta v_o \left\{ 1 + (2/\beta v_o^2) \left[v_{r1}(v_o^2 + B)^{\frac{1}{2}} - B \right] \right\}^{\frac{1}{2}} - \beta v_o \\ &\quad \text{Expanding} \\ &= \beta v_o \left\{ 1 + \left(\frac{1}{2} \right) \left(2/\beta v_o^2 \right) v_{r1} (v_o^2 + B)^{\frac{1}{2}} - B \right\} + \text{terms in } \\ &\quad 1/\beta^n, n > 1 \left. \right\} - \beta v_o \\ &= \beta v_o + (1/v_o) \left[v_{r1}(v_o^2 + B)^{\frac{1}{2}} - B \right] - \beta v_o \end{aligned}$$

Therefore,

$$\lim_{\beta \rightarrow \infty} gI_s = (v_{r1}v_{wl} + B)/v_o \quad (B2)$$

References

¹ Groves, D., "Mini subs," Naval Eng. J. 79, no. 2, 249-255 (April 1967).

² Brady, J. F., "Torpedo propulsion-1964," Astronaut. Aeronaut., 50-54 (March 1965).

³ Greiner, L., "State-of-the-art in torpedo propulsion," Undersea Technol. (February 1965).

⁴ Greiner, L., "Selection of high-performance propellants for torpedoes," ARS J. 30, 1161 (1960).

⁵ Greiner, L., "Torpedo propellants" (published elsewhere in this volume).

⁶ Stull, D. R., JANAF Interim Thermochemical Tables (The Dow Chemical Co., Midland, Mich., December 1960).

⁷ Leary, F., "The Anti-sub submarine," Space/Aeronaut., 52-66 (July 1966).

^a Muehler, J. R. and Greiner, L., "Estimation of performance factors for rocket propellants," Texaco Inc. (1962).

⁹ Gongwer, C. A., "Hydroductor," U. S. Patent 3,079,753 (March 5, 1963).

¹⁰ Gongwer, C. A., "Jet propulsion device for operation submerged in water," U. S. Patent 2,971,325 (February 1961).

¹¹ Badger, W. L. and McCabe, W. L., Elements of Chemical Engineering (McGraw-Hill Book Co., Inc, New York, 1936), 2nd ed., pp. 86-87.

¹² Keenan, J. H. and Keyes, F. G., The thermodynamic Properties of Steam (John Wiley & Sons, Inc., New York, 1936).

¹³ Keenan, J. H., "A steam chart for second-law analysis," Mech. Eng., 195-204 (March 1932).

¹⁴ Sutton, G. P., Rocket Propulsion Elements (John Wiley & Sons, New York, 1956), 2nd ed., p. 375.

UNDERWATER MISSILE PROPULSORS

-- A METHOD TO DESIGN PUMPJETS

R. E. Henderson,* J. F. McMahon,+ and G. F. Wislicenus#

Pennsylvania State University, University Park, Pa.

Abstract

conventional propeller rotating within a shroud. The shroud permits the flow through the rotor to be controlled more or less independently of vehicle velocity. A **pumpjet** can be designed with better cavitation characteristics than an open propeller or, alternatively, smaller in **size** to **reduce** over-all weights. The **pumpjet** may be engineered from knowledge **and** experience with axial-flow compressors and pumps. The meridional flow within the shroud is assumed to be axially symmetrical, and the flow through the vane system to **be generally** cylindrical. Although axial-compressor data can be used in designing the blade profiles for air compressors are not directly suitable for hydrodynamic propulsors because of cavitation requirements. A quasi-one-dimensional method is instead described which uses compressor data but still meets cavitation requirements.

Nomenclature

A_f	= frontal area of propelled vehicle, ft^2
a	= area, ft^2
C_D	= drag coefficient of propelled vehicle $\text{drag}/(1/2\rho V_0^2 A_f)$
C_L	= shroud lift coefficient
C_{L_∞}	= blade lift coefficient based on average relative velocity

*Assistant Professor of Engineering Research, Ordnance Research Laboratory.

+Research Assistant, Ordnance Research Laboratory.

#Head, Department of Aerospace Engineering, and Director, Garfield Thomas Water Tunnel, Ordnance Research Laboratory.

C_{L_2}	■ blade lift coefficient based on unit relative velocity
C_m	■ mass flow coefficient = mass flow rate/ $(1/2\rho V_o^2 A_f)$
C_Q	■ torque coefficient = torque/ $(1/2\rho V_o^2 A_f d_o)$
C_T	■ thrust coefficient = thrust/ $(1/2\rho V_o^2 A_f)$
D	■ drag of propelled vehicle, lb
d_o	■ maximum diameter of propelled vehicle, ft
F	■ thrust, lb
g	■ dimensional constant = 32.2 ft-lbm/lb-sec²
h	■ submergence depth, ft
H	■ $\eta_H H_R$
H_R	■ rotor head = ft-lb/lbm
H_{R_o}	■ dimensionless rotor head = $H_R / (V_o^2 / 2g)$
H'_R	■ incremental rotor head = ft-lb/lbm
H_{SV}	■ total inlet head = ft-lb/lbm
J	■ advance ratio = V_o / nd_o
L	■ length of propelled vehicle, ft
l	■ shroud length, ft
a	■ blade chord length, ft
l_a	■ axial blade chord, ft
m	■ mass flow ratio, slugs/sec
m_0	■ dimensionless flow rate = $m / (\pi / 4 \rho V_o^2 d_o^2)$
n	■ rotational speed, rps (unless otherwise stated)
n	■ coordinate normal to streamline, ft
Δn	■ offset between mean streamline and camber line measured perpendicular to blade chord, ft

Δn_1	■ Δn for NACA 65-series blade operating at $CL_\infty = 1.0$
n_S	■ specific speed [see Equation (15)]
n_p	■ propulsor specific speed [see Equation (18)]
Δp	■ difference between blade pressure face and suction face pressure at the same axial position, psf
p_0	■ freestream static pressure, psf
p_{cr}	■ freestream static pressure at which cavitation appears, psf
p_v	■ vapor pressure of water, psf
P	■ power, ft-lb/sec
Q	■ volume flow rate, cfs
R	■ radial distance from axis of rotation, ft
r	■ streamline radius of curvature, ft
S	■ suction specific speed [see Equation (16)]
s	■ coordinate along streamline, ft
t	■ circumferential blade spacing, ft
U	■ peripheral speed, fps
V	■ velocity, fps
V_a	■ axial component of velocity, fps
V_m	■ meridional component of velocity, fps
V_u	■ circumferential component of velocity, fps
V_0	■ reference velocity, i.e., forward velocity of propelled vehicle, fps
w	■ relative velocity, fps
w_∞	■ vectorial average of relative velocity between inlet and exit of blade, fps
Y	■ coordinate normal to surface, ft

a	= angle of attack
b	= blade stagger angle from axial direction
c	= defined in Fig. 16
d	= vorticity, 1/sec
e	= hydraulic efficiency
f	= Propulsive efficiency
g	= ram efficiency
h	= circumferential direction

i	= fluid density, slugs/ft ³
j	= cavitation index
k	= circumferential blade thickness, ft

Subscripts

- 1 = upstream of vehicle where the static pressure is equal to the freestream static pressure far ahead of the propelled vehicle
- 2 = rotor inlet
- 3 = rotor exit
- 4 = downstream of vehicle where the static pressure is equal to the freestream static pressure far ahead of the propelled vehicle

A. Introduction

A **pumpjet** is a rotating hydrodynamic propulsor operating in a close-fitting casing or shroud. It is the hydraulic counterpart of the ducted-fan aircraft engine. The principal difference between **pumpjet** and propeller is that the flow stream through the former departs from the "natural" or **freestream** surface, as indicated in **Fig. 1**.

An original object of the **pumpjet** was to improve cavitation resistance beyond that of an open propeller. By adding a shroud, the flow velocities through the **pumpjet** rotor can be reduced, and so its cavitation characteristics become essentially

independent of the velocity of the vehicle. However, as **Fig. 1** shows, if cavitation resistance of the blades is to be improved without reducing thrust and with the same rate of flow, the **pumpjet** rotor must be larger than the propeller. This increase in propulsor diameter and the addition of the shroud increase drag which, together lower propulsor efficiency.

The **pumpjet** can also reduce the weight of the propulsor by operating at increased rotational speeds, although this degrades cavitation characteristics. With a boundary-layer intake, this process is promising and analogous to aircraft-engine developments.

~~Although axial-flow aircraft compressors provide a background for the design of axial-flow pumpjets, the two differ in that 1) the pumpjet operates in a liquid, and hence velocity limits are dictated by cavitation, for although an analogy exists between problems when approaching sonic velocity in air and incipient cavitation in a liquid, means for advancing the two limits differ; and 2) the mechanical problems of blade designs are different because bending stresses dominate in the pumpjet, requiring relatively low aspect ratios, whereas centrifugal forces dominate in the air-handling engine (during steady operation), implying long slender blades. Additional background for pumpjet design is provided by extensive cavitation experience with marine propellers and hydrodynamic pumps.~~

The general design philosophy advanced in this report is based on a) extensive use of theoretical and experimental work of NACA and others with axial-flow air compressors; b) important modifications of these aerodynamic developments based on experience taken with marine propellers; and c) information from axial-flow pumps designed for high cavitation resistance.

B. General Relations for Flow and Force Action

Thrust

The general relations for the flow and force actions of a **pumpjet** are the same as for a propeller. Thrust is

$$F = \rho Q (\bar{V}_4 - \bar{V}_1) \quad (1)$$

where subscripts refer to stations 1 and 4 in **Fig. 1**, and pressures at these stations are assumed equal to the free-stream. Under steady self-propulsion, F equals the total drag of the propulsed craft. In coefficient or nondimensional

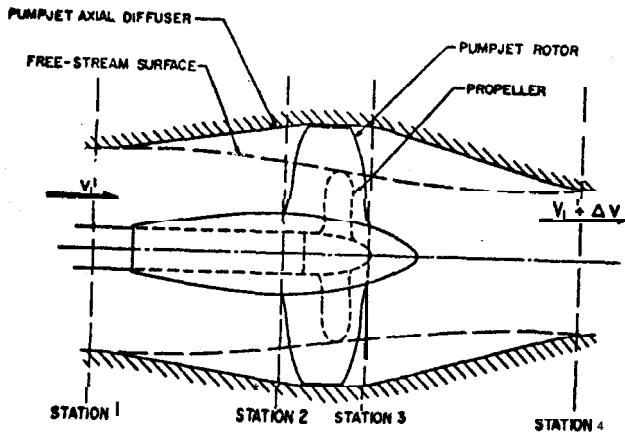


Fig. 1 Comparison of flows through **pumpjet** and **propeller**

Fig. 2 Comparison of typical inlet velocity diagrams for a marine propeller and a corresponding **pumpjet**

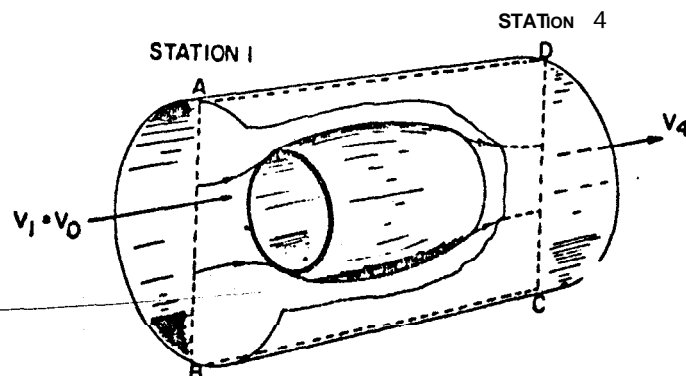
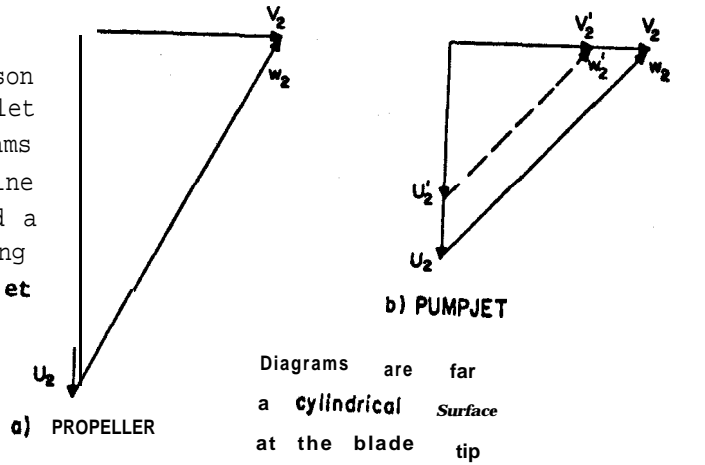


Fig. 3 Isolated pumpjet

form, Equation (1) becomes

$$C_T = C_m \left(\frac{\bar{V}_4}{V_0} - \frac{\bar{V}_1}{V_0} \right) \quad (2)$$

Propulsive Efficiency

The propulsive efficiency, or propulsive coefficient, is the ratio of the thrust work done by a propulsor moving at velocity V_0 to the energy required to increase the fluid velocity from V_1 to V_4 , assuming no frictional losses. For self-propulsion,

$$\eta_p = \frac{DV_0}{(1/2)\rho Q(\bar{V}_4^2 - \bar{V}_1^2)} \quad (3)$$

From Equation (1),

$$\eta_p = \left(\frac{\bar{V}_1}{V_0} + \frac{1}{2} \frac{\Delta V}{V_0} \right)^{-1} \quad (4)$$

where ΔV equals $(\bar{V}_4 - \bar{V}_1)$. In coefficient form,

$$\eta_p = \left(\frac{1}{2} \frac{C_D}{C_m} + \frac{\bar{V}_1}{V_0} \right)^{-1} \quad (5)$$

Hence, the higher the mass flow rate the higher the propulsive efficiency. However, the **pumpjet** adds additional drag that increases with the mass flow rate. So, an optimum flow rate exists for any given application.

Head, Torque, and Power Relations

According to Euler's turbomachinery equation, the input energy per unit mass (or head) along a streamline through the propulsor is

$$H_R = A (V_u U / g) \quad (6)$$

where Δ indicates the difference between the quantity ahead of and behind the rotor. In coefficient form,

$$H_{R_0}' = 2 \Delta [(V_u / V_0)(U / V_0)] \quad (7)$$

The total power required by the blades is

$$P = 2\pi\rho g \int V_m \cdot R \cdot H'_R \cdot dn \quad (8)$$

where n is the direction normal to V_m . If the head H'_R is constant along the entire span of the blade, Equation (7) reduces to

$$P = \rho g Q H'_R \quad (9)$$

If the blades can be designed with a constant head, or an averaged value used, the total energy input per unit mass through the propulsor is

$$H = \eta_H H_R = \frac{1}{2} \frac{\bar{V}_4^2 - \bar{V}_1^2}{g} \quad (10)$$

Consequently,

$$P = (1/2 \eta_H) \rho Q (\bar{V}_4^2 - \bar{V}_1^2) \quad (11)$$

or, in coefficient form,

$$\frac{2\pi}{J} C_Q = \frac{C_D}{\eta_H} \left[\frac{1}{2} \frac{C_D}{C_M} + \frac{\bar{V}_1}{V_0} \right] \quad (12)$$

By equating (6) and (10) [using Equation (1) and nondimensionalizing],

$$\Delta \left[\frac{V_u}{U} \frac{U^2}{V_0^2} \right] = \frac{1}{\eta_H} \frac{C_D}{C_M} \left[\frac{1}{2} \frac{C_D}{C_M} + \frac{\bar{V}_1}{V_0} \right] \quad (13)$$

c. Improvement of Cavitation Resistance of a Pumpjet

Flow through a propeller is essentially dictated by the forward velocity of the vehicle, but is greater than the velocity without the propeller, which pre-accelerates the flow. A shroud (Fig. 1) can reduce the velocity through the rotor, making its cavitation characteristics less dependent on the vehicle velocity.

Cavitation is a function of the flow velocity relative to its rotating blades. Figure 2a shows a typical inlet velocity diagram for a marine propeller. The tip velocity (U_2) is considerably higher than V_2 through the blades. To reduce the

velocity relative to the blades (w_2), U_2 could be reduced by lowering rotational speed. This improves the cavitation resistance of the propeller, or of the "corresponding pumpjet," which has the same torque, speed, and thrust characteristics.

After the peripheral velocity of the blades has been made comparable to the flow velocity through the blades, significant reductions in relative velocity can be realized only by reducing both the through-flow velocity and the peripheral blade velocity. With a shroud, V_2 can be reduced to a lower value (V_2'), as shown in Fig. 2b. If the peripheral velocity of the blades is reduced correspondingly from U_2 to U_2' , the relative velocity is reduced from w_2 to w_2' .

~~Because local pressure reductions at the rotor blades are proportional to w_2^2 , this substantially improves cavitation resistance. In fact, the hull of a vehicle can be made to cavitate before its propulsor blades' will.~~

In aircraft, retardations ahead of an inlet to a jet engine can be made quite high, and resultant "ram" efficiencies are fairly high at low Mach numbers. Since underwater vehicles operate at extremely low Mach numbers, substantial retardations ahead of a pumpjet can be obtained with good ram efficiencies. Reference 4--reports on inlet retardation or "prediffusion", where the incoming stream included the boundary layer of the propelled craft. A limited amount of prediffusion was possible even here with acceptable ram efficiencies.

D. Over-All Design of an Isolated Pumpjet

The principles of pumpjet design will be discussed first with reference to the isolated pumpjet of Fig. 3, which is similar to a jet-engine pod. The pumpjet engine is considered surrounded by a right cylinder control volume, coaxial TO it. The distance from the surface of this volume to the pumpjet large enough that the pressure along its surface equals the value at infinity. Because of axial symmetry, only the two-dimensional control area ABCD need be considered.

Equations (1-5) apply to inlet and discharge velocities at stations 1 and 4 and have no significance with respect to the interior.

Determination of Flow Rate

From Equation (5) the larger the rate of volume flow (Q) of the pumpjet, the better the propulsive efficiency; so, as the diameter is increased, less excess velocity is left in the w

The external-friction drag of the **pumpjet** must be subtracted in determining net thrust. As the frontal area of the **pumpjet** is increased, this drag increases. Figure 4 is a "carpet" plot of the propulsive efficiency of a jet engine or **pumpjet** [from Equation (4)] corrected for the drag of the shroud. The curves for increasing values of duct-loss coefficient k are separated from each other by a horizontal shift of the scale to the left proportional to k . The curve $k = 0$ is for zero drag on the shroud (i.e., an unshrouded propeller) and provides the propulsive coefficient of Equation (4). The numbers on the curves represent the portion of the kinetic energy of the incoming flow per unit mass of fluid passing through the **pumpjet** which is "lost" through drag on the shroud. If 10% is lost, the maximum propulsive efficiency drops to approximately 75%, and $\Delta V/V_1$ for optimum efficiency changes from 0 for the unshrouded propeller to 0.3 for a **pumpjet**. Actually, more than 10% is expected to be lost; accordingly, Fig. 4 indicates that maximum effective propulsive efficiency occurs at $\Delta V/V_1$ in excess of 0.3, presumably optimizing between 0.3 and 0.6. This ratio should be chosen as high as can be justified on efficiency considerations. From Equation (1), at higher values of $\Delta V/V_1$ less mass flow is required to produce a given thrust, and so the diameter of the **pumpjet** can be smaller.

Thus, from the standpoint of over-all efficiency, a **pumpjet** should be smaller than a corresponding propeller, in contrast to the opposite result for the same mass flow rate. This fact is useful as a starting point in estimating the diameter of a **pumpjet** which may be taken as about 15 or 20% less than that of the propeller it replaces.

Preliminary Shroud Design

After mass flow rate is determined, the shroud may be designed on the basis of one-dimensional flow continuity between it and the central body of the propulsor. The shape of this body is usually determined by a mechanical aspect of its mechanism. Stream surfaces of revolution may be drawn around the body for a mean flow velocity between the upstream surface and the body. The rate of volume flow is given by the preceding and Equation (1).

The line marked 1 on Fig. 5 represents a stream surface of revolution corresponding to the velocity inflow (\bar{V}_1) well ahead of the shroud. The line 1' represents the stream surface corresponding to a \bar{V}_1' somewhat lower than \bar{V}_1 . The surface marked 2 represents the stream surface for a \bar{V} at the inlet of the rotor sufficient to allow the required volume

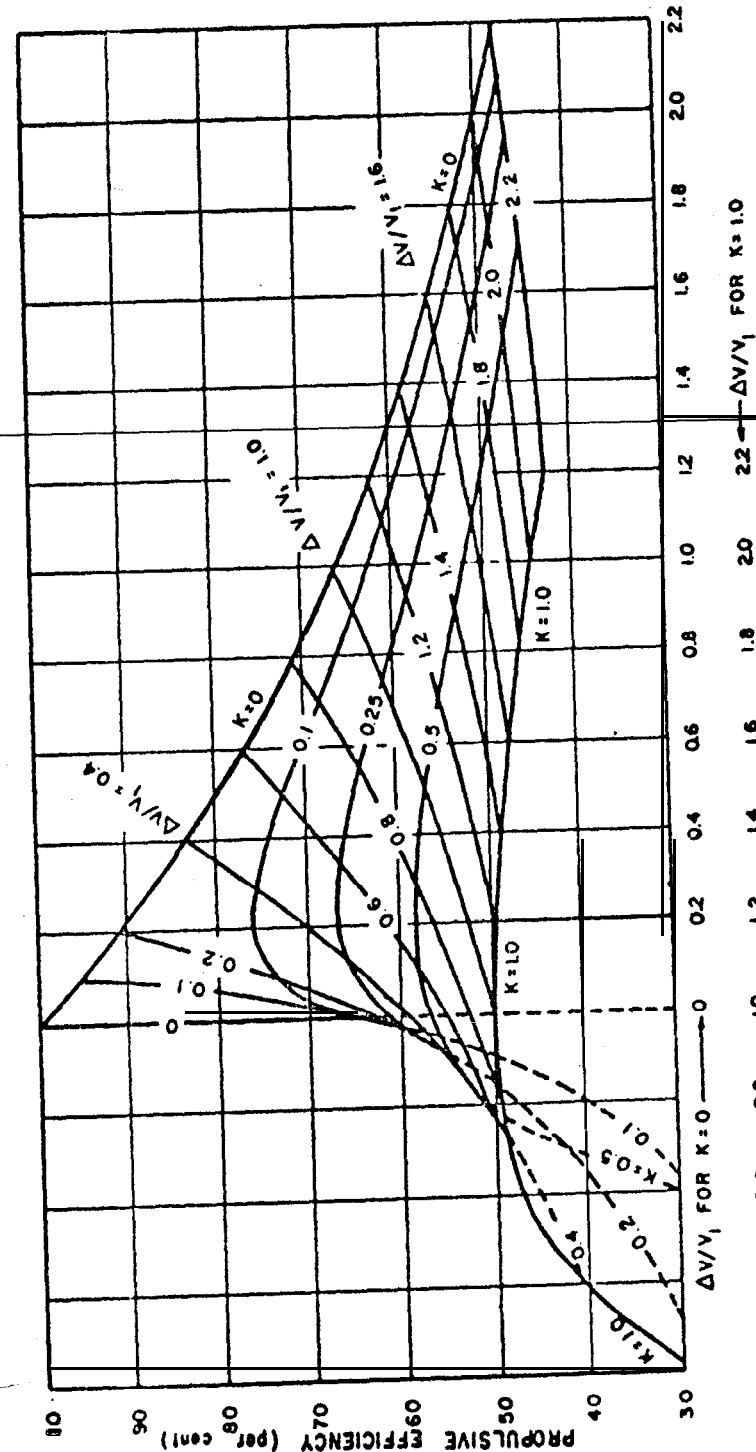


Fig. 4 Propulsive efficiency of a pumpjet for several values of duct-loss coefficient

flow (Q) to pass between it and the central body. Surfaces 3 and 4' are likewise defined from continuity considerations at the trailing edge of the rotor and at the shroud discharge, respectively.

A first estimate of the inside contour of the shroud may now be made. At the inlet, the surface must be slightly outside 1' and pass through 2 and 3 near the estimated inlet and discharge of the rotor (stations 2 and 3). It must end slightly outside 4' because of the slight "vena contracta" at the **discharge**.

As yet, no consideration has been given to the shroud length, i.e., the distance between 1' and 4'. An indication may be obtained from mechanical considerations and the location and general arrangement of the pumpjet; however, a hydrodynamic criterion will be discussed later. Figure 5 also shows a geometric flow criterion that involves the angle of attack between the flow that would exist without the shroud at its approximate geometric center, and a zero lift line between the trailing edge and the center of the shroud profile. This approximation of the zero lift direction is taken from plane flow considerations of airfoils. By analogy, the lift coefficient is roughly equal to one-tenth the angle of attack, measured (in degrees) from the zero lift direction. A lift coefficient of 1.5 is a limit obtainable without separation, and the angle α should not exceed 15° . Despite an apparent crudeness, this leads to practical designs.

Flow between the Shroud and the Central Body

The meridional flow between the central body and the shroud is not uniform because of its curvature. Figure 6 shows a graphical approximation for the velocity distribution, V_m , between the shroud and the central body, obtained from the radius of curvature of the boundaries at the outer and inner ends of the flow cross section. The equation that leads to this distribution in an irrotational fluid is

$$(\partial V_m / \partial n) + (V_m / r) = 0 \quad (14)$$

Starting with radii of curvature, r and r_1 , at the outer and inner boundaries, values for intermediate streamlines can be obtained by **iteration**.

E. Over-All Design Considerations for the Speed of Rotation

The following are part of the over-all design considerations

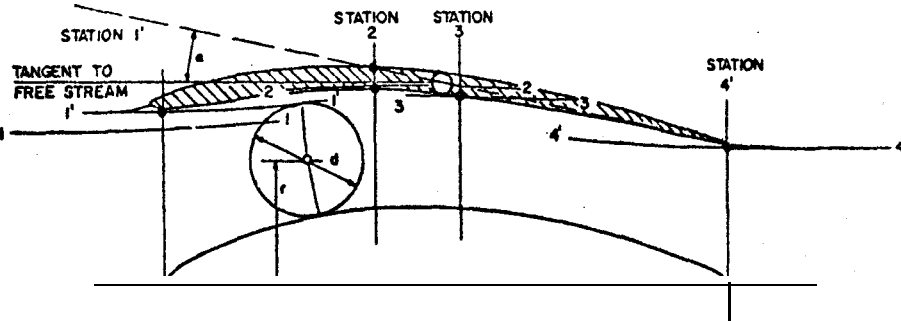


Fig. 5 Fluid flow through shroud with rotor not operating

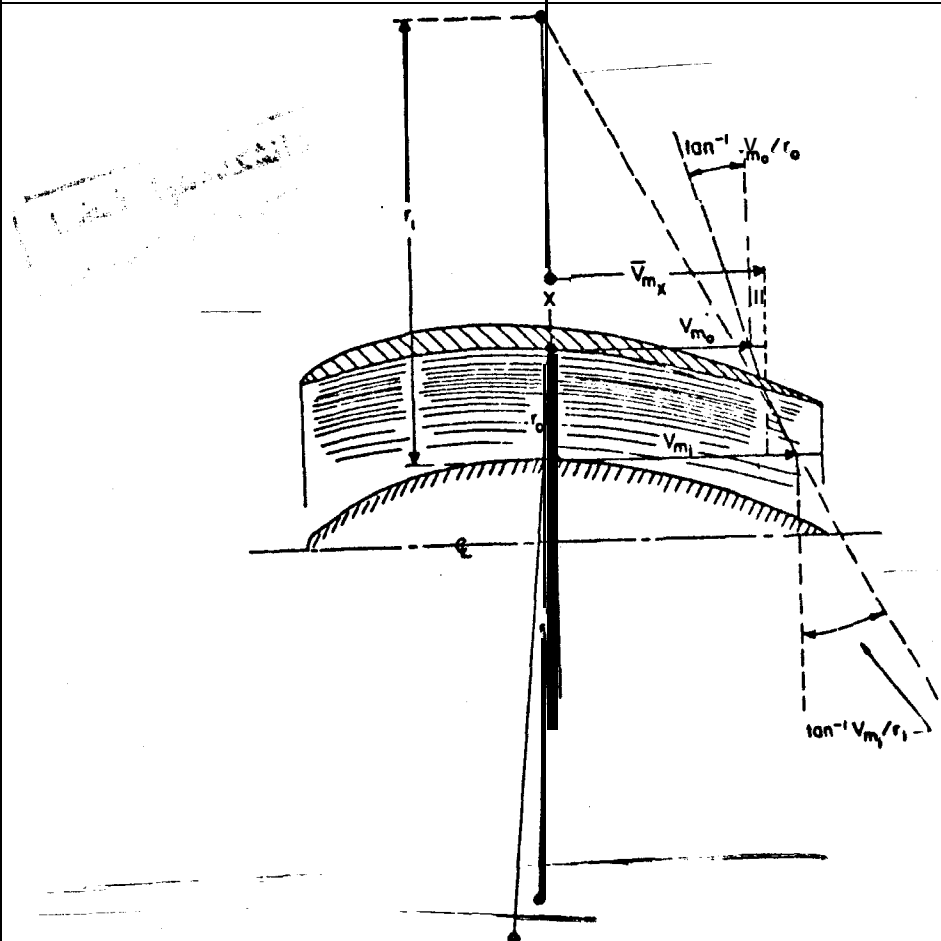


Fig. 6 Approximation of velocity distribution between the shroud and the central body

of a pod-type **pumpjet** and differ from the preceding, which did not include the rotor.

Advance Ratio

The speed of rotation for a **pumpjet** can be determined by selecting an "advance ratio" proportional to the ratio of the through-flow velocity to the peripheral velocity of the rotating element. As stated, this ratio should be for optimum cavitation characteristics. However, this implies a low speed of rotation, which requires large and heavy propulsion machinery and involves danger of flow separation within the **rotor-and-vane system**, according to Equation (6). Therefore, low rotational speeds result in large flow deflections within the rotor (especially near the blade roots) and possibility of flow separation.

Specific Speed

This problem can be resolved by characterizing geometrically similar machines by their "specific speeds",

$$n_s = n \sqrt{Q} / H^{3/4} \quad (15)$$

where Q is in gallons per minute. For a **pumpjet**, the head, H , is the increase in kinetic energy between the inlet and discharge streams [Equation (10)].

From empirical knowledge, n_s of single-stage axial-flow pumps should be between 6000 and 11,000 (for Q in gallons per minute). Values below 600 result in excessive deflections of flow in the roots of the rotors or in an excessively large hub diameter. Values above 11,000 imply high velocities compared to the pump head (the square of the velocity is compared) and, consequently, low over-all efficiencies. (Since a radially nonuniform head can be used for pumpjets, it may be possible to employ n_s lower than 6000.)

Suction Specific Speed

By similarity considerations analogous to the foregoing, judgment of cavitation characteristics in a **pumpjet** can be obtained before it is designed. These characteristics can be expressed by the "suction Specific speed":

$$S = n \sqrt{Q} / H_{sv}^{3/4} \quad (16)$$

For a Propeller or a **pumpjet**, the inlet head is

$$H_{sv} = h + 31 + \eta_{RAM} (\bar{V}_1^2 / 2g) \quad (17)$$

where the 31 is atmospheric pressure minus the vapor pressure of cold water, in feet of sea water.

The suction specific speed can also be related to the internal flow. Figure 7 shows that curves of constant blade pressure or cavitation coefficient vs. the advance ratio (V_m/U) of the rotor tip section have fairly flat optima. Since cavitation-free performance has been achieved with blade cavitation numbers (C) as low as 0.2, it appears that suction specific speeds up to about 10,000 can also be achieved, with very precise blade design. If some local cavitation is tolerable, substantially higher values are possible.

As also shown in Fig. 7, the advance ratio of the rotor tip section must be between 0.25 and 0.35 to obtain s of 10,000 with a blade pressure coefficient not less than 0.2. If it is desirable to maintain a reasonably high speed of rotation, this ratio cannot be chosen simply as low as possible but has an optimum dictated by s .

The relationships in Fig. 7 between s and the other flow characteristics are for a rotor hub diameter of zero. In reality, s is lowered by the square root of the actual inflow cross section of the rotor compared with $D_2 \pi/4$, where D_2 is the inlet tip diameter of the rotor. This reduction is normally small.

Propulsor Specific Speed

The foregoing similarity considerations should be expressed in terms of operating conditions important to **pumpjet** performance, for example, the speed of rotation referred to the thrust and forward velocity of the propulsor. For these quantities, a "propulsor specific speed"

$$n_{ps} = n \sqrt{F} / V_0^2 \quad (18)$$

is defined analogously to specific speed. Propulsors (with the same density of the fluid) that have the same value of n_{ps} and are geometrically similar can be derived from each other by scaling and by changes in absolute velocity and speed of rotation.

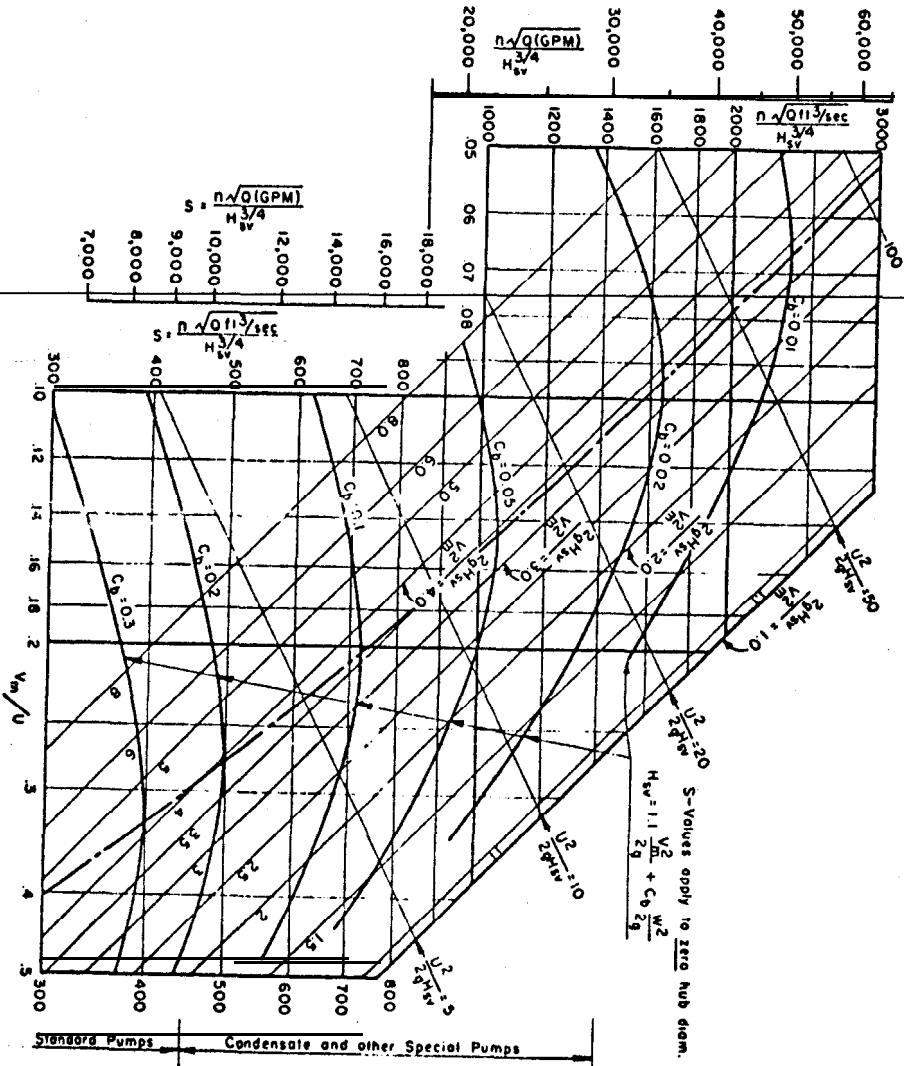


Fig. 7 Relationship of the cavitation parameters of turbomachinery

This similarity criterion is expected to become meaningful after it has been calculated for a number of propulsors and their design and flow characteristics plotted vs. n_p^s .

F. Over-All Design of a Pumpjet on the Aft of a Body of Revolution

This section covers design of a **pumpjet** on the trailing end of a propelled body of revolution, as shown in Fig. 8, which is quite similar to that of Ref. 7. The characteristics of such a propulsor are discussed in Ref. 13.

Average Velocities

~~since the inlet of an aft-mounted pumpjet is exposed to the~~ boundary-layer flow of the body, V is not uniform with distance. A first approximation for a design of passages within the shroud can be obtained by considering average meridional velocities (\bar{V}). This technique is similar to those given in Sec. D with definitions of average velocities as next discussed.

An average of the meridional through-flow velocity is defined from continuity:

$$\bar{V} = \frac{1}{\Delta y} \int_0^{\Delta y} V dy \quad (19)$$

where Δy is thickness of the flow layer entering the **pumpjet** measured normal to the flow direction. Alternately, if flow momentum is being considered,

$$\bar{V} = \sqrt{\frac{\int_0^{\Delta y} V^2 dy}{\int_0^{\Delta y} V dy}} \quad (20)$$

and, if energy transport through the cross section is to be evaluated, the average velocity is

$$\bar{V}^2 = \sqrt{\frac{\int_0^{\Delta y} V^3 dy}{\int_0^{\Delta y} V dy}} \quad (21)$$

Velocity Profiles Ahead of the Shroud

The velocity distribution over the boundary layer of a body of revolution is rarely found theoretically but instead is determined from a wake survey, usually in a plane midway between the leading and trailing edges of the rotor. This distribution may be transferred to another cross section, say ahead of the **pumpjet** inlet, either by assuming the total energy of flow constant along streamlines or by using the laws of vortex

flow through turbomachinery.⁸ The latter becomes identical with the former if the propulsor imparts constant energy per pound of fluid along every streamline.

The general relationship for vortex flow through **turbomachinery** under axially symmetrical flow conditions is

$$(\bar{\zeta} \times \mathbf{v}) / \rho RV = \text{const.} \quad (22)$$

along streamlines. If the vorticity vector is normal to the velocity of flow, which is true in the boundary-layer flow ahead of the **pumpjet** vane systems, Equation (22) simplifies to

$$\left(\frac{\partial V_m}{\partial n} + \frac{V_m}{r} \right) \frac{1}{R} = \text{const.} \quad (23)$$

Equation (23) is valid throughout the **pumpjet** if **all vane** systems have radial or **spanwise** uniform circulation.

Equation (1) and **considerations** of Sec. D are directly applicable to the **average** through-flow velocity on the end of a body of **revolution** when the static pressure some distance ahead of the **pumpjet** inlet and behind its discharge is equal to **the freestream pressure** P_0 . This is a good approximation, because the static pressure on the surface of the body equals the freestream pressure near the after end. Generally, however, **either** theoretical or experimental velocities and pressures should be used.

Shroud Design

The **pumpjet** shroud may now be designed similarly to that in Sec. D and Fig. 5. The configuration on the end of a body is shown in Fig. 9, where the angle of attack α is as defined in Sec. D and is, therefore, near 15°.

Although the lift coefficient of the shroud may also be calculated as suggested in Ref. 7, all approximations ignore separation of flow from the external surface. This could occur with a shroud of zero lift coefficient with a **conical afterbody** and a rather steep angle of convergence. The over-all problem of shroud design is therefore still incompletely solved.

Velocity Profiles Within the Shroud

Velocities of flow inside a **pumpjet** shroud, calculated as described previously, are indicated in Fig. 10 for four stations within the shroud and a fifth at the discharge end. The

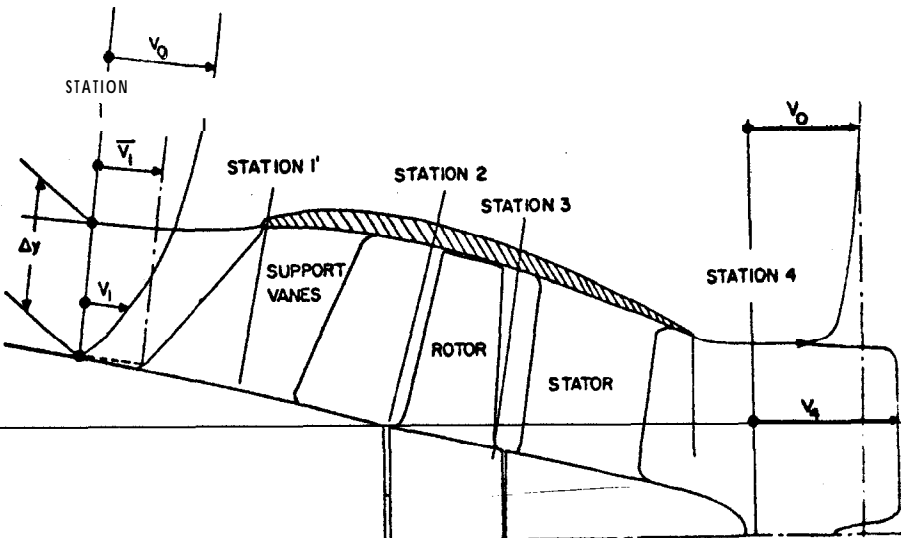


Fig. 8 General arrangement of a pumpjet located at the after end of a propelled body of revolution

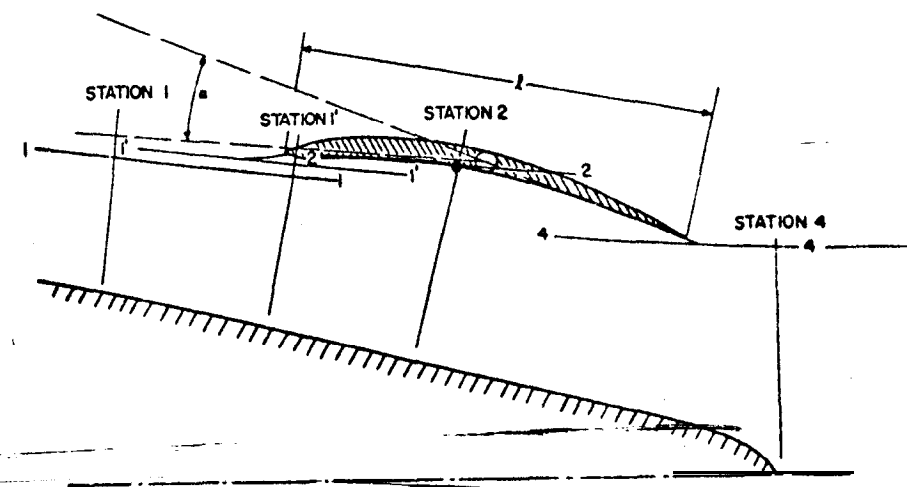


Fig. 9 Pumpjet shroud on tapered afterbody

distributions for stations 2-6 are derived from the bare-body velocity distribution shown, using Equation (23) and successive approximations that satisfy continuity at the flow cross section inside the shroud. The effect of curvature, as expressed by the second term in Equation (23), is approximated separately by the curve α indicated in Fig. 10, which is constructed as described in Sec. D and Fig. 6. Velocity variations produced by flow curvature may be algebraically added to those derived for zero curvature. Figure 10 shows that curvature has very little effect on the flow inside the shroud, for this example.

Frictional Effect

The foregoing derivation is for frictionless flow inside the shroud. Actually, a boundary layer forms on the inside of the shroud and along the central body, but it is usually not practical to estimate its effects because of the influence of the vane systems ahead of and within the shroud. Instead, stations 2-6 (Fig. 10) may be corrected for an estimated boundary-layer-displacement thickness on the walls of the annular passage. If there is retardation between the inlet and station 2, a fairly rapid growth of this thickness is expected, perhaps about 10% of the total cross section. A similar additive correction in cross-sectional area may be justified at stations 3 and 4. At 5 and 6, however, a smaller increase should be used because of acceleration of meridional flow from 4 to 6. These empirical increases in flow areas should later be adjusted with experimental data.

G. Design of Pumpjet Rotor Blades

Design Surfaces

After determining velocity distributions between the shroud and the central body, streamlines may be derived from

$$V_m(\Delta a) = \text{const.} \quad (24)$$

where $a = R\Delta n^2\pi$, and Δn is the perpendicular distance between streamlines.

The meridional stream surfaces so determined are more or less conical. However, the empirical data for the axial-flow compressor of Sec. A apply primarily to straight, cylindrical stream surfaces. Theoretical treatment of flow along such surfaces is far simpler because flow relative to rotating vanes has an inherent vorticity.

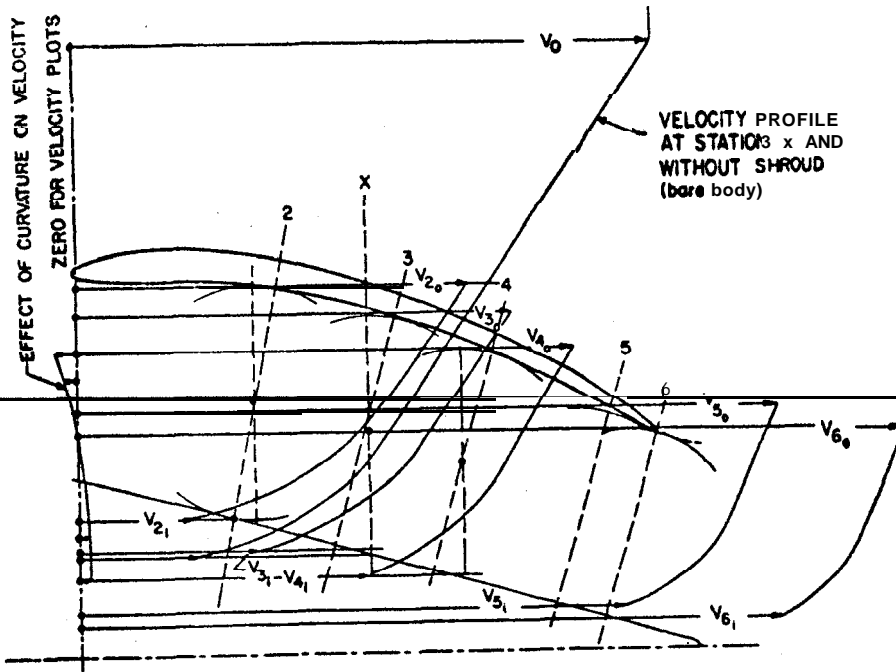


Fig. 10 Velocity distribution within a shroud on a tapered afterbody

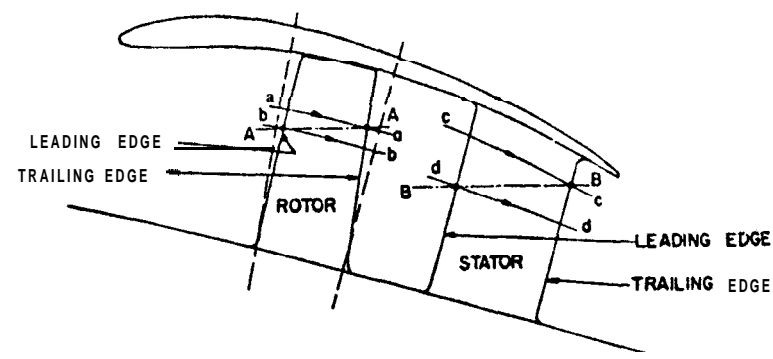


Fig. 11 Flow surface in meridional plane

To apply the cascade data of NACA for straight axial flow and to avoid the theoretical complications of flow along conical surfaces, blade shape is determined by considering only the axial component of the meridional flow. As shown in Fig. 11, flow is examined for a straight cylindrical section A-A. The meridional velocity of the entering flow is determined for the stream surface b-b, and the inlet velocity along section A-A is the axial component of the meridional velocity along b-b at the leading edge. For the discharge, the meridional velocity is that for the stream surface a-a; and the discharge velocity along the cylindrical section A-A is the axial component along a-a where this surface intersects the trailing edges of the vane system. The axial velocity along A-A differs between inlet and discharge, because of changes in the cross section of the meridional flow, which also passes from one surface to another.

The actual meridional flow consists of that along A-A plus a **spanwise** flow that changes this cylindrical flow to one along the conical stream surfaces a-a and b-b. If vane circulation does not change spanwise, it seems reasonable to neglect this component. In reality, however, **spanwise** flow can be neglected only if the blade sections have the same direction as a **spanwise** flow of constant angular momentum.

In practice, **spanwise ("fairing")** sections of the vanes will be determined largely by geometric considerations described later, and, usually **spanwise** flow of constant angular momentum does not occur. However, the previous assumption holds, in principle, if the leading and trailing edges of the vanes fall approximately in a radial plane and the incoming flow has no circumferential component. A method to use when this condition is not satisfied is discussed in Ref. 9.

The Mean Streamline

Blade profiles along cylindrical sections, as A-A of Fig. 11, will be designed by the "mean-streamline" method. It determines changes in the circumferential component of flow through the vane system caused by pressure differences along the blade and departure of the blade camber line from the mean streamline, as determined from a semiempirical analysis of NACA cascade data. An example of a blade layout for a fairly large ratio of axial-to circumferential relative-velocity component is shown in Fig. 12. The relative inlet flow **velocity vector** w_2 and discharge velocity vector w_3 are determined by a) the axial components of the **meridional flow** at inlet and discharge, b) the peripheral velocity of the blade at A-A, and c) the change in circumferential component of the

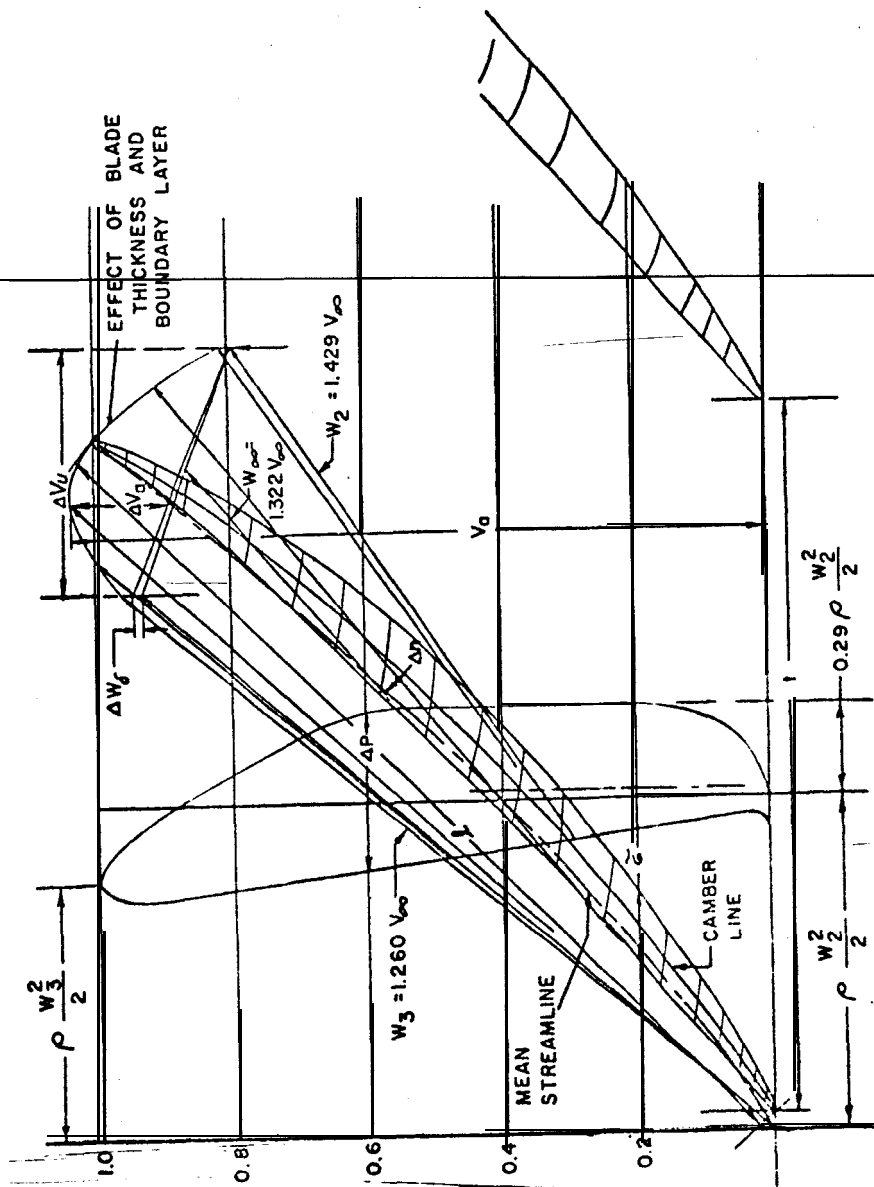


Fig. 12 Typical section of a blade with a high advance ratio

flow V_u from Equation (6). Subscripts 2 and 3 denote stations ahead of and behind the rotor (see Fig. 1).

The axial component of the discharge relative velocity (w_3) is larger than that determined from Fig. 10 by an amount equal to the area reduction at the blade discharge edge plus the displacement thicknesses of both boundary layers leaving the blade profile. Figure 12 shows a typical curve along which the ends of the relative velocity vectors travel. It is difficult to determine the displacement thickness of these boundary layers, but the reduction in meridional cross section caused by the blade boundary layers can be estimated and an appropriate increase made in the axial component of w_3 . The axial component at intermediate locations between the inlet and discharge of the rotor can be similarly obtained.

The circumferential component of the absolute velocity at intermediate locations is determined by a proportion of the diagram of blade pressure vs axial length. The circumferential component of the relative velocity is then obtained by subtracting the blade speed from the component of the absolute velocity. Details are given in Ref. 6.

The mean streamline may now be constructed as tangents to the relative velocity vector at every point.

The Mean Camber Line

The departure of the mean camber line of the blade from the mean streamline is assumed to be proportional to the lift coefficient of the blade. Its distribution along the blade profile is derived from NACA cascade data. A typical departure curve for vane systems requiring high resistance to cavitation is shown in Fig. 13. The unit of departure is the maximum of the standard NACA 65-series cascades of Fig. 14.

The lift coefficient of the blade, written with present notations, is

$$C_{L\infty} = 2 (\Delta V_u / W_\infty) (t/l) \quad (25)$$

or, referred to the inlet relative velocity,

$$C_{L2} = C_{L\infty} (W_\infty^2 / W_2^2) \quad (26)$$

C_{L2} can also be determined from the mean pressure difference

across the blades as derived from the assumed pressure- $w^2/2$ distribution diagram of Fig. 12. This diagram uses $w^2/2$ as the difference between the freestream pressure and the stagnation pressure; therefore,

$$C_{L2} = \frac{2}{\rho W_2^2} \int_0^{l_a} \Delta P dl_a \cdot \frac{1}{l_a} \quad (27)$$

where ΔP is as plotted in the pressure-distribution diagram, l_a is the coordinate of the blade in the axial direction, and l_a is the total axial extent of the blade.

Maximum departures of the blade camber line from the mean streamline are plotted in Fig. 14 vs the "stagger" angle of the vane system measured from its axial direction. The departure Δn is normal to the base or chord line of the blade and is referred to the unit lift coefficient.

Figure 13 shows the distribution of the camber-line departure from the mean streamline along the blade length. The solid curve shows departures derived from the "trailing-edge loaded" profiles investigated by NACA. In this case, the maximum is larger than unity, i.e., greater than that of the standard NACA 65-series profiles.

The actual departure is determined from Fig. 13 by

$$\Delta n = \left(\frac{\Delta n_l}{l} \right)_{MAX} \left(\frac{\Delta n_l}{\Delta n_{l,MAX}} \right) C_{L\infty} l \quad (28)$$

where $\Delta n_l / \Delta n_{l,MAX}$ is the value for various stations along the chord of the blade. On the horizontal axis of this figure, 0 indicates the leading and 1 the trailing edge of the blade.

After determining the blade camber line, blade thickness is found from changes in the axial component of the relative flow, using

$$r/t = \Delta V_a / V_a \quad (29)$$

where V_a is the velocity after effects of thickness are included. The originally assumed curves along which the relative velocity vectors travel will not produce a smooth contour, and generally are "corrected" to hydrodynamically acceptable shape by drawing this contour with minimum curvature along the sides of the blades.

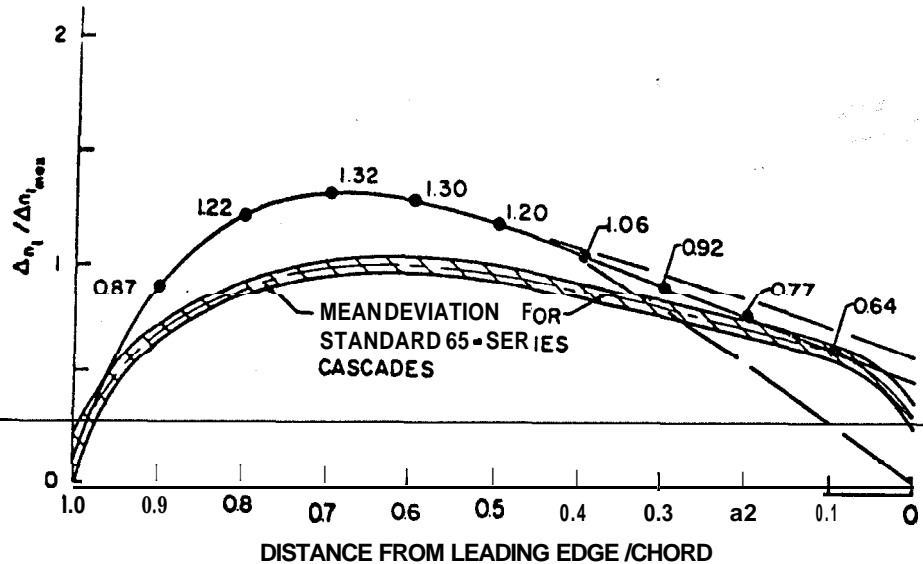


Fig. 13 Chordwise distribution of camber-line offsets

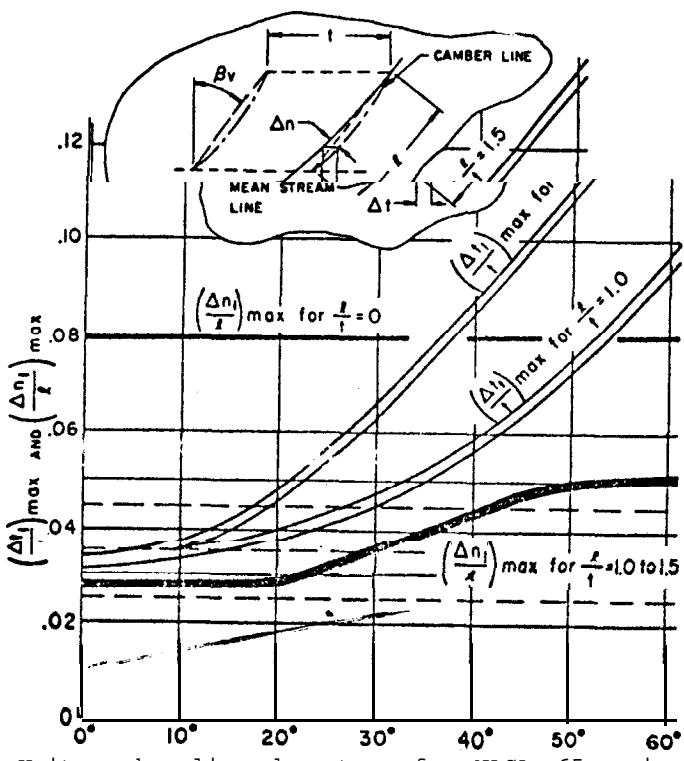


Fig. 14 Unit camber-line departure for NACA 65-series cascades

Design Examples

In Fig. 13, a variation of this departure curve is indicated near the leading edge because the action of the blade is largely determined by its trailing portion. The manner by which this can be exploited is now discussed.

Figure 15 shows the blade profile for the tip section of a **pumpjet** rotor of a much *lower* advance ratio than that of Fig. 12. Figure 16 shows a blade profile for the root section of a pumpjet rotor of fairly low advance ratio. The required flow deflection for this **section** is, of course, much greater than that of the tip, because the change in circumferential component multiplied by the peripheral velocity is constant, as indicated by Equation (6).

The Leading Edge

Figure 16 shows a limitation on the blade shape near its leading edge which is not determined in Fig. 13. The length δ is established by drawing a line perpendicular to the incoming flow and passing through the leading edge of the neighboring blade. δ cannot be obstructed by a blade, since otherwise flow ahead of the vane system would accelerate between **vanes**. — Also, δ is strongly influenced by the departure curves near the leading portion of the blades. For the tip sections, where blades do not usually overlap, the lower departure curve shown in Fig. 13 can be used. For root sections, as in Fig. 16, it may be necessary to use the upper departure curve to be certain that acceleration of the mean flow is not required.

Flow Separation

For strong deflections, such as those in the root sections, it is necessary to consider retardation limits by flow separation at the low-pressure side of the blades ("stall"). As a rule the relative discharge velocity should not be less than 0.6, and never less than 0.5, times the relative inlet velocity. The conditions in Fig. 16 represent nearly a limiting case.

Stator Blades

Design considerations for rotor — also apply to stator vanes behind or in front of the rotor. Again, the more or less conical **meridional streamlines** are replaced by a cylindrical section B-B, as in Fig. 11. A typical diffuser vane section derived by the mean-streamline method is shown in Fig. 17. If the shroud is properly designed, the **meridional**

Fig. 15 Tip section of a blade with a low advance ratio

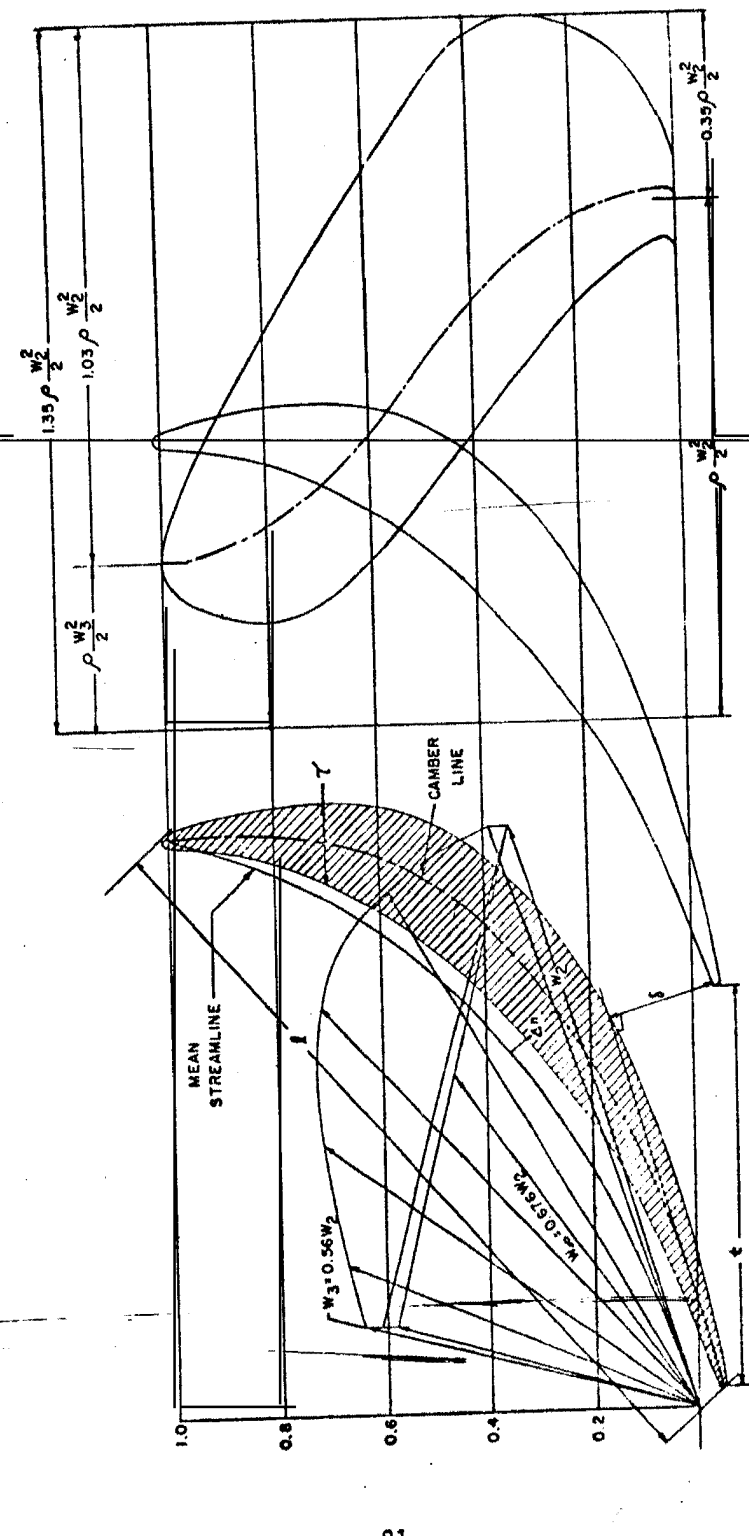
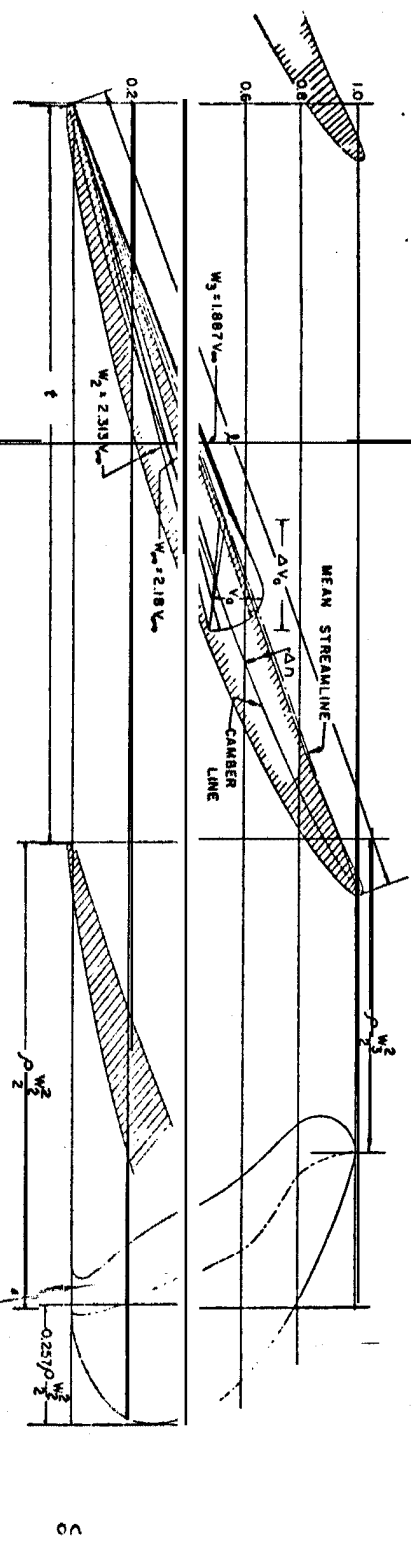
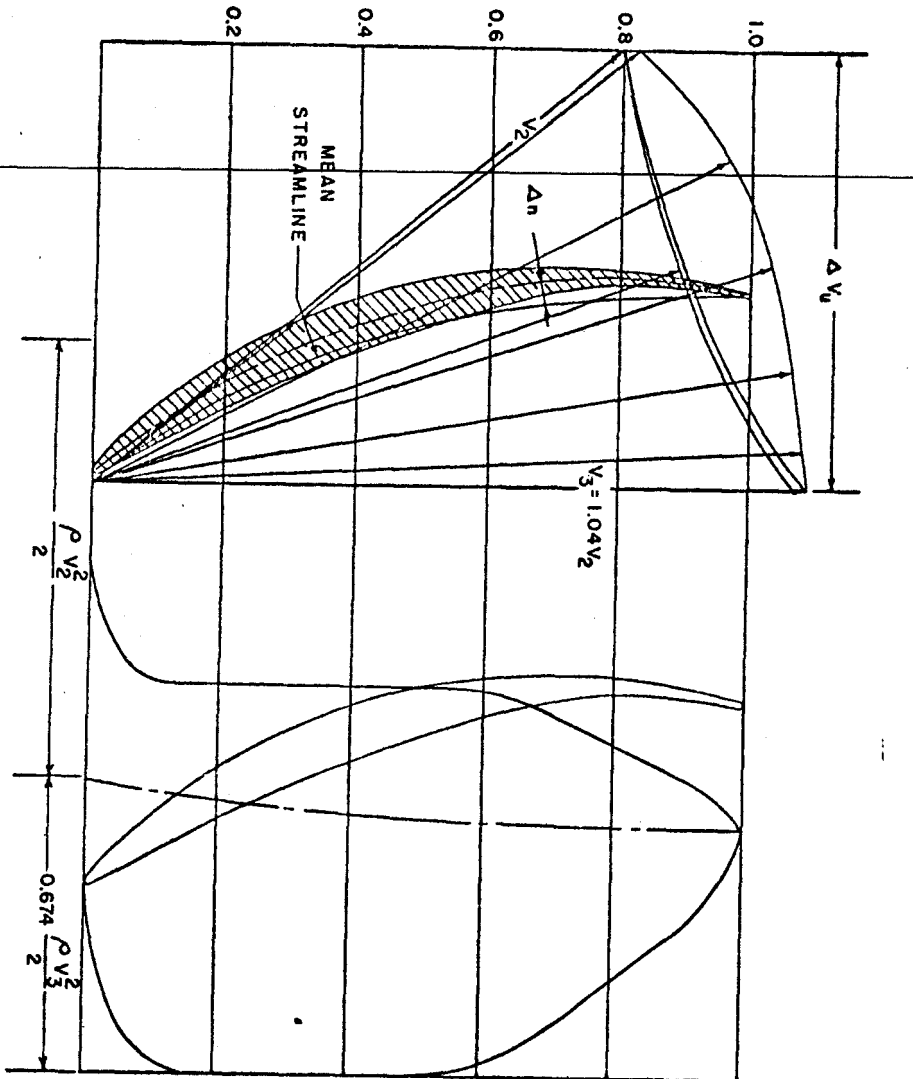


Fig. 16 Root section of a blade with a low advance ratio

Fig. 17 Typical diffuser-blade section



component of the flow (and thereby the axial component in the blade section) can be sufficiently accelerated to avoid retardation within the diffuser-vane system. As a result, boundary-layer growth and corresponding losses within the vane system are minimized.

Final Blade Design

Design of the individual vane sections on the basis of local flow conditions is still incomplete in two respects: a) the relationships between velocities, pressures, solidity (t/l), and lift coefficient [Equations (25-27)] leave considerable freedom in choosing these variables, and b) the pressure difference across the blade (Δp) - as shown, for example, in Fig. 12 - should be determined so that a selected cavitation performance is obtained. For the blade section of Fig. 12, the pressure reduction below the mean static pressure at the inlet is 0.29 ($\rho w_2^2/2$), where w_2 is the relative inlet velocity, and, for the particular example, $w_2 = 1.429 V_0$. Therefore, if the static-pressure difference between the rotor inlet and the freestream is neglected, the cavitation number is

$$\sigma = 0.29 / (V_0^2 / W_2^2) = 0.29(1.429)^2 = 0.59^{(30)}$$

Pressure distributions may now be selected so that cavitation numbers will be about the same for all blade sections. After determining the pressure reduction and thereby, to some extent the average pressure difference over the blade from cavitation considerations, an approximation for the lift coefficient is obtained from Equation (27), and appropriate values of the solidity (t/l) of the various sections may be determined.

The cascade sections are dimensionless, and must be adjusted so that the blade spacing (t) varies with distance from the axis and provides a whole number of blades. The number of blades or the actual aspect ratio is found by considering bending stress and, if possible, elastic deformations.

Even this does not necessarily produce a final answer, because the over-all geometry of the blade may be unsatisfactory. Thus, it is necessary to "stack" the blades, i.e., inspect the cylindrical sections after they are placed one on top of the other. A satisfactory blade design thus requires successive approximations.

H. Experimental Results

These methods have been used to design **pumpjets** for completely submerged, axisymmetric bodies. Low rotational speed **pumpjets** have been fabricated for both torpedoes and submarines, and high-speed **pumpjets** for torpedoes.

A Low-Speed Pumpjet on the Aft of a Body of Revolution

Experimental results with a low-speed **pumpjet** on an 8-in.-diam.**torpedo** model (generally as shown in Fig. 8), are given in Figs. 18 and 19. Its design advance ratio was 2.025, at which value net thrust is zero.

The discrepancy between the design and actual ratios is due primarily to two reasons: 1) the original drag coefficient was overestimated, since design was accomplished before accurate wake data could be obtained from the model; this emphasizes need for wake data; and 2) no adequate method is available to determine the increased drag caused by the **pumpjet**; thus, an analytical estimation of this drag is an important need for **pumpjet** design.

Figure 18 demonstrates the need for model tests. The curves "5%" and "10%" show the effects of respective increases in shroud exit area. The net thrust was notably altered by these minor modifications.

Overestimation of design thrust improves cavitation performance, as shown in Fig. 19. The curves marked "unmodified" are with the **blading** as-designed, and indicate premature suction-surface cavitation on the leading edges. Based on actual wake data, the system was modified so that the slope of the mean camber line was increased approximately 5° near the leading edge, and the new cavitation data are designated "modified". This change, together with the increase of the self-propulsion advance ratio to 2.025, resulted in a cavitation performance that exceeds the predicted critical index of approximately 0.7.

A High-Speed Pumpjet on the Aft of a Body of Revolution

The following are results of an experimental program with a **pumpjet** operated at high shaft rotational speeds (the idea of a high-speed **pumpjet** was first described in Ref. 5), designed using the principles described in this text.

Two propulsors were constructed and experimentally evaluated, the first with a single rotating shaft and the second with

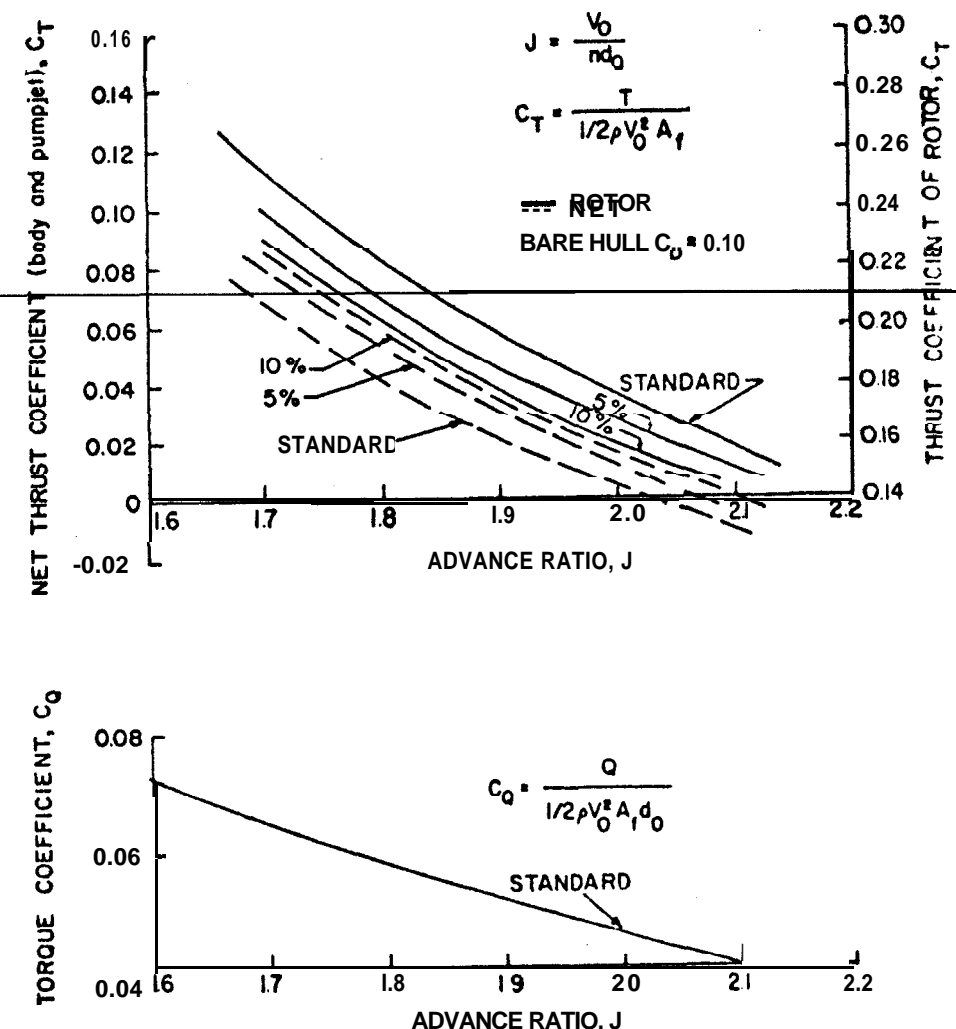


Fig. 18 Thrust and torque coefficients as a function of advance ratio

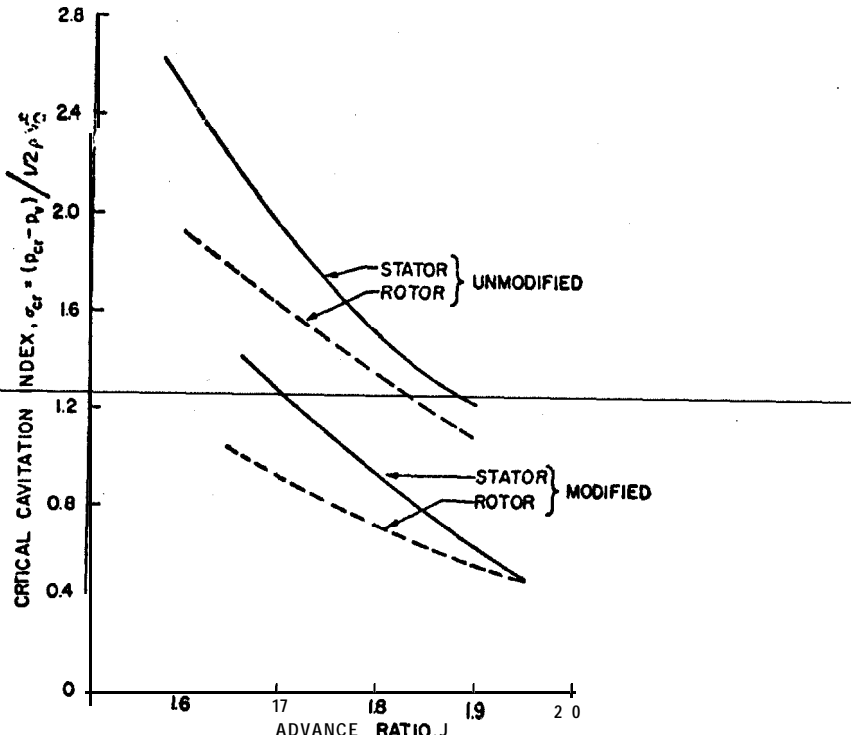


Fig. 19 Cavitation performance of a pumpjet

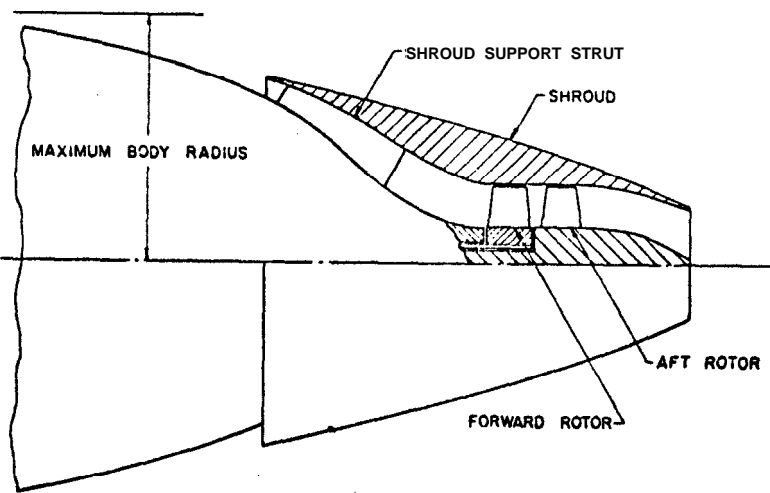


Fig. 20 High rotational speed pumpjet with boundary-layer intake

counterrotating shafts. A sketch of the latter is in Fig. 20 and represents the general arrangement of a high rotational speed propulsor.

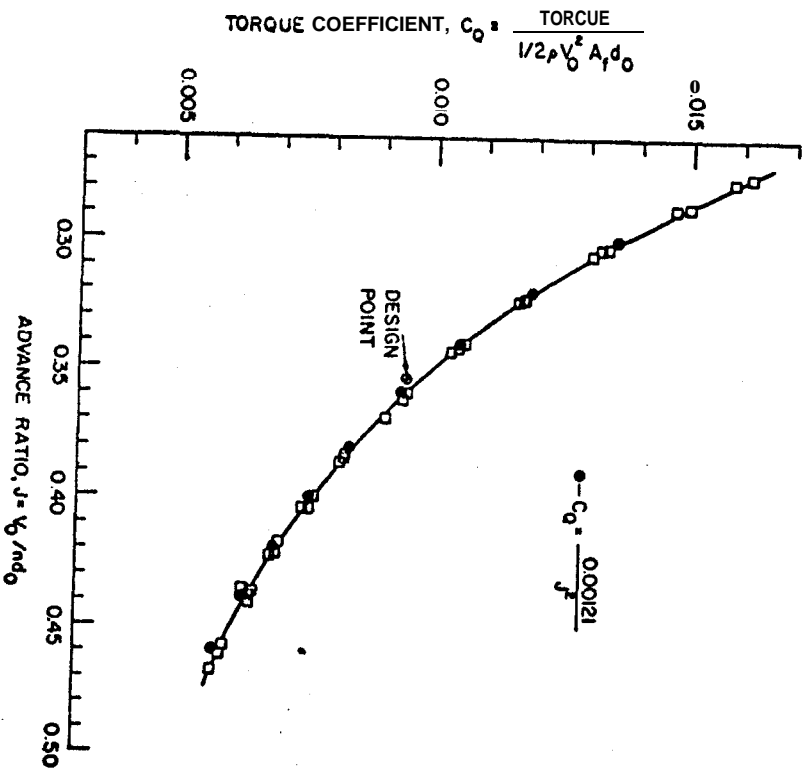
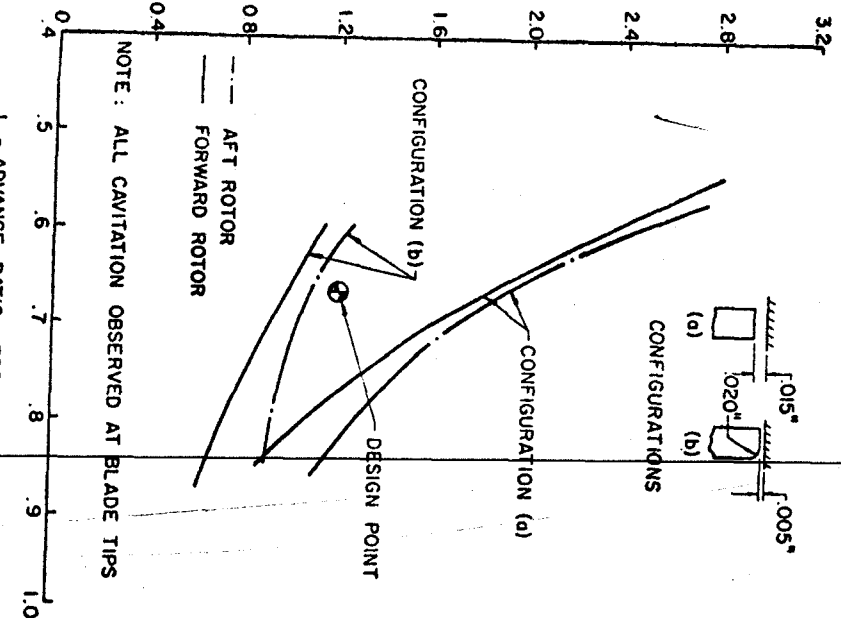
The program for the single-rotor high-speed pumpjet is described in Refs. 10 and 11. It demonstrated the correctness of the duct and shroud design of Fig. 20, but provided much poorer cavitation performance than anticipated, apparently caused by selecting the wrong design velocity profile for the rotating blades. Thus, the counterrotating set of blades was designed to improve cavitation. It was estimated that cavitation-free operation could be obtained at an index of 1.25. Because of greater rotational speed, the critical cavitation index of this pumpjet is greater than that of Fig. 19. Counter-rotation provides intrinsic resistance to cavitation, since the forward rotor operates at a lower rotational speed than the aft, which it effectively supercharges. This pumpjet was cavitation-free at an index of 1.1, as shown in Fig. 21. The critical form of cavitation occurred at the tip of the blade and was caused by the leakage vortex over the blade tip. As shown in Fig. 21 and discussed in Ref. 12, this is strongly affected by the tip shape.

Figure 22 plots rotor torque coefficient vs advance ratio for the single-rotor high-speed pumpjet. It demonstrates a characteristic of a pumpjet rotor; namely, operation at a constant blade inlet angle, as implied by the inverse variation of torque coefficient with the square of the advance ratio¹³ which occurs with all pumpjets in a range of $\pm 20\%$ of the design advance ratio. It implies that the pumpjet has better cavitation characteristics than a propeller during vehicle acceleration or deacceleration, and allows accurate prediction of pumpjet performance at off-design.

I. Conclusions and Recommendations

At the Ordnance Research Laboratory methods have been developed for the hydrodynamic design of pumpjets for the propulsion of underwater vehicles. At ORL these were aimed primarily at attaining high resistance to cavitation, and this has been successfully demonstrated. Three factors have contributed to the success of this program:

- 1) The original NACA cascade data, which was not satisfactory for the design of a pumpjet with high cavitation resistance, was made so by judicious generalization to yield satisfactory blade-section profiles.



2) High-solidity blading has been used to increase the number of blades and **reduce loading** on each, although a sacrifice in efficiency because of added skin-friction drag, which must be accepted to obtain high cavitation resistance.

3) The velocity profiles at the inlet and exit of the rotor and **stator** blades were carefully determined.

Current hydrodynamic designs of **pumpjets** include two major unsolved problems:

1) An analytical method is needed **to** predict the effect of the shroud on the net force produced by the propulsor and on the flow through it. This work would supplement that of Ref. 7, and may include results from Ref. 14.

2) Methods are needed to predict unsteady flows and forces that occur in both **pumpjets** and propellers.

References

¹ Wislicenus, G. F., "Principles and applications of bypass turbojet engines," *Soc. Automotive Engrs.* 64, 486 (1956).

² "Aerodynamic design of axial-flow compressors," Lewis Flight Propulsion Lab. Repts. NACA RM E56B03, NACA RM E56B03a, and NACA RM E56B03b (August 1, 1956).

³ Wislicenus, G. F., Smith, L. H., "Hydraulic jet propulsion and incipient cavitation," Johns Hopkins Univ., Institute of Cooperative Research, Rept. I-6, Part A (March 21, 1952).

⁴ Eskinazi, S. J., Flagle, C. D., Ruetenik, R., and Weske, J. R., "A problem in retardation of a turbulent boundary layer," Johns Hopkins Univ., Institute for Cooperative Research, Rept. I-6, Part B (March 21, 1952).

⁵ Wislicenus, G. F., "Hydrodynamics and propulsion of submerged bodies," *ARS J.* 30, 1140-1148 (1960).

⁶ Wislicenus, G. F., *Fluid Mechanics of Turbomachinery* (Dover Publications, Inc., New York, 1965), Vols. I and II.

⁷ McCormick, B. W. and Eisenhuth, J. J., "The design and performance of propellers and **pumpjets** for **underwater** propulsion," *AIAA J.* 1, 2348-2354 (1963).

⁸ Smith, L. H., Traugott, C. C., and Wislicenus, G. F., "A practical solution of a three-dimensional flow problem in axial-flow turbomachinery," Trans. Mech. Engrg., 75, no. 5 (July 1953).

⁹ Wislicenus, G. F., "The design of mixed-flow pumps," Symposium on Pump Design, Testing and Operation, National Engineering Lab., East Kilbride, Glasgow, Scotland (April 12-14, 1965).

¹⁰ McMahon, J. F., "Design of the ORL high speed pumpjet," Ordnance Research Lab. Tech. Memo., TM 506.3810-01 (November 11, 1963).

¹¹ Gearhart, W. S. and Henderson, R. E., "Results of experimental investigations with a high speed boundary layer intake pumpjet," Ordnance Research Lab. Tech. Memo., TM 506.3810-02 (January 31, 1964).

¹² Gearhart, W. S. "Tip clearance cavitation in shrouded underwater propulsors," AIAA J. Aircraft 3, 185-192 (1966).

¹³ Gearhart, W. S. and Henderson, R. E., "Selection of a propulsor for a submersible system," AIAA J. Aircraft 3, 84-90 (1966).

¹⁴ Dickman, H. E., "Fundamentals of annular airfoil theory (nozzles in a free stream)," Polytechnic Institute of Brooklyn Rept. 353 (August 1956).

APPLICATIONS OF NEW SOLID PROPELLANTS TO UNDERWATER ROCKETS

Donald E. Tryk*

United Technology Center, Sunnyvale, Calif.

Abstract

Techniques of application and limitations of solid-propellant rockets as underwater propulsors are analyzed. At constant vehicle speed, propellant specific impulse and density are of about equal importance. Maximum vehicle speed is limited by the ratio of maximum thrust to frontal area (typically about 50,000 psf) to 400 - 500 knots with conventionally shaped bodies, but cavitation and short range diminish the usefulness of such speeds. Propulsive efficiency of rockets increases with speed, but is only about 25% at 550 knots. Solid rocket grains with thin webs are useful in boost applications, whereas thicker web shapes or end burners are useful in sustainers. A simplified equation for calculating boost impulse requirements is developed. Some characteristics of typical modern solid propellants are given. High-density formulations offer a 15-20% increase in underwater range over conventional solids. The versatility of grain designs now possible, together with the wide range of current burning rates, offers speeds between 30 and 500 knots. Conceptual designs of a 6-in. and a 10-in.-diam rocket are illustrated, and their performances are estimated.

Nomenclature

A	=	reference area (body cross section)
a	=	acceleration of body
At	=	nozzle throat area
Cd	=	drag coefficient
Cf	=	thrust coefficient, actual delivered

Presented as-preprint 64-462 at the 1st AIAA Annual Meeting, Washington, D. C., June 29 - July 2, 1964.

*Chief, Technology Projects Section; presently Project Engineer, Pratt & Whitney Aircraft, Florida Research and Development Center, West Palm Beach, Fla.

c_f	th opt	■ thrust coefficient, theoretical, at optimum expansion area ratio
D		■ drag force
F		■ rocket thrust
F_B		■ rocket boost thrust
I_{sp}		■ specific impulse Eq. (2)
\dot{I}_{tot}		■ total impulse
m		■ mass flow rate
P_a		■ pressure at ambient (depth) conditions
P_c		■ rocket motor chamber pressure
P_e		■ pressure at nozzle exit plane
R		■ range
t_b		■ burning time
Atb		■ boost burning time interval
v		■ velocity
V_p		■ volume of propellant
V_j		■ jet velocity
AV		■ jet velocity, vehicle speed
W_p		■ propellant weight
W_v		■ vehicle weight
γ		■ ratio of specific heats
ϵ		■ nozzle expansion ratio
η		■ efficiency
ρ_w		■ density of water
ρ_p		■ density of propellant
I_{sp}, ρ_p		■ density impulse

Introduction

Simplicity, low cost, nontoxicity, and safe handling are desirable in underwater propulsion systems; they are also characteristics of many state-of-the-art solid-propellant rockets. However, propulsive efficiencies of rocket-propelled underwater vehicles are intrinsically low, because of low running speeds relative to the velocities of their exhaust jets. This makes rockets noncompetitive, in performance, with gas-generator-fed-engine-propeller systems, except in a restricted class of short-range, high-speed missions.

Even in the latter cases, restrictions on practical propellant grain configurations and burning rates severely limit run times, and it has not generally been possible to optimize a design for a specific application. Recent developments in high-energy propellants, which extend burning rates to both higher and lower values, now allow greater flexibility, whereas new high-density propellants also offer somewhat increased performance. Such propellants are theoretically considered below for short-range, high-speed, rocket-propelled underwater vehicles. The analysis is morphological, rather than particular.

Analysis

First, consider the basic relations between design and performance for a constant-speed, fixed-size, rocket-propelled underwater vehicle:

Vehicle drag
$$D = C_D \cdot \frac{\rho_w v^2}{2} A \quad (1)$$

Rocket thrust
$$F = m \cdot I_{sp} \quad (2)$$

With thrust constant
$$F = (W_p/t_b) \cdot I_{sp} \quad (3)$$

At constant speed
$$F = D \quad (4)$$

Combining (1) - (4) and assuming a constant C_D gives

$$v \propto \sqrt{m \cdot I_{sp}} \quad \text{or} \quad v \propto \sqrt{(W_p/t_b) \cdot I_{sp}} \quad (5)$$

Introducing
$$R = v \cdot t_b \quad (6)$$

then
$$R \propto \sqrt{W_p \cdot I_{sp} \cdot t_b} \quad (7)$$

With $V_p = W_p/\rho_p$ fixed,

$$R \propto I_{sp} \cdot \rho_p \cdot t_b \quad (8)$$

For a fixed-size propulsion unit, Eq.(8) shows the desirability of propellants with high "density impulse" (I_{sp}, ρ_p) and the need to maximize burning time when long range is required.

Next, consider vehicle speed. From (1) and (4),

$$v^2 = 2F/C_D \rho_w A$$

or

$$v = \sqrt{(2/C_D \rho_w) (F/A)} \quad (9)$$

With solid-propellant rocket motors, high chamber pressures and, hence, high F/A values are feasible. For example, a rocket nozzle with optimum expansion ratio for 2000-psia combustor operation at 200-ft depth and a nozzle exit area half of its body frontal area has a (calculated) F/A ratio of about 55,000 psf. For a reasonable drag coefficient of 0.10, this gives a maximum speed of 743 fps (440 knots). However, the attendant range, being inversely proportional to the square of the speed, is extremely short. In addition, since gross body cavitation occurs on high speed vehicles, except at great depths, control would be difficult, if not impossible with conventional fins and rudders. So, because of short range and because of control problems, such speeds are of academic interest.

Consider next propulsion efficiency:

$$\eta_p = [1 + 1/2 (\Delta v/v_j)]^{-1} \quad (10)$$

Taking a representative exhaust velocity for a high-energy solid propellant of 6700 fps at a pressure ratio of 20:1, η_p values at various vehicle speeds are plotted in Fig. 1. They show the desirability, from this point of view, of operating underwater rocket-propelled bodies at the highest possible speeds.

The time available for an unguided, negatively buoyant underwater rocket vehicle to attain full speed under its own thrust is very short. But if only sustainer thrust is used, this interval could become several seconds, as shown in Fig. 2 (for a particular vehicle). Therefore, in the interest of vehicle control and rapid starting, it is desirable to include a booster stage.

Booster total impulse requirements may be estimated assuming that 1) sustainer thrust is negligible compared to booster thrust, 2) "drag impulse" ($\int D dt$) is insignificant during booster operation, and 3) booster propellant weight is small compared to vehicle weight. Then

$$F_B = (W_v/g) = a \quad (11)$$

$$V_{final} = a \cdot t_B \quad (12)$$

$$I_{tot, boost} = F_B \cdot t_B, \quad (13)$$

$$I_{tot, boost} = (W/g) \cdot V_{final} \quad (14)$$

since

then

Fig. 1 Propulsive efficiency vs velocity of a typical solid-rocket underwater vehicle.

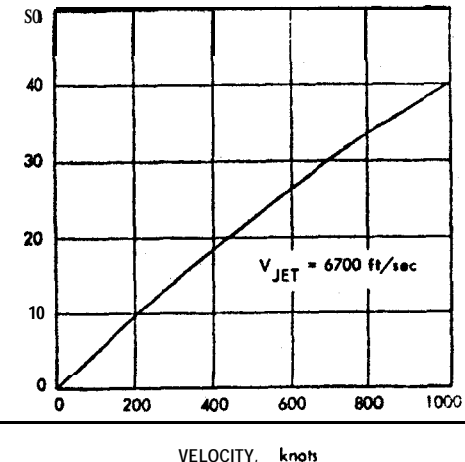


Fig. 2 Calculated starting transient for a vehicle with zero boost (vehicle I at 200-ft depth).

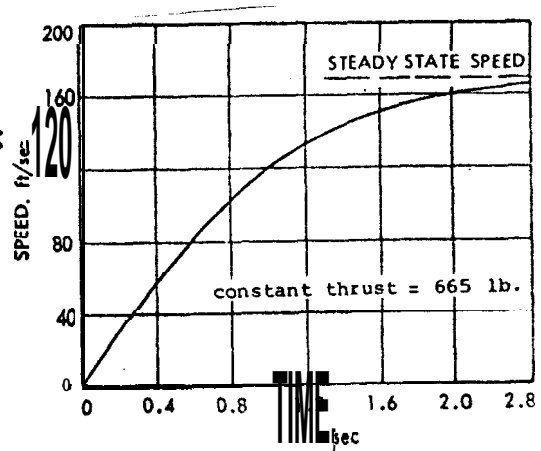
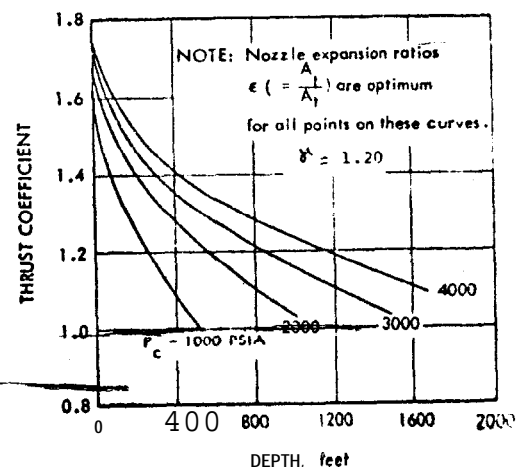


Fig. 3 Thrust coefficient vs depth at various chamber pressures.



Equation (14) will be used later to estimate boost-propellant weights for two vehicles. Although the allowable booster burning time varies with requirements, it is generally low, and 0.1 sec. will be used for the examples, under which condition the preceding assumptions are valid.

Rocket Motor Relationships

Rocket motor thrust, chamber pressure, nozzle throat area, expansion ratio, and specific impulse are related by

$$F = P_c \cdot A_t \cdot C_f \quad (15)$$

$$C_f = \eta \cdot C_{f\text{ th, opt}} + \frac{P_e - P_a}{P_c} \quad (16)$$

$$C_{f\text{ th, opt}} = \sqrt{\frac{2\gamma^2}{\gamma-1} \frac{2}{\gamma+1} \frac{\gamma+1}{\gamma-1} \left[1 - \frac{P_e(\gamma-1)}{P_c} \right]} \quad (17)$$

and

$$I_{sp} = I_{sp\text{ (ref)}} (C_F/C_{F\text{ (ref)}}) \quad (18)$$

Using these relationships and the tables of Seifert and Crum,¹ the graph in Fig. 3 of thrust coefficient vs operating depth at various chamber pressures was made. It provides theoretical values at optimum expansion ratios for a specific-heat ratio of 1.2 and shows need for high chamber pressures at great depths.

High chamber pressure is also desirable to permit small port areas in internal burning grains. On the other hand, it requires heavy case walls and thick insulation, and increases propellant strains in case-bonded grains.

Grain Designs

In a solid rocket, mass flow rate is determined by grain geometry and propellant burning rate. Four representative geometries are shown in Fig. 4 with increasing characteristic web thickness going from 4a to 4d. Propellant slivers (unburned residues) are shown for each design where applicable. Typical insulation configurations to protect case walls from burnthrough are shown for the slotted-tube grain and the end burner.

Approximate limits of practical web thickness and cross-sectional propellant loadings for near-neutral (i.e., constant

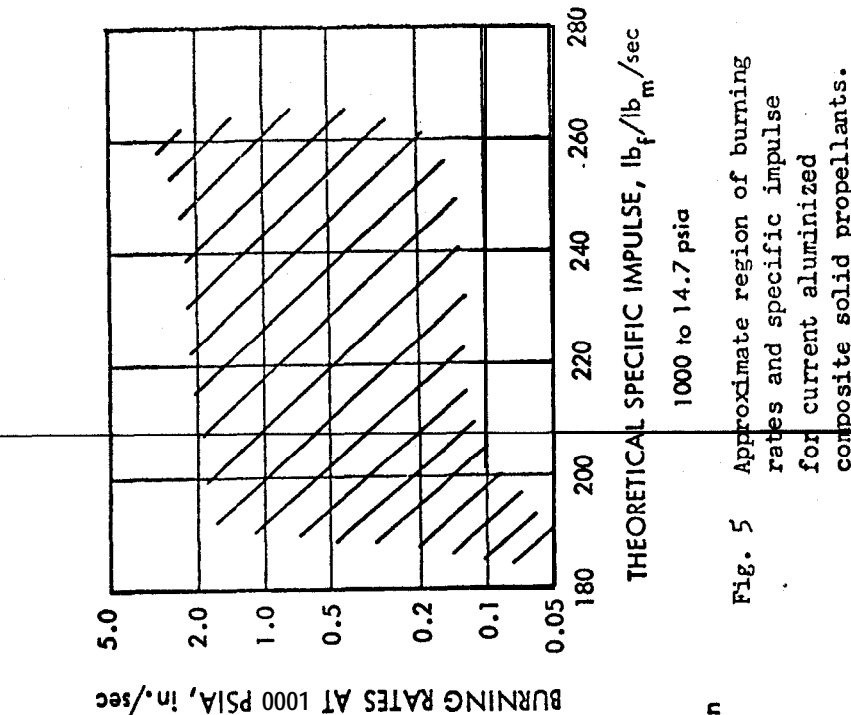


Fig. 5 Approximate region of burning rates and specific impulse for current aluminized composite solid propellants.
1000 to 14.7 psia

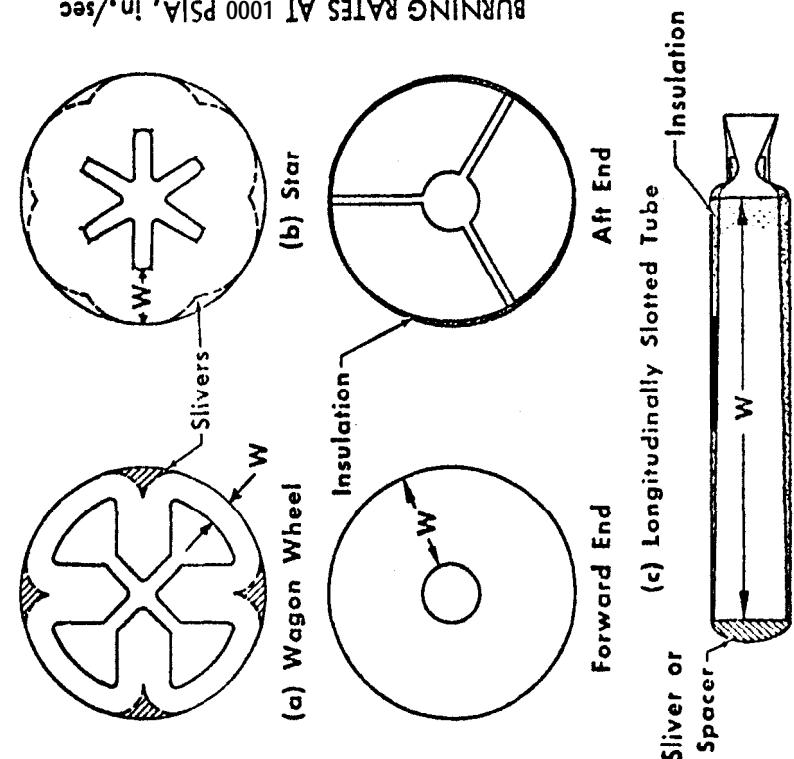


Fig. 4 Representative grain geometries of solid-propellant rockets.

burning surface) configurations are given in Table 1. Wagon-wheel or star-grain designs are best for short-duration boost charges. The slotted tube with a slow burning-rate propellant can be used for comparatively short-duration sustainer thrust. End burners are the choice for long duration, although they produce maximum excursion of the vehicle's center of gravity.

Table 1 - Characteristics of representative grain geometries

Grain type	Web fraction (W/R)	Cross-sectional loading, %	Remarks
Wagon wheel	0.1 - 0.3	40 - 70	Thinnest web for shortest burn times; gives slivers
Star	0.25- 0.5	50 - 95	Suitable for booster or short-duration sustainer; gives slivers
Slotted tube	0.3 - 0.8	50 - 96	Has maximum web thickness for inter- nal burner; requires insulation <u>under</u> slots.
End burner	1 - 20	100 ^a	Suitable for sus- tainer <u>only</u> ; requires insulation

Solid Propellants

A wide variety of solid propellants is currently available with various combinations of burning rates, specific impulses, densities, etc. For simplification, only three propellant ~~types~~ are considered here. As given in Table 2, they include 1) aluminized ammonium perchlorate composite propellants with various polybutadiene, polyurethane, or double-base binders plus suitable burning rate catalysts; 2) "high-density" propellants with heavy metal additives, as tungsten or zirconium, and ammonium perchlorate, all-in polybutadiene binders; and 3) ammonium nitrate and/or ammonium perchlorate with hydrocarbon binders, with or without aluminum.

^aEffective loading of end burner is less than 100% due to peripheral insulation.

Of these, the aluminized composites give highest specific impulses and now offer an extremely wide range of burning rates. This is shown in Fig. 5, which plots approximate burning rates available at various specific impulse levels. The high-density propellants, as seen in Table 2, have the highest theoretical "density impulse" ($I_{sp} \cdot \rho_p^n$). This is of greater importance underwater than in above-water rockets, since for the latter $I_{sp} \cdot \rho_p^n$ with n less than unity is a better performance criterion. Composite propellants with appreciable proportions of ammonium nitrate have the lowest burning rates and so permit the longer burning times that could be of special advantage in an internal-burning configuration.

Table Approximate properties of several solid propellants

Propellant type	Aluminized composite ^a	HDP ^b	CH/AP/AN/ALC ^c
Burning rates in./sec at 1000 psi'	0.2 - 3.0	0.25 - 0.5	0.05 - 0.1
Burning rate exponent	0.2 - 0.7	0.15 - 0.35	0.5 - 0.6
Specific impulse (theoretical)... 1bf/lbm/sec, 1000/14.7 psia	260 - 267	225 - 235	170 - 200
Density, lb/in. ³	0.062 - 0.064	0.070 - 0.066	0.053 - 0.056
Combustion temperature, °F	5200 - 6000	5200 - 6100	2000 - 3500
Density impulse ($I_{sp} \cdot \rho_p^n$, theo.), g - sec/cm ³	440 - 470	450 - 540	250 - 300

^aPropellants with ammonium perchlorate and a polybutadiene, polyurethane, or double-base binder.

^bHDP = high-density propellants with a heavy metal, ammonium perchlorate, and a hydrocarbon binder.

^cPropellants with ammonium nitrate, with or without ammonium perchlorate and aluminum, and a hydrocarbon binder.

To compare underwater rocket performances using these propellants and to show the flexibility afforded by modulating propellant burning rates, both end-burning and internal-burning (slotted tube) grain configurations were considered in vehicles with the external configurations shown in Figs. 6 and 7 for a 6-in.-diam rocket, vehicle I, and a 10-in.-diam rocket, vehicle II, respectively. Vehicle speeds and ranges were calculated over the approximate spectrum of burning rates for each propellant type. A constant insulation thickness of 0.25 in. was used for end burners and 0.050 in. for internal burners. For the latter, all internal port diameters were taken at 0.2 times the grain diameter. The calculations were made with fixed thrust coefficient and for expansion from 2000 psia chamber pressure to 103.5 psia, the depth pressure at 200 ft. Propellant specific impulse values were 92% of the midpoint of the range of theoretical values of Table- 2.

Results of the calculations are gathered as range vs speed in Fig. 8 for the 6-in.-diam vehicle and in Fig. 9 for the 10-in. They show a slight performance advantage of the high-density propellant over the more conventional aluminized composite, at-risk the wide versatility in speed and range available from the latter. Further shown is a restricted area of usefulness for ammonium nitrate propellants • to attain 80 knots in a 10-in.-diam vehicle with an internal burner.

Vehicle Examples

To summarize the analysis, the conceptual preliminary designs for the two underwater, solid-rocket propelled vehicles, shown in Fig. 6 for the 6 in.-diam vehicle and Fig. 7 for the 10-in.-diam, were further analyzed. The former was designed as an end-burning rocket at 100 knots and 200-ft depth with both booster and sustainer chamber pressures of 2000 psia, and the latter as an internal burning rocket at 200 knots and 1000-ft depth with chamber pressure of 3000 psia. The calculations were made without considering vehicle stability or control. Drag coefficients were estimated from Ref. 2. No attempt was made to optimize chamber pressure, body shape, etc. The nozzle expansion ratio properly expanded the combustion gases to the depth pressures in each case.

The calculated weight and performance values are given in Tables 3 and 4. They are rough estimates to illustrate the order-of-magnitude capabilities of the two high-speed underwater missiles. They also illustrate the need to change from end burner to internal burner with increasing diameter and to increase chamber pressure with increasing depth.

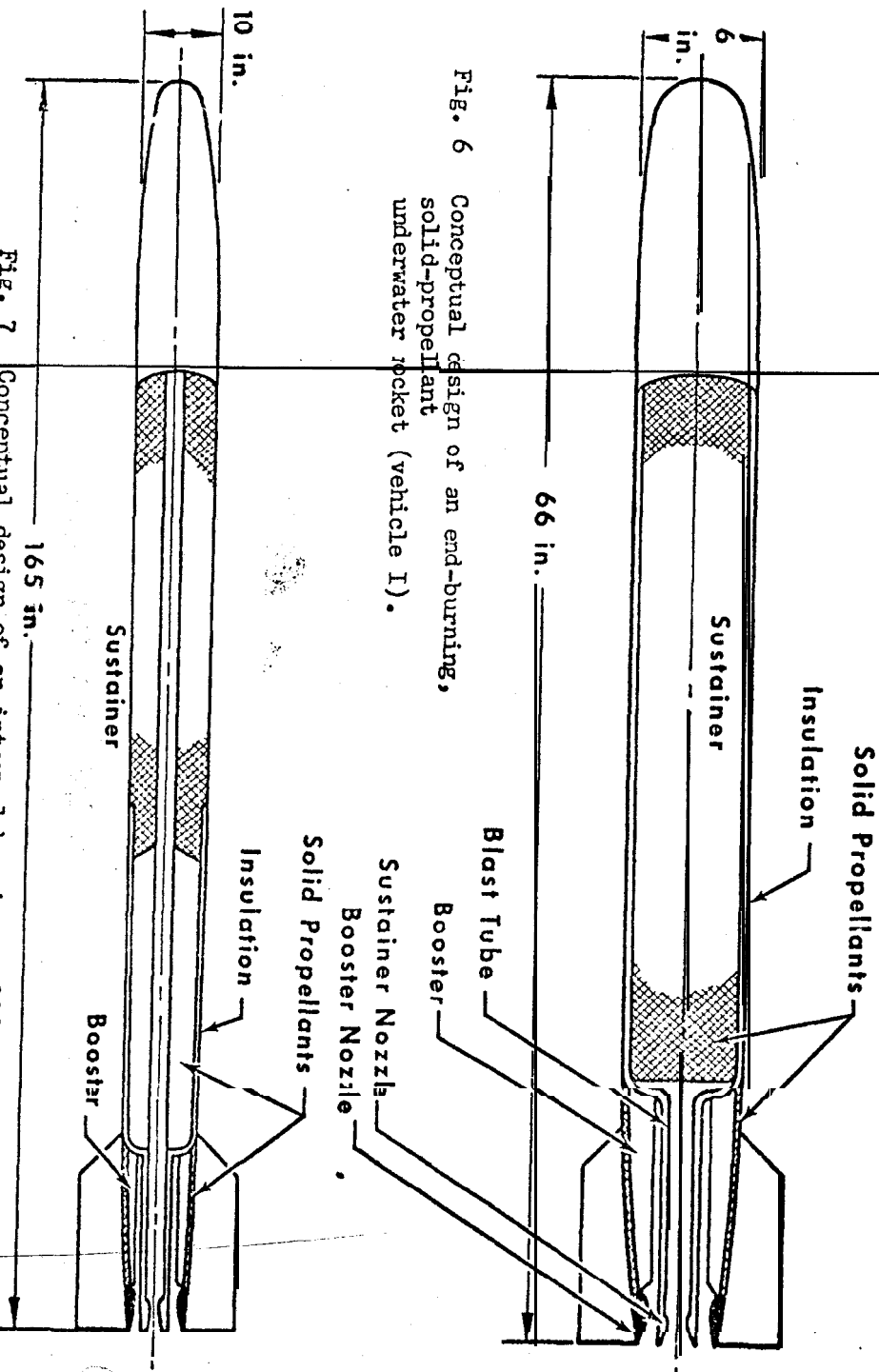


Table 3 - Characteristics of a 6-in.-diam, endburning underwater rocket (Vehicle I)

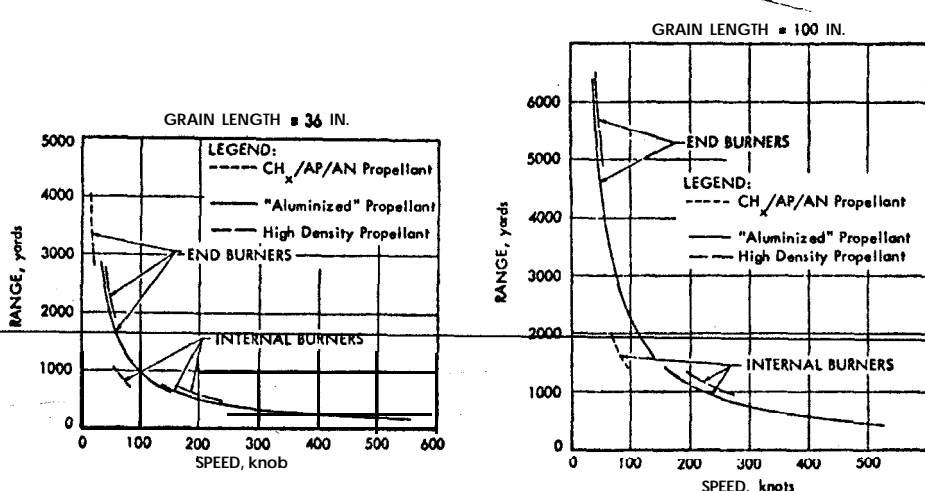


Fig. 8 Calculated range vs speed for three solid propellants; vehicle I at 200-ft depth.

Fig. 9 Calculated range vs speed for three solid propellants; vehicle II at 200-ft depth.

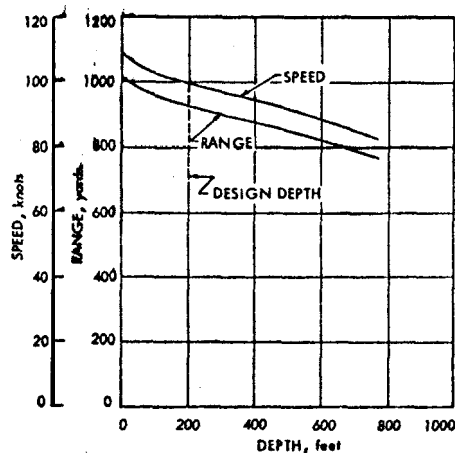


Fig. 10 Estimated performance variations with depth, vehicle I.

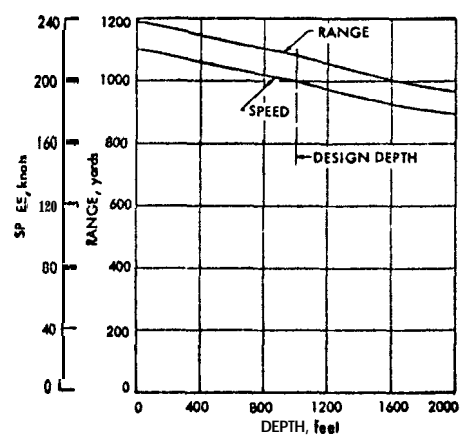


Fig. 11 Estimated performance variation with depth, vehicle II.

Assumed value:	Calculated values
Drag coefficient: 0.12	Range: 930 yds
Chamber pressures: 2000 psia	Propellant weights:
Design depth: 200 ft	Boost: 36 lb
Propellant characteristics:	Sustain: 567 lb
Type: Aluminized composite	Total vehicle weight: 145 lb
I_{sp} : 212 sec	Burning time: 16.5 sec
$\rho = .063$ lb/in. ³	Vehicle Buoyancy: 65 lb
Vehicle speed: 100 knots	

Table 4 - Characteristics of a 10-in.-diam, internal burning underwater rocket (Vehicle II)

Assumed values:	Calculated values
Drag coefficient: 0.15	Range: 1080 yds
Chamber pressures: 3000 psia	Propellant weights:
Design depth: 1000 ft	Boost: 94 lb
Propellant characteristics:	Sustain: 590 lb
Type: High-density composite	Total vehicle weight: 1360 lb
I_{sp} : 151 sec	Burning time: 9.7 sec
$\rho = .086$ lb/in. ³	Vehicle Buoyancy: 460 lb
Vehicle speed: 200 knots	

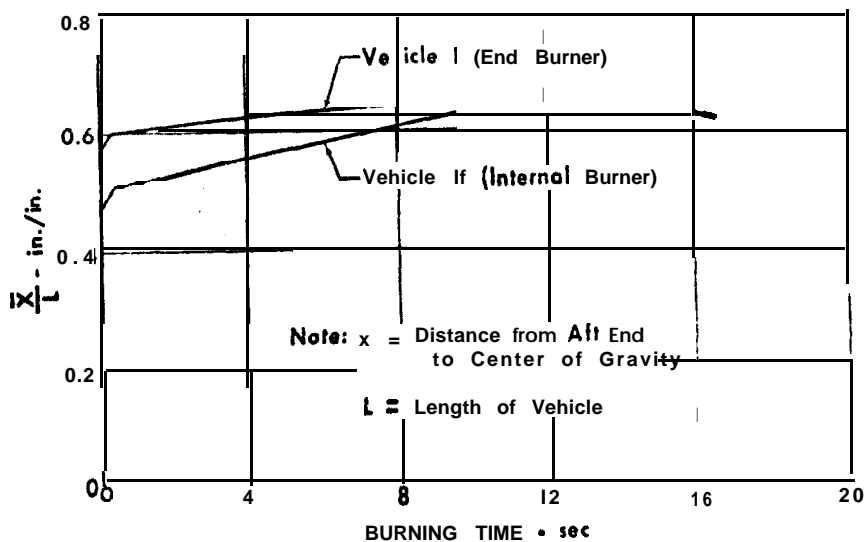


Fig. 12 Estimated center of gravity travel during burning.

Since the two vehicles are capable of operating at depths other than the design values, their performances at other depths were also computed and plotted in Figs. 10 and 11. Although performance diminishes with depth, the effects apparently are not extreme over moderate depth changes.

Finally, estimated variations in the center-of-gravity locations for the two vehicles are plotted in Fig. 12. The short jog in these curves at start-up shows the shift in c.g. during boost. The curves show, respectively, the typical humped variations of an end-burner and the linear shift of an internal burner.

Conclusions

Propellant densities and specific impulse values are about equally important in underwater rocket applications. Current high burning rates of aluminized composite propellants make them attractive as end-burning grains, whereas low burning rate propellants should have slotted-tube grain configurations and be used in comparatively short-burning missiles. High-density-impulse propellants offer a performance advantage over aluminized composites in underwater rockets. However, unless compositions with a wide variety of burning rates are established, they will be less generally useful than the aluminized propellants. Thin web grain designs, such as the internal burning star, are suitable only for very short burning times and therefore primarily as boosters.

References

¹Seifert, H. S. and Crum, J., "Thrust coefficient and expansion ratio tables," Space Technology Labs., Los Angeles, Calif. (February 1956).

²Hoerner, S. F., Fluid-Dynamic Drag (published by the author, 1958).

EFFECT OF STAGING ON THE RANGE OF UNDERWATER ROCKETS

William C. Ragsdale*

U. S. Naval Ordnance Laboratory
White Oak, Silver Spring, Md.

Abstract

A simple relation is derived for computing the range of a solid-propellant multistage underwater rocket. The rocket is assumed to consist of identical stages designed to give constant vehicle velocity and is assumed to travel horizontally. A comparison of the range of two and three-stage rockets is given.

Nomenclature

A	■ total wetted surface area of vehicle, ft^2
C_D	■ drag coefficient, dimensionless
D	■ diameter of vehicle, ft
F	■ drag force acting on vehicle, lbf
g_c	■ conversion factor, 32.2 $\text{lbf}\cdot\text{ft}/\text{lbf}\cdot\text{sec}^2$
I_{sp}	■ specific impulse of rocket motor, $\text{lbf}\cdot\text{sec}/\text{lbf}$
L	■ overall length of vehicle, ft
AL	■ combined length of propellant grain and rocket nozzle for single-stage rockets, ft
AL'	■ length of propellant grain plus nozzle for multistage rockets, ft
n	■ number of stages
N	■ length of rocket nozzle, ft
P	■ length of payload section, ft
R_1	■ range of a single-stage rocket ft
(R_1)	■ maximum possible range for a single-stage rocket, ft
R_{\max}	■ range of a rocket with n stages, ft
T	■ thrust of rocket motor, lbf
v	■ vehicle velocity, fps

* Aerospace Engineer, Applied Aerodynamics Division

w_p	= mass of propellant, lbm
α	= payload fraction, dimensionless
β	= nozzle fraction, dimensionless
θ	= burning time of rocket, sec
ρ	= density of water, lbm/ft^3
ρ_p	= propellant density, lbm/ft^3

Introduction

The forces acting on an underwater rocket are the thrust of the rocket motor, the weight and drag of the vehicle, and the buoyant force. Because of the relatively high density of **water**, the drag force is much larger for underwater rockets than for rockets operating in the atmosphere. As a result, underwater rockets usually travel at a terminal velocity, in contrast to atmospheric rockets, which accelerate during burning and coast after burnout.

The total drag of slender bodies (such as torpedoes) traveling underwater consists almost entirely of skin friction drag and, for this reason, is directly proportional to the total wetted surface area. It is this fact that makes staging an attractive proposition for underwater rockets--under certain conditions. Underwater rockets are inherently inefficient, and as a result, most of the vehicle volume is usually taken up by the propellant. As propellant is consumed, a progressively larger portion of the vehicle becomes an empty shell, contributing nothing to the thrust of the rocket but contributing significantly to the drag of the vehicle. By dividing the rocket into several stages, each having its own nozzle and propellant supply, the spent portions of the rocket may be discarded and the range and velocity of the vehicle increased accordingly.

The effect of one method of staging on the range of underwater rockets is considered in this paper. None of the practical problems of staging are considered.

Analysis

In order to obtain simple relations for estimating the effect of various parameters and staging on the range of underwater rockets, the following assumptions are made:

- 1) Only solid-propellant rockets are considered.
- 2) The rocket travels in a horizontal path. This

implies that the effects of buoyancy and weight on the trajectory are neglected.

- 3) The rocket quickly reaches a constant terminal velocity where thrust is equal to hydrodynamic drag.
- 4) In computing range, periods of rocket acceleration and deceleration are neglected. The range is taken as the product of the terminal velocity and the burning time,
- 5) The specific impulse is constant.
- 6) The drag force acting on the vehicle is assumed proportional to the total wetted surface area.

The assumption of constant vehicle velocity implies, in the case of a single-stage rocket, a constant chamber pressure if the rocket is traveling horizontally (assumption 2).

In order to achieve constant vehicle velocity with a multi-stage rocket, it is necessary to vary thrust between stages. Following assumption 5, this can be accomplished by operating each stage at the same chamber pressure and using in each stage propellant having the same specific impulse but different burning rate characteristics. Under these conditions, variation in thrust is due to variation in the mass discharge rate of the propellant from stage to stage.

Single-Stage Rockets

The following additional assumptions are made regarding the single-stage underwater rocket:

- 1) The vehicle is assumed to be made up of a cylindrical payload section, a cylindrical propellant grain, and a cylindrical nozzle section, as illustrated in Fig. 1.
- 2) The total wetted area is taken to be the lateral area of the cylindrical vehicle,

The thrust of the single-stage rocket illustrated in Fig. 1 is given by the following:

$$T = I_{sp} \frac{w_p}{\theta} = I_{sp} \frac{\pi}{4} D^2 \left[\Delta L - N \frac{\rho_p}{\theta} \right] \\ = I_{sp} \frac{\pi}{4} D^3 \left[\frac{\Delta L}{D} - \frac{N}{D} \right] \frac{\rho_p}{\theta} \quad (1)$$

† At a particular chamber pressure, ambient pressure, and nozzle expansion ratio.

The dray, force acting on the vehicle is given by the following (assumption 6):

$$F = AC_D \frac{\rho v^2}{2g_c} = \pi DLC_D \frac{\rho v^2}{2g_c} = \pi D \left[\Delta L + P \right] C_D \frac{\rho v^2}{2g_c}$$

$$= \pi D^2 \left[\frac{\Delta L}{D} + \frac{P}{D} \right] C_D \frac{\rho v^2}{2g_c} \quad (2)$$

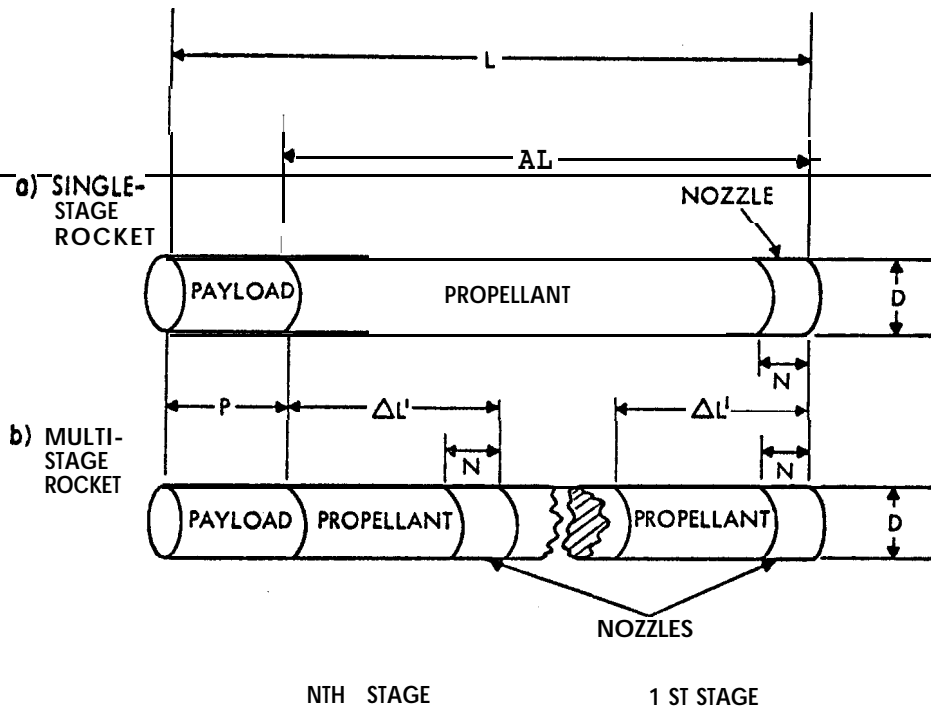


Fig. 1 Idealized underwater rocket configurations. In the comparisons made in this paper, D , L , N , and P are the same for the rockets compared.

Combining Eqs. (1) and (2) and using assumptions 3 and 4 leads to the following approximate expression for the range, R_1 , of a single-stage underwater rocket :

$$\frac{R_1}{D} = \left[\frac{g_c I_{sp}}{2C_D V} \right] \left[\frac{\rho_p}{\rho} \right] \left[\frac{1 - \beta}{1 + \alpha} \right] \quad (3)$$

where

$$\alpha = \frac{P/D}{L/D - P/D} = \frac{P/D}{\Delta L/D}$$

$$\beta = \frac{N/D}{L/D - P/D} = \frac{N/D}{\Delta L/D}$$

The maximum possible range of a single-stage rocket for given values of I_{sp} , ρ_p , C_D , D , and V would occur when $\alpha = 0$ and $\beta = 0$. This corresponds to a hypothetical rocket made up entirely of propellant. Expressing the range in terms of the maximum possible value gives

$$\frac{R_1}{(R_1)_{max}} = \frac{1 - \beta}{1 + \alpha} \quad (4)$$

where

$$(R_1)_{max} = \text{maximum possible range for a single-stage rocket} = D \left[\frac{g_c I_{sp}}{2C_D V} \right] \left[\frac{\rho_p}{\rho} \right] \text{ ft}$$

because of their approximate nature, Eqs. (3) and (4) are more useful as scaling rules to estimate the effect of α and β on range than as relations for determining the **actual** range of single-stage underwater rockets,

Multistage Rockets

The following additional assumptions are made regarding multistage underwater rockets:

- 1) The vehicle is assumed to be made up of **a** cylindrical payload section and a number of identical stages, each consisting of a cylindrical propellant grain and a cylindrical nozzle section, as illustrated in Fig. 1b.
- 2) The stages are assumed to be discarded as soon as they are completely burned.

The range of the multistage underwater rocket is determined by summing the **increments** of range obtained by burning each stage. Following the same procedure as for the single-stage rocket leads to the following:

$$\frac{R_n}{D} = \left[\frac{g_c I_{sp}}{2C_D V} \right] \left[\frac{\rho_p}{\rho} \right] \left[\frac{\Delta L' - N}{D} + \frac{\Delta L' - N}{D} + \dots + \frac{\Delta L' - N}{D} + \frac{\Delta L' - N}{D} \right] + \dots + \left[\frac{\Delta L' - N}{D} + \frac{\Delta L' - N}{D} \right] \quad (5)$$

or

$$\frac{R_n}{(R_1)_{\max}} = (1 - n\beta) \left\{ \frac{1}{n(1+\alpha)} + \frac{1}{n(1+\alpha)} - 1 + \dots + \frac{1}{n(1+\alpha)} - (n-1) \right\} \quad (6)$$

where

$$\alpha = \frac{P/D}{L/D - P/D} = \frac{P/D}{n\Delta L'/D}$$

$$\beta = \frac{N/D}{L/D - P/D} = \frac{N/D}{n\Delta L'/D}$$

Equations (4) and (6) may be used to **compare** the range of multistage rockets with the range of single-stage rockets. It should be pointed out that such comparisons are restricted by the assumptions made in deriving Eqs. (4) and (6). It is important to remember that only one method of staging has been considered, i.e., identical stages designed to give **a** constant vehicle velocity.

Two additional assumptions will now be made:

- 1) The single-stage and multistage rockets compared have the **same** value of α and β , i.e., the same values of D , L , N , and P . Figure 1 illustrates this assumption.
- 2) The rockets compared have the same values of I_{sp} , C_D , and ρ_p .

Combining Eqs. (4) and (6) with these assumptions gives

$$\frac{R_n}{R_1} = \frac{1 - n\beta}{1 - \beta} \left\{ \frac{1}{n} + \frac{1}{n - [1/(1 + \alpha)]} + \dots + \frac{1}{n - [(n-1)/(1 + \alpha)]} \right\} \quad (7)$$

Results and Discussion

Values of R_n/R_1 for two-stage and three-stage underwater rockets were calculated using Eq. (7) and are shown in Fig. 2. These results show that the effect of staging on range becomes greater as either α or β is decreased. In other words, staging becomes more effective in increasing the range of an underwater rocket when the payload and nozzle sections make up a

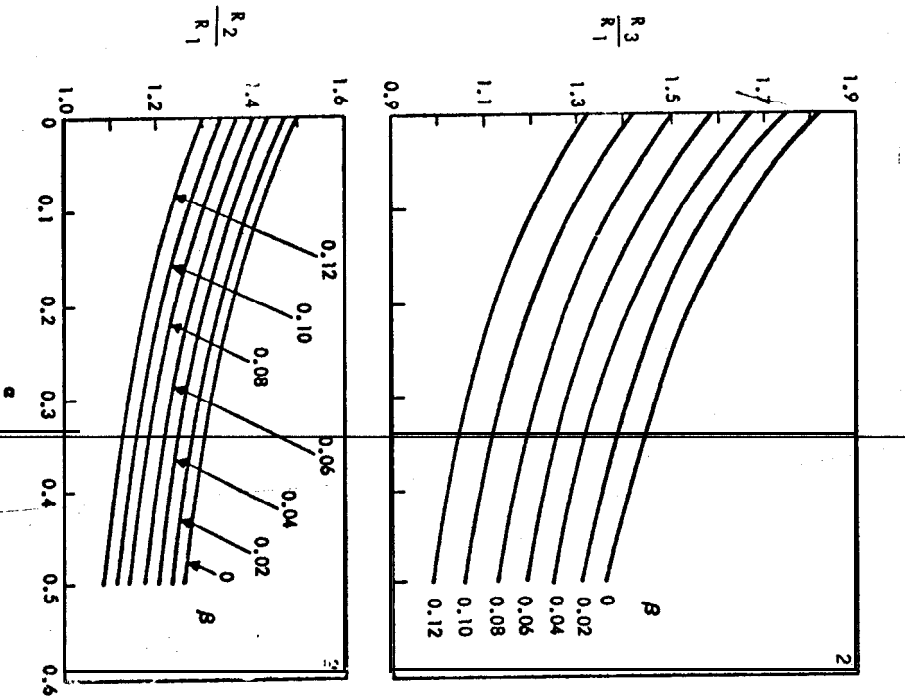


Fig. 2 (left) Comparison of range of two-stage and three-stage underwater rockets with range of similar single-stage rockets.

Fig. 3 (above) Comparison of range of two-stage and three-stage underwater rockets.

small portion of the vehicle. Thus, when α and β are zero, the effects of staging are greatest. Using these limiting conditions, the results show that the range of underwater rockets, under the assumptions made, could be increased by not more than about 50% if two stages were used instead of one and by not more than about 83% if three stages were used,

For large values of α and β the effects of staging are reduced and may actually be adverse. For example, when $\alpha = 0.5$ and $\beta = 0.12$, the range of a two-stage rocket is only 8% larger than a single-stage vehicle, and the range of a three-stage rocket is actually 1% smaller. This is because as the number of stages is increased some propellant must be sacrificed ~~in order to make room for the additional exhaust nozzles~~ required. This effect finally offsets the beneficial drag reduction effect as the number of stages is increased.

The range of two-stage and three-stage rockets is compared in Fig. 3. It can be seen that, over a wide range of values of α and β , the range of three-stage rockets is only slightly larger than that of two-stage rockets and is smaller than the range of two-stage rockets at large values of α and β . Hence, it appears that underwater rockets of three stages or more would be of little practical value.

In this paper, none of the practical problems of underwater rocket staging have been considered, such as stage ignition and separation. A highly idealized situation has been assumed in order to estimate the maximum possible effect of staging on the range of underwater rockets. The increases in range actually realized with a multistage rocket would probably be somewhat smaller than those estimated here.

Only one method of staging has been considered: equal-length stages designed to give a constant vehicle velocity. Many other methods of staging can be imagined, involving stages of different lengths designed to give different vehicle velocities. No attempt has been made to determine the optimum method of staging.

Conclusion

Under the assumptions made here, the following conclusions can be drawn concerning the effect of staging on the range of underwater rockets :

- 1) The range of underwater rockets can be increased by not more than 50% by using two stages instead of one and by not more than 83% by using three stages,

- 2) Staging is effective in increasing the range of under-water rockets only when the payload section and nozzle sections make up **a small portion of** the vehicle.
- 3) Staging **has an adverse effect on range when the nozzle and payload sections make up a large portion of the vehicle.**
- 4) Underwater rockets having more than two stages would be of little practical value,

UNDERWATER **MISSILE** DRAG

SIMPLIFIED METHODS FOR ESTIMATING TORPEDO DRAG

John D. Brooks* and Thomas G. Lang†

Naval Undersea Warfare Center, Pasadena, Calif.

Abs tract

From drag data for a large number of tests of bodies of revolution with and without appendages, semiempirical relations were developed and theory tally-extended. The results, in graphical form, show the variation of drag coefficient with tail shape, nose shape, and cylinder-section length for stably running torpedo configurations with constant volume and velocity. From them, methods are developed for selecting the optimum torpedo configuration with minimum drag for any given set of design specifications. In addition, a method is presented for quick calculation of the drag of a torpedo with arbitrary fin size, roughness, holes, tail cutoff, volume, and velocity.

Nomenclature

- A = cross-sectional area of torpedo, ft^2
 a, b, c = fin dimensions shown in Fig. 13, ft
 C_f = skin-friction drag coefficient = skin-friction drag (1b)/ $q_0 S$
 C_{D_s} = total drag coefficient based on surface area
= total drag (1b)/ $q_0 S$
 $C_{D_s f}$ = fin drag coefficient based on fin surface area
= fin drag (1b)/ $q_0 S_f$
 C_{D_A} = total drag coefficient based on cross-sectional area = total drag (1b)/ $q_0 A$
 $C_{D_{\text{parasite}}}$ = parasite drag coefficient based on cross-sectional area = parasite drag (1b)/ $q_0 A$
 $C_{D_A R}$ = roughness drag coefficient based on cross-sectional area
 C_{D_V} = total drag coefficient based on volume = total drag (1b)/ $q_0 (V)^{2/3}$

*Physicist, Underwater Ordnance Department.

†Research Mechanical Engineer, Underwater Ordnance Department.

$C_{D_{A_c}}$	= drag coefficient from truncated tail cone , based on cross-sectional area
C_p	= prismatic coefficient = $\frac{V}{(\pi/4 d^2)}$
C_τ	= residual or form drag coefficient based on surface area = residual drag (lb)/$q_0 S$
d	= maximum diameter of torpedo, ft
d_B	= diameter of truncation on tail cone, ft
D	= drag, lb
D_f	= fin drag, lb
DR	= roughness drag, lb
ΔC_{D_S}	= added drag coefficient of fins caused by boundary-layer interference, Fig. 14, due to
$\Delta C_{D_S f}$	= boundary-layer interference (lb)/ $q_0 S_{\text{fins}}$
$C_{D_{S_R}}$	= added drag coefficient of torpedo from holes and roughness = added drag due to roughness and holes (lb)/ $q_0 S$
L'_{β_t}	= tail lift coefficient based on cross-sectional area
β_t	= tail lift (lb)/ $q_0 A \beta$
l^{*t}	= length of the torpedo tail cone , measured to the extended tip, ft
l	= torpedo length, ft
l^{*}	= torpedo length, measured to the extended tail cone tip, ft
l/d	= body fineness ratio
$\Delta l_c/d$	= nose-shape correction factor (from Fig. 6)
m	= ratio of the position of maximum thickness from nose to the over-all length of streamlined body
$\Delta p/q_0$	= change in the static pressure ratio on a body
$\Delta q/q_0$	= change in the dynamic pressure ratio on a body along the chord length of the fins
q	= dynamic pressure, psf, = $1/2 \rho V^2$
q_0	= freestream dynamic pressure, psf, = $1/2 \rho V_0^2$
R_f	= Reynolds number based on over-all length = $V_0 l / \nu$
r_f	= local radius of the body at the fin midchord, ft
r_w	= local radius of the body, ft
S	= surface area, ft^2
t	= thickness of a fin, ft
V	= torpedo body volume, ft^3
V	= local velocity, fps
V_0	= freestream velocity, fps
α	= angle between tangent to surface and axis of the body
β	= angle of attack of the body, rnd
δ	= thickness of the boundary layer, ft
θ	= momentum thickness of the boundary layer, ft,
$= \int_0^\delta \left(1 - \frac{V}{V_0}\right) \frac{V}{V_0} d\delta$	

Ω = momentum area of the boundary layer, ft^2 ,

$$= \int_0^\delta \left(1 - \frac{V}{V_0}\right) \frac{V}{V_0} r_w d\delta$$

ν = kinematic viscosity of the fluid, ft^2/sec

Subscripts

b = the longitudinal station **located at the forward end of the cylindrical midsection**

c = the cylindrical midsection

e = the longitudinal station **at the after end of the cylindrical midsection**

F = the forebody of a streamlined shape such as the DTMB series 58

N = any arbitrary nose shape

0 = drag coefficients, Reynolds numbers, etc., **of a specific configuration**

T = the tail section of a streamlined shape such as the DTMB series 58

introduction

Modern undersea warfare **requires** small and compact **torpedoes** with high **speed**, long range, and great maneuverability. To achieve this, the external hydrodynamic shape of the torpedo must be optimized, and it is desirable to use a body form and stabilizing fins with the least drag for its volume.

Theoretical methods, employing boundary-layer theory, are available for estimating torpedo drag, but such computations of ten are prohibitively time-consuming. Also, much of the experimental data on drags of underwater body shapes have considerable scatter. Consequently, the common method for quickly estimating drag of a torpedo consists, first, of calculating the skin friction of its body and fins through turbulent flat-plate drag coefficients and then adding a certain percent to account for body form drag and another percent to account for interference effects and fin-form drag. Refinements are seldom included for differences in nose shape, tail-cone shape, cylinder-section length, and fin size, or for variations in surface roughness and numbers of holes or protuberances.

A method is developed for quickly estimating torpedo drag as a function of these latter differences and variations, using generalized graphs. Other graphs are also included for estimating drags of optimum designs. Then, a modified procedure is given for quickly estimating the drag of any existing torpedo.

The analysis is both empirical and theoretical: an attempt is made to correlate previous experimental data on streamlined body shapes with theory, using additional data on the **effects** of body-shape variations and fin drag.

Drag of Streamlined Bodies

A large number of drag **tests were** conducted on streamlined bodies of revolution at zero angle of attack in incompressible flow, and the data correlated as next discussed. The total drag is composed of frictional and form types. Friction drag is the sum of the viscous shears in the boundary layer, and form drag is the result of the difference in integrated **pressure** over the nose and tail sections caused by the finite **thickness of the boundary layer as it streams off in the wake.**

This paper is concerned only with submerged body shapes over which the flow is fully turbulent and where no separation occurs, except possibly at the tail cone. Thus, data from many **water-** and wind-tunnel tests, which have been conducted at low Reynolds numbers, cannot be used, since some laminar flow is likely to **occur** at the nose. The latter is illustrated in Fig. 1 (Fig. 2 from Ref. 1) for measurements on a model in a Variable-density Wind tunnel. In the **transition** region $2 \times 10^6 < R_f < 2 \times 10^7$, there was considerable scatter, indicating laminar flow, whereas above $R_f = 2 \times 10^7$, there is little scatter, indicating turbulent flow.

The drag data used in this paper are the results of tests on **streamlined** bodies, with results as shown in Fig. 2. Here the skin friction in each instance, including the overvelocity effect, has been adjusted to a standard Reynolds number of 2×10^7 (the limit of the transition region), with the form drag kept constant. The wide scatter in the data results mainly from having tested in the transition region. Also, there are differences in test equipment and technique, in test-fluid nature and turbulence, in model roughness, and in strut interference. Consequently, a mean line was drawn through the points regarded as **most reliable**, as judged by the criteria in Table 1.

The tests at the David Taylor Model Basin (DTMB) are considered the most reliable. They were obtained in a water basin, in accord with the **statement of Hoerner³** that transition from laminar to **turbulent flow** occurs (for an unknown reason) at a lower Reynolds number in water than in air. They were conducted on bodies with fineness ratios of 4 and **larger**. Below this ratio, theoretical drag estimates were obtained from Ref. 2,

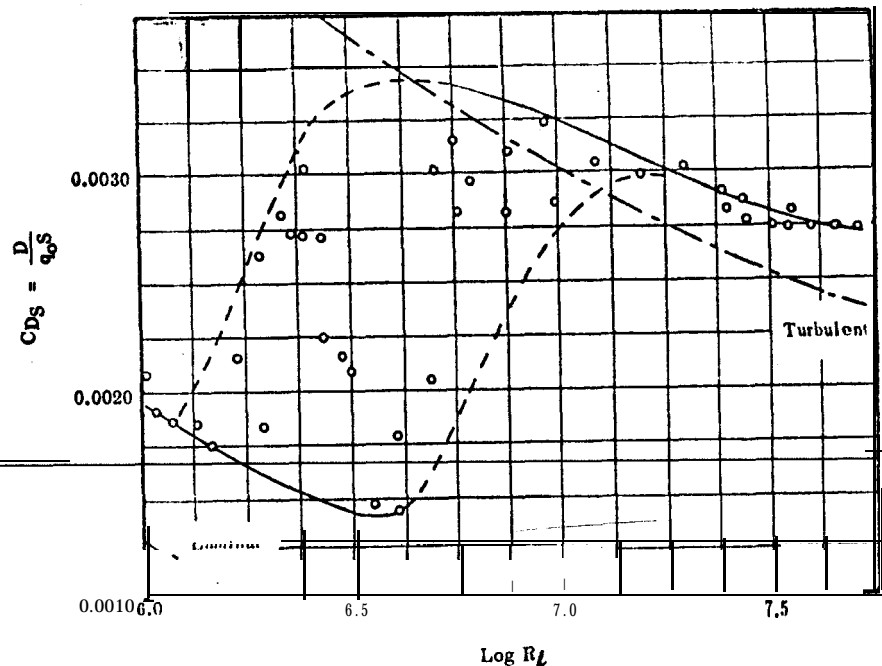


Fig. 1 Drag coefficient C_{D_s} vs Reynolds number R_f for a particular streamlined body in a variable-density wind tunne 1.

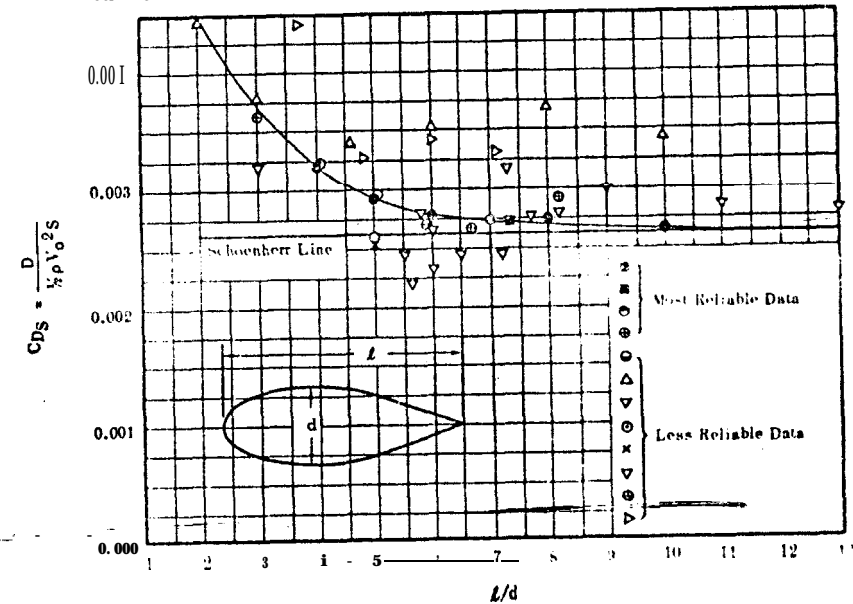


Fig. 2 Drag coefficient C_{D_s} vs fineness ratio l/d for streamlined bodies at R_f of 2×10^7 .

Table 1 Basic drag data^a

Symbol	Reference	Test R_e	Scatter of data	Turbulence stimulation	Type of tunnel	Support correction	
●	DTMB, Ref. 2	2×10^7	Small	Yes	Water	Small	
■	DTMB, Ref. 3	2×10^7	Small	Yes	Water	Small	
○	DTMB, Ref. 4	2×10^7	Small	Yes	Water	Small	
⊕	ARC, Ref. 5	...	Theoretical points for no separation				
○	NACA, Ref. 6	2×10^7	Medium	No	Air (variable density)	Medium	
△	NACA, Ref. 7	7×10^5 to 3.8×10^6	Large	No	Air	Large	
▽	ZWB, Ref. 8	5.4×10^6	Large	No	Air	Large	
○	SIT, Ref. 9	2.7×10^6	...	Yes	Water	Small	
×	NACA, Ref. 10	2.2×10^7	...	No	Air	Small	
▽	SIT, Ref. 11	7×10^6	Large	Yes	Water	Small	
⊕	Ref. 12	4.8×10^6	Large	No	Air (variable density)	Medium	
▷	NACA, Ref. 13	2×10^7	Large	No	Air (variable density)	Medium	

^a The data for the upper four symbols are the more reliable for the current application.

which agrees with data from the National Advisory Committee for Aeronautics (NACA) at a low Reynolds number.

All the drag data of Fig. 2 are for streamlined bodies of similar shapes. Reference 4 shows that small changes in the position of maximum body thickness and in prismatic coefficient* have only a small effect on drag. Consequently, the mean curve is considered valid for streamlined bodies in fully turbulent flow when the prismatic coefficient is approximately 0.6 and the position of maximum thickness is approximately 0.41 from the nose.

A graph of the skin-friction coefficient based on body surface area is plotted in Fig. 3 vs Reynolds number. It was

obtained from the Schoenherr turbulent skin-friction drag of a flat plate, corrected for overvelocity of free stream through theoretical calculations from Ref. 2. Figure 4 shows the form or residual drag coefficient based on body-surface area C_d , obtained by subtracting the drag coefficients of Fig. 3 from those of Fig. 2.

Drag of General Body Shapes

The effect on drag of changes in body shape and of the addition of appendages can be appreciated by considering a viscous boundary layer around the body on which is superimposed the ideal fluid pressure distribution. An increase in length of the cylindrical midsection will cause additional friction drag because of added shear in the boundary layer, and additional form drag because of thickness of the boundary layer at the tail. Also, any change in shape which affects the pressure distribution on the body, such as of the nose, cutoff tail cone, or stabilizing fins, can cause a corresponding effect in form drag; and any change in surface condition or roughness which influences the shear in the boundary layer can cause added friction drag. These effects are investigated in the following sections.

Cylindrical Section

Although the effect on drag of the addition of cylindrical midsections has been tested, results have been inconclusive, since they are usually made at diverse Reynolds numbers and require high strut-drag corrections. Analyses indicate that the best such data for torpedo bodies were those obtained at DTMB.⁵

* See Nomenclature for equation.

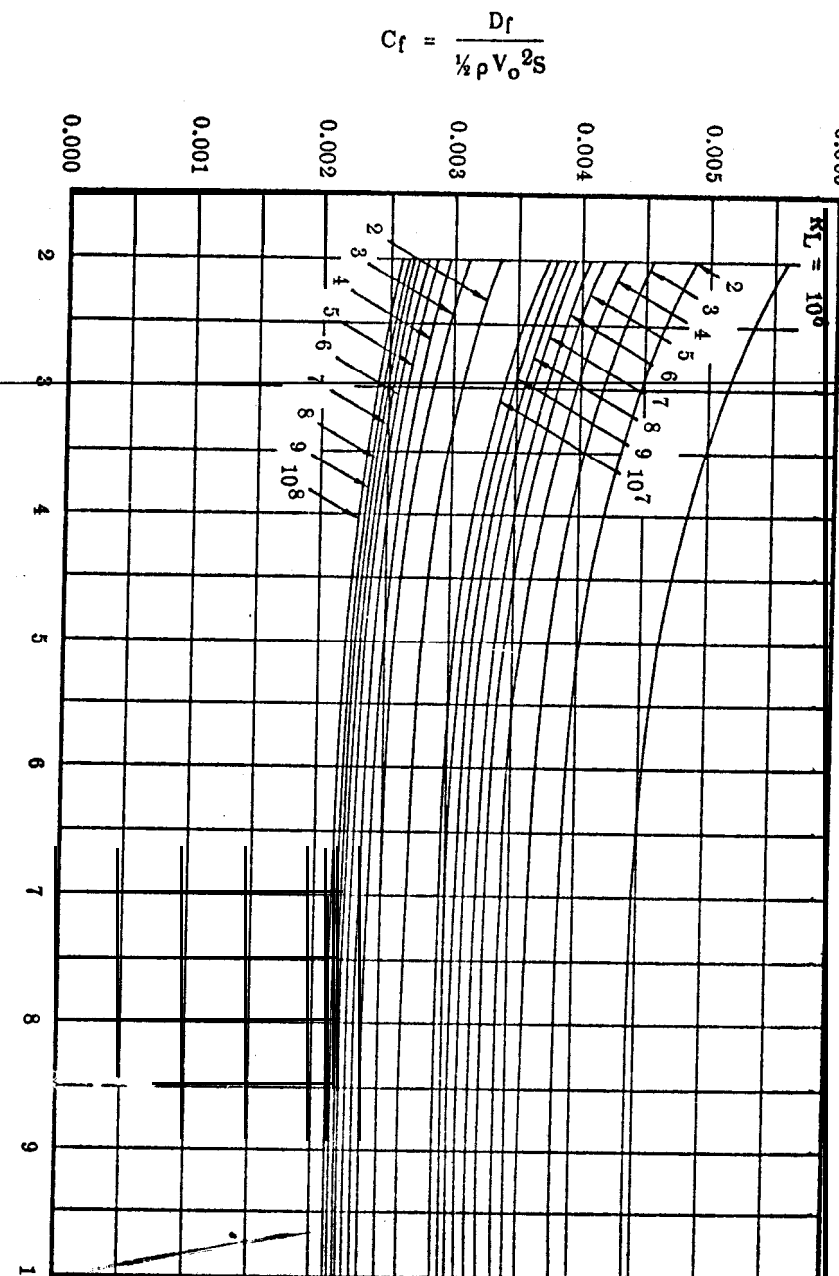


Fig. 3 Turbulent-skin friction coefficients C_f for streamlined bodies of revolution vs fineness ratio l/d .

A theoretical method⁶ for estimating the drag of a body of revolution, modified by the simplifying assumptions described in Appendix A, was used to calculate the added form drag resulting from the increased boundary-layer thickness over the cylindrical section. Results, combined with the tail-cone form drag of streamlined bodies, are given in Fig. 5 as the total drag coefficient of torpedo bodies based on body volume vs tail-cone shape and cylindrical-section length. They are in good agreement with the experimental results of Ref. 5. The theoretical cylindrical-section drag was also estimated for a particular range of Reynolds numbers, as described in Appendix A, but the increase in form drag from this source will probably remain reasonably independent of Reynolds number for torpedoes.

Nose Shape

A number of experimental tests on torpedo models with different nose sections led to the general conclusion that their form drag is independent of nose shape when separation does not occur on the nose section and the boundary layer is fully turbulent. This agrees with the postulate that the form drag of a nose section, which is attached to a very long body, is zero. Therefore, within the practical range of torpedo fineness ratios, the pressure distribution on the nose probably has negligible effect on the pressure distribution on the tail.⁴ Consequently, current nose sections of torpedoes can be considered to have purely frictional drag, and the total form drag can be considered to be a function of the tail-cone shape and the boundary-layer thickness at the tail cone.

Curves of drag coefficients are shown in Fig. 5 for a family of torpedoes with over-all fineness ratios 1.67 times their tail-cone fineness ratios. These curves can be used to estimate the drag of a torpedo of any nose shape, if separation does not occur, by including the nose-shape correction factors of Fig. 6. The latter, effectively, are changes in the cylindrical-section lengths that provide volumes that are equivalent in drag, to the actual torpedo noses plus the volumes of the cylindrical length, and so can be used in Fig. 5. Consequently, to use Fig. 5, the fineness ratio of the actual torpedo cylindrical section is changed by the amount indicated in Fig. 6. It is also assumed that noses with the same volume have approximately the same skin-friction drag, since, for example, the effect of overvelocity on a blunt nose is to increase the

⁶ For very short bodies, the form drag may be influenced by the nose shape.

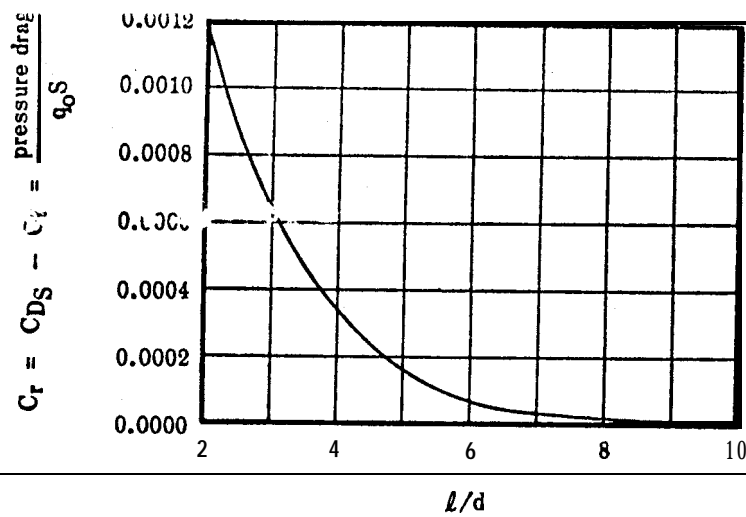


Fig. 4 Pressure drag coefficient C_r for streamlined bodies vs fineness ratio k/d .

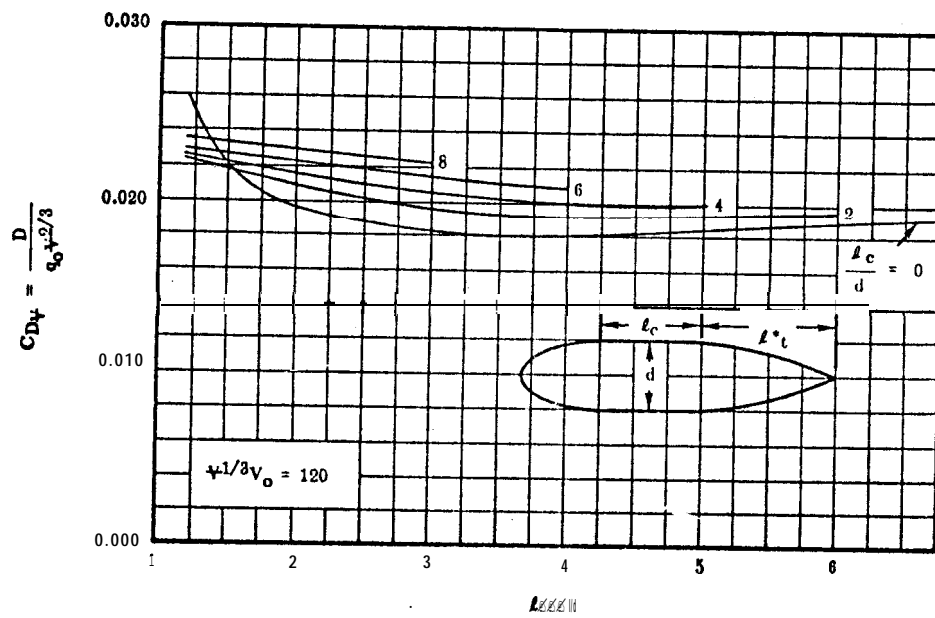


Fig. 5 Drag coefficient C_{D_V} based on volume for streamlined bodies with cylindrical sections vs tail cone fineness ratio $l^* t/d$. Parent tail-cone shape from DTMB series no. 58 for fully turbulent flow.

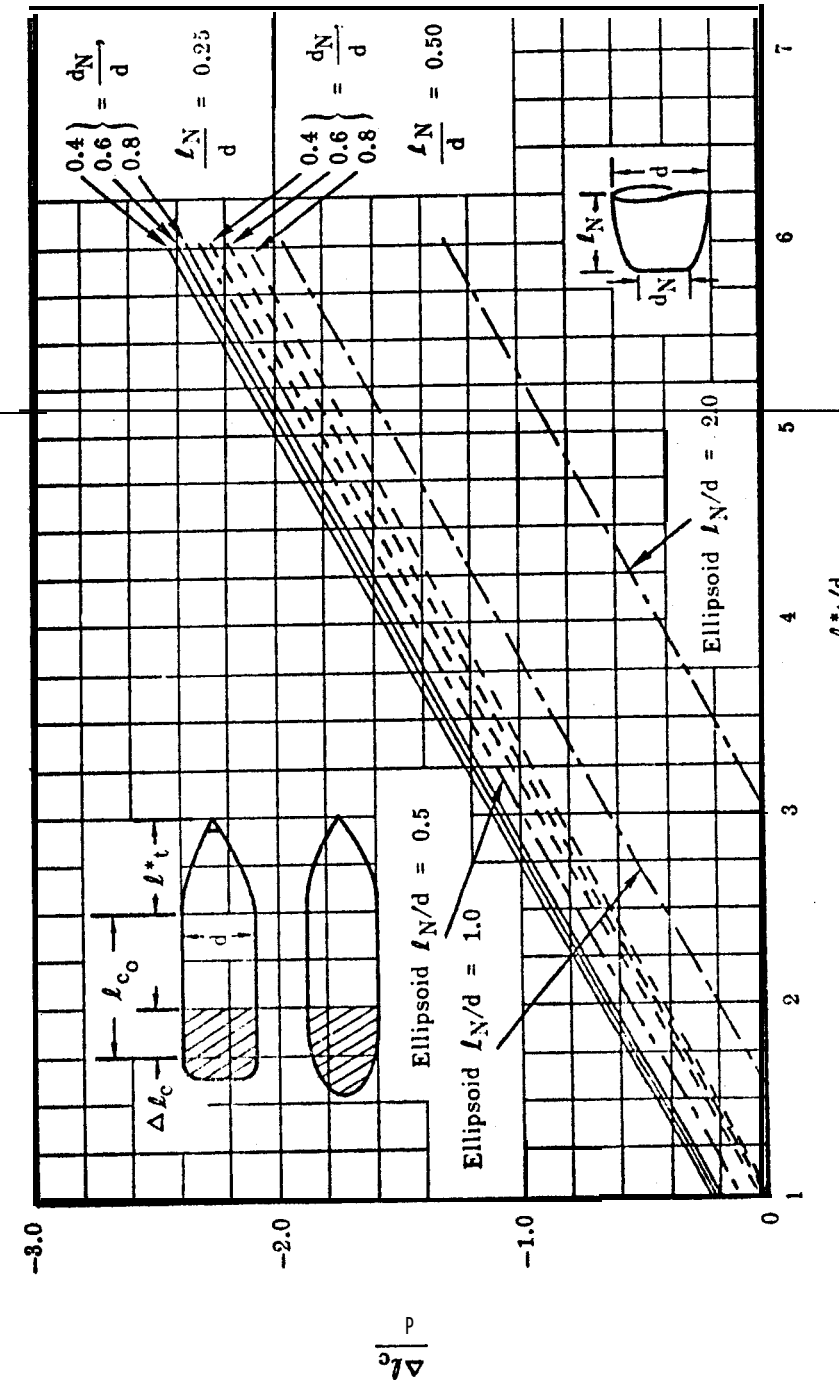


Fig. 6 Nose shape correction factor $\Delta l^*/d$ vs tail-cone fine-ness ratio l_N/d .

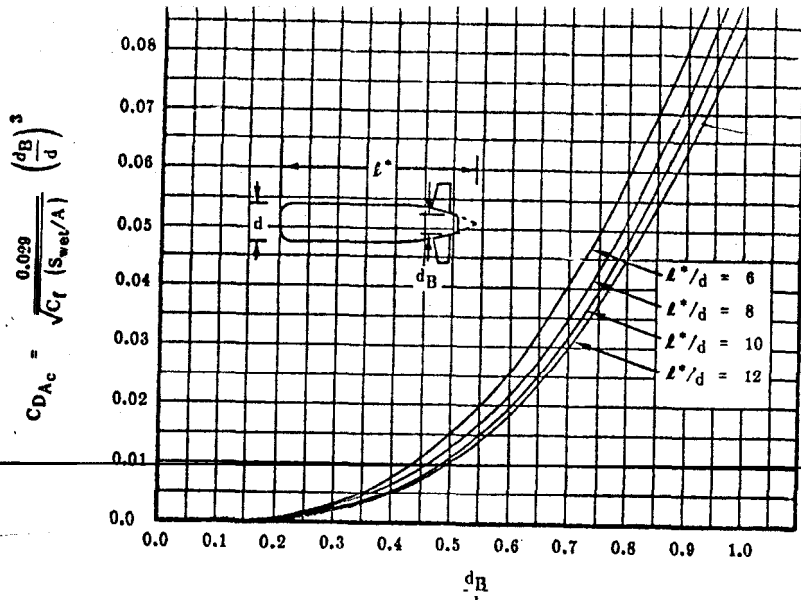


Fig. 7 Drag coefficient CD_{A_c} for truncated tail cone vs cutoff diameter ratio d_B/d for wetted surface coefficient approximately 0.8 and $R_l \approx 10^7$.

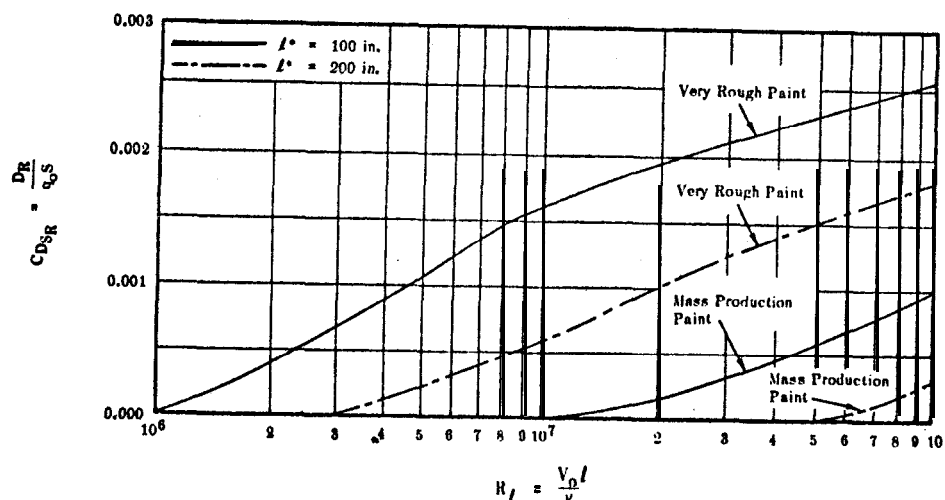


Fig. 8 Roughness coefficient CD_{SR} vs Reynolds number at various torpedo lengths, and surface finishes.

nose, drag, but this tends to be cancelled by its decreased surface area.

Cutoff Tail Cone

When the tail cone of a torpedo is truncated, the added drag is a function of the boundary-layer thickness and the diameter of the cutoff. The drag coefficient for the truncated tail cone is expressed in Ref. 7 as

$$C_{D_{A_c}} = \frac{0.029}{\sqrt{C_f (S_{wet}/A)}} \left(\frac{d_B}{d} \right)^3 \quad (1)$$

For standard torpedoes, $C_f \approx 0.003$, where $R_l \approx 10^7$. Also, $S_{wet} \approx 0.8\pi(l*/d)d^2$ and $A = (\pi/4)d^2$. Therefore,

$$C_{D_{A_c}} \approx \frac{0.29}{\sqrt{l*/d}} \left(\frac{d_B}{d} \right)^3 \quad (2)$$

The latter is graphed in Fig. 7.

Figure 7 is useful in estimating the drag of torpedoes with large cutoff diameters. For normal torpedo bodies with cutoff diameters less than one-fourth, their maximum diameters, Fig. 7 shows that the drag increase is less than 2X, which is negligible. Thus, their drags may be estimated by assuming the tail cone to be streamlined and using a lead tip to the projected tip. When very short tail cones are used and separation occurs, the drag due to truncation is zero, if cutoff is back of the separation point.

Surface Roughness

The drag coefficient correction for roughness, based on body surface area, can be derived from Fig. 8, which was drawn from data reported in Ref. 8 and modified for torpedo use in Ref. Figure 8 is based on cross-sectional area of the torpedo, rather than surface area, and the conversion to body surface area may be made by assuming that $S \approx 0.8\pi l^* d$, from which

$$C_{D_{A_R}} \approx 0.31 C_{D_{S_R}} d/l^* \quad (3)$$

The correction for very smooth surfaces is zero. The added drag of holes and protuberances can be estimated by methods given by Hoerner.⁷

Drag of Stabilizing Fins

The method used here for calculating fin drag is that of Hoerner,⁷ modified by a correction factor **derived from empirical data**. It is developed in detail in Appendix B. As discussed there, the fin drag, based upon the wetted fin-surface area for tail fins located along the rear portion of the tail cone, is

$$C_{DfS_f} = \frac{\text{fin drag}}{q_0 S_f} = 0.93 C_f \text{fin} \left(1.135 + 2 \frac{t}{c} \right) + \frac{t}{b-a} \left(0.16 \frac{t}{c} + 0.017 \right)$$

$$= 0.00024 \frac{c}{b-a} + 0.00093 9.5 - \frac{t^*}{d} \quad (4)$$

The first three terms in (4) represent the skin friction corrected for overvelocity plus body-fin pressure interference effects. The last term is an empirical correction for boundary-layer interference between the body and fins, where t^*/d is the fineness ratio of the body. It was derived from experimental drag data for 12 airships and torpedoes and represents the difference ΔC_{Df} between experimental and theoretical fin drags.

Although the scatter in the data, which are plotted in Fig. 9, is significant, these corrections are the best available.

If fins are attached at positions other than the tail cone, or if cruciform fins of unusual design or a shroud ring are used, a modification of these procedures can be used to estimate drag.

Optimum Body Shape

Much interest has been shown in optimizing the body shape of torpedoes. Reference 4 shows that minimum drag per unit volume for a streamlined body occurs at a body fineness ratio of 6.5, which corresponds to a tail fineness ratio of 3.9. Reference 5 explains the effect of the variation of cylindrical midsection length on the drag of a single parent form. However, there are no systematic tests that show the combined effect on drag of nose shape, tail-fin size, tail-cone fineness ratio, and cylindrical midsection length. These may, instead, be estimated by applying the methods in this paper to torpedo configurations representing different body shapes with proper fins appended to achieve constant torpedo stability.

To illustrate the effect on drag of different body shapes, torpedo volume and velocity were held constant by holding $V^{1/3} V_o$ constant. Drag was expressed in coefficient form,

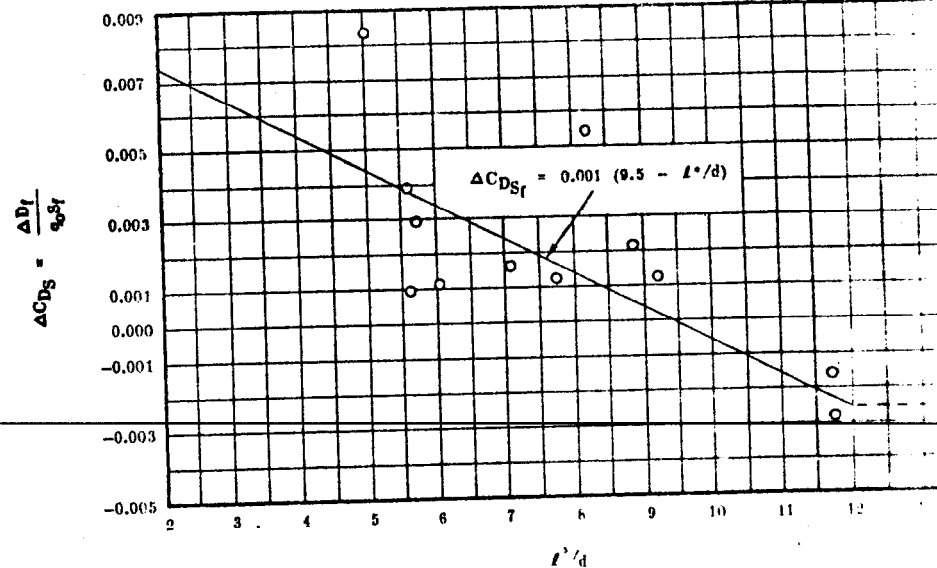


Fig. 9 Drag increment ΔC_{Df} between theoretical and experimental data for stabilizing fin vs fineness ratio t^*/d .

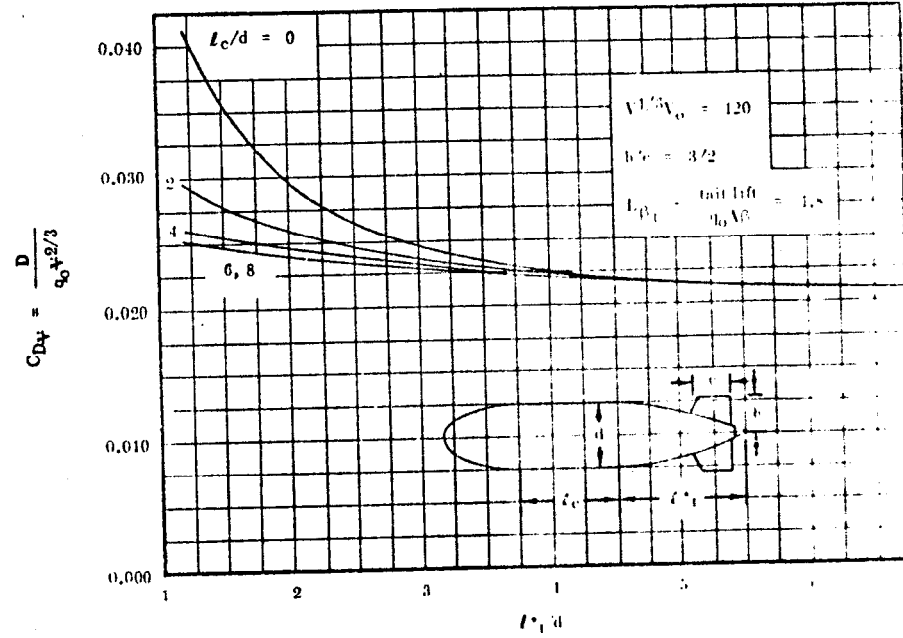


Fig. 10 Drag coefficient based on volume $C_d V$ for torpedoes with stabilizing fins vs tail-cone fineness ratio t^*/d . Parent tail-cone shape from DTMB series 58 for fully turbulent flow.

$C_{Dv} = D/v^2/3 q_0$, which is constant for geometrically similar torpedoes at the same Reynolds number, $R_L = l V_o / v$. Since l is proportional to $v^{1/3}$, R_L is proportional to $v^{1/3} V_o$. Therefore, C_{Dv} measures drag per unit volume. Taking $v^{1/3} V_o$ of 120 provides a useful family of torpedoes with, as examples, a volume of 20 ft³ running at 44 fps, 10 ft³ at 56 fps, or 5 ft³ at 70 fps.

The Reynolds number of torpedo bodies satisfying these conditions varies with fineness ratio. Although the skin friction will change when other sizes or velocities are considered, optimum design point and qualitative difference between shapes will not noticeably vary as long as flow is fully turbulent and without separation over the nose.

The results of computations for such conditions are shown in Figs. 5 and 10, with drag coefficient based upon body volume for bare bodies and for fully appended bodies, respectively, as a function of tail-cone fineness ratio and cylindrical-section length (where $v^{1/3} V_o = 120$ and the nose correction factor is obtained from Fig. 6).

Figures 5 and 10 show that the drag per unit volume of a bare torpedo body is minimized when it is fully streamlined with tail-cone fineness ratio of 3.9, which corresponds to a body fineness ratio of 6.5. Replacing the streamlined nose with a well-designed blunt nose may decrease drag slightly if flow is fully turbulent in both situations. Minimum drag per unit volume of fully appended torpedoes occurs when the tail-cone fineness ratio is 6 or greater. When it is smaller, minimum drag occurs when the cylindrical-section length is equal to or greater than six diameters. Adding a blunt nose in this instance increases drag slightly for low body fineness ratios and has no effect at the higher ratios. Consequently, the minimum drag per unit volume for different body shapes depends on the presence or absence of stabilizing fins. The optimum body shape, however, is not critical for small variations. Figures 5 and 10 clearly show the effect of large body-shape variations.

Drag of the Fully Appended Torpedo

The drag coefficient of a fully appended torpedo can be estimated by the three methods already considered, which are reviewed below.

Method A: Standard Torpedoes[¶] When $v^{1/3} V_o \approx 120$

This method is for body geometrically similar torpedoes with fin size and stability similar to that defined in Appendix I and for which $v^{1/3} V_o$ is approximately 120. It is first necessary to obtain the fineness ratio of the tail cone (measured to the extended tip) l_t^*/d , cylindrical section l_c/d , nose l_n/d , and nose flat d_n/d . The nose correction factor is then found from Fig. 6, and the drag coefficient based on volume from Fig. 10. For convenience, the drag coefficient based on body cross-sectional area is also shown in Fig. 11.

Method B: Standard Torpedoes of Any Volume or Velocity

This method is valid for torpedoes of the same family as those considered in method A but with $v^{1/3} V_o$ markedly diff from 120. Again, it is necessary to obtain the fineness ratios of the tail cone, cylindrical section, nose, and nose flat. The Reynolds number is $R_L = V_o l / v$, where $v = 1.3 \times 10^{-7}$ for sea water at 60°F. The drag coefficient based on cross-sectional area is found from Fig. 12** after the nose correction factor of Fig. 6 is applied.

Since the full-scale Torpedo EX-2A has a fin shape similar to that of this study, its drag may be estimated by this method, as follows.

The specifics of the torpedo are $l_t^*/d = 3$, $l_c/d = 4.9$, $l_n/d = 0.5$, $d_n/d = 0.5$, and $R_L = 3.18 \times 10^7$ (for this analysis). The nose correction factor from Fig. 6 is $\Delta l_c/d = -0.1$. Therefore, $l_c/d = 4.9 + 0.9 = 4.0$.

The drag coefficient from Fig. 11 for these conditions is $C_{DA} = 0.100$, which is 5% above the value of 0.095 measured DTMB for a smooth-body model.

Method C: Nonstandard Torpedoes

This method is valid for all torpedoes, including those whose velocity, displacement, and fin size vary widely from those of the torpedoes considered in this study. To correct the C_{DA} found in

[¶] An arbitrary term designating torpedoes of the geometric similarity, stability, and surface condition selected for this study. Nonstandard torpedoes may have greatly differing characteristics.

*Derived from Fig. 10.

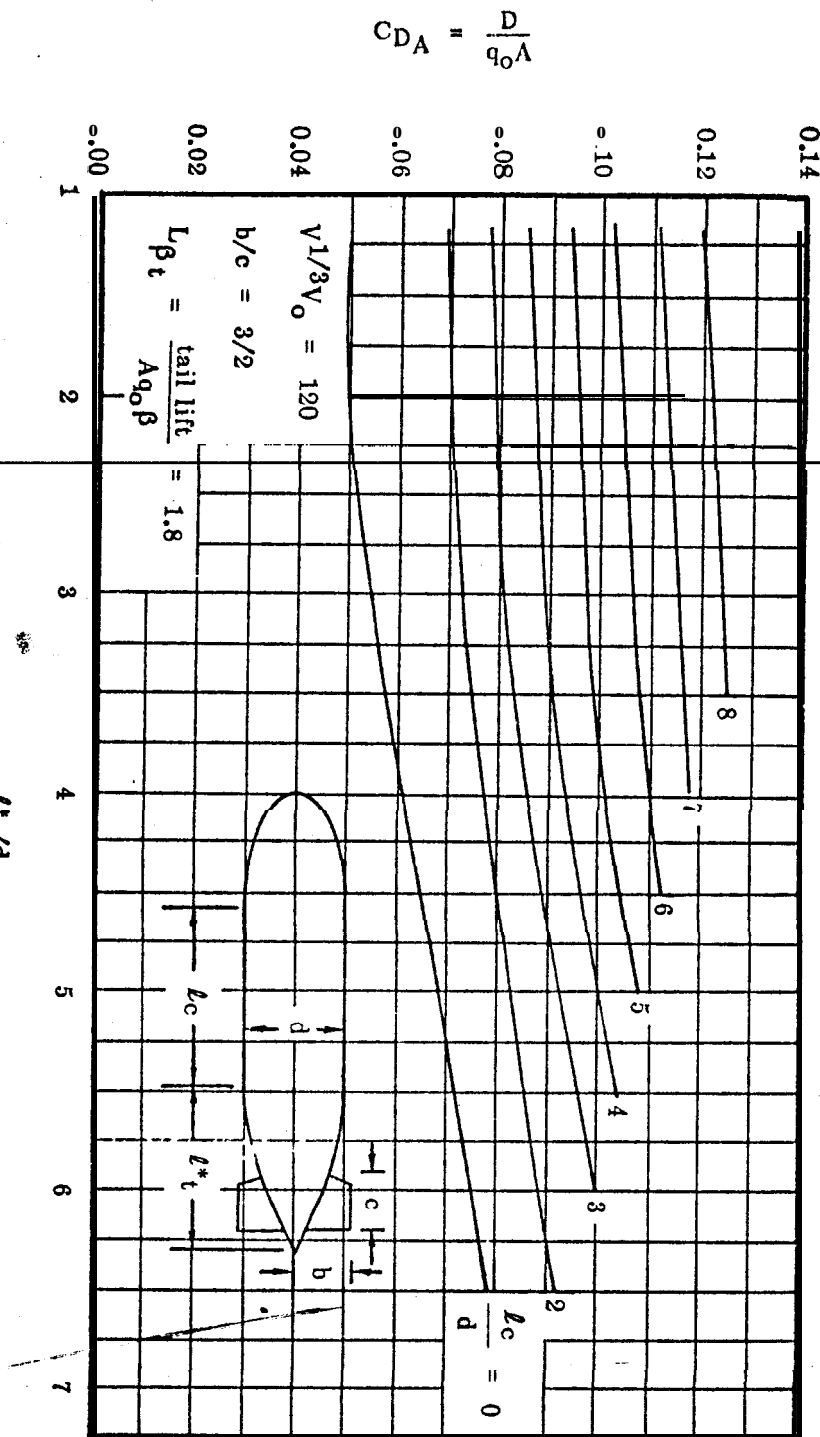


Fig. 11 Drag coefficient based on cross-sectional area for torpedoes with stabilizing fins. Parent tail-cone shape, DMB series no. 58. Fully turbulent flow.

method B for the effect of roughness, protuberances, and fin size. The fin dimensions a , b , c , and t of Fig. 13 are needed. The roughness and parasite drag coefficients C_{DSR} and

$C_{DAPARASITE}$ are obtained from Fig. 8 and Ref. 7, respectively.

The drag of a blunt tail cone, important if the cutoff diameter is greater than one-fourth the torpedo diameter, is obtained from Fig. 7. The fin drag is obtained from Appendix B. For convenience, it is used as a correction, ΔC_{DAf} , to the drag of the standard fins used in method B.

Thus, the fully appended torpedo drag, based on cross-sectional area, is

$$\begin{aligned}
 C_{DA} &= C_{DA}(\text{method B}) + 0.31 d/l C_{DSR} + C_{DAPARASITE} + C_{DAc} \\
 &\quad + AC, A_f \\
 &= C_{DA}(\text{method B}) + 0.31 d/l C_{DSR} + C_{DAPARASITE} + C_{DAc} \\
 &\quad + \left\{ 0.93 C_{f,fins} (1.135 + 2t/c) + \left[t/(b-a) \right] (0.16t/c + 0.017) \right. \\
 &\quad \left. - 0.00024 \left[c/(b-a) \right] + 0.00093 (9.5 - *d) \right\} \left[10.2c(b-a)/d^2 \right] \\
 &\quad - 0.0190 + 0.00122 l*/d
 \end{aligned}$$

Conclusions

Methods described in this paper may be used to determine the optimum torpedo configuration for a given application, or to calculate the drag of a specific (existing) torpedo configuration.

In their development, it is assumed that flow is fully turbulent and no separation occurs at the nose, and empirical data are used despite some scatter. These methods appear sufficiently accurate for preliminary design purposes.

Appendix A: Calculation of Drag of Cylinder Section

A method of calculating the drag of a body of revolution⁶ involves step-by-step determination of the momentum thickness of the boundary layer, from the nose to the tail and into the

wake. Total drag is proportional to the momentum area of the wake far down stream. This method can be used to calculate the drag added by a cylindrical midsection by computing the change in the momentum area of the wake.

A simplified equation for the momentum thickness θ of a turbulent boundary layer, where θ is much smaller than the local body radius r_w , is⁶

$$\left(\frac{v}{v_o}\right)_e^{3.9732} \left(\frac{r_w \theta}{l^2}\right)_e^{1.1686} = \left(\frac{v}{v_o}\right)_b^{3.9732} \left(\frac{r_w \theta}{l^2}\right)_b^{1.1686}$$

$$+ \frac{(1.1686)(0.006361)}{(R_l)^{0.1686}} \int_{L_b/l}^{L_c/l} \left(\frac{r_w}{l}\right) \cdot \left(\frac{v}{v_o}\right)^{3.8046} \sec \alpha \frac{dl}{l} \quad (\text{A1})$$

Along the cylindrical section,

$$r_w b = r_w e = \frac{d}{2} \quad (\text{A2})$$

and, since the angle between the surface of the body and the longitudinal axis is 0,

$$\sec \alpha = 1 \quad (\text{A3})$$

For moderate pressure gradients, the velocity is about the same at the beginning and the end of the cylindrical midsection, or

$$(v/v_o)_b = (v/v_o)_e \quad (\text{A4})$$

Thus, for this case, Eq. (A1) can be simplified to

$$\theta_e^{1.1686} = \theta_b^{1.1686} \quad (\text{A5})$$

$$= 0.001116 \frac{\ell}{(v_o)^{0.1686} (v_{e,b}/v_o)^{3.973}} \int_{L_b/l}^{L_c/l} \left(\frac{v}{v_o}\right)^{3.8046} \frac{dl}{l}$$

To solve for $\Delta\theta$, where

$$\Delta\theta = \theta_e - \theta_b, \quad (\text{A6})$$

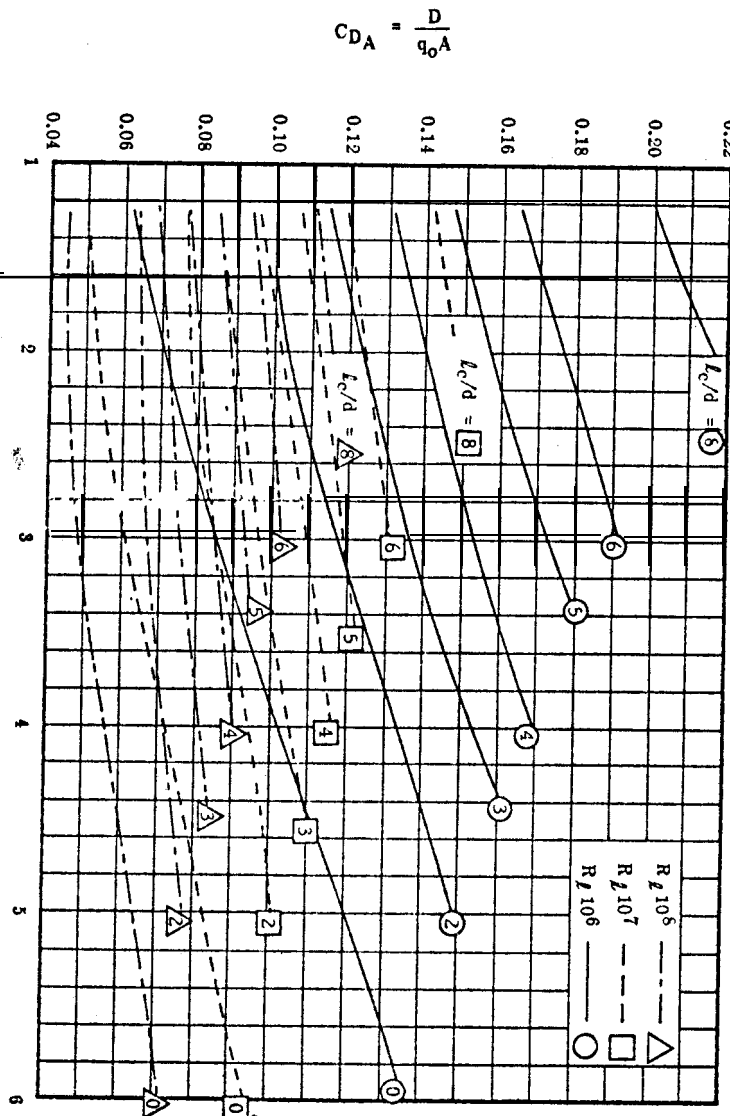
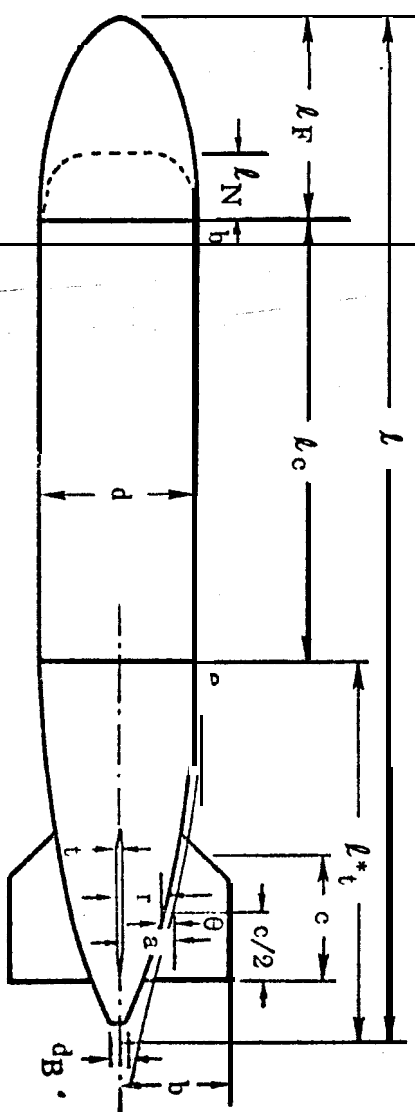


Fig. 12 Drag coefficient based on cross-sectional area C_{D_A} for fully appended torpedoes vs tail-cone fineness ratio l^*/d .

Fig. 13 Parameters of a typical torpedo.



an additional relationship between θ_e and θ_b is necessary which may be approximate since the exponents of θ_b and θ_e in Eq. (A5) are close to unity. For a flat plate in turbulent flow, according to Ref. 10,

$$\theta = \text{const} \times (R_f)^{-1/5} l \quad (\text{A7})$$

and so, approximately,

$$\theta \propto l \quad (\text{A8})$$

$$\theta_e / \theta_b = l_e / l_b \quad (\text{A9})$$

Equations (A5) and (A9) are solved simultaneously for $\Delta\theta$.

The velocity distribution over the cylindrical section is estimated from the experimental results in Refs. 2, 11, and 12, and the integral is evaluated numerically. The increment of momentum area is

$$\Delta \Omega = d/2 \Delta \theta \quad (\text{A10})$$

From Ref. 15, the effect of the velocity distribution over the tail on the change in momentum area in the wake is

$$\Delta \Omega_\infty = (v_e/v_\infty)^{3.4} A R \quad (\text{A11})$$

and, finally, the drag of the cylindrical section is

$$D_C = 4\pi \Omega_\infty q_0 \quad (\text{A12})$$

Drag coefficients calculated by this method for streamlined bodies with cylindrical midsections agree well with the limited test data.⁵

Appendix B: Calculation of Drag of Tail Fins

Two problems are involved in adding stabilizing fins to the **series** of torpedo bodies. First, for purposes of comparison, it is necessary to add the proper-size fins to give equal stability to each body, and, second, the **added** drag of the fins must be determined.

It has been shown¹³ that the stability and controllability of **widely** different torpedo configurations are approximately the same when their tail-lift coefficients, based on frontal

areas of the torpedoes, are equal. The partly empirical, partly theoretical formula developed in Ref. 14 for the lift coefficient derivative of four cruciform fins on a body of revolution is

$$L' \beta_t = 16 \frac{b^2}{d^2} \frac{(1 - a^2/b^2)}{\left(\sqrt{b^2/c^2 + 1} + 1\right)} \quad (B1)$$

Where fin and body dimensions a , b , c , and d are defined in Fig. 13. As an example, $L' \beta_t = 1.8$ will be used, which provides average torpedo dynamic stability.

An average torpedo-fin configuration is also taken, composed of four cruciform fins, each pair with over-all aspect ratio of 3 ($A_R = 3 = 2b/c$). The fins are located on the torpedo with midpoints at an effective diameter of one-half the maximum diameter ($a/b = 1/2$). Thus, the fin-tip radius, b , is $0.62d$, and the chord length, c , is $0.414d$.

The drag of the fins is found by adding the skin-friction drag to that caused by body-f in interference. These drags are expressed as coefficients based on fin surface area and estimated, using Ref. 8 and other sources, as follows:

1) The fin-skin friction drag including the overvelocity effect is

$$\left(C_{D_{S_f}}\right)_{friction} = C_f (1 + 2t/c) \quad (B2)$$

2) The form drag of the fins' is

$$\left(C_{D_{S_f}}\right)_{form} = C_f [60 (t/c)^4] \quad (B3)$$

or, for small t/c ,

$$\left(C_{D_{S_f}}\right)_{form} \approx 0 \quad (B4)$$

3) The correction for the momentum thickness of the boundary layer is applied by reducing the fin-surface area by the amount covered by the torpedo-body momentum thickness θ . The fin drag is defined as

$$D_{f_0} = C_{D_{S_f}} q_0 S_f$$

The reference surface area S_f for four fins is defined as

$$S_f = 8c(b - r - \theta) = 8c(b - a) \quad (B5)$$

where r is the body radius at the fin midchord. An approximate expression for θ is

$$\theta \approx 0.0025 \ell^* \quad (B6)$$

A more exact value, obtained from Ref. 14, is

$$\theta \approx (d/2r) 0.022 \ell_{leading edge}^{-1/6} \quad (B7)$$

4) The interference drag caused by the effect of the fins on the pressure distribution of the body' is

$$\begin{aligned} & \left(C_{D_{S_f}}\right)_{body \text{ pressure}} = 1.6 \frac{(\Delta q/q_0)}{\Delta \ell/\ell} C_{D_s} \\ & \approx 1.6 \frac{\left(\frac{leading \text{ edge}}{q_0} - 0.87\right)^2}{\left(1 - \frac{leading \text{ edge}}{a}\right)} \left(C_{D_{S_f}}\right)_{friction} \end{aligned} \quad (B8)$$

5) The interference drag caused by the effect of the body on the pressure distribution of one fin' is

$$\begin{aligned} & \left(C_{D_{S_f}}\right)_{fin \text{ pressure}} = \left\{ 8 t/c [t/c + 0.25(\Delta/q_0)]^2 \right. \\ & \quad \left. + 0.0005 \left(\frac{c^2}{S_f}\right) \right\} \end{aligned} \quad (B9)$$

or, for four fins where S_f is $8c(b - a)$,

$$\begin{aligned} & \left(C_{D_{S_f}}\right)_{fin \text{ pressure}} = 0.4 [t/(b - a)] [t/c + 0.25(\Delta/q_0)]^2 \\ & \quad - 0.00025 [c/(b - a)] \end{aligned} \quad (B10)$$

6) Because the dynamic pressure over the tail cone is lower than the freestream dynamic pressure, the estimated total drag of the fins is multiplied by the local dynamic pressure ratio:

$$D_f = D_{f_0} q/q_o \quad (B10)$$

7) The drag of holes and rudder gaps, if any, is estimated by the methods of Ref. 7.

8) The thickness of the boundary layer over the tail cone modifies items 4 and 5 by submerging the fins and increasing or decreasing the effect of the pressure interference. To estimate the magnitude of this correction, all available experimental data were used in which both bodies and bodies with fins were tested. To the measured bare-body drag was added the sum of the drags estimated using Eqs. (B2-B10). The difference between this estimated fin drag and the measured fin drag is $\Delta C_{D_S f}$, the empirical boundary-layer interference drag shown in Fig. 9.

Although there is considerable scatter in the data because of the inaccuracy inherent in a small difference between two large drag measurements, the generally decreasing trend of the fin drag as the boundary layer thickens is apparent. Thus, as t/d increases, the momentum thickness increases, and the added drag from pressure interference in the intersection between the body and fins decreases, finally becoming less than that predicted by corrections 4 and 5 and making $\Delta C_{D_S f}$ negative. The equation for this correction is

$$\Delta C_{D_S f} = 0.001(9.5 - t^*/d) \quad (B11)$$

The total drag of the fins, using the corrections given by Eqs. (B2-B11) and Fig. 9, is then

$$\begin{aligned} C_D S_f &= \frac{\text{fin drag}}{q_o S_f} \\ &= \frac{q}{q_o} \left\{ C_f \left[1 + 2 \frac{t}{c} + 1.6 \frac{\left(\frac{q_{\text{leading edge}}}{q_o} - 0.87 \right)^2}{\left(1 - \frac{t_{\text{leading edge}}}{t} \right)^3} \right] \right\} \end{aligned}$$

$$\begin{aligned} &+ 0.4 \frac{t}{b-a} \left(\frac{t}{c} + 0.25 \frac{\Delta p}{q} \right)^2 - 0.00025 \frac{c}{b-a} \\ &+ 0.001 \left(9.5 - \frac{t^*}{d} \right) \end{aligned} \quad (B12)$$

For the case of four fins mounted on the tail cone, it can be assumed that $q_{\text{leading edge}}/q_o \approx 1$, "leading edge" ≈ 0.8 , $\Delta p/q \approx 0.87$, and $q/q_o \approx 0.93$. Then, neglecting higher order terms in t/c ,

$$\begin{aligned} C_D S_f &= 0.93 C_f \text{fin} \left[1 + 2 \frac{t}{c} + \frac{t}{b-a} + \frac{t}{c} + 0.017 \right] \\ &- 0.00024 \frac{c}{b-a} + 0.00093 \left(9.5 - \frac{t^*}{d} \right) \end{aligned} \quad (B13)$$

In estimating the fin drags to be added to the series of bodies, it was assumed that the thickness-to-chord ratio of the fins is 0.05, that the drag of gaps and holes is negligibly small, and that the fin sizes are as described in the first part of this Appendix. The total drag of the fins is then

$$C_D S_f = 1.15 C_f \text{fins} + 0.0102 + 0.00093 \frac{t^*}{d} \quad (B14)$$

In estimating the drag of a torpedo by method A or B, it is assumed that the fin drag is given by Eq. (B14). A more accurate procedure for torpedoes with widely different tail configurations is given by method C. The difference in the fin-drag coefficient from the standard fin size assumed in Eq. (B14) and an arbitrary fin is obtained by subtracting Eq. (B13) from Eq. (B14). Making the simplifying assumption that $C_f \text{fin}$ in Eq. (B14) ≈ 0.0037 , the difference in the fin-drag coefficient based on cross-sectional area of the torpedo is

$$\begin{aligned} \Delta C_{D_A f} &= \left[0.93 C_f \text{fin} \left(1.135 + 2 \frac{t}{c} \right) + \frac{t}{b-a} (0.16 \frac{t}{c} + 0.017) \right. \\ &\quad \left. - 0.00024 \frac{c}{b-a} + 0.00093 \left(9.5 - \frac{t^*}{d} \right) \right] \frac{10.2c(b-a)}{d^2} \\ &- 0.0190 + 0.00122 \frac{t^*}{d} \end{aligned} \quad (B15)$$

where the ratio of fin surface area to torpedo cross-section area is

$$\frac{S_f}{A} = \frac{8c(\pi - a)}{\pi/4 d^2} - 10.2c \frac{(b - a)}{d^2}$$

For the standard fin, $(S_f/A)_{\text{standard}} = (10.2)(0.414)(0.31)$
= 1.31.

References

¹Williams, D.H., Jones, R., and Brown, A.F., "Tests on two streamline bodies in the compressed air tunnel," Aeronautical Research Committee, London, ARC R. and M. 1710 (1936).

²Young, A.D., "The calculation of the total and skin friction drags of bodies of revolution at zero incidence," Aeronautical Research Committee, London, ARC R. and M. 1874 (1944).

³Hoerner, S.F., Fluid Dynamic Drag (published by the author, Midland Park, N.J., 1958).

⁴Gertler, M., "Resistance experiments on a systematic series of streamlined bodies of revolution for application to the design of high-speed submarines," David Taylor Model Basin, Washington, D.C., Rept. C-297 (1950); confidential.

⁵Larsen, C.A., "Additional tests of series 58 forms. Part I-Resistance tests of a parallel middle body series," David Taylor Model Basin, Washington, D.C., Rept. C-738 (November 1955); confidential.

⁶Cranville, P., "The calculation of the viscous drag of bodies of revolution," David Taylor Model Basin, Washington, D.C., Rept. 849 (July 1953).

⁷Hoerner, S.F., Aerodynamic Drag (published by the author, Midland Park, N.J., 1951).

⁸Freeman, H.B., "Force measurements on a 1/40 scale model of the U.S. airship 'Akron,'" National Advisory Committee for Aeronautics, Washington, D.C., NACA Rept. 432 (1932).

⁹Zahm, A.F., Smith, R.H., and Louden, F.A., "Drag of C-class airship hulls of various fineness ratios," National Advisory Committee for Aeronautics, Washington, D.C., NACA Rept. 291 (1928).

¹⁰Schlichting, H., Boundary Layer Theory (McGraw-Hill Book Co., Inc., New York 1955), p. 433.

¹¹Rouse, H. and McNow, J.S., "Cavitation and pressure distribution, head forms at zero angle of yaw," Iowa Institute of Hydraulic Research, Iowa City, Iowa, Bull. 32 (1948).

¹²Eggers, H.A., "A boundary-layer survey of the Mark 41 torpedo," David Taylor Model Basin, Washington, D.C., Rept. C-314 (May 1950); confidential.

¹³Sweat, C.W., "Hydrodynamic design criteria for adequate torpedo stability and response," U.S. Naval Ordnance Test Station, China Lake, Calif., NAVORD Rept. 6428, NOTS TP 2134 (October 29, 1958).

¹⁴Bottaccini, M.R., "The stability coefficients of standard torpedoes," U.S. Naval Ordnance Test Station, China Lake, Calif., NAVORD Rept. 3346, NOTS 909 (July 18, 1954).

¹⁵Schirmer, M., "Aerodynamic model tests with German and foreign airship designs in the wind tunnel of the Zeppelin Airship Works," Zeppelin Airship Works, Friedrichshafen, Rep. F.B. 1647 (April 1942).

¹⁶Strumpf, A., "Model studies of the hydrodynamic characteristics of the proposed Mark 40 torpedo with hydrojets," Stevens Institute of Technology, Experimental Towing Tank, Hoboken, N.J., Rept. 356 (December 1948); confidential.

¹⁷Hill, F.J., Jr., "Wind tunnel tests on an unpowered model of a research torpedo configuration," U.S. Naval Ordnance Test Station, China Lake, Calif., NAVORD Rept. 5428, NOTS 1691 (February 11, 1957).

¹⁸David Taylor Model Basin, Washington, D.C., NRS 724; confidential.

¹⁹ Eggers, H.A., "The Mark 41 torpedo. Resistance and propulsion characteristics with various body lengths," David Taylor Model Basin, Washington, D.C., Rept. C-526 (September 1952); confidential.

²⁰ Peters, B.H., "Model studies of the hydrodynamic characteristics of the Mark 18 torpedo in turn, rise, and dive," Stevens Institute of Technology, Experimental Towing Tank, Hoboken, N.J., Rept. 357 (January 1949); confidential.

²¹ Strumpf, A., "Model studies of the hydrodynamic characteristics of the proposed Mark 36 torpedo," Stevens Institute of Technology, Experimental Towing Tank, Hoboken, N.J., Rept. 387 (November 1949); confidential.

UNDERWATER DRAG REDUCTION

THROUGH OPTIMUM SHAPE:

Bruce H. Carmichael*

North American Rockwell Corp., Anaheim, Calif.

Abstract

A method for reduction of hull plus fin surface area through use of low-fineness- ratio streamline shape is developed and presented graphically. Vehicles with length-times-speed products from 100 to 1000 ft²/sec are theoretically amenable to significant reduction in drag coefficient based on surface area through delay of laminar boundary-layer transition by purely geometric means. However, ambient turbulent eddy velocities 0.001 of vehicle speed, vehicle surface wave height 0.001 of surface wave length, and surface roughness of a few thousandths of an inch may limit the theoretical reduction. Calculations predict a reduction in drag to 1/3 conventional values under ideal conditions for either constant frontal area or constant volume applications. A gravity-powered, fin-stabilized body with a 3.33 length-to-diameter ratio and 5.6 ft³ of volume was fabricated and tested in the Pacific Ocean. It achieved 60% drag reduction compared to a conventional torpedo of equal volume at -15 knots and approximately 50% at 20 knots. Transition length Reynolds numbers of 14 to 18 x 10⁶ were deduced by comparison of experiments with theory. These values indicate acceptable vehicle roughness and waviness plus acceptable turbulence level and contamination-free operation in the ocean.

Nomenclature

A	= hull frontal area = $(\pi/4)d^2$, ft ²
AR	= fin aspect ratio = b/c
b	= fin span, tip to tip, ft
c	= average fin chord, ft
C _L	= fin lift coefficient = fin lift / $(\rho/2)U_{\infty}^2 S_{Fin}$

Presented at AIAA Second Propulsion Joint Specialist Conference, Colorado Springs, Colorado, June 13 - 17 1966.

*Senior Technical Specialist, Research and Engineering, Autonetics Division.

C_{DA}	= frontal area drag coefficient = drag/ $(\rho/2)U_\infty^2 A$
C_W	= wetted area drag coefficient = drag/ $(\rho/2)U_\infty^2 S_W$
C_f	= flat plate friction coefficient = drag/ $(\rho/2)U_\infty^2 S_W$
$C_{DV}^{2/3}$	= volumetric drag coefficient = drag/ $(\rho/2)U_\infty^2 (V)^{2/3}$
d	= maximum hull diameter, ft
F	= hull fineness ratio = l/d
K_1	= longitudinal additional mass as fraction of displaced mass of sea water
K_2	transverse additional mass as fraction of displaced mass of sea water
K_W	= ratio of hull wetted area to lateral area of cylinder of same length and diameter = $S_W/\pi d l$
K_V	= ratio of hull volume to volume of cylinder of same length and diameter = $V/(\pi/4)d^2 l$
l	= hull length along centerline, ft
l_T	= tail length from center of gravity to fin aerodynamic centroid, ft
M	= moment, ft-lb
$M\alpha_H$	= hull moment slope with angle of attack, ft-lb/deg
$M\alpha_F$	= fin moment slope with angle of attack, ft-lb/deg
q	= dynamic pressure = $(\rho/2)U_\infty^2$, psf
R_l	= projected length Reynolds number = $\rho U_\infty l / \mu$
$R_{X_{TR}}$	= projected transition length Reynolds number $\rho U_\infty X / \mu$
R_θ	= boundary-layer momentum thickness Reynolds number = $\rho U_\infty \theta / \mu$
S_F	= fin area in each of two perpendicular planes, ft^2
S_W	= wetted or surface area, ft^2
U	= potential velocity (outside of boundary layer), fps
U_∞	= vehicle velocity, fps
u	= velocity at some location Y in the boundary layer, fps
V	= hull volume, ft^3

X	= distance measured along the centerline, ft
X_{TR}	= distance from nose to boundary-layer transition point, ft
Y	= distance measured perpendicular to surface, ft
P	= fluid mass density, $\text{lb}\cdot\text{sec}^2/\text{ft}^4$
μ	= fluid viscosity, $\text{lb}\cdot\text{sec}/\text{ft}^2$
a	= angle between hull centerline and the relative velocity, deg
A	= length of a surface wave, ft
δ	= boundary-layer momentum thickness = $(u/U) (1 - (u/U)) d_Y \text{ ft}$
δ_0	= boundary-layer total thickness, ft

Introduction

The vehicles considered in this paper are neutrally buoyant, fully submerged, streamlined, finned bodies of revolution which travel linearly within the ocean. Wave drag, cavitation drag, induced drag due to hydrodynamic lift, increased body or fin zero-lift drag due to angle of attack and control deflection, and parasitic drag of large surface excrescences or cavities are neglected. These simplifications are not restrictive for many types of Naval underwater ordnance, since zero wave drag can be achieved five body diameters below the surface, and a typical low-drag body is cavitation-free up to GO knots at a depth of 23 ft. The angle of attack that provides sufficient hydrodynamic lift to support a vehicle twice as dense as sea water is about 1° at modern ordnance speeds, and the angle of attack for good turning performance is also only 1° or 2°.

The drag of concern here is generated by fluid viscosity. For very slender bodies and fins, total drag is almost identical to an integration of the friction over the vehicle wetted surfaces, and flat-plate friction coefficients could be used to predict vehicle drag. For bodies of low length-to-diameter ratio, the average flow velocity about the vehicle is higher than the vehicle velocity; thus the surface area friction coefficient based on vehicle velocity squared is increased over the plate case. In addition, integration of the static pressure distribution about the body results in a net rearward force or pressure drag increment. In the extreme, very blunt bodies, such as spheres, suffer flow separation that results in negative static pressures at the rear and an almost order-of-magnitude increase in drag. Trends in vehicle geometry which tend greatly to

reduce the integrated surface friction appear to lead toward a higher danger of separation.

This paper, then, explores the extent to which drag can be reduced through changes in vehicle shape alone, and the variation in this drag reduction with the size and speed of the vehicle. Discussion of the geometric and hydrodynamic principles involved and the analytical methods available for drag prediction are given. Large-scale experiments in which a large drag reduction was achieved are then reported.

Analytical

Body Geometry Formulas

This discussion is limited to bodies with a circular cross section, which typifies many underwater vehicles. Such a body shape is defined by a) the fineness ratio, $F = l/d$; and b) the longitudinal shape or equation of form. Resistance, or drag, is proportional to surface or wetted area. Because volume V and/or frontal area $A = (\pi/4)d^2$ are usually imposed conditions, it is important to minimize wetted area for constant frontal area when the volume requirement is not dominant, and for constant volume when diameter is not specified.

It is helpful to compare the body surface area S_W to that of a right circular cylinder of equal length and diameter, $K_W = S_W/\pi d l$, and to compare body volume to that of the same cylinder, $K_V = V/A l = 4V/\pi d^2 l$. The absolute length may be removed by substituting the fineness ratio F . Thus, $S_W = K_W \pi d^2 F$ and $V = (\pi/4)K_V d^3 F$.

The following points are then noted:

1) Since the volume or space available for propulsion equipment is proportional to d^3 , whereas the wetted area that influences propulsion requirements is proportional to d^2 , there is a beneficial geometric effect with increased absolute size, i. e., $S_W/V = 4K_W/dK_V$

2) For the constant frontal area case that is not volume limited, it is geometrically desirable to use a minimum acceptable fineness ratio? and a highly tapered body form (low K_W), since $S_W/A = 4K_W F$

3) For the constant volume problem with diameter not limited, the value of d^2 for the wetted area equation may be found by raising both sides of the volume formula to the $2/3$ power. Substituting gives $S_W/(V)^{2/3} = 3.695 K_W (F^{1/3}/K_V^{2/3})$

Thus, low fineness ratio is beneficial in case 3 to the $1/3$ power and in case 2 to the first power. For any given body form, K_V is constant even down to $F = 1$, whereas K_W is almost constant at values of $F > 5$ but changes rapidly for values of $F < 3$. A study of a wide variety of body forms from very highly tapered (double cone) to very full (standard cylindrical boat-tailed torpedo) indicates that differences in $K_W/K_V^{2/3}$ between various body forms at any fixed value of F do not exceed 2%.

Transporting and launching systems often impose diameter, length, and weight limitations. Here, the effects of decreasing length from the maximum allowable value and of departing from more cylindrical forms decrease the power and energy requirements but also decrease the space available to house the powerplant. The optimum design thus requires a detailed design study, using realistic performance-to-volume and performance-to-weight ratios of all vehicle components, together with specific mission requirements. Such a study is beyond the scope of this paper.

Fin Geometry Formulas

A body of revolution moving at angle of attack generates a divergent moment, and any practical vehicle therefore includes stabilizing appendages that should be considered in configuration optimization.

The divergent body moment slope is given by Multhopp¹ as

$$M = (2\alpha^\circ/57.3)q \text{ (volume)} (K_2 - K_1)$$

Substituting $(\pi/4)K_V d^3 F$ for volume yields

$$M/qd^3\alpha^\circ = 0.0274 KVF (K_2 - K_1)$$

K_2 , the transverse assessment coefficient, and K_1 , the longitudinal assessment coefficient, are functions of F . $K_2 - K_1$ is 0 at $F \approx 1.0$. $F(K_2 - K_1)$ being linear with F permits a simple analytical expression,

$$(M/qd^3\alpha^\circ)_{BODY} = 0.0286 K_V (F-l)$$

The opposing moment slope of the fins is

$$(M/\alpha)_{FINS} = C_L q S_F l T$$

Nondimensionalizing in the form used previously for body slope,

$$(M/qd^3\alpha)_{FINS} = C_L \alpha / AR (b/d)^2 (l_T / l) F$$

[†] See discussion on flow separation.

Relating body and fin moment slopes as required for dynamic stability yields the required value of

$$C_{L\alpha}/AR = 0.0286 K_V [(F-1)/F] [M_\alpha_{\text{FINS}}/M_\alpha_{\text{BODY}}]/(b/d)^2 (\ell_T/\ell)$$

The lifting surface theory of Weisinger as applied by DeYoung² can then be used to find the required value of AR. The required fin area in each of two mutually perpendicular planes can be found from AR and b/d.

These equations are now applied to the following practical vehicle situation:

1) Fineness ratio: variable between 2 and 10.

2) Two body forms: a) Reichardt constant pressure, and b) NACA 66 series laminar shape.

3) Four unswept fins: tip chord = 0.5 root chord, fin span = body diameter, tail length = 0.5 body length, and $M_\alpha_{\text{FINS}} = 0.7 M_\alpha_{\text{BODY}}$.†

The fin formulae simplify to

$$(C_{L\alpha}/AR)_{\text{Reichardt}} = 0.0282 [(F-1)/F]$$

$$(C_{L\alpha}/AR)_{66 \text{ series}} = 0.022 [(F-1)/F]$$

$$SW_{\text{FINS}}/A = 5.09/AR$$

$$SW_{\text{Fins}}/(\text{volume})^{2/3} = 4.70 / \left[(K_V)^{2/3} (F)^{2/3} AR \right]$$

Examples of the Constant Frontal Area Situation

Consider the geometric aspect of fairing a vehicle of given cross-sectional area (e.g., a sphere where volume in excess of the sphere is not required). The ratio of body wetted area to body frontal area is shown in Fig. 1. It is not quite linear with F, because of a slight variation of K_W with F. The laminar, NACA 66 body forms have significantly lower wetted areas, compared to the fuller Reichardt forms, at all values of F.

The ratio of fin wetted area to body frontal area is also shown in Fig. 1. The lower wetted area at low F reflects the influence on body instability of both the decrease in body volume and in $K_2 - K_1$.

†Typical for a controlled torpedo.

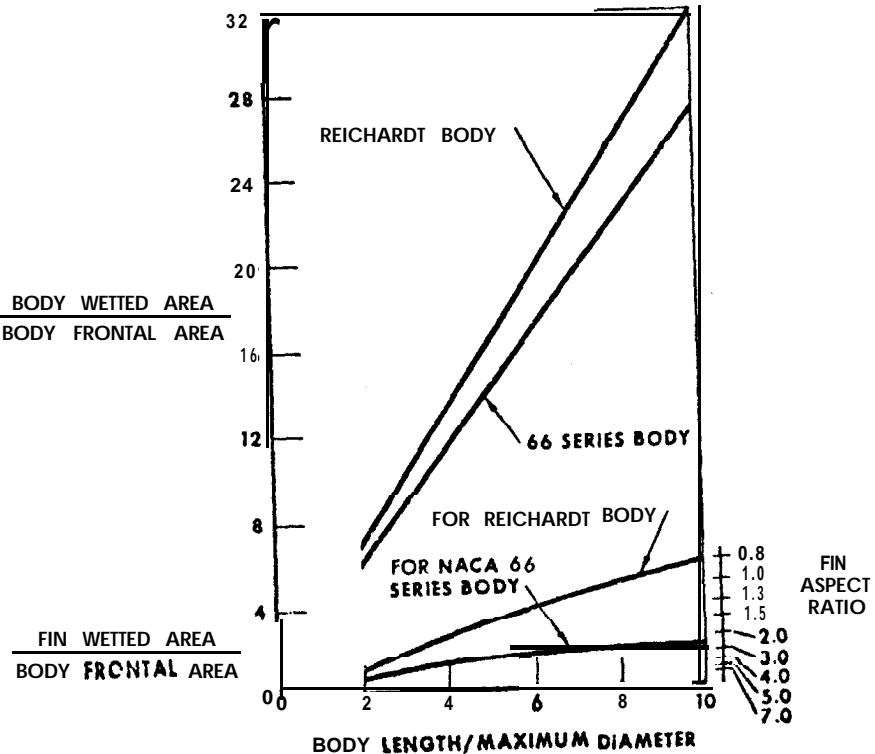


Fig. 1 Wetted area/frontal area relationships for constant cross-sectional area.

At low body instability, the reduction in required fin area leads to higher stabilization per unit fin area due to higher fin aspect ratio, as shown by the right-hand scale. The more rapid rise in fin area with F for the Reichardt form compared to the laminar form illustrates the penalty of low aspect ratio. It is not possible for $M_{\alpha}\text{FIN}$ to exceed $M_{\alpha}\text{BODY}$ (as required for an uncontrolled towed body) at high values of F unless fin span exceeds body diameter, or a ring tail is substituted, or the tail arm is increased with a boom.

Examples of the Constant Volume Situation

The effect of F on body wetted area at constant volume, although not as pronounced as previously, is still appreciable. The trend is shown in Fig. 2. Deviation from $F^{1/3}$ is due to the variation of K_w with F. The negligible effect of body shape at constant volume and at all F values is also apparent.

The effect of body shape on $S_{W,\text{FIN}}/(\text{volume})^{2/3}$ is more pronounced, and even the variation with F is different for the two body shapes. The Reichardt form calls for continually increasing values with increase in F, whereas the laminar body increases up to F = 3.5 and then decreases. This effect stems from the shape of the fin $C_L \alpha$ vs R curve. At $M_{\alpha}\text{FIN} = M_{\alpha}\text{BODY}$, both curves have the same shape as the Reichardt curve in Fig. 2, only steeper. At $M_{\alpha}\text{FIN} = 0.5M_{\alpha}\text{BODY}$, both curves have the same shape as the 66 series curve.

Laminar vs Turbulent Boundary Layer

The average friction intensity, $C_f = \text{DRAG}/qS_w$, on a thin plate varies greatly, depending on whether the flow in the thin friction layer next to the plate is laminar or turbulent. Thus, a slender, all-laminar body has $1/3$, $1/10$, or $1/25$ the drag of a slender, all-turbulent body at speed-times-length products of 10, 350, and 5000 ft²/sec, respectively. Laminar flow on bodies of finite thickness is limited to 60 or 70% of length, if shape alone stabilizes the layer. In addition, local values of laminar or turbulent friction are altered by the potential velocity distribution arising from the finite thickness and shape of the body. Theoretical wetted area drag coefficients are presented in Ref. 3 as a function of body fineness ratio, length Reynolds number, and boundary-layer transition location.

Figure 3, prepared from data in Ref. 3, indicates the regime where extending laminar flow by improved shape may produce large changes in the wetted area drag coefficient. Horizontal scales of length Reynolds number, associated speed-times-length products at

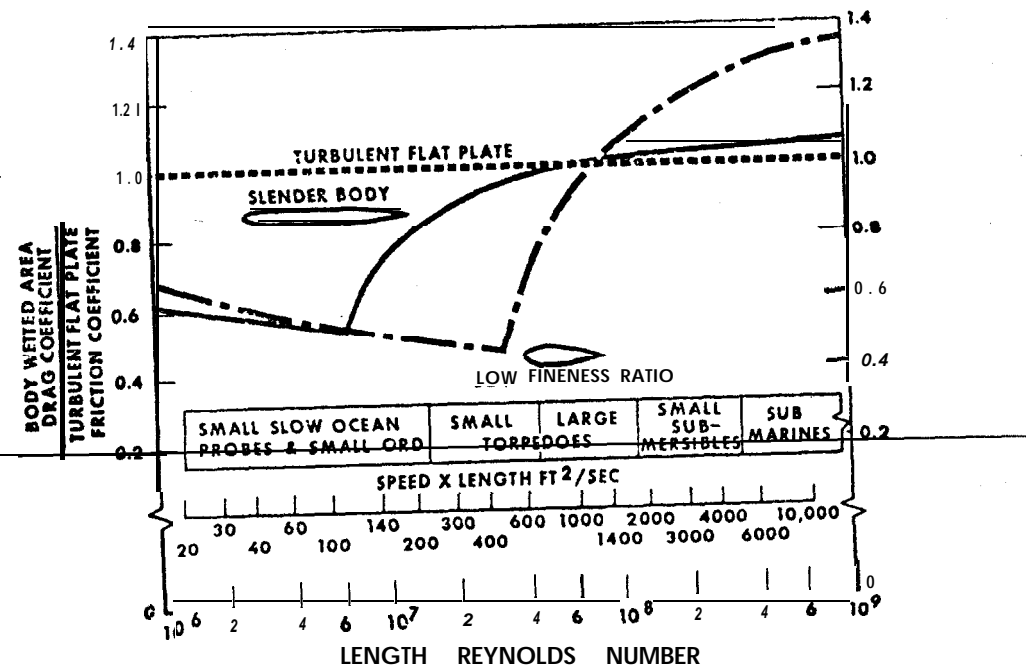


Fig. 2 Wetted area/(volume)^{2/3} relationships for constant volume.

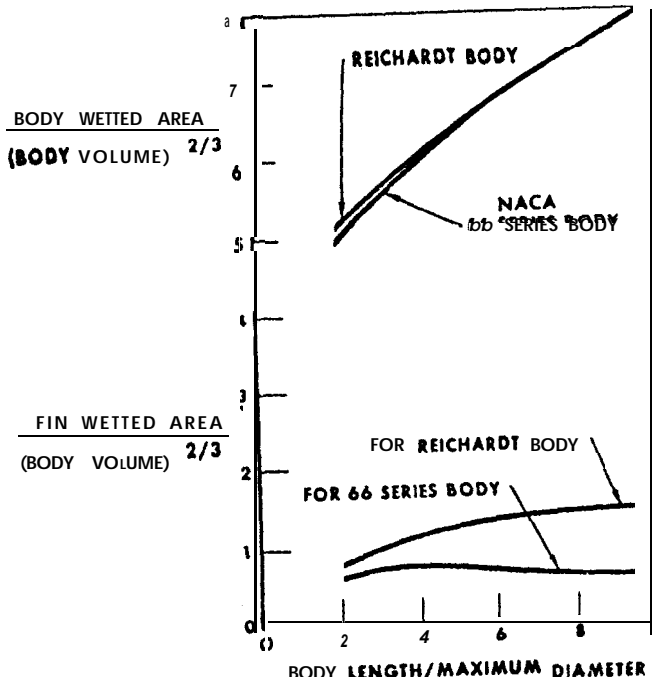


Fig. 3 Wetted area drag coefficients.

50°, and bars representing classes of vehicles are shown. The vertical scale is the ratio of body wetted area drag coefficient to turbulent flat plate friction coefficient. Coefficient reduction under ideal conditions is bounded by two examples: a slender body with transition length Reynolds number of 4×10^6 , and a low fineness ratio body with R_{xTR} of 20×10^6 . Laminar flow is limited to $X/P = 0.6$ by the minimum pressure-point location assumed for both shapes:

Substantial C_w reduction can be achieved even for slender bodies up to a speed-times-length product of $100 \text{ ft}^2/\text{sec}$. Low fineness ratio can extend the reduction to products of approximately $300 \text{ ft}^2/\text{sec}$, which represent small, fast torpedoes. Large torpedoes are in a product regime where C_w approaches the turbulent plate value for even low fineness ratio bodies. Above $1000 \text{ ft}^2/\text{sec}$, all body shapes have very little laminar flow, and C_w exceeds turbulent plate C_f by an amount that increases as fineness ratio decreases. Figure 3 deals with wetted area drag coefficients, and reduction in surface area due to low fineness ratio must be superimposed to obtain true relative drags.

Ideal Boundary-Layer Transition

For bodies of finite thickness, the flow velocity, which is zero at the nose, increases over the forward portion of the body and decreases over the rear. The thin laminar boundary layer separates from the surface shortly aft of the peak velocity point. It then becomes turbulent and reattaches to continue as a turbulent layer. Thus the peak velocity point limits the maximum possible extent of laminar boundary layer,

There is no guarantee that laminar flow will extend to the peak velocity point. Under ideal conditions, transition occurs as the boundary-layer momentum thickness Reynolds number reaches a maximum allowable value, which increases with the slope of the curve of velocity vs body length. A low body length-to-diameter ratio increases this slope and thus increases the allowable R_θ , while decreasing the length of the boundary run and hence the actual R_θ . These effects together delay transition. The semiempirical method of Michalek¹ is available for estimating the location of transition. The pressure or velocity distribution can be computed by the method of Smith et al.,⁵ and boundary-layer growth by a number of methods such as Thwaites⁶.

Causes of Premature Transition

A basic requirement for extensive laminar flow is low turbulence level of the fluid. Schubauer and Skramstad⁷ discovered that laminar flow length on a flat plate in a wind tunnel could be extended as the root mean square velocity fluctuation value was decreased until it

reached 0.1% of the mean stream velocity. Kramer⁸ has stated that the turbulence level below which further reduction is ineffective is even lower than 0.1% for bodies with strong flow acceleration, which ideally permits considerably higher transition length Reynolds numbers. The increased Reynolds number condition is sensitive to even smaller disturbances than those that are critical for a flat plate. A turbulence level of 1% of mean stream velocity reduces the extent of laminar flow on even low-fineness-ratio bodies sufficiently to negate the laminar approach to drag reduction. Previously, absolute values of size and speed were thought to be unimportant in predicting the extent of laminar flow, as long as the Reynolds number was unchanged. Limited data from ocean tests indicate very little laminar flow at low speeds, and Kramer⁸ attributes this to a finite level of turbulence in the ocean. Transition is affected by the ratio of eddy velocity to vehicle velocity, and the higher the vehicle speed the lower the relative turbulence. From the meager data presently available, a vehicle velocity of 30 knots appears to be required to achieve maximum laminar length.

A second requirement for extensive laminar flow is a smooth vehicle surface. Data on critical roughness sizes from tests on plates and wings in air, which are applicable to all but the forward 10% of bodies of revolution, indicate that rough particles and steps (at joints) a few thousandths of an inch in size will trip the laminar boundary layer on high-speed torpedoes to turbulence. The nose region is less sensitive, but the degree has not yet been established.

A third requirement is low surface waviness. Here again, data from high Reynolds number tests in air predict an allowable ratio of wave height to wavelength of about $1/1000$ for two waves in tandem, and about $1/2000$ for continuous surface waves. Short wavelengths, i.e., $\lambda = 0.5 \text{ in.}$, can be seen in glancing light; and intermediate wavelengths, i.e., $1 \text{ in.} < \lambda < 3 \text{ in.}$ can be found by induced jarring of a straight edge rolled along the surface. Magnitude may be obtained from a plot of readings of a dial indicator mounted between fixed legs and moved along the surface. The waviness criterion is not difficult to meet with proper design and fabrication.

The fourth and fifth requirements to prevent premature transition are noise and vibration. Considerable data are available on the effect of noise on laminar flow in air, but none in water, whereas definitive "Vane" vibration experiments have not been made in either medium. "Singing" from fins and propellers, vibrations from ~~propeller~~ machinery sweeping through fin wakes, and vibration in ~~internal~~ Careful, full-scale are all possible sources of premature transition. Careful, full-scale experiments in water are urgently needed.

A sixth requirement to prevent premature transition is low vehicle angle of attack. The resulting variations in the longitudinal pressure distribution on differing element lines of the body lead to transverse velocity components in the boundary layer. The transverse boundary-layer profile is similar to a wake profile and, as such, leads to premature transition in turbulent flow above a critical value of cross-flow Reynolds number. Whether the 1° to 2° angle-of-attack characteristic of a high-speed torpedo is high enough to cause appreciable drag increase on a laminar vehicle is not known. Wind-tunnel experiments at length Reynolds number of 5×10^6 had very little effect, but may have been below the critical Reynolds number.

Flow Separation

~~Geometric design for maximum laminar flow calls for low length-to-diameter ratio and aft location of the minimum pressure point.~~ Such a combination results in a steep pressure rise on the afterbody, causing separation of the boundary layer, which, in extreme cases, may not reattach to the surface. The pressure on the afterbody will be equal to the negative value at separation resulting in very high drag.

The results of an analytical study of separation¹⁰ using the method of Truckenbrodt¹¹ are shown in Fig. 4 for bodies of 30-in. diam, a speed of 45 knots, and minimum pressure at 60% of length. Length-to-diameter ratio was varied from 2 to 3.33 and assumed transition location from 0 to 60% of length. The results are believed to be slightly conservative. Far aft transition permits lower finesse ratio because of the improved ability of a thin boundary layer to withstand a steep pressure gradient. An increase in Reynolds number (all else the same) would have the same beneficial effect.

Estimation of Possible Drag Reduction

To illustrate the factors involved in drag reduction through the geometric approach, two ideal examples are computed below.

Constant Frontal Area. Body parameters: diameter = 21 in., length/diameter = 3.33, velocity = 45 knots, and length Reynolds number = 30.4×10^6 .

Body shapes: a) Reichardt constant pressure body: transition Reynolds number limited to 4×10^6 , transition location = $4/30$, $4 = 0.132$ length, wetted area coefficient = 0.00315 from Ref. 3, and simple slab sectioned tail; b) ideal laminar body: transition at the minimum pressure-point of 0.60 length, transition Reynolds number = 0.6 ($30.4 = 18.2 \times 10^6$), wetted area coefficient = 0.00125 from Ref. 3, and laminar-type tail section.

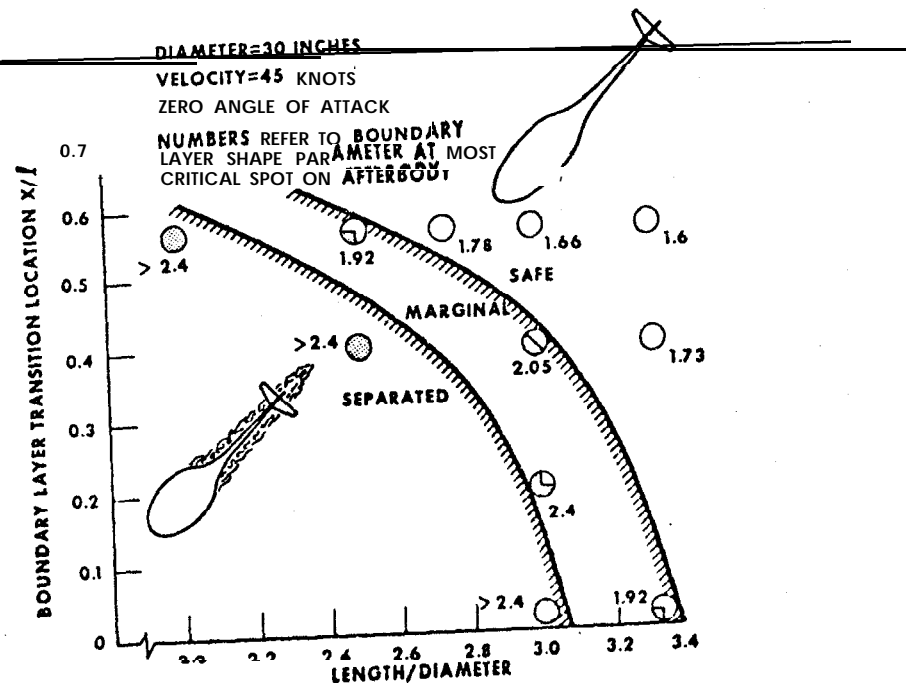


Fig. 4 Theoretical flow separation boundary.

The frontal area drag coefficient is

$$C_{D_A} = C_{W_H} (S_W/A) + C_{W_F} (S_{W_F}/A)$$

Substitution yields

$$\text{Heichardt } (0.00315)(11) + (0.005)(2) = 0.0446$$

$$66 \text{ Series } (0.00125)(9.4) + (0.003)(1.2) = 0.0154$$

Thus, it appears possible to remove almost two-thirds the drag of a low-fineness-ratio turbulent flow vehicle with fixed frontal area by geometric design for maximum laminar flow.

Constant Volume. The possible drag reduction of a torpedo through changing from the conventional full, fineness-ratio 8 form to a laminar form of 3.33 fineness ratio is estimated using wetted area ratios from Fig. 2. The Rechardt constant pressure form is assumed to have $R_{XTR} = 4 \times 10^6$, and the 66 series laminar body to have transition at 60% of length. Wetted area coefficients are from Ref. 3:

<u>Body:</u>	<u>Reichardt:</u>	<u>66 Series:</u>
C_{W_HULL}	0.00245	0.00122
C_{W_FINS}	0.005	0.003
$S_{W_H}/V^{2/3}$	7.4	5.66
$S_{W_F}/V^{2/3}$	1.42	0.75
$CD_{H_V^{2/3}}$	0.0181	0.0069
$CD_{F_V^{2/3}}$	0.0071	0.00225
$CD_{TOTAL V^{2/3}}$	0.0252	0.00915

Thus, the laminar design is predicted to have only 36% of the drag of the conventional torpedo.

Values of S_W/A and S_{WF}/A from Fig. 1.

Experimental

The preceding sections supply theoretical reasons to expect that torpedo drag could be greatly reduced by improved shape alone, but the critical effects of the unknown ambient turbulence level in the ocean and of imperfection in, or contamination of, the vehicle surface necessitate full-scale experiments to verify this prediction. Such tests are discussed below.

Vehicle Design and Fabrication

On the recommendation of M. Kramer, the NACA 66 series form with length-to-diameter ratio of 3.33 was selected for this study, based on the NACA low-drag airfoil data. Kramer applied the relationship between velocity gradients about a sphere and a right circular cylinder to deduce from two-dimensional airfoil data a three-dimensional body form for the experiment. An aluminum casting, tracer machined with an accurate template, produced a body with surface waviness no greater than 1/2000. (The thick shells typical of torpedoes lend themselves admirably to achieving the smoothness and waviness requirements of laminar vehicles.) A slender steel boom and three fixed fins were added to ensure a steady vertical trajectory with minimum appendage drag, resulting in the vehicle shown in Fig. 5. Its 5.6-ft³, 1.575-ft-diam. hull has a wetted area of 18.15 ft². The boom adds 1.33 ft² and the fins 1.54 ft² to the wetted area.

Test Method

The ocean was used for testing, since no water facilities were available where low-fineness-ratio bodies of revolution could be tested at torpedo Reynolds number ($10^7 < R_l < 10^8$) under low turbulence level. The ocean has the added advantage of being the service environment.

Concerning the method of propulsion, mounting or towing from a surface vehicle was impractical at full torpedo scale, and excessive cost ruled out any internal motor-propeller scheme. A vertical downward trajectory was therefore chosen with acceleration from rest just below the surface to terminal speed achieved by lead ballast. The test vehicle design is shown in Fig. 6. It was expected that ambient turbulence would be low at the 800-ft depth where the vehicle reached top speed. Negative buoyancy thrust involves need

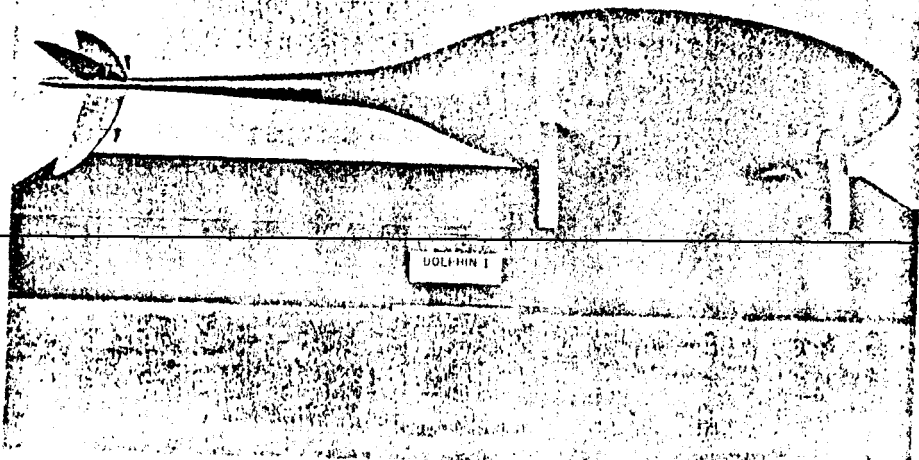


Fig. 5 Photograph of Dolphin 1.

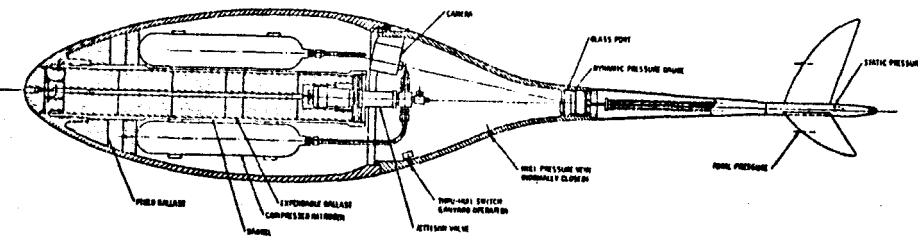


Fig. 6 Inboard profile Dolphin 1.

for ballast ejection for vehicle recovery and a lengthy turn-around time but introduces no disturbances and provides accurately known thrust. Further simplification is achieved by avoiding a control system. Boom and fins ensured dynamic stability and a steady vertical trajectory.

Data System

Since the vehicle was recovered after each run, the data were stored on board rather than transmitted to the surface during **the run**. A camera record of differential pressure, a clock, a compass, and two low-mass, highly damped pendulum vanes provided information on speed, time, rotation about the vertical trajectory, and normal accelerations, respectively. Speed was obtained with pitot-static sensors, whose open-ended total-head tubes protruded from the fin leading edges about a half-span out from the centerline to ensure their being outside the body wake, and whose static orifices were located in the boom, between and aft of the fins. The entire boom was flooded.

An external-type speed measuring system checked the accuracy of the onboard pitot-static system. It consisted of a 0.020-in.-diam piano wire, wound on an accurate drum located on the launch boat, and connected to the end of the tail boom. The drum rotated as the vehicle accelerated to depth, and a cam operated a switch that activated a pen to record the drum revolutions on a scroll, whereas a second pen produced a parallel print on the scroll from a 50-cps oscillator. The vertical motion of the launch boat was graphically faired out from an enlarged plot of speed vs time. The position error of the internal system was found to be negligible; the vanes indicated angle-of-attack variations of only a fraction of a degree at top speed.

Analysis

Velocity was plotted vs time, and the results smoothed. Slopes taken from this curve provided acceleration vs time. Integration of the velocity curve provided the depth history. The equation of motion for the vertical trajectory is

$$\text{thrust} - \text{drag} = (\text{effective mass}) (\text{acceleration})$$

where thrust is the accurately measured weight with the vehicle submerged in water, drag is the sum of body, stabilizing-boom, and fin drags, plus wire drag (when the calibration wire was used); and effective mass is the sum of the weight in air and 11% of the displaced weight of the sea water all divided by the acceleration of gravity. The use of 11% is from Lamb's value¹⁴ of virtual mass in the longitudinal direction for an ellipsoid with length/diameter = 3.33. The error in

to the slight difference in shape of the test body from that of an ellipse is small and becomes negligible near top speed.

It was necessary to estimate the tail drag, but the fact that the boom and a portion of the fins were immersed in the body wake complicated analysts. For this reason, an ogive nose was placed on the boom and the assembly towed at a depth of 1 ft below the surface behind a speed boat. The drag area or drag in pounds divided by the dynamic pressure (p/Z) U_∞^2 was found to be 0.013 ft² at 27 knots, which extrapolates to 0.012 ft² at 45 knots and coincides with a computed value neglecting the body wake. If the wake greatly increased the effective Reynolds number of the boom, the tail drag area at 45 knots could be as low as 0.008 ft². The friction drag of slender rods moving in the stream direction has been found to exceed flat-plate values at equal-length Reynolds number when the boundary layer is of a similar or greater radius than the rod. Thus, an intermediate value of tail drag area of 0.01 ft² is believed to be a conservative estimate. Estimation of wire drag was also complicated, and lengths of 0.020-in. diam piano wire and monofilament line were towed beneath and behind the speed boat, from which a value of drag/ $[(\rho/2)U_\infty^2](\pi d l)$ or wetted area coefficient of 0.0045 was experimentally established.

Performance was computed at 1/2-sec intervals using depth, speed, and acceleration data, by the following:

- 1) Total drag = thrust - (effective mass) (acceleration),
- 2) Total drag area = total drag/ $(p/2) U_\infty^2$.
- 3) Vehicle drag area = total drag area $\sim 0.0045 \pi d_{\text{wire}}$ (depth), when the trailing wire was used.
- 4) Hull drag area = vehicle drag area ~ 0.01 .
- 5) Hull wetted area drag coefficient = hull drag area/hull wetted area.
- 6) Hull length Reynolds number = 68,500 (hull length) (U_∞ fps).
- 7) Transition location in percent of projected body length is deduced by applying the hull fineness ratio wetted area coefficient, and length Reynolds number to a curve plotted from the analytical study of Ref. 3 (see Fig. 8).
- 8) Hull frontal area drag coefficient = hull drag area/ $(\pi/4)d_{\text{hull}}^2$.
- 9) Hull volumetric drag coefficient = hull drag area/(volume)^{2/3}.

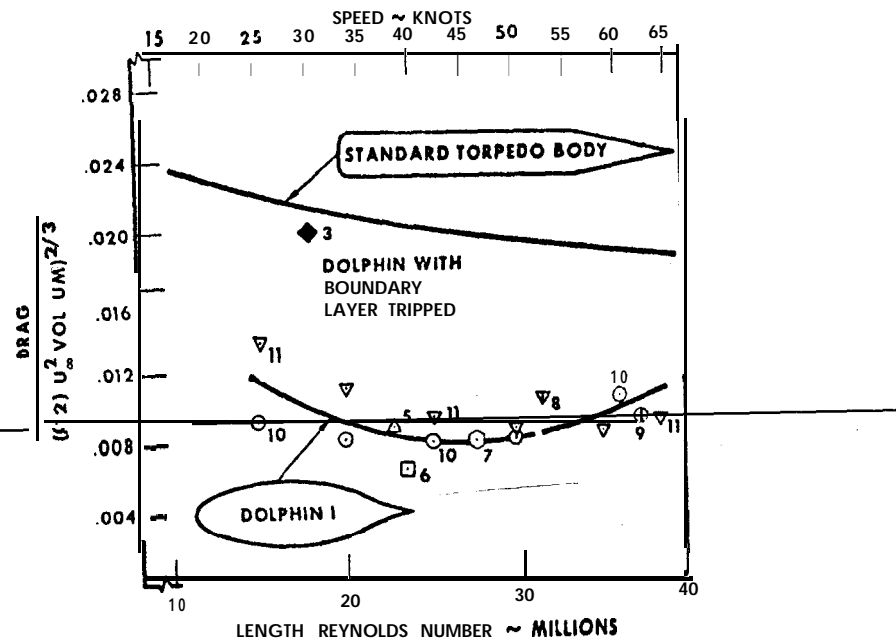


Fig. 7 Experimental drag comparison of Dolphin vs standard body.

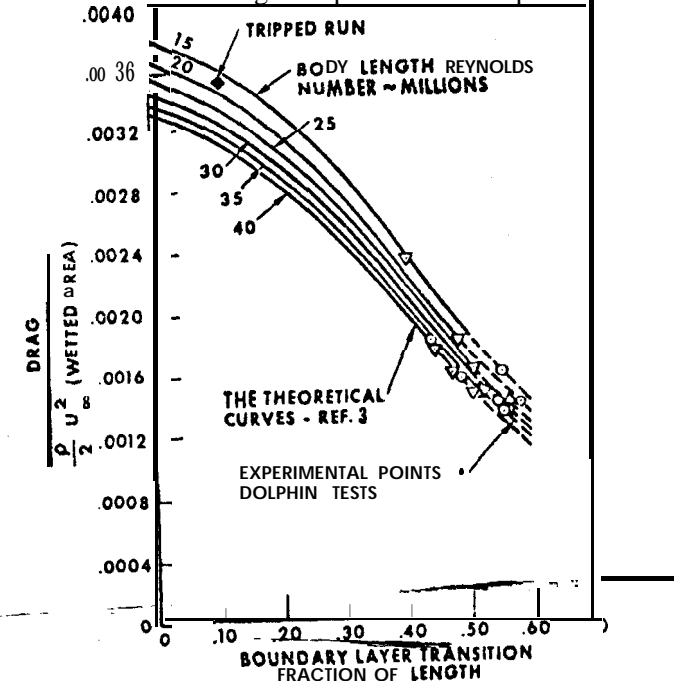


Fig. 8 Transition location deduced from wetted area drag coefficients,

Results

Seven sea tests during the midsummer of 1962¹² confirmed that hull drag was **more** than cut in half through geometric design alone using a vehicle in the **torpedo size-speed** range. Transition of the **laminar boundary layer** was found to be delayed to values of Reynolds numbers larger than those established in air flight. This indicates that the **ambient** turbulence level in parts of the ocean is low in the range of eddy sizes that affect laminar boundary-layer transition. No evidence of surface contamination occurred in the ocean, in sharp contrast to atmospheric flight, where insect and meteorological contamination is serious. Torpedo hulls were found well suited to the production of smooth, wave-free surfaces.

In a second series of tests¹³ with an enlarged ballast ejection system in early 1963, the thrust was doubled, extending the 45-knot, 27×10^6 hull-length Reynolds number of the first experiments to G2 knots and $48 \times 10^6 R_f$. Although the drag coefficient increased somewhat at R_f greater than 30×10^6 , it was still far below that of normal torpedoes.

The experimental hull drag coefficients are presented in Fig. 7 in the volume coefficient form which is most meaningful to torpedoes, along with experimental results for a clean standard torpedo hull (length/diameter = 8.0). They show that the new design (the Dolphin hull) at 45 knots with $R_f = 27 \times 10^6$ has 40% of the hull drag of a conventional torpedo of equal volume. Data from the end of each run (near terminal velocity) were generally used in Fig. 7 to minimize errors in the graphical differentiation required for the acceleration term, and because high speed and Reynolds number are of prime importance. The data in Fig. 7 for runs 10 and 11 include various acceleration values and illustrate the scatter in results when extensive laminar flow is involved. Run 11 had higher drag at low speed and lower drag at high speed, relative to run 10. In run 3, the boundary layer was artificially tripped near the nose. Its volume drag coefficient is slightly below the standard torpedo's, since the Dolphin's favorable volume-to-wetted-area ratio more than compensates for the higher wetted-area coefficient associated with a low-fineness-ratio, completely turbulent boundary-layer body. The large difference in Dolphin drag level when tripped and when clean proves the existence of extensive laminar flow in the latter case. The tripped drag value checks well with the prediction of Ref. 3,

The clean hull volume coefficient of 0.008 at $R_f = 24$ to 30×10^6 can be converted to a frontal area coefficient $CDA = 0.013$. The artificially tripped value at $R_f = 18 \times 10^6$ is ($C_{DA, \text{trip}} = 0.032$), which is lower than found in most turbulent flow applications because

of low fineness ratio, good form, and clean surface. The clean value of $CDA = 0.013$ is remarkably low. This experiment was designed to optimize the constant volume situation important to certain torpedoes. It may be possible to reduce further the fineness ratio and drag for the constant frontal area situation.

The results are reduced, in the foregoing, in terms of volume and frontal area. In Fig. 8, the experimental wetted area drag coefficients are superimposed on curves of wetted area drag coefficient vs transition position (interpolated from Ref. 3) for a fineness ratio of 3.33 and hull length Reynolds numbers of 15×10^6 to 40×10^6 . Extrapolation was required for transition locations aft of 50% length, and deduced to be between 45 and 58% of length. Minimum drag values occur between 20×10^6 and 30×10^6 length Reynolds number. Maxi-

mum length of laminar flow occurs at $R_f = 20 \times 10^6$, whereas the maximum transition length Reynolds number of $R_{XTR} = 18.4 \times 10^6$ occurs at $R_f = 38 \times 10^6$ and 48.5% of body length. These percentages refer to projected or centerline body length, in keeping with Ref. 3. The arc or surface distance Reynolds numbers are 8% larger.

Although more information is needed on small-scale turbulence and its influence on laminar flow experiments in the ocean, the magnitude of drag reduction demonstrated in these tests is so large that there is little question of the worth of this approach.

Conclusion

Underwater vehicle hull surface area can be reduced for either constant frontal area or constant volume applications through reduction in length-to-diameter ratio. The required fin surface area is simultaneously reduced. Surface area drag coefficient can theoretically be reduced by proper hull shape, together with low length-to-diameter ratio through attendant extension of the laminar boundary layer. Analogy with low-drag wing research suggests that laminar flow on submerged vehicles may be most extensive at a length-times-speed product near $500 \text{ ft}^2/\text{sec}$ with a reduction in drag to 1/3 conventional values under ideal conditions.

A gravity-powered, fin-stabilized body with 3.33 length-to-diameter ratio and 5.6 ft³ of volume was fabricated and tested in the Pacific Ocean. It achieved 60% drag reduction compared to a conventional torpedo of equal volume at 45 knots and approximately 50% at 60 knots. Transition length Reynolds numbers of 14 to 18×10^6 were deduced by comparison of experiments with theory. Such high values require low vehicle surface roughness and waviness, lack of vehicle surface contamination, and low ambient turbulence level. The very large drag reduction achieved encourages this simple approach where applicable.

References

- 1 Multhopp, H., "Aerodynamics of the fuselage," NACA TM1036 (1942).
- 2 De Young, J., "Theoretical additional span loading characteristics of wings with arbitrary sweep, aspect ratio, & taper **ratio**," NACA TN 1941 (December 1947).
- 3 Young, A. D., "The calculation of the total and skin friction drags of bodies of revolution at **zero** incidence," British R & M 1874 (April 1939).
- 4 Michel, R., "Etude de la transition sur les profils d'aile... establishment awn critere de determination du point de transition et calcul de la trainee de profil en incompressible," Office Nationale d'Etudes et de Recherches Aeronautiques Rapport 1/1578A (July 1951).
- 5 Smith, A. M.O. and Pierce, J., "Exact solution of the Neumann problem. Calculation of non-circulatory plane and axially symmetric flows about or within arbitrary boundaries," Douglas Aircraft ES26988 (April 1958).
- 6 Thwaites, B., "Approximate calculation of the laminar boundary layer," Aeronaut. Quart. I, 245 (1949).
- 7 Schubauer, G. B. and Skramstad, H. K., "Laminar-boundary-layer oscillations and transition on a flat plate," NACA TR 909 (1948).
- 8 Kramer, M. O., "Hydrodynamics of the dolphin," Hydroscience, edited by V. T. Chow (Academic Press, Inc., New York, to be published): Vol. II.
- 9 Carmichael, B. H. and Meggitt, D. J., "Wind tunnel test results of the **0.42-scale** model North American Aviation towed sonar vehicle," SID 65-1131, Contract N123(953)52188A (August 1965).
- 10 Carmichael B. H. and Nichues, O., "Computer study to establish the lower limit of length-to-diameter ratio advisable for low-drag bodies," North American Aviation SID 64-1938 (October 1964).
- 11 Truckenbrodt, E., "A method of quadrature for calculating the laminar and turbulent boundary layer for plane and axially symmetrical flow," NACA TM-1379 (May 1955).
- 12 Kramer, M. O., Carmichael, B. H., and Knoll, W. A., "Drag measurements in the Pacific Ocean on a 5.6 cubic-foot laminar body at speeds up to 45 knots," North American Aviation S&ID SID 63-43, Project Dolphin Phase I (December 1962).
- 13 Kramer, M. O., Carmichael, B. H., Knoll, W. A., and McNay, D. E., "Drag measurements in the Pacific Ocean on a 5.6-cubic foot laminar body at speeds up to 62 knots," North American Aviation SID 64-1242, Project Dolphin Phase II (May 1964).
- 14 Lamb, H., Hydrodynamics (Dover Publications, New York, 1945), 6th ed., p. 155.
- 15 Richmond, R. L., "Experimental investigation of thick, axially symmetric boundary layers on cylinders at **subsonic** and hypersonic speeds," Doctor of Philosophy Thesis, California Institute of Technology (1957).

EFFECT OF POLYMER ADDITIVES ON FLUID FRICTION

J. W. Hoyt* and A. G. Fabula†

Naval Undersea Warfare Center, Pasadena, Calif.

Abstract

Experimental studies verify that a few weight parts per million of certain high molecular weight, linear molecules lower the turbulent friction of aqueous solutions more than 70% below that of pure water. The phenomena does not appear related to a change in **the** viscosity of water, and does not necessarily occur in concentration regimes where the additives produce non-Newtonian flow.

Introduction

It is well established that very small concentrations of many natural and synthetic high-polymer substances reduce the turbulent friction drag of the liquid in which they are suspended or dissolved. The earliest published data on **turbulent-flow** reductions by dilute polymer solutions appear to be by Toms who studied polymethylmethacrylate in chlorobenzene. Flow of "thickened gasoline" was the subject of a U. S. Patent in 1949.² Work with aqueous solutions of polymers was reported simultaneously by Shaver and Merrill³ and Dodge and Metzner,⁴ all of whom used sodium carboxymethylcellulose. The technique has found commercial use in oil-field applications.^{5,6}

Because early workers attributed the friction-reduction phenomenon to induced "non-Newtonian" fluid properties, the term has become synonymous with the effect. However, it can be observed (indeed, becomes most prominent) at polymer concentrations at which the solutions are Newtonian by conventional viscometry. Further, polymer additives can be

Presented at the **ONR-Skipsmodelltanken**, Fifth Symposium on Naval Hydrodynamics, Bergen, Norway, September 12, 1964.

*Head, Propulsion Division, Underwater Ordnance Department.
†Staff Scientist, Applied Science Division.

effective in concentrations as little as a few weight parts per million (wppm).

Although the exact mechanism of the phenomenon is not known, general rules as to the types of material likely to be effective can be developed, and predictions made of the polymer concentration for maximum effectiveness in several simple flow situations. These generalizations may well apply to all solvent fluids, but the experimental work was with water solutions.

Experiments with Rotating Disks

Because apparatus was on hand, early work at the Naval Undersea Warfare Center (then the U.S. Naval Ordnance Test Station) was performed on large-scale rotating disk facilities. One is shown in Fig. 1 and consists of a 3785-liter water tank in which a 45.7-cm-diam disk is rotated at such a speed that turbulent flow extends over a major portion of it. Disk speed and shaft torque were measured with various concentrations of polymer additives in the tank. Most of the torque is developed near the outer disk edge, so that torque reduction is essentially equivalent to friction reduction, and these terms are used interchangeably.

An example of the type of data obtained is given in Fig. 2. The polymer additive is guar gum.[‡] At constant rotative speed, addition of the polymer immediately lowered the torque until, at 300-400 wppm, it is between 30 and 40% of its pure water value. At higher concentrations, torque increased somewhat, probably because of increased viscosity of the solution.

Much more striking results are obtained with the synthetic polymer poly(ethyleneoxide).^x Figure 3 shows data with the disk at 40 rev/sec for four molecular weights of the chemical. As molecular weight increased, the effect becomes more pronounced, and 70% torque (or friction) reduction is obtained with less than 100 wppm of the highest molecular weight material.

Results of similar tests with a wide variety of natural and synthetic polymers are gathered in Table 1, where wppm to achieve a friction reduction of 35% (half way between no

[‡] "Westco J-2 FP" supplied by the Western Company, Research Division, 2201 North Water-view Parkway, Richardson, Texas.

^xUnion Carbide Corp., 270 Park Avenue, New York, New York.

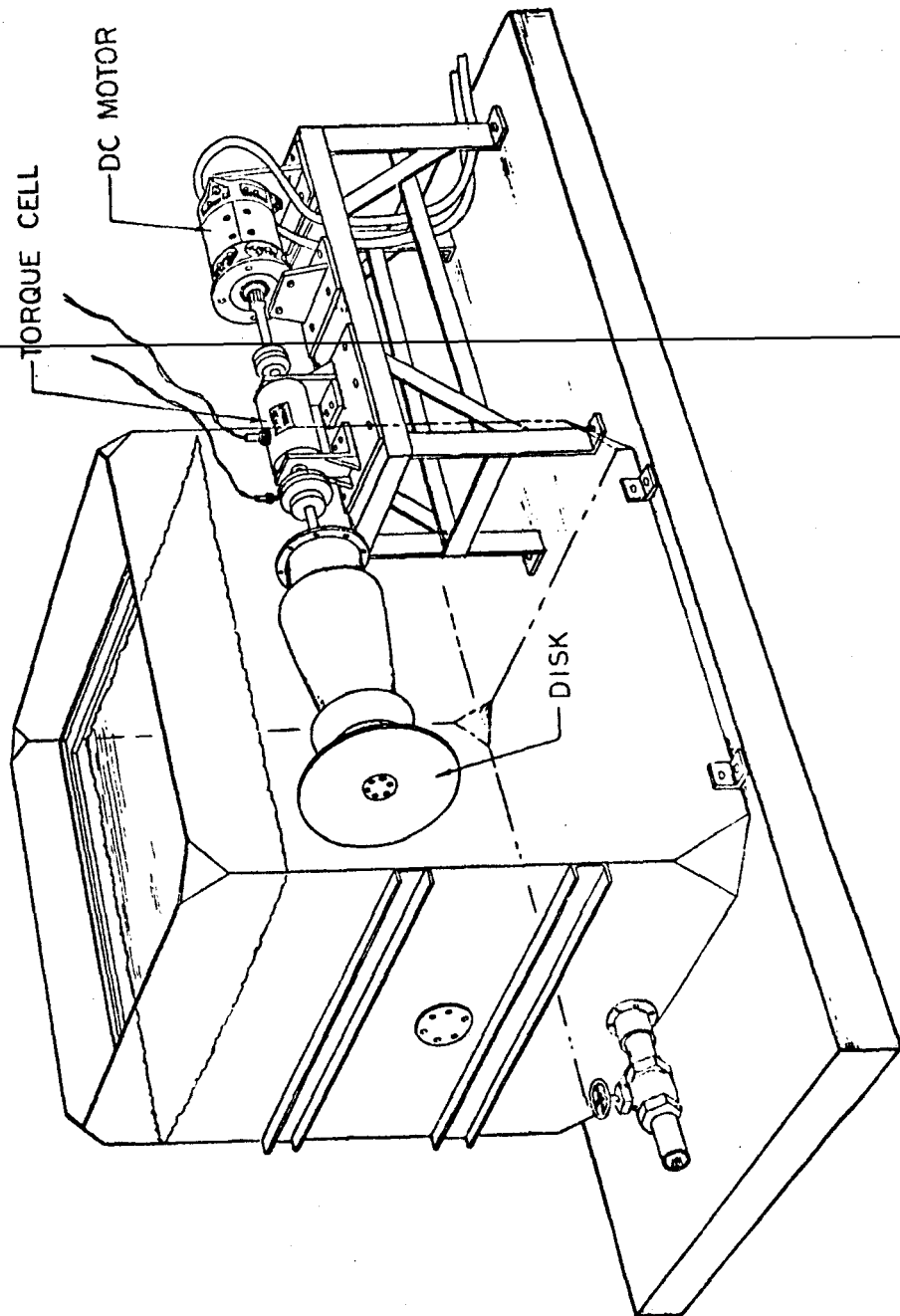


Fig. 1 Large rotating-disk apparatus.

effect and the maximum of about 70% observed at 40 rev/sec) are listed, together with properties of the polymer. It appears that at least three factors significantly affect the ability of a dissolved polymer to lower turbulent frictional resistance: *linearity, molecular weight., and solubility.*

Linearity

The most effective polymers are long-chain materials with essentially unbranched structures. The chemical formulas of guar and poly(ethylene oxide) shown in Fig. 4 indicate such compounds. Although configuration of these molecules in solution is poorly understood, approximate length-to-diameter ratios are from 350 to 500 for guar, and from 22,000 to 165,000 for poly(ethylene oxide), or 6×10^6 molecular weight. Thus, ignoring, for the moment, molecular chain flexibility, the linearity of the molecule appears important.

Molecular Weight

Accompanying linearity is an increase in molecular weight. However, the experiments with Gum Karaya (Table 1) indicate that high molecular weight in itself is not as effective as linearity. Thus poly(ethylene oxide) is some 65 times more effective on a weight basis than the heavier Gum Karaya molecule.

Replotting the disk data of Fig. 3 for a constant rotative speed of 40 rev/sec for poly(ethylene oxide) in the logarithmic manner of Fig. 5 shows the dependence of friction-reduction on molecular weight. Apparently substantial increases are required to achieve better friction reductions. Such unusually large macromolecules approach finite particles, and experiments with woodpulp⁷ show reductions are obtained, although much lower than reported here. This brings up the third requirement for maximum effectiveness, solubility.

Solubility

Referring again to Table 1, tests with Carrageenan indicate the greater the solubility the more the friction reduction. Further, certain molecules, which otherwise would be expected to be very effective, such as Amylose, are not, probably because of poor solubility.

--Further Work with Rotating Disks

Since the large-scale rotating disk apparatus of Fig. 1 required large amounts of experimental solutions, a smaller

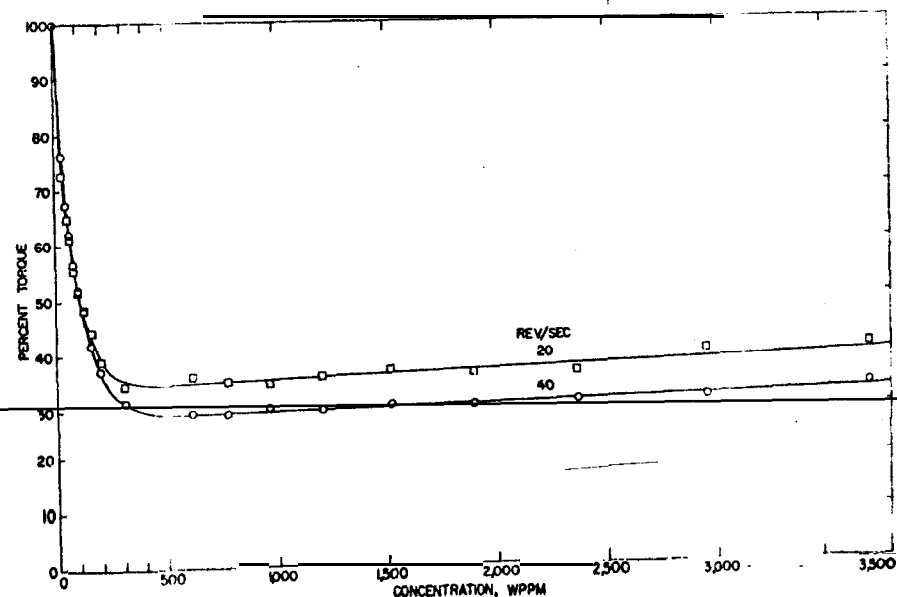


Fig. 2 Rotating-disk torque curves with **guar** additive.

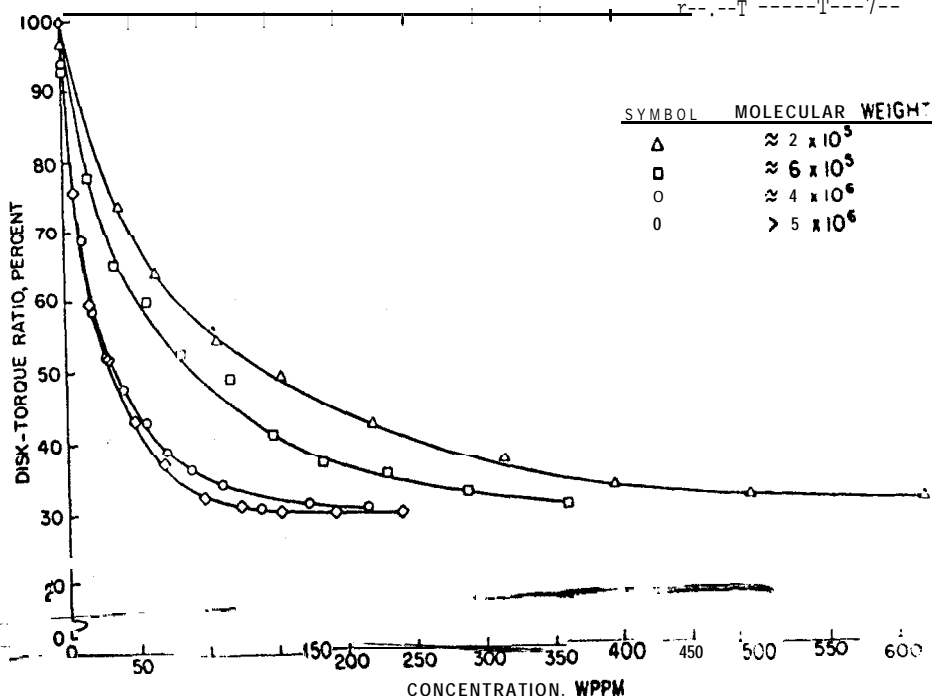


Fig. 3 Rotating-disk torque curves for **poly(ethylene oxide)** additives.

Table 1 Comparative friction-reduction effectiveness of water-soluble polymer additives measured with the rotating-disk facility

Additive	C_R^a	$M \times 10^{-6}^b$	Notable Characteristics
Guar gum, w, s (J-2FP) ^c	60	0.2	Straight chain molecule with single-membered side branches
Locust bean gum, m	260 (260) ^d	0.31	Similar to guar but with fewer side branches , causing reduced solvability and less hydrogen bonding
Carageenan or Irish moss, m (Stamere NK)	650 (420)	0.1 - 0.8	Strongly charged anionic polyelectrolyte
Gum karaya, m	780	9.5	Highly branched molecule; relatively insoluble ; acidic
Gum arabic, b	Ineff.	0.24 + 1	Highly branched molecule
Amylose, s (Superlose)	Ineff.	>0.15	Linear chain molecule; retrogrades rapidly
Amylopectin, s (Ramalin G)	Ineff.	1.2	Highly branched molecule
Hydroxyethyl cellulose, u (Cellosize QP-15000) (Cellosize QP-30000) (Cellosite QP-52000)	220 220 160	Nonionic; formed by addition of ethylene oxide to cellulose ; has side branches of various lengths
Sodium carboxymethyl-cellulose, h (CMC WHSP)	400	0.2 - 0.7
Poly(ethylene oxide), u (Polyox WSR-35) (Polyox WSR-205) (Polyox WSR-30 1) (Polyox coagulant)	70 44 17 12	0.2 0.6 4 >5	Very water-soluble ; no biological oxygen demand; apparently an unbranched molecule with unusual affinity for water
Polyacrylamide, d (Separan NP10) (Separan NP20) (Separan AP30)	26 25 29	1 2 2-3	Nonionic Nonionic Anionic
Polyhall-27, s	130
Polyvinylpyrrolidone, f (K30) (K90)	Ineff. 2900	0.04 0.36	a....
Polyvinyl alcohol, e (Elvanol 51-05) (Elvanol 72-60)	Ineff. Ineff.	0.032 D. 17 - 0.22
Silicone, u (L-531)	Ineff.
Polyacrylic acid, g (Goodrite 773x020 B-3) (Goodrite K-702) (Goodrite K-714)	Ineff. Ineff. Ineff.	0.006 0.090 0.2 - 0.25
Carboxy vinyl polymer, g (Carbopol 941)	Ineff.	...	Inconclusive test due to precipitation upon dilution

^a C_R = concentration required (in weight parts per million) for 35% disk-torque reduction at 40 rev/sec with lake water as the solvent.

^b M = approximate molecular weight of the polymer according to the literature.

^c The source of each polymer for this work is indicated by the letter after its name:

^d Braun Div., Van Waters and Rogers, Inc.; ^e Dow Chemical Co.; ^f E. I. DuPont;

^g General Aniline and Film Corp.; ^h B. F. Goodrich Chemical Co.; ⁱ Hercules Powder Co.; ^m Meer Corp.; ^s Stein, Hall and Co.; ^u Union Carbide Chemicals Co.; ^w Westco Research.

^a C_R values in parenthesis are for solutions given heat treatment to increase polymer solubility.

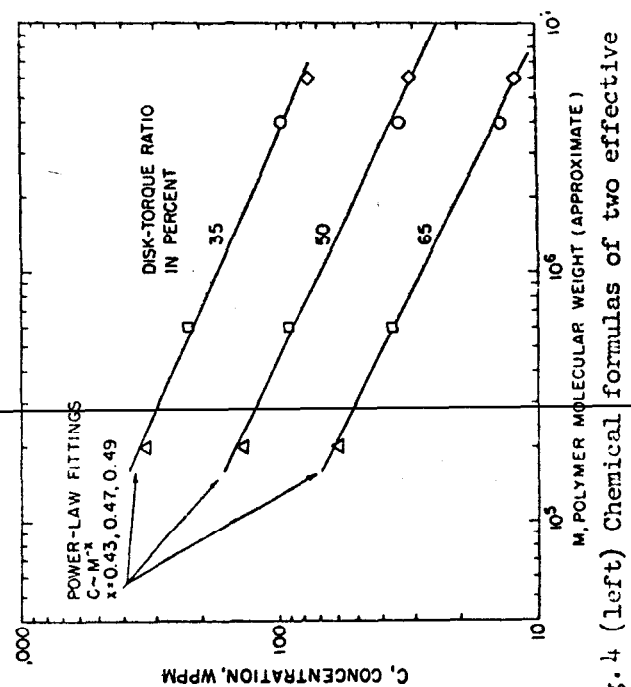
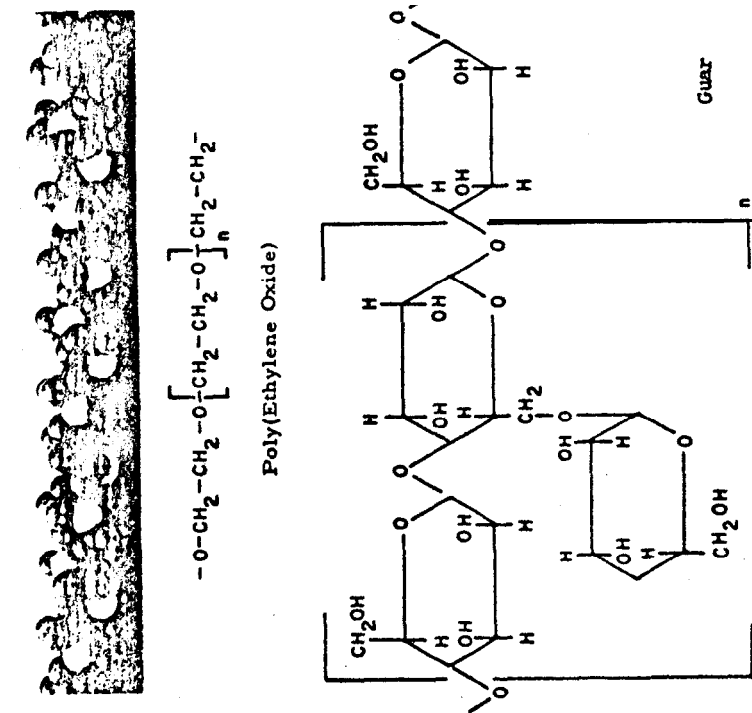


Fig. 4 (left) Chemical formulas of two effective additives.
Fig. 5 (above) Dependence of required concentration for various disk torque ratios on molecular weight of poly(ethylene oxide).



disk of 16 cm diem was developed that required only 2 liters. Figure 6 shows experimental data obtained with it using **guar** gum, with a maximum torque reduction on the order of 40%. Similar data are shown in Fig. 7 for solutions of **poly(ethylene oxide)**.

The torque reductions obtained with the large and **small** disks and their variation with rotative speed suggested plotting results as a function of Reynolds number. Such a plot of maximum torque reduction vs. Reynolds number based on the viscosity of pure water is shown in Fig. 8 for data from the 7.6 cm, the 45.7 cm, and also a **76.2-cm** disk. Typical data points for the **45.7-cm** disk which were used in **Fig. 8 are given in Table 2 and are concentrations of various materials required to attain 70% reduction at a Reynolds number of 1.3×10^6** . Apparently at any Reynolds number, the same **maximum** torque reduction is obtained with **all** of the "effective" polymers, although the required concentrations varied from polymer to polymer.

Table 2 Concentrations (wppm) to achieve 70% torque reduction at a rotating disk $Re = 1,300,000^a$

Guar gum (J-2FP)	500
Locust bean gum	1700
Gum Karaya	2700
Polyhall-27	850
Polyox-WSR 205	250
Separan AP 30	100

^a The source and molecular weight of the above materials is given in Table 1.

Effect of Sea Water

Additional tests-e with the 45.7-cm disk in sea water. As shown in Fig. 9, friction reduction for **guar** in simulated sea water agrees closely with that in fresh water. The tests were made three different temperatures from **10° to 27°C**. **Poly(ethylene oxide)** solutions were found to be even less affected by sea water salts.

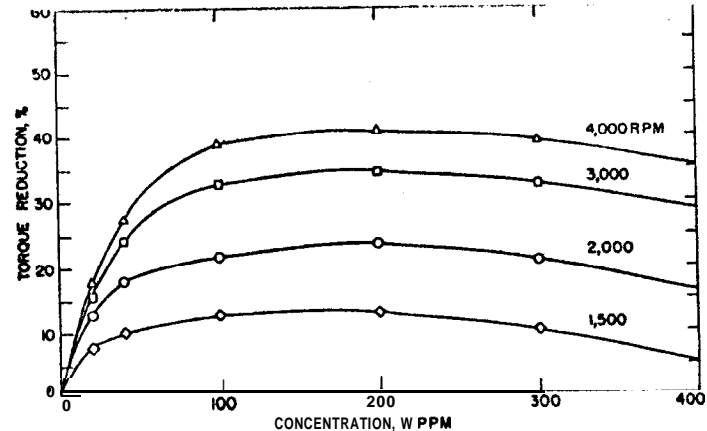


Fig. 6 7.6-cm disk torque reduction vs guar gum concentration.

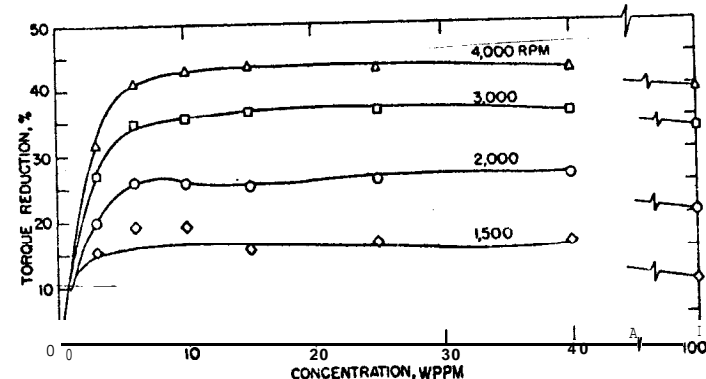


Fig. 7 7.6-cm disk torque reduction vs poly(ethylene oxide) concentration.

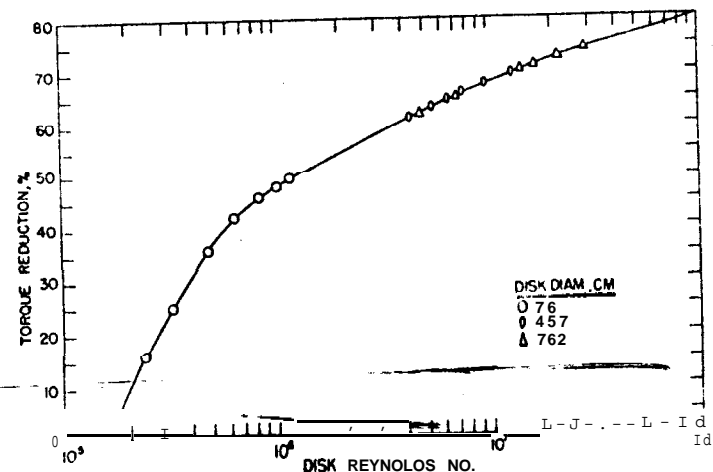


Fig. 8 Maximum torque reduction as a function of Reynolds number.

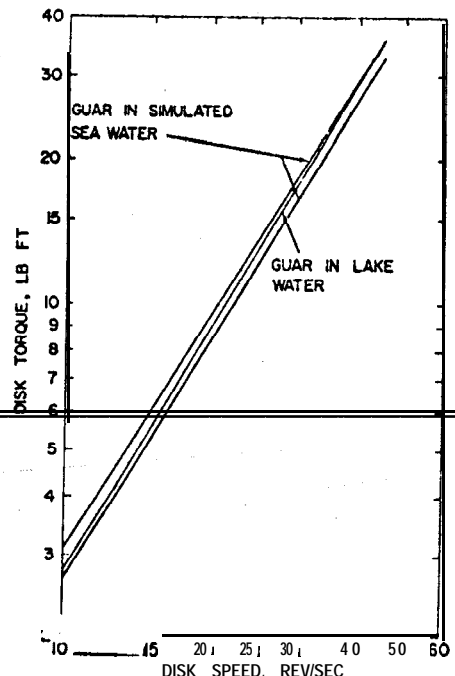


Fig. 9 Effect of seawater on guar solution.

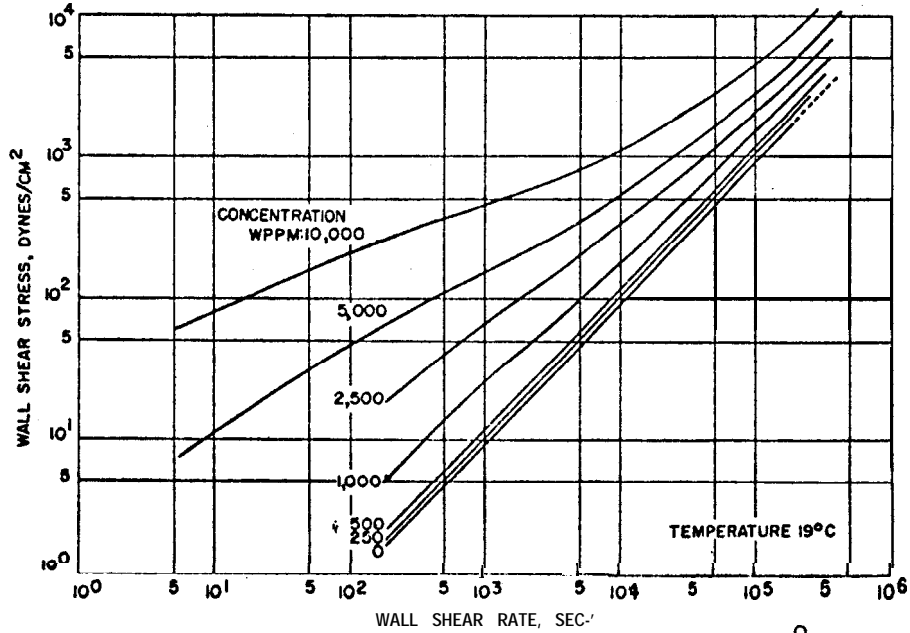


Fig. 10 Rheogram for guar additive in water at 19°C.

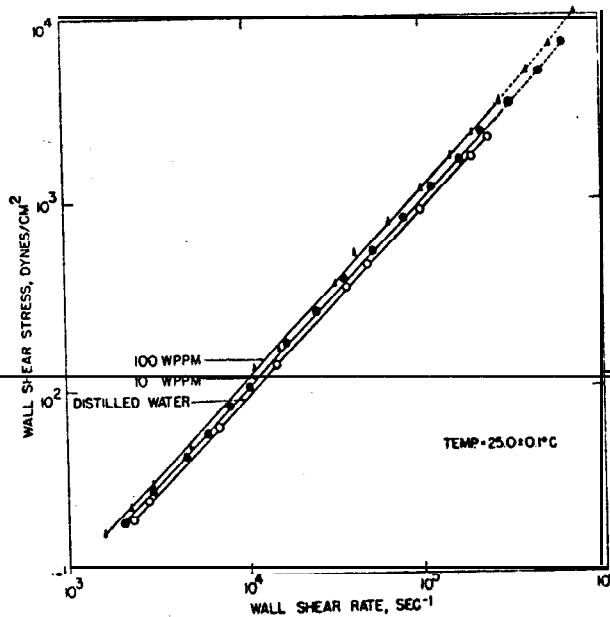
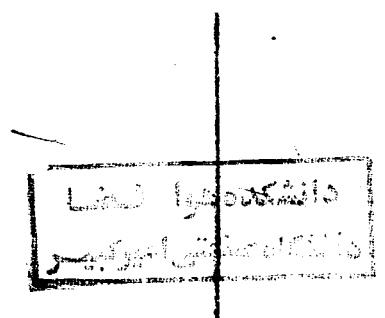


Fig. 11 Rheogram of poly(ethylene oxide) of 4×10^6 molecular weight in water.

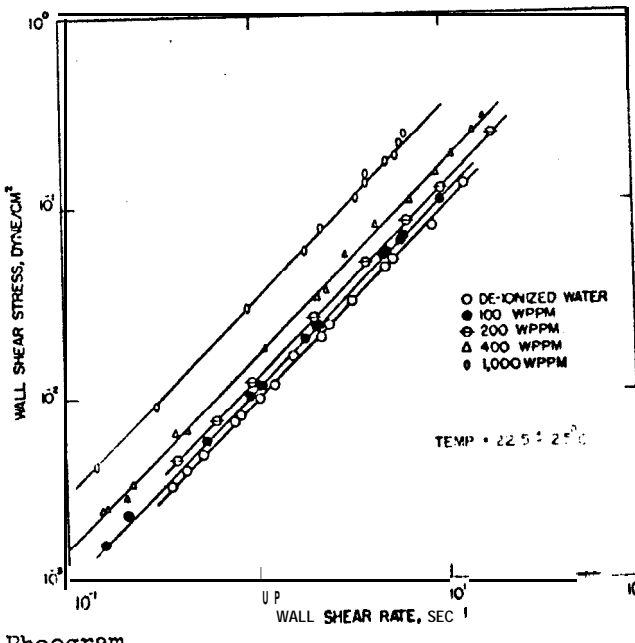


Fig. 12 Rheogram for poly(ethylene oxide) of 4×10^6 molecule weight at low shear rates.

Rheological Studies

Since high concentrations (above 1000 wppm) of these polymers are shear-thinning, early explanations of their reduced friction were based on their variable or "non-Newtonian" viscosity. Considerable study was thus devoted to their rheology and on exploring how this behavior provides drag reduction.

Figure 10 shows a rheogram for guar, and Fig. 11 for poly(ethylene oxide) of 4×10^6 molecular weight.¹ At concentrations under 500 wppm for guar and under 100 wppm for poly(ethylene oxide) it is difficult to ascribe a variable viscosity with shear to the solutions. Constant viscosity extends even to very low shear, as shown in Fig. 12.** The term "non-Newtonian" is inappropriate for these fluids, unless nonsteady measurements show shear rigidities at high frequencies, since their rheograms at polymer concentrations where maximum friction reductions are obtained show the solutions to have essentially constant viscosity with shear as well as a viscosity greater than that of the solvent. Only at higher concentrations were departures from constant viscosity evident.

Lumley⁸ has argued that friction reductions should not be expected in purely viscous, non-Newtonian class of fluids. Although many of the effective additives produce highly viscoelastic solutions in higher concentrations, not all viscoelastic solutions are effective drag reducers, e.g., Carbopol (Table 1). Furthermore, drag reduction was not enhanced by increasing the viscosity of solutions of guar by "complexing" with sodium borate.⁹ In fact, doing so lowered the drag-reduction effect, based upon the weight of guar in solution. In a typical test, viscosity was increased by a factor of 22 over the guar solution alone by adding sodium borate, but the drag reduction was only 70% of that which would have occurred with guar only.

Whatever the method by which friction reduction is produced, it seems clear that the action involves suppression of turbulence intensity. Figure 13 shows test data from the 45.7-cm-diam disk for guar, correlated with disk Reynolds numbers based on water. At concentrations up to 311 wppm, the slopes

¹Data obtained under U. S. Navy contract by the Western Co., Research Division, using Fann and Burrel-Severs viscometers.

^{**}Data obtained by J. M. Caraher of the Naval Undersea Warfare Center, using a helical-coil viscometer of his design.¹

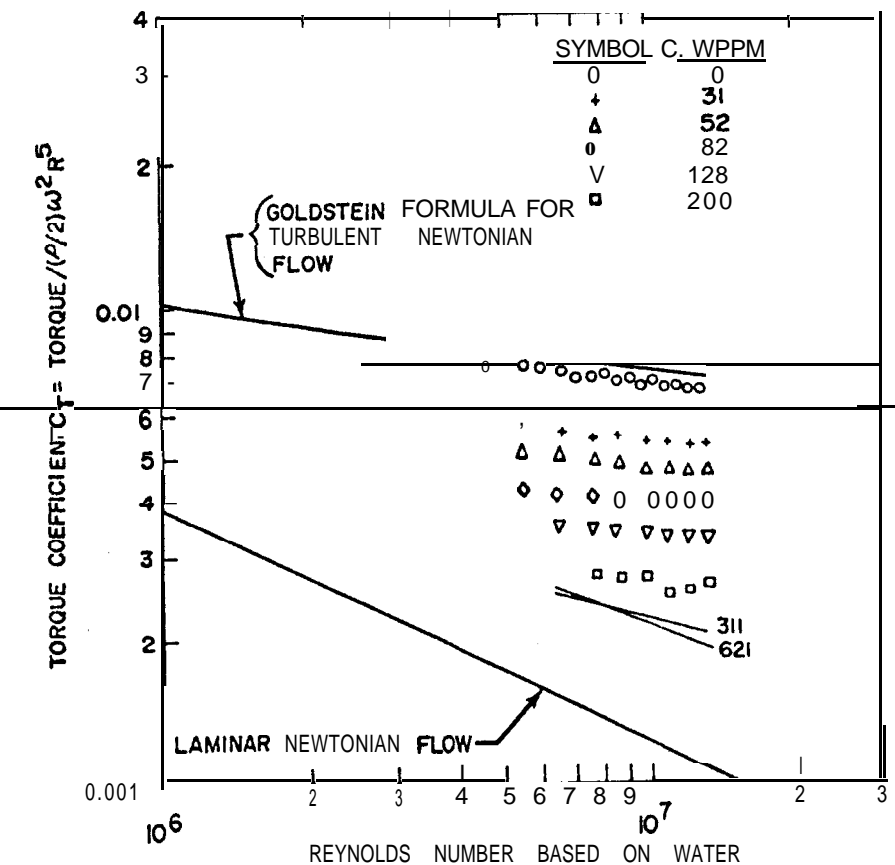


Fig. 13 Torque coefficient as a function of Reynolds number.

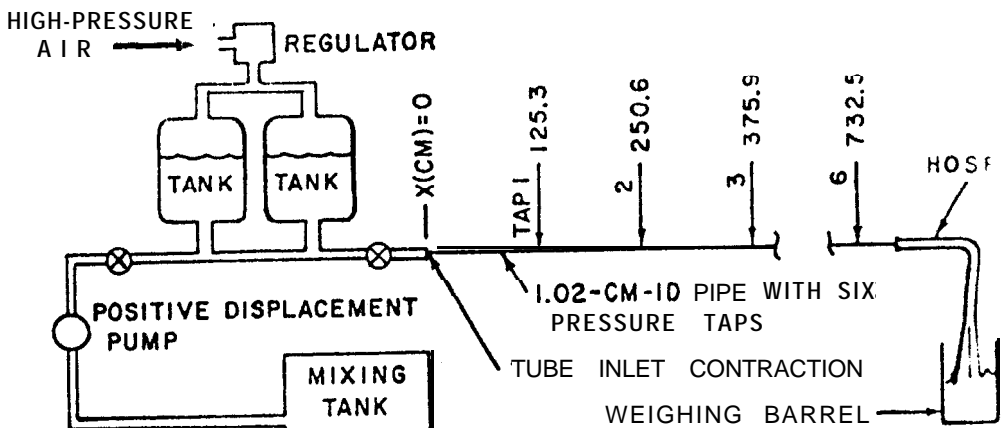


Fig. 14 Schematic diagram of blowdown pipe apparatus.

of the curves are roughly parallel to, but lower than, the turbulent-flow water data. For 621 wppm and above, the slopes are roughly parallel to, but higher than, the laminar-flow water case. Thus, under 500 wppm no significant changes in Fig. 13 would result from use of Reynolds numbers based on the measured viscosities of solutions.

Pipe Flow Experiments

Friction-reducing effects of polymer solutions can be studied by measuring pressure drops in a length of pipe in which the polymer solution is flowing. One such facility is shown schematically in Fig. 14, which uses air-pressure pumping to minimize degradation of test solutions.¹⁰ Polymer solution was forced through the pipe test and its static-pressure gradient measured at various stations. Flow rates were determined by weighing the polymer solution discharged in a given time, and the discharged solution was discarded to minimize shear degradation effects which occur very rapidly in many solutions. Drag reduction was calculated by comparison with similar tests with pure water.

'Typical data for poly(ethylene oxide) of 4×10^6 molecular weight are shown in Fig. 15. Drag reduction of well over 75% was obtained. Similar data for the polymer in sea water (obtained in a similar apparatus¹⁺) are given in Fig. 16.

Another pipe flow apparatus, which is essentially a turbulent flow rheometer, is sketched in Fig. 17. The piston of the cylinder is moved upward at 1.245 cm/sec , forcing fluid through the small diameter pipe. Representative data, taken at a constant flow velocity of 12.65 m/sec (Reynolds number based upon water at 21.1°C of approximately 14,000), are given in Fig. 18.

Reynolds Number Correlation

Data from poly(ethylene oxide) of 4×10^6 molecular weight have been correlated with pipe-flow Reynolds numbers, using the viscosity of pure water. At 100 wppm, drag reduction reaches 78 - 79% at a Reynolds number of about 105. At 30 wppm the effect falls off at higher Reynolds numbers, perhaps because of rapid shear degradation of the polymer.

The envelope of maximum drag reduction in pipes is plotted in Fig. 19 as maximum effects for the polymers as a function

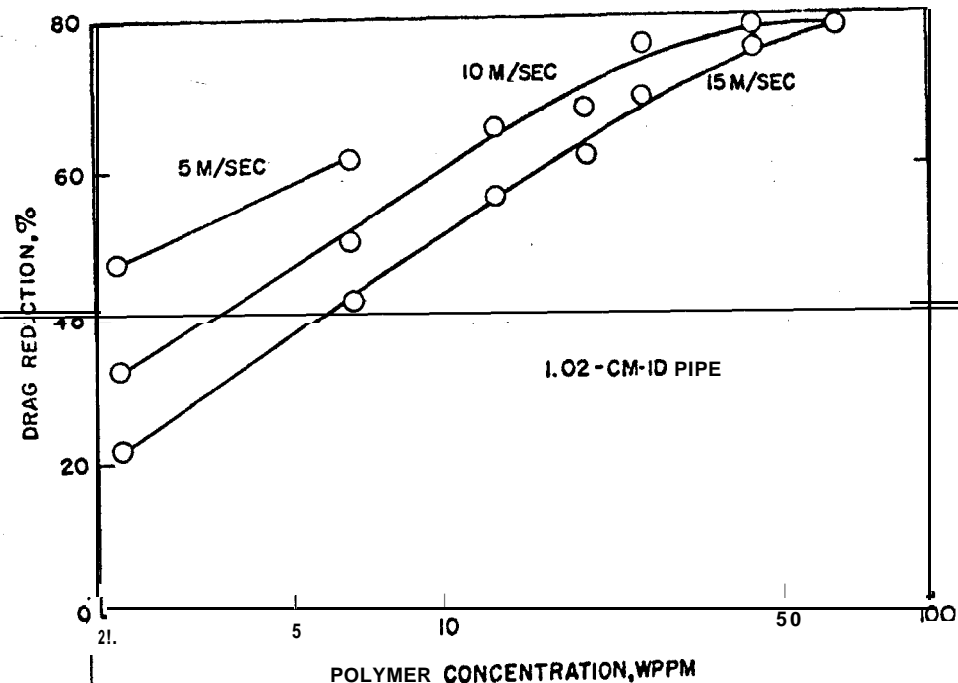


Fig. 15 Drag reduction for poly(ethylene oxide) in blowdown pipe apparatus.

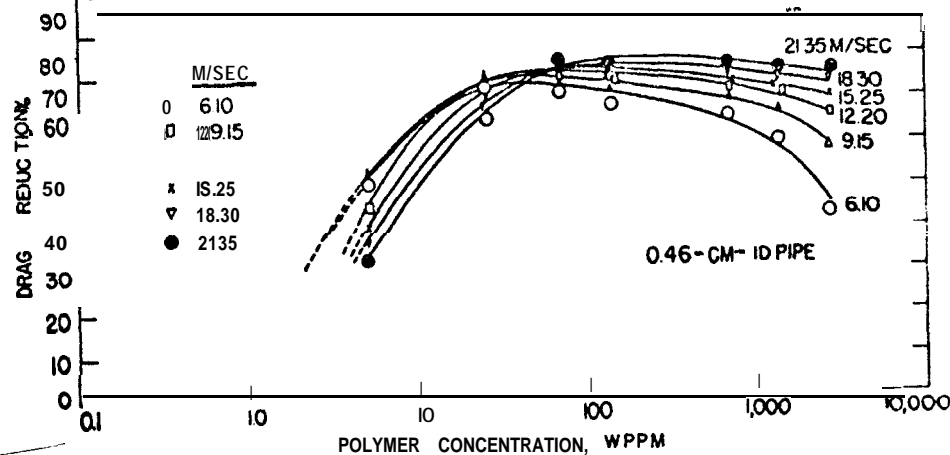


Fig. 16 Friction reduction for poly(ethylene oxide) in pipe-flow apparatus.

*Data taken by the Western Co. under U. S. Navy contract.

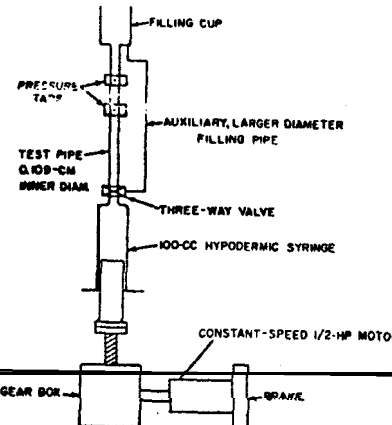


Fig. 17 Turbulent-flow rheometer.

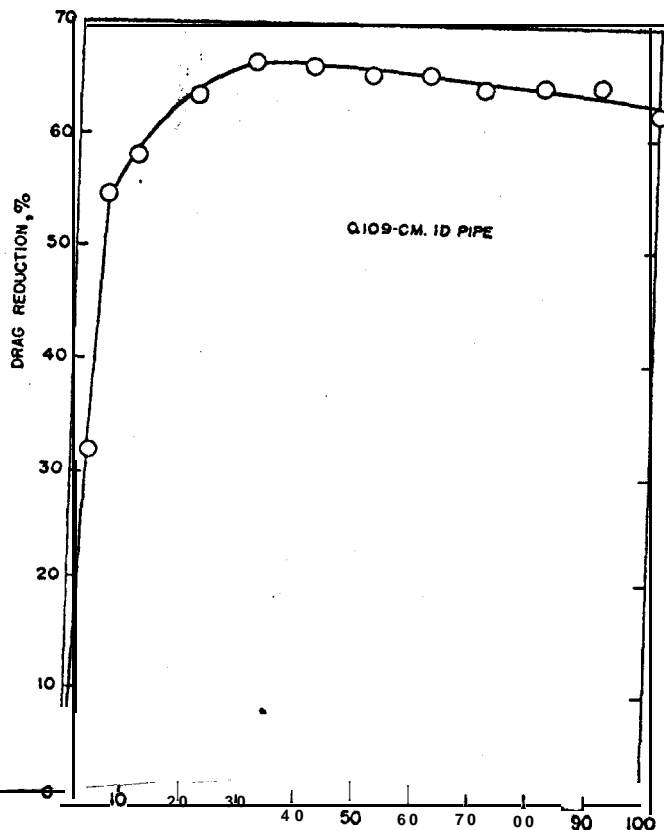


Fig. 18 Turbulent-flow rheometer data for poly(ethylene oxide).

of Reynolds number. It provides an empirical relationship for pipe flows corresponding to that for rotating disks in Fig. 8. The data are consistent with those reported in Ref. 11.

For use in Fig. 19, Table 3 gives some concentrations of materials required to attain the maximum drag reduction of 67% at a pipe flow Reynolds number of 1.4×10^4 .

Table 3 Concentrations (wppm) required to achieve 67% drag reduction in pipe flow at $Re = 14,000$

Guar (J-2FP)	400
Colloid HV-6 ^a (refined Guar)	375
Polyox WSR-301	30
Colloid HV-2 ^a (refined Guar)	500

^aStein, Hall and Co; other materials as listed in Table 1.

Experiments with Marine Organisms

The drag reduction phenomenon has been suggested¹² to explain erratic fluctuations of measured resistance in some towing tanks¹¹, which are always low, and as much as 14%. Many algae and marine organisms secrete mucus or slime, which may act in the manner of the compounds studied. The data of Table 4, (obtained with the turbulent flow rheometer), although not intended to be rigorous or even quantitative, do show this possibility. Sizeable reductions in drag apparently are obtained from a variety of natural substances.

Conclusions

Aqueous solutions of certain polymers exhibit lowered turbulent friction drag than the pure solvents when tested in various types of apparatus. The reduction appears dependent

¹¹It appears that these fluctuations are reduced in tanks where the water is chemically purified.

primarily on the linearity of the polymer molecules, with molecular weight and solubilities also having important effects. Many natural substances also cause lowered drag.

Correlation curves can be constructed which show maximum friction reductions for a variety of substances vs. Reynolds numbers.

Table 4 Drag reduction of living materials

Material	Drag reduction, %
Fresh water algae	
Blue-green (<u>Anabaena floss-aquae</u>)	59.5
Green (<u>Chlamydomonas peterfi</u>)	29.0
Red (<u>Porphyridium aerugineum</u>)	65.0
Seawater algae	
Dinoflagellate (<u>Prorocentrum micans</u>)	32.0
Diatom (<u>Chaetoceros didymus</u>)	52.0
Fish slime	
Small mouth bass	60.0

References

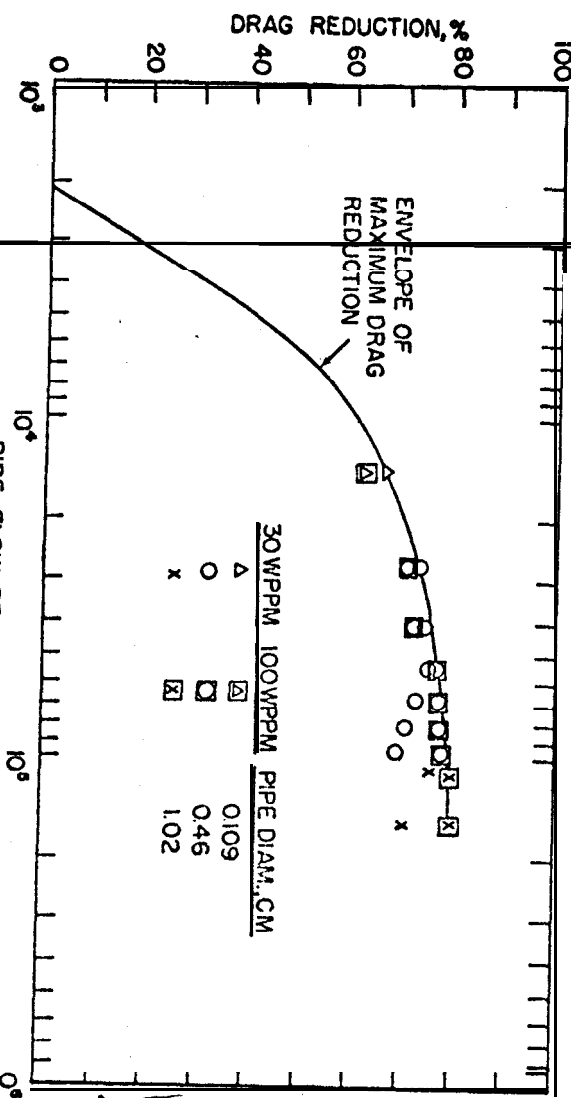
¹Toms, B. A., "Some observations on the flow of linear polymer solutions through straight tubes at large Reynolds numbers," Proceedings of the International Rheological Congress, North-Holland Publishing Co., Amsterdam (1948), pp. II • 135 • 41.

²Mysels, K. J., "Flow of thickened fluids," U. S. Patent 2,492,173 (December 27, 1949).

'Shaver, R. G. and Merrill, E. W., "Turbulent flow of

Fig. 19

Reynolds number correlation for pipe flow.



pseudoplastic polymer solutions in straight cylindrical tubes," Am. Inst. Chem. Engrs. J. 5, 181 (1959).

⁴Dodge, D. W. and Metzner, A. B., "Turbulent flow of non-Newtonian systems," Am. Inst. Chem. Engrs. J. 5, 189 (1959).

⁵Dever, C. D., Harbour, R. J., and Seifert, W. F., "Method of decreasing friction loss in flowing fluids," U. S. Patent 3,023,760 (March 6, 1962).

⁶Melton, L. L. and Malone, W. T., "Fluid mechanics research and engineering application in non-Newtonian fluid systems," Soc. Petrol. Engrs. J. 4 56 (March 1964).

'Daily J. W. and Bugliarello, G., "The effects of fibers on velocity distribution, turbulence and flow resistance of dilute suspensions," Hydrodynamics Lab. TR 30, Massachusetts Institute of Technology (October 1958).

⁸Lumley, J. L., "Turbulence in non-Newtonian fluids," Phys. Fluids 7 (March 1964) 335-337.

Whistler, R. L. and BeMiller, J. N., (eds.) Industrial Gums (Academic Press, New York, 1959).

¹⁰Fabula, A. G., "The Toms phenomenon in the turbulent flow of very dilute polymer solutions," Proceedings of the Fourth International Congress on Rheology, Wiley (Interscience), New York, (August 1963).

¹¹Ripken, J. F. and Palk, M., "Studies of the reduction of pipe friction with the non-Newtonian additive CMC," St. Anthony Falls Hydraulic Lab. Technical Paper 42, Ser. B (April 1963).

¹²Hoyt, J. W. and Fabula, A. G., "Frictional resistance in towing tanks," Tenth International Towing Tank Conference, National Physical Laboratory, England (September 1963).

EXPERIMENTAL MODEL STUDIES OF NON-NEWTONIAN SOLUBLE COATINGS FOR DRAG REDUCTION

S. Thurston* and R. D. Jones+

Northrop Corporation, Hawthorne, California

Abstract

~~Experimental model studies have been carried out to demonstrate the feasibility of using a soluble coating on the surface of an underwater body to reduce friction drag. The coating dissolves in a predictable manner, and the body rides in a boundary layer of non-Newtonian fluid. A model test program was carried out with a small body of revolution in a simple drop-tank facility. The distance-time relationship was measured and drag derived therefrom. Although the tests were not systematic, and the location of the coating was limited to the stagnation region of the nose, reductions in total model drag of 18% with fresh water and 16% with sea water were obtained. This corresponds to reductions in model friction drag of 30 and 27%, respectively.~~

Introduction

The friction drag of marine craft increases exponentially with velocity and consequently represents a major barrier to the attainment of higher speeds and major performance improvements. Therefore, serious attention is being given to techniques for reducing drag. One promising approach for missions of short duration involves the use of soluble coatings to impart non-Newtonian properties to the boundary-layer flow.

An earlier version of this paper was published in the March-April 1965 issue of the Journal of Aircraft. The subject program was conducted while the authors were employed by Astropower, Inc., a subsidiary of the Douglas Nrcraft Company. The authors gratefully acknowledge the work of E. Levy-Pascal and N.R. Byrd of Astropower, Inc., who contributed much valuable information during the program.

*Chief, Advanced Underwater Systems Group, Norair Division.

+Senior Engineer, Nortronics Division.

An insight into the behavior of a non-Newtonian fluid can be acquired by comparing it with pure water. In water, the shear stress is proportional to the rate of shearing deformation adjacent to the body surfaces. This ratio is the coefficient of viscosity and is constant for water that exhibits "Newtonian" behavior. The shear stress at a water-body surface is

$$T_s = \mu (du/dy)_s$$

where

μ is the absolute coefficient of viscosity, and $(du/dy)_s$ is the velocity gradient (rate of shear) at the body surface.

For a non-Newtonian fluid, the ratio of the shear stress to the rate of shear is not constant. Examples are colloids, emulsions, polymer suspensions, and some organic materials.

Typical relationships of the flow velocity in a capillary tube as a function of pressure loss across the tube for various general classes of non-Newtonian and Newtonian fluids are shown in Fig. 1. Newtonian fluids exhibit linearity between velocity and pressure loss, whereas non-Newtonian fluids deviate substantially from linearity, depending on the nature of the liquid.

A number of chemicals have been identified by the Naval Ordnance Test Station² which reduce the friction drag of water flowing in pipes when added in very small quantities. These chemicals are related in that they are polymers with a high molecular weight and a long chain molecular structure. Some promising chemicals are Guar (J-2FP), Colloid HV-6 (refined Guar), and Polyox WSR-301. The coatings used herein utilized similar polymers with high molecular weight and a long chain molecular structure. These were Polyox WSR-35, Dowfax 9N40, and Methocel 4000 cps. It is of interest, as pointed out in Ref. 2, that even living materials in solution reduce friction drag; examples of these are scraped slime from sea fish and from the sea snail. Refs. 3-7 further describe the behavior of friction reducing additives and non-Newtonian flow.

This paper describes an experimental model test program to demonstrate the feasibility of using a soluble coating to reduce friction drag of an underwater body. This coating dissolves in a predictable manner, and the body rides in a boundary layer of non-Newtonian fluid. Model tests of a

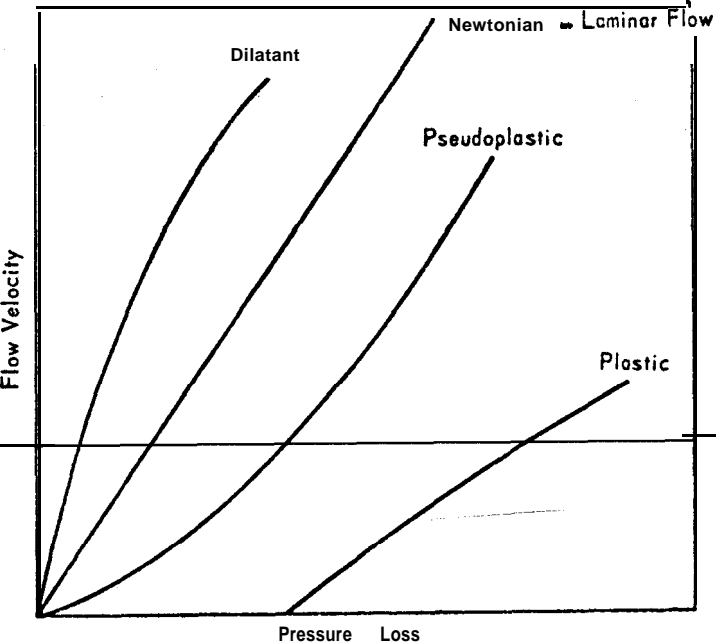


Fig. 1 Variation of pressure loss in capillary tubes with flow velocity for various non-Newtonian fluids.

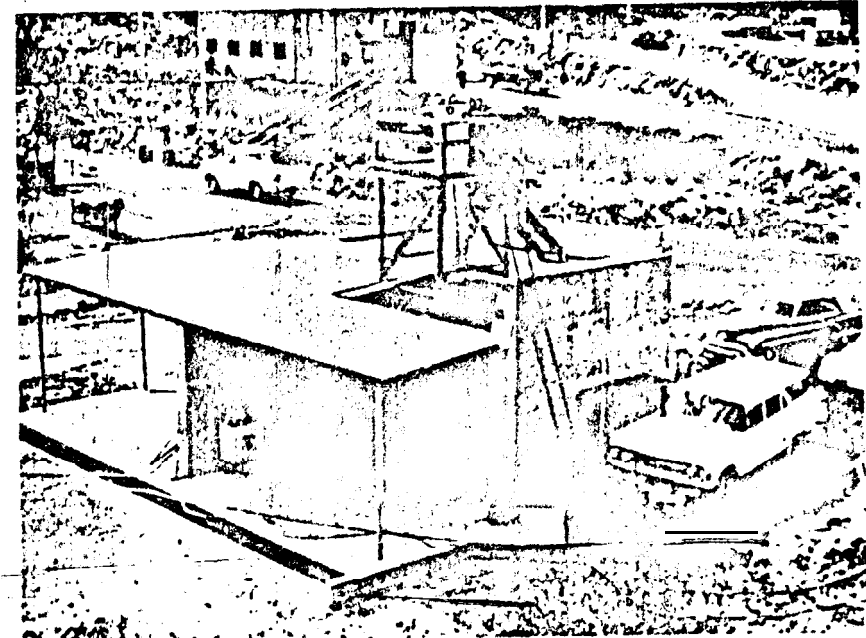


Fig. 2 Test tank.

simple body of revolution have demonstrated a reduction in friction drag of over 30% with fresh water and 27% with sea water. The results of the experimental program are presented herein.

Test Configuration and Procedures

Model Tank

The test program was carried out in the model test-tank facility shown in Figs. 2 and 3. The tank is 2 ft in diameter, 20 ft long, and has a capacity of approximately 500 gal.

The tank was instrumented at nine vertical stations, 2 ft apart, to determine the distance-time relationship. At each station, a floodlight projects a plane of light through a horizontal slit 0.06 in. wide by 3 in. long. Light-sensitive resistors mounted at each end of the light slit register the nearly instantaneous change in light intensity due to the reflectivity of the model as it passes. The models were black, with the exception of a reflective ring around the center section to reflect light to the light-sensitive resistors, whose output was recorded as a function of time on an oscillograph recorder. An electromagnetic release mechanism for the model was located at the top of the tank. Temperature and kinematic viscosity were determined before and after each test. The range of Reynolds numbers attainable and their relationship to the transitional and turbulent regions are shown in Fig. 4. The maximum Reynolds number was 1.2×10^6 .

The basic model is shown in Figs. 5 and 6. Two nose shapes were used: a blunt one and a streamlined one. The blunt nose assured turbulent flow and a high erosion rate of the coatings and the streamlined nose provided laminar flow over a large portion of the body. Only a few tests were made with the latter nose.

The coatings were applied as follows. The chemicals were initially mixed dry and the required amount transferred to the nose cap, which was positioned in an upright position. The amount was determined by practice, so that the final thickness was approximately $1/8$ in. The nose cap was then put into an oven and heated until the coating was liquid. It was then removed and allowed to cool. Sandpaper was used to finish the material to the final contour.

The same coating was used over and over again for the tests. Although the erosion was nonuniform and the surface became

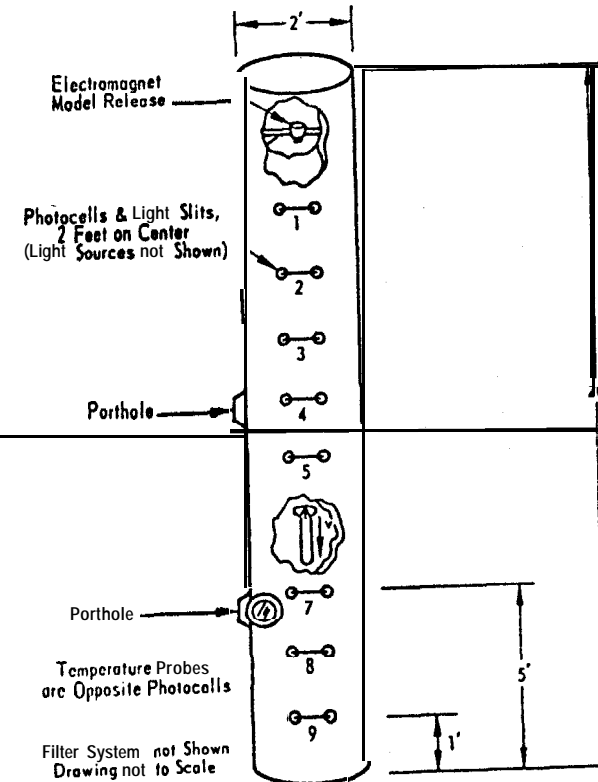


Fig. 3 Sketch of test tank.

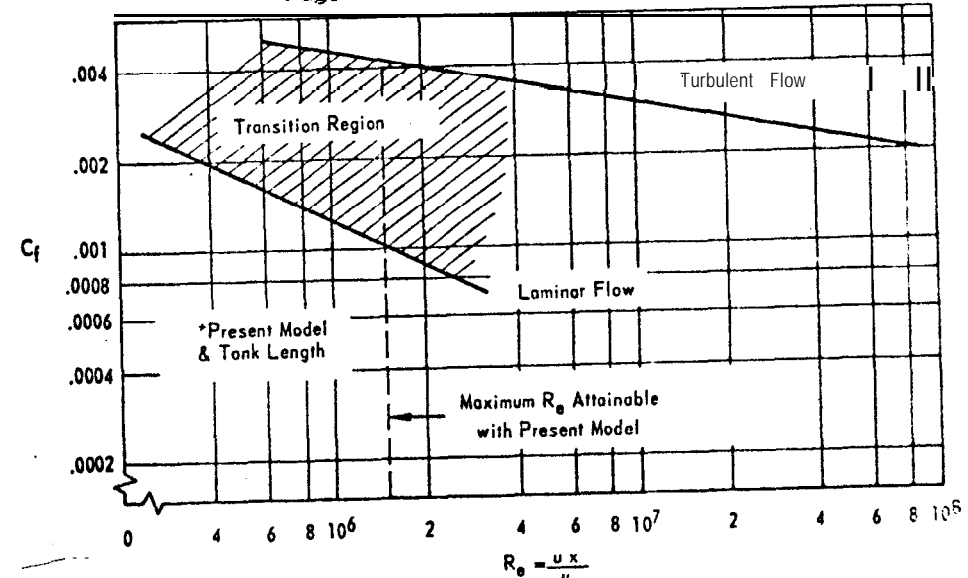


Fig. 4 Flat plate skin friction coefficient as a function of Reynolds number.

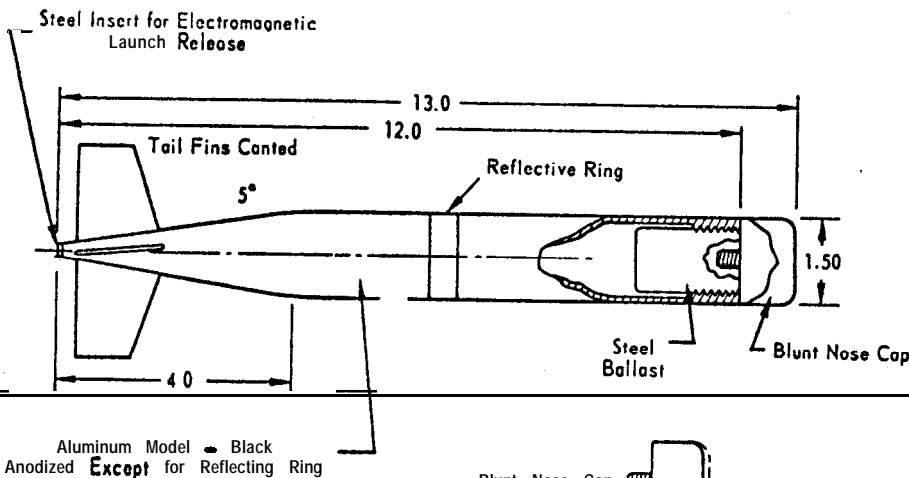


Fig. 5 Test model showing interchangeable nose shapes (Dry weight: 1.258 lb, blunt nose),

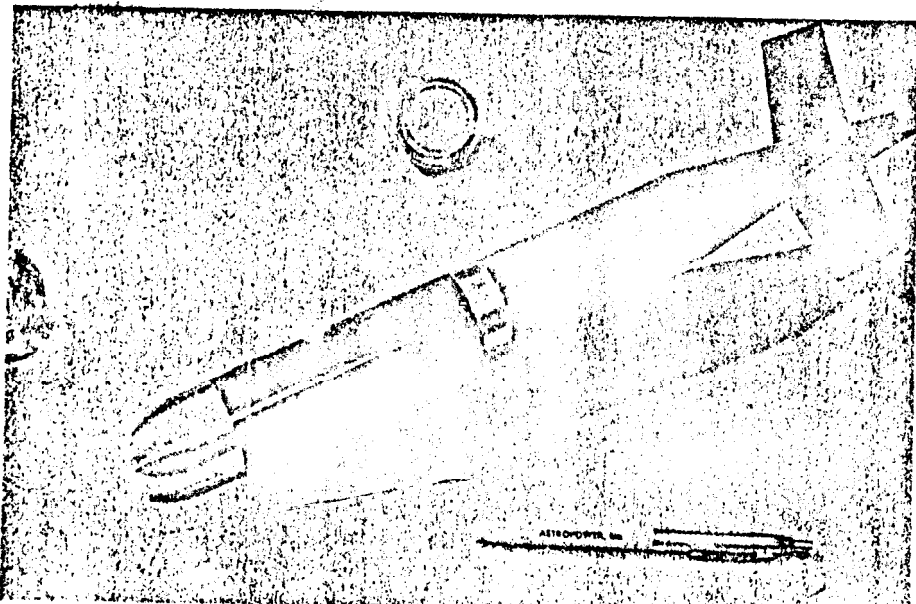


Fig. 6 Test model showing interchangeable nose shapes.

roughened, there was no measurable systematic effect on performance.

The model had four relatively large tail fins canted at 5° to the centerline to produce a controlled clockwise spin of approximately 1 rev/sec. This corresponded to approximately 2 rev for a complete fall. **High-speed motion pictures of a typical test verify a high degree of stability and virtually no dispersion in the trajectory.**

To ensure uniformity of test results and verify that the water had not become contaminated with chemicals that obscured the actual effects, each series of tests was preceded, and followed, by three ~~tests with an uncoated blunt nose model as~~ a standard. If any deviation from its known drag occurred, the tankwater was changed.

Accuracy of Test Results

The velocity of the model was determined as an average

$$\bar{V} = \frac{\text{distance between light slits}}{\text{time to travel this distance}}$$

between any two measuring stations. The acceleration, then, is also an average derived from \bar{V} . Some typical plots showing experimentally measured distance-time relationships and the derived velocity and acceleration curves are shown in Fig. 7. The model approaches terminal velocity very near the end of its run when the accelerations is nearly zero.

An error analysis was carried out to cover the range of anticipated performance conditions and test parameters. The maximum absolute error in time measurement is 0.002 sec. The time to travel the 2-ft increment between measuring stations at a terminal velocity of approximately 13 fps is approximately 0.16 sec, which results in an error of 1.3%. The corresponding maximum error in drag, based on terminal conditions, is estimated to be 2 to 2.5%.

Additional factors that influence accuracy and repeatability include variation in the coating thickness, the surface roughness of the coating, and the slight changes, in shape due to erosion. In addition, some vertical temperature gradients were present. Considering all, it is estimated that the measured drag coefficient did not vary more than ±5%. The data at the higher Reynolds number, when terminal conditions are approached, are the most accurate.

Experimental Results

A summary of the fresh-water test results is shown in Fig. 8. Each curve is the average of three to six runs. The ordinate is the percentage decrease in total measured drag of the coated model compared to the uncoated model, and the abscissa is the Reynolds number. A reduction in the measured model drag of approximately 18% resulted over almost the entire trajectory. A maximum Reynolds number of approximately 1.2×10^6 reached at the end of the trajectory closely represented terminal conditions.

Some of the tests were repeated with sea water, with results shown in Fig. 9. In all aspects, the coating behavior was similar in fresh water and sea water, although the drag reduction in sea water was a little less. The total drag reduction in sea water was 16%.

Pipe flow and rotating disk tests² demonstrates that non-Newtonian additives act to reduce friction drag. Therefore, the equivalent friction drag reduction that corresponded to the measured reduction in total drag was determined. A graphical presentation of total drag reduction as a function of skin friction drag reduction at various ratios of friction to total drag is shown in Fig. 10. Design calculations for the model gave a ratio of friction-to-total drag of approximately 0.59, displayed as the dashed line. This low value results from high form drag and induced drag contributions. The 18% reduction in total drag, which was experimentally obtained during the fresh-water tests, therefore, corresponds to a reduction of approximately 30% in body skin friction drag; and the 16% reduction from sea-water tests corresponds to 27% reduction in body skin friction drag. These results are predicated on the postulate that the coating reduced body skin friction drag alone.

Some limited tests were also made with the streamlined nose section in which laminar flow was obtained on a large portion of the body. The experimental results showed that the drag of this configuration (uncoated) was 30 to 40% lower than the blunt-nose configuration (uncoated). A portion of the streamlined nose was coated; however, a reduction in drag did not occur. It was suspected that either the erosion rate was insufficient, due to the low mixing rate within a laminar boundary layer, or that the flow mechanism which caused the drag reduction was different for laminar flow than for turbulent flow.

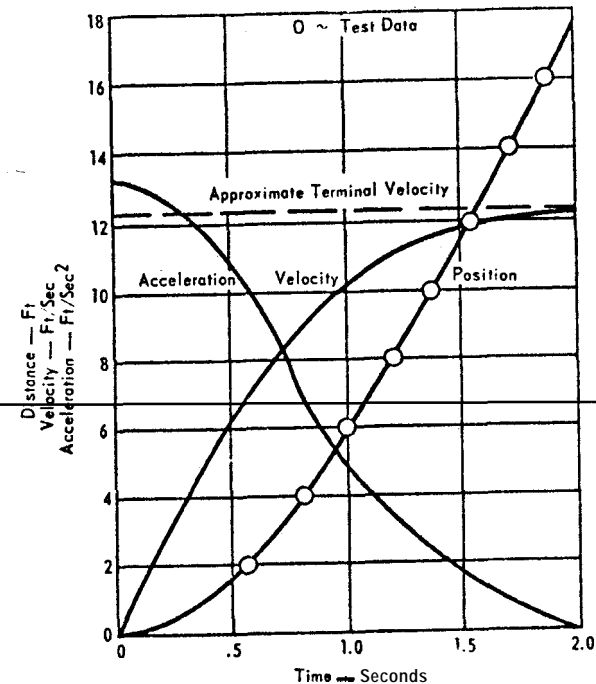


Fig. 7 Typical results of model test (Fresh water at a temperature of 60°F; blunt-nose configuration).

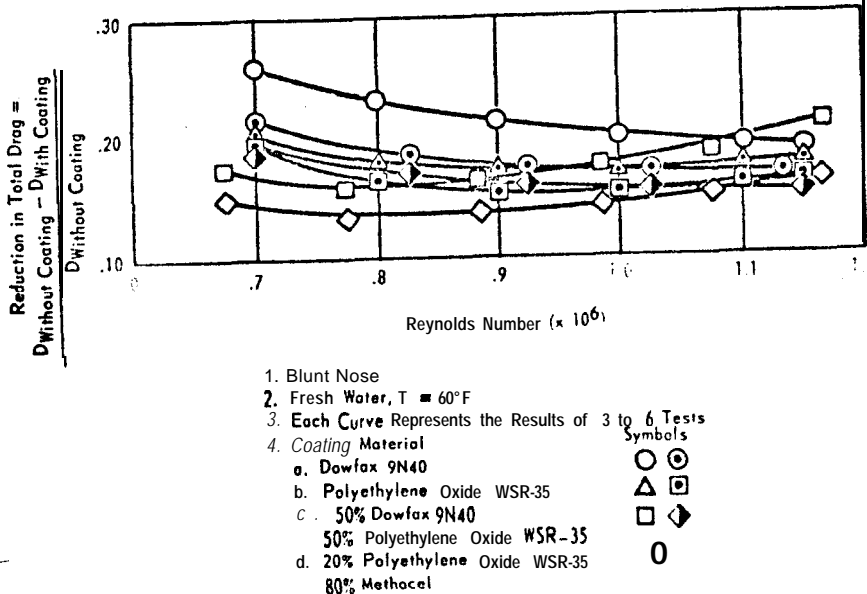


Fig. 8 Reduction in total drag by using soluble coatings from model tests in fresh water.

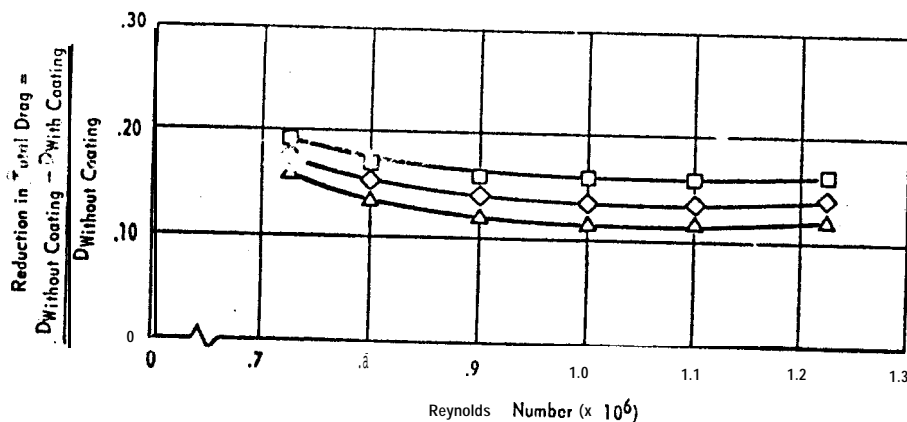


Fig. 9 Reduction in total drag by using soluble coatings from model tests in sea water.

1. Blunt Nose
 2. Sea Water, $T \approx 60^\circ F$
 3. Each Curve Represents the Results of 3 Tests
 4. Coating Material
 - a. 50% Polyethylene Oxide WSR-35
 - b. Polyethylene Oxide WSR-N-10
 - c. Polyethylene Oxide WSR-N-8
- Symbols
- \square a. 50% Polyethylene Oxide WSR-35
 - \diamond b. Polyethylene Oxide WSR-N-10
 - \triangle c. Polyethylene Oxide WSR-N-8

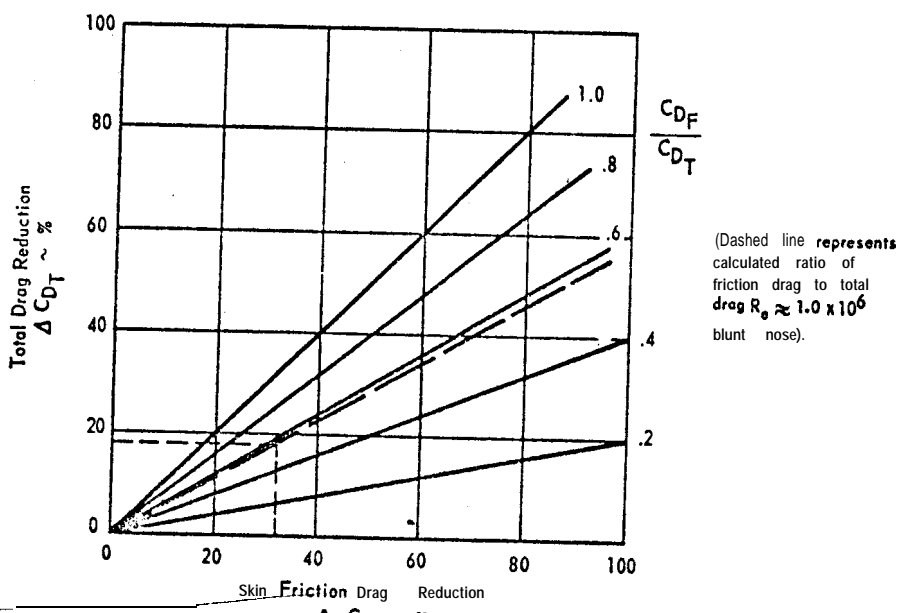


Fig. 10 Variation of total drag reduction with skin friction drag reduction.

Conclusions

The results of the experimental studies demonstrate the feasibility of using a soluble coating material to reduce drag of an underwater body. A body so treated rides in a boundary layer of non-Newtonian fluid, a phenomenon of direct interest for increasing the range and speed of vehicles that operate in water and have missions of short duration. The results obtained thus far are sufficiently promising to merit serious consideration for engineering applications of coatings even at this early development stage.

References

- 1 Thurston, S., "Drag reducing means," Patent #3,196,823 (July 1965).
- 2 Hoyt, J.W. and Fabula, A.G., "The effect of additives on fluid friction," Fifth Symposium on Naval Hydrodynamics, Bergen, Norway (September 1964).
- 3 Ripken, J.F. and Pilch, M., "Studies of the reduction of pipe friction with the non-Newtonian additive CMC," St. Anthony Falls Hydraulics Lab., Tech. Paper 421, Ser. B (April 1963).
- 4 Granville, P.S., "The frictional resistance and boundary layer of flat plates in non-Newtonian fluids," J. Ship Res. 6, 43 (October 1962).
- 5 Dodge, D.W. and Metzner, A.B., "Turbulent flow of non-Newtonian solids," J. Am. Inst. Chem. Engrs. 5, 109-204 (June 1959).
- 6 Wilkinson, W.L., Non-Newtonian Fluids (Pergamon Press, New York, 1960).
- 7 Bogue, D.C. and Metzner, A.B., "Velocity profiles in turbulent pipe flow, Newtonian, and non-Newtonian fluids," Ind. Eng. Chem. Fundamentals 2 (May 1963).

ELECTRICAL ENGINES FOR
UNDERWATER MISSILES

BATTERIES FOR TORPEDOES

Francis G. Murphy*

Naval Underwater Weapons Research and Engineering Station
Newport, R. I.

Abstract

Advancements in hot-gas (thermal) torpedo propulsion systems have not been matched by improved batteries for torpedoes. To take maximum advantage of their potential, torpedo batteries should be of primary type, of pile-type construction, and integrated with the torpedo shell. They should operate at maximum allowable temperature and be reusable (by design) as insert packs. Recently, battery development effort at the Naval Underwater Weapons Research and Engineering Station (NUWS) has been expanded along these lines. Feasibility tests of an improved silver-zinc pile were successful, and development contracts were let for a full-size battery. Contracts were also let for state-of-the-art sea water batteries. This paper describes the various candidate couples for torpedoes batteries, with regard to their background, current status, and potential.

Introduction

Developmental effort over the past decade has resulted in major improvements to hot-gas torpedo propulsion systems. As a result, electrical propulsion has, at least temporarily, lost a competitive edge. Both battery and thermal torpedo propulsion systems utilize energies of chemical reactions. Batteries are essentially isothermal, with energy transformed directly from chemical to electrical. Thermal systems are adiabatic, with the chemical energy heating high-temperature

Combined paper presented at the AIAA Torpedo Propulsion Conference July 23-26, 1963 at Naval Underwater Weapons Research and Engineering Station, Newport, Rhode Island and the AIAA Second Annual Meeting, San Francisco, California July 26-29, 1965. The author wishes to recognize the most helpful assistance of the associates of the Research and Development Publications Division.

*Head of the Electrical Engineering Division, Research Dept.

working fluids that power heat engines. At low discharge rates, batteries are capable of directly converting chemical to electrical energy at nearly 100% efficiency. However, high discharge rates are used in practice, and battery efficiencies are often as low as 30%, although subsequent conversion of electrical to mechanical energy is near 90%. The conversion of chemical energy to useful power in a thermal system is inherently inefficient, since only a modest fraction is thermodynamically available, and only a part of this is actually utilized.

Aside from high potential efficiency, battery propulsion systems are potentially simpler than heat engines, have higher over-all reliability, leave little visible wake, have minimum noise-making auxiliaries, and operate at constant weight, which simplifies hydrodynamic problems. On the contrary, present electrical propulsion systems have lower energy-densities than thermal systems, and so have greater over-all weights and volumes at high horsepower levels. They are also high in cost and difficult to recover after exercise, because their weight remains constant.

Thus for electrical propulsion to regain its competitive position, batteries are needed with increased energy-density, reduced cost, and designs that exploit their practical and theoretical potentials. Possible means of accomplishing these objectives and the status of various battery couples are next discussed.

Optimum Battery Design

Better torpedo battery designs require developing the battery-motor specifically for the torpedo, noting that, in the trade off between battery and motor, preference should be given to the former. The battery should take advantage of the torpedo shape and environment, and its chemical reaction should be chosen on bases of best energy, output rate, and practicability.

The energy-density of a battery depends on the energy produced by the reaction, losses in transferring this energy, and the amount of support and inactive materials required. All three are interrelated and depend on the rate at which energy is produced. Optimum energy-density is obtained when the battery is specifically designed for the torpedo. Such a battery would be 1) of primary design (i.e., not capable of recharge); 2) integrated with the torpedo shell to eliminate battery-case weight and make maximum use of available volume; 3) made of

pile-type construction to make maximum use of volume, provide support to the torpedo shell and thereby reduce its weight, and minimize power lost as heat in intercell connections; and 4) operated at maximum temperature consistent with its active materials.

With regard to item 1, the energy-density of a primary battery is far greater than that of secondary types, and a secondary battery is not amenable to items 2-4 and hence cannot be substantially improved through future efforts. Therefore, only primary batteries should be considered for high-performing torpedoes.

To clarify items 3 and 4, pile batteries are based on bipolar electrodes, which consist of positive and negative electrodes joined together as an integral unit. With several assembled in series, the space between adjacent electrodes constitutes a cell and separate intercell connections are eliminated. If the electrodes are also circular with outside diameter equal to the inside diameter of the torpedo shell, then the shell serves as battery case, and the entire volume of the battery compartment is essentially utilized. This ideal, of course, is reduced to allowing for housing fitting tubes, cell venting, conduit for cables between head and afterbody, and space for the electrolyte reservoir. Figures 1 and 2 show such proposed design concepts. Further savings of 1/3 the battery space and 1/5 the weight could be achieved by locating the electrolyte reservoir outside the torpedo, although system complexity would be increased.

Turning to item 4, operation at maximum temperature increases the rate of the chemical reaction. For a battery to operate at maximum efficiency, its reaction rate must equal the rate at which the resultant electrical energy is used. Each battery has an operational temperature where it produces energy at this optimum rate and related current density. To maintain it, excess heat must be dissipated; but, with conventional torpedo batteries, essentially no heat is transferred during its short period of operation, which means that the permissible current density is reduced. For this reason, development of an effective heat-transfer medium is under study. If successful, the electrolyte could be preheated to bring the battery to its optimum working temperature and then maintained there-by heat transfer to sea water. For the zinc-silver oxide battery, doing so would double the current density.

In establishing an optimum torpedo battery 1) the chemical reaction should also produce free energy at the rate (current)

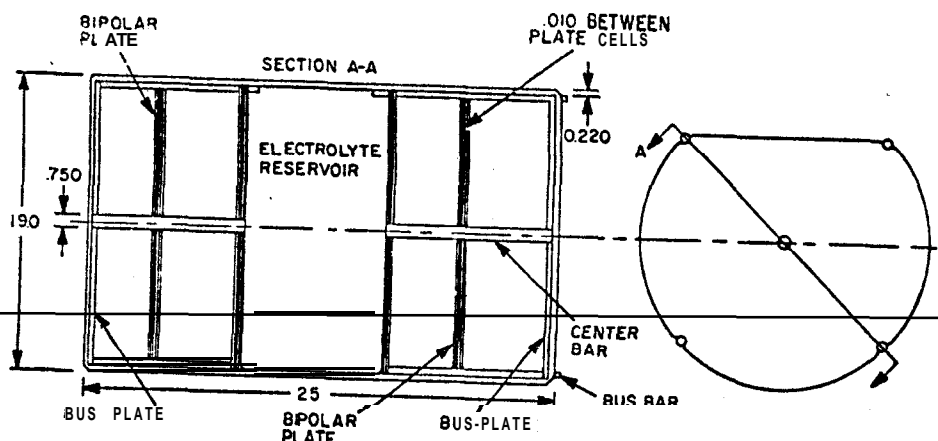


Fig. 1 Optimum torpedo battery configuration.

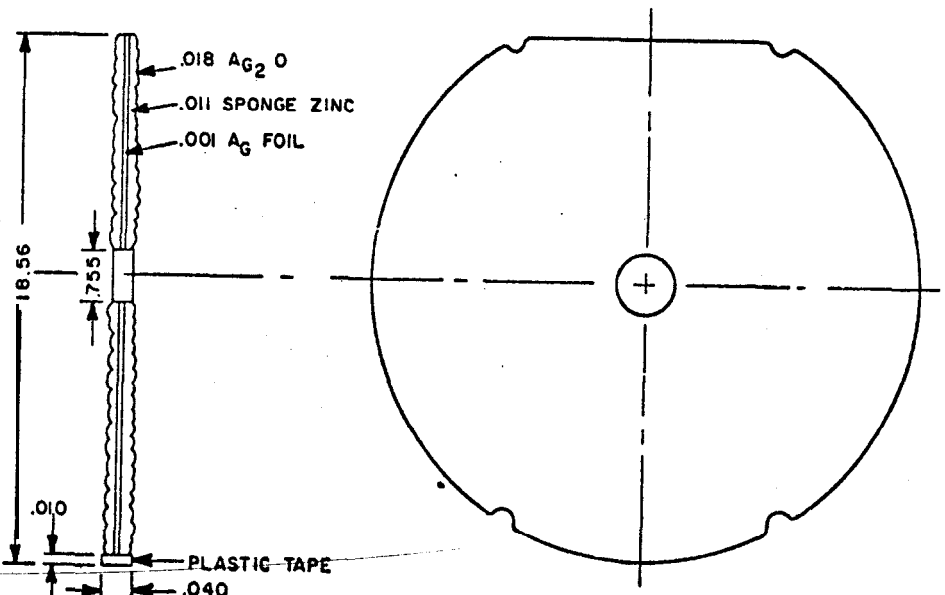


Fig. 2 Typical bipolar configuration of optimum battery cell.

density) that the electrical energy is expended; 2) its active material should be light, stable, and of minimum electrical resistance; 3) the **electrolyte** should be highly ionized to provide maximum conductivity, and, if it does not take part in the cell reaction, only a minimum should be used; and 4) there should be no side reactions.

In the following, potential torpedo battery types are compared, and the background and status of current couples are given.

Actual Battery Types

Sea Water Battery

The sea water battery was originally designed by the Bell Telephone Laboratories during World War II. General Electric Company (GE) continued engineering development and has manufactured battery sections for torpedoes. Only this battery type has been designed purposely for a torpedo. GE estimates that specialized battery cartridges with an energy-density of 60 w-hr/lb can be constructed. With shell, bulkheads, sea water electrolyte, etc., the complete energy package would provide 40 w-hr/lb and 2.5 w-hr/in.³.

Operation of this battery is explained by discussing the original Fleet battery. It is activated by flowing the electrolyte, sea water, through the cells. Its bipolar electrodes are shown in Figure 3. They are constructed of 0.01-in. thick magnesium (Dow alloy J-1Z), a barrier layer of 0.001-in. silver foil, and then 0.014-in. silver chloride whose surface has been activated by partial chemical reduction to silver with a developer. The assembly is cemented together and the edges sealed with lacquer. The electrode spacing of 0.017-in. is maintained with glass beads forced into perforations in the silver chloride.

The unit-cell pack is shown in Figure 4. It is rated at 90 amp at 135 v for 15 min and consists of 110 cells in a laminated plastic box. Supporting ribs at the bottom and at the top form ducts that direct the sea water electrolyte to pass up through the cells in parallel paths. Several such unit-cell packs comprise the battery, which is enclosed in an aluminum shell. As shown in Figure 5, the aft section has a water scoop. This is slid through the shell after the torpedo leaves the firing tube by a spring-powered mechanism triggered by a squib. It directs a continuous flow of sea water through the cell packs and then back to the sea.

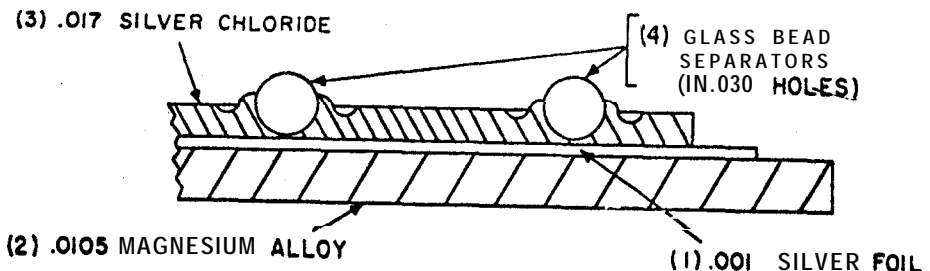


Fig. 3 Bipolar electrode for sea water battery.

(1) The 0.001-thick silver foil is glued to the 0.010-thick Mg alloy sheet.

(2) Mg-Ag foil assembly is edge-dipped in paint to ~~reduce internal losses.~~

(3) Beaded AgCl is glued to the silver foil.

(a) AgCl has been perforated and its **surface** reduced with Kodak D72 developer to decrease "come-up time."

Size: sheet - 11 1/8 x 11 7/8

Mg foiloy - 11 1/16 x 11 13/16

AgCl - 11 x 11 3/4

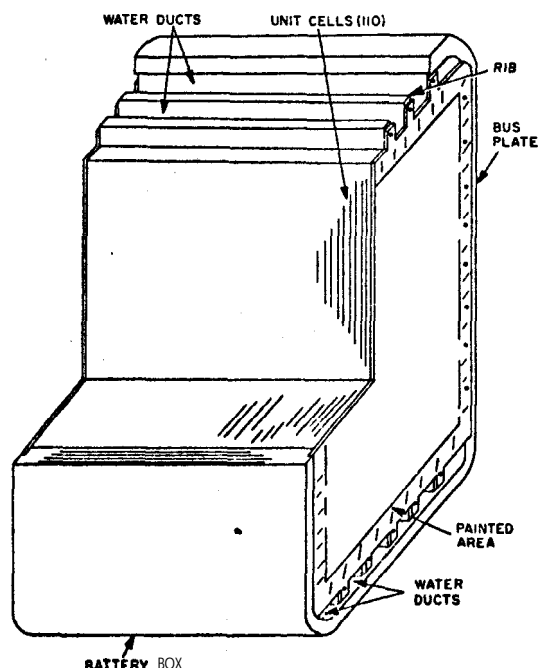


Fig. 4 Unit cell pack of sea water battery.

The power output depends on the temperature and salinity of the sea water. Since its temperature coefficient is approximately $0.75\%/\text{°F}$, a battery operated with 32°F sea water delivers 65% the *energy* it will at 80°F . A 50% decrease in the nominal salinity of the water will lower output approximately 25%, and fresh water will decrease it practically to zero.

In some batteries, a thermostatically controlled valve provides steady-state operation that is independent of **ambient** water temperature. In others, a voltage-control valve regulates the flow to maintain constant voltage. Toward the end of discharge, the flow of new sea water is reduced almost to zero. Recirculation during discharge tends to maintain operation that is independent of water salinity, etc., consistent with providing the flow necessary to dispose of reaction products. Such flow control and recirculation increase the time that the battery maintains its voltage **above** the 90% nominal value.

The simplicity and reliability of the sea water battery are considered good. It is inert and safe until its scoops are opened and sea water enters. High storage temperature does not adversely affect the battery, and it is adequately protected against moisture. It has a theoretical output of 0.273 hp-hr/lb of active material; however, side reaction of magnesium and internal resistance of the cell reduce efficiency to 30%. The desired reaction is $2 \text{ AgCl} + \text{Mg} = 2 \text{ Ag} + \text{MgCl}_2$, but corrosion of the magnesium, $\text{Mg} + 2 \text{ H}_2\text{O} = \text{H}_2 + \text{Mg(OH)}_2$, is an important side reaction that produces heat, a gaseous wake, and passivation of the anode by coating with the hydroxide.

The high resistance of the AgCl electrode is alleviated somewhat by converting portions to metallic silver. The conductivity of the sea water electrolyte, which is relatively poor, is accentuated by the need for a spacing between electrodes of 0.25-in. to permit electrolyte flow. The electrolyte is common to all cells, and so intercell electrical leakage occurs which reduces efficiency. The latter, coupled with the side reaction, results in approximately 1.4 times as much heat produced as electrical power produced. The total plate area thus acts as a heating surface, and the battery operates near the boiling point of sea water, modulated by its rate of flow. Since energy-density is affected by electrolyte flow, an improvement in its transport would reap major dividends -- made even greater because of the large numbers of cells involved. The efficiency of heat exchange, disposal of reaction products, conductivity within the cells, and electrochemical and chemical reactions are all affected by this flow.

GE is conducting a company research program to improve the battery, looking into flow characteristics, magnesium alloys with higher operational potentials, and additives to reduce corrosion. NUWS recently directed contract efforts to increase the output of the sea water battery from 245 to 500 v., increase current density from 1.7 to 3.25 amp/in.², and to study a new magnesium alloy. The higher voltage increases arcing possibility, and so hazards from venting the hydrogen gas were diminished by locating the flow-control valve in the inlet scoop, rather than in the exhaust. The higher current density and the new magnesium alloy, caused increased sludging, and so fresh sea water flow and recirculation flow was increased.

Zinc-Silver Oxide Battery

The zinc-silver oxide couple was developed by Andre of Paris between 1921 and 1943. In 1947, world patent rights were acquired by Yardney Electric Corporation (Yardney) with licensee/manufacturers in several countries. In 1949, the Electric Storage Battery Company (ESBC) received a contract to develop a zinc-silver primary battery for torpedoes.

Development of thin sintered positive plates allowed construction of very high-rate cells. They were constructed with expanded silver mesh introduced into the main powdered silver before it was pressed and sintered. This provided better current distribution and increased rated capacity of the cells as much as 50%. The negative plates for primary cells consist of compressed zinc powder, zinc sheet, zinc wool or mesh, or zinc sprayed on various backings; and each has individual advantages. Plates of zinc powder have been developed with current densities as high as 15 amp/in.². Important factors are the current density that the plate can withstand without becoming passive, and the necessity of ensuring adequate electrolyte solution around and in the plate structure, since the plate operates almost entirely around the liquid reaction. The electrolyte is 45% aqueous potassium hydroxide.

The electrochemical and chemical reactions of the silver-zinc battery includes the aqueous cathode reaction $\text{AgO} + \text{H}_2\text{O} + 2e^- = \text{Ag} + 2\text{OH}^-$ and the anode reaction $\text{Zn} + 2\text{OH}^- = \text{Zn(OH)}_2 + 2e^-$; the complete cell reaction is $\text{AgO} + \text{H}_2\text{O} + \text{Zn} = \text{Ag} + \text{Zn(OH)}_2$. The battery operates with little or no "free" electrolyte; rather, the electrodes are separated by approximately 0.02-in. of absorbent tissue that contains electrolyte. This spacing provides minimum resistance and limits the amount of zinc that dissolves. Since the dissolved metal can pre-

cipitate at places other than the anode, thus allowing more of the anode to dissolve than electrically consumed, secondary batteries have extra thick anodes to compensate for such loss, which, however, increases cell resistance.

The zinc-silver oxide couple has a theoretical of 0.314 hp-hr/lb of active material. There are no significant side reactions and the cell resistance is low. With proper design, it can operate at an efficiency of 75% even at high-rate discharge. It holds the most promise for immediate development. At 50 w-hr/lb, a current density of 1.2 amp/in.², and 75% efficiency, its temperature rises 20°F/min without cooling. Discharge times at high rate can be greatly extended by taking advantage of pressure to raise electrolyte boiling point.

In recent tests by Yardney with a primary design of pile-type construction, three 50-cell, 18.5-in.-dia batteries were constructed and discharged with minor modifications in each succeeding discharge. Figure 6 shows performance for the third discharge and Table 1 lists pertinent data. Table 2 summarizes results of all three tests. Based on such successes, parallel contracts were given to Yardney and to ESBC to develop a full-size battery of 50 w-hr/lb, 4.5 w-hr/in.³, \$1/kw-min. Research areas include determining the optimum method for producing the duplex electrodes, sealing the cells, integrating the piles into the torpedo shell, optimizing the activation procedure, and operating at maximum temperature with simple methods to dissipate excess heat.

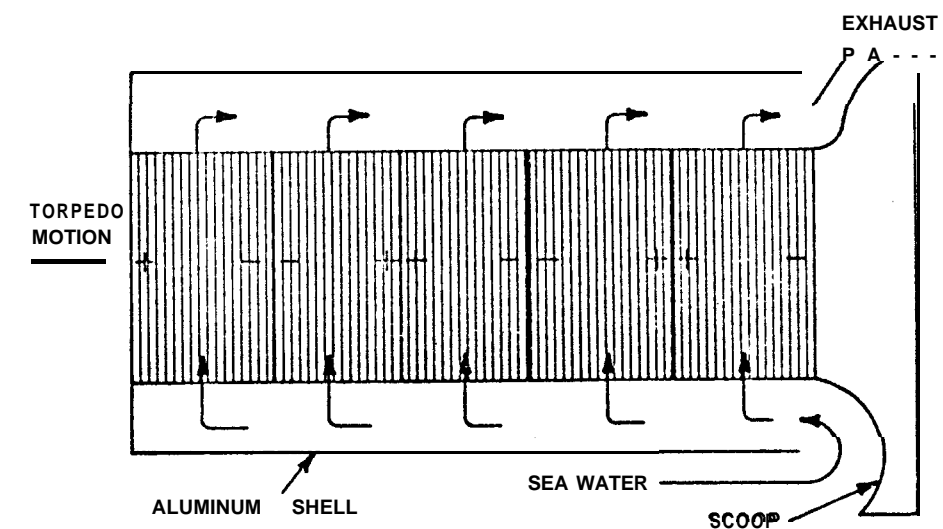


Fig. 5 Sea water flow in battery Mk 35-2.

Table 1. Data of Third Yardney Silver Cell Test

No. of Cell, 50	Current density, 1.2 amps/in. ²
Cell Dia, 17 inches	Open circuit voltage, 1.77
Cell thickness, 0.060 inches	Plateau Voltage, 1.45
Electrolyte, 31% KOH	Time to 1 v, 20 min
Central. manifold	Utilization grams AH AgO 3.37 Zn 2.45

Activation: 40 psi into
Evacuated Cells

Table 2. Summary of Yardney Silver Cell Tests

Test No.	Wt/lbs	Vol/in.3	HP min	lbs/HP min	in.3/HP min
1	76	763	255	0.3	3
2	83.5	732	326	0.26	2.25
3	92.5	732	410	0.23	1.8

Recent results indicate that chemically formed divalent silver oxide and zinc dust can be locked into a 2-mil steel foil to produce an economical and efficient duplex electrode. Tests at NUWS have demonstrated that a 1/4-in. thick aluminum shell, resting on a 1/4-in. thick rubber perimeter gasket seal and supported by closely packed cells, will withstand great depth pressure. Figure 7 illustrates the design, with roughly 280 in.2 of active area on each circular electrode. At approximately 1 amp/in.², each cell delivers 300 amp at 1.47 v. The internal cell resistance has also been reduced and the battery will operate for 20 min without excessive temperature rise.

Zinc-Chromic Acid Battery

Yardney acquired rights to the zinc-chromic acid battery from its inventor, Mr. Tamminen, of Finland. Preliminary information indicated an operating cell voltage of 1.5 v, a size equivalent to the sea water battery, and cost one-third that.

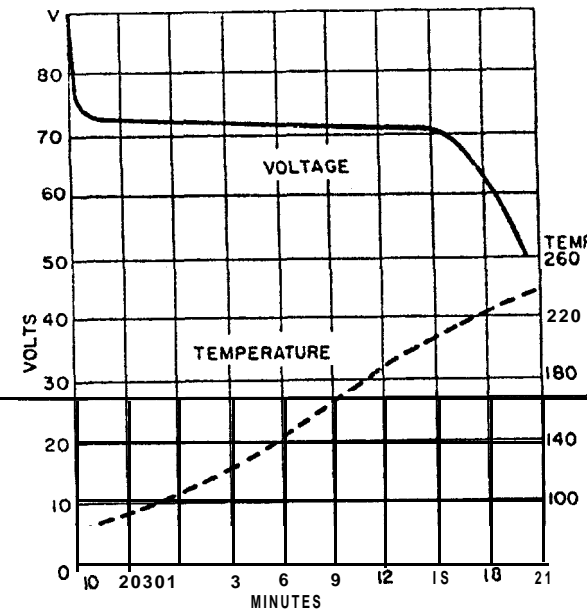


Fig. 6 Voltage and temperature vs run time of third Yardney silver cell test.

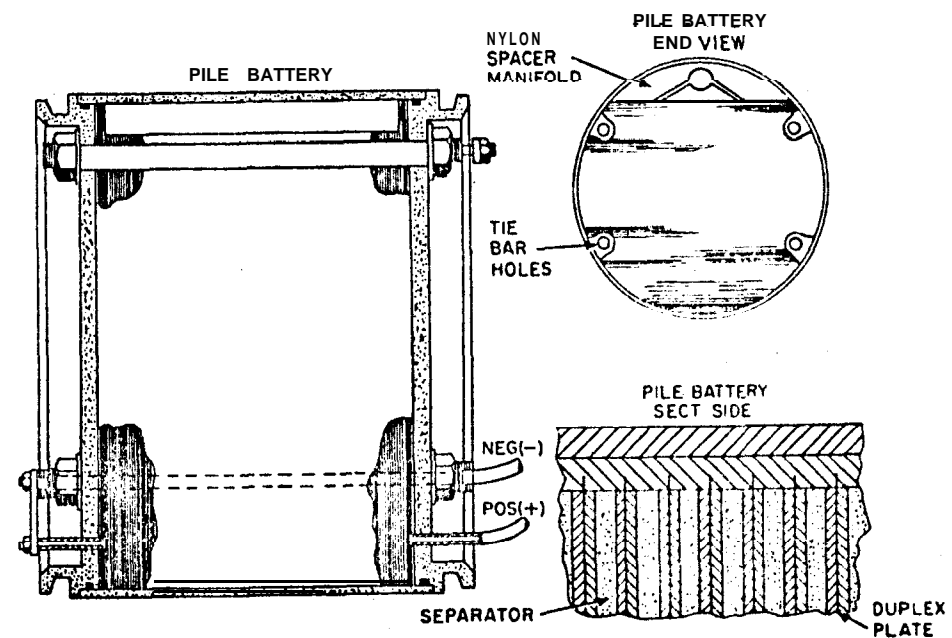


Fig. 7 Views of NUWS silver cell.

Table 3. Test Data on Chromic Acid Battery

	d = 0.10"		d = 0.050"	
N _R	4000	7000	4000	7000
30°C	1.03	1.31	1.11	1.11
60°C	1.14	1.18	1.35	1.09
80°C	1.38	1.00	1.39	1.60

Variability attributable in part to hydrogen gas evolution

2. Design data

Plate size, 12 x 15 inches Watt-hr/lb 175 theoretical
 Plate spacing, .050" O.C.V. 2.1
 Electrolyte, 10 CrO₃,
 $23\text{H}_2\text{SO}_4$, 67 H₂O Oper. V 1.30
 Time to 1.25 v 10.5 min

Vacuum Activation

Temperature, 175°F

of the silver battery if silver is included. For such reasons, the system appears promising.

$\text{H}_2\text{O} + \text{CrO}_3 + \text{H}_2\text{SO}_4 \rightarrow \text{Cr}_2(\text{SO}_4)_3 + \text{H}_2\text{O}$

The overall cell equation includes both the electrical-producing reaction and one whose output is only heat, which leads to lowered efficiency. A second conflicting reaction is oxidation of zinc by the sulfuric acid.

A statistical series of approximately 50 scale tests and 10 full-size, 'j-cell tests has been performed to optimize cell design. Other tests to improve electrolyte flow are also nearing completion. Because of certain similarities, sea water battery technology is being applied to the chromic acid battery. Thus, sea water is used as diluent for concentrated chromic-sulfuric acid. Doing so involves the added complexity of a chromic-sulfuric acid tank and a mixing tank. Figure 8 illustrates a current concept of the chromic acid battery. Figure 9 illustrates recent results, and Table 3 summarizes the data.

Organic Cathode Batteries

Although there is considerable research activity in organic cathode materials for batteries, temperature limitations, poor conductivity, and toxic products have precluded their use, as yet. The organic n-halogens, such as trichloromelamine, bear investigation in a sea water battery. Coupled with a magnesium anode in a magnesium chloride-magnesium bromide electrolyte activated by water, it produced nearly twice the energy of a comparable magnesium-cuprous chloride battery.

Present evaluation indicates that these materials should be looked into further because of their high theoretical energy and the scarcity of research effort in high-rate discharges. However, an order-of-magnitude improvement in conductivity appears required, as well as increased rates of reaction.

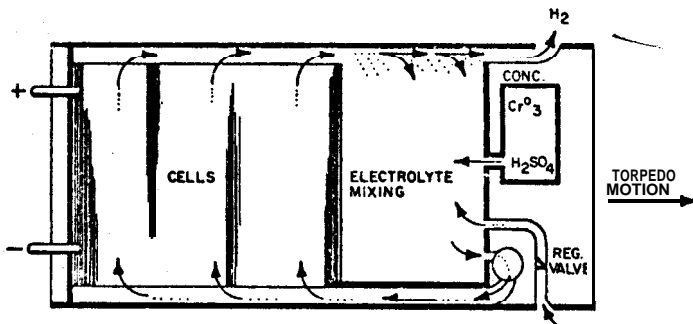


Fig. 8 Concept of chromic acid battery

Activation requires:

1. Vacuum in cells and electrolyte tank.
2. Squib to open sea water scoops and pressurizing mechanism for conc electrolyte tank.

Use same tank for activation as for steady state:

1. H₂ separation
2. Electrolyte enrichment
3. Temperature stabilization

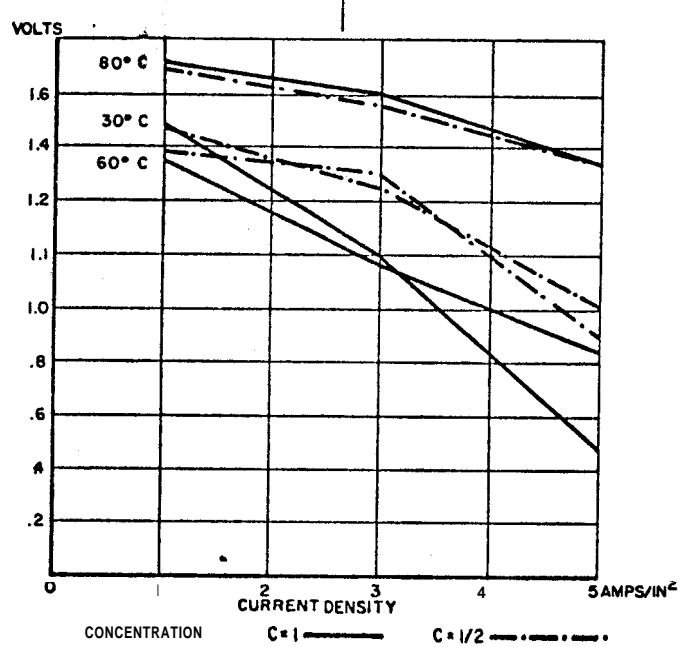


Fig. 9 Voltage vs current density of various internal conditions for chromic acid battery.

Fused Salt Batteries

Research effort sponsored by the Bureau of Naval Weapons has uncovered a number of fused-salt systems with theoretical energy densities as high as 0.948 hp-hr/lb of active material. Maximum efficiency has been 50%. Production costs and complexity of a battery operating at the necessarily high temperatures of about 1200°F make these systems questionable for torpedoes.

In 1953, a contract was awarded to Union Carbide Corporation to determine the feasibility of developing a torpedo battery capable of 100-kw output for 15 min, 250 w-hr/lb and 19 w-hr/in.3. From the Stefan-Boltzman radiation law, the steady state temperature of such a battery at 50% efficiency is above 1100°F, which sets the electrolyte as molten inorganic salts. The actual combination chosen melts at about 800°F and, in practice, might be maintained at (say) 750°F before firing, with additional heat then supplied for final melting. Energy densities of 180 w-hr/lb have been obtained in single cell tests. The same surface used originally to transfer heat into the battery (for melting) would be used to radiate excess heat to the sea, with surface temperatures increasing from the original 800° to about 1400°F.

Liquid Ammonia Batteries

A number of theoretically attractive couples have been proposed with liquid ammonia as electrolyte. However, side reactions and internal cell resistance have resulted in low efficiencies.

The Naval Ordnance Laboratory (NOL) is studying such a battery with m-dinitrobenzene as cathode and lithium as anode. NOL estimates that 1.00 w-hr/lb can be obtained for 10 min. This cathode melts at 194°F and has poor conductivity but a high density of 1.57. The vapor pressure of ammonia is quite high, its density is low, and its conductivity only about half that of aqueous potassium hydroxide. The over-all utility of this system is questionable, based on volume and temperature considerations. Poor safety makes it of little interest for submarine-carried torpedoes.

Nonaqueous Electrolyte Batteries

Besides ammonia, a number of nonaqueous electrolytes have been proposed, but poor conductivity and temperature limitations have reduced their permissible current densities.

Proposals for a battery based on a new class of electrolyte solvents that are compatible with the direct use of alkaline metals as anodes have been received. For a complete battery, energy densities of 130 w-hr/lb and 5.6 w-hr/in.³ are estimated.

Zinc-Iodate Battery

A zinc-iodate system has been under development by the Naval Ordnance Test Station (NOTS), starting in 1958. Its theoretical output is 0.231 hp-hr/lb of active material, but temperature limitation and poor conductivity have lowered permissible current densities.

Magnesium-Silver Oxide Battery

The magnesium-silver oxide couple has a theoretical of 0.652 hp-hr/lb of active material, and research indicates that electrolytes can be found to reduce the magnesium-water side reaction and so provide an efficient, high-rate battery.

Magnesium-Chromic Acid Battery

The magnesium-chromic acid couple, proposed by Graham, Growly, and Associates, is a dynamic system in which electrolyte is pumped through a pile array. The reaction is complex and its theoretical energy-density uncertain. Plumbing difficulties have led to its abandonment.

Battery Costs

Sea water and zinc-silver oxide batteries used in torpedoes use government furnished silver that is later recovered and reused. Hence, the major cost is in battery processing and handling. Here, a significant reduction could be accomplished if modern, high-production methods were employed, and the battery purposely designed to be reusable. Were the same electrode structure used in both exercise and warshot torpedoes, instead of a secondary cell for the former and a primary cell for the latter, production quantities would be increased and the processing would lend itself to mass production.

Summary of Battery Comparisons

Table 4 is a working comparison of present and proposed battery systems. Weights and volumes include the complete energy section: torpedo shell, bulkheads, contactors, etc. Estimates of energy densities of new systems are based on maximum

Table 4. Comparison Summary Conventional and Proposed Battery Systems

Battery Name	Type	Press.	Press.	Press.	Press.	Poss.	Poss.	Poss.
Lead-sulfuric	Sec.	4	35	1.5	1.5	5	5	5
Lead-perchlorate	Pri.	5	35	5	5	2	2	2
Nickel-cadmium	Sec.	4	30	2.5	2.5	5	5	5
Zinc-silver oxide	Sec.	0.83	27	1.5	1.5	5	5	5
Zinc-silver oxide	Pri.	0.83	27	5	5	2	2	2
Mag.-silver chloride (sea water)	Pri.	0.42	0.33	5.7	5.7	9	9	9
Zinc-iodate	Pri.	0.52	0.5	18.2	18.2	11.3	11.3	11.3
Mag.-chromic acid	Pri.	0.52	0.25	0.25	0.25	2.5	2.5	2.5
Zinc-silver oxide	Pri.	0.11	0.11	0.11	0.11	2.4	2.4	2.4
Mag.-silver oxide	Pri.	0.08	0.08	0.08	0.08	5	5	5
Fused salt	Pri.	0.1	0.1	0.1	0.1	5	5	5
Mag.-organic	Pri.	0.3	0.3	0.3	0.3	1	1	1
Liquid ammonia	Pri.							
Organic electrolyte	Pri.							

current density at which the battery can operate efficiently. The first five batteries of the table are conventional and the remainder are specific designs for torpedo propulsion. The last nine incorporate design concepts discussed previously, which is one of the reasons for their greater potentials.

• Conclusions

Batteries for propulsion of torpedoes have not been fully exploited. Their potential advantages of little, or no, gas evolution at depth, performance independent of depth, and inherent simplicity warrant further developmental effort. These should be aimed at 1) integrating the battery structure with that of the torpedo, 2) use only of primary batteries, and 3) developing optimum battery couples with good theoretical potential that are capable of efficient high-rate discharge. Such studies are in progress and are meeting with a degree of preliminary success.

Bibliography

Vinal, G. W., Primary Batteries (John Wiley and Sons, Inc., New York, 1950).

Chapman, C. L., "Technical problems associated with the silver-zinc battery," Proceedings of 1958 International Symposium on Batteries (1958).

Lemmon, M. J. H. and Casson, W. E., "Chloride depolarized water activated batteries," Proceedings of 1958 International Symposium on Batteries (1958).

"Evaluation study on torpedo propulsion batteries and on program for future requirements," Graham, Crowley and Associates (1954).

Latimer, W. M., Oxidation Potentials (Prentice-Hall, Inc., Englewood Cliffs, N. J., 1952).

WIRE TRANSMITTED ELECTRICAL POWER FOR TORPEDO PROPULSION

R. M. Dunlap* and W. R. Cox†

Naval Underwater Weapons Research
and Engineering Station, Newport, R.I.

Abstract

The use of a wire to transmit guidance intelligence from firing ships to certain torpedoes suggests the use of this link to transmit electrical propulsion power-to the missile. Direct current power transmission for this purpose is superior to alternating current since the latter has excessive charging current, line losses, corona, and insulation bulk. The power transmittable is influenced by the heat generated in the coiled line. Since wire insulation is the primary resistance to rejecting this heat, more than a 40% increase in power can be achieved by tapering the insulation thickness from sending to receiving end and by grading its permittivity radially. With good line cooling, much more power can be transmitted. High-voltage d.c. power transmission over a single wire with sea water return promises to be compact and simple, has no wake, and is not depth dependent. The major unsolved technical problem is to design a d.c. motor for much higher speeds and voltages. New developments which offer promise here are use of high-voltage silicon controlled rectifiers for mechanical commutation and the motor field as a rotating member which permits removing field windings from the rotor.

I

Nomenclature

- a = conductor radius
- b = radius over insulation
- d = relative power density
- D = power density (power received per unit volume of insulated wire)
- E = dielectric strength
- E_c = voltage generated in the armature

*Associate Director for Research.

†Head, Power Branch, Electrical Engineering Division,
Research Department.

h	=	a/b
H	=	magnetic intensity
I	=	current
I_d	=	current in the armature conductors
K	=	a constant dependent on the number of poles, the number of armature conductors, etc.
l	=	line length
N	=	relative between the flux or field and the armature conductors
p	=	relative power
P	=	power received
P_d	=	power developed in the armature
R	=	resistance
S	=	stress
v	=	relative voltage
V_r	=	received voltage
V_s	=	sent voltage
γ	=	line efficiency
ρ	=	resistivity
ϕ	=	the flux per pole

Introduction

The idea of conveying both electric power and control signals over **the same** transmission line dates to 1872 with the Foster torpedo, powered and controlled from shore, and the similar Sims-Edison torpedo in 1877. The latter, patented in 1885 by **Winfield Sims**,¹² used a steam-powered d.c. generator or battery on shore, and a dual-conductor wire cable paid out of the torpedo during the run. One conductor carried current to propel and guide the torpedo and to fire the explosive charge, and a second actuated relays in the steering and exploder mechanisms. Though sea water electrical return was used, the large volume required for storing the insulated cable within the torpedo limited its range and discouraged further development.

During World War II, both Germany and Italy experimented with electric torpedoes powered and guided by cable transmission. Italy abandoned her attempts while Germany, although achieving some success, concentrated on electric propulsion efforts on a battery-powered torpedo.

To the present day, **electric** torpedoes have limited speeds and ranges, primarily because of necessary limitations on battery size. Many torpedoes use a wire link to obtain guidance information from the launching ship. If this same wire could be used for transmission of electric power, with elimi-

nation of the carried battery, an electric torpedo could result that is competitive with **thermal** powered torpedoes in both speed and range and with added benefits of **wakelessness**, and independence of performance on depth of operation. Certain new problems are brought into focus which are **investigated** in this report.

Direct vs Alternating Current Transmission

In the proposed system, the transmission line initially would be wound in two coils, one in the torpedo and the other in the launching vessel, as shown in Fig. 1. As the two move apart, their lines would uncoil and remain essentially stationary in the water.

A transmission line in sea water **consists** chiefly of series resistance and of shunt capacitance to ground. Initially, there may be a large lumped inductance at both ends, in the coils in the firing ship and the torpedo. It is not possible to compensate this shunt capacitance by inductive loading without prohibitive increase in the bulk of the line. Thus, with long a.c. transmission lines, the **charging** currents **and** losses are excessive. Moreover, with sinusoidal a.c., the dielectric stress is roughly $2\sqrt{2}$ times that with d.c. voltage equal to the root-mean-square a.c. value. This makes for extra insulation bulk. The dielectric stress also reverses with twice the line frequency, which shortens insulation life and causes continuous corona noise which interferes with signal transmission. There is little corona noise on a d.c. line.

Thus, for reasons of excessive charging current, line losses, corona, and insulation bulk in a.c. lines, a.c. power transmission for torpedo propulsion **appears** less promising than d.c. Excellent additional general information is given in Refs. 1 and 2.

Heat Generated in the Coiled Line

Because of the small wire size required for efficient packaging in the torpedo, a large amount of heat will be generated in the coiled line. Nevertheless, even for the adiabatic case (no heat dissipated), **Lucal**³ showed that a worthwhile amount of power could be transmitted without overheating the insulation, and with good line cooling much more power could be transmitted. Test of the **Naval Underwater Weapons** Research and Engineering Station, adapting the methods of **Tong and London**,⁵ calculated heat transfer rates for porous

TORPEDO LAUNCHED FROM SUBMARINE

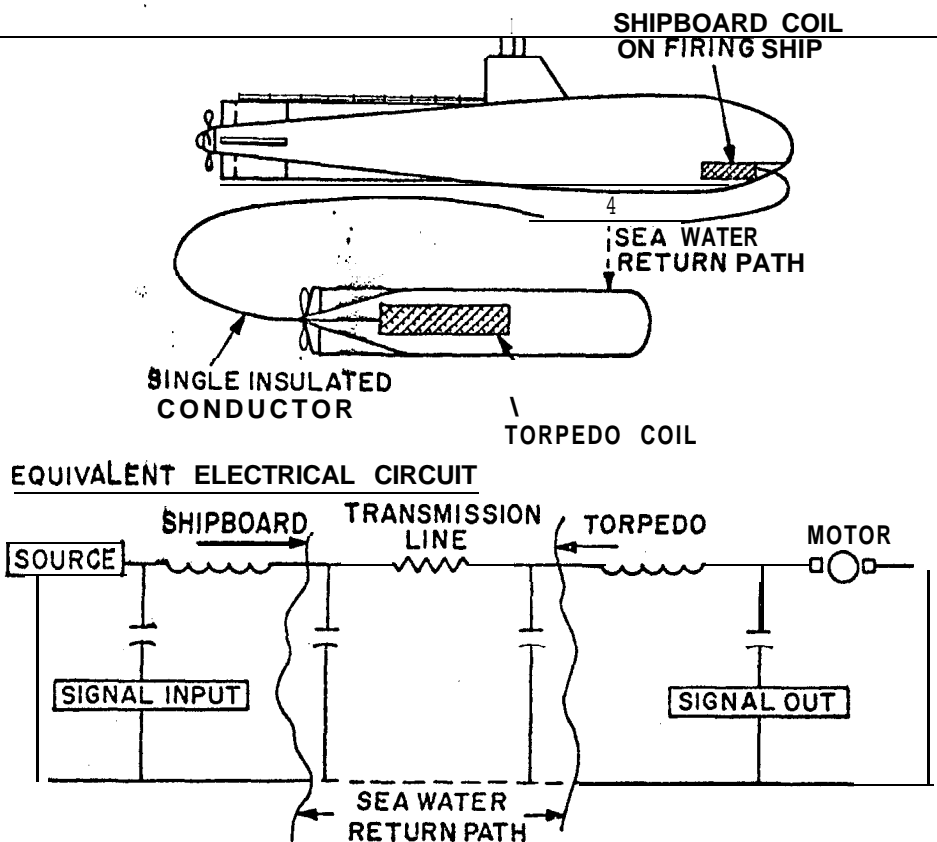


Fig. 1 Wire-powered torpedo propulsion system.

coils, wound as universal coils, as described in Ref. 6, and concluded that at least $25 \text{ kw}/^{\circ}\text{F}$ of heat can be absorbed by cooling water flowing through the matrix. The relatively slow torpedo speed of 25 knots would provide the 10 psi pressure drop required to flow water through the matrix. The primary source of resistance to heat flow turned out to be that due to the wire insulation.

Insulation

The prime requirements of satisfactory wire insulation are high dielectric strength at high temperature, flexibility, and freedom from weak spots over very long lengths. These are best met by Teflon*, grades TFE or FEP 100. Teflon on FEP 100 is melt-extrudable in-a-single layer over very long lengths of wire. It also may be made into tape which is wrapped around the conductor with subsequent fusion of the layers to make a homogeneous pinhole free insulation. Teflon TFE may be applied in layers of tape with silicone oil used to exclude the air. Each form of insulation apparently is satisfactory and experimentally withstood dielectric stresses higher than 2700 v/mil d.c. applied for long periods without breakdown. Since 600 to 1000 v/mil dielectric strength levels provide electric systems competitive with advanced battery and thermal types, the latter assures an ample safety factor.

As mentioned, insulation failure from corona is not anticipated as a major problem since direct current is used. Also the required operating life is less than 1 hr, and literature references indicate that the insulation life of Teflon, as affected by corona, is many times greater at zero frequency than at 60 to 1000 cps. This phenomenon is explained in Ref. 11.

Adverse effects caused by necessary bends in the wire, the physical relations of various coil turns, and the stress of winding the cable into the reeled configuration, which lowers the corona initiation voltage, are important but have not been evaluated.

D.C. Power Transmission through a Well-Cooled Insulated Conductor

For a **circular** conductor of constant diameter and **uniform** insulation thickness, application of **Ohm's law** and realization that the maximum dielectric stress is at the sending end of the line, such that

*Registered trademark

$$E = V_s / (a \ln b/a)$$

leads to the following:

$$P = n(1-n)\pi h^4 b^4 E^2 \ln^2 h/\rho L$$

$$b = [P \rho L / n(1-n)\pi h^4 E^2 \ln^2 h]^{1/4}$$

$$I = -\pi(1-n)h^3 \ln h E b^3 / \rho L$$

$$V_R = 0.15 E b$$

$$D = -E h^2 \ln h / L^{3/2} n(1-n) P / \pi \rho^4$$

which, by setting $\partial D / \partial h$ and $\partial D / \partial n = 0$ in turn,

$$D_{max} = 0.0517 E/L^{3/2} [P/\rho]^{\frac{1}{2}}$$

which occurs at $n = 0.5$ and $h = 0.605$, as indicated in Fig. 2.

More effective utilization of insulation for a given total coil volume is obtained by 1) tapering the insulation thickness from sending to receiving end and 2) grading the permittivity of the insulation in the radial direction.⁴ The optimum power density b is increased 15% by 1) and 37% by 2), while over 40% improvement may be expected by combining the two.

Line Efficiency

The relative power density varies with line efficiency in accordance with $d = 2[n(1-n)]^{1/2}$ and the relative voltage received in accordance with $v = \sqrt{2} n^{3/4} (1-n)^{-1/4}$. These relations are plotted in Fig. 3.

As a consequence, if $n = 30\%$ and $d = 0.916$, then $v = 0.625$. Thus, a reduced line efficiency will cause a large reduction (37.5%) in motor voltage but only a slight reduction (8.4%) in power density in the line. Therefore, lower line efficiency, which requires more power at the sending end and more heat dissipation in the coil, but also lowers motor voltage, may provide lesser problems than designing a high-voltage d.c. motor. However, the latter approach appears optimum and is primarily considered in this paper.

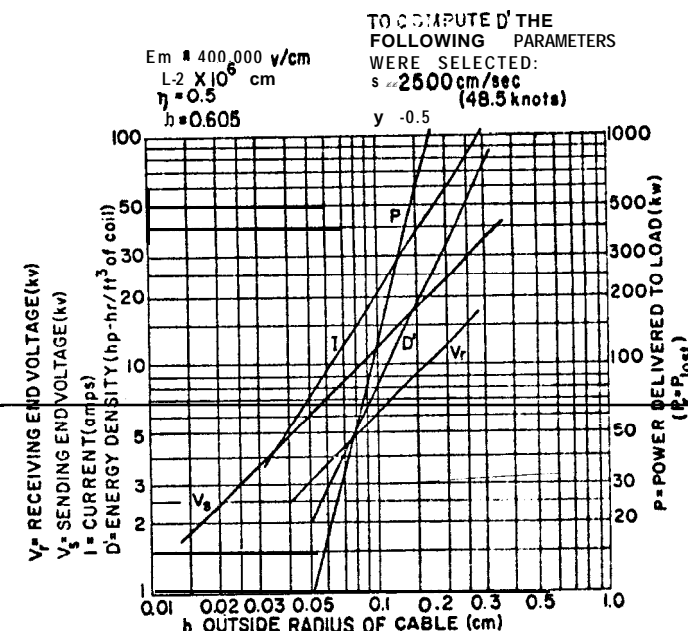


Fig. 2 Variation of I , V_r , V_s , P , D' as function of b for optimum uniform line.

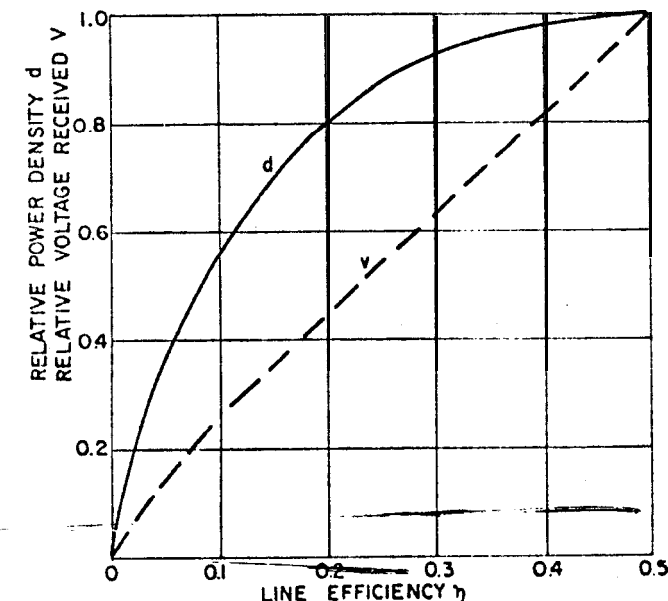


Fig. 3 Relative power density and voltage received vs line efficiency (line diameter has been varied to keep delivered power constant).

Transmission Line

For a conservative voltage stress of 1000 v/mil, the power densities of the reeled transmission line can be over 10 hp hr/ft³. The potential for increased power density is directly proportional to the dielectric stress.

With regard to mechanical stresses, careful attention will have to be given to the cable during high-speed unreeling. As shown in the analysis and data in Ref. 10, operation in air has a speed limitation from the need to dissipate energy equal to $1/2 mv^2$. Operation in water may eliminate this problem of energy dissipation, but stress from the increased drag of the water will be encountered.

Motor Design

In general, motor design is basically regulated by $P_d = E_c I_d = K \phi N I_d$. The power per unit of motor volume is proportional to the product of motor speed, magnetic flux density in the iron and current density in the conductors.

Advances in motor design are needed to convert high-voltage d.c. electrical power to mechanical power. These include operation of the motor at both much higher voltages and speeds than normal. These are now limited by commutation, which is basically a switching problem. Here the use of carbon brushes and copper segments are satisfactory only when there is a difference of 100 v or less between commutator bars, when the commutator surface speeds are 20,000 ft/min or less; the two conditions apparently have not been achieved simultaneously.

There is no problem from the inrush of starting current, since the resistance of the proposed transmission line will limit this to approximately 170% of the full load current. Thus, with a conventional commutator, the danger of arcing and burning will be minimized greatly. The necessity for reducing the voltage on starting also will be eliminated, although it may prove desirable for other reasons.

Bergman⁷ describes an early-design high-voltage d.c. generator which successfully incorporated many features needed for high-voltage motors. However, its speed was low, and its size was not limited. Shobert and Diehl⁸ describe a method of investigating commutation which may be useful in developing a high-voltage d.c. motor.

New developments which offer the most promise for a breakthrough to high-speed commutation are 1) substitution of high-voltage silicon-controlled rectifiers (SCR) for mechanical commutation and 2) use of the field as the rotating member and removing field windings from the rotor, thereby making the rotational stress in solid steel and bearings the only limitations. Katz⁹ describes an elementary development which might be adapted to high-voltage d.c. motors.

Shipboard Installation

High-voltage d.c. would be obtained most readily from a three-phase high-frequency and voltage alternator, after rectifying by cascades of silicon diodes in a bridge circuit.

Little or no filtering will be required, the load would be connected and disconnected at the a.c. side of the power supply, and a fault in the high-voltage d.c. line could be cleared on the a.c. side. Switching at current zero is possible twice each cycle on the a.c. side, where it is accomplished easily. This eliminates the need for heavy contactors to interrupt the high currents, as used in conventional battery-propelled torpedoes.

The coil on board ship must contain enough wire to permit maneuvering the ship after torpedo launch. For example, if the speed of the torpedo is 45 knots and that of the ship is 15 knots, the shipboard coil should have 1/3 the length of the wire in the torpedo. Since space is more available on a ship than in the torpedo, a wire diameter triple that in the torpedo may be used by the shipboard coil. Its resistance is 1/27 that of the torpedo coil and, therefore, is negligible.

Magnetic Detection

From considerations of symmetry and Biot-Savart's law, a wire-powered torpedo with a sea water electrical return that is well aimed at a relatively slow-speed target will produce a vanishingly small magnetic field at the target. At a target y yards from the torpedo axis and x yards range, this field is $HP = Iy/1830x^2$ oe. Thus, a target at x = y = 1000 yd will sense a field of 1 gamma (10^{-5} oe) from a line current of 18.3 amp, which is considered well below the level of detectability.

If two conductors were used to eliminate magnetic detection completely by removing the sea-water return, each would be at equal and opposite voltages and would carry equal power. It follows that the volume of the two-conductor line, at best,

will be 41% greater than that of the single conductor, and motor voltage under similar conditions would be 68.4% higher. Should one of the wires fail, the torpedo speed could be as high as 80% of its original speed. Despite such advantages, the added volume required to store a two-conductor wire makes this approach undesirable.

Conclusions

Electrical torpedo propulsion with high-voltage d.c. power transmitted over a single wire link with a sea-water return promises to be compact and simple. There is no wake present to interfere with homing systems or to permit detection by the target. ~~Speed adjustments may be achieved easily on board ship by simple voltage adjustments. Operation is not depth-dependent, and mid-course guidance information may be transmitted over the same wire. The major technical problem to be solved is the design of a high-voltage d.c. motor. Objections to the system include the need for a power supply on board ship, restricted maneuverability of the ship after torpedo launch, hazards of wire breakage, and magnetic detection.~~

References

1 Adamson, C. and Hingorani, N. G., High Voltage Direct Current Power Transmission (Garroway, London, 1960), pp. 1-10, Chap. 1.

2 Taylor, E. O., "D.C. Power transmission," (3 parts), Electr. J. (London) 163, No. 23, pp. 1227-1231 (December 4, 1959); 164, No. 1, pp. 22-27 (January 1, 1960); 164, No. 5, pp. 294-299 (January 29, 1960).

3 Liscal, H. M., "An electric transmission line for supplying d.c. power to a torpedo," Naval Underwater Weapons Research and Engineering Station, Newport, R. I. TM No. 255 (U), (October 1960).

4 Nizinski, S. J., "Silicone rubber graded construction for high voltage insulation," prepared for presentation at Tenth Annual Wire and Cable Symposium, Asbury Park, N. J., November 29-December 1, 1961, printed by Dow Corning Corporation, Midland, Mich.

5 Tong, L. S. and London, A. L., "Heat transfer and flow-friction characteristics of woven-screen and crossed-rod matrixes," Trans. Am. Soc. Mech. Engrs. 79, 1558-1570 (October 1957).

6 Querfurth, W., "Coil winding," Geo. Stevens Mfg. Co., Chicago, 111. (March 2, 1954).

7 Bergman, S. R., "Direct-current generators of very high voltage," Gen. Elec. Rev. 31, 596-599 (November 1928).

8 Shobert, E. I. and Diehl, J. E., "A new method of investigating commutation as applied to automotive generators," Power and Apparatus 16 (February 1955).

9 Katz, L., "Brushless d.c. and universal motors," Military Systems Design (November-December 1961).

10 Wilson, L. T., "A study of the mechanics of withdrawing a flexible filament from a source at rest," Signal Corps Engineering Laboratories, Fort Monmouth, N. J., Rept. E-1141.

11 Gore, W. L., "Corona resistant 'Teflon' for high voltage," Insulation, pp. 17-19 (November 1961).

12 Sims, W. S., Torpedo boat (or submarine vessel) propelled and steered by electricity, U. S. Patent 319,633 issued June 9, 1885 (English patent No. 2614 issued May 25, 1883).

ANALYSIS OF HIGH-PERFORMANCE
ELECTRIC TORPEDO POWERPLANTS

M. L. Henderson*

General Electric Company, Pittsfield, Mass.

Abstract

Battery-powered, electrical torpedoes **are** discussed in general **and** their components briefly **analyzed** with respect to component interface, radiated noise, **voltage** modifier, **transformer**, inverter, motor type, speed adapter, **and** propulsor. Since each component affects the characteristics of the **others**, their selection as an integrated unit is examined to provide **information on the** usefulness of the total system. Doing so on the basis of the state of the art and reasonable extrapolations, it appears that there **are** several electrical systems that are capable of **400-hp** output within the total weight **range** of 500 to 650 lbs. although some will require additional development. Although not done in this paper, combining these results with expected battery performance improvements should result in **electrical** propulsion systems whose weights are comparable to thermal systems in this power range.

Presented as paper at the AIAA Torpedo Propulsion Conference, U. S. Naval Underwater Ordnance Station, **Newport**, Rhode Island, **July 23 -26, 1963**. The conclusions and relative comparisons are believed to remain **fairly** valid on a total system basis. The General Electric Company has tested a very quiet, conventional DC motor weighing 420 pounds which **produced** over **430 hp** for **12** minutes (over **1 hp/lb**), not as good as projected in the paper. On the other hand, advances **in** solid state electronics should **make these** components lighter than **projected**. **Comments on** **radiated** noise and competitiveness of electric with thermal propulsion systems, **and** the **necessity** of **considering the** total systems, are still valid.

***Staff Engineer, Electromechanical Systems** (Consultant, **General** Electric-South America, Brazil.)

Introduction

Propulsion of large high-speed torpedoes with **sophisticated** controls calls for a high level of performance per unit weight and per **unit** volume from power sources, prime movers, and control systems. Furthermore, utmost attention must be given to reducing radiated noise, desirably below **that** of torpedo hydrodynamic and flow noise, and here electric systems have an inherent advantage compared with certain thermal systems.

Electric Propulsion System

The block diagram of Fig. 1 applies to an electric torpedo **propulsion system. Feedback loops and control** are omitted for simplicity.

Speed control, if needed, may be incorporated into any one of the blocks, with varying effects on the **overall weight** and performance.

Greatest advantage is taken of the capabilities of the **electric** system when the electrical and mechanical "interfaces" are chosen to optimize the performance of the entire system, rather than individual components. For example, in a battery-powered system, the weights of both battery and motor are **critically** affected by the choice of operating voltage. The **essential** need is to minimize the combined weight, including, of course, connections; and even the control scheme selected **must** be evaluated for its effect on **overall** weight. Similarly, contributions of various components to noise must be studied and appropriate tradeoffs made.

Radiated Noise Characteristics

To **minimize** the noise radiated from a torpedo propulsion system, it is **important** to identify and quantify the principal noise and vibration sources, and to determine the extent that these are transmitted to the torpedo structure and eventually to the water. Thus, a noise-reduction program must concentrate on reducing vibration at the **source** and on preventing its transmission to the outside.

Because of the large mismatch in acoustic impedance between air (or any **gas**) and the shell, and thence to the water, acoustic energy perceived near components on bench tests performed in air is but a small contributor to in-water noise. On the other hand, vibration at mountings, perhaps unnoticed in bench testing, may be amplified by direct transmission to the

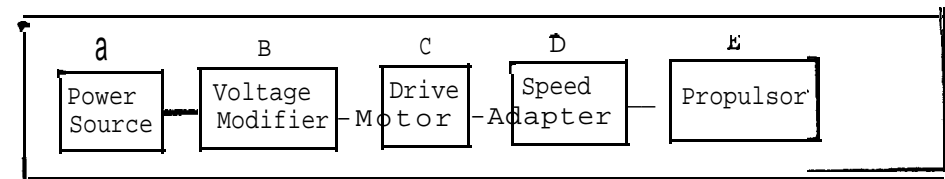


Fig. 1 Block diagram of electric propulsion system.

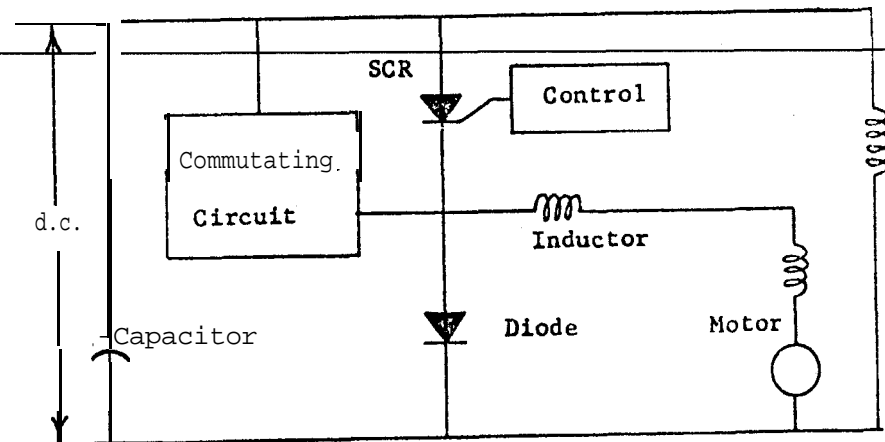


Fig. 2 Time-ratio control circuit.

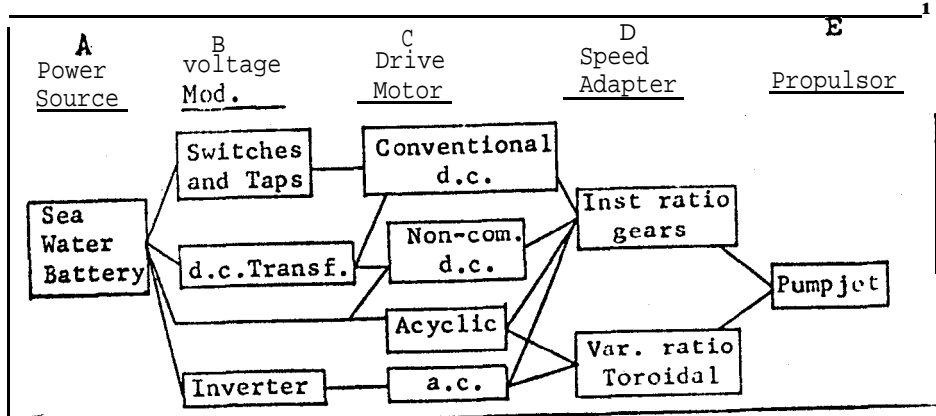


Fig. 3 Propulsion system choices.

relatively flexible shell. **For** this reason, it **is important** to know not only the amplitudes and frequencies of internally generated vibrations but also the **motional** impedances of the part concerned and of the enclosure at the point where it is mounted.

Since a **torpedo** shell has easily excited resonances over a wide frequency range, it is generally impracticable to inhibit noise by "de-tuning". This is particularly true when operation is expected over a significant speed range. **Thus**, design of the **entire** system and its mountings must be carefully coordinated to minimize external noise. Solid friction damping, properly used, will minimize some modes of vibration that cannot be controlled otherwise.

System Components

There are several internal possibilities for each of the blocks shown in Fig. 1. Although even after eliminating incompatible systems the number of feasible combinations is too large to analyze in detail here, some comments **on** principal components will **facilitate** a comparison of the systems. The components considered **are** those for a torpedo requiring some 400 **shp** for a **12-min. run**.

Block A: Power Source

This discussion is **devoted** to batteries as power supplies. **Although** fuel-cell batteries are developing rapidly, they are not **considered** here, since they are basically low-power, long-life devices and do not yet have the concentration of power per unit volume necessary for a high-performance torpedo. For our purposes, it will suffice, instead, to concentrate on sea **water-activated** batteries with silver chloride and magnesium as electrodes, although the use of another type with equivalent energy **storage** would **not** greatly affect the analyses.

Batteries produce no appreciable noise, but careful hydrodynamic design of inlet and outlet scoops and valves is necessary to prevent cavitation noise. Pumps **for** water circulation can be minor noise sources.

Block B: Voltage Modifier

A voltage modifying means may be used to change the battery **input from direct-to-alternating current or to provide voltage variation** for speed control. If neither is required, this

block is eliminated.

1. Switch-Controlled Taps on Batteries. If a few discrete reduced voltages are needed, properly selected taps or series-multiple connections will serve. Solid-state electronic devices may supplement mechanical switches, reducing the contact duty. Means may also be needed to limit transient currents during switching. Because of internal resistance of the battery, a half-voltage tap or connection gives somewhat more than half voltage under load, especially since the load current is lower at the resulting reduced speed. Noise from switches is confined to short-time shocks at the time of major speed change, presumably at infrequent intervals, and is **ndt** expected to cause any problem.

2. D.C. Transformer. A number of electronic **inverter-rectifier** circuits have been devised to effect a change in **d.c.** voltage. Of these, the "time-ratio control" is particularly applicable.¹ A simplified circuit is shown in Figure 2.

Pulsating current is supplied to the motor through the silicon-controlled rectifier (SCR) which is "turned **on**" by the control circuit and "turned off" by the commutating circuit. When the SCR is not conducting, the diode permits current to continue to the motor. The average voltage impressed on the motor is determined by the ratio of "time on" to "time off" of the SCR. Efficiency is very high, since the principal loss is from voltage drop in the rectifying elements during their tiny conducting periods.

This circuit contains small reactors, and therefore pulsating **magnetic** forces may be present. But its components are much smaller than the motor it controls, and so proper mounting should result in negligible external noise.

3. Invertcr. Conversion from direct to alternating current by electronic **devices** permits use of more-or-less conventional a.c. motors. Both voltage and frequency **variation** may be used in the latter's speed control. Several varieties of inverter circuits have been devised to fit motor-drive applications. As in the case of the d.c. transformer, their efficiency is high, and their noise is minor.

Block C: Drive Motor

Several **types** of drive motors can be used, depending on the power supply and the means of speed control. Among them are the following.

1. Conventional d.c. Commutator Motor with Shunt, Series, or Compound Characteristics. Speed control is accomplished by voltage and/or field strength variation. Chief limitations are in commutator construction and heat dissipation. By the use of compensating windings, high-temperature insulation and improved heat-transfer means, such a motor can be built with less than 1 lb/hp. For direct drive of counter-rotating propellers, the motor may also have its inner and outer members rotating in opposite directions. This, however, requires an additional set of brush contacts, and added weight is needed to make the outer member rotatable, even if at the same relative speed.

2. A.C. Induction or Synchronous Motor. A significant advantage of such motors is removal of speed limitations imposed by the commutator on a d.c. machine. To best exploit this, frequencies of a few hundred cycles can be used, which raise speeds above 10,000 rpm. An induction motor of this type will, however, generally suffer from high slip, low efficiency, and low power factor. The synchronous motor avoids these but requires a means of nonsynchronous starting and some method of assuring synchronism with the a.c. source when under load.

3. D.C. Motor with Electronic Commutation. Here the field poles are on the rotor and the commutated circuits on the stator, and the usual mechanical commutator is replaced by many electronically controlled rectifiers. Thus it is a hybrid between d.c. and a.c. motors. With a reasonable limitation on the number of commutating circuits, the efficiency of this machine is less than that of a good a.c. motor, and torque pulsation will generally be much greater than in normal a.c. or d.c. motors.

4. Acyclic Motor (Homopolar). Operating on direct current on the principle of the Faraday disk and requiring no commutator, this motor is adapted to very high currents at low voltages. A high-current collection means is required to make connection to the rotor. This motor type has been described by Harvey and Burnett² and by Burnett and Kaestle.³ It can be designed for high speed, attaining an output in the neighborhood of 1.4 hp/lb. Its basic efficiency is high, but, because of its need for high current, transmission losses in even a few feet of conductor between battery and motor may be 2 or 3%.

With regard to noise comparisons, any imperfectly balanced motor will give rise to vibratory forces at the rotational frequency. Precision balance and stable dimensions are there-

fore essential. In addition, magnetic flux variations cause vibration at multiples of the fluctuation frequency. The acyclic motor has a constant flux throughout and is therefore free from this type of vibration and noise. The field member of a conventional d.c. motor has little flux variation as compared with the excited stator of an a.c. motor or of an electronically commutated d.c. motor. On the other hand, the conventional d.c. machine may produce noise and vibration from brush-action on the commutator. Any motor may be a source of air-flow noise from rotating parts. A factor less obvious than direct transverse vibration is torque pulsation. This produces reactions at the supports, may excite resonant vibrations of the frame, and will also react on shaft-coupled members, such as splines, gears, and even propellers unless flexible couplings are used.

Block D: Speed Adapter

1. Direct Shaft Connection to the Motor. This can only be used if the motor speed is suitable for the propulsor. This eliminates the weight and noise of a transmission (gear) link but may require considerable compromises in other elements, since efficient motor speeds are generally much higher than that of usual propulsors. It works well with counter-rotating motors and propellers, but otherwise results in greater overall weight than a speed reducer with a fast motor.

2. Constant-Ratio Speed Reducer. Reduction gear units have been a serious source of torpedo noise in the past, but progress in their noise reduction gives promise of order-of-magnitude improvements. Good results have also been reported from friction-type drives, although at somewhat lower efficiency. With expected weights and noise about a standoff, the geared drive is preferred for constant-ratio speed reduction. (It is used in the following system analysis because of higher efficiency and greater engineering experience.)

3. Variable-Ratio Drive. Multiratio, mechanical, gear-shifting devices are a possibility, but they tend to be relatively heavy, involve several gear trains, and so present noise problems. The combination of a variable pump with a hydraulic motor, such as in aircraft auxiliary drives, is a compact variable ratio device, but present equipment is far too noisy.

A continuously variable-ratio toroidal drive designed by Wright Aeronautical Division of Curtiss-Wright Corporation gives adjustable speed reduction by rolling-friction elements.

Noise is expected to be low, and efficiency above 90%. (For purposes of this study, it is selected as a promising component.)

Block E: Propulsor

The present selection is limited to the following: 1) fixed pitch propeller, either a single or a counter-rotating pair; 2) **pumpjet**; and 3) variable-pitch propulsor, although a routine solution in aircraft and an occasional one in marine applications, has not yet been developed for torpedoes.

(Since a constant-pitch **pumpjet** has been devised for the current RETORC II torpedo development program, it is used in the following comparisons, as representing an advanced state of the propulsor art.)

System Comparisons

A few of the more promising systems may now be combined, based on a desired speed range of approximately **2:1**. Expanding Fig. 1. with the preferable components in each block and selecting combinations that can be expected to give good results, Fig. 3 is derived.

The resulting systems are in two groups. In one, the motor speed **is** variable, and the transmission ratio is fixed. Since its motor and all rotating parts will slow down with the torpedo, radiated noise **is** reduced at low speed. In the other, the motor speed is relatively constant, and the propulsor is driven by a variable-speed transmission. Its **motor** remains at full speed (or may go higher, because of rise in battery voltage) as the torpedo slows down, and so the only noise improvement at low speed is due to transmission of less power. This is tolerable only if the motor itself is extremely quiet and can operate satisfactorily at over-voltage and perhaps resultant over-speed. This **is** true of the acyclic motor and of some types of **a.c.** motors, but is not expected of **commutator-type** d.c. motors.

The systems thus emerging from Fig. 3 are shown in Table 1. Here, A and B have essentially constant motor speed and variable-ratio transmission, and the others have **variable-speed** motors and **constant-ratio** transmission. Table 1 identifies the principal components of the **several** systems. Below each component is its roughly estimated weight, based on an output of 400 hp; and the total weight is shown for each system, including speed control, motor, and transmission. In-

Table 1 Comparison of 400-hp torpedo propulsion systems

Sys-tem	Voltage	Auxil. speed	Total	Battery adder, equiv. wt.	Overall length, in.	
modif.	Motor	control	Transm. wt.	lb.		
<u>Systems with constant motor speed and variable - ratio transmission</u>						
A	Heavy bus 50	Acyclic 280	None ...	Toroidal 190 520	0.88 25	545 35
B	Inverter 350	A.C. 300	None ...	Toroidal 190 840	0.82 105	945 51
<u>Systems with variable motor speed and constant - ratio transmission</u>						
C	Var. freq. inv. 400	inv. A.C. 300	None ...	Ger. 55	0.85 65	820 50
D	Heavy bus 5t	Acyclic 470	Sh. fld. 25	Ger. 55	600 0.90 ...	600 36
E	Comm. & contr. 32:	Noncom. D.C. 280	None ...	Ger. 55	660 0.85 65	725 47
F	D.C. transf. 22:	Conv. D.C. 355	None ...	Ger. 55	635 0.85 65	700 44
G	Switch & taps 4:	Conv. D.C. 440	Sh. fld. 25	Ger. 55	565 0.88 25	590 38
<u>Three-speed systems</u>						
H	Switch & taps 45	Conv. D.C. 355	None ...	Ger. 55	455 0.88 25	480 34
J	Switch & taps 235	Noncom. D.C. 280	None ...	Ger. 55	570 0.85 65	635 41

addition to these weights, some allowance should be made for the additional battery capacity needed to compensate for higher losses in the less efficient systems. Accordingly, Table 1 also shows a "battery adder" of 13 lb for each 1% that the (estimated) system efficiency falls below 90%. This allowance is based on a battery output of 3 kw-min/lb and a run of 12 min.

Comparison between systems is finally made on the basis of "equivalent weights" given in the next-to-last column. The final **column** in Table 1 shows the estimated **overall** length of the Propulsion section, less battery, in a **21-in.-dia.** torpedo shell. An "adder" might be computed also to allow for extra battery size in less efficient systems. However, the correction is small, compared to uncertainties in the estimated lengths, and is neglected here.

Comments on the individual systems of Table 1 are as follow.

System A: Acyclic Motor and Toroidal Transmission

With good efficiency and low weight, this combination merits consideration, although both components require development for this application. Noise performance should be good in spite of high motor speed at low torpedo speed,

System B: Fixed Frequency Inverter, a.c. Motor, and Toroidal Transmission

The highest in weight and length and lowest in efficiency, this system is least attractive. Noise performance would be only fair because of the large number of components.

System C: Variable-Frequency Inverter, a.c. Motor, and Gears

The inverter presents some problems, as it should produce voltage proportional to frequency to avoid magnetic saturation of the motor at low frequencies. Motor noise would be moderate.

System D: Acyclic Motor with Shunt Field Control and Gears

Field control of speed **results** in a very heavy motor, but all other components are light. Development is needed for the **motor**. **Noise should be very low.**

System E: Noncommutator d.c. Motor and Gears, with Speed Control Combined with Electronic Commutation

The electronic circuits appear to be heavier than the **motor**, but further development of the **circuits should** uncover means of combining functions and reducing weight. Noise Performance is questionable because of difficulty of isolating large torque pulsations.

System F: D.C. Transformer with Conventional d.c. Motor and Gears

The **d.c.** transformer has been demonstrated in a smaller **rating**, and a **400-hp** motor is under construction, as described below. Expected noise performance is good.

System G: Switched Taps and Shunt Field Control Applied to a Conventional d.c. Motor and Gears

Besides being one of the lightest systems, it has the most technological background. The shunt field could be controlled by a time-ratio circuit to give it fast response.

System Weights and Dimensions

Although none of the estimated weights and dimensions in Table 1 are precise, they are believed to be of the right order of magnitude, say to **± 10%**. More refined figures **will** depend on design and development to the hardware stage. The results imply, however, that there are several electric torpedo propulsion systems that appear entirely feasible in the weight range of 500 to 650 lb, including **speed** control, motor, and transmission. As a choice among the continuously variable-speed systems, F or G looks best for immediate application, and system A has excellent potential for the longer term.

To comment further on the noise to be expected from the several systems, it must be recognized that there **is** no ultimate substitute for actual **tests**. However, much can be done to predict and control in-water noise **from** bench tests of components, if proper recognition is given to the complexity of the dynamic structures.

Multispeed Systems

All of the foregoing systems are for a continuously variable speed range of **2:1**. It seems reasonable to inquire whether or

not continuous variability is really necessary, and system H and J, at the bottom of Table 1, show the results of specifying three discrete speeds, say approximately 50, 75, and 100% of maximum.

System H. Switched taps with conventional d.c. motor and gears. This compares with system G but is 110 lb lighter.

System J. Switched taps with electronically commutated d.c. motor and gears. This compares with system E but is 90 lb lighter.

Thus, some 20% weight savings can be obtained by substituting three discrete speeds for continuous variability. It is a valid future study, therefore, to examine weapon effectiveness under those circumstances which have minimum complexity and weight.

Auxiliary Power

The power supply for essential torpedo auxiliaries is now considered. These normally include power for sonar gear, for data-processing electronics, and for steering. These have frequently been supplied by mechanically driven generators or by hydraulic systems. The electric torpedo with an adequate battery on board can supply such electrical loads either directly or through an electronic inverter without the noise of rotating machinery. Electric steering motors have proved satisfactory on torpedoes at lower speeds, and an electrically actuated steering system based on proportional control can be used on a high-speed torpedo, which does not need as high a maximum response rate as an hydraulic "bang-bang." The net result is quieter torpedo auxiliaries on an "all-electric" basis.

Current Motor Development

It is evident from the foregoing that the conventional, **commutator-type d.c.** motor is a component of several of the more promising systems and is quite close to state of the art. On this basis, the General Electric Company is independently developing a 408-hp, 450-v motor to run at 8000 rpm. It employs a special **commutator** structure, compensating windings, high-temperature insulation, and some unique cooling features; and its estimated weight is 355 lb.

Summary and Conclusions

From this analysis of components for **electric** torpedo **propulsion**, it is seen that there are several systems capable of **400-hp** output within the range of 500 to 650 lb, including speed control, drive, and transmission. Some are nearly state of the art, whereas others require additional development. Combining these results with expected improvement **in** battery performance, the weight of the electric propulsion system should become comparable to that of thermal systems in this power range.

Application of developed techniques to the quieting of motors ~~and of transmissions and to the isolation of residual vibration~~ from the torpedo shell has excellent promise of resulting in the really quiet torpedo essential to modern antisubmarine warfare.

References

- ¹**Turnbull, F. G.**, "Controlled rectifier dc to dc 30 hp motor drive," Am. Inst. Elec. Engrs. Paper 62-1066 (1962).
- ²**Harvey, L.** and **Burnett, J.**, "A new look at acyclic generation," Am. Inst. Elec. Engrs. Paper CP 61-504 (1961).
- ³**Kaestle, F. L.** and **Burnett, J. R.**, "Acyclic generator design and its application to electrolytic processes," Am. Inst. Elec. Engrs. Paper CP 62-403 (1962).

APPLICATION OF A SPECIAL MAGNETOHYDRODYNAMIC
INDUCTION COMPRESSOR TO UNDERSEA PROPULSION

Eugene Migotsky* and Joseph L. Neuringer†

AVCO Corporation, Wilmington, Mass.

Abstract

A magnetohydrodynamic induction compressor for undersea propulsion is described and theoretically analyzed. The analysis shows that its output is a function of the non-dimensional magnetic Reynolds number, R_m , and the nondimensional thickness of the conductor annulus, kh , in addition to geometric parameters and the ampere turns of the coils. The compressor output is maximum when $R_m = 4.12$ and $kh = 0.309$. The electromechanical conversion efficiency is 0.50 or less, and is 0.368 when the magnetic field strength is minimized for a fixed output. The preliminary feasibility study indicates that the compressor can provide the pressure rise required to propel large and small undersea craft. The speed of the traveling current wave in the coils should be as large as possible, but is limited by cavitation, to the order of the vehicle speed, although somewhat greater. The frequency of the wave is inversely proportional to the size of the propelled vehicle. For a torpedo, approximately 50 cps appears appropriate, with lower values for a submarine. Magnetic field strengths required to propel undersea vehicles at 30 knots are between 10^3 and 10^4 gauss, independent of the size of the craft. Minimum magnetic field strength is needed when the compressor operates at $R_m = 4.12$ and $kh = 0.309$. Conductivities required for minimum magnetic field strength are inversely proportional to the size of the craft and are attainable with liquid metals; lithium, for example, appears suitable for a torpedo.

The authors wish to thank Edwin L. Resler Jr. of the Cornell Graduate School of Aeronautical Engineering, who originally suggested the induction compressor concept to them, for many helpful and stimulating discussions.

*Senior Consulting Scientist, Applied Physics Section
†Senior Consulting Scientist, Applied Physics Section

Nomenclature

\vec{E}	= electric Intensity vector
\vec{v}	= velocity of conductor relative to magnetic field
\vec{B}	= magnetic induction vector
\vec{j}	= current density vector
f	= vector force per unit volume
j_θ	= azimuthal component of current density
B_r	= radial component of magnetic induction vector
B_x	= axial component of magnetic induction vector
V	= speed of traveling current sheet, also equal to speed of water through compressor
F_c	= total axial force on compressor
l_c	= length of compressor
<u>outer radius</u>	
R_1	= mean position of diaphragm
h	= annulus thickness of liquid conductor
n	= ratio of thickness of water to liquid conductor annuli
A	= cross-sectional area of water annulus
σ	= conductivity of liquid conductor
σ_o	= conductivity of liquid conductor corresponding to minimum magnet. field
μ_0	= free space magnetic permeability
k	= wave number, ω/v
ω	= circular frequency, rad/sec
ν	= frequency, cps
ν_o	= frequency corresponding to minimum magnetic field
R_m	= $\mu_0 \sigma V/k$ = magnetic Reynolds number based on wave speed and wavelength
N	= number of turns per unit length
I_o	= required current in coil
B_o	= magnetic field equivalent corresponding to the required current in coil
G_1	= dimensionless function of R_m and kh
G_{1o}	= dimensionless function of R_m
H	= power dissipated by joule heating in liquid conductor
η	= electromechanical energy conversion efficiency
γ	= dimensionless function of R_m and kh
m	= mass flow rate of water
T	= thrust
u_1	= exhaust speed at freestream pressure
U_∞	= forward speed of craft
p	= static pressure
p_∞	= freestream static pressure

Units are in the mks system.

P_c	= static pressure at compressor entrance
ρ	= density of sea water
g	= gravitation constant
d	= water depth
d_o	= depth of equivalent water corresponding to atmospheric pressure
η_p	= propulsive efficiency
A_s	= wetted area
$C_D s$	= drag coefficient based on wetted area
D	= drag
r, e, x	= cylindrical coordinates
$\hat{r}, \hat{\theta}, \hat{x}$	= unit vectors corresponding to cylindrical coordinate directions

Introduction

Recently, considerable interest and some success have been shown in applying the principles of magnetohydrodynamics to compression and acceleration of conducting gases and liquids. For example, Covert and Haldeman discuss the traveling-wave pump with emphasis on the acceleration of ionized gases, and Blake describes various magnetohydrodynamic pumps for liquid metals in nuclear reactors. Applications of these principles, however, to the direct interaction of a magnetic field with sea water shows that extremely large field strengths are required to produce significant forces because of the low conductivity of sea water:

A scheme is described which overcomes limitation with realistic magnetic field strengths, and a simplified theoretical analysis of an applicable induction compressor is given. Also included are a feasibility study of its application to the propulsion of undersea craft.

Analysis

The MHD Induction Compressor

The magnetohydrodynamic (MHD) induction compressor considered here is shown schematically in Fig. 1. It consists of a coil around a circular cylinder on which a sinusoidal traveling current is impressed. Adjacent to the coil is an annulus of a conducting liquid which is constrained from moving axially and is separated from the internal nonconducting fluid (water) by a flexible diaphragm. The traveling current has a sinusoidal traveling magnetic field associated with it, which induces azimuthal (ring) currents

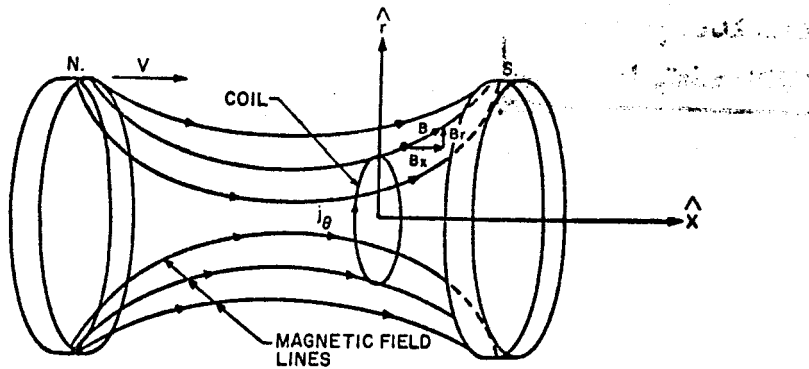


Fig. 1 Schematic of magnetohydrodynamic induction compressor.

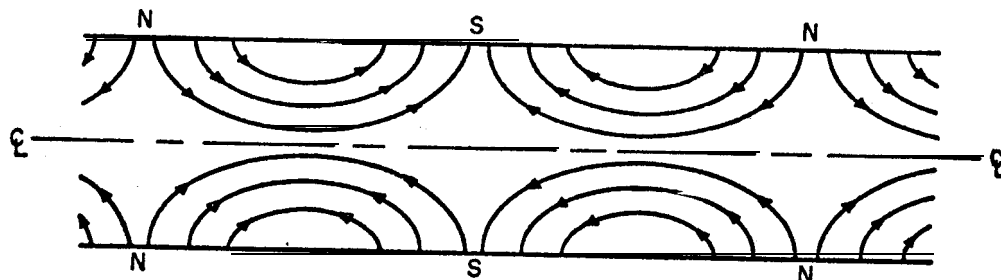
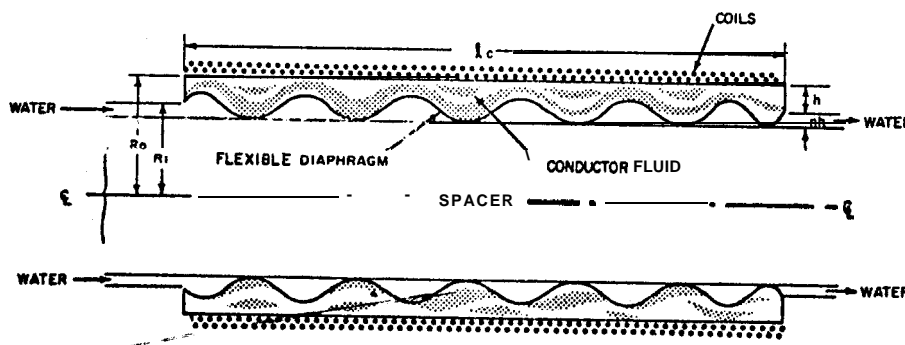


Fig. 2 Simplified case of a coil imbedded in an axially symmetric magnetic field.



Mg. 3 Schematic variation of magnetic field inside the coil.

in the conducting liquid. The interaction between the magnetic field and these currents results in **Lorentz** forces, with radial and axial components, within the liquid conductor. Independent of the direction of the magnetic field lines within the liquid conductor, the instantaneous axial force is positive (or zero), and the radial force does change sign. Inasmuch as the liquid conductor **is** constrained from moving axially, an axial pressure gradient is induced in it. If the radial forces in the liquid conductor are sufficient to pinch and trap the water (see Fig. 1), this pressure gradient will be transmitted to the flowing water via the flexible diaphragm. This results **in** motion of the water as trapped packets, traveling from left to right with the wave speed of the diaphragm, which resembles a series of compressors, each giving a finite pressure rise to the pumped water and each wavelength **corresponding** to a compressor stage.

To understand the operating principle involved, recall the **motional** form of Faraday's induction law, Ohm's law, and the Lorentz force law. The **former** states that an electrical conductor, moving with a **velocity** V relative to a magnetic field B , has an electric **field** E induced in it,

$$\vec{E} = \vec{V} \times \vec{B} \quad (1)$$

The vector cross product indicates that lines **of** magnetic flux must be cut by the moving conductor before induction takes place. The resultant current density \vec{j} , which flows in a conductor with electrical conductivity σ , **is** obtained from Ohm's law, written as

$$\vec{j} = \sigma \vec{E} \quad (2)$$

Finally, a conductor carrying current density \vec{j} in a magnetic field B experiences a force per unit volume f ,

$$\vec{f} = \vec{j} \times \vec{B} \quad (3)$$

Now apply these laws to the simplified geometry of Fig. 2, where a circular coil with **axis** \hat{x} **is** imbedded in an **axially** symmetric field of the N-S magnet. The motion of the coil along the negative direction of its axis in the field of the **fixed** magnet is electromechanically equivalent to a **stationary coil with the magnet moving to the right with the same** velocity. The field of the magnet, being **axisymmetric**, has only an axial **component** B_x and a **radial component** B_r .

Applying Eq. (1) yields $E_\theta = -V B_r$, and, from Eq. (2), the current density is

$$j_\theta = \sigma V B_r \quad (4)$$

Thus, the current density induced in the coil is in the azimuthal direction, is proportional to the electrical conductivity and the relative velocity, and depends only upon the radial component of the magnetic field. Substituting the expression for j_θ into Eq. (3) yields

$$\vec{f} = \sigma V B_r^2 \hat{x} - \sigma V B_x B_r \hat{r} \quad (5)$$

Thus, the coil is subjected to a positive (or zero) force in the axial direction and a pinch or squeeze in the radial direction. Regardless of the direction of the magnetic lines threading the coil, the axial force is never negative; the radial force, however, does change sign.

The preceding can now be applied to the configuration of Fig. 1: a cylindrical tube on which a coil and its return are azimuthally wound. The two wires are connected to a power source at the left end and terminated to a characteristic impedance at the other. This constitutes a transmission line, and the magnetic field configuration inside the tube is shown schematically in Fig. 3. The traveling current wave moving to the right in the coils has a traveling magnetic field associated with it, which can be considered as a sequence of traveling N-S magnetic poles. Azimuthal currents and body forces would be induced in salt water placed in an annulus inside the tube and adjacent to the coils. because the conductivity of salt water is so low (i.e., orders of magnitude less than ordinary liquid metals) pumping or accelerating salt water requires extremely high current levels to produce the necessary magnetic fields.

For the latter reason, an annulus of highly conducting liquid is introduced next to the coils in which significantly larger body forces are induced, and, by restraining the liquid conductor from moving axially, an axial pressure gradient will occur. A first approximation of this gradient is obtained from the axial momentum equation, neglecting the Inertia terms:

$$\sigma V B_r^2 = \partial p / \partial x \quad (6)$$

Since liquid metal annulus is internally bounded by a flexible diaphragm, this pressure gradient is transmitted mechanically to the water.

An approximation for the total force on the compressor is obtained by solving Maxwell's equation for magnetic field components inside a solenoidal coil for the case where conductivity vanishes outside the coil, the conductivity inside the coil has a finite value, and the current in the coil is a sinusoidal wave traveling axially with speed V . The expression for the radial component of the magnetic field is substituted in Eq. (6) to obtain the pressure gradient within the compressor, and the gradient integrated to give the total force acting on the compressor. Although exact solutions of Maxwell's equations were obtained in Refs. 3 and 4, they involve Bessel functions with complex arguments. To obtain more tractable expressions, asymptotic expansions These do not solution were also developed in the references place any restriction on the value of the conductivity; the only restriction involved is geometric, in particular, $kR_o \gg 1$. This asymptotic expression for the total force acting on the compressor is

$$F_c = \left(\frac{1}{R_o} \right) \frac{A}{h \left[1 - \frac{h}{R_o} \right]} G_1(R_m, kh) \frac{B_o^2}{2\mu_0} \quad (7)$$

where

$$G_1(R_m, kh) = \frac{(kh)R_m \exp \left\{ -kh(2+2\sqrt{R_m^2 + 1}) \right\}^{1/2}}{\left[(1/2)(2+2\sqrt{R_m^2 + 1})^{1/2} + 1 \right]^2 + \frac{R_m^2}{(2+2\sqrt{R_m^2 + 1})}} \quad (7a)$$

and

$$B_o = \mu_0 N I_o \quad (7b)$$

The variation of the nondimensional function, G_1 , with magnetic Reynolds number, R_m , for several values of the non-dimensional parameter, (kh) , is shown in Fig. 4. The various curves have an envelope curve denoted by G_{10} , whose expression is derived from the preceding one for G_1 by differentiating with respect to (kh) , setting the derivative equal to zero, solving for the resultant variation of $(kh)_o$ with magnetic Reynolds number, substituting the resulting expression into the original function G_1 , and simplifying to obtain

$$(kh)_o = (2 + 2\sqrt{R_m^2 + 1})^{-1/2} \quad (8)$$

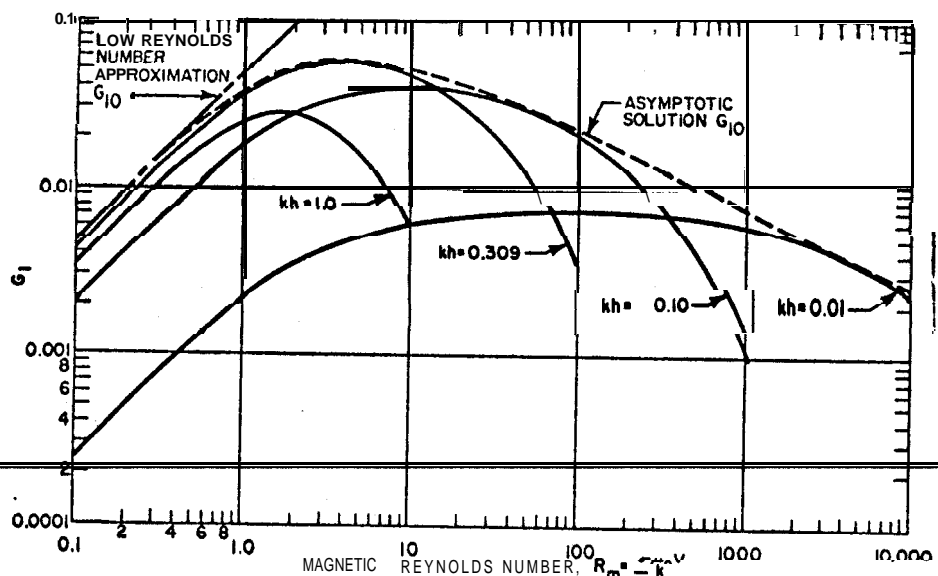


Fig. 4 The nondimensional function G_1 vs magnetic Reynolds number for several values of kh .

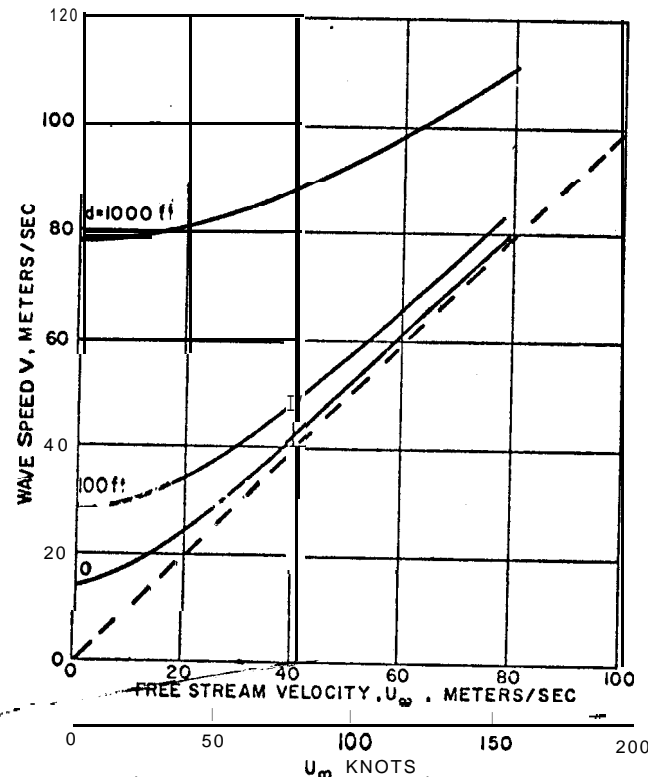


Fig. 5 Wave velocity vs forward velocity for three minimum depths ($R_c=0$).

and

$$G_{10} = \frac{1}{e(2+2\sqrt{R_m^2 + 1})^{1/2}} \quad (9)$$

$$\times \frac{R_m}{[1/2(2+2\sqrt{R_m^2 + 1})^{1/2} + 1] + \frac{R_m^2}{(2+2\sqrt{R_m^2 + 1})}}$$

G_{10} has a maximum,

$$G_{1\max} = 0.0553 \quad (10)$$

where

$$(kh)_{\text{opt}} = 0.309 \quad (R_m)_{\text{opt}} = 4.120 \quad (11)$$

The simplified expression for the function G_1 , obtained by expanding about $R_m = 0$ and retaining only the linear term, is

$$G_1 = \frac{R_m (kh) \exp \left[-2kh \right]}{4} \quad R_m \ll 1 \quad (12)$$

and the corresponding optimum is

$$G_{10} = \frac{R_m}{8e} \quad R_m \ll 1 \quad (13)$$

which occurs at

$$(kh)_0 = 1/2 \quad (14)$$

In Fig. 4 is a plot of Eq. (13). It is valid only if $R_m \ll 1$, and will lead to incorrect conclusions if this is not so.

The existence of a maximum and the subsequent reduction of G_{10} , as the magnetic Reynolds number is increased indefinitely is related to the well-known skin-depth effect: that is, attenuation of an oscillatory electromagnetic field as it penetrates a conducting medium.

The total power delivered to the liquid conductor is the sum of the pump power and the power expended in the joulean heating resulting from the circulating currents in the conductor. Defining an electromechanical conversion efficiency η_e as the ratio of the pumping power to the total power delivered to the conductor,

$$\eta_e = \frac{F_c V}{F_c V + H} = \frac{1}{1 + \frac{H}{F_c V}} \quad (15)$$

where F_c is defined in Eq. (7), and

$$H = 2\pi \int_0^{l_c} \int_{R_o-h}^{R_o} \frac{j\theta^2}{\sigma} r dr dx \quad (16)$$

Evaluating Eq. (16), with the asymptotic form for the current density distribution obtained in Refs. 3 and 4, Eq. (15) becomes

$$\eta_e = \frac{1}{1 + \frac{e^\gamma - 1}{\gamma}} \quad (17)$$

where

$$\gamma = (2 + 2\sqrt{R_m^2 + 1})^{1/2} \quad (kh) \quad (18)$$

Application to Undersea Propulsion

A preliminary study was made to evaluate the feasibility of an induction compressor as a jet propulsion system for undersea craft. The craft considered includes a water inlet at its forward end, ducts to bring sea water to the compressor, an annular induction compressor around the hull, and ducts leading from the compressor to an exit nozzle. It was assumed that shapes could be coordinated in a final design so that losses due to internal or external flow separation would be largely avoided.

Consider this jet-propelled craft moving through a fluid with velocity U_∞ and static pressure p_∞ . For a mass flux through the system of m , the relative exhaust velocity is u_1 , the exhaust pressure p_1 is equal to the free-stream static

pressure p_∞ , and the thrust T becomes

$$T = m(u_1 - U_\infty) \quad (19)$$

The ratio of the work done in unit time TU_∞ to the sum of the work done and the kinetic energy left in the slip-stream (i.e., $TU_\infty + \frac{1}{2}m(u_1 - U_\infty)^2$) and using Eq. (19) gives propulsive efficiency

$$\eta_p = \frac{2}{1 + \frac{u_1}{U_\infty}} \quad (20)$$

From the continuity of mass flow,

$$\dot{m} = \rho AV = \text{constant.} \quad (21)$$

To propel the vehicle at constant velocity, the thrust must equal drag, or

$$D = (C_D S A_S) \frac{\rho U_\infty^2}{2} = \rho AV (u_1 - U_\infty) \quad (22)$$

where $C_D S$ is the nondimensional drag coefficient corresponding to a reference area A_S , which is taken as the wetted area of the vehicle.

The work done on sea water by the compressor per unit time is the product $F_c V$, where F_c is the total force on the compressor and V is the velocity of the internal sea water. The velocity V also equals the speed of the wave traveling down the flexible diaphragm, which equals the speed of the electromagnetic wave traveling down the coils. The expression for the rate of doing work by the compressor provides another propulsive efficiency, $\eta_p = TU_\infty / F_c V$, which may be solved for the total force

$$F_c = \frac{TU_\infty}{\eta_p V} \quad (23)$$

From Eq. (23), a vehicle moving at a specified speed with a given propulsive efficiency will require a total force that decreases with V . From Eq. (7), the required current in the coils will be minimum when the velocity of the traveling current sheet is maximum. This velocity is limited by cavitation inception at the compressor entrance. Thus, denoting by P_c the minimum allowable pressure at the entrance, the

allowable fluid velocity (which equals the traveling wave velocity) is determined by Bernoulli's equation between the freestream and this station:

$$p_{\infty} + \frac{1}{2} \rho U_{\infty}^2 = p_c + \frac{1}{2} \rho V^2 \quad (24)$$

The freestream static pressure is

$$p = \rho g (d + d_0) \quad (25)$$

where d is depth below the surface and d_0 is the height of water equivalent to 1 atm. Solving Eqs. (24) and (25),

$$V = U_{\infty} \left[1 + \frac{2g(d + d_0)}{U_{\infty}^2} - \frac{2p_c}{\rho U_{\infty}^2} \right]^{1/2} \quad (26)$$

Equations (7, 19-23, and 26) define the Induction compressor in a jet propulsion system for an undersea craft. In particular, if ρ , U_{∞} , η_p , $(C_D A_S)$, R_o , I , p_c , n , d , and μ_0 are given, one can obtain the following as functions of the two nondimensional parameters R_m and (kh) :

1) The frequency of the traveling wave, V ,

$$V = \frac{\mu_0 n}{\pi R_o} (kh) \left(\frac{\pi R_o^2}{C_D A_S} \right) \left(\frac{1 - \eta_p}{\eta_p} \right) \left(1 + \frac{2g(d + d_0)}{U_{\infty}^2} - \frac{2p_c}{\rho U_{\infty}^2} \right) \quad (27)$$

2) The amplitude of the magnetic field in the neighborhood of the coil, B_0 , from which the required ampere-turns per unit length of coil, NI_0 , can be determined,

$$B_0 = \mu_0 NI_0 \approx$$

$$\left[\left(\frac{\mu_0}{n} \right) \left(\frac{R_o}{Ic} \right) \left(\frac{C_D A_S}{\pi R_o^2} \right) \frac{1/2 \rho U_{\infty}^2}{\eta_p (1 + 2g(d + d_0)) - 2p_c} \right]^{1/2} G_1^{1/2} \quad (28)$$

assuming that the total area of the water annulus may be written $A = 2\pi R_o (nh)$, which is valid when $h/R_o \ll 1$.

3) The conductivity of the liquid conductor,

$$\sigma = \frac{8n}{\mu_0 R_o U_{\infty}} \left(\frac{\pi R_o^2}{C_D A_S} \right) \left(\frac{1 - \eta_p}{\eta_p} \right) R_m (kh) \quad (29)$$

4) The thickness of the Water annulus, nh ,

$$(nh) = \frac{R_o}{8} \left(\frac{C_D A_S}{\pi R_o^2} \right) \left(\frac{\eta_p}{1 - \eta_p} \right) \left[1 + \frac{2g(d + d_0)}{U_{\infty}^2} - \frac{2p_c}{\rho U_{\infty}^2} \right] \quad (30)$$

Results and Discussion

To illustrate characteristics of the application of the magnetohydrodynamic compressor to the propulsion of undersea craft, calculations were made for vehicles with a length/diameter ratio of 10 to 1, a drag coefficient of 0.003 (based upon wetted area and fully turbulent flow), and a velocity of 30 knots with a propulsive efficiency of 90%. The ratio of compressor length to total length of the craft was taken as one-half, and two values of total length were selected. The larger was 376 ft, a value typical of a submarine, whereas the smaller 17.5 ft, representing a torpedo. The minimum pressure at the entrance to the compressor, p_c , was taken as zero. The thicknesses of the conductor annulus and of the water annulus were assumed the same ($n=1$).

The variation of wave speed with vehicle forward speed for three values of minimum depth of operation is shown. The maximum allowable wave speed (i.e., the wave velocity but the same order of magnitude as the vehicle velocity) approaches the vehicle speed as the magnetic Reynolds number is reduced. The maximum wave speed depends upon the mechanical properties, and not upon magnetohydrodynamic characteristics or vehicle size. The variation of the frequency of the traveling wave required for minimum magnetic field strength with magnetic Reynolds number is shown in Fig. 6. The frequency of the traveling wave is less than 100 cps for these conditions. From Eq. (27), frequency varies inversely with the size of the vehicle; thus, the frequency for the smaller vehicle is greater than that of the larger vehicle by a factor of 21.5.

The dependence of the minimum magnetic induction, which corresponds to choosing the envelope curve G_{10} , on magnetic Reynolds number is presented in Fig. 7 for operation at the surface ($d=0$). Also shown is a comparison of the low Reynolds number approximation and the asymptotic solution. These results (see Eq. (28)) are independent of the size of the craft. The two curves differ greatly at magnetic Reynolds numbers greater than unity. The approximation under-estimates the required magnetic field strength by an order of magnitude

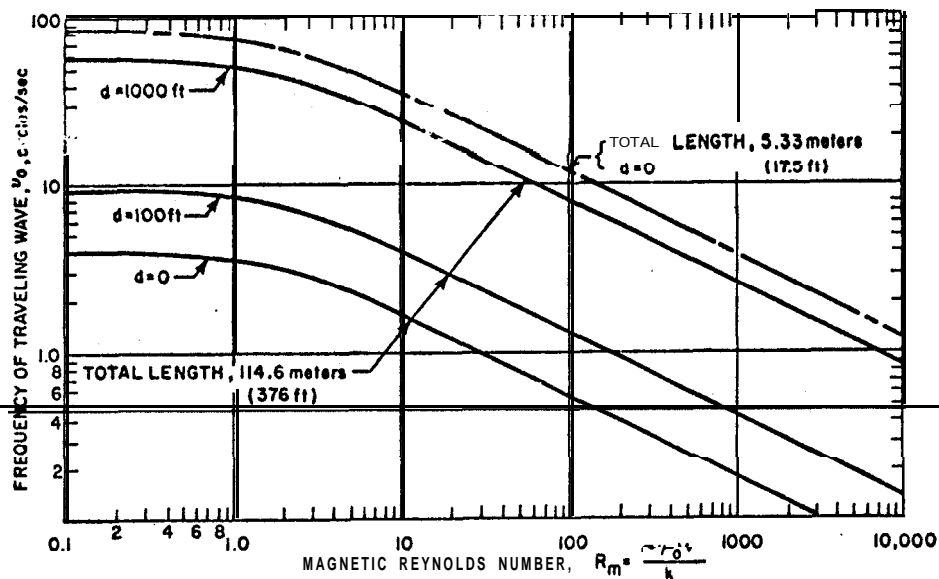


Fig. 6 Frequency of traveling wave required for minimum magnetic field strength vs magnetic Reynolds number. Reference case.

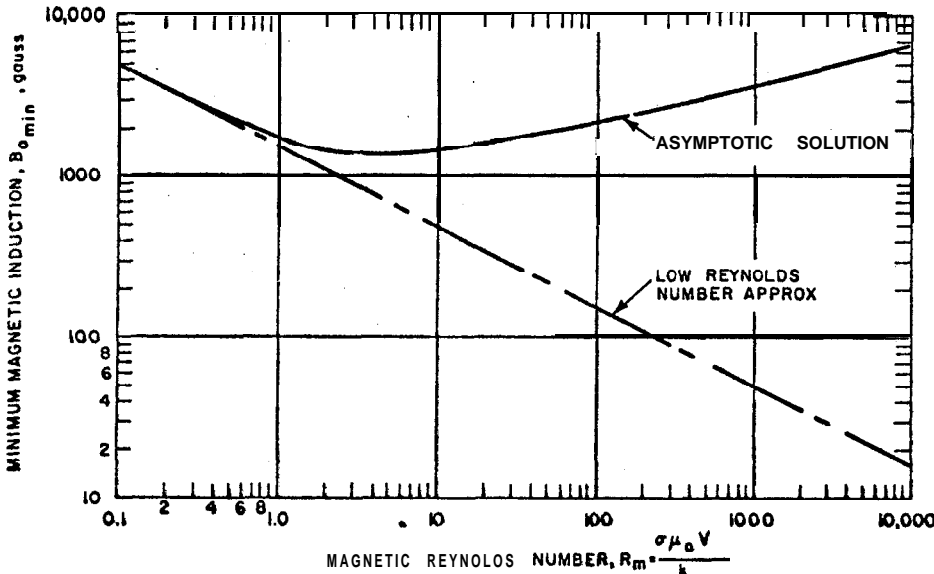


Fig. 7 Minimum magnetic induction vs magnetic Reynolds number. Reference case; minimum depth of operation $d=0$.

when the Reynolds number is 50, and at higher numbers the divergence increases. The minimum value of magnetic induction $B_{0 \min}$, which occurs at a value of $R_m = 4.12$, is 1440 gauss for surface operation ($d=0$). The dependence of $B_{0 \min}$ upon minimum depth of operation is rather weak, as is seen in Eq. (28), where B_0 varies inversely as the fourth root of d . In fact, allowing the minimum depth of operation to be 1000 ft reduces the value of $B_{0 \min}$ only to 730 gauss.

The curve of Fig. 7 has a rather flat minimum: over a wide range of Reynolds numbers, field strengths are of the order of 10³ gauss. For a coil with 10^2 turns/m, this corresponds to currents of the order of 10^3 amps. Coil cooling requirements under this condition do not appear excessive. However, operation at higher magnetic Reynolds numbers, where the field requirements are of the order of 10^4 gauss, increases the joulean dissipation a hundredfold (since it depends on the square of the current) and would probably require superconducting coils.

The depth of the water annulus, equal to that of the liquid conductor annulus, increases linearly with the size of the propelled vehicle (see Eq. (30)). Calculated values of the ratio h/R_o , of thickness of water annulus to the radius of the coils were 0.074, 0.049, and 0.020 when the minimum depth of operation was 0, 100, and 1000 ft respectively. Thus, the annuli are small fractions of the coil radius.

The variation of conductivity required for minimum magnetic field strength with magnetic Reynolds number is shown in Fig. 8. Referring to Eq. (29), it does not depend upon minimum depth of operation and is inversely proportional to the size of the propelled vehicle. Shown in Fig. 8 are conductivities for molten lithium and bismuth. For the smaller body (typical of a torpedo), the conductivity of lithium is very close to the required value. For the larger body (typical of a submarine), a conductivity about one order of magnitude smaller is indicated.

The variation of electromechanical efficiency, which is a function of only one nondimensional parameter $\gamma = (kh)$. $(2 + 2\sqrt{R_m^2 + 1})^{1/2}$ (see Eq. (17)), is presented in Fig. 9. The maximum η_e is 0.5 and occurs when γ vanishes; the curve then decreases monotonically and approaches zero as γ increases. Of particular interest, at the minimum value of magnetic field strength, the parameter γ becomes unity (since $R_m = 4.12$ and $kh = 0.369$), and the electromechanical efficiency is 0.368. Thus, improvement in efficiency is possible by designing the induction compressor to operate at values of γ between zero

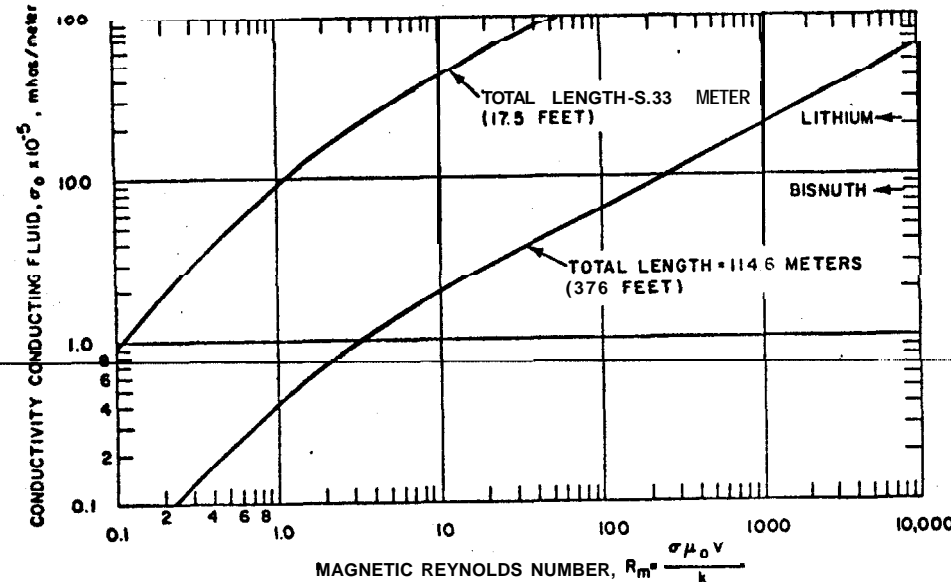
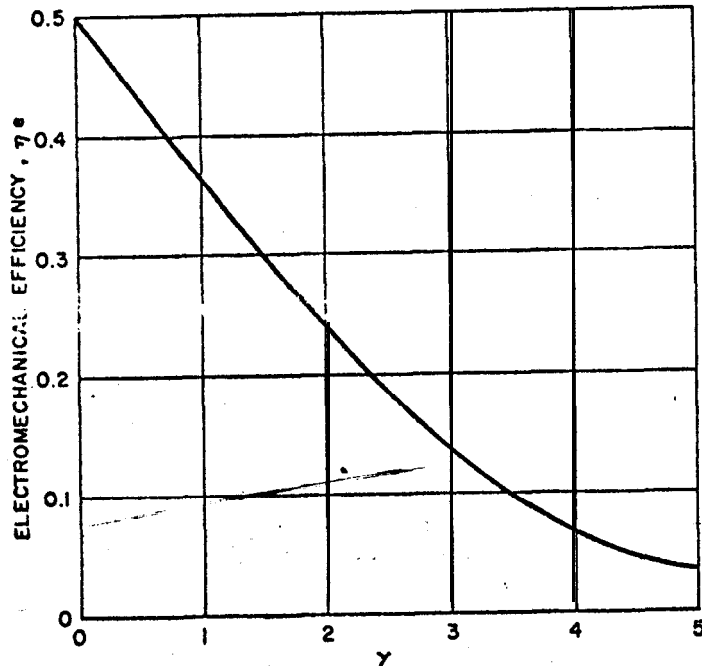


Fig. 8 Conductivity required for minimum magnetic field strength vs magnetic Reynolds number for two craft lengths. Reference case.



Fin. 9 Electromechanical efficiency of induction compressor

and unity. Although this is at the expense of an increase in magnetic field requirement, near the minimum value of magnetic field strength the latter increases are quite small.

Concluding Remarks

This analysis of the magnetohydrodynamic induction compressor shows that its output is a function of the nondimensional magnetic Reynolds number, R_m , and the nondimensional thickness of the conductor annulus, kh , in addition to geometric parameters and the ampere turns of the coils. The compressor-output is maximum when $R_m = 4.12$ and $kh = 0.309$. The electromechanical conversion efficiency is 0.50 or less, and is 0.368 when the magnetic field strength is minimized for a fixed output.

The preliminary feasibility study indicates that the compressor can provide the pressure rise required to propel large and small undersea craft. The speed of the traveling current wave in the coils should be as large as possible, but is limited by cavitation, to the order of the vehicle speed, although somewhat greater. The frequency of the wave is inversely proportional to the size of the propelled vehicle. For a torpedo, approximately 50 cps appears appropriate, with lower values for a submarine. Magnetic field strengths required to propel undersea vehicles at 30 knots are between 10^3 and 10^4 gauss, independent of the size of the craft. Minimum magnetic field strength is needed when the compressor operates at $R_m = 4.12$ and $kh = 0.309$. Conductivities required for minimum magnetic field strength are inversely proportional to the size of the craft and are attainable with liquid metals; lithium, for example, appears suitable for a torpedo.

This theoretical analysis assumed that the effect on the electromechanical interaction of motion of the liquid conductor can be neglected. Actually, the conductor's fluid motion affects this interaction and, in addition, acts as an energy drain, since its kinetic energy ultimately is converted by viscosity into heat. It was also assumed that the amplitude of the current wave does not vary with axial distance along the coils, although, by analogy to a loaded transmission line, the amplitude of the current wave is expected to decay as it travels down the coils.

References

1 Covert, E. E. and Haldeman, C. W., "The traveling wave pump," **ARS J.** 31, 1252 (1961).

2 Blake, L. R., "Electromagnetic pumps for liquid metals," **J. Nucl. Energy** 1, 65(1959).

3 Neuringer, J. L. and Migotsky, E., "Skin effect in magneto-fluid dynamic traveling wave devices," **Phys. Fluids** 6, 1164 (1953).

4 Neuringer, J. L., Migotsky, E., Haag, R. M., and Turner, J. H., "Theoretical investigation of an Induction compressor," Avco Research and Advanced Development Division, Final **TR RAD-TR-63-51**, (March 1964). prepared for office of Naval Research Contract **N(ONR)4047**.

HEAT ENGINES FOR
UNDERWATER MISSILES

TORPEDO PROPELLANTS

Leonard Greiner*

United Technology Center, Sunnyvale, Calif.

Abstract

Propellants for torpedoes must be selected with consideration to mission requirements. Because underwater speeds are necessarily slow and torpedo ranges relatively great, rocket-type propulsors are less effective than rotating types, and so the propellants are used to power engines that supply torque. Their relative performances are best screened through theoretical work output/volume. Values given for a number of candidates show metal-fueled systems to be best and, thus, likely to be used in the future. The products of the propellant reaction must be compatible with the power plant, whether turbine or reciprocating, and the specialized underwater power cycles. Some of the latter are unaffected by the high ambient pressure of the environment. As metal-fueled systems become utilized, unique feed and combustion methods will be needed.

Introduction

A modern torpedo is a guided missile that often travels a great distance underwater to deliver its explosive payload to a target. To do so effectively in its high-drag environment, relatively slow speeds are required which are best obtained by a rotating propulsor shafted to a torque-producing power plant. Heat engines are potentially and practically competitive with other power sources if the propellants that drive them can be safely stored, can produce exhaust products that uniquely match the engine requirements, and can liberate sufficient energy to perform the mission requirements. The last two require consideration of the type of engine and of its thermodynamic cycle which, together with the propellants, must provide for effective operation for a sufficient length of time at a deep enough depth, and must fit into the relatively small volume available in a torpedo.

* Technical Assistant to Manager, Research and Advanced Technology Department. (Scientist, Research and Development, CETEC Corp., Mountain View, Calif.)

In contrasting the processes of choosing propellants for underwater torpedoes and above-water missiles, greater emphasis has been placed, in the former, on practical aspects, with attainment of truly high performance relegated a secondary role. Yet, as underwater requirements increase, skillfully manipulated combinations of potential propellants and feasible methods for propelling torpedoes can provide better performances within the practical specifications. Information on selecting propellants that fulfill these goals is given below.

Propellant Performance Analysis

The heat engines of torpedoes include a combustion chamber, like that of a rocket, wherein the propellants are reacted to liberate their energy. Liquid bipropellants, monopropellants, solids, or hybrids are used. Liquids are pumped to the chamber directly or by being displaced by pumped sea water. Sea water often is part of the propellant—generally diluent to lower temperatures and to augment working gases, but it may be oxidizer as well. Because speeds of torpedoes are necessarily relatively low in the high-drag underwater environment but ranges of thousands of yards are required, jet-type propulsion that requires high-speed bodies for efficient energy utilization is of little interest. Thus, the hot propellant products power a mechanical engine, either turbine or reciprocating, which provides torque to a rotating propulsor.

Considering the carried propellant alone, which excludes sea water from the environment, a torpedo has a certain space where expendable propellant is stored. Thus, a good propellant performance indicator represents the effect of filling this (fixed) space with candidate fuels. This compares strictly on an energy/volume basis and neglects weight effects. However, they usually are not definitive, as discussed next.

The proportion of the torpedo weight which comes from the carried propellant probably never exceeds 0.5 and is usually less, in contrast to above-water rockets where ratios exceeding 0.9 are common. Thus, the total torpedo weight is relatively independent of the propellant used, which therefore is not critical to either propulsive performance or to missile-handling difficulties on shipboard. However, space on most torpedo launch platforms is limited, and missile size becomes more critical than weight. The notable-buoyancy experienced in water greatly reduces effective weight and this lowers the angle-of-attack requirements for torpedoes traveling horizontally. Since torpedo flights are usually at constant speed, the power plant is primarily countering drag and not accelerating the body. At nominal torpedo speeds, drag can be very

great since coefficients in water are three orders of magnitude above those in sea-level air at similar speeds. Thus, the weight of the torpedo is usually small compared to its drag, but this drag increases with missile size. All these factors tend to make propellant energy/volume far more important in torpedoes than energy/weight.

Another consequence of torpedoes moving primarily in sustain modes is that theoretical work output of the propellant is a more convenient propellant performance comparison than jet-thrust capability, since the former can be directly converted through efficiencies (ordinarily about 50%) to the work output of the rotating thruster. Also, the power plant operates against a constant force (drag) which is tantamount to the classical concept of work-moving an object against a force.

In view of previous discussions where volume and weight effects are shown to be relatively unimportant and work output is a useful means of characterizing torpedo performance, the parameter most conveniently used in grading torpedo propellants is work/volume in customary units, $\text{hp}\cdot\text{hr}/\text{ft}^3$. However, a final choice among closely competitive propellants requires a rigorous assessment at exact flight conditions.

Thus, weight-(i.e., mass) is important when the missile changes velocity and must be considered in trajectories where this is involved. Weight cannot be ignored when the torpedo is essentially a second-stage: a payload of ASROC or SUBROC, of a DASH helicopter, or of an ASW fixed-wing aircraft. Weights are also important when they affect missile trim, or recovery after an exercise run when this depends on floating the spent missile to the surface.

Theoretical values of work output for torpedo propellants are calculated by a process resembling that for rocket propellants, which take into account the energy and the type of working gases produced by the chemical reaction. One assumes adiabatic combustion to chemical equilibrium, followed by isentropic expansion that is either frozen or shifting, depending on conditions. Computations for a number of propellants are gathered^{1, 2} in table 1 for 20.4/1 expansion ratio and in figs. 1 through 4 for 1,000/14.7 and 300/14.7 ratios. Some of these were computed by approximation techniques, as exemplified in the appendix and all are accurate to 10%, which is sufficient for comparisons.

Performances on rocket and power bases are plotted versus moles of free sea water for three water-oxidized systems in the figures. In the table, only power parameters are listed.

Fig. 1 Approximate theoretical power on weight and volume bases for some water-reacted propellants versus moles of free water (expansion ratio, 300/14.7 psia; open data points indicate combustion temperature about 1,800°F).

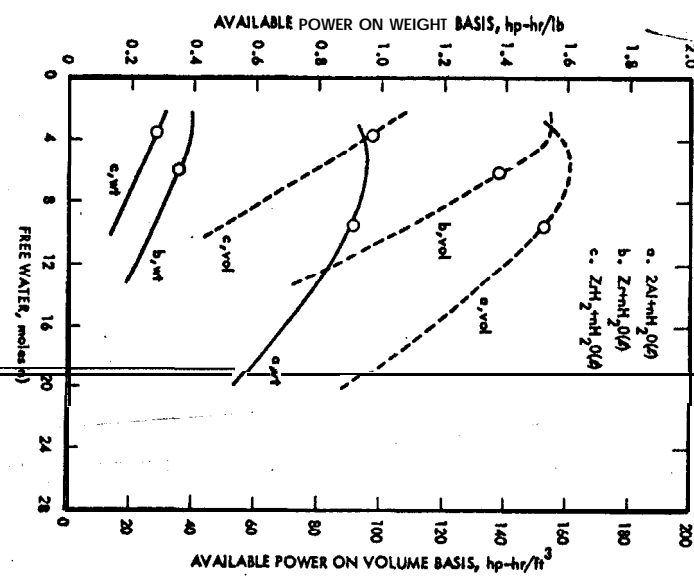
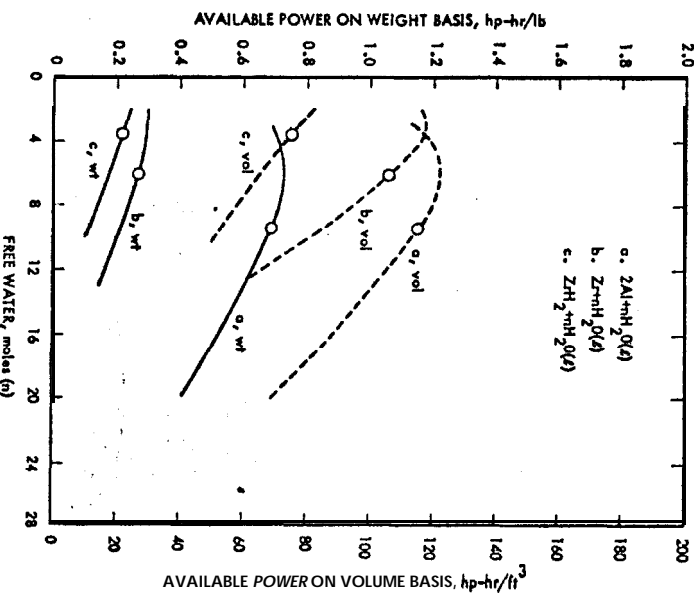


Fig. 2 Approximate theoretical power on weight and volume bases for some water-reacted propellants versus moles of free water (expansion ratio, 1,000/14.7 psia; open data points indicate combustion temperature about 1,800°F).



They are usually computed with sufficient free water added to lower combustion temperature to 1,800°F (so that the products can be handled by a state-of-the-art turbine), and results are arranged in descending order of $\text{hp-hr}/\text{ft}^3$ for reasons previously mentioned. The energy required to pump this water for operation at normal combustion pressures (300 to 1,000 psia) can be ignored, in contrast to the parallel situation with air-breathing power plants where pumping work is important. In a torpedo the water pump is powered by a shaft geared to the engine.

It is evident from the table and figures that high performance with respect to weight and volume generally does not simultaneously characterize any single propellant, which shows the need to select the proper performance parameter for their evaluation. The highest work/volume propellants are those in which the fuels are metals, as aluminum, zirconium, magnesium, and lithium, approximately in that order. Although the best combinations use free water as oxidant, some that use carried oxidizers are quite competitive. As shown in the figures, performances peak at an intermediate amount of free water. This peaking is more pronounced with water-breathing than with air-breathing systems because of the competing effect on available energy of the high heat of vaporization of water. Systems that do not use metals as fuels have lowered performances; nevertheless, for practical reasons these are used in current torpedoes.

Practical Aspects

In choosing propellants for torpedoes, performance can be less important than toxicity or other potential hazards in case of accident, because the missile is stored in closed environments (say, in a submarine) and often shares the living quarters of the crew. Also, the propellants must be adaptable to the power cycle and to practical construction of the engine, as next discussed. The properties of the combustion products are critical here.

In the most simple, common torpedo heat engines, the propellant products are piped directly from the combustor to the engine and exhausted overboard. A primary problem here is compatibility of the products with the engine. Generally, a turbine can tolerate a greater amount of nongascs in its working medium than can a reciprocating engine, and the latter can accept gases of somewhat higher temperature. Even with a turbine problems are to be expected if the exhaust includes extremely hard solids, as aluminum oxide (corundum); and both turbines and reciprocating engines will have operating

difficulties when materials are present which form glass-like coatings (as boric oxide), or which are highly corrosive, as hydrogen fluoride. Also, such open-cycle systems can diminish the effectiveness of the weapon system by emitting a bubble trail behind the torpedo which can give away the launch platform and/or affect the torpedo's internal guidance. A critical problem of these simple **systems stems** from the fact that the engine directly feels the external (i.e., back) pressure, so that its operational pressure ratio decreases with depth, and this reduces the thermodynamically available energy.

A means of compensating, within reason, for the effect of **depth on the performance of an open-cycle system** is to operate **at very high internal pressures**.^{4, 5} However, this requires heavy structural materials and sturdy pumps that take up volume otherwise occupied by propellant or by other power plant components. If extremely high pressures (15,000 psi) are chosen, the work required to pump the propellants (or sea water) to the combustor significantly subtracts from the power delivered to the propellor shaft.

In case one chooses propellants for an open-cycle system, all of whose gaseous products are condensable to **nongases** on contacting cool water (e.g., aluminum-hydrogen peroxide balanced to aluminum oxide and water), then addition of a special **jet-ejector**, called a condensuctor, to the exhaust of the power plant will make the system depth-insensitive.²⁹ This is because the pressure sensed by the power plant is that within the **condensuctor**,⁶ which can approach the vapor pressure of the (heated) internal aqueous solution, and this bears no relation to the ambient pressure. The free water stream is **educted** into the condensuctor by the waste enthalpy in the power plant's exhaust, which also provides **sufficient** momentum for diffusion and expulsion against the ambient pressure. Thus, there are no energy or propellant losses chargeable to the condensuctor, the sole requirement being that all gaseous products formed by the propellants be condensable to **nongases** on cooling, and this is a problem for the propellant formulator.

Generally, the propellant products will not comply with the requirements of a condensuctor because of practical formulation problems, nonequilibrium on combustion, or the intrinsic chemistry of the propellants. Under these conditions, depth independency can be **obtained with an increase** in system complexity by adopting a power plant cycle in which the propellant products exchange their energy to an enclosed working medium. The latter powers the engine in a closed loop wherein the heated working medium first energizes the engine, is then cooled by heat exchange to sea water to reject the thermo-

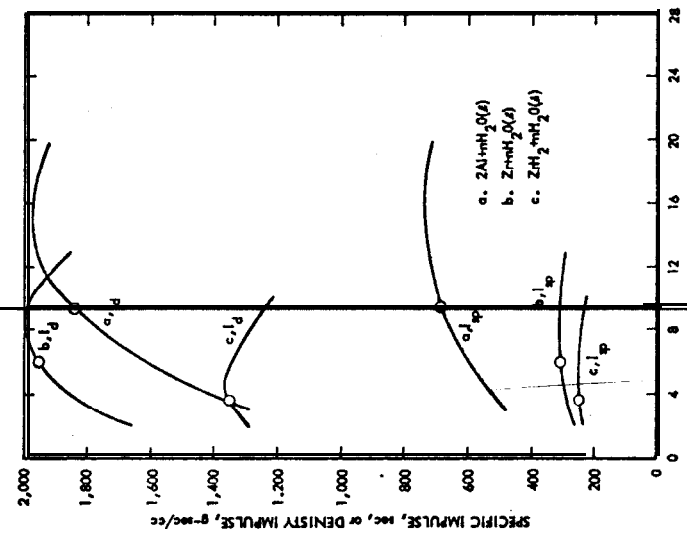


Fig. 4 Approximate theoretical specific impulse and density impulse of some water-reacted propellants versus moles of free water (expansion ratio, 1,000/14.7 psia; open data points indicate combustion temperature about 1,800°F).

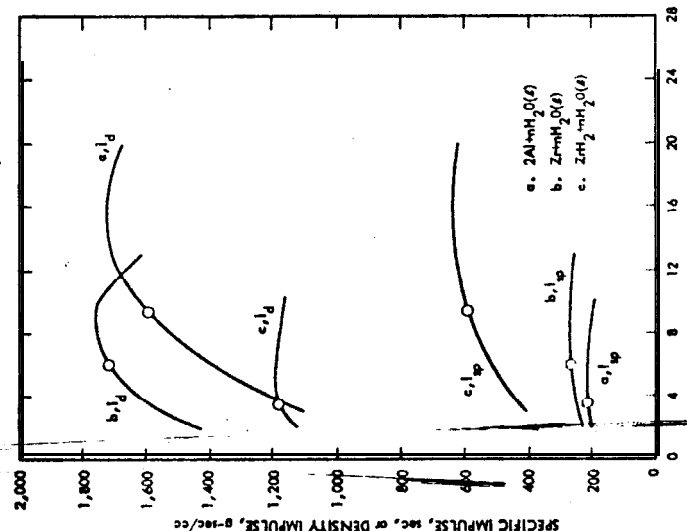


Fig. 3 Approximate theoretical specific and density impulse of some water-reacted propellants versus moles of free water (expansion ratio, 300/14.7 psia; open data points indicate combustion temperature about 1,800°F).

dynamically unusable energy, is next repressurized by a pump, and subsequently is reheated by exchange with the propellant products to repeat the cycle.

Metal-Fueled Systems

Turning to the propellant systems per se, at present they resemble the liquid and solid types used in rockets, although their feed and combustion systems are engineered to handle repetitive runs of several minutes duration. As performance requirements increase and metallized propellants are needed, specialized combustors and feed methods will be used. For example, the metals could be heated to the molten state and then treated as a liquid, incorporated into a thixotropic slurry whose pumping characteristics resemble homogeneous liquids,* or they could be formulated as part of a solid propellant and reacted with a liquid oxidizer by means of hybrid technology.*

Conclusion

The propellants used by a torpedo greatly affect the practicality and performance of the missile. In the first place, they must be safe enough to be stored in confined environments in close proximity with the crew. Then, since they necessarily power a torque-producing engine, they must be compatible with the latter's materials of construction, its mechanical features, and its thermodynamic cycle. Metal-fueled propellants theoretically provide the highest performance, since energy/volume is the definitive criterion; but their exhaust products, which may be hard particles of solid oxides, must be manageable by the engine. The reduction in performance with depth through the lowering of pressure ratio which characterizes any open-cycle system can be minimized by using a condensuctor or adopting a closed-cycle system. Which of these proves more amenable depends on the particular propellant formulation: if it is such that all gaseous propellant products are completely converted to nongases on contacting water, then the simple condensuctor can be used; if not, the more complex closed cycle is required. As greater performance capability becomes required for torpedoes and metal-fueled propellants are called for, specialized means to effect combustion and pumping of the metals will be required.

Appendix: Estimation of Theoretical Performances of Torpedo Propellants³

Candidate torpedo propellants often are screened through **theoretical jet horsepower-hours per cubic foot for fixed-**

equilibrium expansion with sufficient free sea water added to the propellants to lower combustion temperatures to 1800°F. To determine these accurately, iteration computations are required. However, they may be estimated accurately enough for screening by multiplying theoretical heats of reaction to major products at 298°K/unit volume of the propellants ($-\Delta H_{r298}/V$) by empirical values that depend on the major species.

For an expansion ratio of 300 psia/1 atm and input energies in kilocalories per cubic centimeter, respective multiplying factors are 13.65 when all products are gases (as CO₂ plus H₂O), 12.94 when they contain a diatomic nongas [as MgO(c)], and 11.76 when they contain a penta-atomic nongas [as Al₂O₃(c)]. For stoichiometric magnesium 90% aqueous hydrogen peroxide (H₂O₂.0.2 H₂O) as propellants, the reaction is Mg(c) + H₂O₂.0.2 H₂O = MgO(c) + 1.2 H₂O(g), where $-\Delta H_{r298} = [(0.0 + (-59.1)] - [(-143.7) + (1.2)(-57.8)] = 154.0 \text{ kcal}$, and $V = (24.3/1.74) + (37.6/1.39) = 41.0 \text{ cm}^3$. Theoretical power output is estimated as $(154.0/41.0)(12.94) = 48.6 \text{ jet hp-hr/ft}^3$, which is less than 2% below the accurately computed value.

References

¹ Greiner, L., "Selection of high performing propellants for torpedoes," ARS J. 30, 1,161 (1960).

² Brody, J. F., "Torpedo propulsion - 1964," Astronaut. Aeronaut. 50, (March 1965).

³ Greiner, L., "Estimation of theoretical performances of torpedo propellants," J. Spacecraft Rockets 3, 149 (1966); Erratum, 3, 608 (1966).

⁴ Sirmalis, J. E., "A theoretical study of the thermodynamics of noncyclic turbine-drive propulsion systems for torpedoes at deep depths" (published elsewhere in this volume).

⁵ Greiner, L. and Hansen, F. A., "A sea water-aluminum torpedo propulsion system" (published elsewhere in this volume).

⁶ Miguel, J. and Brown, G. A., "An analytical and experimental investigation of a condensing ejector with a condensable vapor" (published elsewhere in this volume).

⁷ White, W. D., "Lithium and sodium as water-reactive fuels for torpedo propulsion" (published elsewhere in this volume).

Table 1 Approximate theoretical performances^{1, 2} of some underwater propellants, computed for 20.4/1 expansion ratio with frozen equilibrium and generally after dilution with free sea water to 1,800°F

Fuel	Oxidizer	hp-hr/ft ³	hp-hr/lb
Al	Free sea water	118	0.72
Zr	Free sea water	106	0.27
Al	LiClO_4	78	0.57
Mg	Free sea water		0.64
Mg	LiClO_4	60	0.55
Zr	BrF_5	59	0.29
Al	H_2O_2 (90%)	55	0.55
Mg	H_2O_2 (90%)	50	0.58
Li	LiClO_4	45	0.72
Li	Free sea water	41	1.27
Li	H_2O_2 (90%)	40	0.68
N_2H_4	H_2O_2 (90%)	28	0.36
Diesel fuel	H_2O_2 (90%)	28	0.35
Alcohol (92.5%)	H_2O_2 (90%)	26	0.34
Hydrazine mono-propellant ^a	...	23	0.28
Solid propellant ^b	...	23	0.31
Na	LiClO_4	21	0.31
OTTO fuel-II ^c	...	16	...
H_2O_2 (90%) mono-propellant	...	12	0.14

Table 1 Approximate theoretical performances^{1, 2} of some underwater propellants, computed for 20.4/1 expansion ratio with frozen equilibrium and generally after dilution with free sea water to 1,800°F (Continued)

Fuel --	Oxidizer	hp-hr/ft ³	hp-hr/lb
Na	H_2O_2 (90%)	10	0.34
Na	Free sea water	5	0.24
Alcohol (17%) ^d	O_2 -gas (3,000 psi)	3	0.16

^a 8% N_2H_4 -72% $\text{N}_2\text{H}_5\text{NO}_3$ -20% H₂O.

^b Typical ammonium nitrate type.

^c Nitrate-base liquid monopropellant.

^d Includes carried diluent water.

LITIUMANDSODIUMAS

WATER-REACTIVE FUELS FOR TORPEDO PROPULSION

William D. White*

Naval Undersea Warfare Center, Pasadena, Calif.

Abstract

The potential performances of lithium and sodium reacting with sea water as torpedo propellants are discussed. combustion chambers are described in which efficient reaction can be achieved continuously for long periods. These **combustors** can be used in torpedoes where specific fuel consumption on a weight basis is of great importance and high-temperature storage of the fuels in the molten state can be tolerated.

Introduction

The concept of water-reactive fuels for underwater propulsion utilizes the sea as a copropellant, in much the same manner as oxygen is used in an air-breathing engine. This study ~~+~~ was aimed at developing means of handling and reacting molten sodium and lithium with sea water to produce a working fluid at high temperature and pressure for driving a gas turbine in a torpedo powerplant.

Theoretical Considerations

Sodium metal melts at 98°C and reacts violently with water even at room temperature. Lithium metal melts at 186°C and reacts quietly with water at room temperature. Although molten lithium reacts rapidly with water, **it** is much less reactive than molten sodium.

Thermodynamic **calculations** were made ^{1,2} on the reactions of these-metals with water and on the effects of adding excess

*Head, Thermodynamics Branch.

~~+Conducted~~ at the U. S. Naval Ordnance Test Station, Pasadena Annex, by the Propulsion Division under Dr. R. C. Brumfield.

water to **lower** flame temperature and increase the gas content of the working fluid, based on the following general equations:

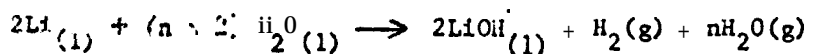
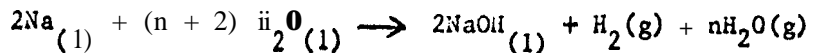


Figure 1 shows combustion temperatures (T_c) and temperatures (T_e) after expanding the reaction products with shifting equilibrium from 300 psia to atmospheric pressure calculated for various weight ratios of water to lithium. Horizontal portions of the curves indicate regions where an equilibrium exists between two different forms of the reaction products. For instance, the plateau near a mixture ratio of 4 to 5 indicates **equilibrium between lithium oxide and lithium hydroxide**, and the small flats at ratios of 8 to 10 reflect the melting at 735°K of solid lithium hydroxide to liquid. At mixture ratios higher than 12 or 13, the heat generated is insufficient to vaporize all of the water, and an equilibrium exists between liquid and vapor H_2O in the reaction products.

Figure 2 gives performance parameters calculated from the enthalpy drop between the temperatures shown in the first graph. Maximum specific energy⁷ (E_{sp}) occurs at the fairly high ratio of about 9 lb of water per pound of lithium, corresponding to a combustion temperature of only about 850°K (1070°F).

Figures 3 and 4 are results of similar calculations for the sodium-water system. Maximum specific energy is at a mixture ratio of about 2, again at a combustion temperature of about 850°K . The second maximum, at a mixture ratio of 5, is a result of the heat liberated in dissolving sodium hydroxide, which can occur only when liquid water is present in the reaction products. The dashed curves of Fig. 4 are obtained when this heat of solution is ignored.

The lithium system produces five times the energy per pound of fuel as the sodium system. For a turbine operating with 50% efficiency at a 20-to-1 pressure ratio, the **lithium-water** system has a specific fuel consumption of 1.5 lb/shp-hr, whereas the sodium system requires 7.6 lb/shp-hr. Thus, the former is the preferred fuel. Nevertheless, much of the experimental work was with sodium because of its lower cost,

⁷Specific energy is the kinetic energy of the jet in horse-power-seconds per pound of expendable fuel.

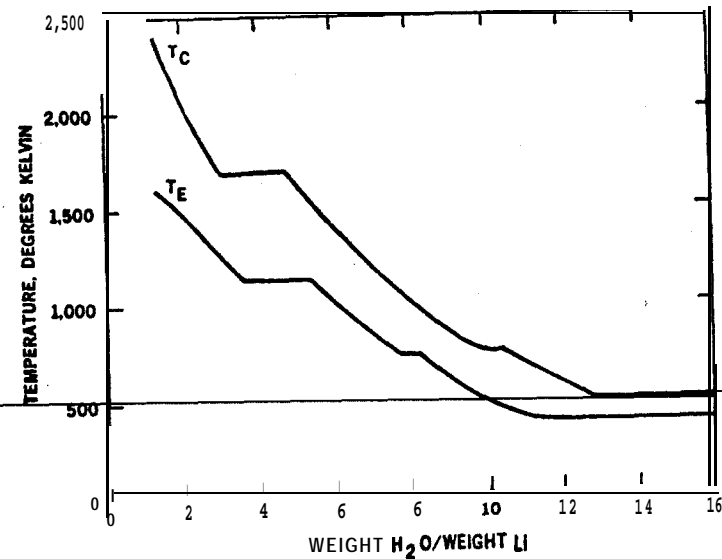


Fig. 1 Combustion and exhaust temperature vs mixture ratio for lithium-water system (pressure ratio 20.4).

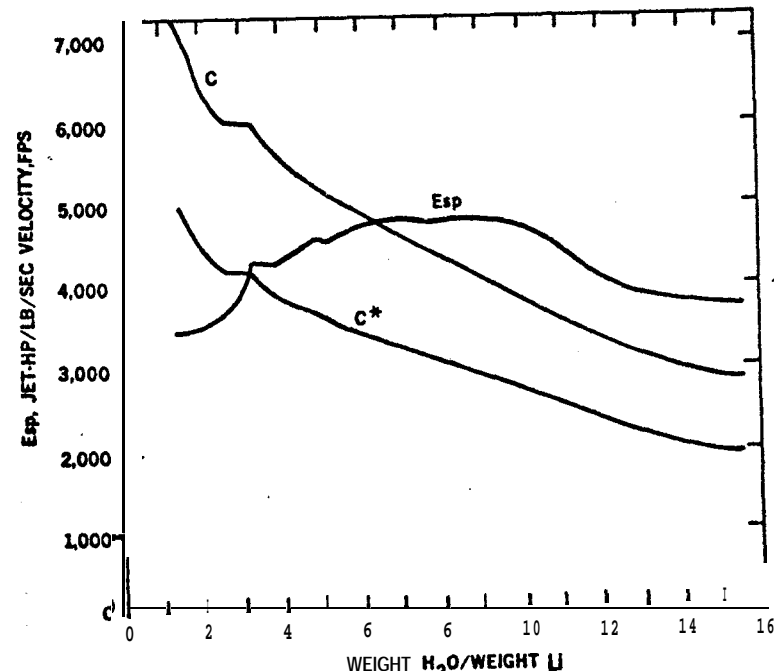


Fig. 2 Gas-generator performance vs mixture ratio for lithium-water system (pressure ratio 20.4).

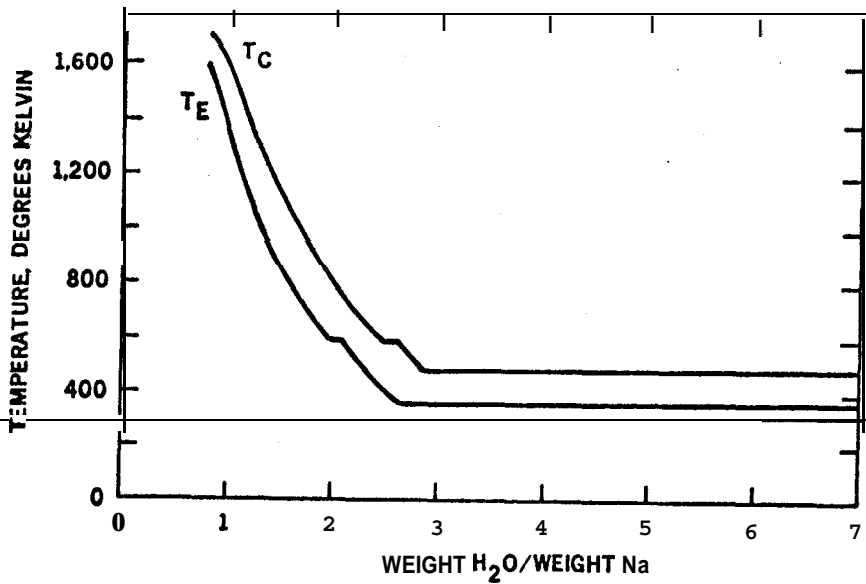


Fig. 3 Combustion and exhaust temperature vs mixture ratio for sodium-water system (pressure ratio 20.4).

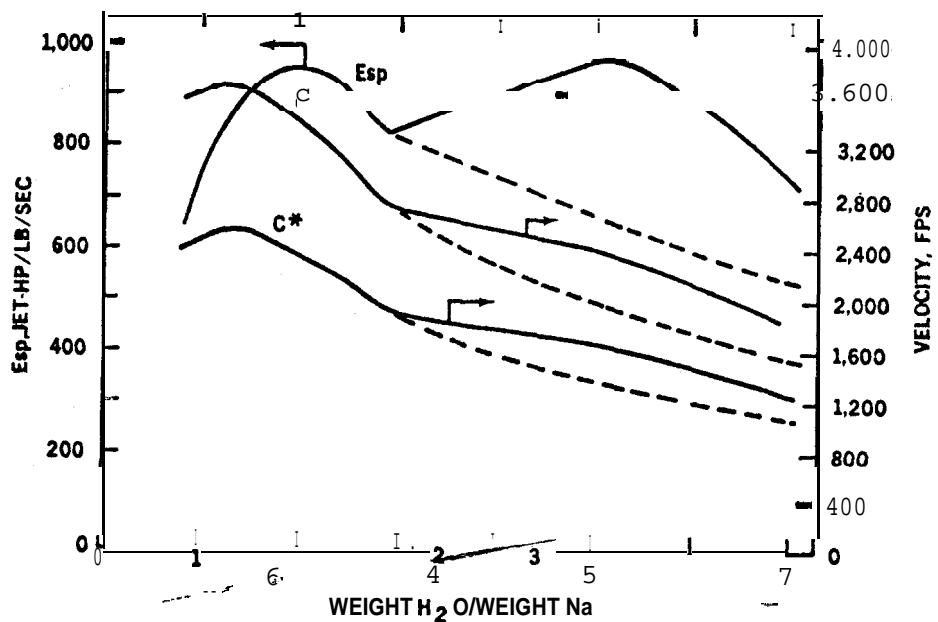


Fig. 4 Gas-generator performance vs mixture ratio for sodium-water system (pressure ratio 20.4).

lower melting point, greater reactivity, and general similarity to lithium.

Experimental Studies

The experimental phase was conducted in small rocket-motor test cells, as shown in Fig. 5. Most tests were at about 200-lb thrust, equal to about 600 jet-hp. Sodium or lithium was melted within a thin stainless-steel tank placed in a steel pressure vessel. Electrical resistance heaters were installed between the walls of the two tanks, and the fuel lines and valve3 were heated to prevent solidification before the fuel entered the combustion chamber. Helium was used to pressurize the fuel tank, because the metals, especially lithium, react

quite rapidly with nitrogen at elevated temperatures. The plastic-lined steel tanks, which contained synthetic sea water for oxidizer and diluent, were pressurized with air. Water flow rate, tank pressure, chamber pressure, and thrust were measured directly with standard instrumentation. Fuel flow rate was calculated from the duration of the test and the weight of sodium or lithium consumed. Near the end of the program, cavitating venturis were very successfully used in both the fuel and oxidizer lines, and provided constant flow rates, irrespective of the combustion-chamber pressure,

Many different types of injectors were investigated. The fuel-on-oxidizer multiple-impinging jet injector with an enzian-ring splash plate, illustrated in Fig. 6, showed considerable promise from a reaction-efficiency standpoint, but its small fuel orifices were easily clogged by foreign material or by cooling of fuel in its passages. Also, small misalignments or deviations of the jets resulted in rapid burnout in case the molten fuel struck a steel part of the combustion chamber before reacting with water.

The final design of the combustion chamber is shown in Fig. 7. It avoided the preceding problem by using a single fuel orifice with a swirler to produce a hollow-cone spray, and a series of tangential water orifices to form a moving wall of water. The fuel impinged upon the wall of water, which also protected the steel parts from contact with the molten metal. An enzian ring directed excess water away from the wall and into the hot flame core, to promote mixing and rapid attainment of equilibrium in the downstream portion of the combustion chamber. --

This design worked very well with sodium, but required modification for lithium because of its lower reactivity and the higher proportion of water needed. Therefore, part of this

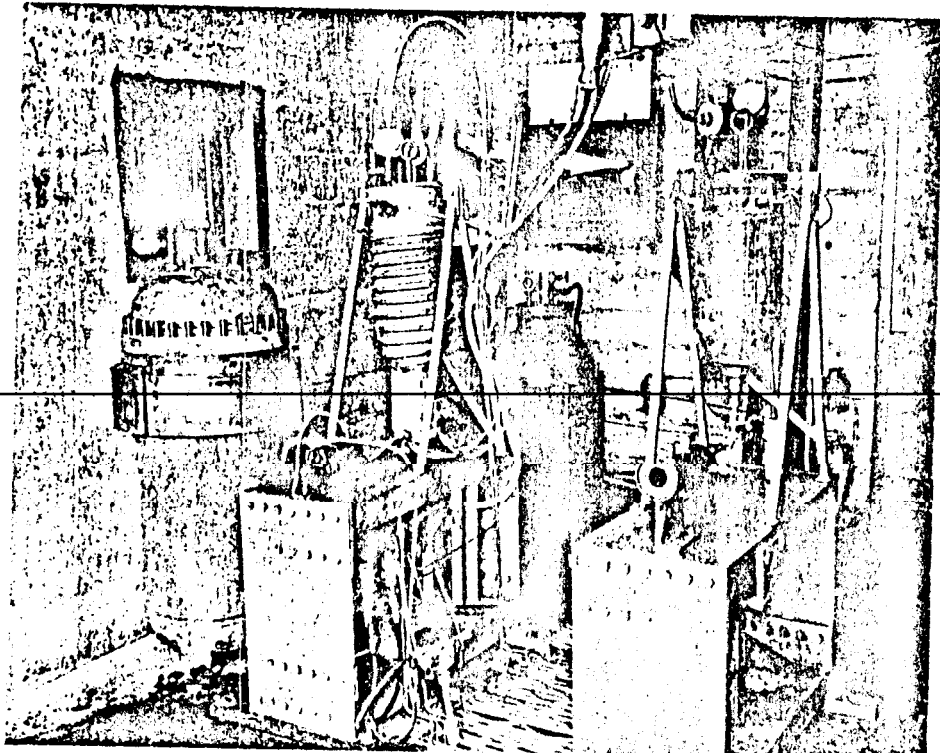


Fig. 5 Teat cell setup.

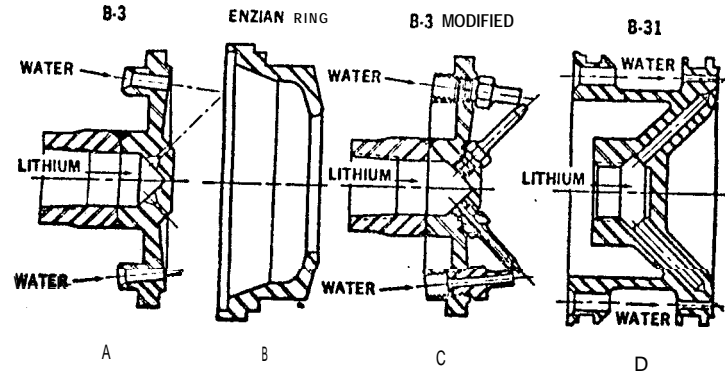


Fig. 6 Multiple-impingement injector.

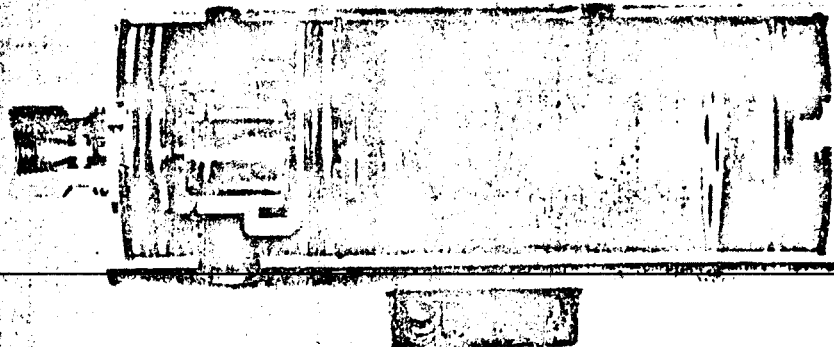


Fig. 7 Sodium-water gas generator with hollow cone fuel and tangential water Injectors.

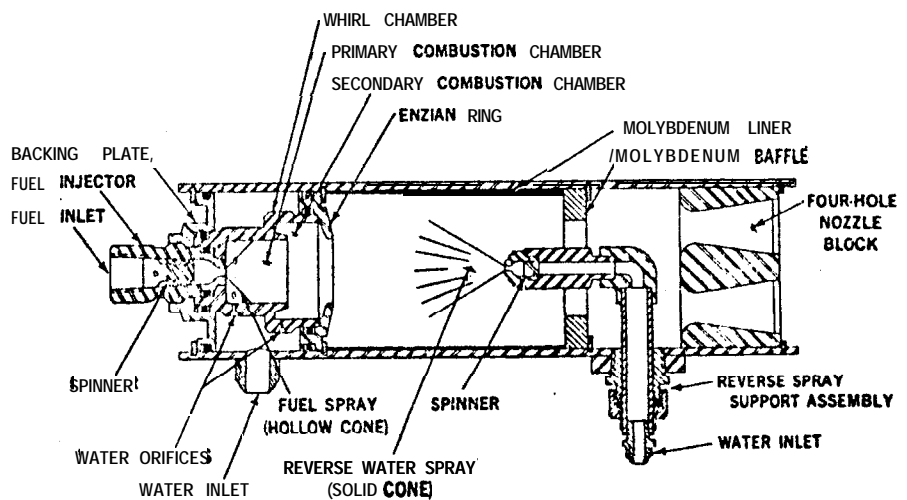


Fig. 8 Lithium-water gas generator with reverse water spray.

additional water was introduced through a separate spray injector placed downstream from the first with its flow counter to the main flow, as shown in Fig. 8. This created a hot primary reaction zone and produced the more vigorous mixing required by the larger quantity of diluent water.

Several hundred combustion **tests** were made, mostly at chamber pressures between 250 and 350 psi, and at 400 to 600 jet-h p. Many of the tests were from 20 to 30 sec, which was long enough to evaluate combustion-chamber design changes and mixture-ratio variations. A few tests **were** run continuously for 2 to 3 min. to check endurance,

The impinging-jet injectors had a combustion efficiency of about 80%, as determined by the ratio of measured to theoretical characteristic velocity (c^*). The injector that sprayed a hollow cone of fuel against a curtain of water gave about 90% of theoretical c^* , and the counterflow water spray, added in adapting the system for lithium, increased combustion efficiency to about 95%.

Conclusions

The theoretical performance of lithium and **sodium** reacting with water has been examined, and an experimental program has developed chamber designs for obtaining efficient combustion for several minutes.

These light-metal propellant systems have inherent disadvantages, such as fuel preheating, the nature of the solid reaction products, and low density, which reduces performance on a volume basis. But in applications where specific fuel consumption is of primary importance, these troublesome aspects can probably be tolerated, and the use of molten lithium, especially, as a water-reactive fuel can **result** in a superior propulsion system,

References

¹White, W. D., Carter, J.M. and Rapp, L.R., "Theoretical performance calculations for the sodium-water system," U. S. Naval Ordnance Test Station, Pasadena, Calif., NAVORD Rept. 1155 (NOTS 210) (May 1949).

²White, W. D., "Thermodynamic analysis of the lithium-water system as applied to chemical power generators," U. S. Naval Ordnance Test Station, Pasadena, Calif., NAVORD Rept. 1202 (NOTS 258) (April 1950).

A SEA-WATER-ALUMINUM TORPEDO PROPULSION SYSTEM

Leonard Greiner* and F. A. Hansen Jr†

Texaco Experiment Inc., Richmond, Va.

Abstract

A heat engine torpedo propulsion system, powered by chemical reaction between aluminum and sea water, is discussed. Its potential performance exceeds others examined at depths to 5000 ft and is achieved by operating at very high internal pressure. The system is designed so that the effective storage density of the aluminum fuel is close to that of the bulk metal; solid oxidizer or other extraneous material is not used; and the means for feeding the aluminum appears feasible, reliable, and capable of improving the efficiency of reaction with sea water. Although much of the proposed system is straightforward, an unexplored area is the development of an aluminum-water combustor that operates at high efficiency, will not be clogged by its solid reaction products, and produces these solids in very small particles.

Introduction

It is well known that the most energetic chemical combinations for powering underwater-propulsion heat engines are certain metals as fuels in combination with sea water from the environment as oxidant, diluent, and coolant. The need for metal fuels stems from the fact that only they provide notable energy on chemical reaction with water.

Within the ocean, waterbreathing propulsion systems potentially have the same performance advantages over nonwater-breathing systems as airbreathing propulsion systems in air

Presented at the AIAA Torpedo Propulsion Conference, Newport, Rhode Island, July 23-26, 1963 (not preprinted).

*Research Associate, Texaco Experiment Inc., Richmond, Va. (Scientist, Research and Development, CETEC Corp., Mountain View, Calif.)

†Project Engineer, Texaco Experiment Inc., Richmond, Va. (Project Engineer, U. S. Navy Marine Engineering Lab., Annapolis, Md.)

have over rockets which must carry both fuel and oxidizer. Indeed, because water is relatively simple to pump while air often requires complex mechanical parts, specialized inlets, and voluminous internal ducts, waterbreathing systems appear more amenable to successful exploitation. However, water is denser than air, and so increasingly high ambient pressures are encountered at depths. These reduce engine efficiencies by lowering pressure ratios over the power cycle unless special means are employed. One such is a condensuctor that reduces the back-pressure felt by the engine. But this is only usable with propellants whose products contain no water-insoluble gases, which is not true of metal-water combinations that produce hydrogen gas. Alternatively, the products could heat-exchange their energy to the working medium of a closed-cycle engine which intrinsically is depth insensitive. Finally, the system could operate at an internal pressure sufficiently high that an adequate pressure ratio would exist even at the greatest design depth. The latter is examined here.

Other difficulties with waterbreathing systems are that water normally reacts slowly, at best, with the metals capable of producing the highest torpedo performances, and the normal physical form of metals generally diminishes reactivity even further. Also, feeding metals into a combustion chamber cannot be accomplished by common means, especially when efficient utilization of the fuel-storage volume and optimization of conditions for subsequent reaction with water have to be considered simultaneously.

The metals that theoretically provide the best performance with free water as oxidizer, in terms of range at a given speed, are beryllium, boron, aluminum, and zirconium, approximately in descending order. Of these, aluminum appeared the most tractable as a torpedo fuel, as it is free of hazards, available, and inexpensive. A preliminary paper study, made by Texaco Experiment Inc. (a company effort coordinated by the Bureau of Naval Weapons as Project 61-5) to verify the practical potential and uncover problem areas in utilizing aluminum and sea water as a propellant for torpedoes, is described.

Goals

Because of expected competition with other torpedo propellants and the certainty that the aluminum-water system would be unusual, the study was aimed at exploiting all of its potential advantages to justify its later development. This meant that the effective storage density of the fuel should remain close to that of the bulk metal, that no solid oxidizer be added to degrade performance or increase hazards, that the means for

feeding the aluminum be feasible and reliable, that the system have notable performance at sea-water depths to 5000 ft, and that there be a high likelihood of achieving efficient chemical reaction between the fuel and sea water - obviously a stringent set of requirements.

Fuel Storage, Feeding, and Combustion with Water

The intimate interrelation between aluminum storage, feeding, and combustion with water in the design which evolved is shown schematically in Fig. 1 and will be discussed.

The means of minimizing performance degradation with depth is to operate at the very high internal pressure of 15,000 p

The aluminum is stored in a pressure vessel whose wall is also the torpedo shell. It is displaced into the combustion chamber by pressurization by pumping sea water to the forward end of the fuel tank via a tube passing axially through the fuel. The combustion chamber for the aluminum-water reaction is integral with the aft enclosure of the fuel tank, and its forward surface contacts the aluminum fuel. At steady state, heat is transferred from the combustion chamber to the fuel at this contact area to form a puddle of molten aluminum that subsequently is injected (as liquid) into the chamber.

The latter requires that most of the heat transferred from the combustion chamber to the fuel remain near the contact area and not be lost by conduction through the bulk of the aluminum. On the other hand, radial heat transfer from this contact area is desirable for reasons to be mentioned. To assure these, the fuel is in the form of thin, contoured sheets, tightly packed in layers, whose over-all density is close to that of bulk metal. Axial heat flow between such sheets is reduced by the insulating layer of aluminum oxide normally present at their surfaces; however, radial conductivity is not affected. Because of the former, the molten puddle will not lose heat to the main body of the fuel; because of the latter, the outer portions of those sheets whose centers contact the hot combustion chamber will be warmed considerably. The latter decreases the tensile strength at the edges of the sheets, as shown in Table 1, so that the internal pressure of 15,000 psia is sufficient to cause extrusion. Consequently, at steady state, the molten metal in the puddle, which is injected into the chamber, is renewed by aluminum entering the puddle by axial bulk movement and radial inward extrusion.

The minor aluminum extrusion required is not expected to be troublesome. Extrusion difficulty increases with metal tensile strength, extrusion speed, area-reduction ratio, and surface

Table 1 Tensile strength of aluminum
(grade 1100-o) vs temperature

Temperature °F	Tensile strength psi
75	13,000
300	8,500
400	6,000
500	4,000
600	2,500
700	2,000

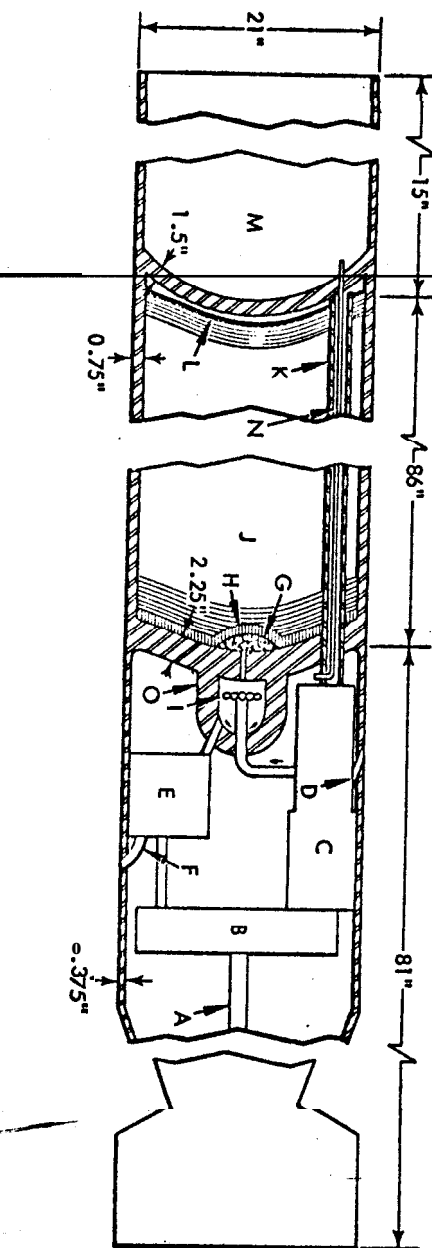
friction.² Tensile strength, which is also the minimum pressure required for extrusion, is only about 2000 psi for aluminum (Table 1) at the predicted minimum temperature of 750°F at the periphery of the sheets; the required extrusion speed is only about 0.03 in./sec; and the required reduction in area between the original sheets and the molten puddle is only about 10. From the empirical equation for estimating extrusion pressures, a value less than 5000 psi is computed for these conditions, ignoring friction. Although friction is difficult to predict, it should not exceed the available over-pressure of at least 10,000 psi. Frictional drag along the length of the aluminum is not an issue, because the metal away from the end enclosure is cool, so its tensile strength is high and radial expansion (mushrooming) will not occur.

Because the aluminum enters the combustion chamber as a molten liquid, the optimum injection schemes for obtaining efficient chemical reaction may be selected. Also, the molten metal is considerably more reactive than the solid metal. Despite such aids, development of an effective aluminum-water combustor is expected to be a major problem. For this reason, in the chamber of Fig. 1, part of the incoming sea water, in stoichiometric ratio with the incoming aluminum, is preheated to more reactive steam by passing through a flat, spiral heat exchanger within the chamber. This flat heat exchanger also divides the combustor into a forward zone for the stoichiometric reaction, whose high temperature should aid in effecting reaction and in achieving heat exchange to the chamber wall, and an aft zone, where diluent water is added to cool the products to the lower temperature required by the engine hardware. The water may enter the latter zone along the inner walls of the chamber to cool them so they will retain their strength.

To form the aluminum puddle, heat transfer through the combustor wall must raise the fuel temperature to about 1250°F. Calculations of the necessary heat flux were made for a molybdenum 5%

- A Propeller shaft
- B Gear train
- C Water pump
- D Water inlet
- E Turbine
- F Turbine exhaust
- G Molten zone
- H Extrusion zone
- I Spiral heat exchanger
- J Aluminum plates (fuel)
- K Pipe for displacement water
- L Piston
- M Space for fuel contingency
- N Wire conduit
- O Combustion chamber

Fig. 1 Diagram of aluminum-sea-water system



titanium alloy as forward end of the combustion chamber with a layer of graphite on both sides. Because an accurate estimate of the film coefficient within the hot section of the combustion chamber (which contains molten Al², gaseous H₂, and quantities of unreacted material) was impossible both optimistic and pessimistic values were used, from which required combustor temperatures of 3500° and 4000°R, respectively, were found necessary. Either is below the theoretical stoichiometric temperature for the aluminum-water reaction of about 6000°R, as shown in Fig. 2.

To start the feed and combustion process, a small solid rocket propellant is burned in the combustion chamber. Its liberated heat brings the system to temperature, and its evolved gases start the mechanical process. If necessary, a few layers of easily extruded and highly reactive lithium also could be substituted for the initial sheets of aluminum.

Because torpedo range is proportional to the volume of propellant, the wall thickness of the fuel tank is minimized by using high-strength metal. One such is Rocoloy 270 with a yield strength of 270,000 psi and other steels with similar strengths are becoming available. Taking a value of 250,000 psi, a wall thickness of 0.63 in. will withstand the internal pressure of 15,000 psi; 0.75 in., was chosen to provide a safety factor. The effect of the thickness of the tank end enclosures on space available for propellant is small; therefore, a forward enclosure thickness of 1.5 in. was used. The aft enclosure, which is heated and so requires special materials (such as molybdenum 5% titanium alloy), was increased to 2.25 in. These three thicknesses were used in computing system performances.

Power Turbine and Water Pump

A conventional turbine powerplant was selected, so that performances could be compared directly with other propellants. Thus, the exhaust products of the high-pressure reaction power a turbine connected to a gear box that operates the torpedo propeller shaft and a water pump. The latter supplies water to the combustion chamber and to the fuel tank for pressurization.

A special turbine may be required because of the large energy content per unit flow of working medium, the very high working pressure, and the presence of aluminum oxide particles. As a point of departure, a Silvern drag-type turbine of about 4 to 5 in. in diameter, operating at 40,000 rpm, should be considered.⁵ At a "specific speed" of 1.5, which fits that of the aluminum-

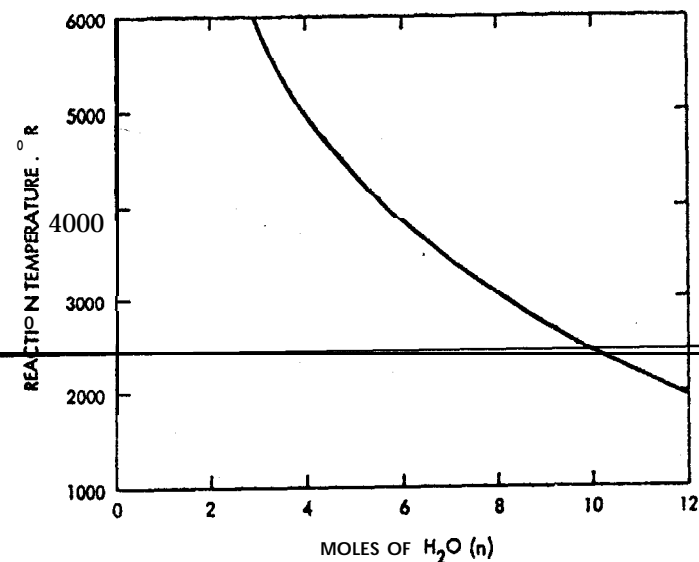


Fig. 2 Theoretical combustion temperature for the system 2 Al + n H₂O, vs n moles for H₂O

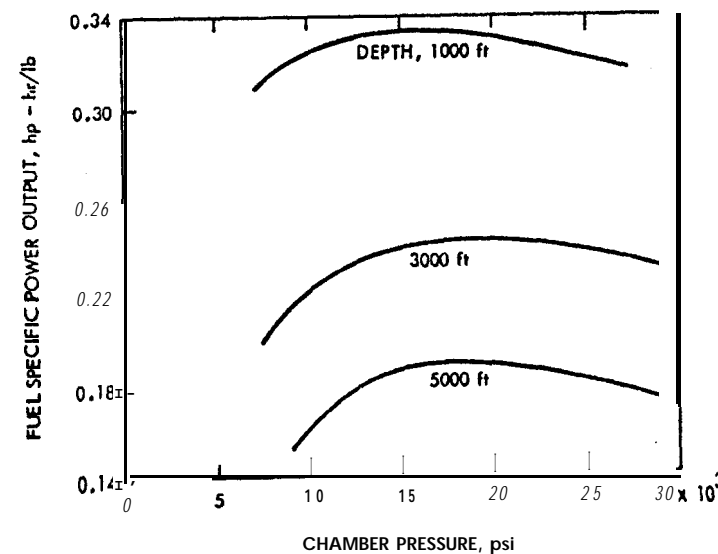


Fig. 3 Fuel specific power output for the Al-H₂O system vs chamber pressure at various depths

water system, an efficiency of 50% is indicated with a further growth potential.⁶ Also, a single-row impulse turbine may be satisfactory.

In computing working-gas properties, the solid Al2O3 particles were assumed in velocity and temperature equilibria with the gases. This requires very small particle sizes so the combustor must be developed with this as a goal. Potentially serious problems from these solids are likely within the turbine, such as clogging of the orifices and erosion of the blades. However, clogging of very small nozzles by carbon particles has been prevented in certain turbine systems, and blade erosion is diminished by small particle sizes.

Although efficient, reliable piston-displacement pumps for the proposed water flow rates and pressures are available, they are at least 25% too large for the proposed application. However, as an example, the Cosmodyne Corp. Model CL-5 pump appears amenable to the required size reduction.

Capability of the Conventional Powerplant

In this powerplant, a large amount of turbine work is used to pump water to very high pressure. Since this lost work increases with operating pressure, which in turn increases turbine output, the operating pressure for maximum shaft output passes through a peak. This is shown in Fig. 3, based on approximate calculations for a 55% efficient turbine and a 70% water pump. From it, a pressure of 15,000 psi was chosen.

To permit comparisons with previous studies,⁸ a combustion temperature of 1800°F (about 2250°R) was used. Based this time on exact equilibrium calculations at 15,000 psia with all known reaction products included, theoretical combustion temperatures at various water concentrations were computed and are shown in Fig. 2. The desired combustion temperature is at a molar ratio of 2 Al to 10.8 H₂O. Isentropic enthalpy drops at this ratio for expansion from 15,000 psia to various back pressures are plotted versus water depth in Fig. 4.

Torpedo propellants are best compared when within a standard missile. For such a missile, dimensions and other information on the spaces available for fuel and for mechanical parts were taken from Ref. 8 and applied to the aluminum-water system (Fig. 1) with due allowance for its increased wall thicknesses. These parameters were used:

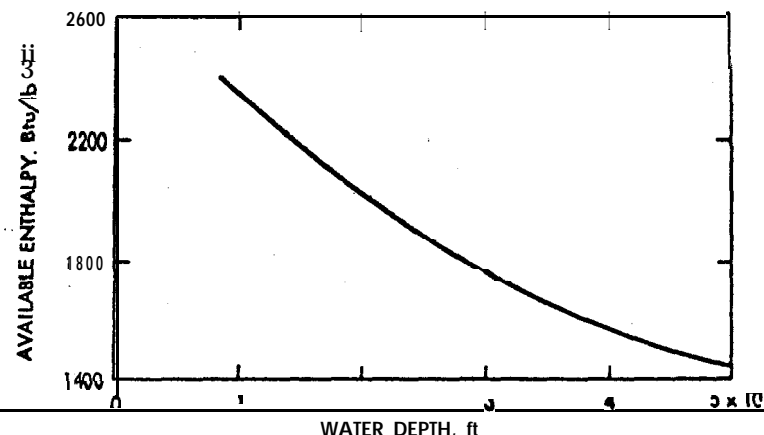


Fig. 4 Isentropic enthalpy drop for expansion of the system 2 Al + 10.8 H₂O from 15,000 psia to ambient pressure at various sea-water depths

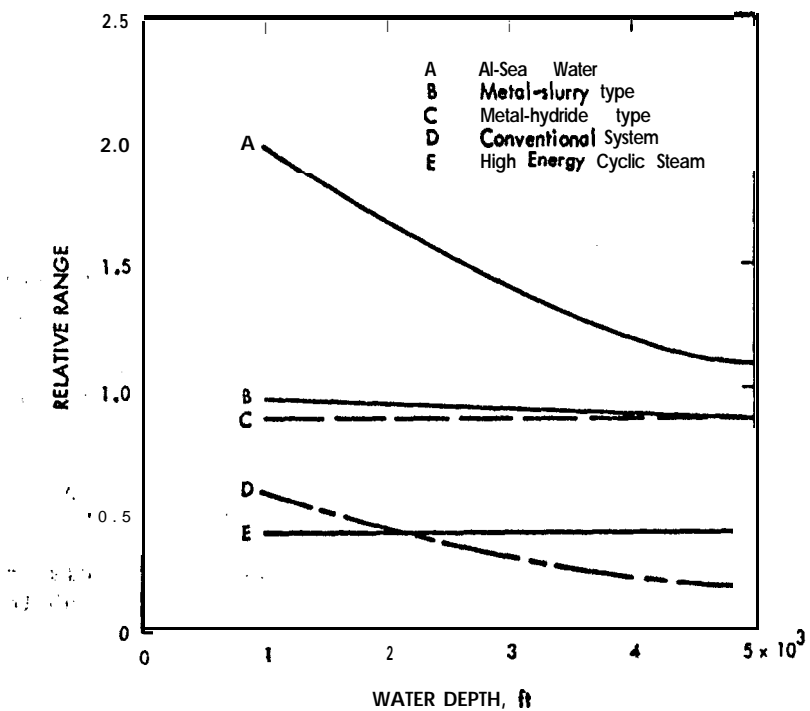


Fig. 5 Relative range at high speed vs sea-water depth for selected propulsion systems in the standard torpedo

Turbine efficiency	55%
Turbine exit pressure	ambient at <u>depths</u>
Propellant combustion efficiency	100%
Propellant combustion temperature	1800°F
Water pump efficiency	70%
Propeller efficiency	80%

Relative high-speed ranges of torpedoes powered by the proposed aluminum-water system and by other systems³ at various depths (for these conditions) are shown in Fig. 5. They show that the performance capability of the aluminum-water system notably exceeds all others considered.

Conclusion

A torpedo turbine propulsion system, which exploits reaction between aluminum and sea water as power source, has been analyzed. It appears capable of at least doubling the performance of other systems at moderate depths and of at least a 25% improvement at great depths. The system appears capable of practical development, with only the combustor requiring extrapolation beyond the current state of the art. The suggested aluminum-feed system should minimize problems in this area, because it injects the fuel into the combustor as a hot, molten metal which is relatively easy to react. This aluminum-sea water system appears capable of the greatest performance possible from a chemically powered torpedo powerplant.

References

¹ Greiner, Leonard, "Selection of high performing propellants for torpedoes," ARS J. 30, 1161-1163 (1960).

² Brown, G., and Sirmalis, J. E., "Condensuctor, a back pressure reduction device," presented at the ARS 17th Annual Meeting, November 1962, (confidential).

³ Pearson, C. E., and Parkins, R. N., The Extrusion of Metals (John Wiley & Sons, Inc., New York, 1960), 2nd ed. rev.

⁴ Bhat, B. K., "Evolution of ultra-high strength steels, and research on materials and various novel techniques of fabrication of high performance rocket motor cases," Mellon Inst. Ind. Research (October 1961).

⁵ Stephens, C. W., Spies, R., and Menetrey, W. R., "Dynamic thermal converters," Vol. 3 of Energy Conversion Systems Reference Handbook, (Electra-Optical Systems, Inc., September 1960) EOS Report 390, WADD TR 60-699.

⁶ Brady, J. F., and Shivell, E., "Turbines for torpedoes," presented at ARS 17th Annual Meeting, November 1962
(Confidential)

⁷ Cosmodyne Corporation, Hawthorne, Calif., Bull. CE-1.

⁸ Brady, J. F., Kaye, J., and Fields, A., "Power cycles for deep operating torpedoes," presented at Joint ARS-IAS National Meeting, June 1961 (Confidential).

A CLOSED-CYCLEPROPULSION SYSTEM FOR DEEP SUBMERGENCE

K. E. Smith* and L. G. Hidde[†]

Naval Undersea Warfare Center, Pasadena, Calif.

Abstract

A conventional solid propellant was used as heat source for a closed-cycle propulsion torpedo system with its combustion products passing through a heat exchanger to generate steam for the prime mover, and then overboard. A proposed liquid-bipropellant version will permit higher performance, and injection of fuel in several stages limits maximum combustion temperature without need for diluent. With fuel oil and hydrogen peroxide as propellant, the entire volume of noncondensable exhaust products can be contained within the torpedo, so that operation is wakeless and independent of depth.

Introduction

There is continuous effort to develop torpedo propulsion systems that operate effectively at widely varying depths. This report on a program to demonstrate the feasibility of a particular closed-cycle system for deep-operating, air-launched, high-speed torpedoes, and a subsequent study to uncover refinements to attain a wakeless torpedo. A comprehensive comparison of many of the propulsion systems proposed for deep submergence is presented in Ref. 1, and a qualitative comparison is made here of the effects of increasing operating depth on three types of thermal propulsion systems.

An open-cycle system is the simplest, since the energy is extracted directly from combustion products through an expansion engine; but its performance deteriorates sharply as depth increases. A modified open-cycle system, with a back-pressure reduction device (such as a jet condenser) to produce

*Engineer (General), formerly Head, Torpedo Design Branch, Torpedo Development Division, Underwater Ordnance Department, now with North American Aviation, Inc., Downey, Calif.

[†]Mechanical Engineer, formerly Turbomachinery Branch, Propulsion Division, Underwater Ordnance Department, now with United Technology Center, Sunnyvale, Calif.

an artificial, low-pressure at the exhaust, is a **partial** solution, provided exhausting the various products into the sea is acceptable; but beyond intermediate depths, the pump power required to produce this artificial back pressure is **limiting** unless the exhaust products are completely condensable. If they are not, a closed-cycle system must be used, or at least one in which negligible power is required to pump fluid across the system boundaries.

Combustion products from common propellants contain a high percentage of noncondensables. Even so, a semiclosed system that uses them can be devised in which the *gases* pass through a heat exchanger that operates at only a sufficiently high pressure to be able to exhaust overboard. Here *energy* is **extracted by a working fluid, such as water, and is used in** a closed steam cycle. Such a system was built and its feasibility demonstrated. The chief remaining problem is to **eliminate** exhausting noncondensables into the sea, which places a practical limitation on operating depth and causes a detectable wake; a solution is indicated in the latter part of this paper.

Background

In Fig. 1, typical curves of available energy vs depth are indicated for each of three system types and are shown to pass through common points. At **shallow** depths, a closed-cycle system compares poorly with the two others because a large amount of *energy* is rejected to the condenser. However, its performance is not affected down to its design **depth**, and so crossovers are reached at depths below which the performances of the other two systems deteriorate. Crossover depth depends on the particular propellants and components, characteristics of which may only be feasible for one type of system. Therefore, a specific closed-cycle system may not be directly amenable for comparison with a specific open, **direct-expansion** system, though the curves are generally applicable.

The current project . . . is directed to an advanced **air-launched** torpedo 12.75 in. in diameter by 105 in. in length. A constant speed was required, independent of depth.

Solid-Propellant System

Beginning in 1958, the Naval Ordnance Test Station (NOTS) designed and **built** the semiclosed-cycle steam propulsion system **diagrammed** in Fig. 2, where gas from a solid propellant **passed** through a heat exchanger, and then overboard through a pressure regulator. Steam generated in the heat exchanger

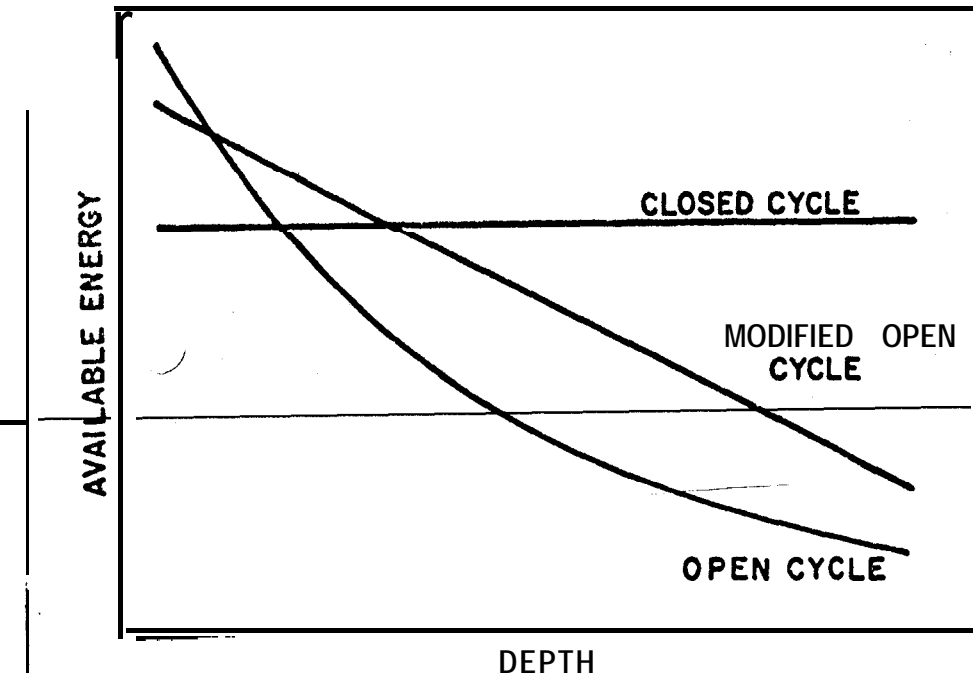


Fig. 1 Characteristic performance curves of three types of powerplants. Coordinates not defined because of the many possible design variations

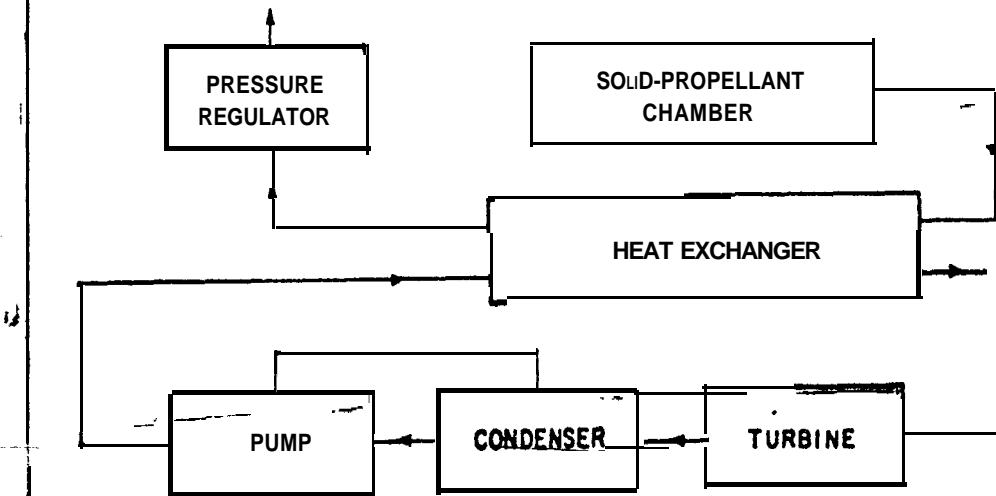


Fig. 2 Block diagram of solid-propellant system

operated a turbine before being condensed for re-use. The solid propellant was an ammonium nitrate-base end-burning grain. Its combustion products contained a high percentage of noncondensables, which precluded closing the gas side of the system. The solid propellant was of relatively low energy since performance was a secondary consideration. Its use eliminated the complexity of a liquid system and allowed concentration on the critical problems of boiler and condenser performance and stability and control of the steam system. The exhaust pressure regulator on the solid propellant side of the system was set at 1300 psi to achieve the desired energy-release rate and allow operation independently of ambient pressure variations to about 3000 ft.

A layout is shown in Fig. 3. The heat exchanger was located within the propellant chamber. The annulus between the chamber and the outer shell of the vehicle was the condenser. The turbine, gearbox, pump, and controls were in the after-body. On the steam side, feed water was pumped from the condenser by a gear pump driven directly by the turbine. Excess water was routed through a bypass valve and injected into the turbine exhaust duct to cool the superheated exhaust steam to saturated vapor before entering the condenser. The condenser, shown in Fig. 4, was of 6061-T6 aluminum and consisted of shell, end rings, stiffeners, and inlet duct. Twenty-five longitudinal stiffeners were attached by dip brazing and the I.D. machined to provide 0.0- to 0.010-in. clearance when the liner was installed. SAE 4130 steel was used for the inner wall of the condenser which also served as the combustion chamber for the solid propellant grain. When pressurized, the chamber expanded to contact the stiffeners and provide uniform load distribution between the chamber and the outer shell. The stiffeners also set the flow path of the condensing steam. Turbine exhaust steam entered the upper passages, flowed forward, split, and passed back and forth to be collected as condensate at the bottom of the annulus.

Unknowns in the condenser design included possible progressive deterioration of the condensing surfaces on storage and rerun, and the effect of air permanently retained in the condenser after the vent valve closed on startup. Therefore, the condenser was designed generously in terms of surface area.

The boiler was operated at much higher temperature and pressure than normally encountered in stationary powerplants or marine boilers. This, plus high mass velocity in conjunction with the high temperature helped provide the compact design shown in Fig. 5 and 6. The design was a single,

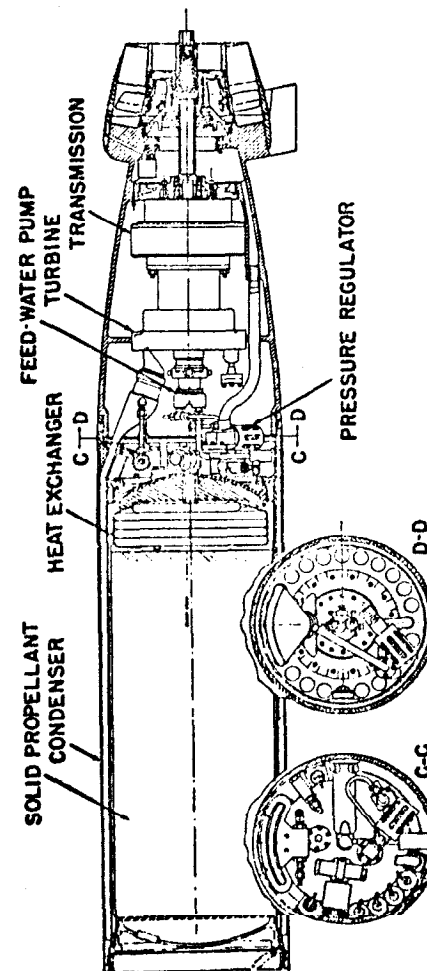


Fig. 3 Solid-propellant powerplant

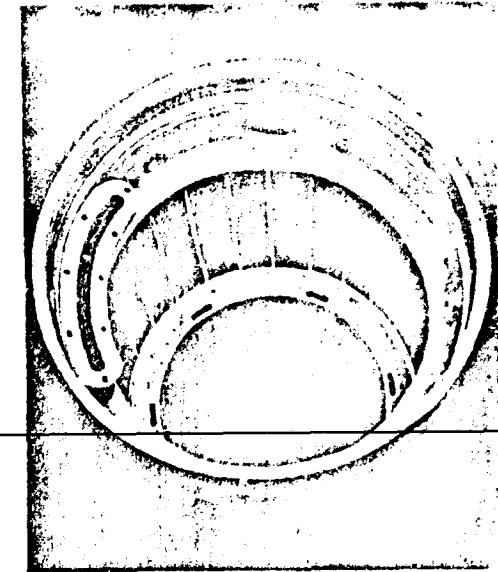


Fig. 1 Condenser shell with combustion chamber partially withdrawn

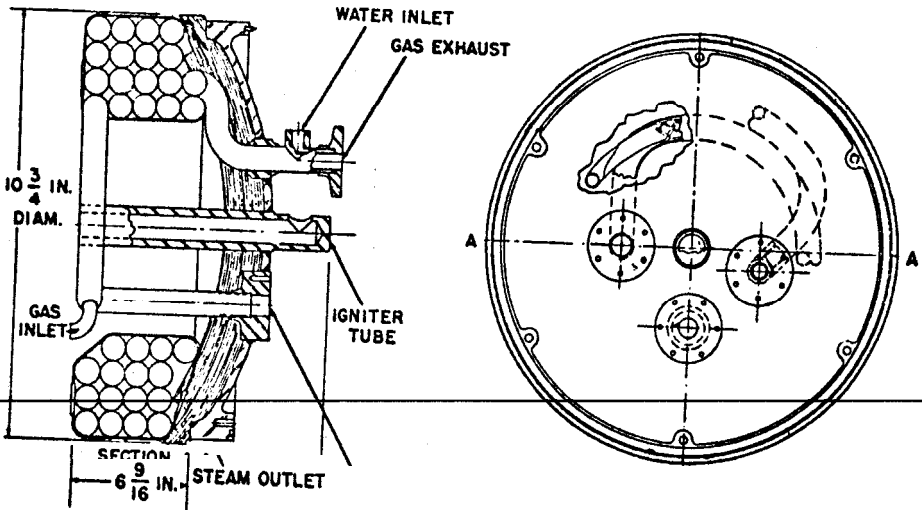


Fig. 5 Heat exchanger assembly for solid propellant power-plant

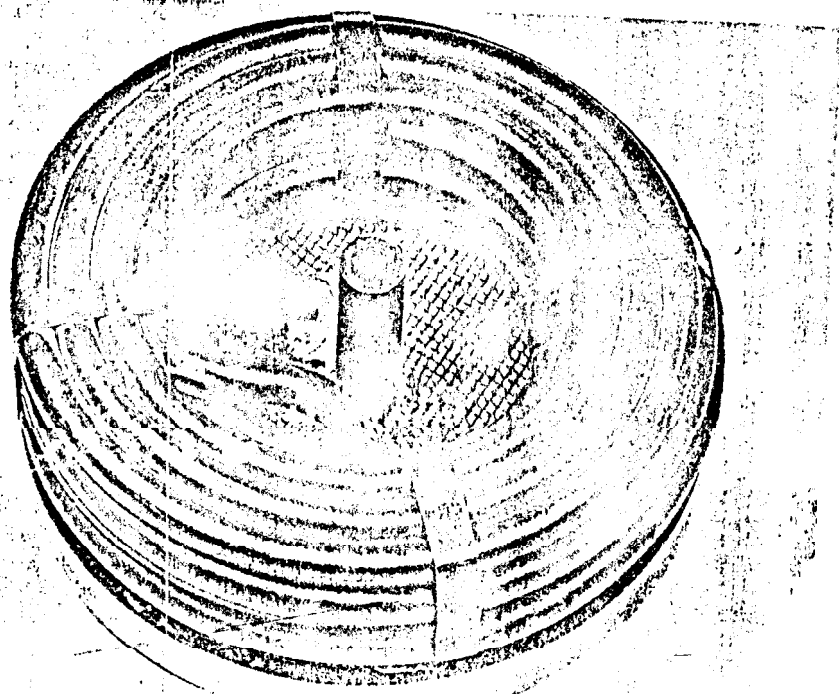


Fig. 6 Heat exchanger assembly in manufactured form

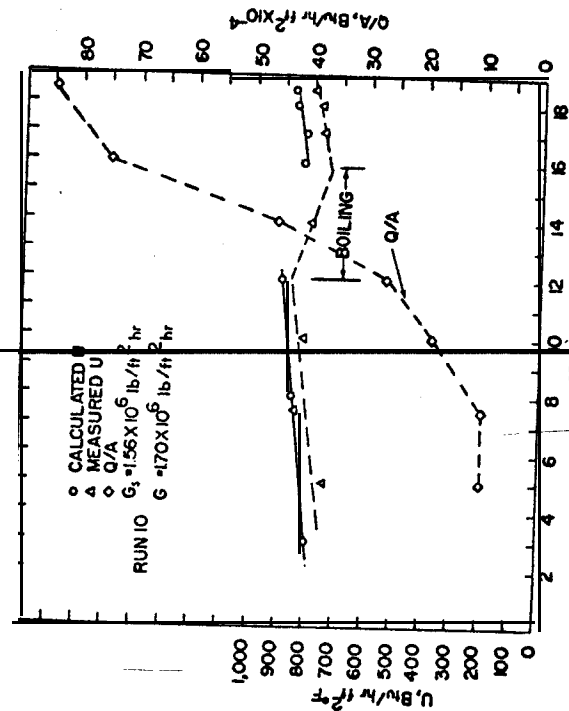


Fig. 7 Experimental heat exchanger test facility and unit heat flux, Run No. 10

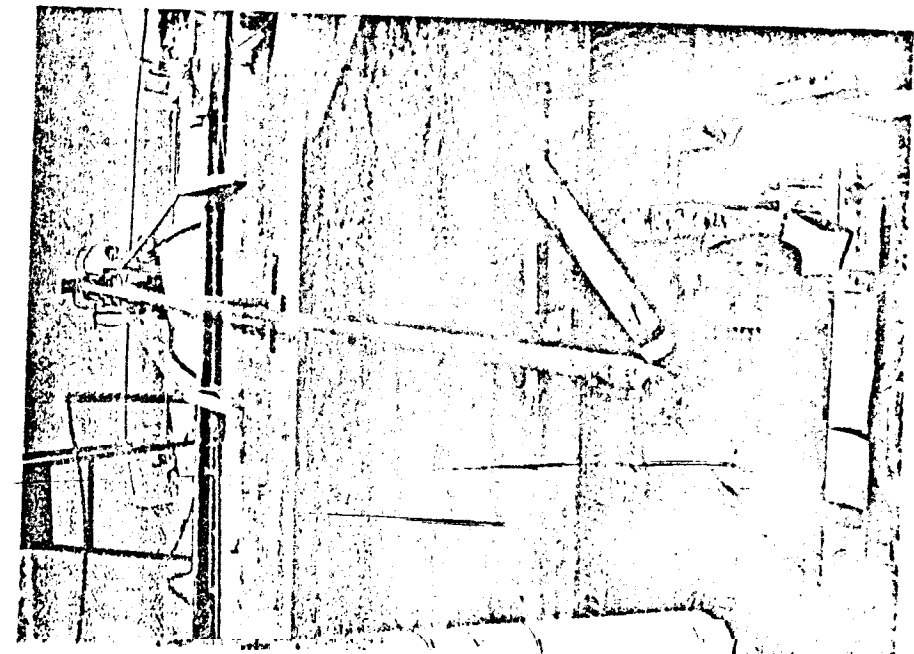


Fig. 8 The long tube encloses the heat exchanger

concentric-tube, counterflow arrangement with gas passing through the inner tube and steam through the annulus. Gas entered the center tube at 2200° F and 1500 psi and exhausted at 425° F and 1300 psi. About 15% of the exhaust products condensed as water.

The boiler was constructed of two concentric 38-ft-long tubes of AISI-316 stainless steel, coiled to fit within the 11-in. dia chamber and welded to the after chamber head. Concentricity of the two tubes was maintained by four wires wound in a 45° helix around the inner tube. Mass velocities in the order of 0.6×10^5 to 1.6×10^6 lb/hr/ft² resulted in a pressure drop of about 200 and 400 psi on the gas and steam sides, respectively.

Feed water at 2500 psi was furnished to the coiled boiler by an Adel gear pump, directly driven from the turbine at 29,000 rpm. Pump inlet conditions were 15 psia and 70° to 100° F, with water taken from the condenser. The flow rate to the boiler was 0.17 lb/sec; steam temperature out of the boiler was 1600° F. By locating the boiler within the grain chamber, pressure balance across the superheater outlet was obtained, which minimized tube-wall stresses and high boiler reliability was achieved despite the high steam temperature. An experimental straight-tube heat exchanger, built to verify the design, is shown in Fig. 7. Steam temperatures and heat-flux curves were constructed from these data, and Fig. 8 shows corrected results of a typical test from Ref. 2. A somewhat greater heat loss was encountered with this test assembly than with the coiled heat exchanger.

The turbine, shown in Fig. 9, was a re-entry two-stage Impulse design. Design performance was not attained, because case warpage and shaft growth necessitated increasing nozzle clearance. Turbine speed was 29,000 rpm and speed reduction to 2500 rpm was accomplished through a planetary gearbox designed by the Eendix Corporation, Utica, N.Y.

System tests were conducted as shown in Fig. 10. A cooling jacket over the condenser simulates external sea-water flow. Treated feedwater was stored in the entire heat exchanger and the system started by firing an igniter to set off the grain. As the hot gas began to boil the water, steam passed into the turbine, driving the direct-connected feedwater pump to bootstrap the system to full power. As the system achieved operating speed, excess water, stem, and some trapped air were exhausted overboard through a flapper valve at the condenser inlet. A typical starting transient of power-vs-time is shown in Fig. 11. The system self-stabilized in about 15 sec,

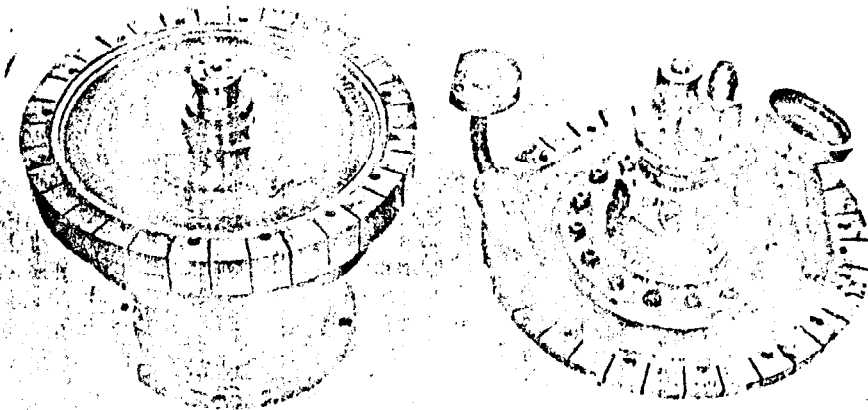


Fig. 9 Turbine with cover removed; the feed-water pump is shown mounted on the cover

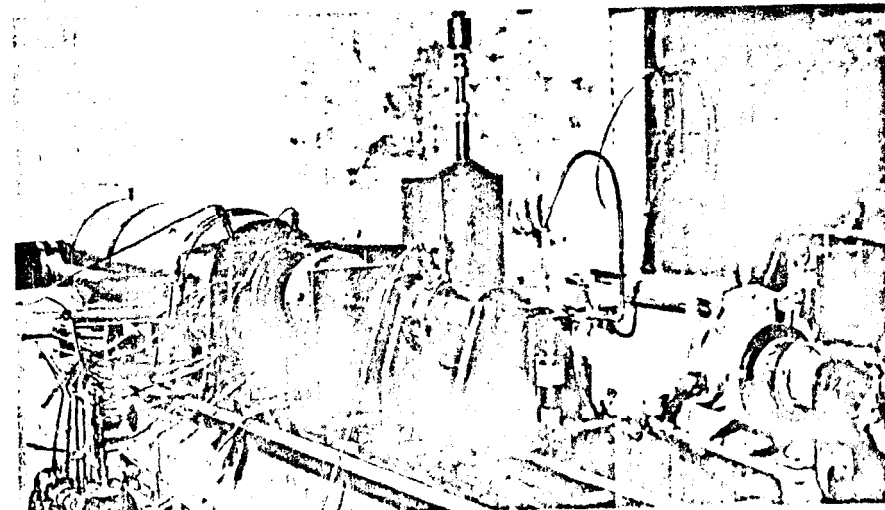


Fig. 10 Complete solid-propellant powerplant assembled for testing

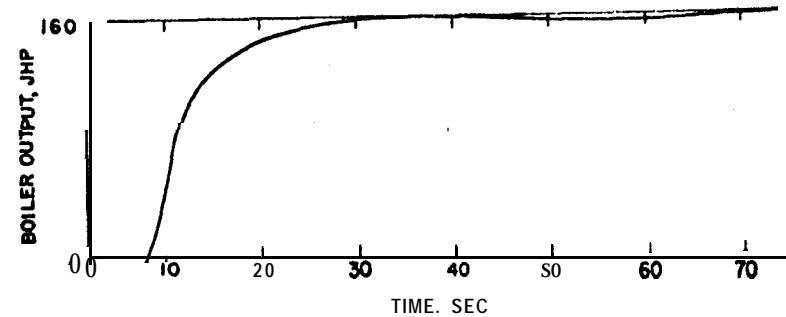


Fig. 11 Typical power characteristic

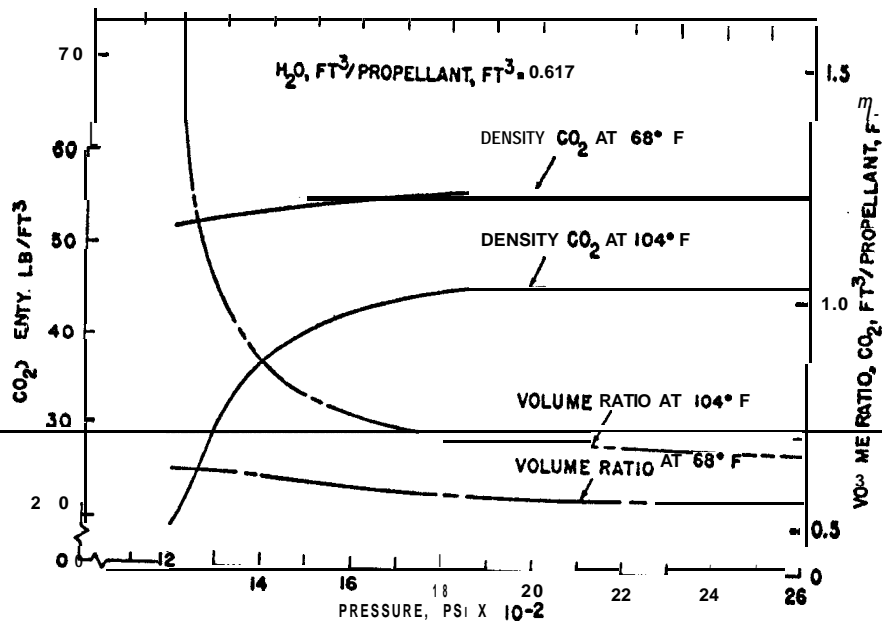


Fig. 12 Density and volume-ratio curves

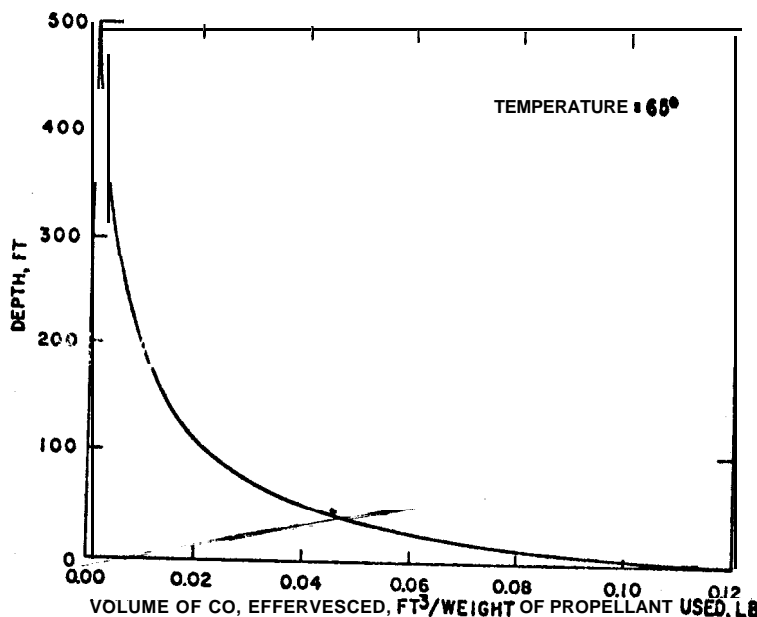


Fig. 13 Maximum carbon dioxide effervesced at depth

and would have produced full power for up to 6 min. with a proper grain length, though runs were limited to 2 min. to conserve propellant.

Because of low turbine performance, a maximum of only 40 shaft horsepower was attained, as compared with the design value of 64. However, performance of the remainder of the system was as predicted and sufficient design information was obtained on boiler, condenser, turbine components, and system controls, to enable design to proceed on a high-performance version with a high degree of confidence.

High-Performance System

After demonstrating feasibility with the solid grain a redesign was begun with inhibited red fuming nitric acid (IRFNA) and unsymmetrical dimethylhydrazine (UDMH) as propellants. Combined with powerplant improvements, it could provide about three times the available energy of the solid-propellant powerplant, and liquids are throttleable to permit more precise power control. However, as with the solid propellant, the exhaust from these liquids produced large quantities of non-condensable gases, principally nitrogen. Since experience showed that a gas wake can interfere with the torpedo guidance system, it became necessary that the combustion products be contained within the system. For this reason, bi-propellant hydrogen peroxide-diesel oil was substituted for IRFNA-UDMH, since its products of combustion, carbon dioxide and water, have unique characteristics in this application.

To elaborate, water vapor, after passing through the heat exchanger, is almost entirely condensed, and the carbon dioxide remains supercritical and nearly as dense as liquid water. In this regard, Fig. 12 shows the density of carbon dioxide at pressures of interest³, and the volume of carbon dioxide and water relative to the volume of unburned propellant. If the water condensate is separated and exhausted, or pumped overboard, there is more than enough volume in the emptying propellant tanks to store the carbon dioxide remaining.

Gas-exhaust conditions from the preheater of this system were expected to be 1900 psi and 440°F, a pressure-temperature combination that produces considerable liquid water. This water was successfully separated in a small cyclone separator. Although some carbon dioxide was carried overboard dissolved in the water, the majority did not and instead passed through a cooling coil and into the tanks at 1800 psi.

Figure 13 shows the maximum volume of carbon dioxide per

pound of propellant that might effervesce at depth in the worst case³ on being carried overboard dissolved in the exhaust water. Figure 14 shows the estimated time necessary for this gas to redissolve⁴, based on bubble diameter. At shallow depths, the wake redissolves in 26 sec from an initial bubble diameter of 1 mm. With adequate design, the effervescence can be considerably reduced, or even eliminated, by diluting the exhaust with sea water at the exhaust-pressure regulator.

The stoichiometric combustion temperature of 98% hydrogen peroxide and diesel oil is 4800°F , high enough to cause excessive tube-well temperatures in the boiler. The normal solution for torpedoes to limit this temperature is by injecting diluent water, but this adds the complexity of another pump

and its controls, plus the necessity to store or recover fresh water. Since even a slight salt deposit on the heat exchanger tubes would affect heat transmission adversely, completely eliminating the need for a coolant additive was considered attractive.

Thus partial injection of fuel into the oxidizer-rich gases at various stations along the heat exchanger was chosen as means to limit maximum temperatures. A simple counterflow routing of gas and steam then could be used without complicated crossovers to accommodate the superheater in a high-temperature system. Also the mass flow that must be handled was decreased, compared to a system with diluent.

A schematic diagram is shown in Fig. 15, and its temperature diagram in Fig. 16. Hydrogen peroxide enters the decomposition chamber and oxygen and steam emerge from it at 1800°F . These are cooled in the superheater section to 1000°F before entering the first combustion chamber. Here 25% of the diesel oil is injected, which brings the temperature (after reaction) to 2350°F . Cooling the gas and then raising its temperature by such partial fuel injection takes place four times as the gas passes through the successive superheater, evaporator, and preheater sections.

At start, the products of decomposition are below the temperature necessary for autoignition with diesel oil, so that ignition is attained by a thermoignition stitch in each combustion chamber together with a small pilot line carrying liquid hydrogen peroxide into each combustion chamber. The latter passes through a small tube located in the gas stream, then through a catalyst tube, and is finally injected into the chamber at 1800°F . This system lends itself to good packaging and simple heat-exchanger design and has no moving parts.

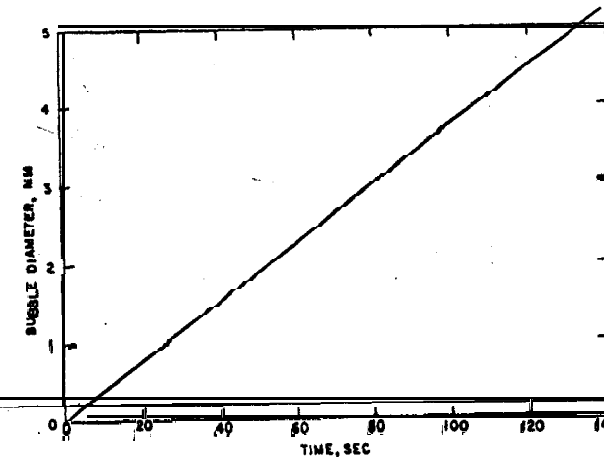


Fig. 14 Time required to dissolve carbon dioxide bubbles in water, est.

Fig. 15 Schematic of high-performance heat exchanger

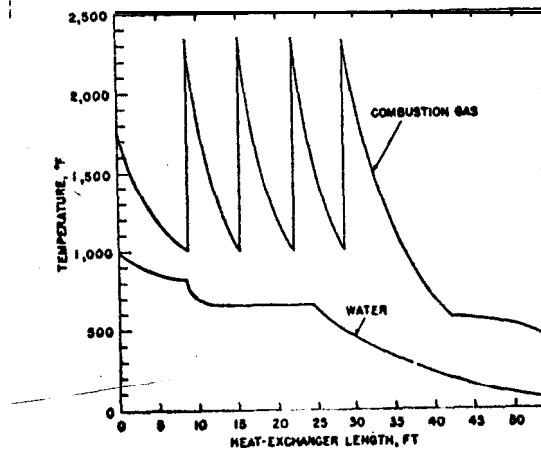
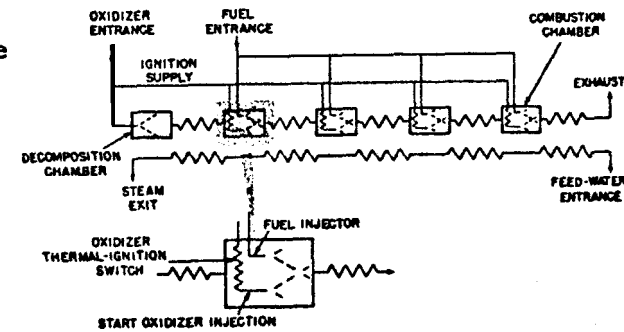


Fig. 16 Temperature characteristic of the proposed heat exchanger

A trial layout of the heat exchanger is shown in Fig. 17. It is similar to that used in the solid-propellant powerplant with added combustion chambers at approximately 6-ft intervals (measured helically). A block diagram of the powerplant is shown in Fig. 18. The steam loop is similar to the solid-propellant version with the addition of a water reservoir. Exhaust products of water and carbon dioxide are separated while still warm and a substantial density difference exists. Excess water is removed in a separator and ejected into the sea via a pressure regulator. Carbon dioxide and the remaining water are cooled before venting into the tanks, to increase density and prevent propellant overheating.

The propellant pumps are initially driven by a cartridge-powered auxiliary turbine for 15 sec. Before the end of this period, the prime mover overrides the starter and the powerplant operates self-sustained.

The principle of staged, partial fuel injection into the heat exchanger limits the combustion temperature and controls temperature throughout the heat exchanger. Conditions are similar to those in a diesel engine, except that combustion is continuous. The first three chambers with fuel injection are oxidizer-rich, whereas the fourth (and final) combustion chamber operates stoichiometrically. Nearly all water is condensed in the preheater over a notably small temperature range, so that the exhaust temperature can vary between the design value of 440°F to above 500°F with only a small loss of energy.

As additional benefit, the differential temperatures in the preheater are relatively high, so the preheater section may be kept small. In contrast, a system with a single combustion chamber required diluent water to reduce the extremely high temperature of the gases. For high efficiency, the latent heat of the diluent water must be removed in the low-temperature section of the heat exchanger, which requires a large preheater where the temperature differential between the feed water and the condensing diluent is small.

Conclusions

Feasibility of a closed-cycle power loop to operate independently of depth was demonstrated on a test stand with torpedo-type hardware and a solid-propellant gas generator as a heat source.

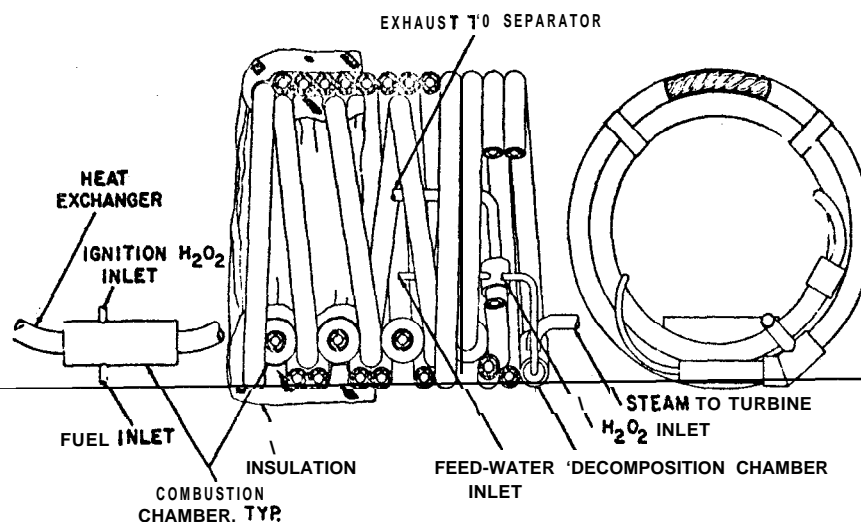


Fig. 17 Proposed heat-exchanger assembly for the high-performance powerplant

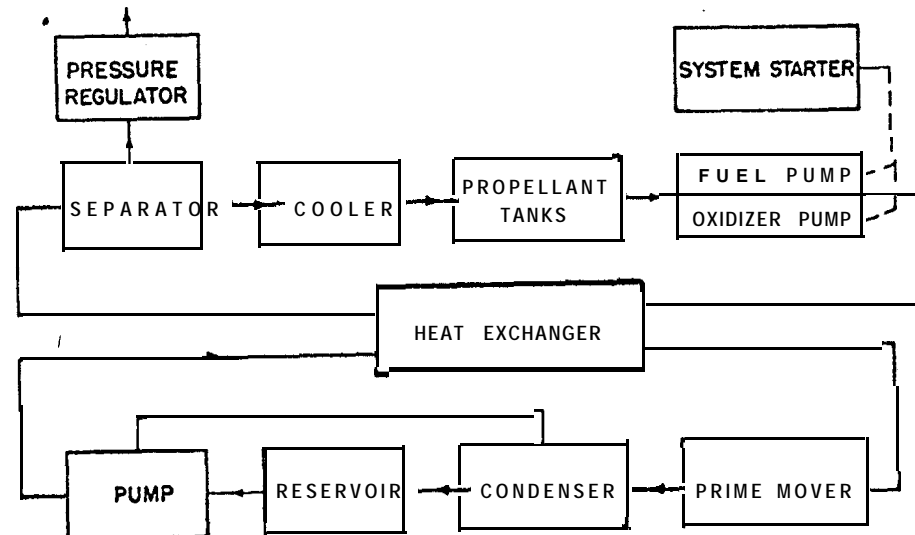


Fig. 18 Block diagram of high-performance system

Analysis and limited experimentation indicate that if water is needed for diluent, it can be extracted in a separator from the products of combustion located downstream of the heat exchanger and injected into the combustion chamber.

Analysis also indicates that use of bipropellant hydrogen peroxide-diesel oil, in conjunction with staged injection of the oxidizer, eliminates need for diluent and allows the non-condensable products of combustion to be contained in the torpedo, resulting in a wakeless system. The operation of such a wakeless system has yet to be demonstrated. Although design and demonstration of the powerplant require no major breakthrough, its success requires solution of component problems.

Most important, inability of the system to contain all non-condensable products of combustion, while using partial injection with some possible decrease in combustion efficiency, must be demonstrated.

References

¹ "Prediction and comparison of performance of propulsion systems for deep-running torpedoes," Joseph Kaye and Co., Inc. Cambridge, Mass., Rept. 40, (September 8, 1961).

² Karig, H. E., Jackley, D. N. and Hidde, L. G., "Experimental investigation of a once-through coaxial steam generator," AIAA Paper 64-468 (1964).

³ Perry, J. H. (ed.), Chemical Engineer's Handbook, (McGraw-Hill Book Co., Inc., New York, 1950), 3rd ed., pp. 206, 674.

⁴ Dorsey, E. N., Property of Ordinary Water Substance. (Rheinhold Publishing Corp., New York, 1950), pp. 552-553.

INVESTIGATION OF A ONCE-THROUGH STEAM GENERATOR

H. E. Karig,* D. N. Jackley,[†] and L. G. Hidde[‡]

Naval Undersea Warfare Center, Pasadena, Calif.

Abstract

For possible application to a closed-cycle torpedo propulsion engine, tests were conducted with a straight-tube coaxial heat exchanger to determine heat-transfer rates on generating superheated steam from cold water using hot gas from a solid propellant. The steam outlet was at 1600°F and 1500 psia and the gas inlet at 2200°F. Repeated runs were without burnout or noticeable decrease in heat-transfer efficiency. Stable equilibrium conditions were obtained in 60 sec., and sufficient steam was generated within 10 sec. to provide partial power for a turbine powerplant. Measured overall heat-transfer rates for superheat, boiling, and preheat regions at high heat flux and large temperature differences were in satisfactory agreement with calculations for forced convection inside tubes. Average rates of over $0.25 \times 10^6 \text{ Btu/hr-ft}^2$ were obtained for both steam and hot gas, with local rates as high as $0.85 \times 10^6 \text{ Btu/hr-ft}^2$ at a mass velocity of $1.5 \times 10^6 \text{ lb/hr-ft}^2$ and a Reynolds number of 1×10^6 .

Nomenclature

A = cross-sectional area, surface area, ft^2

C = wetted perimeter, ft

c_p = specific heat at constant pressure, $\text{Btu/lb-}^{\circ}\text{R}$

D = diameter, ft.

D_e = effective diameter, $D_e = 4A/C$, ft.

f = friction factor in Fanning equation

G = mass velocity, $G = w/A$, lb/sec-ft^2

An earlier version of this paper was published in the May-June 1965 issue of the Journal of Spacecraft and Rockets.

*Consultant, Underwater Ordnance Department.

Formerly Mechanical Engineer, Underwater Ordnance Department; now commercial pilot, United Air Lines.

[†]Formerly Mechanical Engineer, Underwater Ordnance Department; now with United Technology Center, Sunnyvale, Calif.

g = gravitational acceleration, ft/sec^2

H = enthalpy, Btu/lb

h = coefficient of heat transfer between fluid and surface, $\text{Btu/hr-ft}^{\circ}\text{F}$

k = thermal conductivity

L = length

Nu = Nusselt number = hD/k

Pr = Prandtl number = $c_p\mu/k$

P = pressure

Q = rate of heat transfer

R = gas constant

Re = Reynolds number

r_h = hydraulic radius

r = radius

St = Stanton number = h/c_pG

T = absolute temperature, $^{\circ}\text{R}$

t = time

U = overall heat-transfer coefficient, $U \approx Q/A\Delta T$

V = velocity, fps

v = specific-volume

w = mass flow rate

ν = viscosity

ρ = density

Subscripts

b = bulk

f = film

m = mean

Introduction

Recent investigations of thermal powerplants for deep underwater vehicles indicated that a closed-cycle steam system would prove satisfactory if a very compact boiler and condenser were used. Preliminary calculations suggested that a "once-through" coaxial-tube steam generator, or boiler, would provide satisfactory heat-transfer rates, based on equations generally used for forced convection. However, high temperature differences were involved and only limited experimental data were available for forced convection boiling at bulk-temperature differences exceeding 500°F .

A critical question concerned stability in the evaporation zone with high-temperature differences normally considered in the "burnout" or film-boiling region. However, the calculated heat-transfer coefficients for steam in the superheat region were sufficiently high that it appeared that the coefficient for film boiling would be satisfactory, if instability pulsations did not occur. Warm-up time was difficult to predict for dynamic starts, but estimates were less than 1 min to

attain full-flow steam with annular steam passages initially filled with water at room temperature.

Test Setup and Procedure

The once-through boiler for the closed-cycle propulsion system consisted of the single-pass concentric tube exchanger shown in Fig. 1. Hot gas from a solid-propellant gas generator passed through the inner tube, and counter-current water-steam through the annulus. The outside tube was $5/8$ in. in diameter, and the inside tube $7/16$ in. each with 0.035 -in. wall thickness. The annular space was held concentric by four wires wound in a 45° helix on the inner tube. The tube were ~~35 ft. long and spiraled into a four-row-long, four-row-deep coil, less than 4 in. in length and 11 in. in outside diameter.~~ It weighed approximately 15 lb.

Since a coiled tube was difficult to instrument, a straight concentric tube of similar size and length mounted within an insulated guard tube was constructed, as shown in Fig. 2. Thermocouples were placed every 2 ft. along the outer tube for measuring water or steam temperatures in the annulus. Water-inlet and steam-outlet pressures were also determined.

Hot gas was provided by a slow-burning ammonium nitrate-base, end-burning solid-propellant grain. Its inlet and exhaust temperatures and pressures were measured. The burning rate varied with pressure, but flame temperature was relatively constant at approximately 2200°F . No attempt was made to vary the hot gas flow during a test, because stability was considered important.

As shown in Fig. 3, feed water was supplied to one end of the annular space of the straight double-tube boiler. A predetermined mass flow rate, measured by a Waugh flowmeter, was maintained constant using a cavitating venturi or a Waterman flow regulator. A fixed orifice in the steam-discharge line maintained high pressure,

Combustion products from the grain passed into the inner tube of the test boiler. The gas pressure was controlled at approximately the same pressure as the steam's by throttling after leaving the heat exchanger. Temperatures and pressures were determined in the feed line from the grain chamber and in the exhaust line. The hot-gas flow was varied by using either a single grain alone or two grains simultaneously. Runs of 1 or 2 min were made, and stable conditions were attained in less than 1 min. Test data were taken from oscillograph records of steady-state conditions. The heat exchanger

Fig. 1 Spiral heat-exchange boiler

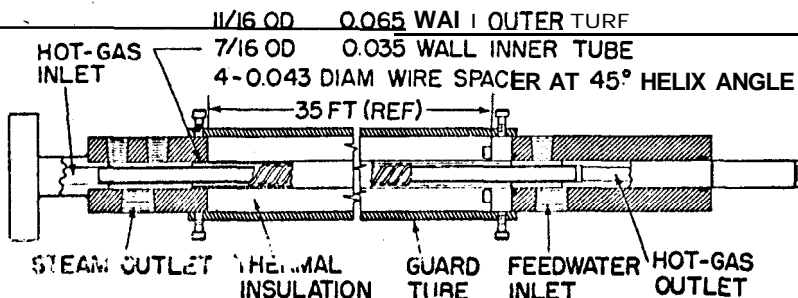
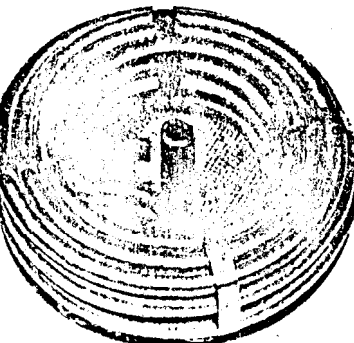


Fig. 2 Coaxial-tube test boiler

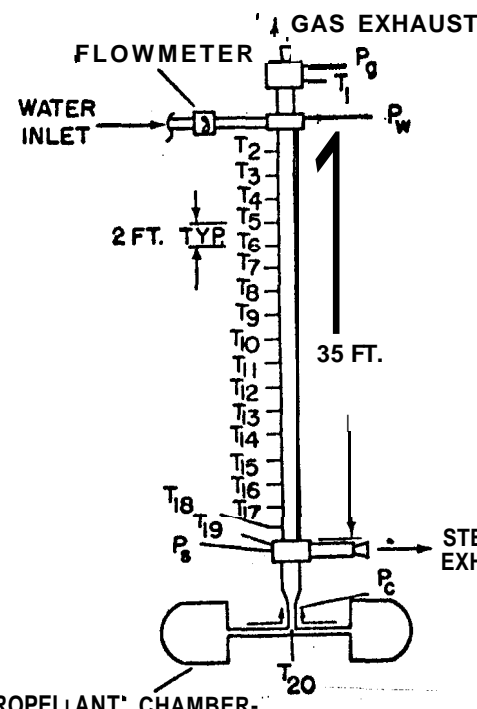


Fig. 3 Experimental heat-exchanger instrumentation

was not cleaned between runs.

Twelve runs were made on the straight-tube boiler, 8 with hot gas and 4 with either water or steam for pressure-drop or for low-temperature determinations. In the last two runs steam from the boiler operated a turbine. A coiled-tube boiler of similar length and tubing size (Fig. 1) was then used for propulsion system tests and its warm-up time and pressure drop correlated with results for the straight-tube holler.

Heat-Transfer Correlation

Experimental

Table 1 contains typical data. Because the high temperatures reduced tube strength, thermocouples were soldered to the outside surface of the steam tube, and although the tube and thermocouples were insulated, a slight correction for heat losses was necessary. Figure 4 shows corrected temperature-tube positions for two runs.

The characteristic area A used in the heat-transfer equations was the inside surface of the propellant-gas tube. Figure 5 is a cross section of the heat exchanger with dimensions, effective diameters, and other details.

Gas temperatures were calculated at various tube positions from the heat absorbed by the steam and the known propellant-gas temperatures at two tube positions. The equations used were:

$$\Delta H_g = AH, \quad w_s/w_g \Delta T_g = \Delta H_g/c_{pg} \quad (1)$$

The mole fraction of each of the five gases in the propellant exhaust as a function of temperature, which was needed to calculate physical properties, was determined by standard methods. Figure 6 shows mole fractions and specific heats at constant pressure (c_p) vs temperature. Dew points were 410°F at 1360 psia and 406°F at 1290 psia. Specific enthalpies of steam were obtained from the corrected temperature and estimated pressure. For the latter, pressure drop along the tube was assumed linear between either end and the saturation points.

⁴ Calculations by J. M. Caraher, Naval Undersea Warfare Center.

Table 1 Typical recorded heat-transfer data (run 10)^a

P _c	1570	T ₅	345
T ₂₀	2250	T ₆	442
P _g	1360	T ₇	390
T ₁	398	T ₈	420
P _s	1315	T ₉	455
T ₁₉	1370	T ₁₀	Not connected
P _w	1780	T ₁₁	540
T _w	90	T ₁₂	640
w _g	0.346 (calculated from P _c)	T ₁₃	605
w _s	0.1795	T ₁₄	590
T ₂	173	T ₁₅	580
T ₃	267	T ₁₆	590
T ₄	310	T ₁₇	825
		T ₁₈	1145

^a P = pressure, psia; T = temperature, °F;
w = flow rate, lb/sec.

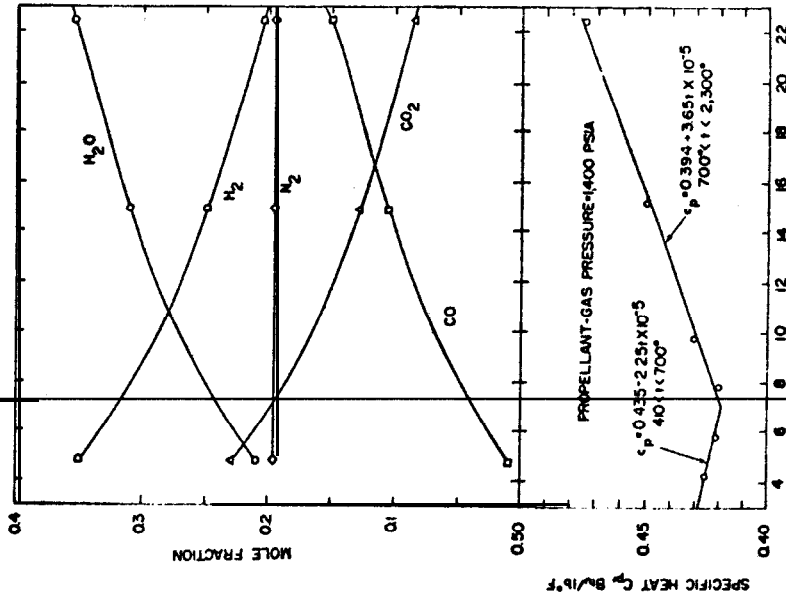


Fig. 4 Typical temperature profiles

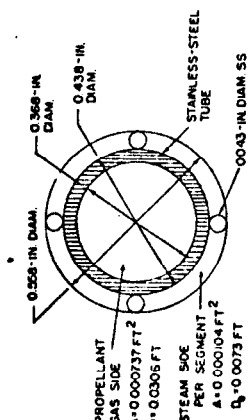


Fig. 5 Detail of tube cross section

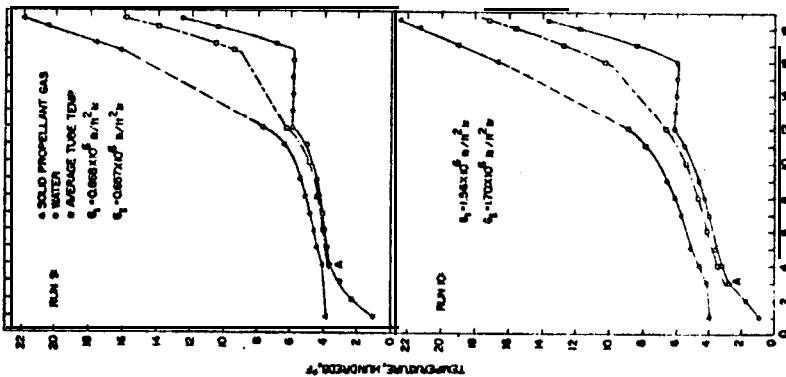


Fig. 6 Specific heat at constant pressure

Figures 7 and 8 are calculated enthalpies of propellant gas vs temperature. They are based, respectively, on zero enthalpy at 2230°F, working down (Fig. 7), and at 400°F, working up (Fig. 8). The base points were station 19 of Fig. 3 at the hot end and the dew point at the cold end. The point where water started condensing from the propellant gas was assumed to be where the water-temperature-vs-tube-position curve abruptly changed slope, such as point A on Fig. 4.

Figure 4 shows calculated propellant-gas temperature vs tube position for two runs, and Table 2 tabulates one of them. Overall heat-transfer coefficients were calculated from

$$Q = UA\Delta T_m = w\Delta H, \quad (2)$$

Where ΔT_m = log mean temperature difference,

$$A = C\Delta L$$

$$U = \frac{w\Delta H}{C\Delta L} \text{ for finite tube lengths} \quad (3)$$

$$U = \frac{w}{C} \frac{dH}{dL} \frac{1}{(T_g - T_s)} = \frac{w}{C} c_p \frac{dT}{dL} \frac{1}{(T_g - T_s)} \text{ for point values} \quad (4)$$

Theoretical

Figure 9 has experimental values of U vs tube station for two runs. These were used to check the theoretical values calculated with a modified forced convection equation.

The basic equation for the latter is

$$hD/K = 0.023 (Re)^{0.8} (Pr_f)^{0.4} \quad (5)$$

It was modified through McAdams' suggestion that, for large temperature differences, a mean or film temperature should be used to evaluate such physical properties. Thus, rewriting Eq. (5),

$$h = 0.023 c_p V_b \rho_f (DV_b \rho_f / \mu_f)^{-0.2} Pr_f^{-0.6} \quad (6)$$

and, using the mass velocity of the fluid and equation of state ($p = \rho RT$) and continuity ($w = \rho_b V_b A$),

$$V_b \rho_f = G (\rho_f / \rho_b) = G (T_b / T_f) \quad (7)$$

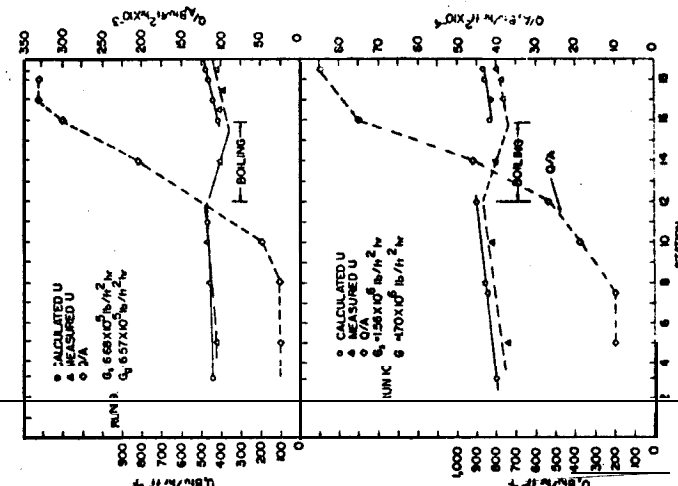


Fig. 9 Overall heat-transfer coefficient and unit heat flux, runs 9 and 10

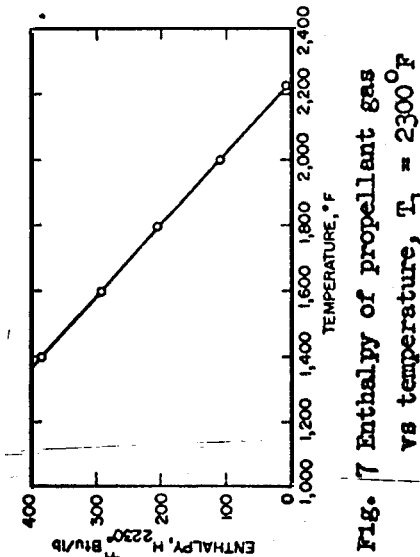


Fig. 7 Enthalpy of propellant gas vs temperature, $T_1 = 2300^{\circ}\text{F}$

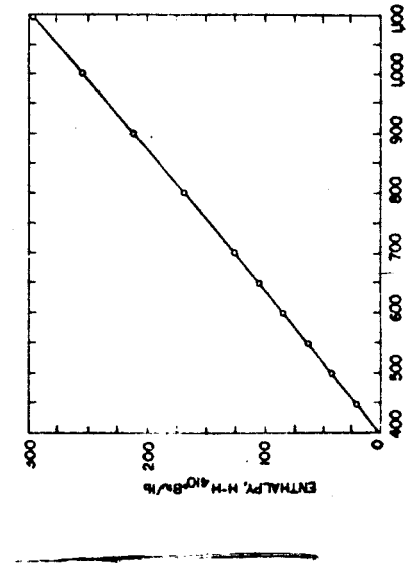


Fig. 8 Enthalpy of propellant gas vs temperature, $T_1 = 400^{\circ}\text{F}$

$$h = 0.023 c_{P_f} G \left(T_b/T_f \right) \left(Dg/\mu_f T_b/T_f \right)^{-0.2} Pr_f^{-0.6} \quad (8)$$

$$\text{or } St_f Pr_f^{0.6} \left(T_f/T_b \right)^{0.8} = 0.023 / Re_f^{0.2} \quad (9)$$

The latter equation separates the temperature-dependent **from** the independent factors.

The thermal properties of the two fluids **are** described by Keenan⁵ and Hilsenrath.⁶ The propellant-gas properties were averaged on a mole fraction basis, using values for each constituent at its temperature and partial pressure. Where temperatures were higher than given in the reference table, generalized properties were determined, and the standard atmosphere data of Kreith⁶ were utilized. Generalized properties are presented by Comings⁷ as a function of reduced temperature and pressure.

For the noncircular cross-sectional area in the annulus, the effective diameter, D_e , was used. Very little heat-transfer work **had** been done at the extremes of temperature **and** temperature difference encountered, and these were largely **confined** to Reynolds numbers less than 10^5 (Bergles and Rohsenow⁸). Results of the present work **allowed** independent determination of such film coefficients.

By analyzing the thermal properties of the hot gases⁵ and from available thermal properties of steam,³ satisfactory correlations of the test data with heat-transfer calculations for forced convection were obtained. Although the hot-gas temperature could not be accurately determined in the **boiling** region, calculation of the overall heat-transfer coefficient from steam to the hot gas during forced convection boiling indicated that it was comparable to that for single-phase conditions, as shown in Fig. 9. In Fig. 10, results of four runs are compared with the forced convection equation. Much better correlation was obtained when film temperatures **were** used instead of bulk temperatures, as noted by McAdams.⁴

Pressure Drop Correlation

The overall pressure drop for both steam and hot-gas **passages** **was measured** across the heat exchanger but not at intermediate points because of the danger of tube failure at pressure taps (as discussed). The pressure drop **through** the steam **passage annulus** was initially determined with cold water at **various** mass velocities, as shown in Fig. 11 for both the **straight-tube** and coiled-tube boilers. The calculated **pressure**

Table 2 Typical propellant-gas temperature calculation (run 10)^a

Sta.	T_s °F	P_s psia	h_s Btu-lb	Δh_s Btu-lb	Δh_g Btu-lb	T_g °F
19	1370	1315	1707	2250
18	1180	1338	1599	108	56	2130
17	845	1390	1399	308	160	1905
16	600	1430	1186	521	271	1665
12	615	1723	639	390	202	885
11	555	1730	558	309	16-1	790
9	465	1738	451	202	105	660
8	430	1745	413	164	85	610
7	400	1752	380	131	68	570
5	358	1766	335	86	45	515
4	315	1773	290	41	21	460
3	275	1780	249	410

$$a_{w_s} = 0.180 \text{ lb/sec.}; w_g = 0.346 \text{ lb/sec.}$$

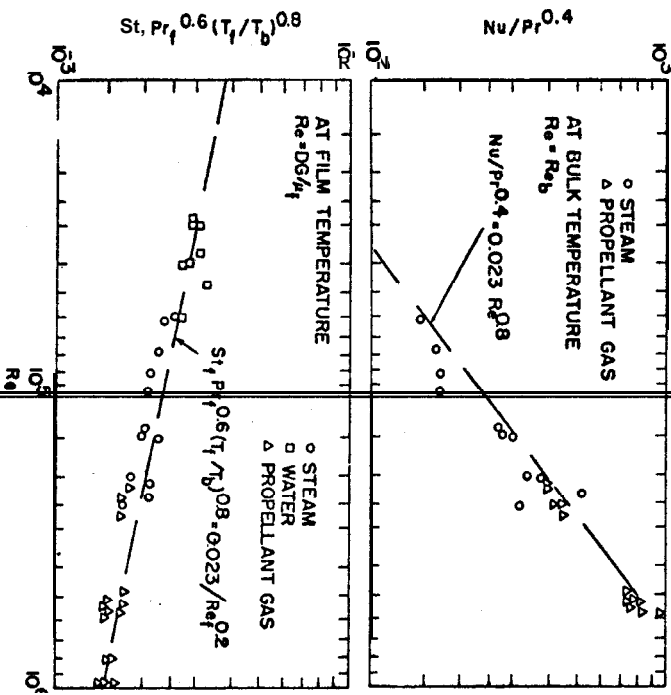


Fig. 10 Correlation of forced-convection data.

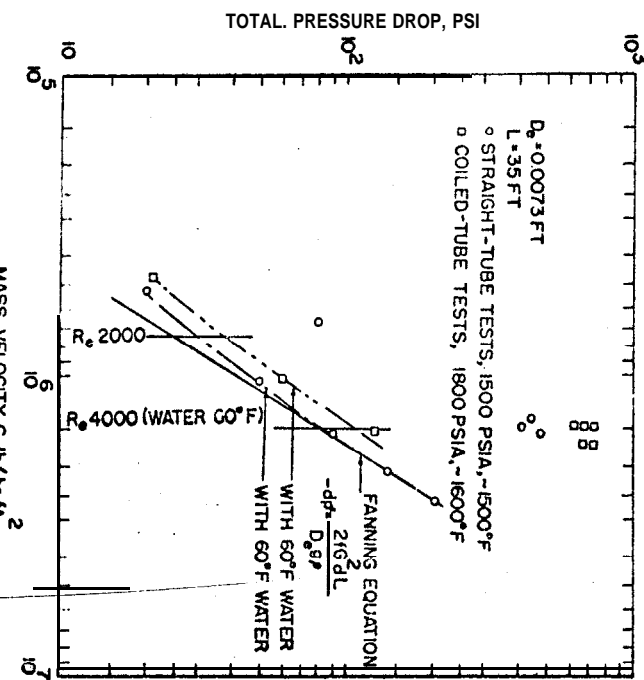


Fig. 11 Pressure drop in annulus of co-axial tube boiler.

drop, based on the Fanning equation,

$$dp = 2f \frac{G^2}{D_e} \frac{dL}{g} \rho \quad (10)$$

is also shown in Fig. 11 for water at 60°F. Good agreement was obtained for the straight-tube boiler at the higher mass velocities, but calculated values were as much as 30% less at lower flow rates, corresponding to Reynolds numbers of 1500 to 2000. The tests with water on the coil-tube boiler indicated a pressure drop approximately 25% higher than in the straight tube.

As expected, the pressure drop during heat-transfer tests with two-phase flow was much higher, especially with high superheat, where Reynolds number exceeded 10³. Correlations for these test conditions were not made because intermediate pressure drops were not determined.

The pressure drop across the inner-tube hot-gas passage was measured during the heat-transfer test runs. The modified Fanning equation for gases,

$$p_1 - p_2 = \frac{G^2(v_2-v_1)}{ag} + \frac{f_m G^2 v_m^2 L}{2gr_h} \quad (11)$$

gave fairly good correlation with test data. With a grain producing approximately 0.345 lb/sec of hot gas at 1500 psia which entered at 2200° and exited at 400°F, the average pressure drop from three runs was 190 psi, compared to 179 psi calculated from the foregoing equation, or 206 psi if the first term (for pressure regain due to gas cooling) is neglected. The pressure drop for similar flow conditions with the coiled tube was about 50% higher.

With a lower gas flow rate of approximately 0.15 lb/sec, the average pressure drop from three tests was 52 psi, compared to a calculated value of 44 psi, or of 52 psi when pressure-regain was neglected.

The warm-up time for the straight-tube test boiler to attain steady-state was approximately 1 min, but the boiler insulation added to its heat capacity. Tests on the coiled-tube boiler mounted with the grain combustion chamber were considered more significant, and warm-up times are indicated in Fig. I.2 for tests with it supplying steam to a turbine. Partial power was available at 10 sec and full power in less than

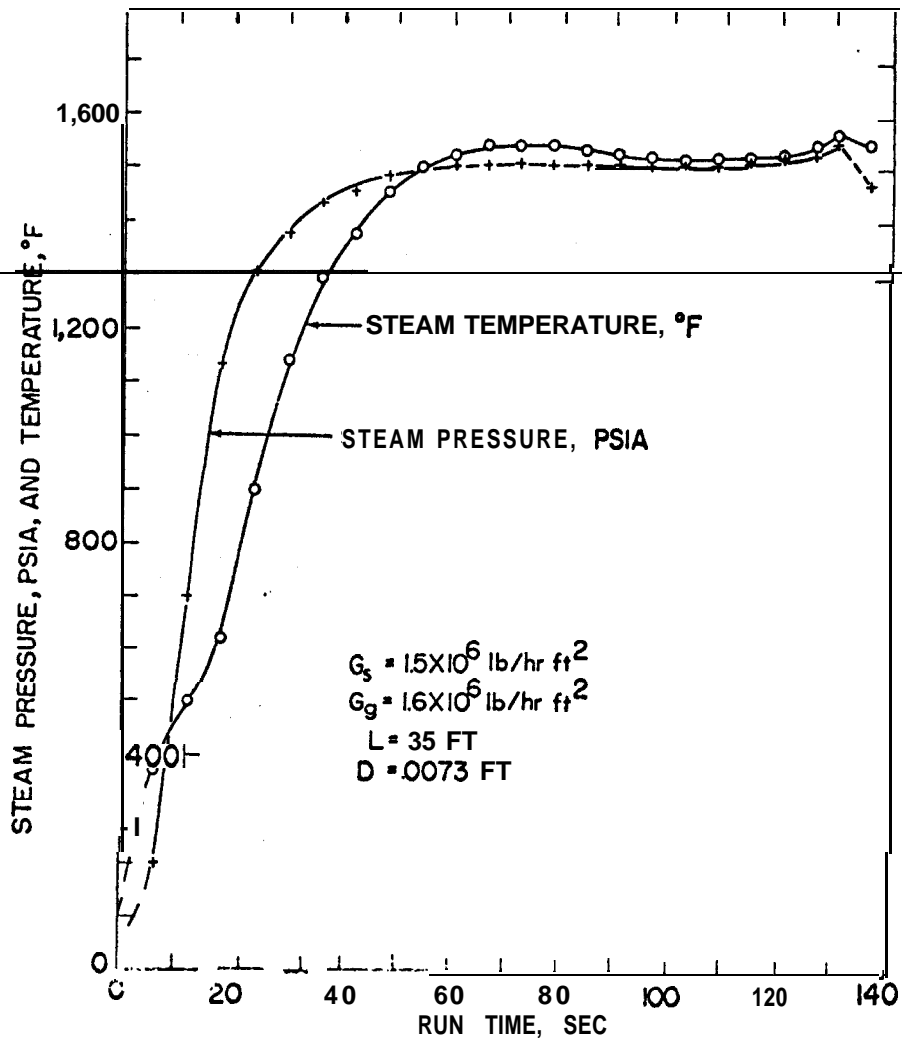


Fig. 12 Warm-up time for steam with coiled tube boiler, run 7

1 min. No instability or pressure fluctuation occurred during buildup to steady state.

Overall heat-transfer tests on the tightly coiled coaxial-tube boiler indicated approximately 20% greater heat-transfer coefficients and an increase in overall pressure drop of 50%. Correlating the forced convection heat transfer equation (5) with the Fanning equation (10) for flow inside tubes, and assuming friction factor, $f \propto Re^{-0.2}$ for turbulent flow, the heat transfer relationship can be shown to vary as

$$h \sim \left(\frac{dp}{dl} \right)^{4/9} \quad (12)$$

This closely approximates the heat transfer and pressure drop relationship experimentally determined for the straight tube and coiled-tube boiler.

Conclusions

Experimental data from tests on a straight coaxial-tube boiler indicates that conventional heat-transfer relationship for forced convection can be used with steam up to 1600°F and 1500 psia, and for a hot-gas source up to 2000°F, when either is at mass velocities as high as $1.5 \times 10^6 \text{ lb/hr-ft}^2$ with temperature differences up to 800°F. Stable conditions were obtained with forced convection boiling between mass velocities of 0.5 and $1.5 \times 10^6 \text{ lb/hr-ft}^2$, and no instability was noted.

References

- ¹Smith, K. E. and Hidde, L. G., "Design of a closed-cycle propulsion system for deep submergence," NAVWEPS Rept. 8039, U. S. Naval Ordnance Test Station, Pasadena, Calif. (November 1963); confidential.
- ²Zemansky, M. W., Heat and Thermodynamics (McGraw-Hill Book Co. Inc., New York, 1957), 4th ed.
- ³Keenan, J. H. and Keyes, F. G., Thermodynamic Properties of Steam (John Wiley and Sons Inc., New York 1936).
- ⁴McAdams, W. H., Heat Transmission (McGraw-Hill Book Co. Inc., New York, 1954), 3rd ed., p. 221.
- ⁵Hilsenrath, J., Beckett, C. W., Benedict, W. S., Fano, L., Hoge, H. J., Masi, J. F., Nuttall, R. L., Touloukian, Y. S., Woolley, H. W., "Tables of thermal properties of gases,"

National Bureau of Standards, Circ. 564, U. S. Dept. of Commerce (1955).

6 Kreith, F., Principles of Heat Transfer (International Textbook Co., Scranton, Pa., 1953).

7 Comings, E. W., High Pressure Technology (McGraw-Hill Book Co. Inc., New York, 1956), Chap. 8.

8 Bergles, A. E. and Rohsenow, W. M., "Forced-convection surface boiling heat transfer and burnout in tubes of small diameter," TR 8761-21, Dept. of Mechanical Engineering, Massachusetts Institute of Technology (May 1962).

RADIOISOTOPE AND REACTOR NUCLEAR POWER

FOR UNDERSEA MISSILE PROPULSION

K. E. Buck* and H. K. McCluer†

Aerojet-General Corporation, San Ramon, Calif.

Abstract

Nuclear power for undersea missile propulsion may offer

unique advantages, particularly in long-duration unattended missions. Nuclear heat-source shielding can be a large fraction of the powerplant weight and must be optimized for mission criteria, such as total allowable missile weight and radiation damage to missile components, and missile surface-handling procedures. Cobalt-60 is attractive for radioisotope-fueled powerplants because of its potentially large availability and low cost, its 5.3-year half-life, and its high power density. A Dowtherm-A Rankine power conversion system is well suited for use with this heat source, and an overall efficiency of about 15% and a total plant weight of about 3000 lb (fully shielded) can be achieved at a **3-kw** (electric) plant output. A fast fission spectrum, gas-cooled nuclear reactor appears to merit the majority of the desirable criteria for larger undersea missile powerplants, and can be used with **Brayton** and Rankine systems, including the Loeffler variation of the latter. All three plants will fit within a **5-ft-diam** cylinder. At 2000 shp, plant efficiencies of 18.0 to 21.5% and specific weights of 6.5 to 8.5 **lb/shp** (lightly shielded) are possible.

Introduction

Nuclear power for underwater missile propulsion can offer unique advantages. Since no oxidizer is required, closed-cycle powerplants are utilized; also, fuel **burnup** is negligible. The extended life of nuclear-powered plants makes possible missions that are impossible with chemical energy. Although the heat source weights are high compared with conventionally fueled systems, for long duration missions a nuclear power propulsion

*Principal Nuclear Engineer, Nuclear Engineering and Manufacturing Operations.

†Senior Mechanical Engineer, Nuclear Engineering and Manufacturing Operations.

system may be the lighter. Nuclear-powered missiles will have higher initial cost; however, since the missile with nuclear power need not be removed from service frequently for battery recharging or for refueling, its higher productivity can result in a lower cost per hour of mission time. In addition to high capital cost, nuclear heat **sources** are potentially hazardous. Hence, potential missions are restricted to those where there is a high probability of recovering the unit.

Two types of nuclear propulsion systems are considered. One is a cobalt-60 (Co-60) fueled radioisotope heat source that is coupled to a Dowtherm-A Rankine power conversion system with a plant output of 3 kw (electrical). The second is a gas-cooled nuclear reactor, which can be coupled to a Brayton-Rankine or a Loeffler variation of the Rankine power conversion system. All three of these plants are compared at a plant output of 2000 shp.

General Characteristics of Nuclear Reactor and Radioisotope Heat Source

In a radioisotope nuclear power source, thermal power output is a linear function of the number of unstable, spontaneously decaying nuclei present. Thus, power is produced at all times, regardless of the amount of radioisotope present, and no control of power output is needed or possible. The shielding required depends on the nature of the radiation emitted during decay. Here, the least costly (most plentiful) radioisotopes require the most extensive shielding. The energy of radiation is generally lower than that emitted by a nuclear reactor during its operation, and neutron activation of external components does not occur.

In a nuclear reactor containing sufficient fissionable materials to sustain its reaction, the power output is primarily limited only by heat transfer, and control from zero to full output is possible and necessary. High-energy radiation is emitted, even during operation at low power, and, after an initial period of operation, the reactor (and, possibly, external components) will continue to emit radiation even after reactor shutdown. In the extremes, the reactor 1) may be fully shielded, which permits personnel to approach during full-power operation, or 2) may employ limited shielding, which only protects adjacent components and/or permits access to selected parts of the reactor during shutdown. Which type is selected depends on mission requirements.

The difficulties in handling a nuclear-powered missile is dependent on the shielding used. If close access is required during operation, then sufficient shielding will have been used to permit close access at the air/water interface and during maintenance on board a service ship. However, if only light shielding is used, as for the reactor powerplants discussed herein, some form of expedient shielding will be required at the air/water interface during handling and during servicing. This could be the sea itself, or specialized external structures of concrete or other dense materials. In general, severely weight-limited missiles will force the use of limited shielding (with either radioisotope, or reactor power) and will produce more severe handling problems.

Radioisotope Propulsion Systems

The radioisotope most frequently considered for high power levels is cobalt-60 (**Co-60**). This is because 1) Co-60 can be made available in larger quantities and at a lower price than any other radioisotope presently under intensive study (large-scale production of Co-60 in operational reactors could produce about 1 mw per reactor-year at an estimated cost of about \$10/w); 2) its half-life, 5.3 years, makes it suitable for many missions; and 3), it can be produced at a relatively high power density (25 w/cm^3), although cost increases with power density. Co-60 is therefore exclusively considered in this paper.

A fully shielded Co-60 heat source is relatively heavy, as shown in Fig. 1. The weight of a fully shielded heat source may represent about half of the total plant weight.

The powerplant used to convert the thermal energy produced by the radioisotope to mechanical or electrical energy must generally be highly efficient because of the high cost of the radioisotope. It also should operate reliably for a long period without maintenance to take full advantage of the long-life characteristics of radioisotopes.

Although Brayton, Stirling, and Rankine power conversion cycles offer particular advantages, only the Rankine is considered here. Such a cycle, with Dowtherm A as the working fluid, has been studied at power levels that satisfy missile propulsion requirements. Its heat source, shown in Fig. 2, consists of cylindrical capsules of Co-60 embedded in the center of a spherical tungsten shield. Heat is conducted through the shield to a helical-coiled tube in which the Dowtherm A is flashed to vapor. A liquid metal (NaK) fills the space between shield and coil to facilitate this heat transfer.

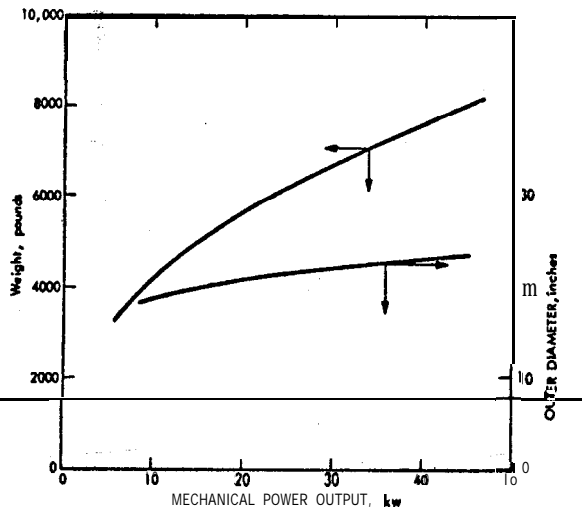


Fig. 1 Size and weight of fully shielded Co-60 heat sources.
Shield material: tungsten; conversion efficiency: 20%;
dose: 10 mr/hr at 1 meter.

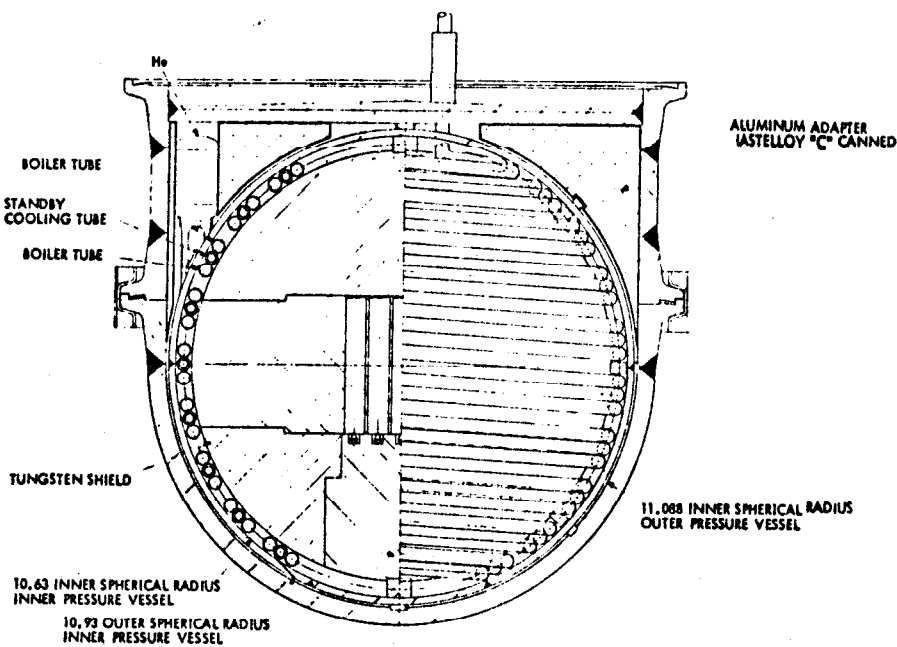
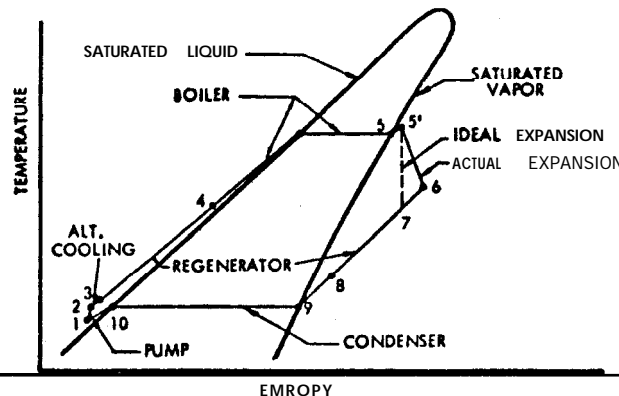


Fig. 2 Proposed Co-60 radioisotope heat source for under-water Rankine cycle powerplant; vertical section.

The shield and coil are surrounded by a double-walled pressure vessel, the space between whose walls is normally evacuated to limit heat loss during operation. In an emergency, the space can be filled with helium from a storage bottle, to provide adequate heat transfer to the sea.

The power conversion system is a closed Rankine cycle with a turbine directly coupled to an alternator and a liquid pump. The cycle processes are shown in Fig. 3, superimposed on the temperature-entropy diagram for the working fluid which also indicates conditions at pertinent points. A characteristic of Dowtherm A is the positive, or reverse slope, of the saturated vapor line, contrasted with the negative slope saturated vapor lines of most fluids. The expansion process for a positively sloped saturated vapor line will progress into regions of increasing superheat, which simplifies turbine design, whereas expansion from a negatively sloped vapor line will progress into regions of increasing wetness. This characteristic, together with high molecular weight and attractive vapor pressure, makes Dowtherm A an excellent turbine working fluid.

The flow schematic of the power conversion system is shown in Fig. 4 with the various cycle locations identified by numbers that correspond to the points in Fig. 3. At point 1, subcooled fluid from the condenser hot-well enters the suction side of a jet pump. The fluid is discharged from the jet pump to the inlet of a partial-emission centrifugal pump. The jet pump provides sufficient pressure to the centrifugal pump to prevent inlet cavitation. The fluid is discharged from the centrifugal pump at point 2 and directed to the cooling passages in the alternator, where it absorbs heat losses. On leaving the alternator, the fluid enters the primary side of a recuperative heat exchanger (regenerator), where it absorbs some of the waste heat in the turbine exhaust. Next, the fluid enters the boiler, where it absorbs energy from the radioisotope and is boiled to dryness and slightly superheated. The vapor leaving at point 5 enters the turbine, where its expansion produces shaft power to drive the alternator and pump. The highly superheated vapor at point 6 (see Fig. 3) enters the secondary side of the regenerator, where it is cooled by the regenerator primary side flow. The vapor then leaves the regenerator and enters the condenser (point 8), where additional desuperheating and condensation occur. The saturated condensate is subcooled in another heat exchanger and, subsequently, returned to the jet pump inlet. At 3 kw(e), an overall efficiency of about 15% can be achieved under these conditions.



POINT	PRESSURE, psia	TEMPERATURE, °F	EMHALPY, Btu/lb
1	0.5	283.0	99.02
2	0.5	286.8	100.77106.85
3	*104.4	286.8	100.77106.85
4	104.4	670.519.3	215.31414.55
5	104.4	700.592.6	415.75371.26
6	104.4	552.6	353.35
7	0.75	329.3	262.80
8	0.5	290.0	248.80
9	0.5	290.0	102.20
10	0.5	290.0	102.20

* Nominal boiler pressure is shown, but condensate pump power calculations are based upon a conservative 30 psi pressure drop from pump outlet to boiler outlet.

Fig. 3 Rankine cycle with Dowtherm-A.

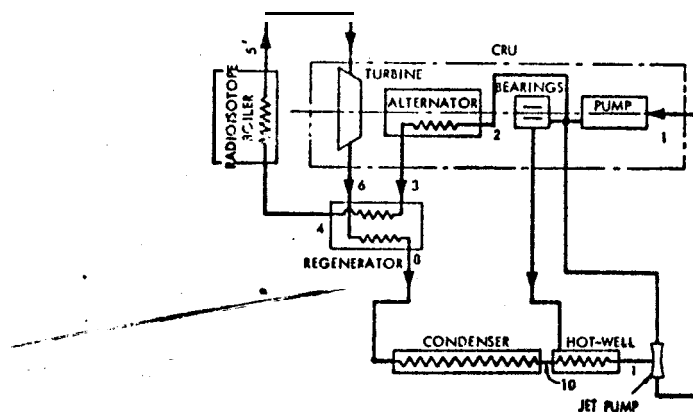


Fig. 4 Rankine power conversion flow diagram.

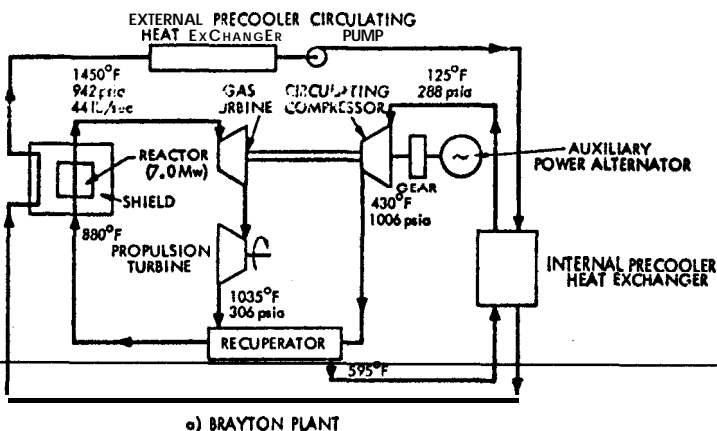
During operation, the thermal power generated by the radioisotope heat source is absorbed by the power conversion system. At other times, such as during assembly, transport, and placement, a standby cooling system is provided. It consists of a separate heat exchanger tube wrapped around the tungsten shield (see Fig. 2). Dowtherm A is circulated by a small pump through this tube to an external heat exchanger, where the heat is dumped to the environment. This system operates on **external** power or internal batteries. It is automatically activated whenever the power conversion system is inoperative, and it deactivates before it restarts. In the event that other heat removal systems are inoperative, an emergency cooling system floods the evacuated space between the double-walled pressure vessel with helium to transfer the radioisotope heat directly

to sea water. This cooling system requires no external signal or source of power and is extremely reliable; helium is released by the melting of a fusible alloy link when the inner pressure vessel overheats (approximately 1000°F). No provision is made for restarting after such emergency cooling, since a failure serious enough to cause its initiation would almost certainly have rendered the power conversion equipment inoperative.

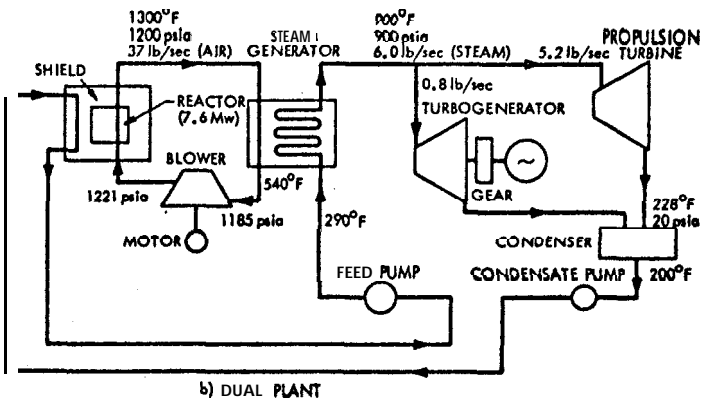
Gas-Cooled Reactor Propulsion Systems

A fast-fission neutron spectrum, gas-cooled reactor with metal-clad ceramic fuel elements appears to satisfy the majority of the desirable criteria for underwater missile propulsion. The reactor can be safely flooded with water without an increase in reactivity, if an appropriate thermal neutron poison, such as gadolinium or europium, is included in the ceramic fuel. Experience with the fuel element of the ML-1, the mobile low-power gas-cooled nuclear powerplant developed under the Army Gas-Cooled Reactor Systems Program by Aerojet-General for the United States Atomic Energy Commission, has demonstrated that a reactor outlet temperature in excess of 1400°F is attainable without exceeding the demonstrated hot-spot temperature of 1750°F. This high outlet temperature provides high powerplant efficiencies. The reactivity change of a fast reactor during fuel burnup is inherently small, and so reactor control is relatively simple. Finally, more than eight years of design, development, and test experience provides an extensive technology base to minimize developmental cost and time.

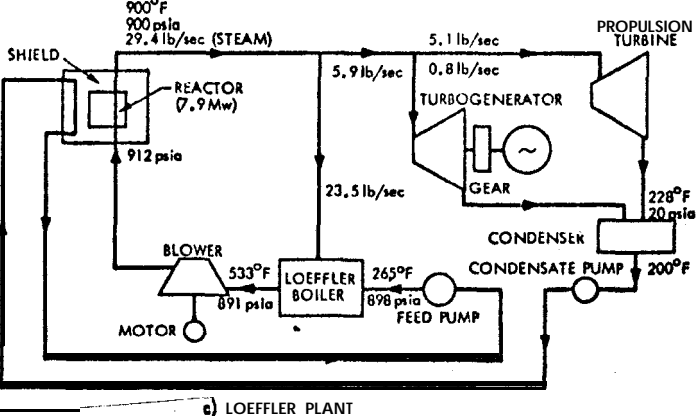
The fast-spectrum, **gas-cooled** reactor can be used as the heat source for powerplants using the Rankine (dual) cycle, the Brayton cycle, or the Loeffler² variation of the Rankine cycle. Typical plants are shown schematically in Fig. 5 and will be



a) BRAYTON PLANT



b) DUAL PLANT



c) LOEFFLER PLANT

Fig. 5 Power plant schematics for nuclear reactor heat source.

described later. Parameters to be considered in selecting the optimum system include allowable plant weight and dimensions, plant efficiency, reactor gas coolant, power transients and response requirements, plant startup, shutdown, and steady-state control, afterheat removal, attitude restrictions, simplicity and reliability, cost, and local ambient pressure.

Aerojet-General has performed studies of a "standard" gas-cooled reactor in the cycles mentioned to establish the trade-offs among these three plants and to define the minimum diameter plant configurations. The "standard" reactor characteristics are summarized in Table 1, and the reactor conceptual design is shown in Fig. 6. Reactor state points were varied as necessary to permit comparison of all three plants at 2000-shp output. Steam was selected as the working fluid for the two Rankine cycle plants because of well-developed machinery technology for high power levels. Air was used in the Brayton cycle because of the well-developed equipment technology and the ready availability of air at sea.

The primary components of the dual Rankine plant (Fig. 5b) are the reactor, reactor-coolant circulating blower, steam generator, propulsion turbine, auxiliary power turbine, condenser, and condensate and feedwater pumps. The steam generator is composed of a steam drum and three small shell-and-tube exchangers as economizer, evaporator, and superheater. The propulsion turbine is a four-stage, axial-flow machine; the auxiliary power turbine has two axial stages. The condenser is on the hull exterior. The single-stage, radial-flow, gas-circulating blower, auxiliary power alternator, feed pump, and condensate pump are directly driven from the auxiliary power-turbine shaft. The component arrangement for the dual plant in an undersea missile configuration is shown in Fig. 7. The Brayton and Loeffler plants are similar.

The primary components of the Brayton plant (Fig. 5a) are the reactor, recuperator, precooler, turbines, and compressor. The plant working fluid is air. The recuperator is a conventional shell-and-tube heat exchanger. The precooler includes two heat exchangers with an interconnecting water loop; one exchanger is located in the hull to transfer plant waste heat to the water loop, and the second is on the hull exterior to transfer heat from the water loop to the sea water. This arrangement eliminates need for introducing high-pressure sea water into the hull or for incorporating large air ducts through the hull which lead to an external heat exchanger. Two single-stage radial turbines are employed, one attached directly to the propeller shaft and the second to a single-stage radial compressor

Table 1 Gas-cooled reactor characteristics

Core characteristics	
Active dimension	16- by 16-in. right circular cylinder
Fuel	3073 fuel pins
Moderator	4-in. BeO
Fuel pin characteristics	
Dimensions	16-in. active length, 22-in. over-all length
Cladding	0.25-in.-o.d. Bastelloy X, 0.025-in. wall
Fuel	$\text{UO}_2\text{-BeO-Eu}_2\text{O}_5$, 0.198-in.-diam pellets
Pressure vessel	
Dimension	27-in. o.d., 42.5-in. length (with elliptical plenums), 0.5-in. thick
Material	Type 347 stainless steel
Control elements	
Type	16 absorber-reflector drums, driven by 8 rotating actuators
Location	Reflector
Composition	$\text{B}_{10}\text{C-UH}$ (absorbing), BeO (reflecting)
Dimensions	4-in. diam
Coolant	Air
Weight (unshielded)	Approximately 3000 lb

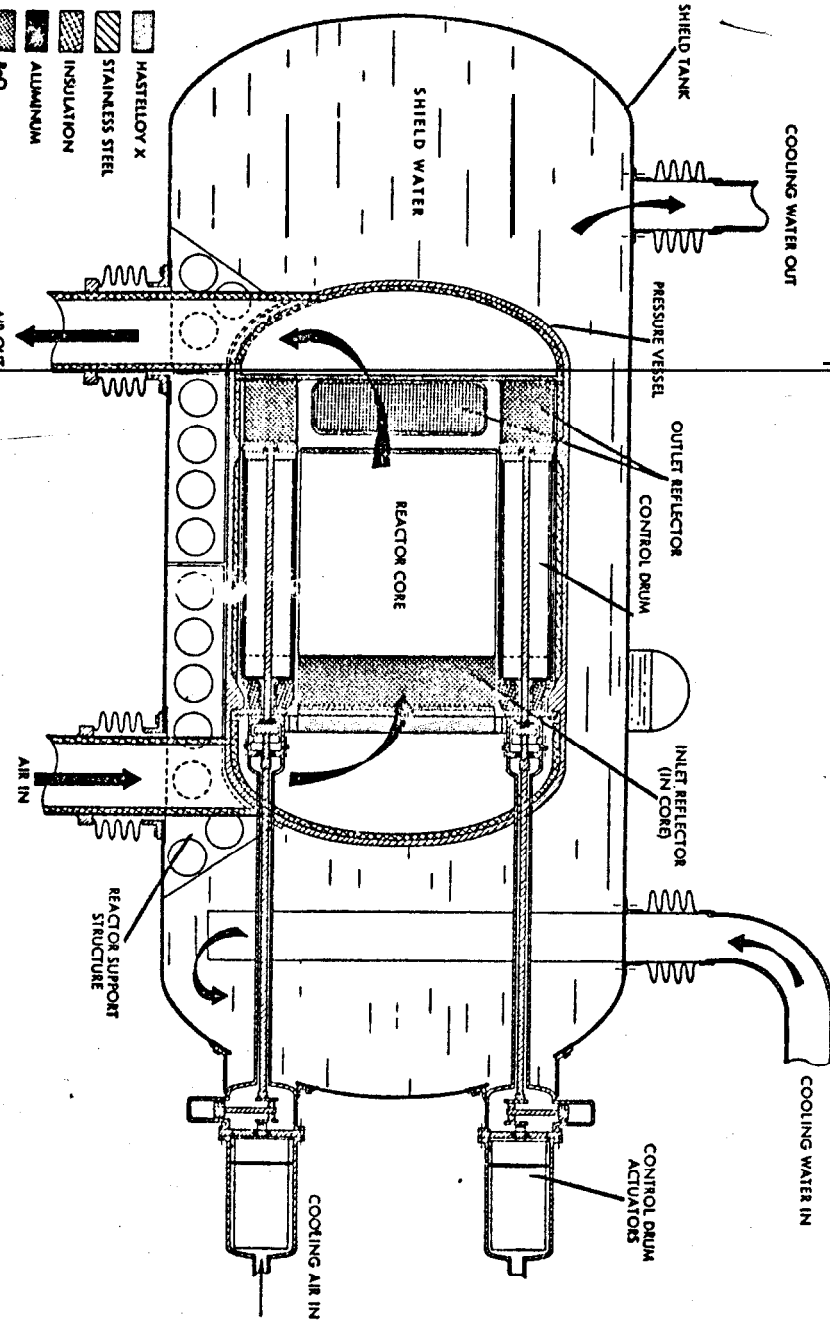


Fig. 6 Nuclear reactor conceptual design.

that circulates the plant working fluid. A constant-speed auxiliary power alternator is also connected to this shaft.

The main components of the Loeffler plant (Fig. 5c) are the reactor, steam circulating blower, Loeffler boiler, propulsion turbine, auxiliary power turbine, condenser, and condensate and feedwater pumps. The steam-circulating blower is a single-stage axial machine. The Loeffler boiler is a small drum in which superheated steam and condensate are mixed to generate saturated steam. The remainder of the components are identical with those of the dual plant.

Specific weights and efficiencies of the three plants at 2000 shp are shown in Table 2. With minimal radial biological shielding, all plants fit within a 5-ft-diam cylinder.

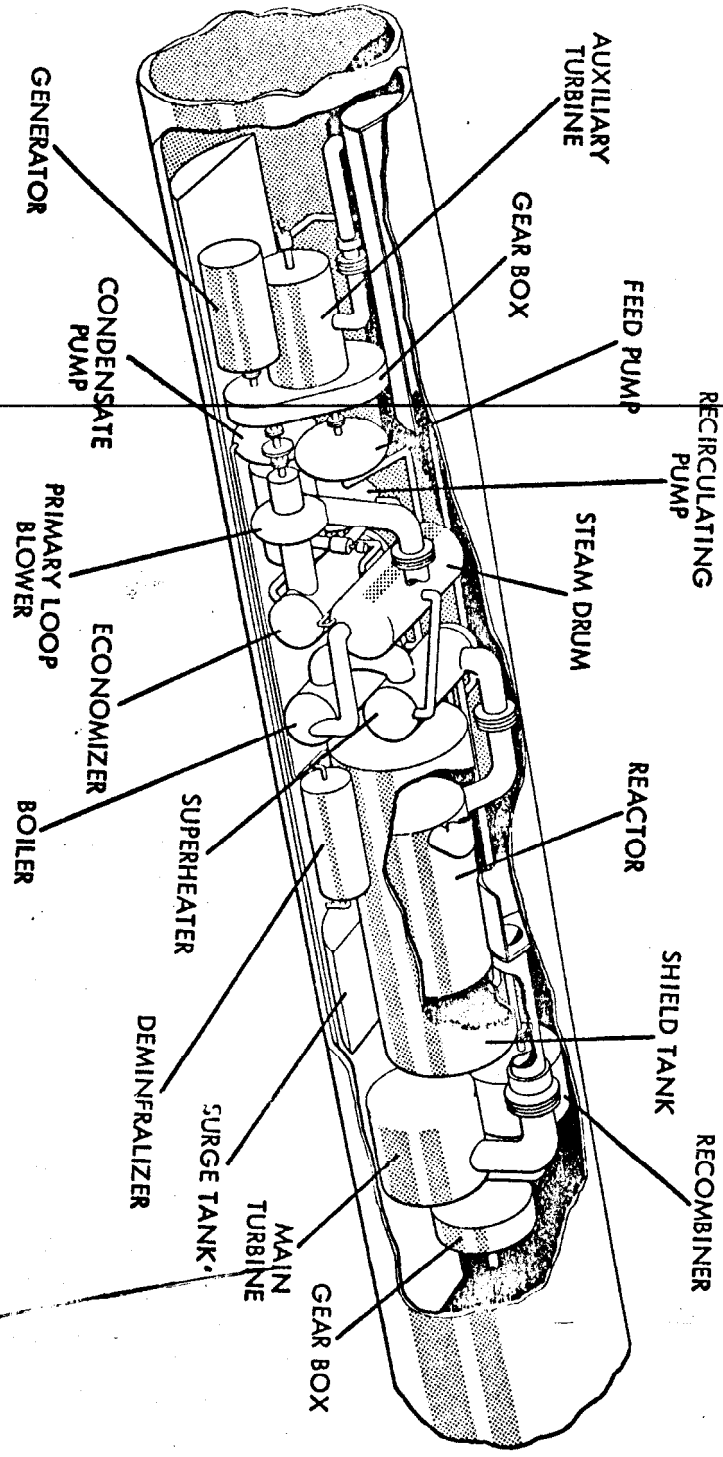


FIG. 7 Nuclear reactor dual-cycle powerplant for undersea missile. Configurations for Brayton and Loeffler plants are similar.

Table 2 Specific weight and efficiency summary

	Specific weight ^a	Efficiency, %
Dual cycle	8.0	19.6
Brayton cycle	8.5	21.5
Loeffler cycle	6.5	18.0

^aInstrumentation shielding only, pounds per horsepower.

In a Brayton-cycle plant, about 80% of full reactor power is required at self-sustaining conditions even when no shaft power is produced. As a consequence, the shaft power can be increased from 0 to 100% in less than a minute. The other two plants can match this response by dumping large amounts of steam to the condenser at low shaft power.

Startup of the dual and Brayton plants is achieved by blowing air through the reactor with an external electrical source until the plant reaches self-sustaining conditions. For the Loeffler plant, steam must be generated in the Loeffler boiler with supplemental electric heaters until the plant becomes self-sustaining.

After about a day of operation, a reactor core continues to generate significant amounts of heat even after shutdown because of decay of radioisotopes formed by fission of the uranium fuel. This afterheat is removed from the dual plant by circulating air through the reactor, generating steam in the boiler, and condensing in the condenser. In the Brayton plant, it is removed by air blown through the reactor by a separate loop located in the shield water, which is circulated to the external heat exchanger. In the Loeffler plant, afterheat is removed by circulating steam through the reactor and condenser with most of the condenser blocked off to prevent steam condensation.

The steam-condensate interface in the condenser, and other equipment of the dual and Loeffler plants will restrict allowable missile attitudes somewhat. However, the Brayton plant, whose coolant is always gaseous, has no such restriction.

In all systems, the propulsion equipment and instrument compartments are separated by compartments flooded with sea water, which acts as biological shielding. Therefore, only a relatively thin pure-water shield around the reactor is needed to reduce to acceptable levels the neutron flux to which the plant electronics and rotating machinery are exposed.

The **Brayton** plant involves fewer valves, pumps, and similar equipment than the dual or Loeffler **let** plants and, as a consequence, is probably the most simple and inherently reliable. The fabrication costs of the three plants are probably comparable, although the development cost of the Loeffler plant may be somewhat greater than for the **Brayton** and dual plants. If the powerplant module is pressurized to the exterior ocean pressure to reduce hull weight, removal of gas that accumulates in the condenser will be difficult with the dual and Loeffler plants. There are no significant effects of module internal pressure on a **Brayton** plant.

In consideration of the several points just discussed, it is apparent that a gas-cooled reactor can provide heat for either of three powerplants with different characteristics, and the plant with the best combination of characteristics can be selected for any given application.

Conclusions

Nuclear powerplants of the types described herein can be attractive for underwater propulsion power. The primary advantages of both reactor and radioisotope power sources are their long lifetimes. Nuclear power may provide the lightest powerplants for some missions. A negligible amount of fuel is consumed during a mission; and completely closed-cycle powerplants are normal. On the other hand, these power sources are expensive and potentially hazardous, and so they are probably applicable only for very long total duration vehicles and where recovery is fairly certain. Also, lightly shielded nuclear powerplants will require special care during handling at the surface and during maintenance operations.

Powerplants of both radioisotope and nuclear reactor types are well within the existing technology of both the nuclear heat sources and power conversion equipment. A serious engineering effort would undoubtedly result in their practical development.

References

¹"Radioisotope applications in hydrospace," AGN-8163, **Aerojet-General Corporation**, San Ramon, Calif. (October 1965).

²Loeffler, S., "Steam generation at high pressures and temperatures," **Power Mag.**, 524-527 (March 26, 1929).

GEAR NOISES OF UNDERWATER MISSILES

INTRODUCTION TO ACOUSTICAL ENGINEERING
OF GEAR TRANSMISSIONS

Darle W. Dudley*

General Electric Company, Lynn, Mass.

Abstract

Gear transmissions can be developed to meet specified requirements for either airborne sound or structural vibrations. Doing so requires selection of the proper type of gear, maintenance of sufficient accuracy in machining, and employment of sound attenuators at appropriate locations.

Introduction

There is long-standing art on sizing and proportioning a gear transmission to achieve a specified load-carrying capacity. Lately, there has been a rapidly growing demand for gears that also meet rather stringent sound requirements. Such design, however, was assumed *not* amenable to logical engineering, and the usual solution was to make the gears as accurately as possible and then tolerate the noise they produced. Recent work indicates, on the contrary, that acoustical engineering can develop gear transmissions that meet specified requirements for airborne sound or structural vibrations.

Gear Noise Sources

Gear sound comes from a variety of sources, the more obvious ones including a) variations in gear tooth spacing, b) deviation of gear teeth from true involute, c) "waves" on tooth surfaces, d) roughness of tooth surface, e) eccentricity of a tooth rotor, f) misalignment of tooth rotor, g) deflection of gear teeth, h) unbalance of tooth rotor, i) windage by tooth rotor, j) disturbance of oil by pumping anti

* Presently associated with Solar, A Division of International Harvester, San Diego, Calif., as Chief of Gear Technology.

splashing by tooth rotor, k) noise of rotor bearings, 1) noise of flexible couplings, m) seal rub or squeal, and n) vibrations transmitted from driving **or** driven equipment.

In the foregoing items, a, b, c, e, f, and g primarily create non-uniform velocity in the driven gear, even when the velocity of the driving gear is absolutely perfect. Such a tendency causes velocity variations in both the driving and driven rotors. These result in accelerations, or changes in forces, that set up vibrations and ultimately produce sound waves.

Roughness of the tooth surface, item d, will cause friction noise as the tooth surfaces slide and roll over each other. However, this does not appear to be serious in high-speed power gearing, which is generally very smooth (20 μ in. or less) and is lubricated with an oil film. As a rule, surface roughness will not result in significant noise unless the pitch line velocity is below 2000 ft/min or the surface roughness is over 25 μ in.

Although unbalance, item h, creates noise, it is generally possible to balance gears so well that this effect is negligible. Only for very large rotors at high speed does balance become critical, and then it results in relatively low frequency disturbances.

In a well-designed gear set, windage and oil splashing, items i and j, have very little effect **on** overall sound.

Usually, sound from sleeve bearings, item k, is negligible. In some cases, rolling element bearings may contribute appreciable sound, but this can be largely eliminated by standard procedures.

In most cases, seal rub or squeal, item m, is not a problem. It can be avoided entirely by labyrinth-type seals.

Proper design of the complete installation usually avoids vibratory effects from driving or driven equipment, items 1 and n. Thus, if the drive is a piston engine with a small number of cylinders, it may be expedient to incorporate a fly wheel or a torsion-isolating coupling. This may also be done. ~~when vibrations from a driven propeller blade tend to feed back,~~

By elimination, therefore, the predominant source of gear sound is the teeth themselves, in inaccuracies or deflections that create

variations in velocity as they mesh.

Acoustical Design of Gears

In a typical spur gear set, there will be important acceleration tendencies from both inaccuracies in the teeth and their deflections. As the teeth roll through mesh, the instantaneous stiffness of the teeth at the point of mesh will tend to vary. This creates accelerations and decelerations, even if the teeth are geometrically perfect involutes. Although it is theoretically possible to modify involute profiles to compensate for varying stiffness, in practice it is a hard manufacturing job to do so exactly. Furthermore, the required modifications change as the load changes, and so the design can be optimized for only one particular transmitted torque and will become progressively more improper as the torque varies.

In contrast to simple spur gears, helical gears usually have three or more sets of teeth in simultaneous contact with their contact line oblique to the tooth. As a result, a well-designed helical gear will have essentially constant stiffness for any phase angle of tooth engagement. This eliminates a major source of noise, and so helical gears are generally quieter than spur gears.

Table 1 lists gears that are apt to have 1) variable and 2) constant stiffness at the meshing point. The designer of very quiet gears should choose from the latter.

Table 1 Gear Types

Variable stiffness at mesh	Constant stiffness at Mesh
Spur	Helical
Circarc (Novikov)	Spiral bevel
Straight bevel	Hypoid
Zerol	Spiroid
Planoid	Helicon
Beveloid	Single enveloping worm
Face gear	Double enveloping worm

Waves in Helical Gears

In a well-designed helical gear, the combination of various tooth manufacturing errors may show up as waves on the tooth surface,

often lined up axially. Figure I is a photograph of such a wave pattern. As a result, a small angular acceleration and deceleration will occur as the point of mesh progresses from wave peak to wave trough. Experimental and analytical data have shown that wave variations as small as 10 pin. can lead to appreciable sound. With actual gears, waves with heights of as little as 50 pin. have produced definitely objectionable sound, and reduction to 20 pin. or less was very **beneficial**.

It is necessary to use specialized equipment to measure such small waves. Figure 2 shows an undulation checker, developed by General Electric Company, in use on a large gear.

Gear Noise Equations

The sound potentially produced by a specified inaccuracy in the **gears**, because of errors and changes in stiffness, may be computed from

$$PSL = 10 \log C \cdot (e^2 f^3 / d^2)$$

where PSL = potential sound level, decibels (see Table 2)

C = constant for a particular gear mesh; includes conversion factors, geometry, mass, inertia, pitch line velocity, etc.

e = double amplitude of inaccuracy, millionths of an inch

f = frequency at which inaccuracy occurs, cps

d = distance from acoustic center of gear case, ft

Table 2

Change, decibels	Ratio of change in sound energy
1	1.26
3	2.00
6	3.98
10	10.0
20	100.0
30	1,000.0
40	10,000.0

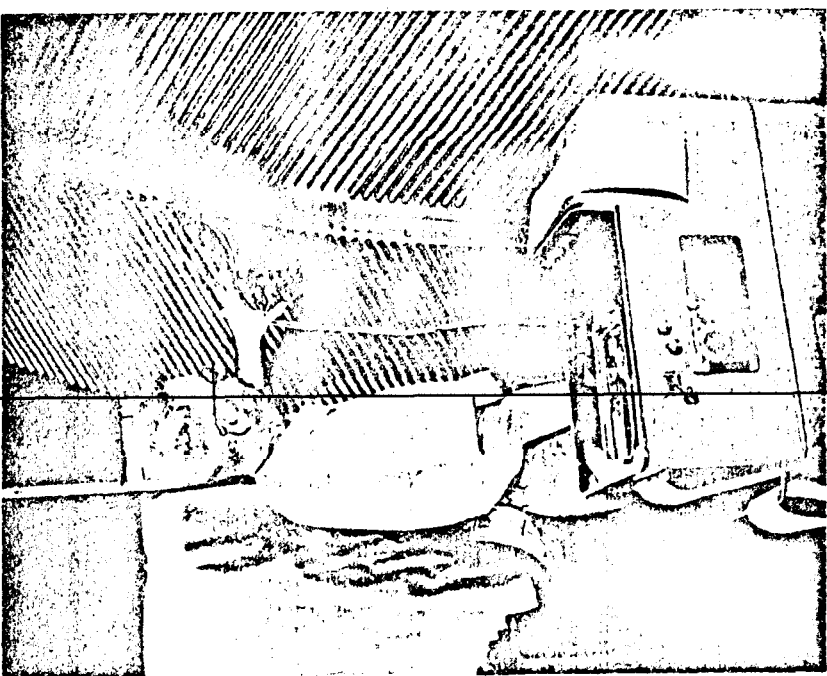


Fig. 2 Undulation checker, courtesy of General Electric Company, Lynn, Mass.

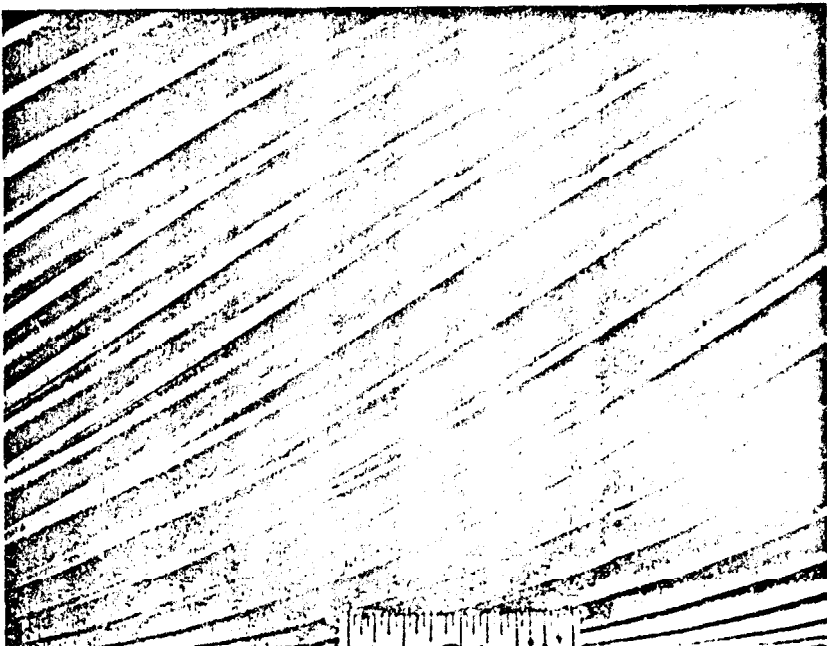


Fig. 1 Wave pattern on large helical gear teeth.

This equation is quite general, and modifications can be adapted to specific cases. It is expected that two or three years of further analysis and experimentation will be necessary to cover the whole field of gear applications with suitable noise formulas.

Figure 3 shows calculated and measured noise output for a large marine unit at about 10 ft. The calculations were based on measured inaccuracies in the various tooth rotors. Although part of the sound developed at the mesh was probably lost before measurement, the experimental and theoretical plots are parallel.

Noise Insulation

After the gear sound leaves the gear mesh, its principal path is 1) from gear teeth through gear rim and web to shafts, 2) from shafts to bearings, 3) from bearings to casing, 4) from casing to air and supporting structure, and 5) from supporting structure to other structures or (with torpedoes) to water.

Figure 4 is a schematic of a simple gear arrangement, showing where the sound from tooth mesh might be blocked by attenuation devices.

As an example of sound attenuation on a gear rim, recent work has shown that a gear with 30 in. pitch diameter and 18 in. face width could have as much as a 25-db reduction in the sound transmitted from the rim to the shaft by the use of a relatively complex sound attenuating design in the rim.

As an example of sound attenuation between a gear bearing and a gear casing, recent work has shown that the use of a special device to attach the bearing to the casing could reduce sound transmission as much as 10-db.

As an example of sound attenuation between the gear mesh and the gear casing, the addition of sound-attenuating devices to the outer surface of the gear casing provided an approximately 10-db reduction. Thus, Fig. 5 is a plot of sound intensity vs octave bands for a large gear casing. The upper curve is for the original machine, and the lower curve was obtained with a moderately sophisticated treatment of the machine.

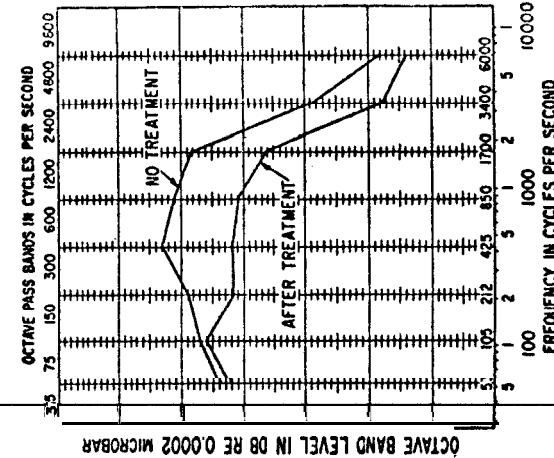


Fig. 5 Effect of casing treatment on airborne sound.

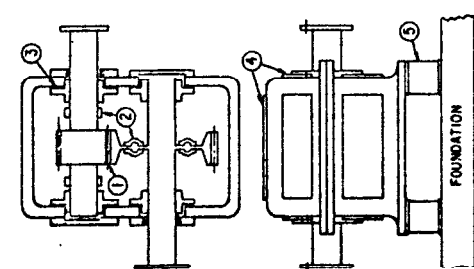


Fig. 4 Typical gear train showing points for sound insulation.

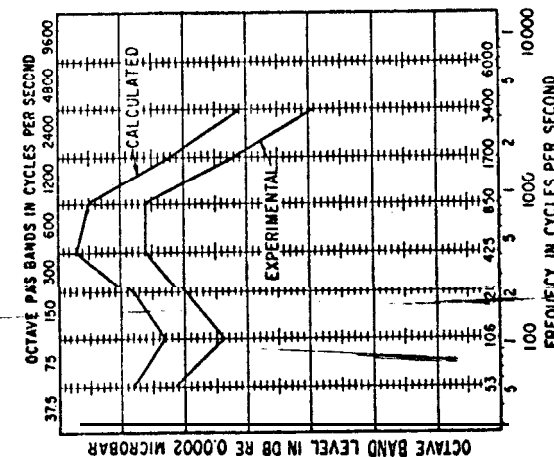


Fig. 3 Example of calculated and recorded airborne gear sound.

Fig. 4 Typical gear train showing points for sound insulation.

Where water-borne sound is important, it is very important to block the transmission of sound energy from the casing to the supporting structure. Vibration isolators are a powerful means of doing so. In selecting such devices, consideration must be given to alignment, torque, and other operational problems; and the flexibility of these isolators must be substantially greater than the structure to which they are attached. In several such applications, reductions in the order of 20 -db have been achieved.

Summary

If necessary to meet very critical limits on gear sound, the designer should 1) minimize the generation of sound at the gear mesh by the right choice of gear teeth, an appropriate geometric design in regard to pitch, pressure angle, etc., and by rigid control of tooth accuracy within manufacturing limits; and 2) block the transmission of the sound to air or water with special attenuating devices at appropriate locations.

Acoustical engineering of a gear set is as reasonable and logical as is engineering of gear power capacity or efficiency. The basic engineering and experimental work on the latter has been going on for about 100 years and is now highly developed, although only in the last few years has there been real concern about gear sound. Thus, formulas, principles, and data relative to the acoustical design of gear units only now are developing into full-fledged practice. Nevertheless, it now appears possible to achieve desired quietness in almost any field of gearing. However, expense and work are involved in doing so.

ACOUSTIC STUDIES ON POWER TRANSMISSIONS

Moe William Rosen*

Naval Undersea Warfare Center, Pasadena, Calif.

Abstract

A program of experimental research, using a special facility to study precision gears, has uncovered new fundamental information on straight toothed (spur) gear noises. The experiments were performed at speeds which ranged from 2500 rpm to 27,500 rpm. The data obtained include spectra analyses and total noise energy outputs of the gears as a function of power and speed. The gears were considered as nonuniform point sources radiating into a sphere, and the total noise output was obtained by integrating data taken at numerous points. Apparently gear noises are caused by the impact of teeth upon each other as they mesh, and by a bouncing action of the teeth while they remain in mesh. This produces intense acoustic radiation at mesh frequencies; and also at harmonics of the mesh frequencies which were detected and measured up to the sixth. Magnification of gear noises occurs when mesh frequency approaches the natural vibrational frequencies of the gear discs or transmission case. At very high speeds, "white" noise is produced over a wide band. Also at high speeds, much of the noise output appears associated with shock waves as air is displaced from meshing teeth. A new acoustic energy rule for gears was discovered: the total acoustic energy radiated by spur gears at constant tooth velocity is directly proportional to the power transmitted. Finally, methods to decrease noise output of spur gears, which were uncovered during these experiments at the U.S. Naval Ordnance Test Station, are detailed.

Introduction

A program of experimental research was undertaken at the U. S. Naval Ordnance Test Station (NOTS) to improve the basic knowledge on gear transmission noises.

This paper was also published as Naval Ordnance Report 6560, U. S. Naval Ordnance Test Station, China Lake, Calif.

*Senior propulsion Research Engineer and Scientist, Propulsion Division.

The work was carried out in a special "transmission drive facility",¹ built at NOTS to power transmissions smoothly and quietly at speeds up to 30,000 rpm. Its noise at these speeds is almost negligible, thus permitting valid measurements of transmission noises.

The first two transmissions studied, identified as the Mk 40 and Mk 42, are representative of the finest spur-gear (straight-toothed) conventional transmissions available for powerplants. They are both of the planetary type. A description of the experiments upon them is given below. The work brought to light a number of important phenomena basic to the noises of transmissions as next discussed. Methods for decreasing noises of spur gears, developed from these and other studies at NOTS, are enumerated in the Appendix.

Description of Tests

Figure 1 shows the Mk 40 transmission and Figs. 2 and 3 show the Mk 42 transmission installed in the high-speed acoustic drive facility. The transmissions are out-of-doors in an acoustically dead environment. A steam turbine in a closed concrete room is connected to them by a long high-speed shaft through the wall. Power is transferred out of the transmission to an enclosed electric dynamometer through a heavy shaft and sleeve-bearing system. It absorbs the load by generating current dissipated in an electrical resistance grid. Accurate torque and speed measurements can be made with this dynamometer. An electric eye registers turbine speed.

The drive facility is capable of exceedingly smooth and quiet operation, even when the turbine and the 39 inch long shaft are running at 30,000 rpm. Carefully designed elastic mounts isolate (vibrationally) the transmission from the support structure and the shafting, with the results that the noise measurements reflect a true picture of the primary transmission radiation, and practically no radiated noise from the drive.

Measurement and Theory

A concept of "spherical measurement" was adopted in which the transmission is considered a nonuniform point source of radiation. Because of the anechoic environment and the quietness of the driving machinery, we may consider the transmission acoustically as if it were suspended in space, apart from any other material object and driven by a remote source of power. A swinging apparatus carries a sensitive microphone on the surface of an imaginary hemisphere about the machine while it is running at 8 steady rate and at constant power. The instru-

ment takes many readings (a typical set on one meridian is shown in Fig. 4), and these are integrated into the total radiated acoustic energy.

$$E = 2\pi I A \quad (1)$$

where I is the intensity (w/cm^2) of noise observed at each point, and A is the spherical area (cm^2) applicable to the intensity reading and the factor 2 comes from assuming identical lower and upper hemispheres.

The noise intensity I is computed from instrument decibel (db) readings as follows:

$$\text{db} = 20 \log_{10} (p/p_0) = 10 \log_{10} (I/I_0)$$

$$10^{\text{db}/10} = I/I_0$$

Therefore,

$$\text{intensity } I = I_0 \cdot (10^{\text{db}/10})^2$$

where

db = decibel observation of overall sound pressure level
 p = sound pressure observed, dyne/cm^2
 p_0 = reference sound pressure, 0.0002 dyne/cm^2
 I_0 = reference intensity of sound, 10^{-16} w/cm^2 (corresponding to 0.0002 dyne/cm^2)

The spherical technique permits comparison of the acoustic properties of different machines and measurements of their absolute radiations. Through systematic tape recordings and the frequency spectrum analyses that were made, the characteristic structure of the noises was shown. The resulting data show smooth and consistent progression with operational changes that are amendable to logical interpretation.

The sensing instrument was a Western Electric 640AA microphone, operating on the condenser-diaphragm principle and designed for 1 to 30,000 cps.

Mk 40 Transmission

The Mk 40 gear train is a single-stage planetary system with straight spur teeth. A central pinion running at turbine-input speed drives three planets on fixed centers, which deliver the torque to a single internal-toothed ring gear connected to the output shaft. Figure 5 shows the design of this transmission. The ratio of the machine is 3.09756 to 1. After

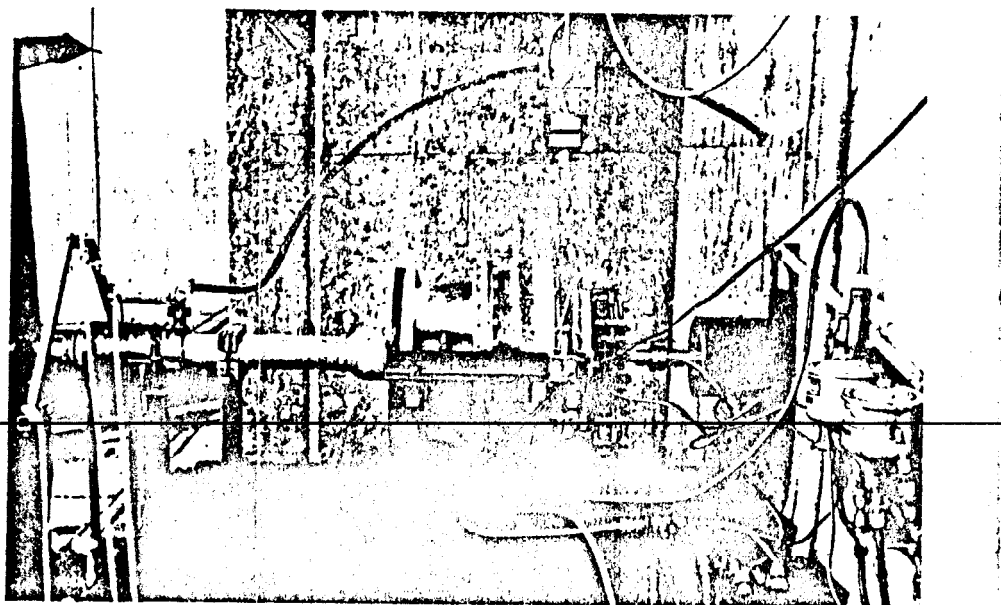


Fig. 1 Mk 40 transmission mounted in test section of acoustic facility. Microphone is at top.



Fig. 2 Mk 42 transmission mounted in acoustic drive facility. Input power is from shaft at right, and output goes to dynamometer at left.

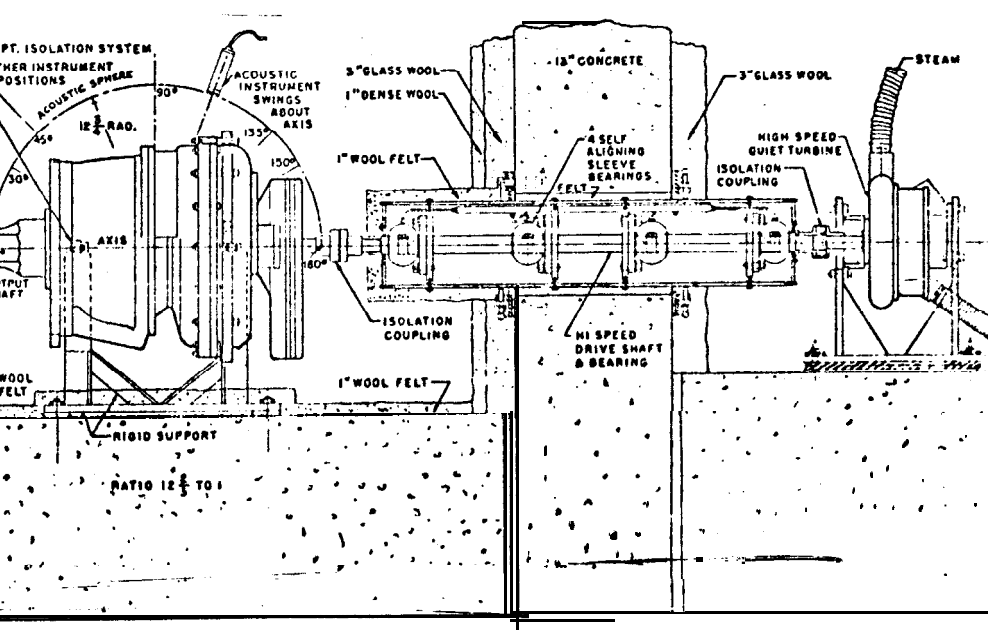
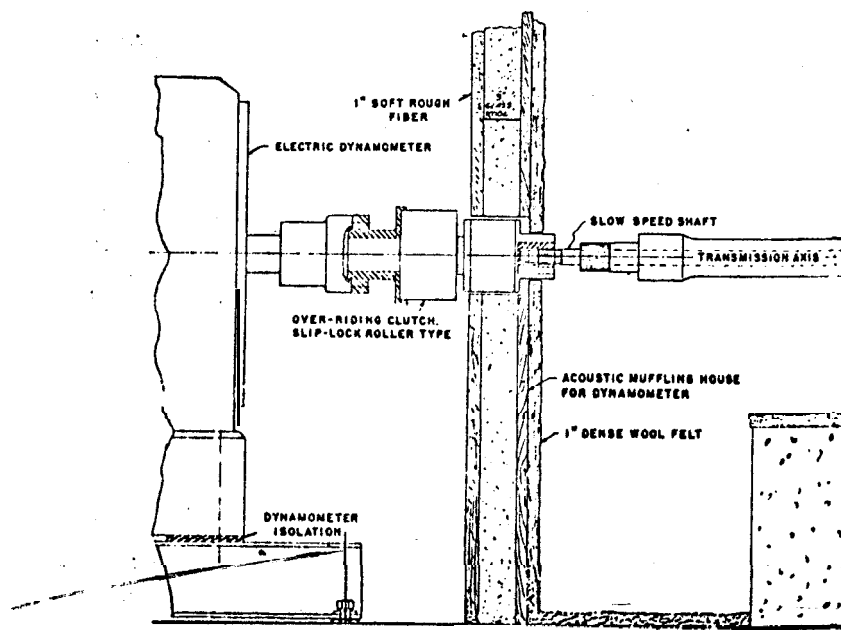


Fig. 3 Drawing of Mk 42 transmission installed for tests, showing design of turbine drive and high-speed power shaft.

having been run, the teeth measured to an accuracy within 0.0002 in. in the shape of the involute curve, the tooth spacing and the concentricity. An occasional error of 0.00025 in. was found. These are gears of great accuracy.

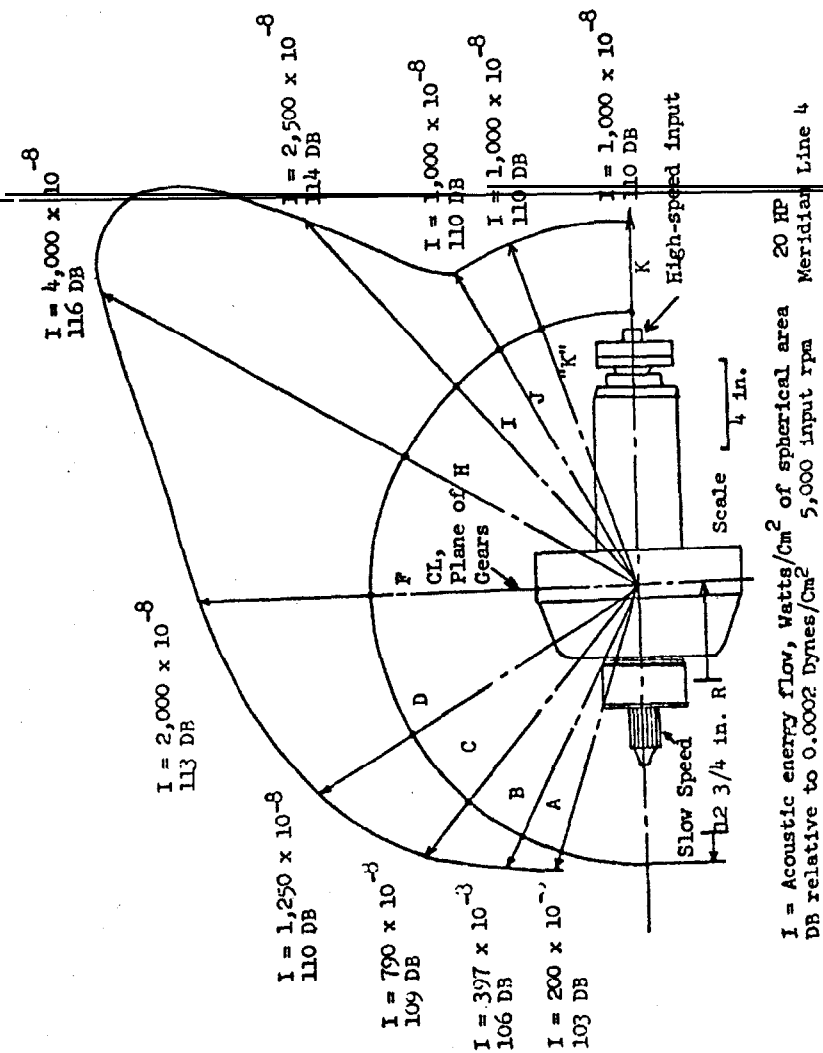
The transmission was isolation-mounted and lubricated and cooled with a fine internal spray of oil. Its rotating parts and shafts were balanced precisely and the machine lined up to the drive within 0.001 in., connected through specially designed isolation couplings. It was operated at steady speeds from 2500 to 27,500 rpm and at steady powers up to 70 hp. This gear train was designed for 1000 hp.

The machine was operated in a series of runs, each systematically higher in speed or power. While operating steadily at each particular constant speed and power, 37 observations of total acoustic intensity at points around the hemisphere were made. Each reading was a measurement of total sound-pressure level in decibels relative to 0.0002 dyn/cm² in the frequency range 0 to 30,000 cps. The readings were integrated by Eqs. (1) and (2) to give the total acoustic energy radiated by the machine.

Figure 6 presents a series of these integrated readings and shows the changes of noise energy as speed and shaft power are increased, thus providing a chart of the total noise radiation versus rotational speed, tooth speed, and mesh frequency. The natural frequencies of some of the transmission components--case parts, shafts and gear bodies--experimentally determined by oscilloscope are located on the chart as vertical lines.

The rapid rise of noise energy between 0 and 5000 rpm occurs in a region where case parts evidently resonate to the tooth mesh. Resonance of the planet gear disks, evidenced by the second peak, results from their thinned-down "I" construction, which causes them to "ring". The pinion, solidly constructed and of approximately the same size as the planet, stays level or declines from the resonant region as the speed is increased to 20,000 rpm, where it rises sharply again. Although the machine was not run above 27,500 rpm, indications (Instrumental and aural) were that a very rapid jump was imminent at 30,000 rpm.

At 20 kc, the response-of the microphone is down 5 db compared with the lower frequencies. Consequently, the curves above 15,000 or 20,000 rpm actually rise at a faster rate than shown. The integrated data on Fig. 6 are presented exactly as measured without microphone correction.



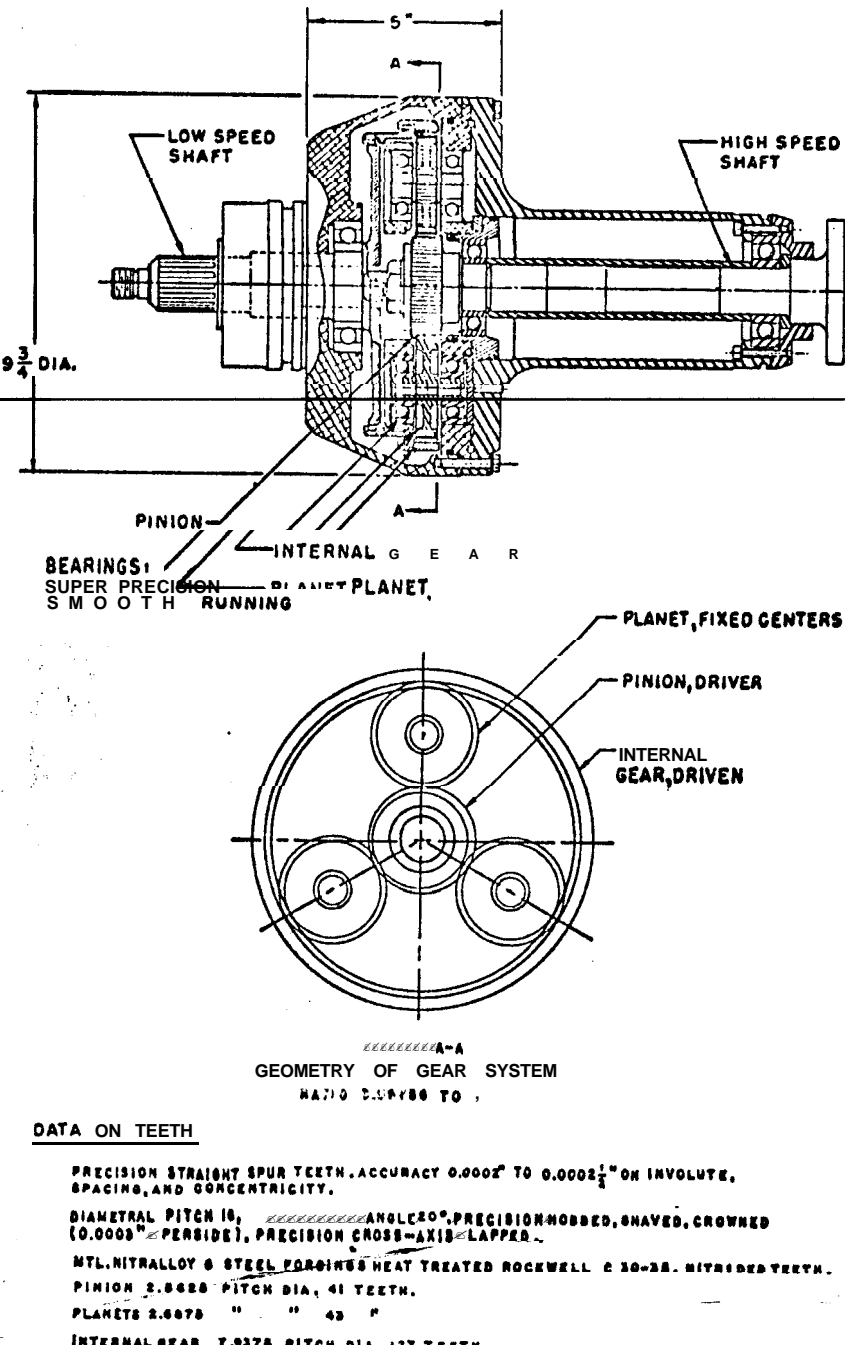


Fig. 5 Drawing of Mk 40 spur gear transmission.

The maximum individual noise readings (not shown on Fig. 6) were obtained 1 in. from the surface of the transmission on the input side. They registered 119 db at 27,500 rpm with 60 hp output.

In addition to total-noise measurements, magnetic-tape recordings were made at each speed and power and then machine-analyzed to provide the frequency spectrum analysis of Figs. 7 and 8. The upper charts show the intensity residing in a **bandwidth** of 1 cps span when the distance from the center of the transmission to the microphone is $12\frac{3}{4}$ in. The sum of all the noises at all frequencies --the total noise pressure--has a **considerably** higher decibel value than the unit decibel values shown. The lower plots in Figs. 7 and 8 give the noise spectra calculated on the basis of a bandwidth of 1000 cps and include a microphone correction.

Figure 7 clearly shows the tooth-mesh frequency and its first six harmonics. The vertical arrows indicate the points where the harmonics are computed to be, these coincide with the experimental peaks. Note that the sixth harmonic is detectable even at 30 kc. The figure also shows that the second harmonic of the tooth mesh is about 10 db higher than the fundamental tooth mesh frequency itself and about 5 times wider in range of frequency disturbance, approximating 50 times the energy of the fundamental.

It is believed by this writer that the intense harmonics of the tooth mesh are caused by "bouncing" of the teeth. When a tooth first strikes its mate, the blow causes elastic deformation in the tooth, in the gear and in the shaft. The gear mass vibrates about its rotational axis, thus bouncing the tooth several times on its mating tooth, which is also vibrating. With each bounce, the driving torque slams the tooth against its mate with a force that may be many times greater than the average driving force. This may explain the "dynamic force" between teeth: gear teeth experience actual forces considerably greater than the computed average driving force and should be designed to resist them. The intense harmonics are attributed to the fact that the number of bounces can only be a discrete multiple of the number of times the teeth are placed into mesh.

Figure 8 plots data taken at 27,500 rpm and 60 hp. The valleys are filled in and peaks do not occur. There is largely "white" noise, and the very high plateau extends to 30 kc. (There may be a peak at the second harmonic of the tooth mesh at 38 kc which the microphone could not measure.) Although this curve looks smoother, the energy it displays is considerably greater than that of Fig. 7. More complete sets of charts for

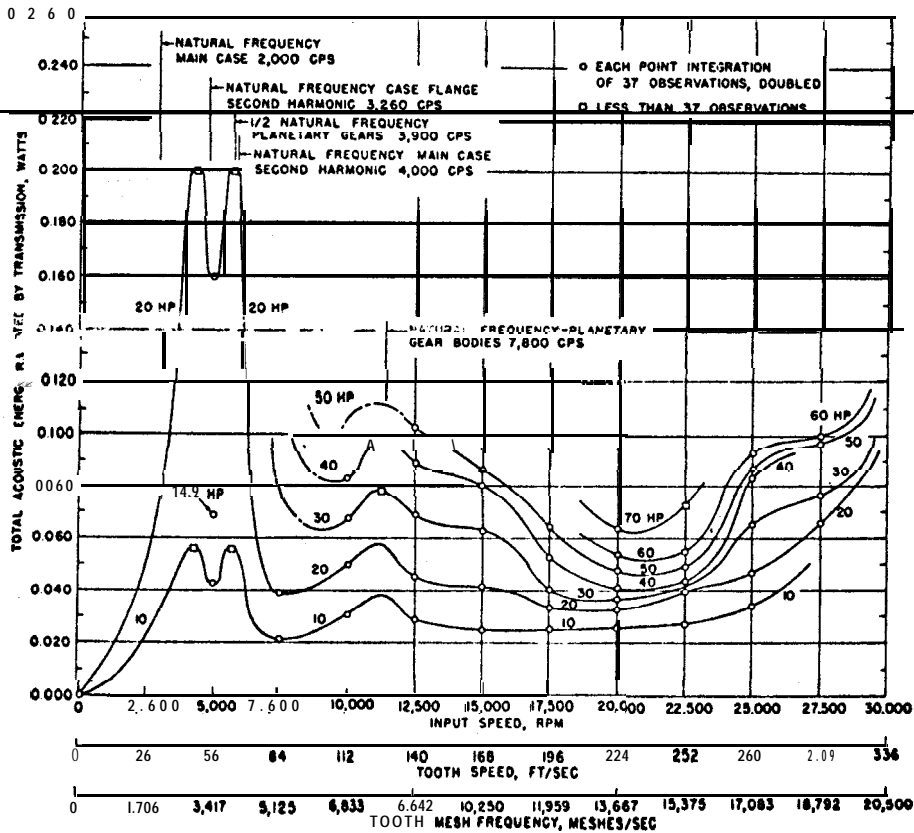


Fig. 6 Mk 40 planetary spur gear transmission noise output at constant shaft power.

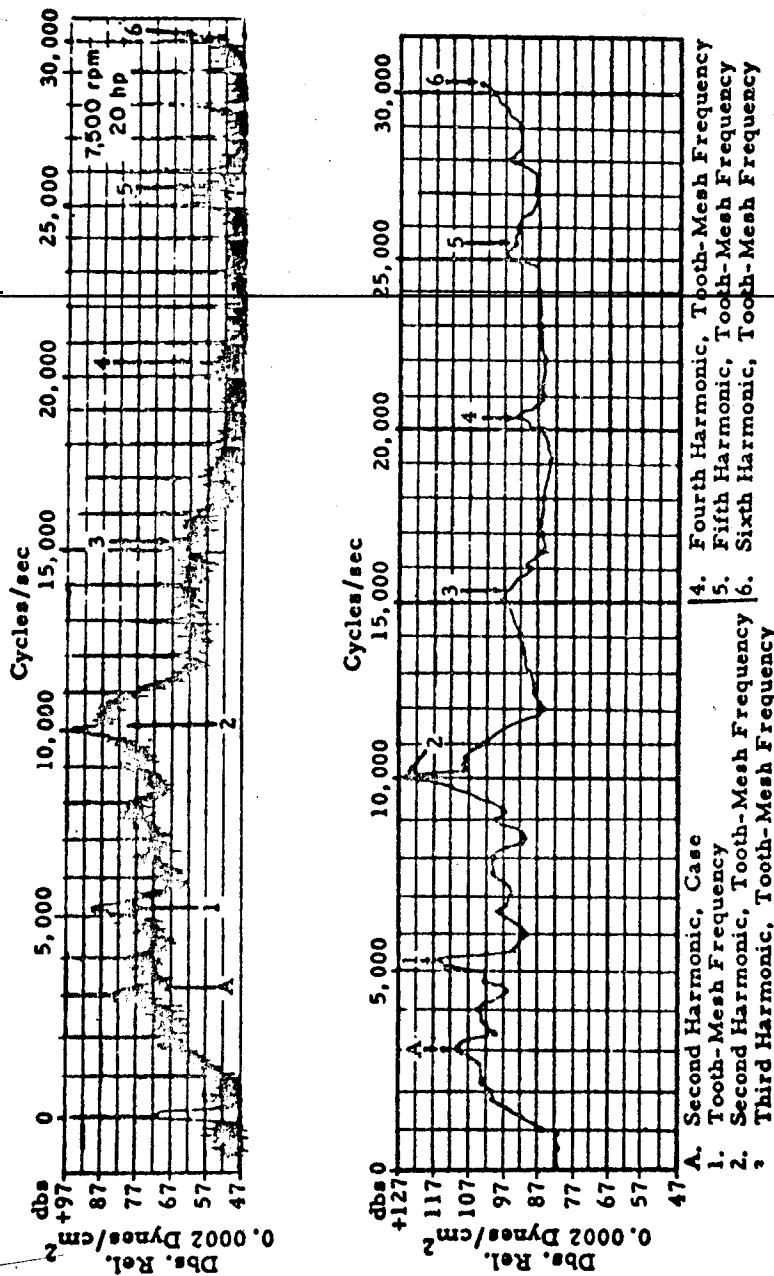


Fig. 7 Typical frequency spectrum analysis of the Mk 40 transmission at 7500 rpm and 20 hp. Sharp peaks occur at tooth mesh frequency and its harmonics. (Lower plot is derived from upper spectrum using 1000-cps bandwidth and correcting for microphone response.)

this transmission may be found in Ref. 2. Figure 8 illustrated that, at high speeds, geared transmissions radiate **intense** acoustic energy over an entire broad spectrum.

Another interesting phenomenon brought to light by these experiments is that the radiated acoustic energy is directly proportional to the shaft power when speed is constant. This is shown in Fig. 9, where **total** acoustic energy is plotted vs shaft power in constant-speed curves: the points fall into straight lines with a few exceptions and the slope of each is different at each speed. This relationship was also obtained with the Mk 42 transmission, as shown in Fig. 10. Since each point is the integrated value of any observations, this proportionality demonstrates an "acoustic energy rule".

Mk 42 Transmission

The Mk 42 transmission is a double planetary system with straight spur teeth delivering **contrarotating** power on two concentric output shafts. Since both shafts are locked together by the gear action, the dynamometer was connected to the central output shaft **only**. The transmission was suspended on isolation mounts (Fig. 3). The machine normally contained two turbine wheels, which were removed for the tests. An auxiliary gear train was also disconnected.

These gears have straight spur teeth of steel, carburized and hardened to Rockwell 60. Other specifications are as follows: 14 diametral pitch of first planetary set (powered); 18 teeth on pinion of first planetary set (powered); 1.2857-h. diametral pitch of second planetary gear (powered); 20° pressure angle of tooth form; and 18 diametral pitch of second planetary set (unpowered). Manufacturing accuracy was measured at 0.0002-0.00025-in. error in involute, tooth spacing and concentricity. Backlash was 0.004 to 0.008 in.

The machine was operated at 2500 to 20,000 rpm and up to 40 hp. It was designed for 600 hp and as a powerplant normally operated at 200 to 250 hp. Measurements were made with the same instruments and following the **same** principles as described previously, except that 25, instead of 37, observations were made on the hemisphere at each steady operating speed and power.

Figure 11 is the resultant chart of integrated points of **total radiated energy**. The rise between 5000 and 10,000 rpm indicates case-component resonances near tooth-mesh frequencies. The upward "swoop" between 15,000 and 20,000 rpm again emphasizes

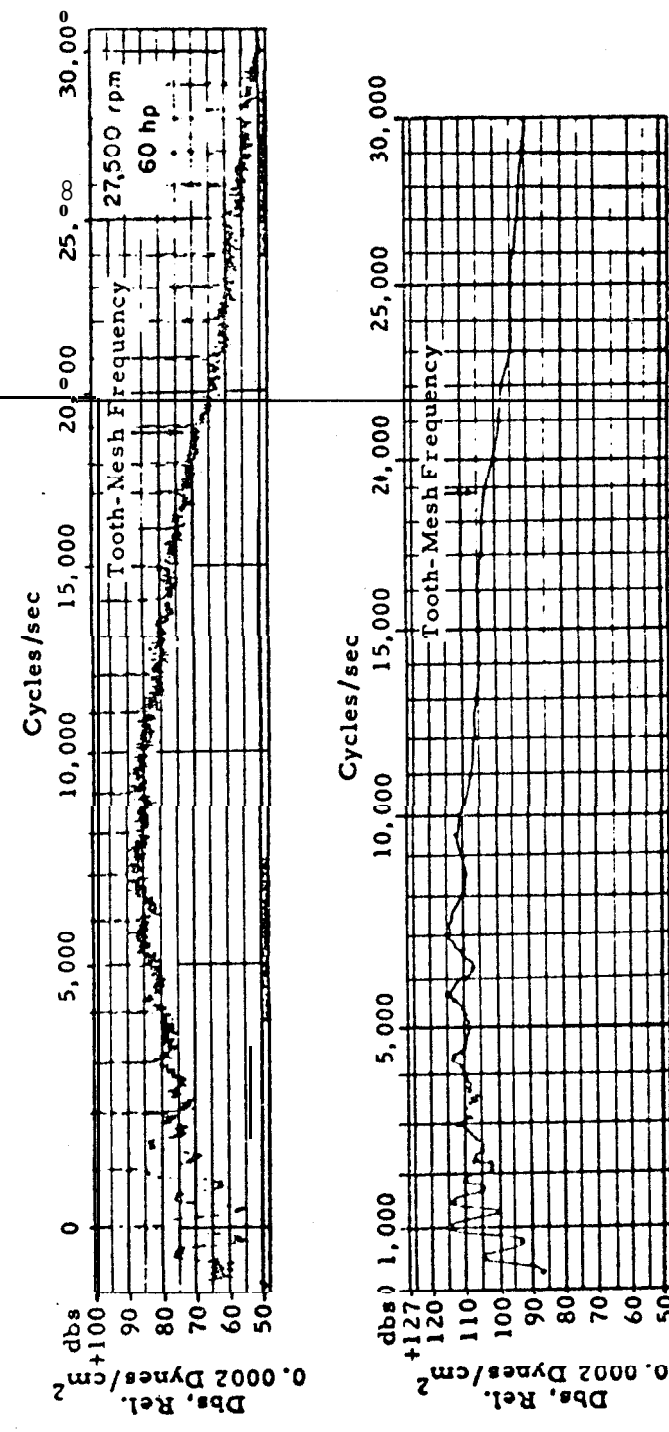


Fig. 8 Frequency spectrum analysis of Mk 40 transmission at 27,500 rpm and 60 hp. Noises are at high level at both low and high frequencies and transmission radiates essentially "white" noise.

entire design capabilities under conditions duplicating those at sea. It immediately and simultaneously controls, indicates, and records all parameters of significance in evaluating propulsion performance.

This paper reports the present basic capabilities of the facility, which can be modified to meet further test requirements.

General Facility Configuration

The facility comprises a control room, dynamometer room, main test cell, air cell, fuel cell, oxidizer cell, and sea water cell, all identified in Fig. 1. It was designed to test torpedoes with high-energy fuels and oxidizers, and so the building containing the five cells is constructed with 18-in. reinforced concrete walls and ceilings. The fuel cell, oxidizer cell, and main test cell are designed for rapid and unidirectional release of gases in case of explosion. All entrances to cells and rooms are from the outside, and there are no interconnecting doors.

A zone-type carbon dioxide fire-extinguishing system, shown in Fig. 2, is provided. Each cell and room has an independent system with automatic thermostatic detector. Manual controls are also provided.

The fuel cell and oxidizer cell are provided with independent dilution-type floor drains, each discharging into larger, independent exterior pits. In an emergency, the fuel and oxidizer may be rapidly discharged from their tanks and diluted to a safe condition.

Each cell has its own high-volume, induced-draft ventilating system to remove combustible gases. These ventilators automatically shut off if the CO₂ fire-extinguishing system is energized.

Control Room

The control room of Fig. 3 contains the control console, the electrical-transducer signal-conditioning equipment, and a multichannel oscilloscope recording system. The console has a control section located immediately in front of the test operator(s), and an instrument section with function-indicating meters located on a graphical representation of the entire facility. The control section contains and identifies all switchgear and has fault-indicating lamps that give notice of

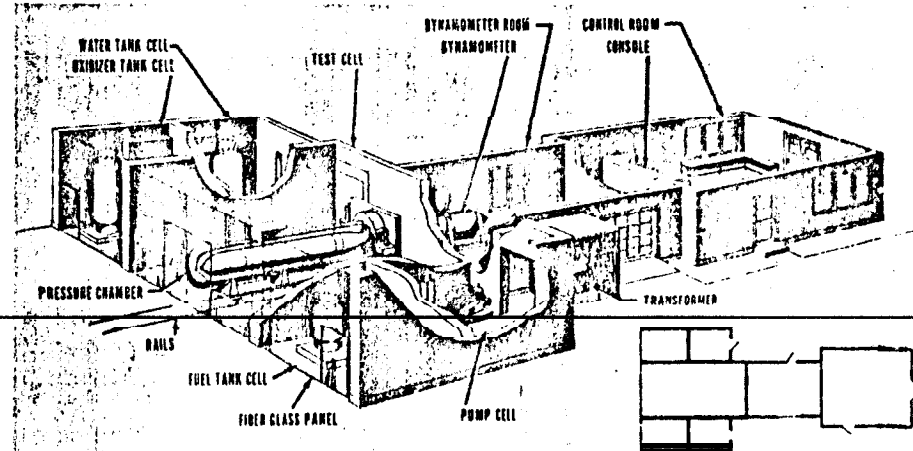


Fig. 1 An artist's view of the Torpedo Propulsion Test Facility.

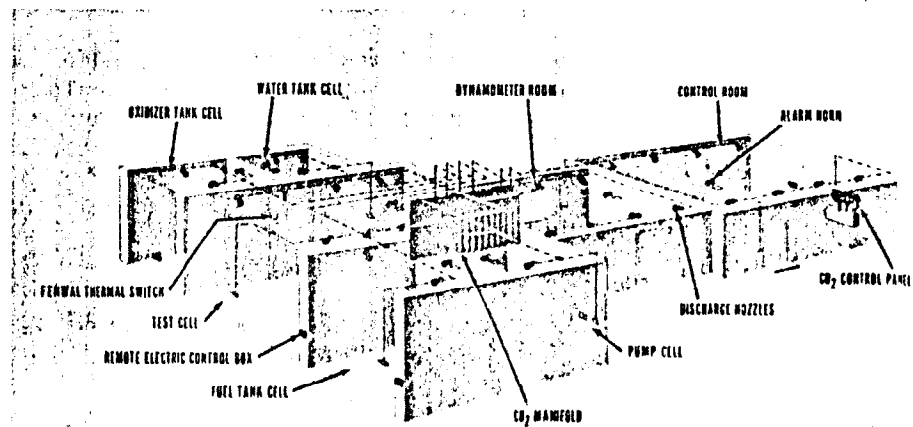


Fig. 2 The CO₂ fire extinguishing system.

possible trouble, such as low oil pressure, Low liquid levels, abnormal temperatures, etc.

The facility can test torpedoes under programmed simulated depth conditions. Thus, the test engineer may lay out a depth schedule for a particular test and program it into the depth controller, as indicated in Fig. 4. The operator may manually override the programmed condition, if necessary. The system can attain simulated depths to 5600 ft in sea water at programmed variations up to a maximum of 56 fpm, which is equivalent to a 34-knot vertical ascent or descent.

Test torpedoes discharge the exhaust gases independently of the ambient sea water pressure against a pressure regulated within a range of ± 100 psi of the ambient sea water pressure. With the exhaust gas pressure set differentially in this manner, it will vary in accordance with the programmed sea water pressure. Fig. 4 shows the control units that indicate ambient sea water depth and exhaust gas differential pressure.

The tripropellant tankage is graphically represented on the instrument panel where the liquid level, tank pressure, and liquid flow rate are indicated for each tank. An air pressure-over-liquid (POL) system controls the propellant delivery pressure in accord with the programmed sea water depth conditions. The controllers, shown in Fig. 4, indicate and regulate pressures differentially with respect to depth pressure, and each may be set within a range of 0 to 200 psi. The operator's console contains a sequence timer for actuating the three propellant delivery valves leading from the external propellant tanks.

The torpedo power absorption dynamometer is graphically represented on the instrument panel (Fig. 3). Torpedo propeller shaft speeds from 0 to 2000 rpm are measured, and torques from 0 to 3500 ft-lb.

Eight meters along the top of the instrument panel shown in Fig. 5 indicate temperatures, pressures, liquid flows, etc., within the test torpedo. Each can be set for a maximum safe condition, and if the preset value is exceeded, an indicating lamp will turn on.

Signal-conditioning equipment to convert the low-level a.c. and d.c. electrical signals from the test transducers to the higher-level d.c. signals needed for the indicating and recording system is located in cabinets adjacent to the control console. The resultant signals are compatible with analog-to-digital data analyzing computers.

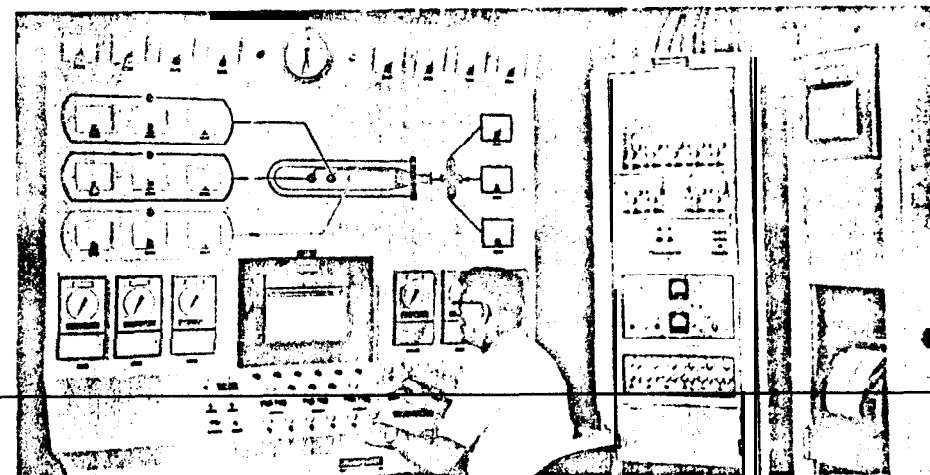


Fig. 3 The control console and signal processing equipment in the control room.

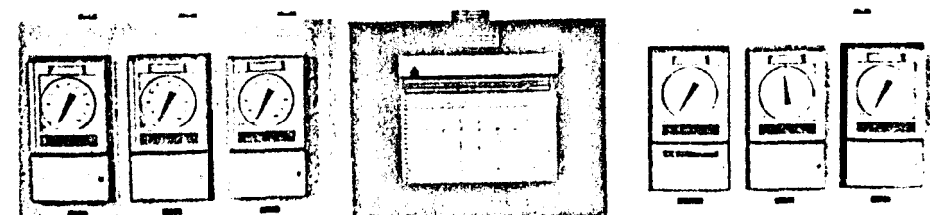


Fig. 4 Indicating controllers.

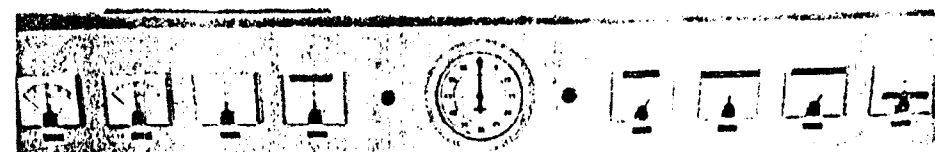


Fig. 5 Torpedo data indicators.

A 24-channel recording oscilloscope is used to record low- and high-frequency transient signals. The facility wiring and junction boxes can accommodate up to 60 variables, and so additional recorders can be added, or channels on the existing recorder can be ~~re~~ ^{selectively} commutated between incoming signals.

Dynamometer Room

The dynamometer room contains the hydraulic absorption dynamometer of Fig. 6, the sea water pump of Fig. 7 and associated electrical switchgear, and the valving and tankage for the CO₂ fire-extinguishing system.

The dynamometer can absorb 1000 hp at shaft speeds from 900 to 3000 rpm in either direction of rotation. The unit is cradled and provided with a tachometer for measuring speed and with a strain-gage load cell for measuring torque. Water circulated through heat exchangers dissipates the absorbed energy.

The pump supplies sea water to the test pressure vessel at a nominal rate of 75 gpm and at pressures from 0 to 2500 psi. The sea water circuit can pump make-up from the supply line, recirculate within the circuit, or make-up and recirculate. The circuit includes heat exchangers to vary the sea water temperature.

Test Cell

The test cell contains control components of the depth system, transducers for instrumenting the torpedo, and equipment for propellant delivery. The two tanks, shown in Figs. 8 and 9 are used to test the torpedoes. One is for depth-simulation studies and is closed with a working pressure of 2500 psi, whereas the other is open and is for testing at sea level conditions. The tanks are on rails and may be easily moved into place. Both accommodate torpedoes up to 30 in. in diameter and 24 ft in length and include necessary torpedo support systems. Each mates with the fixed bulkhead of Fig. 10. The latter supports a seal system that passes the torpedo propeller shaft through a 24-in. reinforced-concrete wall to the absorption dynamometer. Exhaust gases from the propeller shaft are discharged into an exhaust accumulator, released through a pressure control valve, and discharged external to the building.

Ports through the bulkhead deliver propellants from the external tankage to the torpedo (if required) and permit

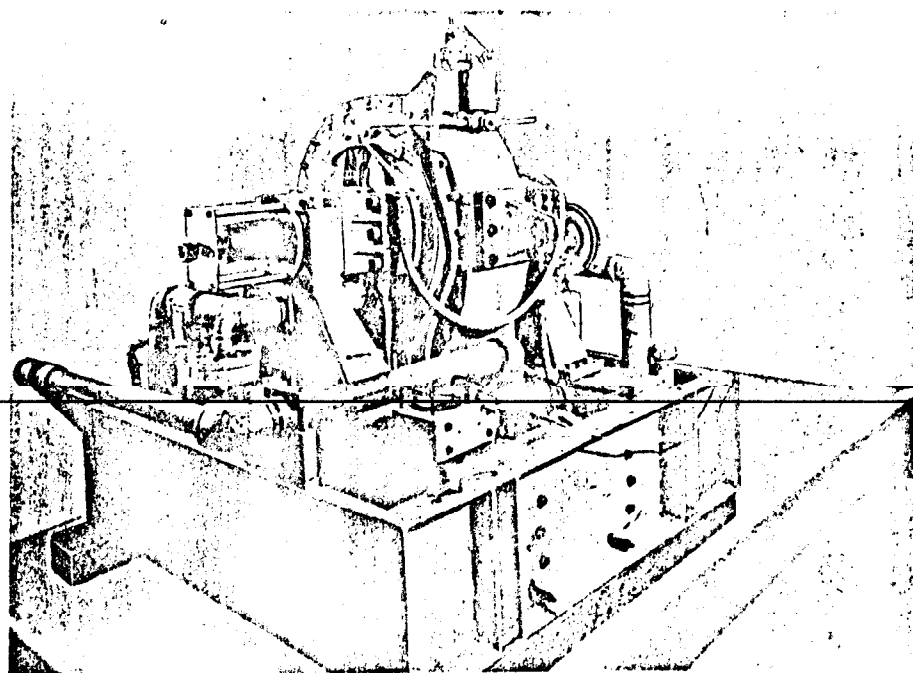


Fig. 6 Power absorption dynamometer.

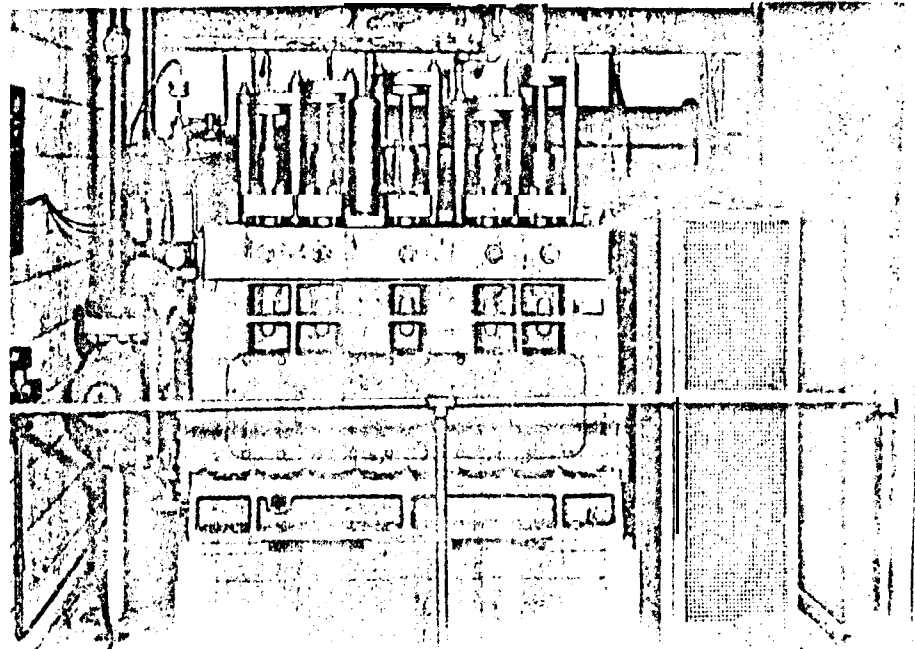


Fig. 7 High pressure seawater pump.

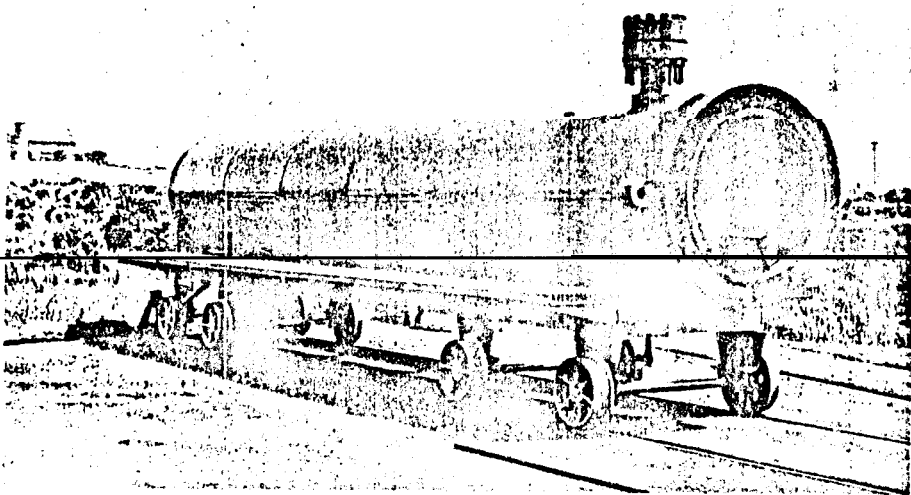


Fig. 8 Open torpedo test tank for surface conditions.

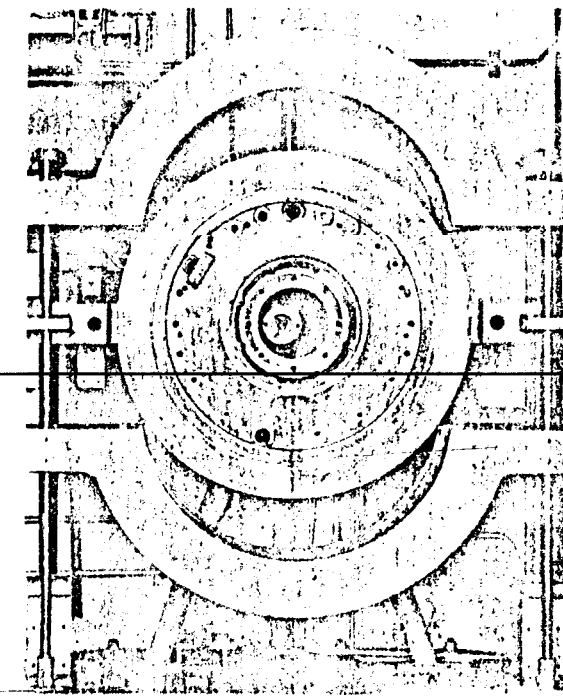


Fig. 10 Fixed bulkhead.

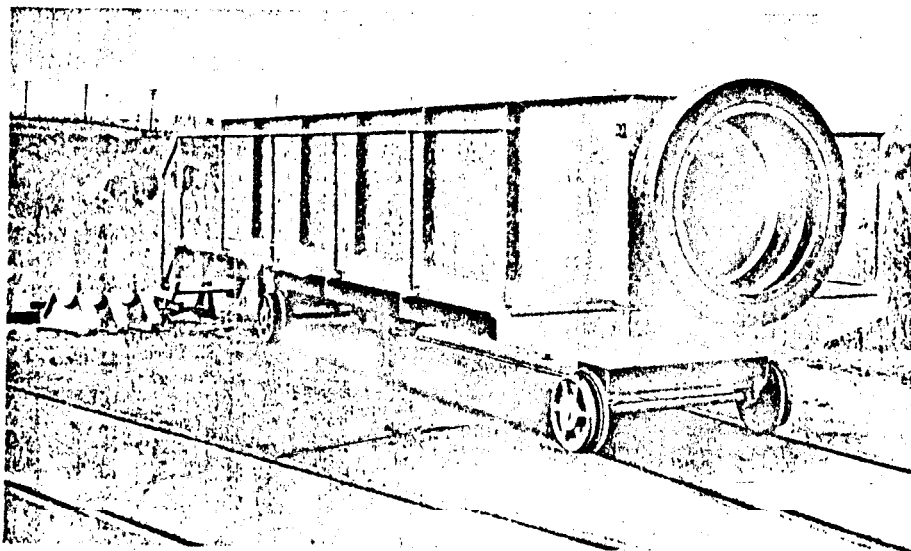


Fig. 9 Closed torpedo test tank for depth simulation.

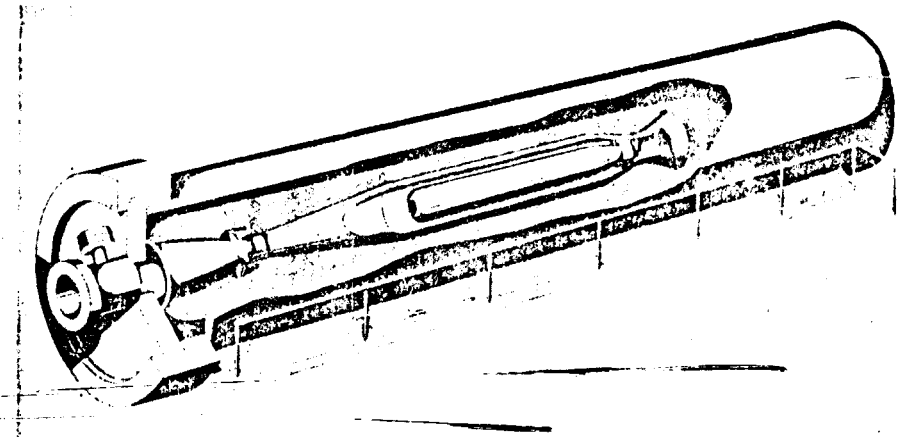


Fig. 11 Test installation.

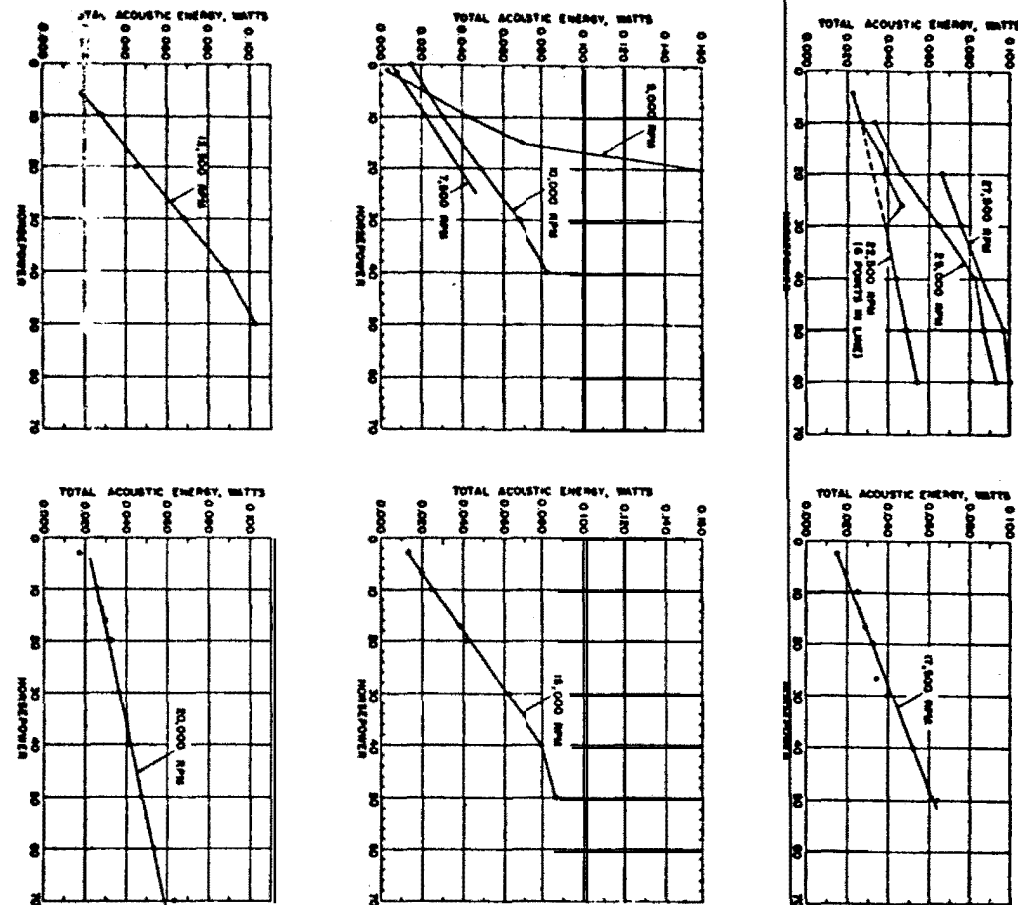


Fig. 9 Acoustic energy vs. horsepower for the Mk 40 transmission at constant speeds. Each data point represents the integration of 37 observations.

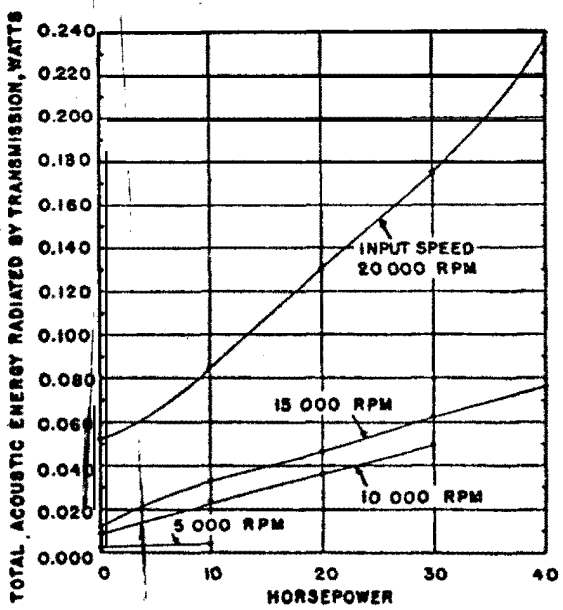
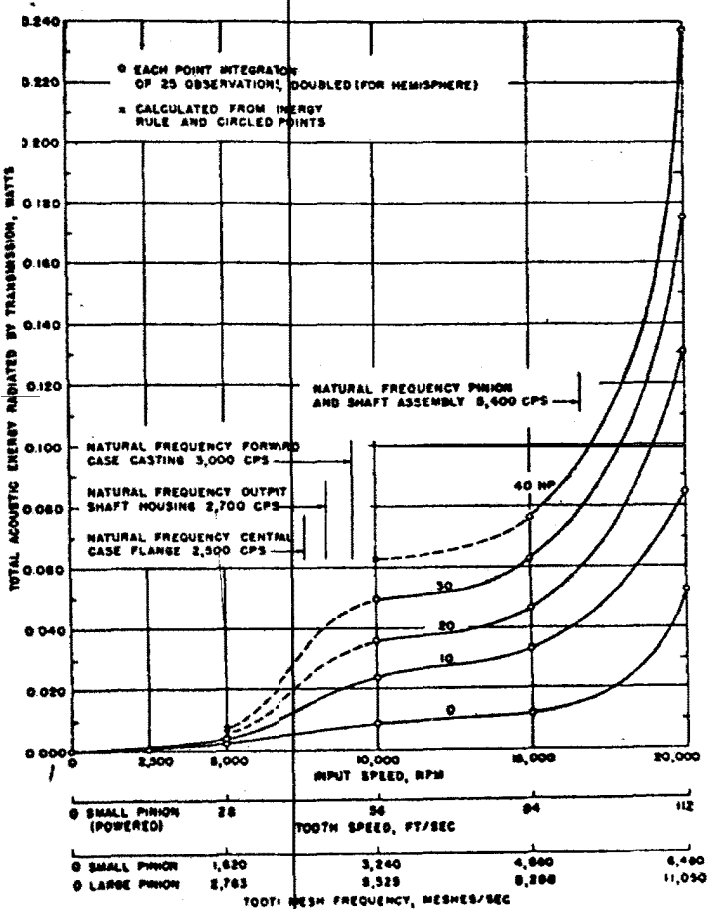


Fig. 10 Acoustic energy vs. horsepower for the Mk 42 transmission at constant speeds. Each data point represents the integration of 25 observations.

Fig. 11 Total noise energy radiation of the Mk 42 transmission vs. various speed functions.



TOOTH MESH FREQUENCY, MESHES/SEC

	0 SMALL PINION (POWERED)	28	34	44	64
0 SMALL PINION	1,620		3,240	4,960	6,480
0 LARGE PINION	8,763		8,329	8,298	11,050

sizes that large noise increases can result from relatively moderate speed increases.

The maximum individual total noise readings obtained with the Mk 42 transmission were 118 db at 12 3/4 in. from the center on the input side near the axis, and 130 db (extremely intense) at the opening of the exhaust duct in the case. (There were no exhaust gases.) Both readings were taken at 20,000 rpm and 40 hp.

The runs were recorded on magnetic tape from which frequency spectrum analyses were made as before. Figure 12 shows some of these spectra. Vertical arrows were placed on the frequency scale of these charts by calculation. As before, they fall on

experimentally found peaks or hills. The charts of Fig. 12 show the intensity residing in a bandwidth of 1 cps span. The changes which occur as speed and power are systematically increased may be seen. The frequency spectrum analysis shows that the chief source of noise in the Mk 42 transmission is also the action of the meshing teeth, and harmonics of the tooth action are clearly evident up to the sixth. The second harmonic is again sometimes more powerful than the fundamental (see complete charts of Ref. 2). Energies in the 20-to 30-kc regions are not as high as in the Mk 40, but the greater share of acoustic power now lies below 20 kc, probably because of the lower tooth speeds.

The total noise at 20,000 rpm and 40 hp exceeded that of the Mk 40. Aurally, the Mk 42 produced a roaring, howling noise at high speeds. The Mk 40, as well as roaring, produced a piercing whine at high speeds. As its speed increased, the whine rose out of hearing range, while another whine took its place and in turn rose up and out, and so on.

Hypothesis of Air Noise

It is suggested that, at very high rotational speeds, air plays a role in gear noises. As a tooth enters the space between its two mates, air that occupied the space is forced out. Estimating the changing instantaneous area through which the air must flow provides a clue about the flow of air. This was done for the pinion and mating planet teeth on the Mk 42 transmission by first drawing curves of volume and area. Together these yielded a final curve for the velocity of air discharge through the variable orifice area:

$$v = (dv/dt)/A$$

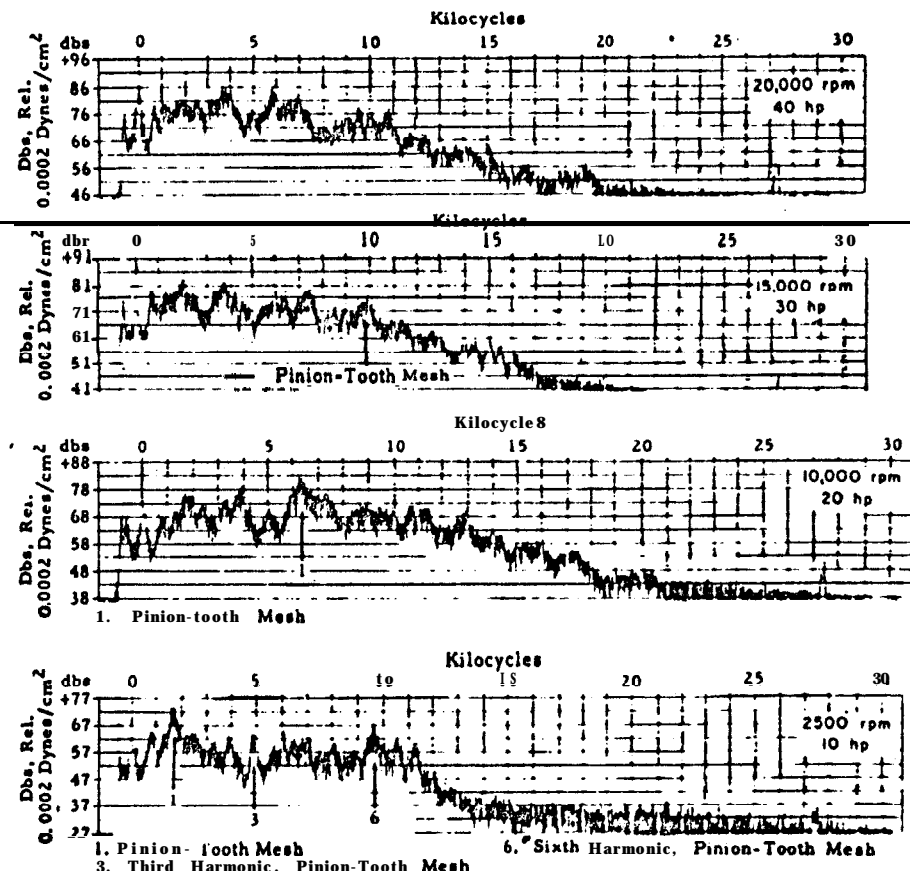


Fig. 12 Noise analysis for the Mk 42 transmission showing changes as speed and power are increased.

where

v = instantaneous velocity of air discharge

A = instantaneous area of discharge

V = instantaneous volume of air between meshing teeth

t = time, which may be related to the angular position of moving tooth

This velocity vs. the angular position of the teeth is shown in Fig. 13. With the mesh of each tooth, it is seen that the air reaches a velocity nearly 10 times that of the pitch line. With the Mk 42 pinion, the air mathematically reaches nearly sonic velocity+ at 20,000 rpm. This corresponds with the sudden rise in noise which occurs experimentally as 20,000 rpm is

approached (Fig. 11). Local shock waves begin to form when air over streamlined objects reaches about 0.8 sonic velocity; and when air is discharged around the sharp edges of gear teeth the local velocities may reach Mach 1 considerably sooner. It seems, therefore, that noise can be attributed to air shock waves, formed in rapid succession at the fundamental tooth mesh frequency when gears are operating at very high speeds. This adds to the noises produced by the dynamic forces of the metal teeth striking one another at high velocity.

Greater backlash and greater clearance between the tip of the tooth and the root of its mate would tend to reduce the air discharge velocity, and thus, the air noises, by providing greater escape area. At low to moderate gear speeds, such air noise is probably not a large factor.

Summary of Results

The important phenomena found by these experiments are summarized below. They relate to spur-gear transmissions at high speeds:

1) A small increase in tooth speed while power is held constant can result in very rapid rises in acoustic energy output. Noises resulting from a speed rise increase more rapidly than those resulting from power increases.

+Calculated for ambient temperature. Air compression will cause sonic velocity to be somewhat higher than shown. Actual local air velocities flowing about the sharp edges of the teeth will also be higher than computed here.

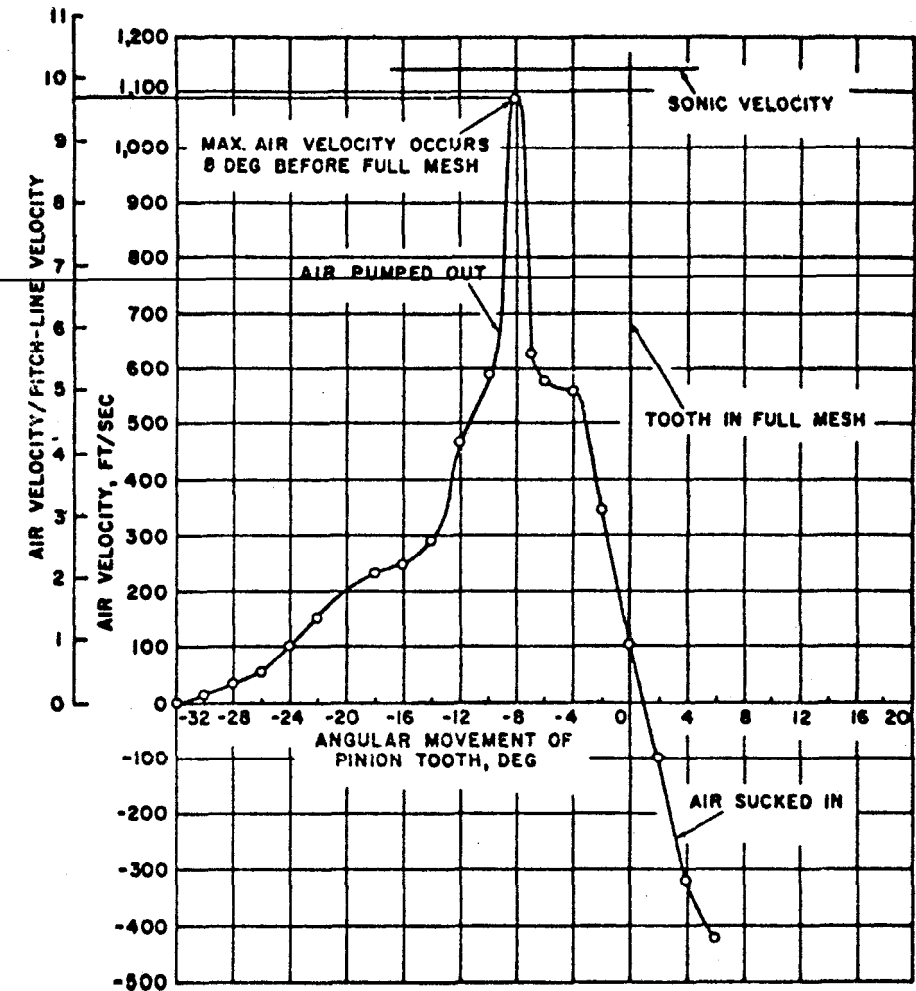


Fig. 13 Computed velocity of air discharge between teeth of the Mk 42 transmission at 20,000 rpm or 112 fpm pitch line velocity of the teeth. The air velocity reaches nearly 10 times the pitch line velocity.

2) The primary source of gear noise is the meshing, metal-to-metal action of the teeth, with the Gear-wheel disks and the case responding to this stimulus. (Ball-bearing noises are minor if the bearings are in good condition and installed and lubricated properly.)

3) A rough correlation is indicated between transmission noise and high-frequency shock waves formed as air is pumped out of the spaces between the meshing teeth. At high gear speeds, this air noise may be substantial, tiding to the foregoing metal-to-metal mesh noises.

4) The generated noise, of spur gear transmissions have major spectral components that extend from low frequencies to ~~30 kcs per sec and higher~~. Low-frequency noises can also be intense when transmissions are operating at high speeds.

5) Gear noises show the presence of strong first, second, third, fourth, fifth, and sixth harmonics of the tooth mesh frequency. The existence of harmonics as high as this was not generally known and appears of significance in acoustic design. At very high speeds, the noises become "white" and are very intense over a wide band of frequencies.

6) The second harmonic of the tooth mesh is sometimes considerably more intense than the fundamental.

7) The most intense noises in the high-frequency bands are at the tooth-mesh frequency and its second harmonic. The predominant noises at lower frequency are at the revolutions per second of the pinion, and the natural and second harmonic frequencies of the gear disks and the case components. Even though the tooth-mesh frequency may not correspond to the natural frequencies of these components, the gear disks and the transmission case respond to the tooth-mesh energy with vigor. Resonance creates sharp rises in noise when the tooth-mesh frequency approaches the natural frequency of a gear disk or of case components.

8) At 20,000 rpm and only 40 hp, the Mk 42 transmission generates about $\frac{1}{4}$ w of total acoustic energy. When measured in the normal manner by microphone 1 in. from the transmission surface, the noises produced by the Mk 40 and Mk 42 machines at high speeds were 118 and 130 db, respectively.

9) A significant new relationship found is the "acoustic energy rule": the total acoustic energy radiated by a spur-gear transmission is directly proportional to the power transmitted when the tooth velocity is held constant. This may apply to all spur gears.

Appendix: Methods of Lessening Spur-Gear Noises

During the experimental studies at NOTS, several methods of lessening the noises of spur gears became apparent:

1) The web or body of the gears should be solid, about as thick as the tooth length. Thinning webs to save weight makes them resonant, ringing diaphragms. For moderate-sized gears, the weight penalty is small to use solid, thick webs.

2) The case should be extremely rigid. External ribs dampen the amplitude of vibration without adding much weight. The shaft should also be rigid and with larger diameter than required from stress considerations. Deflections are important noise considerations.

3) The tooth speed should be low. --

4) Dedendwns and root clearance should be large enough for easy exit of oil and air. Backlash should be generous. The space for oil and air to escape at the two ends of the teeth should be large.

5) Ball bearings should be of the deep-groove super-precision type, selected by "hand feel" to detect roughness. They must not be heavily press-fitted onto their shafts or into the holding case. The inner bearing race should be locked to its shaft by a nut or other means, but not by heavy press-fit. In these ways, roundness of the ball races is maintained.

6) Alignment of the prime-mover shaft to the input shaft of the transmission must be within 0.001 in. The concentricity of rotation of each shaft at the mating point of the two shafts must be within 0.0005 in. total indicator reading. An alternative is a flexible torque link capable of offset at two ends. These measures help prevent generation of large rotating forces that create vibration and loud noises and could damage teeth and bearings at high speeds.

References

¹Rosen, M. W., "High speed acoustic drive facility", Naval Ordnance Report 6594, U. S. Naval Ordnance Test Station, China Lake, Calif., 22 September 1959.

²Rosen, M. W., "The noises of two spur gear transmissions", ,

GEAR NOISE CONTROL BY

MANIPULATING TOOTHCOMPRESSIVXSTRESSES

John Maddock*
Lomita, Calif.

Abstract

Vibration-isolation devices are generally too bulky for incorporation into torpedo gears. Instead, surface compressive stress is shown to be a significant variable in the relationship between noise level and gear-tooth loading. A numerical example is given which shows a method of reducing compressive stresses, without size or weight increase, by means of non-standard gear-tooth height proportions. This technique is an alternate to superprecision manufacture and successfully limited noise output of gears in an acoustic torpedo. The procedure may also bring about further noise reduction in gears already being produced at the limits of precision.

Introduction

Gears that transmit power resemble devices that deliberately produce sound. These force an elastic member into vibration, and couple the vibration to the surroundings by means of a connecting member with suitable dimensions relative to the wave length of the sound. Similarly, a small mass of material is displaced elastically and then released, resulting in a vibratory motion whose frequency corresponds to the number of teeth that engage in unit time. This vibration is conducted to parts of the machine which couple the energy to the environment.

Conventional Gear-Noise Reduction Techniques

Sound passes from a gearbox by vibration of the surrounding air and by conduction through the supporting structure. In underwater missiles, the internal airborne path is usually unimportant because of poor impedance match. Structure-transmitted noise, however, may be effectively coupled to the surrounding water, since it can cause the whole missile hull to vibrate. Isolation methods reduce the transmission of vibration to the hull, and absorption techniques attenuate airborne noise, but

*Consulting Engineer

these expedients often are bulky, heavy, and complex and may introduce serious functional problems.

The rim on which the gear teeth are cut and the spokes or web that connect this rim to the shaft possess a number of natural vibration modes. If these become excited within an operating mode of the machine, they may be damped with loose-fitting rings. Alternately, the use of soft nonmetallic gear flanks may avoid such resonances, but steel gears are required if significant power is transmitted. In real gears, mating teeth are neither completely conjugate nor exactly evenly spaced. Under rotation, these inaccuracies result in minor and erratic angular accelerations that give rise to corresponding forces. The tooth material is again displaced elastically in phase with these forces, resulting in the production of additional frequencies of vibration. Noise reduction has been approached largely by reduction of these inaccuracies; as a result, the amplitude of the sound pattern is decreased by stripping away overtones, but even theoretically perfect teeth would not be silent.

Helical gearing is generally believed to be relatively quiet because its screw-like action appears to transfer the load gradually from one tooth to the next. When directly attached to high-speed turbines, however, the act of gear tooth engagement represents almost a classic shock situation. For example, at 30,000 rpm, each tooth on the smallest practical pinion passes from zero, to full load, and back again in about 0.10 msec. Experience (especially in engine rooms of turbine-driven ships) shows that helical gears can be distressingly noisy and the few extremely high-speed gear units in industrial service with straight-spur teeth are no more noisy than the best helical counterparts.

Gear noise increases more or less linearly with tooth loads, and a simple route to relatively quiet gears is by arranging things so that the teeth are lightly loaded. Although tooth loading can be reduced by increasing the size of the machine, this is permissible only when there are generous limitations on weight and volume.

Compressive Stress-Limiting Techniques

A review of requirements relating to gear noise in torpedoes, where acoustic guidance demands quiet operation, showed that weight and mechanical rigidity requirements almost forbid isolation schemes and that the gear drives must be small and compact. The fundamental nature of gear tooth contact was therefore examined in the hope of uncovering means to keep the

loading intensity at a reasonable level without increasing gear size.

Gears are subject to bending and surface compressive stresses. In bending, particularly at high speed, stresses are often relatively low and change only moderately as design parameters (other than size) are varied. Compressive stresses can, however, be manipulated, as will be discussed.

As a pair of gear teeth enter, pass through and leave the load zone, they experience a varying surface-compressive stress as the contact moves along the profiles. If contact, for instance, occurs close to the base circle, this stress rises steeply and theoretically becomes infinite at the base circle. As the contact moves toward the pitch circle, these stresses are initially lower but increase again as the tip of the tooth approaches the base circle of its mate during the path of recess.

The properties of the involute are such that contact between two meshing teeth always occurs at some point along the line AB, in Fig. 1, which is the common tangent to the two base circles. Since contact cannot occur outside the tips of the teeth, the actual path of action is within CD, the intersection of the outside circles of the mating gears with AB. If O represents any point at which the teeth are in contact, AO is the instantaneous radius of curvature at that point for the tooth on the left, and OB for the tooth on the right.

At O, the instantaneous compressive stress can be computed for the dimensions of and the torque acting on the gears by treating the teeth as two cylinders of radius AO and OB in elastic contact. For steel gears, the Hertz equation for curved surfaces in contact under load may be simplified to determine maximum compressive stress, s_c , at the center of the contact bond:

$$s_c = \left(\frac{W}{F} \frac{r_1 + r_2}{r_1 - r_2} \right)^{1/2}$$

where:

r_1 = AO, in.;

r_2 = OB, in.;

W = tangential force, lb; and

F = width of face, in.

As illustration, the gear combination in Fig. 1 will be taken with the standard tooth proportions tabulated in table 1

and the pinion **delivering** 21 lb-in.

Table 1 Standard Gear

	Pinion	Gear
Number of teeth	21	224
Diametral pitch	40	40
Pressure angle, ϕ	20°	20°
Center distance, DC	3.0625 in.	3.0625 in.
Base radius, BR	0.2467 in.	2.6311 in.
Outside radius, OR	0.2875 in.	2.8250 in.
Face width	0.25 in.	0.25 in.

The compressive stress at the tip of the gear tooth is **calculated** below:

$$r_1 + r_2 = DC \sin \phi = 1.0474$$

$$(OR^2 - BR^2)^{1/2} = 1.0286$$

$$r_1 = 0.0188$$

$$r_1 + r_2 = 0.0197$$

$$\text{Pitch radius} = 21 \div (40 \times 2) = 0.2625$$

$$w = 21 \div .2625 = 80$$

Substitute in eq. (1):

$$SC = 2290 [(80/0.25)(1.0474/0.0197)]^{1/2} = 301,000 \text{ psi}$$

Compressive stresses for other sets of instantaneous radii along AB may be calculated to show the variation of stress along the line of action (as plotted in Fig. 1). Since the meshing action does not utilize the entire length AB, one might inquire if the unused part should not be the high-stress portion, i.e., eliminate the addendum of the gear wheel. For practical reasons, however, a reasonable length of action must be included between the two outside circles to promote smooth load take-up by succeeding teeth. Otherwise, momentary accelerations (cogging action) will occur which bring each fresh pair violently into contact with the introduction of potentially large inertia forces. Thus, if we reduce the gear outside diameter, that of the pinion usually must be increased.

Minor inaccuracies and elastic deformation of the parts in actual gear drives tend to concentrate loads in an unpredictable fashion. Actual stresses, for that reason, cannot be calculated and should only be considered proportional to theoreti-

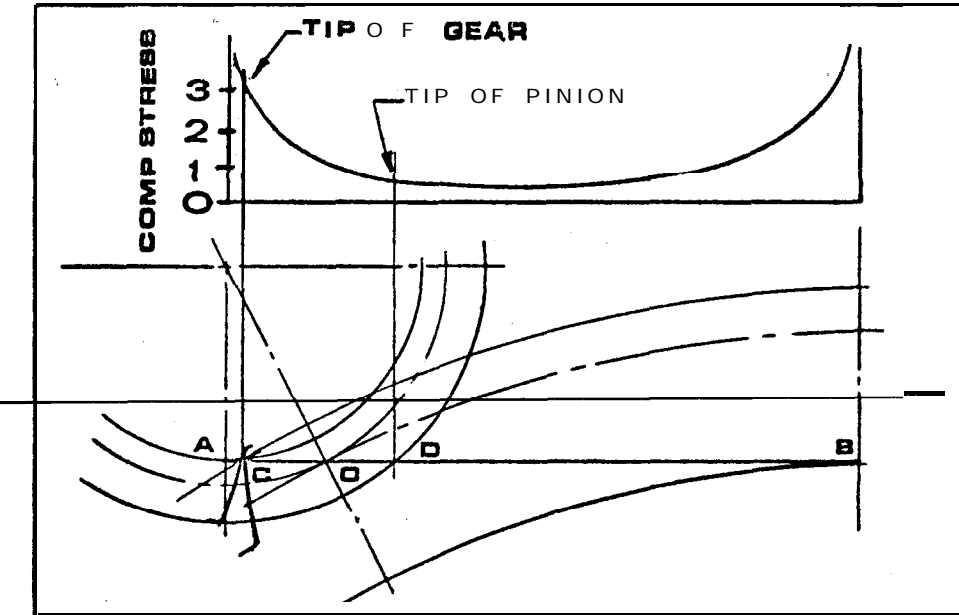


Fig. 1 Comp stress along line of action: standard gears.

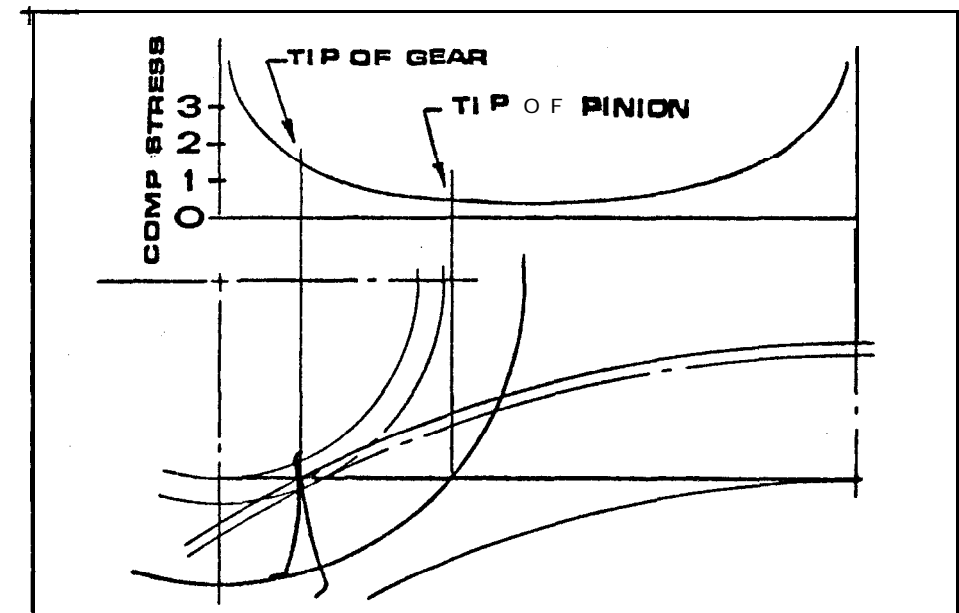


Fig. 2 Comp stress along line of action: Modified gears.

ical values. This analysis omits effects from more than one pair of teeth in a simultaneous contact during part of the action. In real gears, of course, this condition is never completely achieved: gear teeth cannot be so precise that load is exactly divided, and some if not all single teeth carry practically all of the load during their entire passage through the load zone. These teeth are subjected to a theoretical stress program indicated in Fig. 1 & 2.

The effect on stress of revising the outside circle radii is illustrated in Fig. 2 where the maximum stress is less than 57% of that shown in Fig. 1, although the load is the same and the gears are identical except for modified outside diameters. ~~Thus, calculating the stress at the tip of the modified gear,~~

$$\begin{aligned} \text{OR gear} &= 2.8105 \text{ in.} \\ r_1 + r_2 &= 1.0474 \text{ (as before)} \\ r_2 &= 0.998 \\ r_1 &= 0.0594 \\ r_1 \cdot r_2 &= 0.0585 \\ SC &= 2290 [(80/0.25)(1.0474/0.0585)]^{1/2} = 170,000 \end{aligned}$$

The outside radius of the pinion was increased to 0.2995 to keep the total length of action the same as before.

This value of compressive stress could be attained with the original gear if the load were decreased by 50% and experience has shown that a significant improvement in noise level normally results from reducing gear load by half. However, this modification of compressive stress by revising the outside circle radius is accomplished without decreasing gear load. The range within which this procedure is practical depends largely on the radius at which the pinion teeth become pointed and the depth of case hardening. It is not a substitute for careful design and manufacture and is applicable to both spur and helical gears.

Its effectiveness in reducing noise was demonstrated in the machine shown in Fig. 3, which is a step-up unit that drives various pumps and an alternator at over 20,000 rpm in a torpedo. Space limitations dictated use of a high gear ratio in a single step and a narrow bull gear. Teeth are straight spur, loaded sufficiently to require case hardening. Involute form is unmodified throughout the profile, but addendum proportions are nonstandard and were derived by the procedure outlined previously. Although the exact noise level cannot be reported in this paper, it was so low that it did not interfere with the torpedo acoustic system. The nonstandard teeth functioned reliably under gear conditions generally considered difficult:

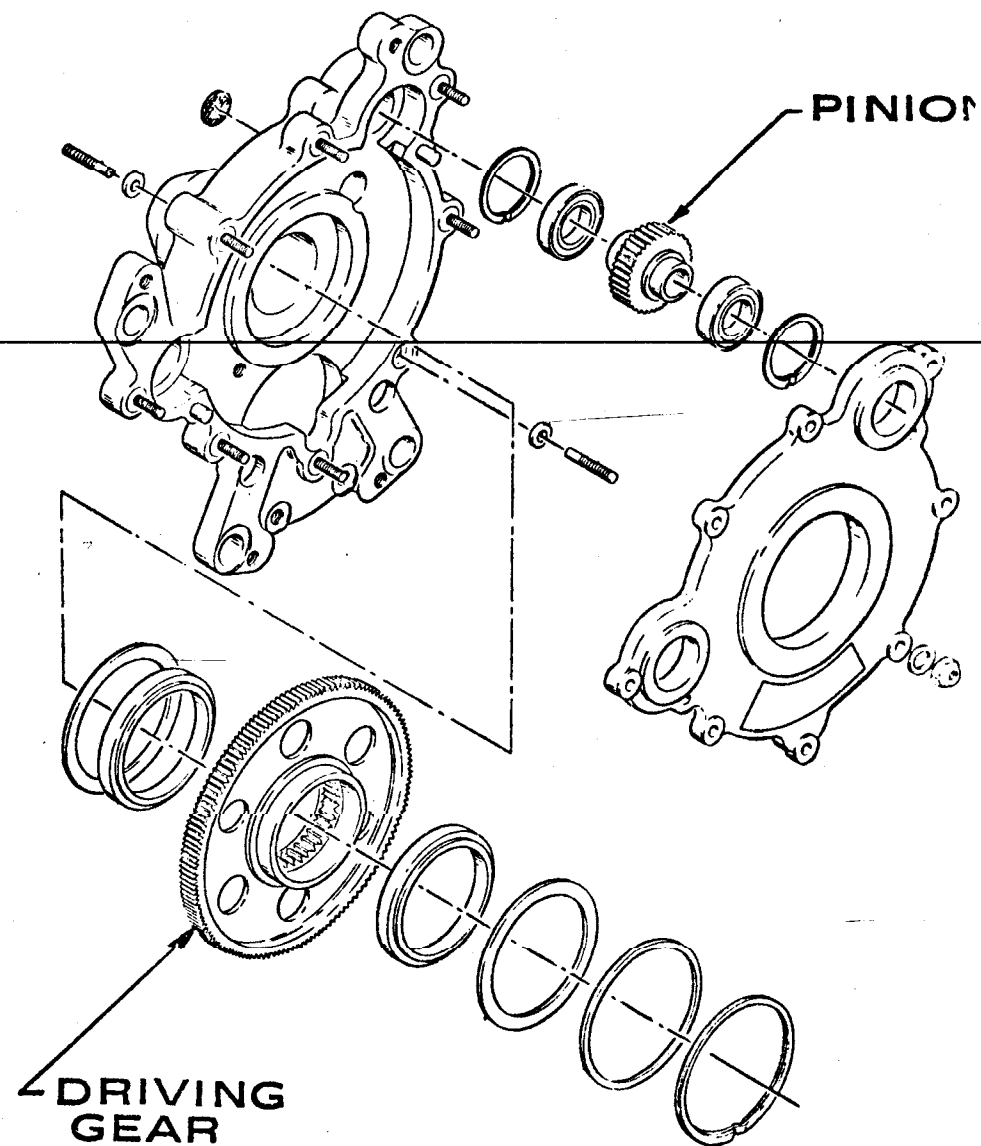


Fig. 3 Step-up gear assembly.

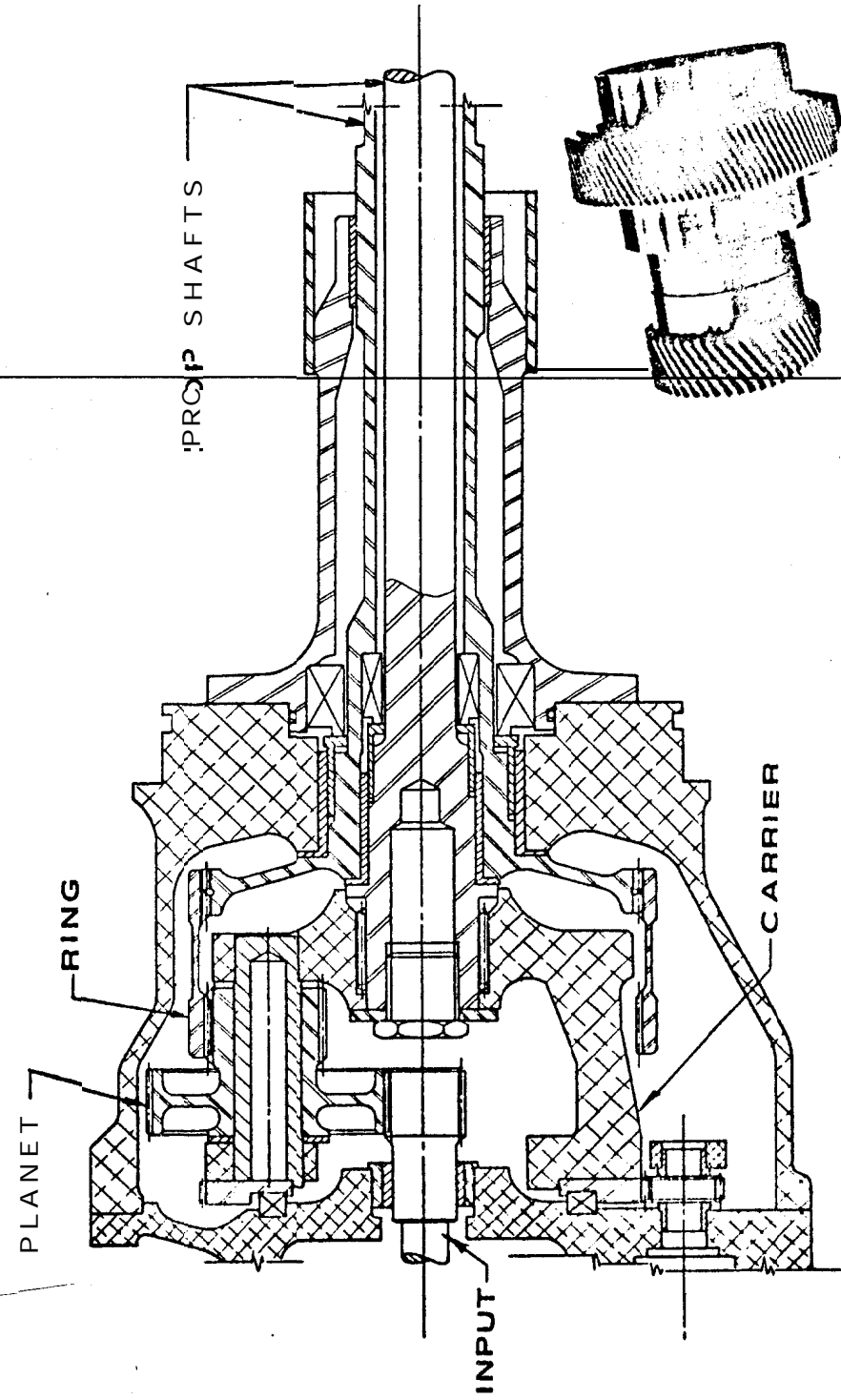
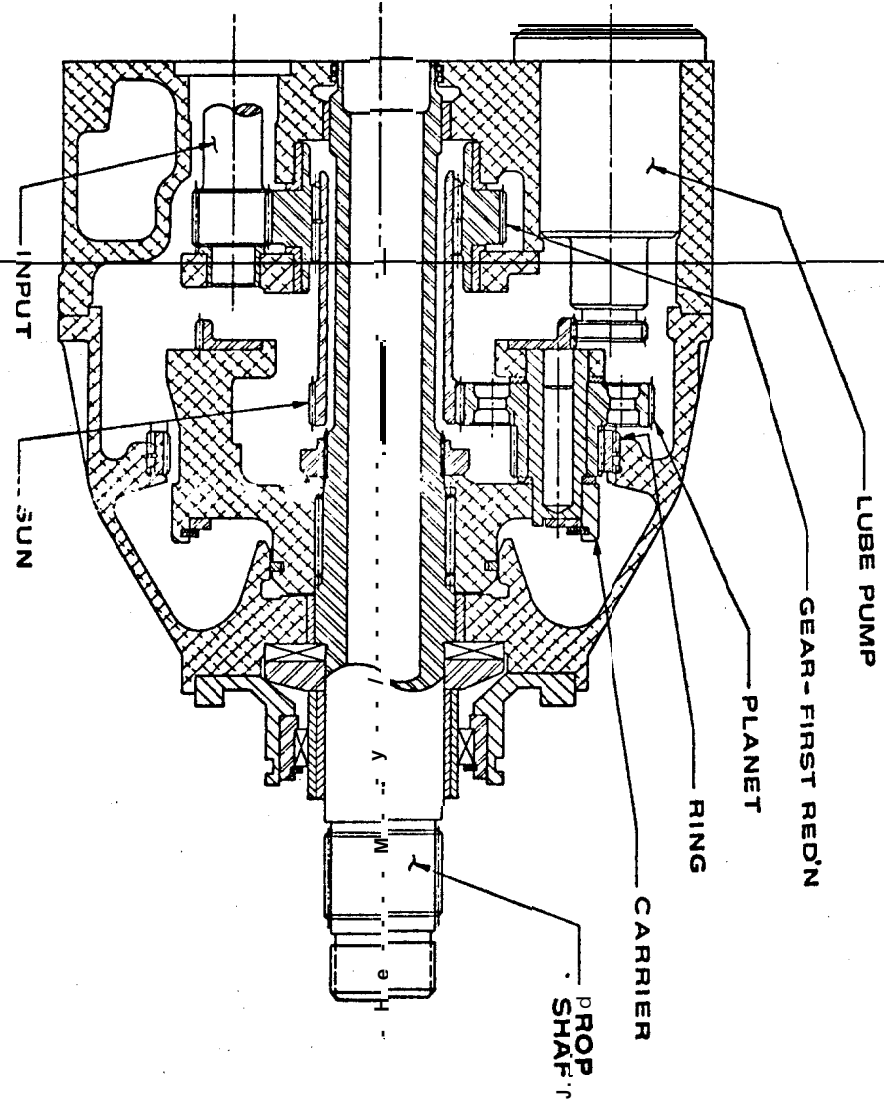


Fig. 6 Sun gear assembly.

high speed, high ratio and speed increasing.

Geared Turbine Systems

For torpedo propulsion reduction gears, where torque loading may be high, planetary machines are attractive because they can divide the load among several paths. This arrangement permits the lowest tooth load and hence the lowest noise output within a given envelope. The examples next shown were constructed during developmental testing of a turbine driven torpedo.

Figure 4 shows a single rotation output. The second reduction sun gear is splined to the output of the relatively conventional first stage. The small ends of the compound planets engage a fixed internal gear. The planet carrier, splined to the output shaft, rotates at a speed ratio of 1:23 with the turbine.

Figure 5 shows a counter-rotating propeller drive. Here the turbine is concentric with and directly connected to, the sun gear. Speed is reduced by a ratio of about 27.5. Weight, including propeller shafting, accessory drive gearing and lubrication pump, was less than 0.2 lb/hp.

In both of these machines, single-helical gearing was used, with fine pitch teeth and a generous helix angle. Figure 6 shows the sun-gear assembly for the single output machine of fig. 4. Loads were high enough to require case-hardened teeth.

No grinding was done after hardening the gear teeth, although lapping was performed, as required, to achieve good tooth contact. Final acceptance was based on visual inspection of tooth contact. The gears were, therefore, not in the super-precision class; instead, the teeth were carefully proportioned to minimize compressive stress. The fact that their noise level was low enough not to disturb the acoustic system of its torpedo indicates the validity of the design philosophy.

Conclusion

Gear noise comprises a complex sound pattern resulting from numerous forms of forced vibrations. Conventional methods of controlling such noise are subject to space, weight and mechanical problems. The technique of optimizing compressive stresses proved an acceptable alternate to super-precision manufacture and successfully limited noise output of gears in an acoustic torpedo. This procedure may also be useful for further noise reduction in gears where manufacturing precision has already been carried to practical limits.

PROPELLION TEST FACILITIES FOR UNDERWATER MISSILES

TORPEDO PROPULSION TEST FACILITY

G. E. Anderson*

U. S. Naval Underwater Ordnance Station, Newport, R. I.

Abstract

~~This paper reports on the capabilities of the Torpedo Propulsion Test Facility of the U. S. Naval Underwater Ordnance Station. The facility, built within a reinforced-concrete building for conducting hazardous tests, has instruments for testing thermal or electrical torpedoes while operating in water tanks under programmed simulated depths from 0 to 5600 ft in sea water. It includes tanks for storing high-energy liquid fuels and oxidizers, and a dynamometer capable of absorbing 1000 s-hp from 900 to 3000 rpm. It accommodates torpedoes up to 30 in. in diameter and 24 ft in length. Planned improvements include means for controlling the ambient water at temperatures from 35° to 90°F, varying its salinity, and passing it over the torpedo surfaces at selected velocities.~~

Introduction

A major problem in research and development of long-range, high-speed, deep-depth torpedoes for antisubmarine warfare is testing their propulsion systems, thermal or electrical, throughout their entire designed operating depth range. The normal dynamic method to test complete torpedo propulsion systems is in a launching at sea, programmed to operate at extreme conditions, with a section included which contains instruments to monitor important parameters. If, however, a critical component fails, the torpedo may be lost, along with data on the cause of failure. This testing is also costly and time-consuming and requires the services of launching and recovery vessels and their crews. The U. S. Naval Underwater Ordnance Station designed and constructed the Torpedo Propulsion Test Facility to test torpedoes on land throughout their

Presented as Preprint 2593-62 at the ARS 17th Annual Meeting and Space Flight Exposition, November 13-18, 1962.

*Project Engineer, Experimental Test, Research Department.

mechanical, **electrical**, and instrumentation connections between the torpedo and the control console. Electrical **connections** are provided for monitoring a minimum of 24 parameters.

Facility Capability

The Torpedo Propulsion Test Facility is designed to test and evaluate high-power, deep-depth, research torpedoes with tripropellant thermal propulsion systems with either open- or closed-cycle thermal systems, as well as electric torpedo systems. The liquid-propellant tankage and delivery systems are neither mandatory nor limited. Depending on compatibility, various types of liquid fuels and oxidizers can be used in the ~~sea water and fuel tanks, which are made of~~ corrosion-resistant steel, or in the oxidizer tank, which is aluminum-lined.

The open test tank is for preliminary "debugging" tests at shallow water conditions with minimum hazard and with observation by closed-circuit television. External propellant tankage permits testing with only a minimum of propellant ~~within the torpedo for safety in~~ preliminary runs, and also ~~allows~~ extended-duration runs.

The first tests conducted in this facility were with a small battery-powered, electric-motor-driven torpedo, as shown in Fig. 13. It was set in a small water tunnel, water circulation over it was provided by an external electric motor driving a pump jet, and the unit was satisfactorily *run* in a very close simulation of open sea conditions to depths of 900 ft.

The Garfield Thomas Water Tunnel

August F. Lehman*
Oceanics Inc., New York, N. Y.

and

Thomas E. Peirce+
Pennsylvania State University, University Park, Pa.

Abstract

The purpose of the Garfield Thomas Water Tunnel is to advance the science and art of the hydrodynamic design of submerged bodies. Of specific interest are hydrodynamic propulsion and control, cavitation, hydroelasticity, **hydro-acoustics**, turbulence, and boundary layer control. **Emphasis** is placed on the particular phenomenon, **whether** the program is basic *or* developmental. A high-speed water tunnel (60-fps velocity) with a 48-in. diam cylindrical working section is the main test facility. It is supplemented by a smaller water tunnel, a subsonic wind tunnel, a very small ultra-high-speed water tunnel (300 fps), a hydraulic flow system, and a boundary layer research tunnel. The large water tunnel is equipped for visual and acoustic observation of cavitation. Steady-state forces and moments can be measured on bodies up to approximately 15 in. in diameter. Propulsor characteristics can be measured on any model. In some instances, bodies up to 25 in. in diameter have been tested by eliminating wall interference effects through special tunnel liners. A capability of measuring and controlling fluid turbulence level permits basic investigations at high Reynolds numbers and testing of drag-reduction methods.

Presented as Preprint 2594-62 at the ARS 17th Annual Meeting and Space Flight & Position, Los Angeles, California, November 13-18, 1962.

*Head, Water Tunnel Division; formerly Project Leader, Water Tunnel Operations, and Associate Professor of Engineering Research, Pennsylvania State University.

+Project Leader, Drag Reduction Program, The Garfield Thomas Water Tunnel, Ordnance Research Laboratory.

Facilities

There are three major facilities^{1,2} at the Garfield Thomas Water Tunnel : a large high-speed water tunnel, a small high-speed water tunnel and a subsonic wind tunnel.

Large Water Tunnel

The large water tunnel is capable of variable speed and pressure. It is a closed-circuit, closed-jet type in which powered models can be placed that drive single or counter rotating propellers or propulsors. As shown in the photograph and circuit sketch in Fig. 1, it is about 100 ft long and 32 ft high with a maximum diameter of the approach to the working section of 12 ft. In this approach; commonly called a "settling section," is a honeycomb to reduce large-scale rotations and undulations in the test stream. Recently, a large-mesh unit was replaced with considerably finer mesh to reduce finer scale turbulence and permit more meaningful turbulence and boundary-layer investigations.

The cylindrical working section is 4 ft in diameter and 14 ft long. Its water velocity is continuously variable up to about 60 fps, as controlled by a four-bladed, adjustable-pitch, 95-in. diam. impeller, driven by a 2000-hp electric motor. The pressure in the working section may be reduced to about 3 psia and raised to about 60 psia, which provides a wide range of cavitation numbers.

The lower limit of testing without cavitation on support appendages is at a cavitation number of about 0.4, which is defined as the available static head minus the vapor pressure divided by the dynamic head. Investigations to indices between 0.2 and 0.3 can be run when cavitation is permissible on the support appendages or the induced form of cavitation on the body itself is of interest. Still lower cavitation numbers can be simulated by injecting air or gas into the cavity.

Water temperature can be varied from 40° to 120°F, which changes the Reynolds number by a factor of two through temperature alone. Numbers on the order of 47×10^6 , based on the tunnel diameter, can be achieved in practical tests.

Operated under Bureau of Naval Weapons Contract NOrd 16597.

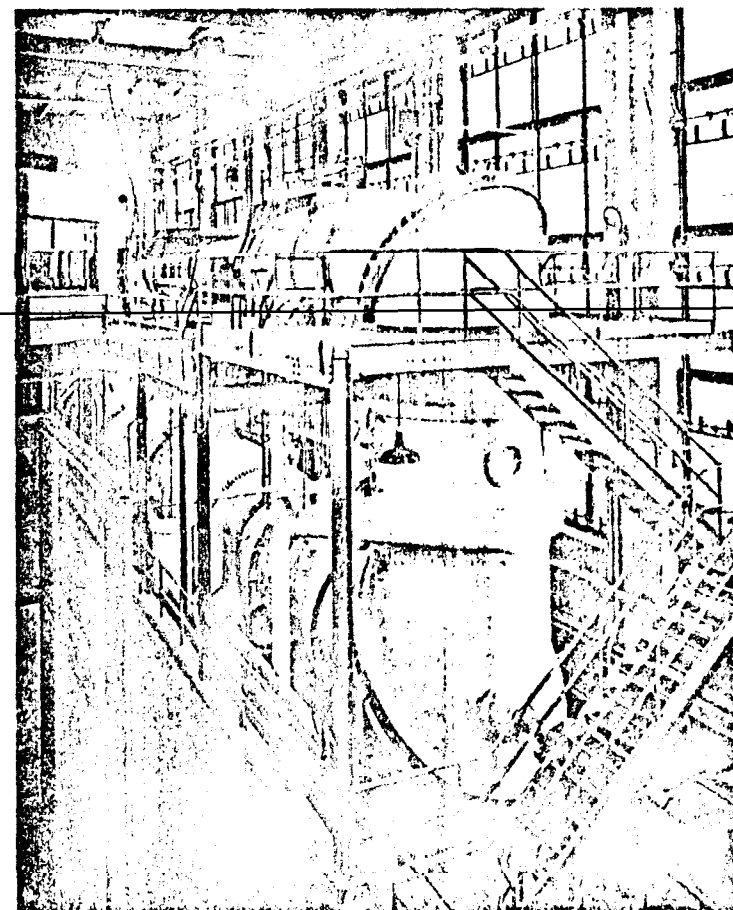


Fig. 1a Large (48-in.) water tunnel.

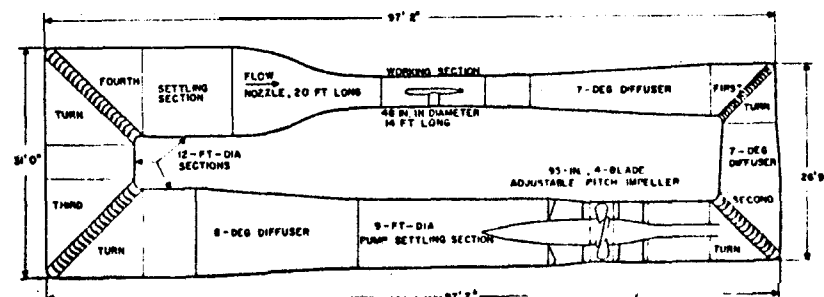


Fig. 1b Circuit of large water tunnel.

The air content of the water is controlled through a degasser and, in the working section, can be made less than saturated, regardless of pressure. Air content is important in cavitation investigations and in studying bodies which purposely liberate gas into the stream, as in certain methods of boundary-layer control.

The working section has Plexiglas windows along both of the horizontal sides for visual and acoustic observations. The hatch cover, containing 12 luminaires for lighting, is removable to permit installation, access to, and removal of test bodies. Acoustic measurements are obtained with specifically designed hydrophones positioned in the tunnel as needed, or through a narrow beam hydrophone in a reflector within a tank of water on the opposite side of the working section from that used for viewing.

Control of tunnel and model variables is done at a console in a glass-enclosed room facing the observation window. From it, water velocity, pressure, and the speed of the rotating test elements can be varied. The room also contains consoles for acoustic and force-measuring equipment.

Small Water Tunnel

The small water tunnel³ supplements the large one. It is also a closed circuit with circular cross section at most points, as shown in Fig. 2. Its length is 26 ft, excluding the drive system, and the maximum height is approximately 20 ft. Approximately 80-fps velocity and a pressure range of 3 psia to 60 psia, independent of water velocity, is attainable in the working section.

The small tunnel has the capability of interchanging its test sections. In this instance "test section" identifies the upper horizontal leg of the tunnel circuit between turns. There are two sections: one is 12-in. circular and the other is 20 x 4 1/2-in. rectangular; both are 30 in. long. The circular section is used to study bodies with three-dimensional flow and the rectangular section to study hydrofoils, slots, and other two-dimensional flow situations.

The drive is in part of the lower leg and one turn of the circuit. The pump is driven by a 150-hp electric induction motor through a variable-speed fluid coupling and reduction gear. To cool the water, a shell-and-tube-type exchanger that is an integral part of the circuit is used, with tunnel water flowing through the tubes and the cooling water

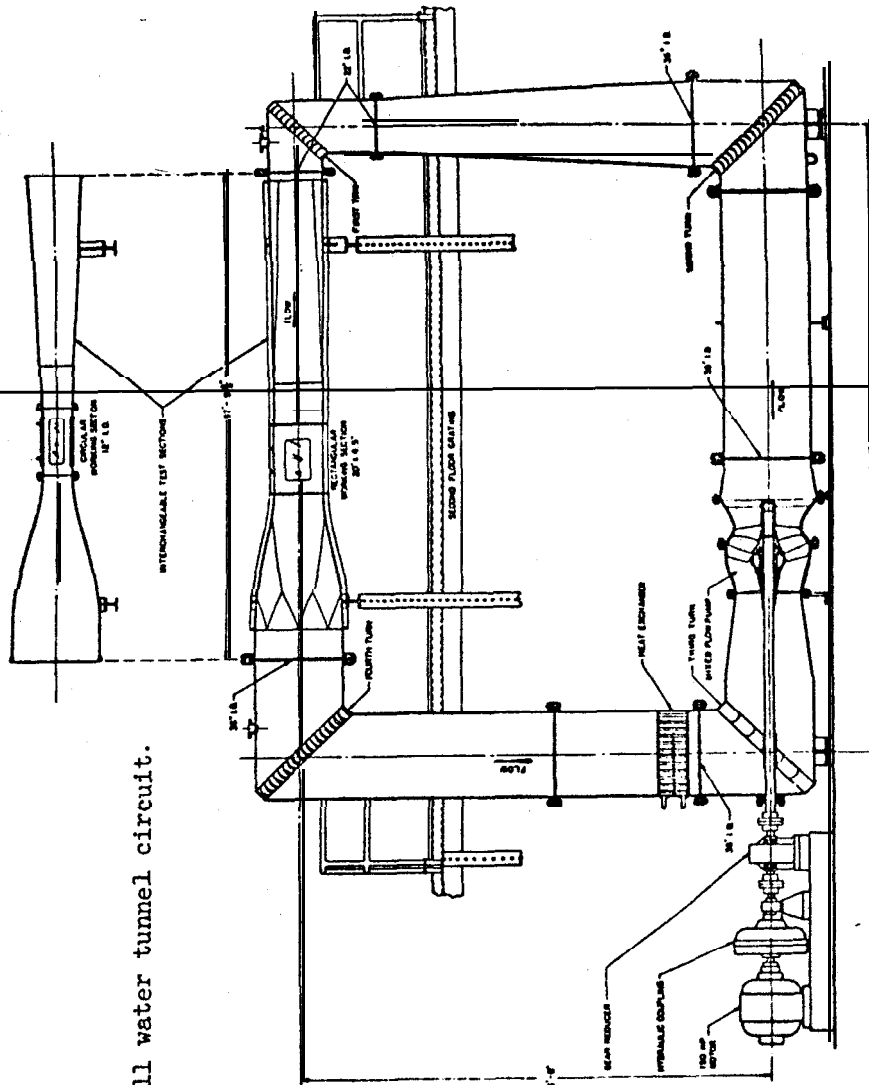


Fig. 2 Sketch of small water tunnel circuit.

circulating around them. It is located *after* the pump to act as a honeycomb and reduce turbulence.

Subsonic Wind Tunnel

The subsonic wind tunnel contributes to many hydrodynamic studies, since flowing air is ideally suited for detailed investigations about bodies or *in* and *about* propulsors. The data can be used, as well, to evaluate cavitation potenti-alities, as shown by Rouse and Ball.^{4,5}

Substitution of low-velocity air for water reduces structural requirements of models and test apparatus, eliminates leakage problems, and generally simplifies the required test instrumentation. Also, air-turbulence measuring instrumentation is considerably more advanced than instrumentation for water, although Lumley recently developed thermistor probes for accurately measuring turbulence intensity in water.

The wind tunnel⁶ is a closed-return type with the cross section varying, respectively, from an octagonally shaped nozzle, the working section, the diffuser, and the rectangular return leg. The working section is 48 in. across the flats and 16 ft long, and the settling section is 9 ft across the flats. The tunnel has an overall length of 60 ft and is approximately 20 ft high, as shown in Fig. 3. The maximum working section velocity of about 170 fps is produced by a 70-in.-diam. axial flow fan driven through a Vickers hydraulic speed control unit powered by a 150-hp synchronous motor. The impeller pitch and its drive speed are variable. A turbulence level of 0.1% is achieved through a honeycomb and screens in the nozzle. The practical Reynolds number for tests (based on the tunnel diameter) is of the order of 3.5×10^6 .

Other Facilities and Supplementary Equipment

Among other facilities in the tunnel building are a hydraulic system, for a controlled supply of water at 2500 gal/min against a head of about 100 ft, and a small, ultra-high-speed, high-pressure water tunnel with a test section velocity of 335 fps, a maximum pressure of 1000 psi, and a temperature up to 250°F, as shown in Fig. 4.

A new water tunnel with a test section length of 25 ft was specifically designed for the investigation of boundary-layer flows in the laminar sublayer.

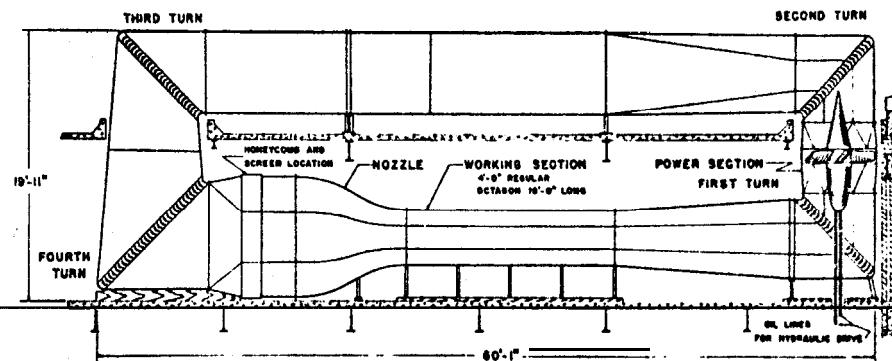


Fig. 3 Sketch of the subsonic air tunnel circuit.

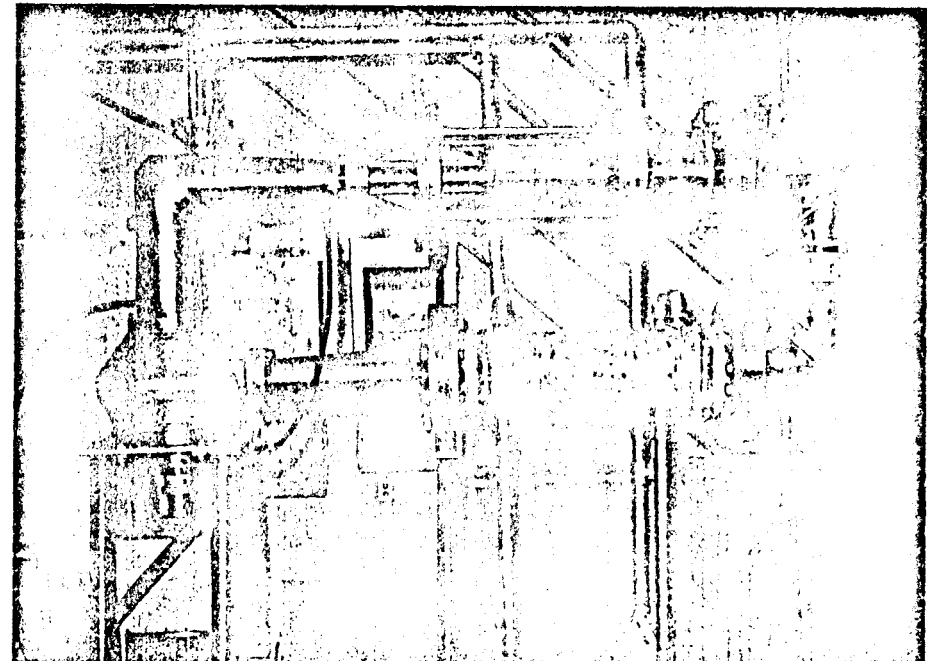


Fig. 4 Small, ultra-high-speed water tunnel.

The building also contains shops for machining **high-precision** blade elements or test shapes. Since experimental tests **often** are undertaken to prove design **criteria, extreme** precision is required so the shape and form will be close to design. This is particularly necessary, for example, in cavitation testing, where very minute deviations **cannot** be tolerated.

Experimental Test Equipment

Test Bodies--Tunnel Installation--Powering

Bodies investigated in the large water tunnel can vary from several inches, to 25 in. in diameter, as shown in Figs. 5, 7. In general, the models have **one** major support strut through which power and instrumentation leads pass to the tunnel exterior. In submarine investigations, the conning tower or "sail" serves as this support.

The interior of powered models contains either electric motors or a small **hydraulic** turbine in case the mass and moment distribution of the model must be maintained. Such a turbine, shown in Fig. 8, was developed at the Laboratory. It weighs 11 lb and develops slightly over 50 hp at 5000 rpm. Electric motors are either 20-hp units, which fit into 8-in. minimum diam models, **or** 70-hp units, which fit into 12-in. minimum diam models. The latter have a variable frequency power supply.

Force and Moment Measuring Equipment

The original purpose of the tunnel was to verify theoretical propeller designs for cavitation-free performance. Thus, determination of "**steady-state**" propeller thrust and torque was **necessary**. With higher **speed** vehicles it also is necessary to measure forces and moments on the body as well, if the vehicles are to be designed for proper maneuverability. Recently, unsteady forces **from** the **propulsor** unit and the vibrations of the underwater vehicles also have **become** increasingly important.

Propeller thrust, power, and torque. Steady-state or "time-averaged" thrust and torque is measured with strain-gage devices. For power or torque, one method is through direct calibration of the electric motors with a dynamometer. **Another** is measurement of torque on the shaft itself, which is either directly "**strain** gaged" or connected to a torque **cell**.

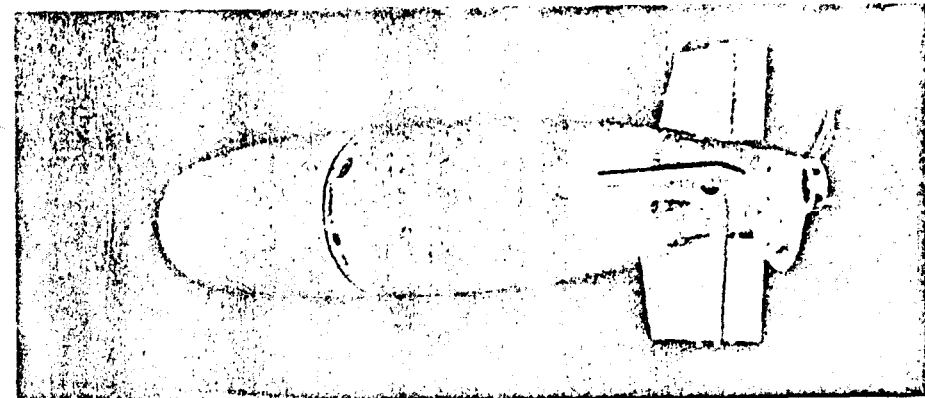


Fig. 5 A 3/4-in.-diam (powered) test body.

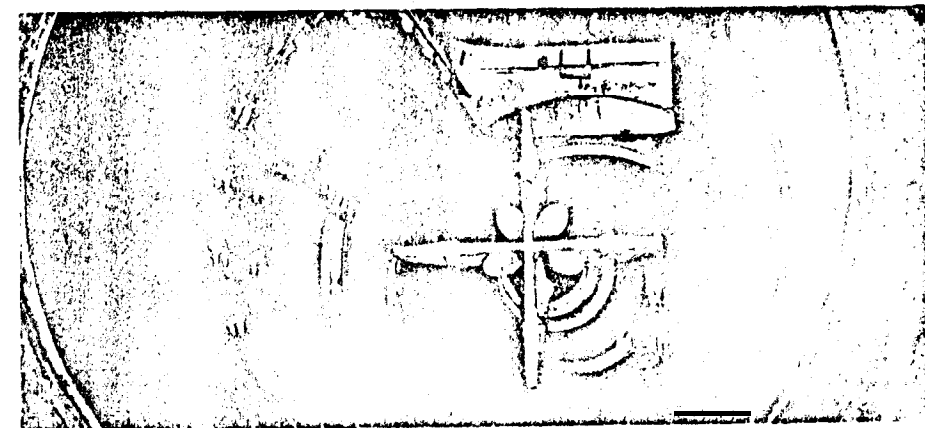


Fig. 6 A 25-in.-diam (powered) test body.

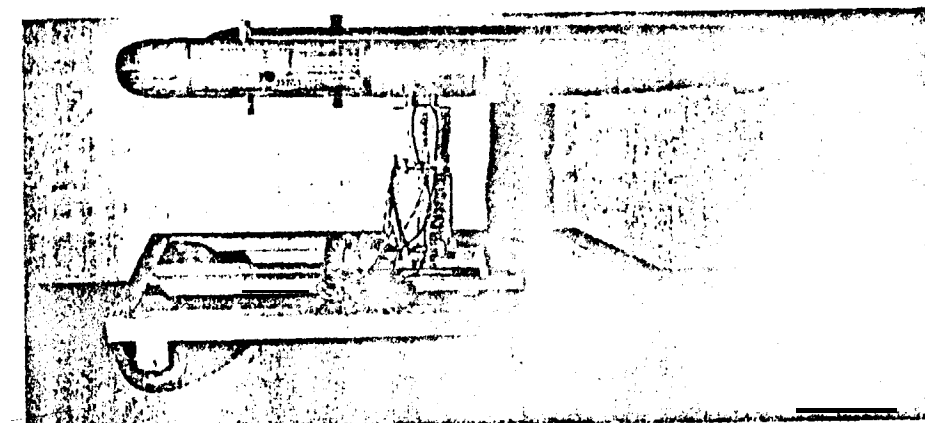


Fig. 7 An 8-in.-diam (unpowered) test body.

Body forces and moments. To measure body forces and moments, a steady-state balance was evolved. It uses tension, rather than bending, members as the force-sensing links to eliminate many vibrational difficulties normally encountered. A sketch of the four-component balance for models 8 in. and larger in diameter is shown in Fig. 9. A smaller internal balance, also operating on strain gages, to measure body lift, axial force, and pitching and rolling moments on unpowered models on a sting-mounted system, is shown in Fig. 10.

Dynamic Measurements

Dynamic measuring techniques involve carrier-frequency dynamic train gages, accelerometers, and piezoelectric dynamic force gages. Recording equipment includes an oscillograph measuring to 3 kc, augmented by magnetic tape which can be analyzed to about 7 kc, with a lower limit of approximately 2 cps. For limited indications at frequencies above resonant, comparison measurements over narrow ranges are employed. Calibration is with electromagnetic shakers delivering up to 200 lb at up to 450 cps. The systems can measure dynamic forces of less than 0.01 lb at frequencies up to 400 cps.

Propeller, thrust, and torque. Using carrier-frequency, dynamic strain-gages; records of Fig. 11 were obtained on a turbomachine, where variations in thrust and torque output are shown. The predominant frequency is the shaft rpm times the number of blades. Thrust variations in this investigation were about 24% of the static value.

Body forces and moments. Investigations also have been made with modeling techniques for predicting mode profiles, vehicle-shell frequency response, and mode resonance performance for full-scale vehicles.

Hydrodynamic stability derivatives. A planar motion mechanism installed to measure dynamic hydrodynamic coefficients is modeled somewhat after the David Taylor Model Basin planar motion mechanism?.

Tunnel Liners

The original objective of the tunnel was to develop design criteria for propulsors and their subsequent design, and finally, to test them. Therefore, the tunnel working section was sized in view of the limits placed on manufacturing propulsor blades.

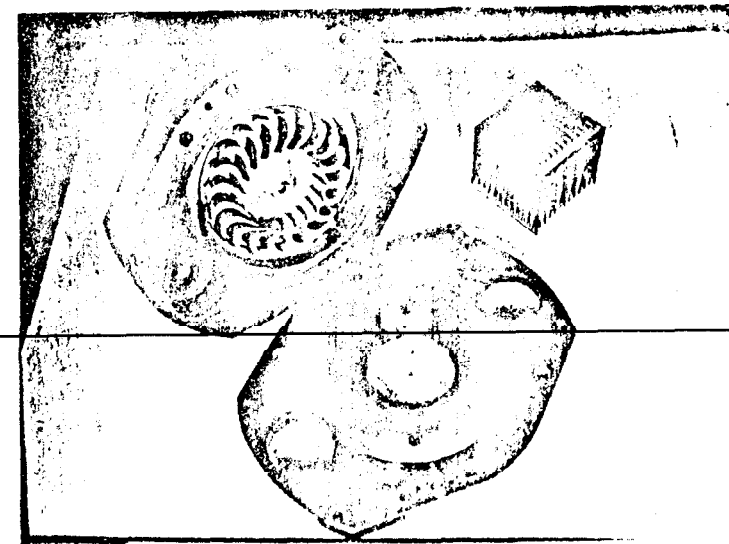


Fig. 8 50-hp hydraulic turbine.

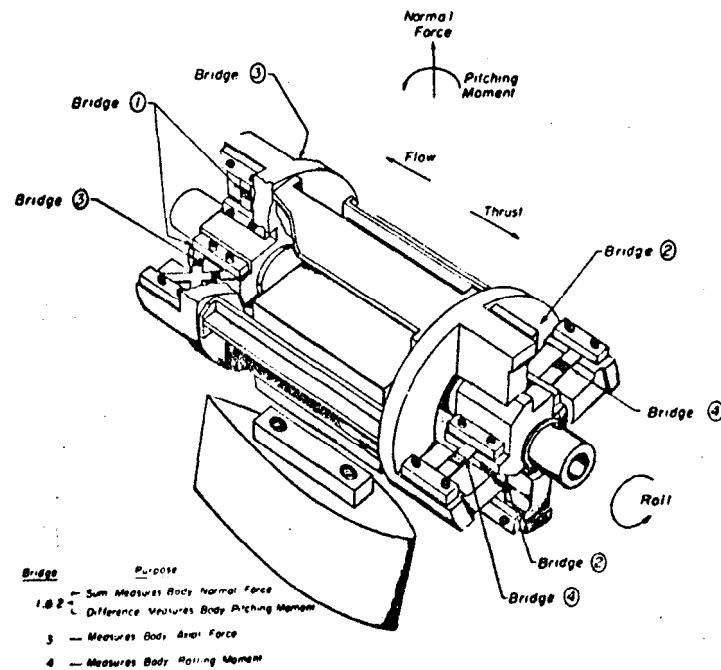


Fig. 9 Four-component balance for models 8 in. in diameter or larger

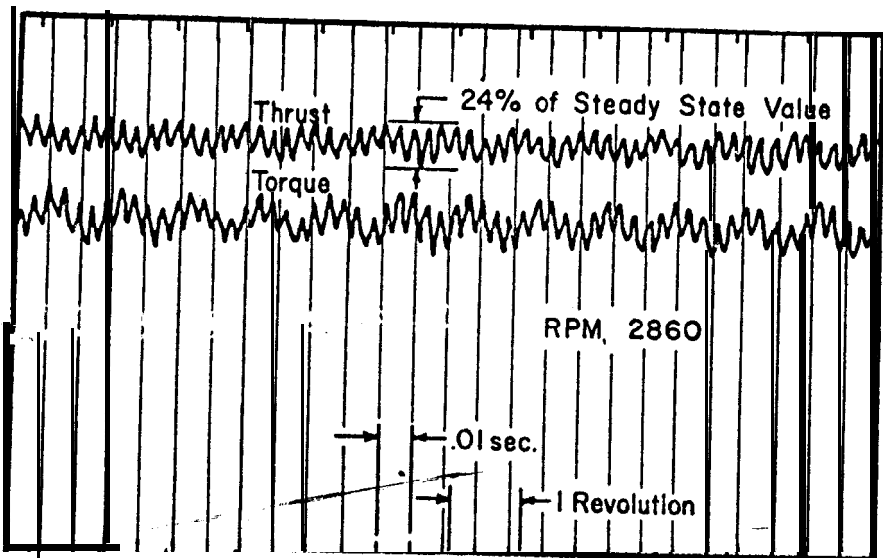
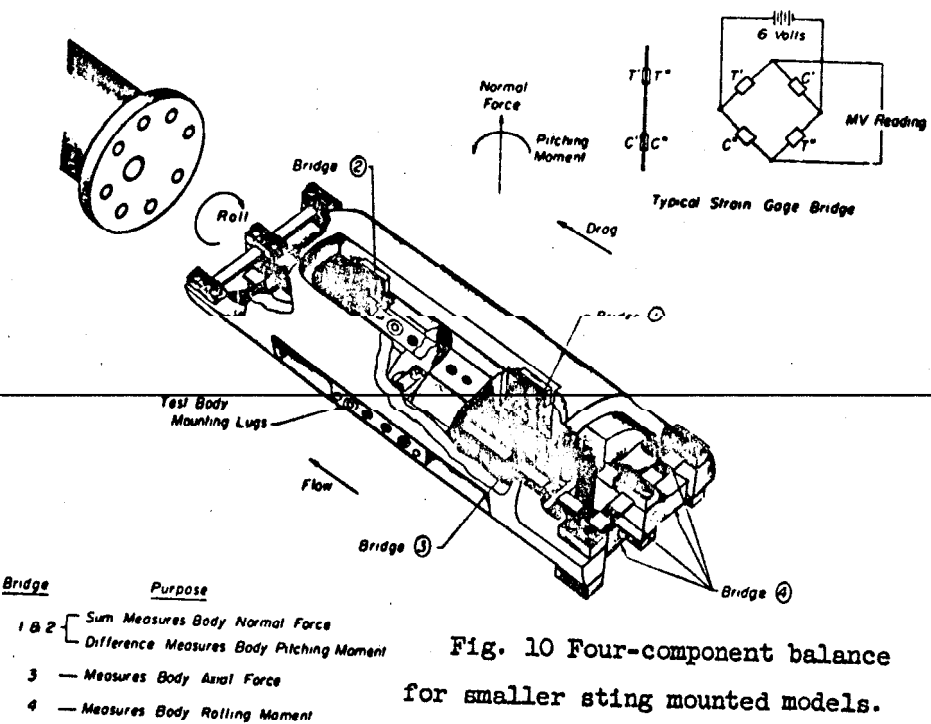


Fig. 11 Traces of thrust and torque variations of a turbo machine.

A review of tunnel test techniques originally led to selection of a ratio of 6:1 between the tunnel and model diameter as being satisfactory. Later the tunnel was used to test bodies approximately 12 in. in diameter, which is a ratio greater than the design ratio. For this reason, a technique of modifying the flow so that it conformed to the pattern which would exist in the free-stream of the larger bodies if the wall were not there was developed, using tunnel liners. This is shown in Fig. 12 for a body with constant-value stream surfaces drawn around it. Were a tunnel wall superimposed on such flow conditions, some of the normal stream paths would pass through the walls. But proper flow conditions would exist if all the flow were forced along normal free-stream paths through slightly curved liners. With this technique finally developed, excellent agreement between tunnel results and free-stream results have been achieved on test objects up to 25 in. in diameter.

The original method used to determine the shape of the tunnel-correcting liner was suggested by Von Karman⁸ and employs a distribution of line sources and sinks along the axis of the body. It was first used to design a liner for use with the 25-in. diameter model of the Albacore submarine. The shaping technique was later simplified⁹, and subsequently work by Smith and Pierce¹⁰ resulted in an improved design method which is adaptable to an IBM 1620 computer.

The liner is constructed of mahogany with sheet metal fairings into the tunnel wall. Figure 13 is a sketch of the liner installation, which conforms to the calculated contour within $\pm 1/16$ of an inch. It consists of two fabricated sections with the tunnel wall as the center section. The liner technique can be used for axially symmetrical bodies at a zero angle of attack.¹¹

Research and Test Capabilities

Testing at the tunnel can be either primarily basic areas or in areas where experimental data are needed to verify hydrodynamic design criteria or to solve developmental problems.

Included in basic research are studies of cavitation inception; flow characteristics over a body of revolution at various attack angles, as shown in Fig. 14; interactions in turbomachinery between stationary and rotating elements; noise characteristics of profusely cavitating blades, as shown in Fig. 15; and investigation of turbulence.

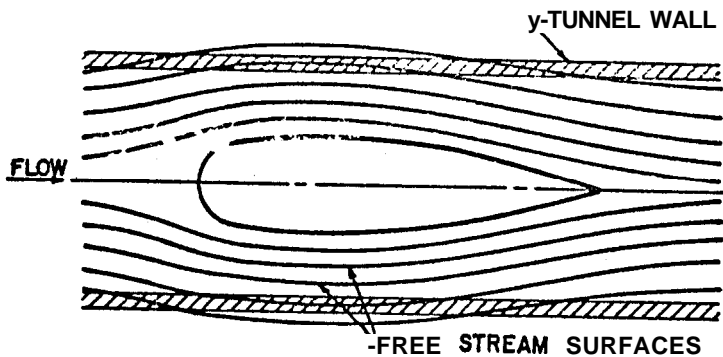


Fig. 12 Sketch of Interference of tunnel wall with free stream flow.

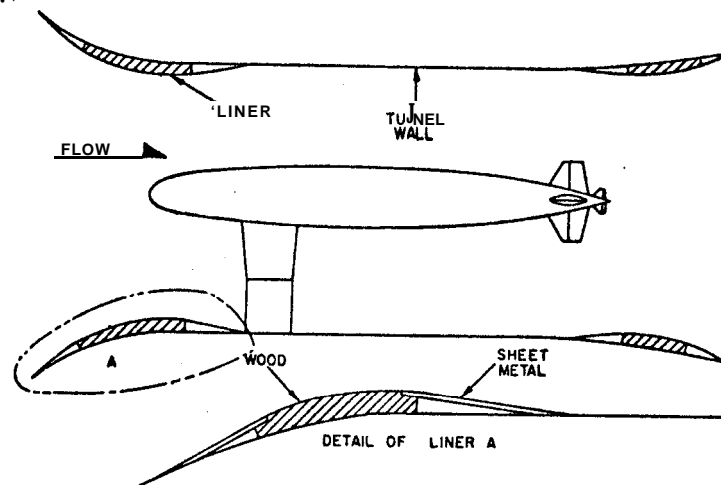


Fig. 13 Typical liner installation in the large water tunnel.



Fig. 14 Test setup for flow field observations over a body of revolution.

Under applied research, propulsion, cavitation, and vehicle control have been investigated on bodies such as those shown in Figs. 16 and 17.

With regard to basic research into turbulence, water is a better test medium than is air, provided the time responses of the instrumentation in both media are approximately the same. This last condition has been obtained by Lumley,¹² who developed a turbulence probe for water.

Next we consider cavitation. Figure 18 illustrates this condition on an ogival nose. Surface cavitation is shown in Fig. 19, and vortex cavitation in Fig. 20. Cavitation creates noise, reduces performance characteristics, and erodes or destroys wall material. The formation and growth of cavitation, and its effect on the flow characteristics of the fluid over the remainder of the body, are thus of interest in design of underwater vehicles. They are best studied in a water tunnel.

Cavitation investigations include the physics of changing from liquid to vapor state and perturbations of the boundary conditions that affect its formation. McCormick investigated, both theoretically and experimentally, the variation in the minimum pressure in the trailing vortex system of elliptic, rectangular, and delta wings as a function of the aspect ratio, angle of attack and Reynolds number¹³ as indicated in the trailing vortex systems of families of wings shown in Fig. 21. Holl extensively investigated incipient cavitation resulting from surface irregularities.¹⁴ Harvey's experiments showed that water which is air-saturated will support tensions up to 300 or 400 psi after being subjected to high pressure for several minutes.¹⁵ Holl and Wislicenus have prepared a summarizing treatise on the scale effects of cavitation.¹⁶ The properties of the gas content, as presented by the work of Ripken and Killen,¹⁷ also play an important part in the scale effect of cavitation.

List of Development and Research Capabilities

The following lists specific areas for which the Garfield Thomas Water Tunnel is well suited from both theoretical and practical aspects: a) propulsor, including both propeller and pumpjet designs; b) cavitation; c) stability and control; d) hydroelasticity, including hydroacoustics and e) boundary-layer control and turbulence research in general.

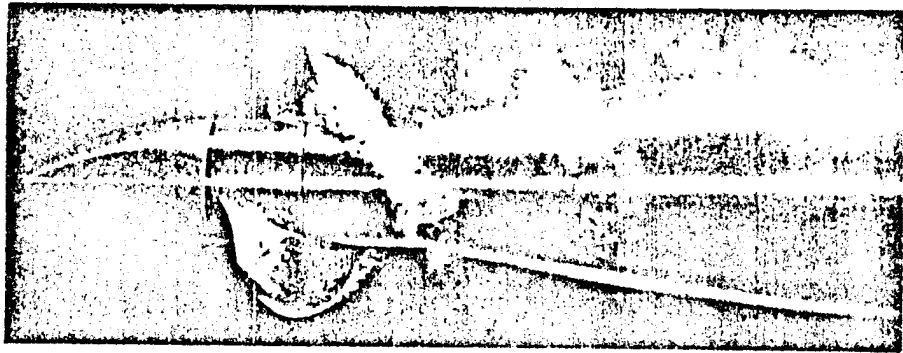


Fig. 15 Super cavitating propeller

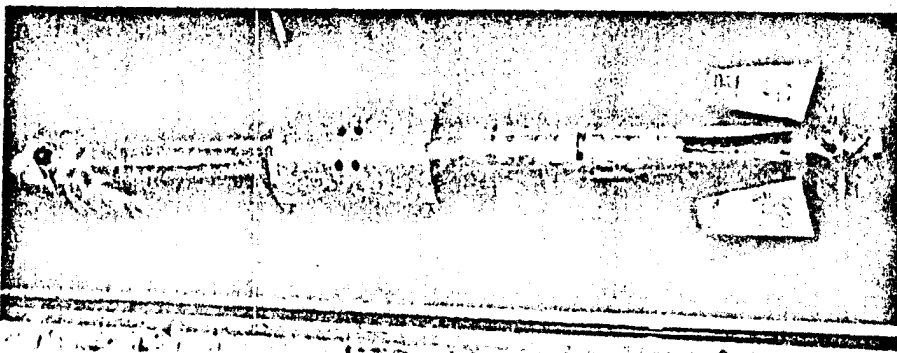


Fig. 16 12-in.-diam test body mounted in the large water tunnel.

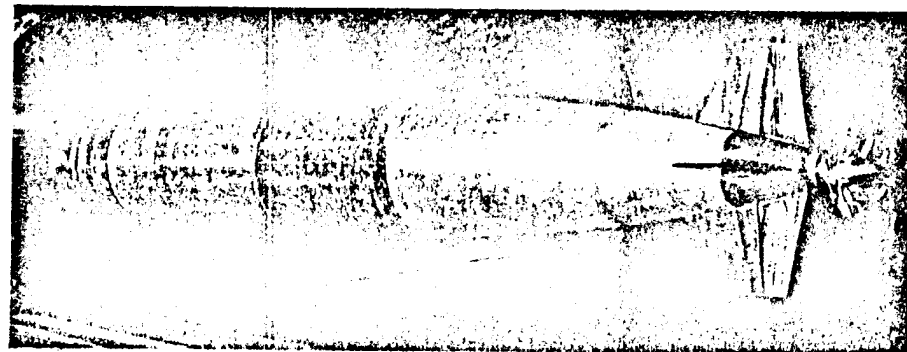


Fig. 17 20-in.-diam test body mounted in the large water tunnel.



Fig. 19 Blade surface cavitation on a free-stream propeller.



Fig. 18 Cavitation on an ogival nose.

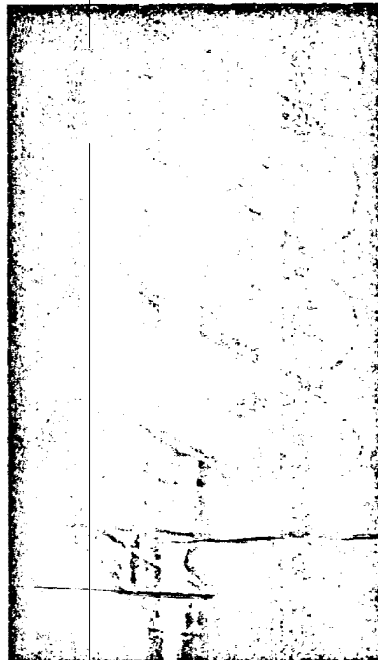


Fig. 20 Tip vortex cavitation on a body-propeller system.

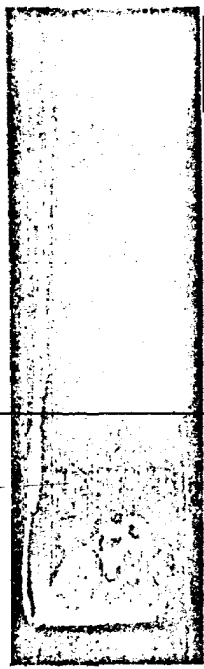


Fig. 21 Tip vortex and blade surface cavitation on a wing.

Conclusions

The Garfield Thomas Water Tunnel is a facility that treats hydrodynamics as an applied science. Its purpose is to increase knowledge in hydrodynamics, and thus to improve the performance of submerged equipment. Here, an understanding of the laws of the behavior of a fluid as a body moves through it, is necessary.

With both large and small high-speed water tunnels (velocities to 60 fps and pressures of 3 to 60 psia), a small ultra-high-speed water tunnel (335 fps and 1000 psia), a subsonic wind tunnel (170 fps at atm. pressures), and the necessary supporting equipment and instrumentation, the possible types of fluid flow investigations which can be undertaken in the tunnel are extensive.

References

1 Power, R. B., Robertson, J. M., "Garfield Thomas Water Tunnel operations," Rept. NC-7958-211, Ordnance Research Laboratory, The Pennsylvania State University (May 1951).

2 Lehman, A. F., "The Garfield Thomas Water Tunnel," Rept. NOrd 16597-56, Ordnance Research Laboratory, The Pennsylvania State University (September 1959).

3 Steele, R. L., "The design of a small water tunnel," M. S. Thesis, The Pennsylvania State College Graduate School, Dept. of Mech. Eng. (June 1951).

4 Rouse, H., "Use of the low velocity air tunnel in hydraulic research," Proc. Third Hydraulic Conference, June 10 - 12, 1946, University of Iowa Studies in Engineering, Bull. No. 31.

5 Ball, J. W., "Model tests using low velocity air," Proc. Am. Soc. Civil Engns. V. 77 (June 1951).

6 Calehuff, G. L., "The design of a small subsonic air tunnel," M. S. Thesis, The Pennsylvania State College Graduate School, Dept. of Eng. Mech. (June 1952).

7 Gertler, M., "The DTMB planar-motion-mechanism system," Proc. Symposium on the Towing Tank Facilities, Instrumentation and Measuring Techniques, Paper No. 6, Brodarski Institute, Zagreb, Yugoslavia, September 1959, (published 1960).

8 Von Karman, T., "Calculation of pressure distribution on air ship hulls," NACA TM No. 574 (July 1930).

9 Lehman, A. F., Light, J. H., and Peirce, T. E., "Elimination of water tunnel interaction with a coaxial test body by a flow correcting liner, and application to the test of an albacore model," Rept. NOrd 16597-39, Ordnance Research Lab., The Pennsylvania State Univ. (July 1958).

10 Pierce, J. and Smith, A. M. O., "Exact solution of the Neumann problem. Calculation of non-circulatory plane and axially symmetric flows about or within arbitrary boundaries," Douglas Aircraft Co., Inc. Rept. ES 26988 (April 25, 1958).

11 Peirce, T. E., "Tunnel wall interference effects on the drag and pitching moment of an axisymmetric body," Phd. Thesis, The Pennsylvania State Univ., Dept. of Eng. Mech. (December 1963).

12 Lumley, J. L., "The constant temperature hot-thermistor anemometer," Proceedings of Symposium on Measurements in Unsteady Flow, ASME Hydraulic Division Conference, Worcester, Mass., pp. 75-82 (my 1962).

13 McCormick, B. W., "A Study of the minimum pressure in a trailing vortex system," Phd. Thesis, The Pennsylvania State Univ. Graduate School, Dept. of Aeronaut. Eng. (June 1954); also see ASME Paper No. 61-WA-100.

14 Holl, J. W., "The effect of surface irregularities on incipient cavitation," Ordnance Research Lab., TM 5.3410-03 (June 1958); also, Trans. ASME, Ser. D, J. Basic Eng., V. 82, 169-183 (1960).

15 Harvey, E. N., Whitley, A. H., and McElroy, W. D., "On cavity formation in water," J. Appl. Phys., V. 18, 162-172 (1947).

¹⁶ Holl, J. W. and Wislicenus, G. F., "Scale effects on cavitation," *J. Basic Eng.*, v. 83, 385-398 (1361).

¹⁷ Ripken, J. F. and Killen, J. M., "A study of the influence of gas nuclei on scale effects and acoustic noise for incipient cavitation in a water tunnel," Tech. Paper 27, Series B, St. Anthony Falls Hydraulic Lab., Univ. of Minnesota (September 1959).

THE HIGH SPEED BASIN AND INSTRUMENTATION
OF THE

NAVAL SHIP RESEARCH AND DEVELOPMENT CENTER

K. E. Schoenherr* and W. F. Brownell†

Naval Ship Research and Development Center,*
Washington, D. C.

Abstract

This paper describes the **2968-ft** high-speed water basin and instrumentation systems for testing a variety of models, such as full-scale towed and self-propelled torpedoes, hydrofoils, planing boats, pumpjets, propellers and various high-speed vehicles. Information on the basin, towing carriages; and on propulsion, force and speed measuring instrumentation is presented. Typical test procedures and uses of the carriages are discussed. New instrumentation nearing completion will further extend the testing capabilities. The carriages are capable of speeds to **55** knots and will soon be controlled to 0.01 knot, which will permit measuring drag to 0.01 lb, despite total weight of 100,000 lb. The requirements to achieve such accuracy are extremely stringent and are met by overdesigning body structures and powerplants, operating instrumentation well within capacity and holding dimensions of large bodies to fine tolerances.,

Introduction

Hydrodynamic facilities for measuring drag and propulsion

**Formerly David Taylor Model Basin.

The facilities and the instrumentation of David Taylor Model Basin are the result of the work of many members of the **Model Basin** staff, of the Bureau of Ships, of the Bureau of Yards and Docks and of many contractors. This is freely acknowledged by dedicating this paper to them. Permission granted by the Commanding Officer and Director of the **Model Basin**, Captain **J. A. Obermeyer**, U. S. Navy, to publish this paper is also gratefully acknowledged.

*Past Technical Director, Hydromechanics Laboratory.

/Assistant Head, Hydromechanics Laboratory (Facilities and Instrumentation).

characteristics of surface and underwater vehicles often tow the test model or body through the surrounding water. Advantages are the ability to maintain steady speed relative to the medium, well within 1/100 knot, which permits measuring drag to 1/100 lb, and to use large models and large ratios of channel cross section to model cross section without excessive power requirement. Disadvantages are the high first cost of the facility, because a towing basin has to be quite long, carefully constructed and powerfully motorized to allow for acceleration and deceleration as well as the steady speed run, and a relatively inefficient operating cycle. Testing of fully submerged bodies, such as torpedoes, with primarily frictional drag requires Reynolds scaling for similitude of flow conditions. Consequently, the test speed must be relatively high to avoid large scale-effect errors, and carriage speed of 50 knots and higher are desirable.

This paper is concerned with facilities for the testing of torpedoes and similar underwater bodies and only the high-speed test facility of the Taylor Model Basin is described. However, it should be mentioned that the Model Basin's low-speed facilities are of impressive size: they comprise three basins end to end with a total overall length of about 3000 ft, a width of 51 ft and a depth of 22 ft for all but 300 ft of the length.

High-Speed Basin

The high-speed basin at the David Taylor Model Basin (DTMB) tests both model-scale and full-scale torpedoes, hydrofoils, pump jets, planing boats, sonar domes, wetted, ventilated and super-cavitating propellers and other high-speed bodies. Tests may relate to measurement of propulsion characteristics, forces and moments acting on the model, or in some cases model-generated noise. The basin is housed in a reinforced concrete arch structure, alongside a surface ship model test basin. Figure 1 shows an outline plan of the interior of this structure. The roof of the building has a free span of 110 ft and a rise of $24\frac{1}{2}$ ft. It is heated and ventilated to maintain about the same inside temperature throughout the year with some control over sweating through cork insulation on the walls above the concrete abutment.

The present high-speed basin is rectangular in cross section as shown in Figure 2 and is 2968 ft long. It is 21 ft wide and 10 ft deep for 1168 ft of its length and 16 ft deep for the remaining 1800 ft. The basin walls are of monolithic concrete sections. Each section is 38 ft long separated by 2 ft gaps that were filled with reinforced concrete after the

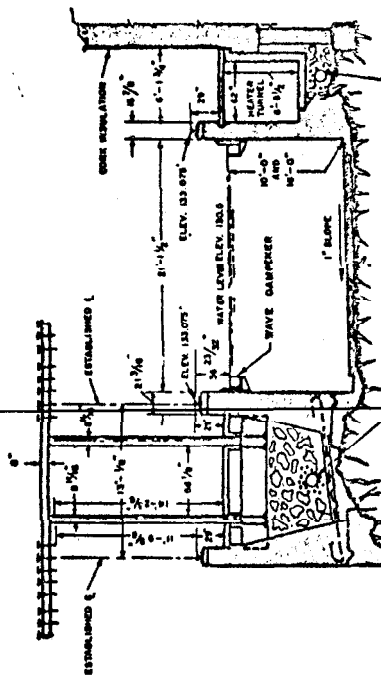


Fig. 3 Model showing track construction.

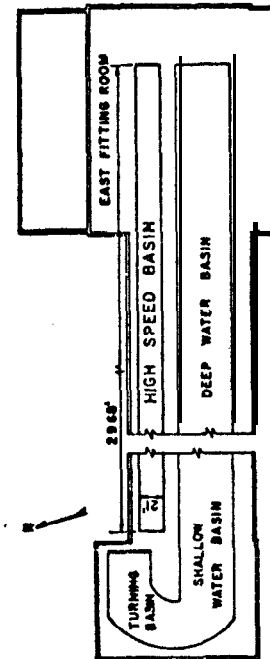
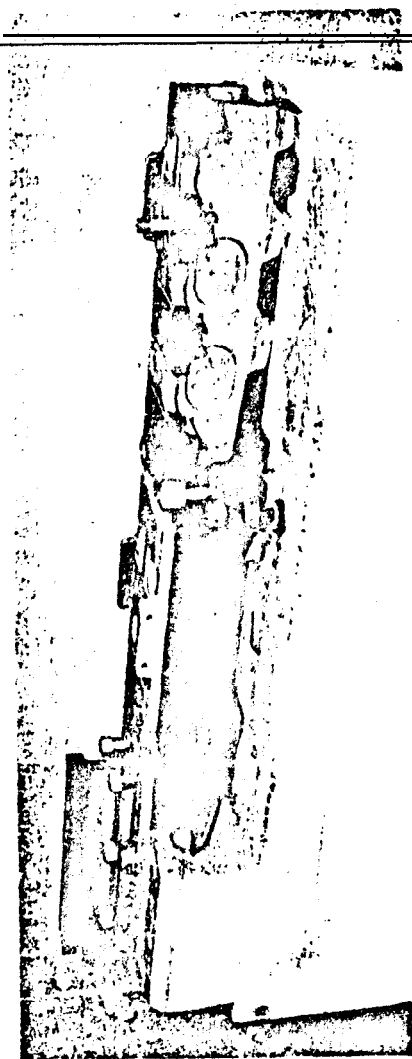


Fig. 1 Outline plan of high speed basin.



sections had set and shrunk. During construction, the basin was enclosed by the building to prevent large temperature variations.

The basin walls are concrete and support the steel tracks on which the towing carriages run. The concrete walls and the bottom of the basin go down to bedrock to furnish a solid foundation for the tracks, which are set precisely. A typical detail of the track construction is shown by the model in Fig. 3. The rails are bolted to high-strength cast iron chairs, which in turn are bolted to the concrete walls. The steel rails are of railroad type and weigh 165 to 185 lb/yd. In general they are about 31 ft long and welded together. The top and sides of the rail heads and the bottom of the rails are ground flat and the top rail is set within \pm 0.005 in. of the water level along the length of the basin. The sides of the rail heads are parallel within 0.005 in. in either direction throughout their length to a vertical plane through the center of the basin.

The basin is filled with fresh water fed by gravity from a conduit of the District of Columbia water supply. The water is clarified by continuous passage through a sand bed filter to facilitate underwater photography, which is taken through glass viewing ports set into the north wall about midlength. Waves and other disturbances generated during the measuring run are quenched by wave absorbers, shown in Fig. 2, which are U-shaped troughs attached to the walls with their upper edges about $\frac{1}{4}$ in. below the water surface.

DTMB carriages 3 and 5 serve the high-speed basin. Carriage 3 has a top speed of 40 knots (46 mph) and carriage 5, 60 knots (69 mph). The latter has interchangeable wheels, with one set equipped with rubber tires for noise tests.

Propulsion dynamometers, force balances, etc., with their associated indicating and recording devices, are available in great numbers and diverse capacities, as later discussed.

Towing Carriages

60 Knot Towing Carriage 5

The towing carriages at the DTMB were designed on a deformation rather than on a stress basis to provide platforms of great stiffness with minimum deflections. Carriage 5, which is pictured in Fig. 4, is a large precision instrument² for conducting model tests at speeds up to 60 knots (69 mph).

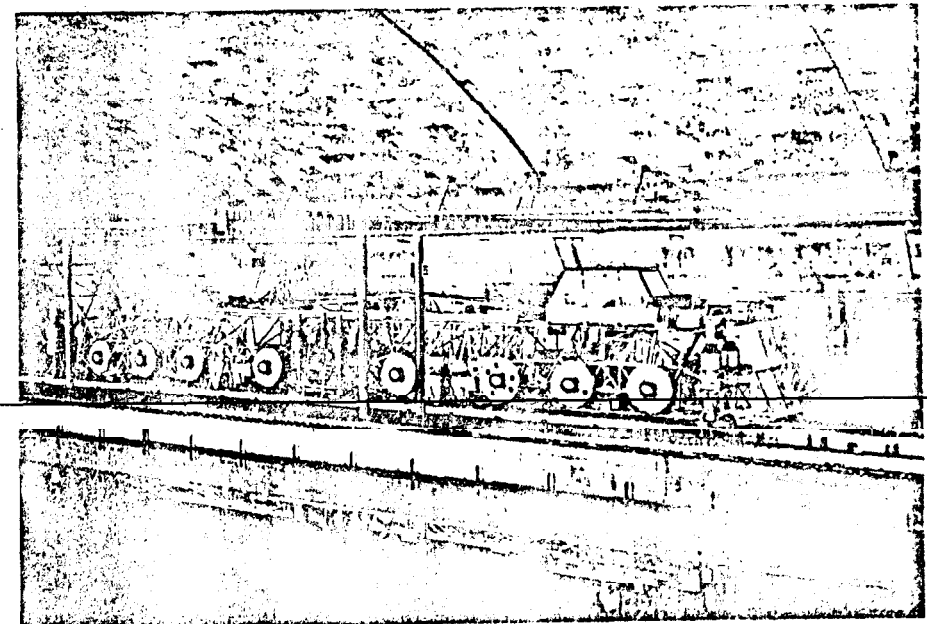


Fig. 4 Carriage 5 with steel wheels.

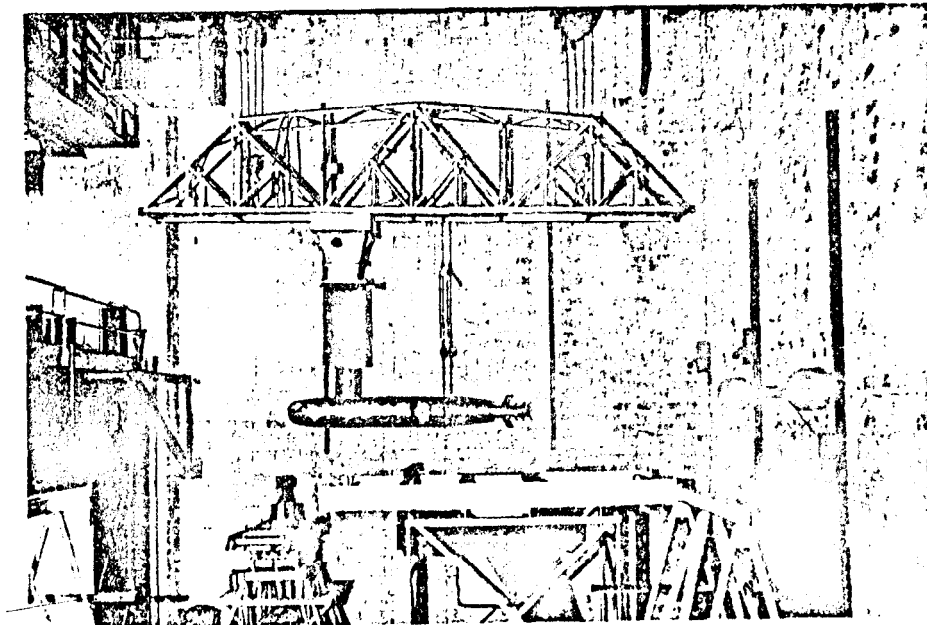


Fig. 5 Towing bridge with strut and torpedo attached.

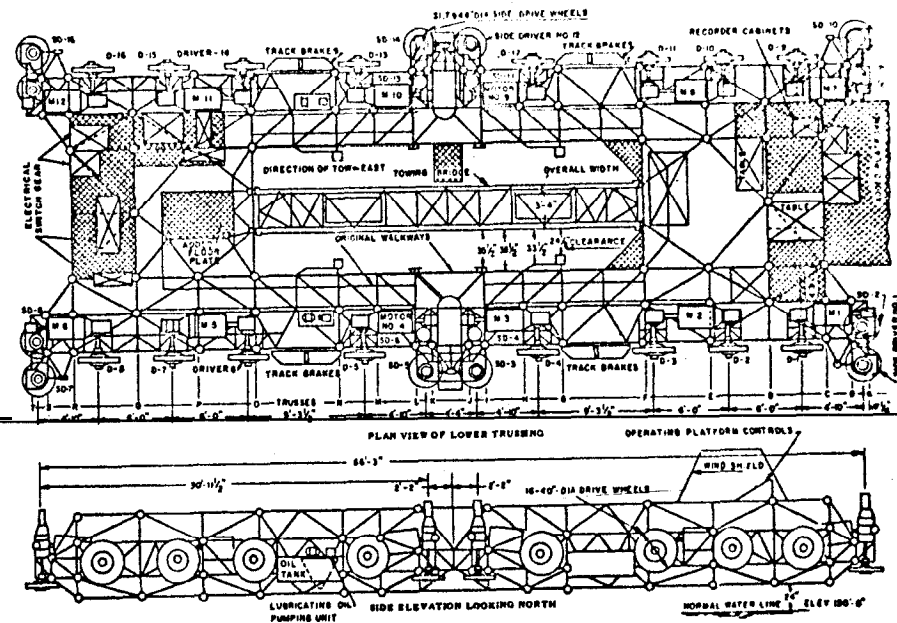
This carriage is a welded tubular steel trusswork 70 ft long by 26 ft wide.³ The tubular members range from 3-in o.d. by 0.183-in wall to 1-3/4-in o.d. by 0.156-h wall. An open rectangular test bay, 31 $\frac{1}{2}$ ft long by 10 ft wide, is provided for mounting the towing bridges to struts and test vehicles, as is shown in Fig. 5. These bridges can be readily disconnected for model fitting without affecting use of the carriage. The carriage with its basic drive equipment weighs about 100,000 lb., its drag load capacity is 9000 lb. (Its structurally safe drag load limit of 20,000 lb, cannot be reached because it exceeds the available traction.) The average length of run during which steady carriage speed can be maintained is about 2100 ft at 20 knots and 680 ft at 55 knots without a model attached and somewhat less with a model.

As can be seen in Fig. 6, the carriage is driven by twelve 250-v, 3500-rpm (maximum), dc motors. These are rated at 165 hp, but each can develop 400 hp during the short time the carriage accelerates. Motor armatures are series connected to equalize loads. A 17-bar trolley system installed along the north side of the basin provides the required power and control supplies. The carriage drive is an adjustable voltage dc system with automatic feedback which regulates steady speed to ± 0.06 knots or 0.1% of full scale. A program is underway to improve carriage speed regulation further.

The carriage motors drive 32 steel wheels. Sixteen wheels, 40 in. in diameter, are vertical and carry the weight of the carriage. The remaining 16 are horizontal side drivers, 31.285 in. in diameter which are located opposed pairs and press against the sides of the rail head to provide the additional tractive effort needed. The side drivers on the south side of the carriage are guide as well as drive wheels. The maximum tractive effort of the carriage is about 20,000 lb and the maximum average acceleration rate about 0.16 g.

The 16 vertical-drive wheels can be fitted with rubber tires with steel cords which are water-inflated to 280 psi. Acoustic tests are run with these tires. Side drivers are not used with the rubber tired wheels, as the latter's coefficient of friction provides sufficient traction for acceleration.

Carriage braking is by regenerative action, with the drive motors acting as generators to feed power back into the lines. When a quicker stop is needed or a power failure occurs, the carriage is stopped by mechanical track brakes mounted on the carriage, consisting of spring-loaded shoes that grip the sides of the rail heads and provide a deceleration of about 0.5 g. If both braking systems fail, emergency braking can be obtained



by tapered nose runners on the underside of the main frame of the carriage which enter spring-loaded shoes attached to the basin walls at the extreme end. Deceleration in this case is about 2 g.

Power supplies of 2500 and 1000 amp supply up to 400-v of direct current to powered models and a 609-v ac, 300-kva and a 50-kw model power supply is also available.

40-Knot Towing Carriage 3.

Carriage 3, with a top speed of 40 knots (46 mph), weighs about 30,000 lbs. The main towing dynamometer mounted on the carriage has a drag capacity of 150 lb. This carriage is used primarily for model testing of planing craft, hydrofoil boats, high-speed craft, and calibration of special devices such as speed logs. It is pictured towing a motor boat in Fig. 7.

This carriage is a triangular shaped welded tubular steel trusswork 24-ft. 7-in. wide. It is 33-ft long on the south side and 11-ft. 4-in. long on the north. Figure 8 shows its general arrangement. The tubular members range from $3\frac{1}{2}$ -in. o.d. to $1\frac{1}{2}$ -in. wall thickness to $1\frac{1}{2}$ -in. o.d. by 0.065 in. wall thickness. The dynamometer bay is 3-ft 6-in. wide by 8-ft 5-in. long.

The carriage is driven hydraulically by a 200 hp synchronous motor. There are four 40-in. vertical steel drive wheels on the south side of the carriage and two 20-in. vertical steady-wheels on the north. It is guided in a horizontal plane by groups of four 8-in. guide wheels at each end of its south side.

Each drive wheel is driven by a direct connected oil motor powered by a pump attached to the shaft of the 550-v ac synchronous motor. The latter obtains power from a trolley system located over the south side. In addition to the synchronous motor, there are two oil pumps and four oil motors. The synchronous motor drives the pump at constant speed, whereas the variable control of the hydraulic system accelerates and drives the carriage at any selected speed. The same system decelerates the carriage by using the oil motors as pumps and the synchronous motor as a generator. This carriage operates from east to west, whereas carriage 5 operates from west to east. A spring loaded mechanical track system, similar to that used with carriage 5, is provided for emergency braking at the west end of the basin.

Power supplies available for model power on carriage 3 include

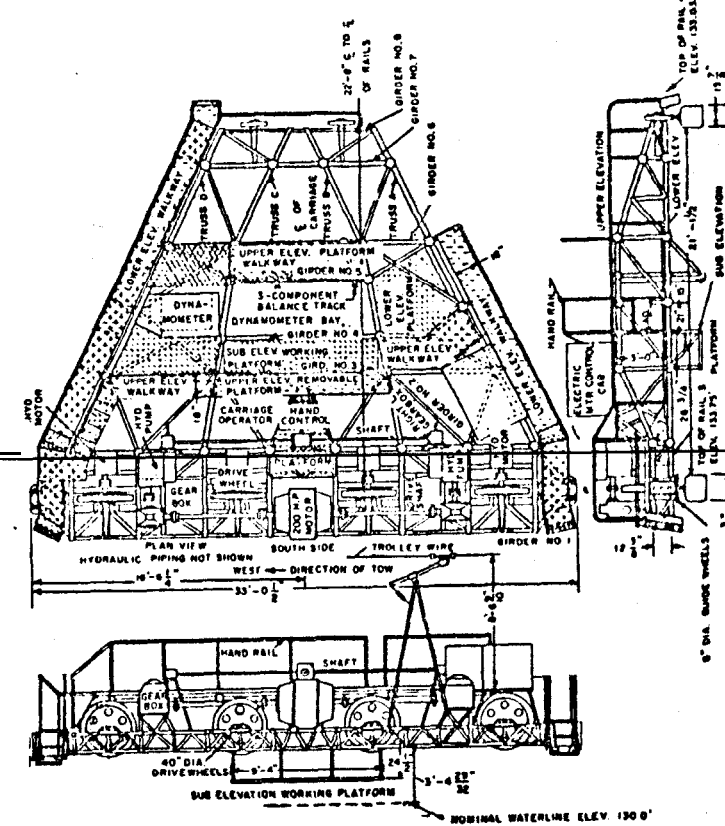


Fig. 8 General arrangement of carriage 3.

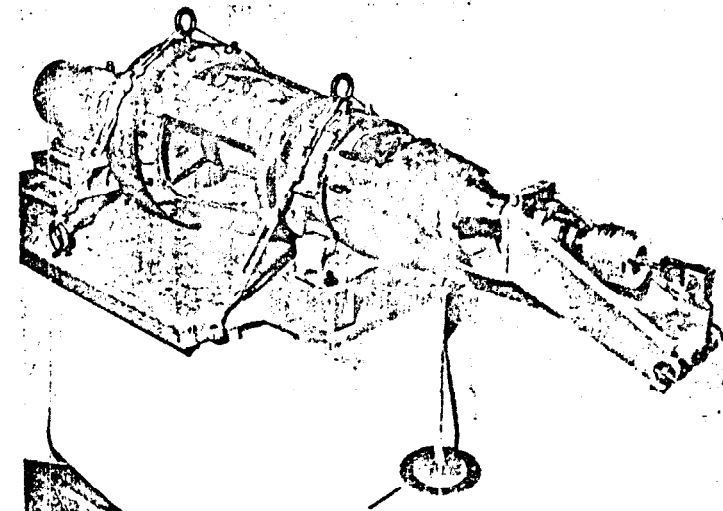


Fig. 9 315 hp contrarotating torpedo dynamometer.

a 0 to 400-v dc, 5-kw supply; a 600-v ac, 100-kva supply; and a 50-kw shore-based supply.

Instrumentation

Some of the wide variety of instrumentation available for model testing in the high-speed basin is next described.

Transmission Dynamometers

Transmissiodynamometers⁴ of the differential reluctance type are used to measure model propeller-shaft torque, thrust and revolutions. They are fitted into the shaft between the drive motors and the propellers. Reluctance type transducers⁵ include a displacement gage (magnigage) which is combination with flexure joints measures forces or-moments; a torque gage (magnitorque); and a thrust gage (magnithrust). Digital indicators and graphical recorders are used for readout, supplemented by a direct writing oscillograph for dynamic conditions. An electromagnetic counter pickup measures shaft revolution. It consists of a copper disk with 10 radial slots and a fixed pair of coils that pick up a pulse as each slot passes. These are counted over time intervals and indicated digitally in rpm or rps. The dynamometers have an overall accuracy of at least 1/2%.

315 Horsepower Contrarotating Torpedo Dynamometer

The dynamometer shown in Fig. 9 measures torque and thrust in contrarotating shafts of full scale torpedoes and is mounted inside the torpedo housing with the propulsion motors. The entire body is then connected to one or two struts attached to a towing bridge mounted in the dynamometer bay of carriage 5. Propeller thrust is measured by magnigage transducers and torque by magnitorque units. The capacities of the dynamometer are 330 lb-in. of torque and 600 lb of thrust at 3000 rpm/shaft. Readings are digitally indicated or graphically recorded.

35 Horsepower Propeller Dynamometer

A 35-hp propeller dynamometer⁶ is used for open water characterization of propellers up to 20 in. in diameter. It consists of an underwater body that houses a transmission type dynamometer. To avoid interference, the test propeller is extended well forward of the main body, as shown in Fig. 10. The assemblage is supported by struts secured to the towing carriage. The dynamometer motor, which is located above water, drives through a vertical shaft and right angle gear box within the underwater body. Signals from the transducers are

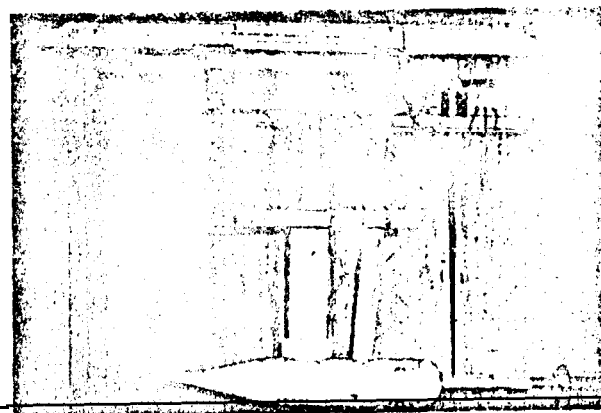


Fig. 10 5hp propeller dynamometer.

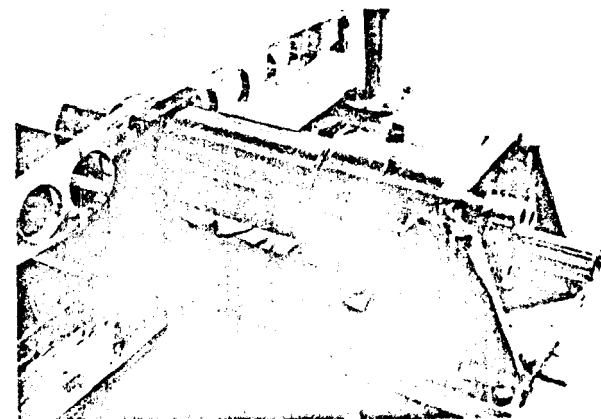


Fig. 11 500 hp nacelle dynamometer in calibration stand.

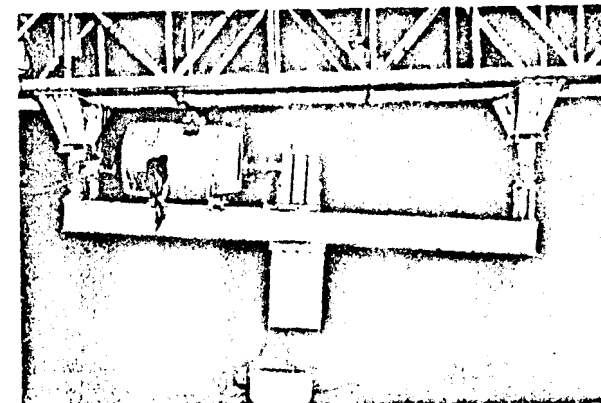


Fig. I.2 500 hp nacelle dynamometer test setup.

transmitted through slip rings and converted to digital readings. The capacity of this dynamometer is 35 hp through the shaft at 1000 to 2500 rpm. Its thrust capacity if 700 lb in "ahead" operation and 200 lb in "astern" and maximum torque capacity is 21,600 in-lb.

500 Horsepower Nacelle Dynamometer

This dynamometer, shown in Fig. 11, is installed inside the nacelles of model hydrofoil boats to measure torque, thrust and rpm. A strut attached to a girder secured to the towing bridge supports the nacelle. The dynamometer is driven by a motor located above water through a 1:2 speed-up right angle gear box, a vertical shaft, and a right angle gear box located in the nacelle, as shown in Fig. 12. Magnithrust and magnitorque transducers of the differential reluctance type are used on this dynamometer also. Its capacities are 3000 lb-in. torque, 2000 lb of thrust and 10,000 rpm, maximum.

General Purpose Dynamometers

The capacities of several propulsion dynamometers of the transmission type, available for surface and submerged model tests, are listed in Table 1.

Table 1 Capacities of Some Transmission type propeller dynamometers

		Thrust, lb	Torque, lb-in	Rpm
5 hp,	40 lb-in. torque	± 60	± 40	8500
5 hp,	50 lb-in. torque	± 50	± 50	5400
8.5 hp,	100 lb-in. torque	± 100	± 100	5400
5 hp,	150 lb-in. torque	± 150	± 150	5400
5 hp,	200 lb-in. torque (contrarotating)	± 50	± 50	5400
20 hp,	400 lb-in. torque	± 250	± 400	3600

Figure 13 shows a typical propeller dynamometer connected to a propulsion motor and Fig. 14 shows an exploded view. The outer diameter of its cylindrical portion is 2 5/16-in. and the overall length of the housing is 11 1/4-in.

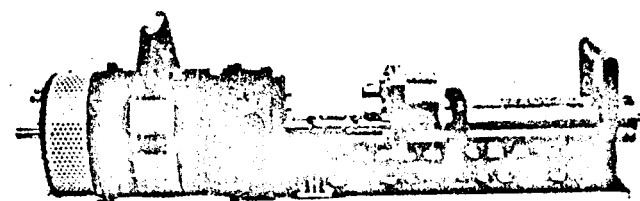


Fig. 13 5 hp, 100 lb-in. propeller dynamometer and motor ready for surface model installation.

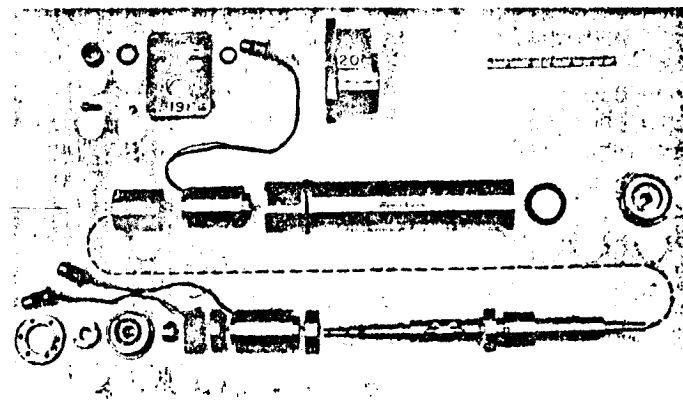


Fig. 14 Exploded view of 5hp, 50 lb-in. propeller dynamometer

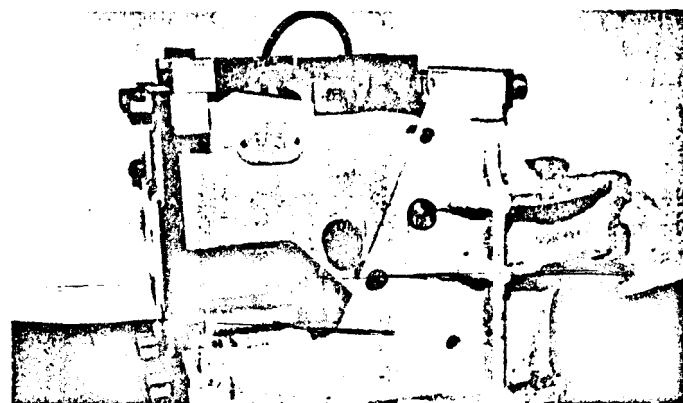


Fig. 15 4000 lb internal resistance dynamometer.

Internal Resistance Dynamometers

Two dynamometers are available to measure the **drag to full scale** or model torpedoes and similar bodies. They also utilize **magnigage** transducers installed between the end of a strut rigidly connected to the **carriage** and the model. Out-put is recorded on a digital recorder⁷ located **on the carriage**. The capacities of these dynamometers are 15 and 4000 lb, respectively, the latter is shown in Fig. 15.

Hydrofoil Dynamometers

A hydrofoil dynamometer measures forces and moments **on hydrofoils towed in a straight line at various angles of attack**. It is attached to the tow bridge on **carriage 5**, as shown in Fig. 16.

The dynamometer uses modular force gages with **magnigage** type transducers as measuring elements. Each is in the form of a 4 in. cube, as shown in Fig. 17. The gage responds to forces in only one direction and so must be properly orientated and combined to measure forces and moments. Capacities are as follows: lift, 5000 lb; drag, 1000 lb; side force, 1500 lb; pitching moment, 40,000 lb-in.; rolling moment, 40,000 lb-in; and yawing moment, 20,000 lb-in.

Since **modular** force gages are available in capacities up to 2000 lb, it is possible to vary the range of operation of the dynamometer over an extensive range.

Induction Motor Dynamometers

Induction motor dynamometers of the cradle-frame type are used to calibrate large propulsion motors, as shown in Fig. 18 for full scale torpedo motors. After calibration, they provide torque as a function of electrical current and shaft horsepower is calculated from torque plus measured rpm.

The dynamometer consists of two 400-hp induction motors that can be used as generators to absorb power or as motors to deliver Dower and Toledo scales to measure forces at the end of the torque arms. The motors and shafts are arranged so that contrarotating propeller motors up to 400 hp each can be simultaneously calibrated and their shafts can be coupled to deliver or absorb up to 800 hp. They are each rated as 265 amp, 800/1065-v and 3000/4000 rpm.

The dynamometer has five scale ranges and accuracies of 1/20% of scale range have been obtained under static conditions.

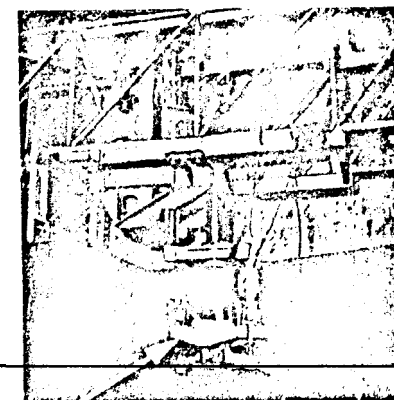


Fig. 16 Hydrofoil dynamometer with tow bridge.

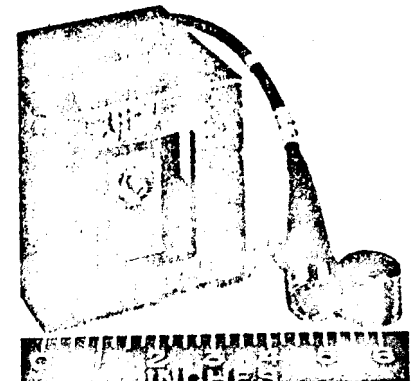


Fig. 17 Modular force gage.

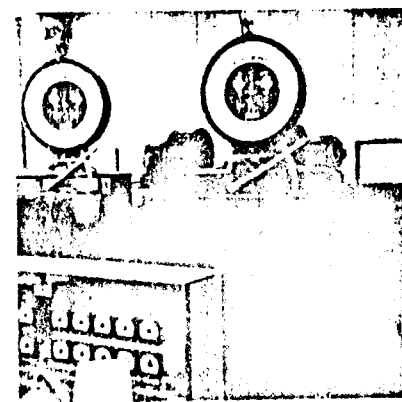


Fig. 18 400 hp induction motor dynamometers.

In addition to the 400 hp unit, a 25 hp induction motor dynamometer of the cradle type is available for calibrating **smaller** propulsion motors. It consists of two 25 hp induction motors and has the same operating flexibility as the **larger** unit.

Carriage Speed Measurement

The speed of **carriage** 5 is generally measured by **an electro-magnetic** revolution counter that provides 100 pulses/f% of carriage travel. An electronic pulse counter and printer **indicates** and records speed. It is planned to **install** a higher resolution system **in the near future**.

Two speed measuring systems are available for carriage

One is similar to that on **carriage** 5, and the other **measures** the distance between marks scribed each second on a sensitized paper "card" rolled on a drum. With a **special** scale, **carriage** speed in knots is **read** directly from this record.

Carriage 3 Towing Gear and Dynamometer

The resistance dynamometer on **carriage** 3 is attached to the lower end of a **pantograph** frame whose other end is fastened to a weight plus a spring **balance**. Spring extension is recorded by a stylus **on** a waxed paper **card** rolled into a drum, which also serves as the speed recorder.

As illustrated in Fig. 19, towing gear No. 1 automatically moves up as the model rises, so that the towing force **is** always along-the shaft line. Towing gear No. 2, which is shown in Fig. 20, test6 planing surfaces and models **of** the hulls of the seaplanes and hydrofoil boats. The **drag** force capacity of the towing gear is 150 lb.

New Instrumentation

To **carry** out an extensive hydrofoil program **in the high-speed basin**, additional major **instrumentations** are planned. They include a **planar** motion mechanism for obtaining both static and dynamic stability coefficients of models, a pitch heave oscillator to measure unsteady hydrodynamic forces **and** moments, a 1000 hp supercavitating propeller dynamometer, a wave maker and a wave absorb& **and** an underwater TV **camera** and housing.

Conclusions

The high-speed basin with its associated **instrumentation** is a versatile facility for obtaining design data on the high speed

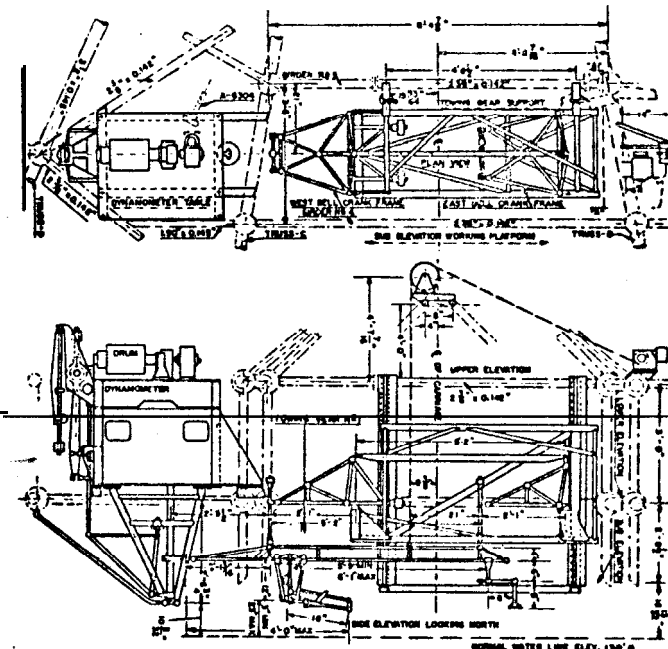


Fig. 19 Carriage 3 dynamometer and **towing** gear No. 1.

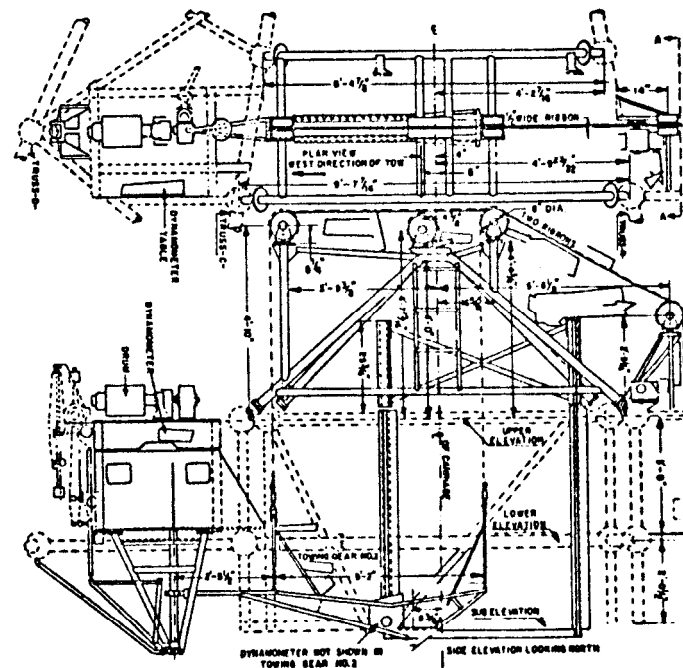


Fig. 20 Carriage 3 dynamometer and **towing** gear No. 2.

performance of underwater and surface test vehicles is still an and roughwater. By its instrumentation, numerous problems can be studied: directional stability and control of torpedoes, hydrofoils and submarines; propulsion characteristics of propellers, torpedoes, pumpjets and other underwater devices; resistance of planing and other high speed craft; performance of hydrofoils under fully wetted, partially cavitating, ventilated and supercavitating conditions; and propeller "singing" and other acoustic phenomena. The precision, size and speed range of this facility make it unique in this country in that both model and full scale testing of vehicles can be accomplished.

References

¹Saunders, H. E., "The David W. Taylor Model Basin", ^{part 2}, Trans, Soc. Naval Architects Marine Eng. (1938, 1940, 1941).

²Wright, E. A., "New research resources at the David Taylor Model Basin", David Taylor Model Basin Rep. 1292 (January 1959).

³DeShazer, G. A., "An arc welded high speed model towing carriage", Design-for-Progress Award Program, James F. Lincoln Arc Welding Foundation (June 1947).

⁴Norman, G. J. & Wilson, M. W.; and Bryant, F. B., "Propeller dynamometer instrumentation at the David Taylor Model Basin", David Taylor Model Basin Rep. 1068 (July 1956).

⁵Wilson, M. W., "A differential reluctance measuring system and its application to model and ship testing", American Institute of Electrical Engineers Middle Eastern District Meeting Paper (April 1958).

⁶Santore, G. L., "Dynamic calibration of 35 hp propeller dynamometer", David Taylor Model Basin Rep. 805 (February 1952).

⁷Pimlott, J. R., "The DTMB magnetic micrometer MK II", David Taylor Model Basin Rep. 847 (May 1953).

⁸Gertler, M., "The DTMB planar-motion-mechanism system", Symposium on Towing Tank Facilities, Instrumentation and Measuring Technique, Paper 6, Zagreb, Yugoslavia (September 1959).

⁹Brownell, W. F., Asling, W. L. and Marks, W., "A 51 foot pneumatic wave maker and a wave absorber", David Taylor Model Basin Rep. 1054 (August 1956).

THE AEROJET RING CHANNEL

Joseph Levy*

Aerojet-General Corporation, Azusa, Calif.

Abstract

The Aerojet Ring Channel, a hydrodynamic test facility, is an annular tank with inside radius 35 ft and outside radius 55 ft in which objects as large as a torpedo are towed by a double-ended rotating boom. Present maximum attainable speed is 99 knots at 50-ft radius. At top speed, the boom can support up to 10,000 lb at each end on the 40-ft radius. Several internal and external force-measuring balances are available, and various sources of power can be used for driving self-propelled vehicles or propulsion devices. Underwater ports permit visual and photographic observations. Hydrophones, tape recorders, and sound analyzing and measuring equipment are used, plus a closed-circuit-TV-camera mounted on the boom. The ring channel is used also for free-flight tests of underwater vehicles - from small, high-speed, underwater rockets to a two-man submersible.

Introduction

This paper describes the Aerojet Ring Channel as it is today, and outlines some planned improvements. This hydrodynamic test facility, located at Aerojet-General Corporation's Von Karman Center in Azusa, Calif., was built under Contract Noori-10 with the Office of Naval Research. Completed in June 1948, it was first operated as a Navy-owned facility, and now has been acquired by Aerojet.

The facility was designed to test subsurface or near-surface high-speed vehicles. Thus, it moves at higher speeds and sustains and measures larger forces than are normally met in traditional towing tanks, which mainly study surface ships. It is particularly suited for studying hydrodynamics of underwater rockets, torpedoes, submarines, foils, struts, and air cushion vehicles.

*Manager, Hydrodynamics Staff.

The ring channel with its circular layout corresponds to a towing tank of infinite length, permitting continuous testing for appreciable distances and periods of time. Among advantages, it allows damping coefficients and apparent mass coefficients to be measured without resorting to oscillating balances. The circularity creates problems, such as running into the wake generated in previous passes, but these will be eliminated or minimized by improvements planned for the near future.

Fixed Structures

The channel is a circular well with outer peripheral vertical walls of 110-ft diam and a concentric 70-ft-diam island, making a working channel 20 ft wide, as shown in Figs. 1 and 2. The normal water depth increases from 10 ft at the north to 12 ft at the south, due to a sloping bottom for ease of draining. It holds 466,000 gal of water with 18 in. of freeboard. The reinforced-concrete walls and floor are 10 in. thick to withstand moderate underwater explosions.

A three-story observation and control tower houses, at its ground level, electrical transformers and switch gear for the main drive and auxiliary power. The upper story is built with a viewing window of explosion-proof glass and contains the boom control console and necessary instrumentation. The bottom subterranean level has six rectangular explosion-proof glass windows set in the outer wall of the channel and used for underwater viewing and photography. A similar observation room is located directly opposite the tower under the island.

A 4- by 6-ft tunnel running under the channel connects the control tower to underground areas on the island which house the drive machinery for the boom, the support bearing of the rotating boom, and the slip ring assembly. The tunnel serves as a cableway for wiring and permits access to the island during boom operation. To minimize hazards, the side of the control tower facing the ring channel is protected by a thick, reinforced-concrete wall with outside steel plate, and the paved area around the ring channel is surrounded by an earth dike.

Rotating Room

The rotating boom is a box-type truss supported at its center. The main steel tubular framed structure is welded throughout and consists of seven central bays, each 5.5 ft wide and 7.5 ft high, and four outer bays, slightly tapered in plan, the over-all length being 80 ft and weight 18 tons. The boom is supported under the central bay by four feet resting

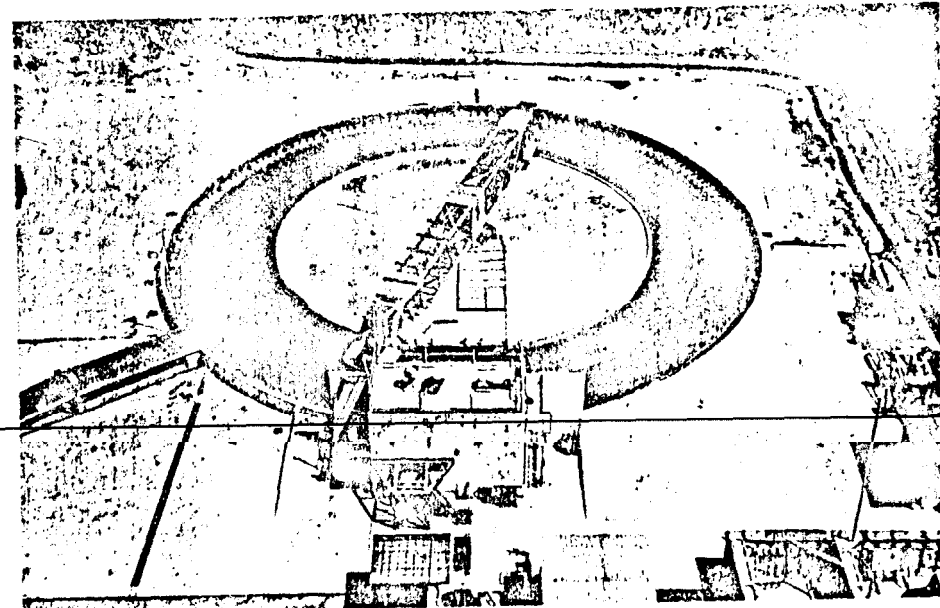


Fig. 1 View of the ring channel while operating at 30 knots.

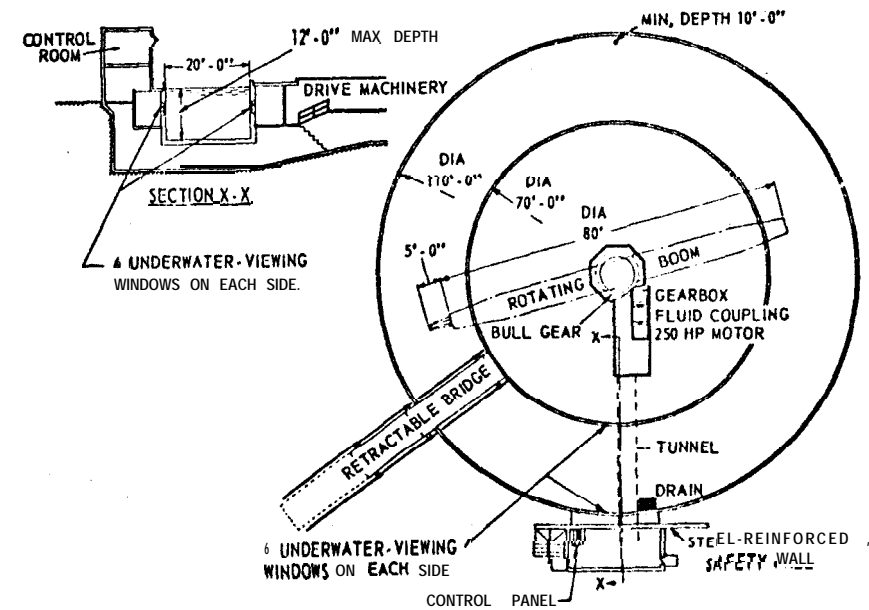


Fig. 2 Schematic diagram of the ring channel.

on the rotating element of the main bearing. Two are bolted down and two are unrestrained, permitting free thermal expansion and elastic elongation (0.020 in. under maximum radial tension).

Support equipment permits testing at either end, boom design conditions being 10,000 lb at each end while rotating at 40 rpm (99 knots at 40-ft radius). Boom extensions of comparable strength and of 2.5, 5.0, and 7.5 ft may be attached at one end. Others of 5.0 and 10.0 ft, but of lower strength, are for attachment at the other end.

To minimize radial forces, the boom is balanced by lead weights for which steel counterweight chests are provided at each end. The central bay of the boom is enclosed to form an auxiliary control room that may be occupied at low speeds.

Main Bearing

A single, large-diameter roller bearing supports the rotating boom without need for a center kingpost. This bearing must resist a large over-turning moment (designed for 901,000 lb-ft), since test objects are usually suspended up to 8 ft below the boom while counterweights at the other end are placed directly on it. The static rating of the bearing is 1,200,000 lb vertical and 548,000 lb radial. At 40 rpm, this is reduced to 500,000 and 227,000 lb. The level of the boom was checked after mounting to be within 0.005 in. in 82 ft. The bearing friction is so slight that one man, by pushing, can easily rotate the fully laden boom.

Main Drive Machinery

The boom is rotated by a 250-hp induction motor through a variable-speed fluid-coupling, a double-reduction bevel gear, and finally, a 30-in. pinion that drives a 10-ft pitch-diameter bull gear mounted on the bearing housing, as shown in Fig. 3. The motor may be overloaded to above 500 hp for short periods. A remotely controlled oil pump permits the fluid-coupling to provide stepless variation in speed from a few feet per second to maximum. This drive can tow unpowered test objects to approximately 100 knots at the 50-ft radius, whereas speeds up to 125 knots can be attained when the test object provides additional power.

Auxiliary Equipment

Controlled nitrogen gas to 1800 psi is available for driving turbines or other prime-movers in self-propelled vehicles, for



Fig. 3 Boom drive machinery.

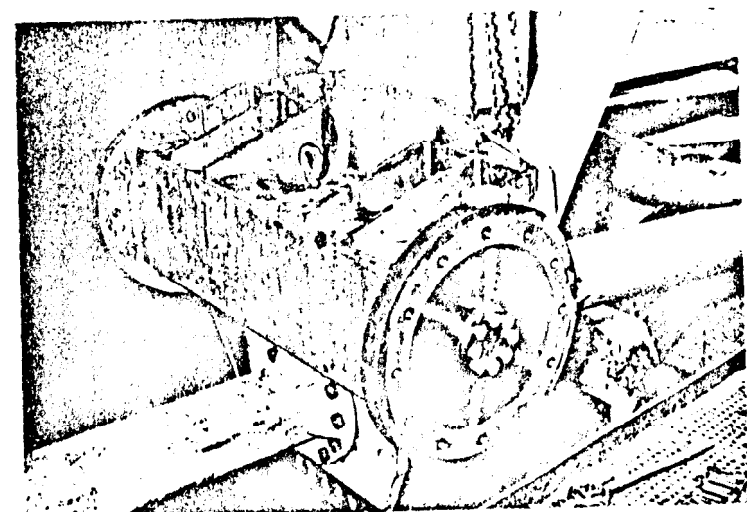


Fig. 4 Thrust suspension balance.

inflating cavities in cavitation flow, or for venting flows over hydrofoils or propellers. Gaseous fuels or oxidants can be handled in tests of thermal powerplants.

An electrically powered steam generator can be mounted on the boom for condensable-exhaust studies, and a small electrically heated tank is available for molten-metal fuels.

A 250-hp gasoline engine with a complete mechanical transmission system is available for supplying large amounts of power for pump, propeller, or other rotating machinery studies. The engine is mounted on the roof of the central cab, and shafting runs over the top of the boom with two right-angle gear drives providing a power train to any underwater vehicle that may require it. Shaft-power dynamometers are used with this system.

A short, free-fire missile test range is located on the floor of the channel for launcher development work and ignition, propulsion, and cavitation studies. It is approximately 60 ft long and instrumented and illuminated for high-speed motion and microflash photography. It is provided with a ballistic box for missile recovery. Speeds to 136 knots have been measured in it.

Water Purification and Wave Suppression

The water in the channel is kept clean by continuous skimming of the surface and continuous treatment with chlorine.

Wave dampers of the capacitance-resistance type are installed around the ring channel walls. They are open-top rectangular boxes, divided by bulkheads into 2-ft cubical compartments with circular holes in bottom and sides. They may be observed in Fig. 1.

Force-Measuring Balances

Thrust-Suspension Balance

A one-component balance is permanently mounted at one end of the boom at the 40-ft radius to measure the force component in the direction of motion (either drag or thrust). It is made up of two steel diaphragms rigidly attached at their peripheries to a ret-tangular frame bolted to the boom. A rigid bar connects the centers of the diaphragms and supports a bolting flange to which test objects are attached. Fig. 4 shows this balance, without the streamlined enclosure that normally surrounds it. Drag and thrust up to 2000 lb can be measured.

Six-Component Internal Balance

A high-precision, six-component balance, manufactured by the Task Corporation of Anaheim, Calif., is installed in submerged test bodies and can simultaneously measure lift and cross-forces to 3000 lb, yaw and pitching moments to 1500 lb-ft, drag to 400 lb, and roll torque to 600 lb-in. Its maximum diameter is 2.500 in., and its over-all length is 18 in. It is of the strain-gage type, as used in wind-tunnel models (but is waterproofed), and has a precision of $\pm 0.5\%$.

Six-Component External Balance

~~Aerojet~~ designed balance is used for studying the hydrodynamics of hydrofoils, struts, air cushion vehicles, etc. It consists of a fixed frame (attached to the boom above water level) and a floating frame which supports the test object. The two frames are joined by six flexured suspensions, each containing a strain-gage load cell (see Fig. 5). This schematic shows the floating frame, the suspensions, the load cells (cylindrical elements) and the points of attachment to the fixed frame (indicated by hatched lines). The bellows of a centrifugal-force compensator, CFC (described below), is interposed between the floating and fixed frames.

The three forces and three moments are resolved about mutually perpendicular axes, as shown. Brag force, cross force, lift, yaw moment, pitch moment, and roll moment can each be calculated from various combinations of load cell readings.

Figure 6 shows the balance mounted on the boom and supporting a surface-piercing, base-vented strut. The box-like structure of light color is the fixed frame, and the darker, gusseted, T-shaped structure is the floating frame. Normally, the balance is enclosed in a wind-proof, streamlined housing (observable in Fig. 1) to eliminate aerodynamic forces on the floating frame.

Centrifugal Force Compensation (CFC)

During testing, the model and floating frame are subject to unwanted centrifugal forces. To remove them, the CFC system applies a force to the suspended parts of the balance which is equal to, but in opposite direction from, the centrifugal force. It consists of a piston pressurized by a mercury column in a tube running inboard along the boom. Hydraulic pressure is created by the centrifugal force integrated along the length of this tube, and this length is adjusted for the weight to be counterbalanced. The mercury column ends in a small, spherical

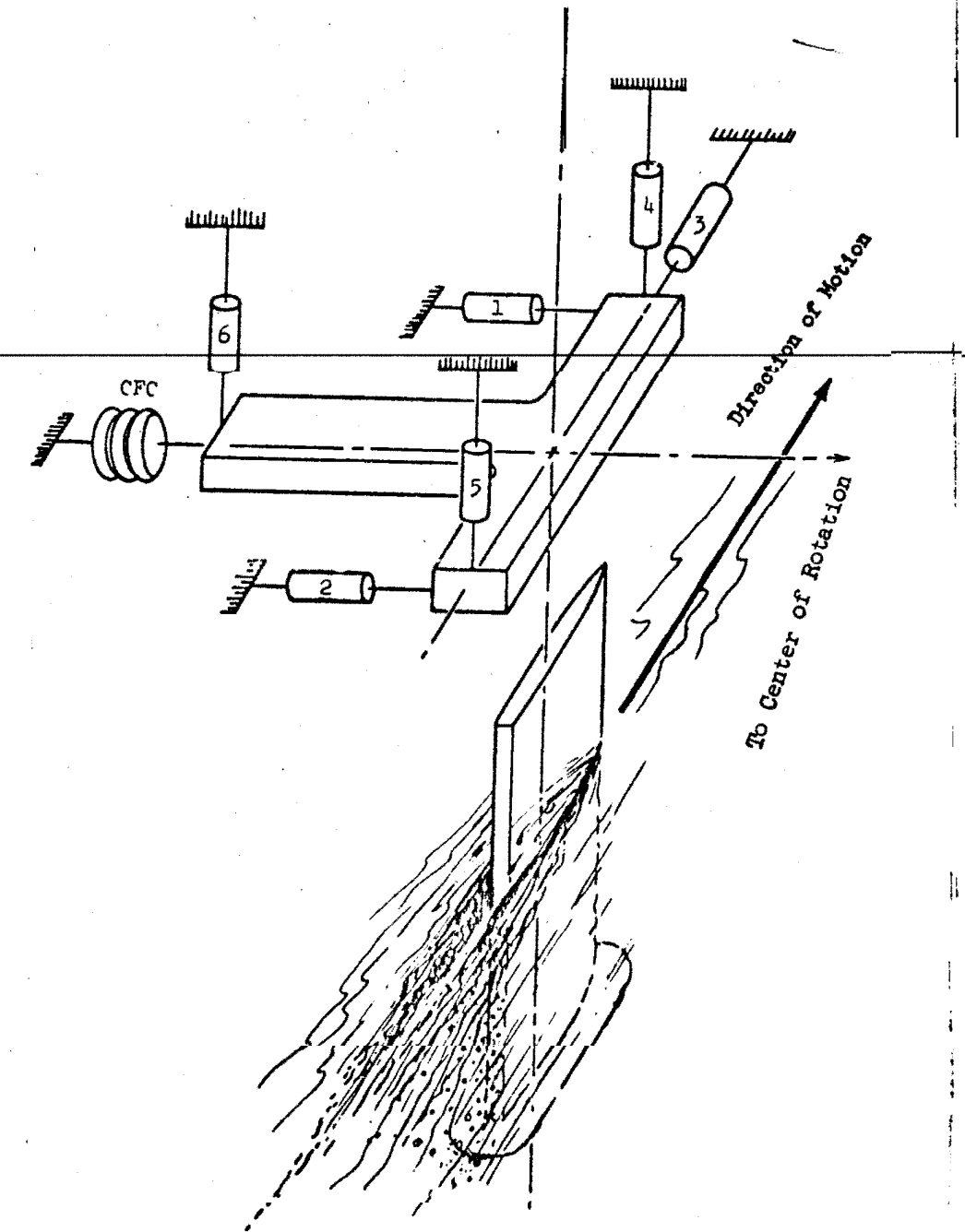


Fig. 5 External six-component balance, schematic arrangement.

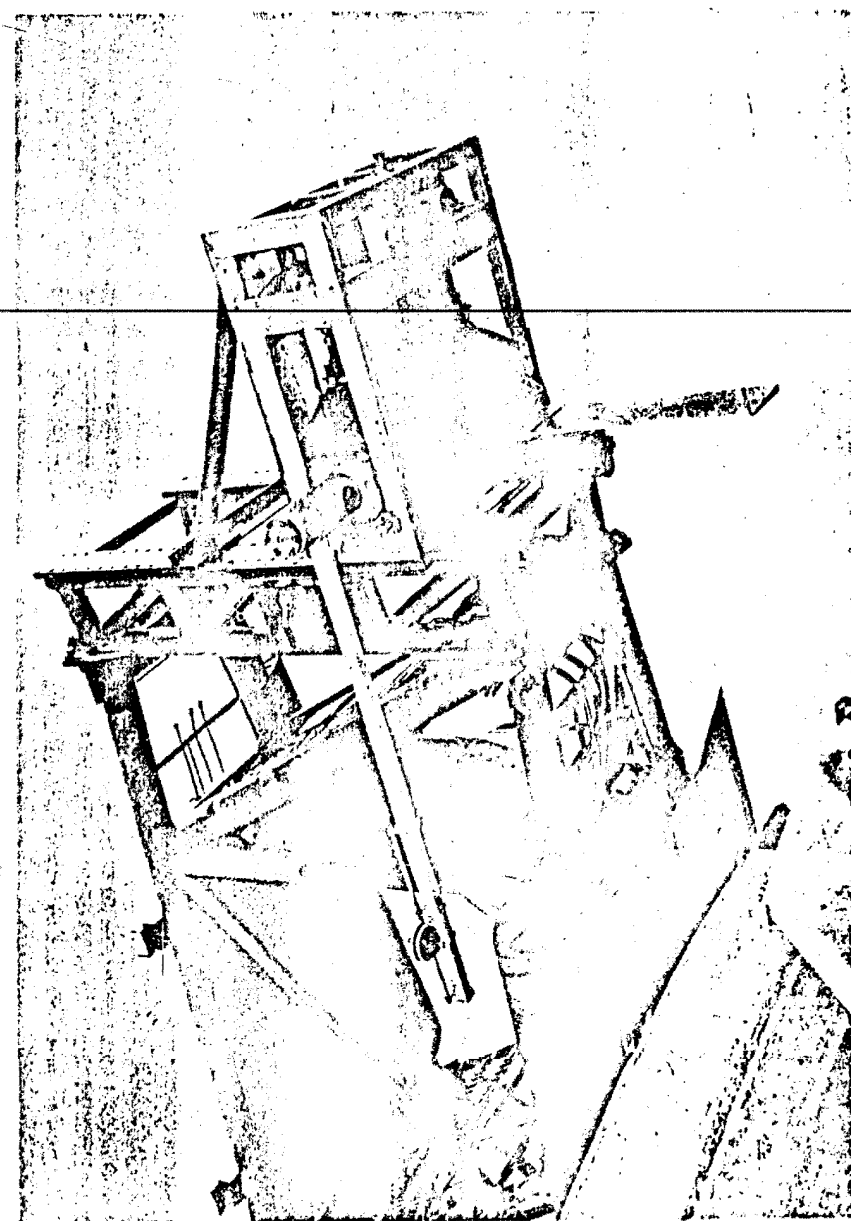


Fig. 6 The external six-component balance and vertical ways mounted on end of boom.

tank, shown in Fig. 6, on the long, square rod extending inboard from the balance.

Capacity and Calibration

The present force-measuring capability of the balance is 20,000 lb in the lift direction, 10,000 lb in the cross force direction, and 1000 lb in the drag direction. However, different force ranges can be obtained by substituting other load cells. Calibration is achieved by direct application of known forces, either by dead weights or by a precision load cell.

Instrumentation and Control

Control and Data Transmission

An array of unshielded slip rings, accommodating up to 100 leads, is mounted under the main bearing. It transmits, between the rotating boom and shore stations, power, on-off signals, and readout of signals in the nature of step functions. A smaller assembly, below the first one, has 48 additional fine, fully shielded slip rings for noise-free transmission of data signals of the proportional type. The slip rings are shown in Fig. 7.

Electrical Instrumentation

Voltage-regulated, d.c. power units provide inputs for strain-gage sensors. Low-level output signals are amplified by differential d.c. amplifiers (NEFF) prior to transmission across the slip rings. Honeywell potentiometer recorders (Brown Electronic) are used for recording steady-state data, while oscilloscopes (CEC and Midwestern) are used where high-frequency response is required.

Towing Speed Measurement

Ground speed of towed objects is measured by a photoelectric tachometer mounted on the boom-drive shaft on the output side of the fluid coupling. The photocell generates an electric pulse for each 0.100 ft of motion at the 50-ft radius. The pulse frequency is counted, and displayed electronically or recorded with a timing pulse on an oscilloscope for determination of instantaneous speed and acceleration. Relative speed between the towed object and the water is measured by a pitot tube and a solid-state pressure transducer.

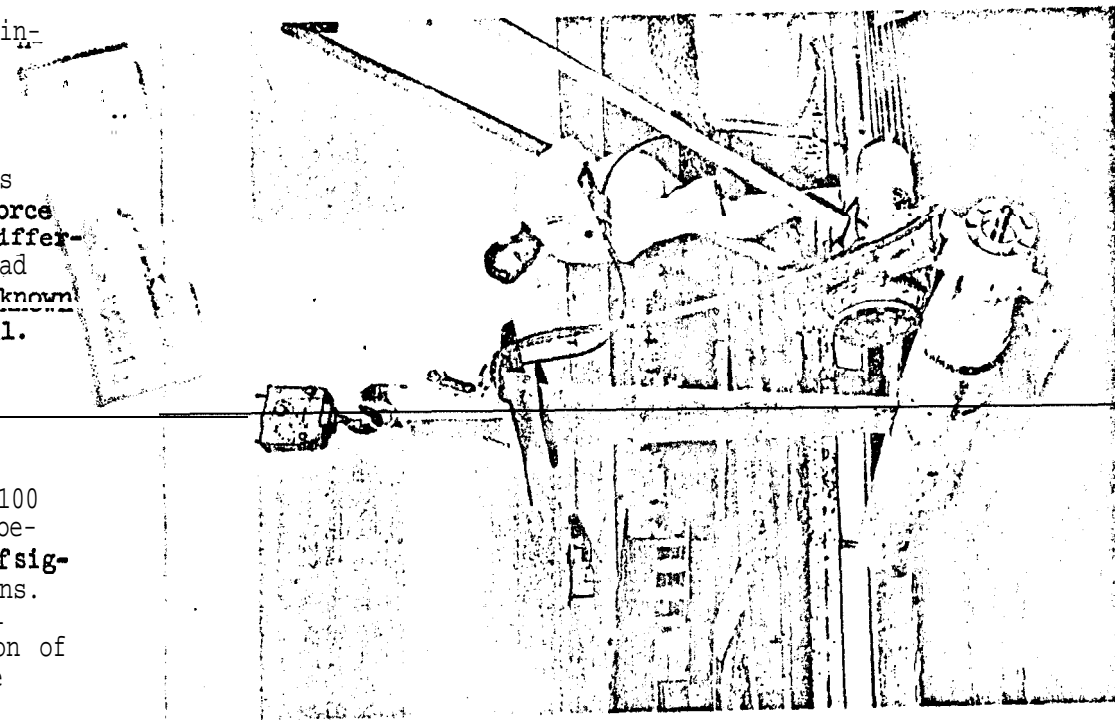


Fig. 8 Full-size torpedo arm strut.

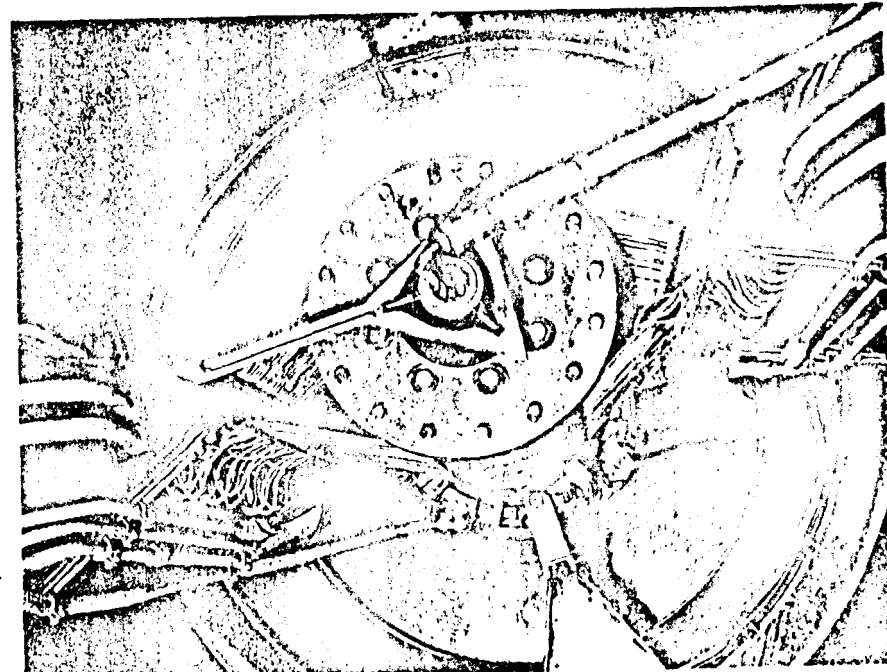


Fig. 7 Slip-ring assembly.

Control Console

The control console consists of panels containing the permanent instrumentation and controls for the boom drive and auxiliary equipment. Interchangeable panels are used, as required, for individual test programs.

Television Monitoring

A General Electric closed-circuit television camera, Model 9TE, is emplaced on the boom for constant close-up viewing of models undergoing tests. The monitor **screen** is in the instrument panel of the control tower.

Photographic Instruments

Camera and lighting equipment is available for photographic observation and recording of the test object and flow around it. These range from large-plate still cameras to high-speed motion picture equipment.

Acoustic Measuring Equipment

The ring channel is provided with acoustic measuring equipment useful from 2 cycles to 100 kc. It consists of hydrophones, suitable amplifiers, sound-level meters, sound-level recorders, a vibration analyzer (2-1/2 to 750 cycles), variable bandpass filter (0.2 cycles to 100 kc), and magnetic tape recorders.

Capabilities and Experience

Scope and Capacities

The ring channel is suitable for a wide range of experiments. In addition to towing bodies either underwater or at the surface, it may be used for underwater rocket firing, for water entry and water exit studies, for underwater sound measurement, and for underwater explosion studies. The rotating arm serves also as a centrifuge for testing missile components under accelerations up to 16 g.

Generally, the maximum speed **is limited** only by the structural strength and **torsional rigidity** of the test object and the **supporting strut**, or by the force and moment capacity of the **force** measuring balance.



Fig. 9 Hydropulse vehicle at **60** knots.

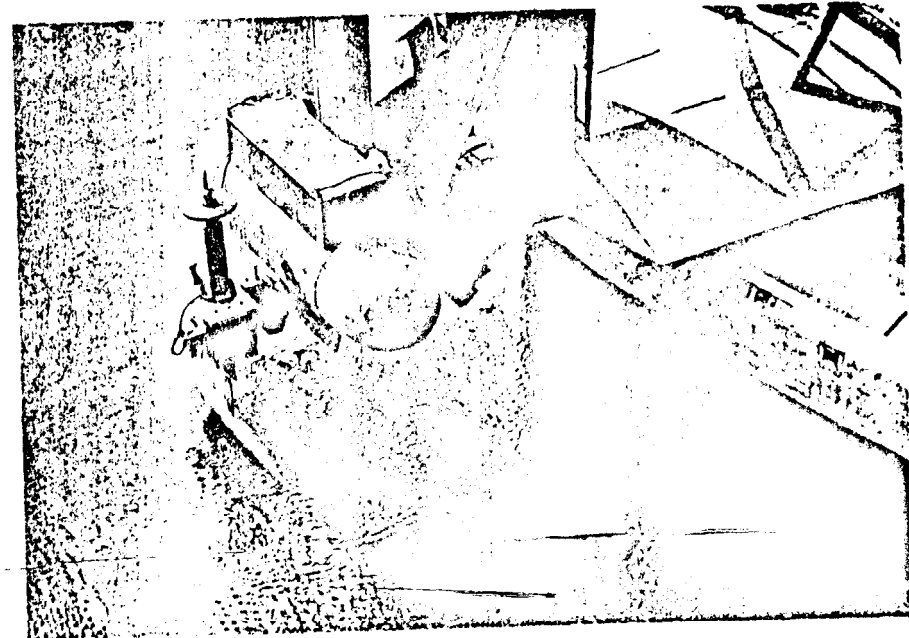


Fig. 10 Streamlined body of revolution at shallow depth.

Past Experience

In its first decade, the ring channel was used ~~almost exclusively~~ as a test and development tool on Aerojet projects under contract with governmental agencies. Recently, the work has included research studies and test programs in the general field of hydrodynamics. Among programs of interest are the following:

- 1) Hydrodynamics of surface-piercing hydrofoil struts for the Bureau of Ships. Model chord lengths ranged up to 2 ft, and speeds to 70 knots.
- 2) Hydrodynamic problems involved in the development of the ~~Torpedo Mk-46~~ for the Bureau of Weapons.
- 3) Effects of polymer additives upon hydrodynamic drag and upon self-noise of torpedoes and of thin plates.

The following examples illustrate the range of experimentation:

- 1) Figure 8 is a strut carrying a full-size, 500-lb torpedo that during test would be 5 ft below the water surface.
- 2) In Fig. 9, a full-size, self-powered hydropulse vehicle is being tested at 60 knots. In Fig. 10, a small, streamlined body of revolution is ready to be towed, whose forces range from a few ounces to 3 lb.
- 3) Figure 11 is a self-powered, wet-hull, miniature submarine (**Minisub VII**) with two men aboard during free-flight tests in the ring channel.
- 4) Figure 12 shows a 10-ft model of an underwater tanker being towed by a cable at 4 knots.
- 5) Figure 13 is a hydrofoil and strut assembly tested for Grumman Aircraft Engineering Corporation up to 70 knots.
- 6) Figure 14 shows the cavitating cores shed by a ~~surface-~~ piercing strut, as photographed during a study of hydroelastic flutter.
- 7) Figure 15 shows vapor cavitation on a base-vented strut operating at 5° yaw and 60 knots.

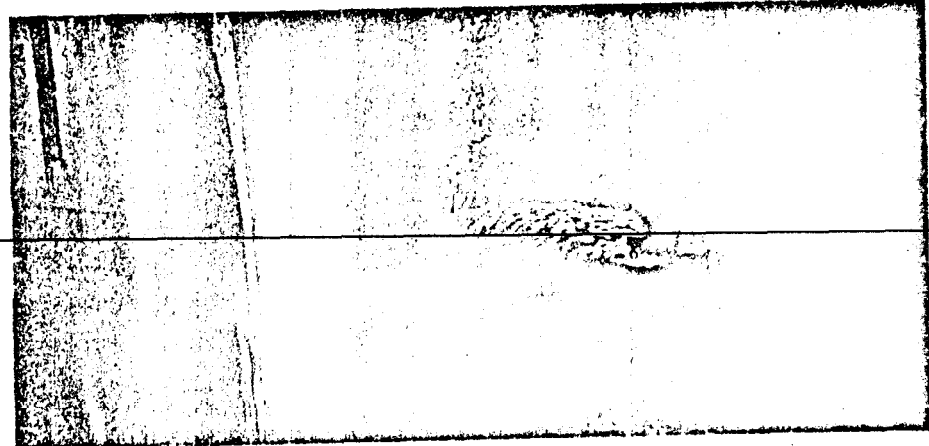


Fig. 11 **Minisub** Mk VII operating in ring channel.

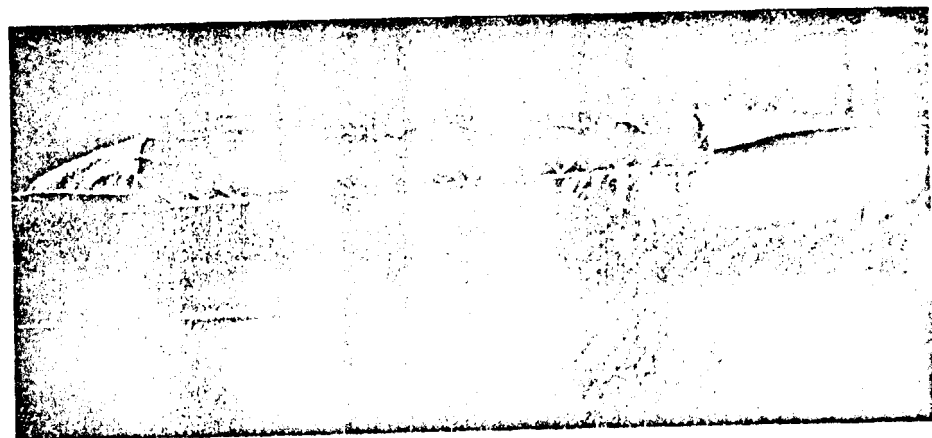


Fig. 12 Model of underwater tanker in tow.

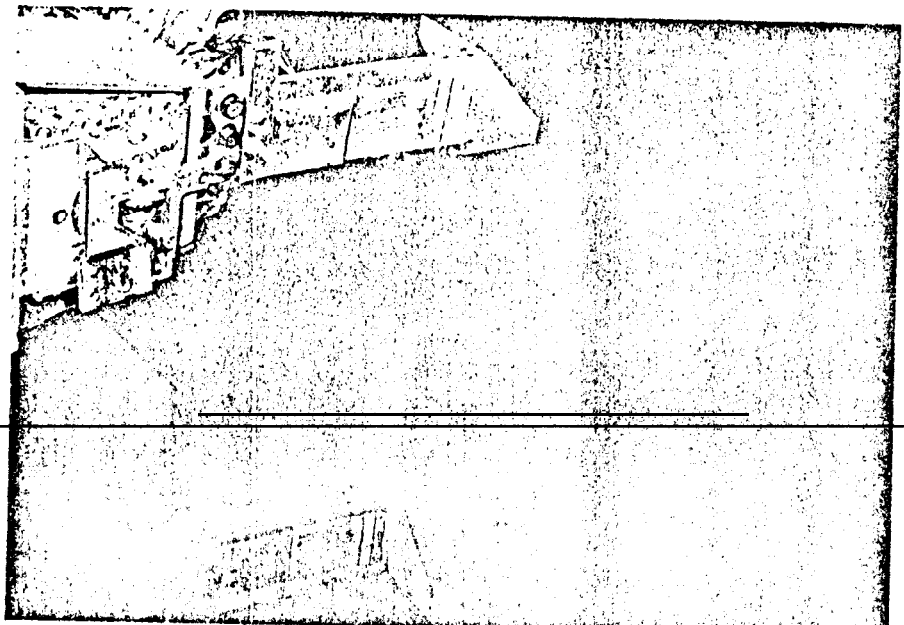


Fig. 13 Hydrofoil with surface-piercing strut, shown rotated 90° counterclockwise from normal position.

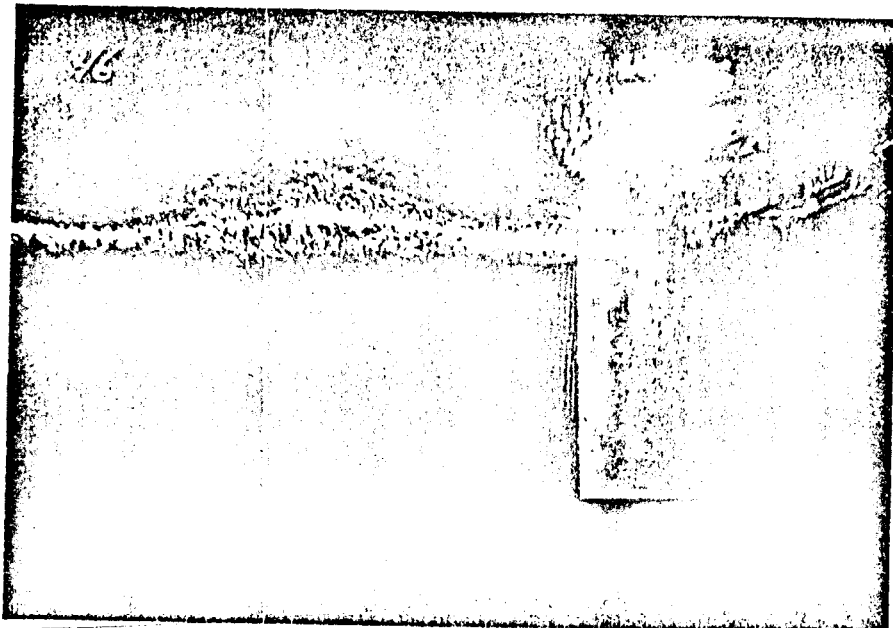


Fig. 14 Cavitating vortex street shed from vertical strut.

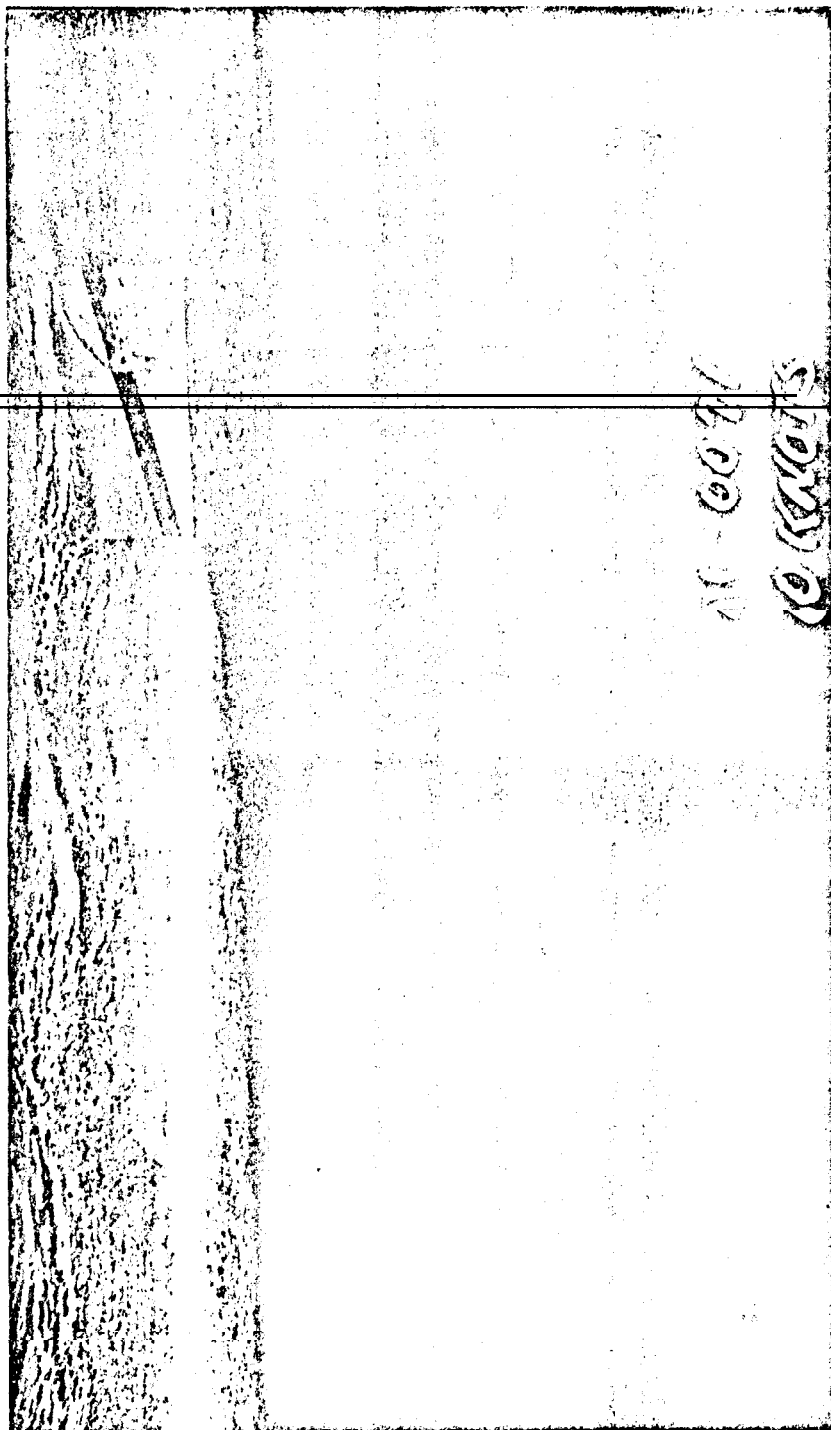


Fig. 15 Vapor cavitation on base-vaned strut at 5° yaw and 60 knots.

Plans for Improvement

The two major improvements being planned for the ring channel are discussed in the following paragraphs.

Additional Power

The power for **driving** the boom is to be at least doubled by an additional power train that will incorporate a **variable-** ratio, remotely controlled, gearbox making possible full power at **low** boom speeds and materially decreasing time to come up to operating speed. Incorporation of a brake will decrease the time required for deceleration. Using the present and the new systems together, the boom speed will be brought to the 40 ft/min for which it was designed; at 50-ft radius, this corresponds to 125 knots and a centrifugal acceleration of 25 g.

Model Immersion Mechanism

To mitigate problems from waves and **wake** previously formed in the channel, it is planned to incorporate a mechanism to hold in the model above water until the boom reaches test speed and **then** lower it to the desired submergence in about one-third of a revolution. This will leave about 200 **ft** of run in absolutely undisturbed water.

THE UNDERWATER CABLEWAY

J. W. Hoyt*

Naval Undersea Warfare Center, Pasadena, Calif.[†]

Abstract

An underwater cableway that provides realistic conditions for testing torpedoes without danger of loss at sea is described. It consists of a pair of parallel steel cables stretched in a shallow catenary under the surface of a lake with test vehicles attached to the cables by runners. The test vehicles are propelled under their own power, and instrumented to accurately measure acceleration, thrust, radiated noise, and interaction of power-plant with thrust producer.

Introduction

An important need in developing underwater propulsion systems is tests under realistic conditions. Measurements of acceleration, thrust, radiated noise, and interaction of power-plant with thrust producer are difficult to handle in a static facility. Conventional hydrodynamic facilities are of limited usefulness for power-plant work, since recirculating water tunnels quickly become contaminated with exhaust products, and towing tanks usually have rather slow speed. Free-running tests of the complete underwater vehicle require that all components be reliable, especially the torpedo steering control, and offer the real possibility of losing the vehicle. Then, too, power-plant operation is only one part of such tests, and consequently can be only allotted a portion of the limited data-recording channels.

Faced with such problems at the **U. S.** Naval Ordnance Test Station, Dr. R. C. **Brumfield** devised an underwater cableway. It consists of a pair of parallel steel cables stretched in a shallow catenary under the surface of a lake. Test vehicles slide along the cables on runners or shoes and are self-

Earlier version presented at American Rocket Society 17th Annual Meeting, Los Angeles, Calif., Nov. 13, 1962.

*Head, Applied Science Division, Ocean Technology Dept.
{Formerly U. S. Naval Ordnance Test Station

propelled by their thrust-producer; In this way, open water is provided for the propellers, large amounts of gas can be discharged without problems from recirculation, and no restriction needs to be set on the size of the test body or propeller. Accurate velocity-time data can be obtained on a predetermined trajectory. Above all, the facility is relatively inexpensive to install and operate.

Facility

The underwater **cableway** facility is shown in Fig. 1. It is located at *Morris Dam*, near *Azusa, Calif.* Two steel cables, anchored near the spot from which the photograph of Fig. 1 was taken, pass through the open well of the barge shown in the foreground, and are fixed above water level at the far end of the lake. The cables are $3/4$ in. in diameter and extend approximately 1000 yd. within the water to a maximum depth of about 60 ft. They are a commercial type frequently used for aerial tramways with a fairly smooth exterior. Tension of about 15,000 lb. is applied to each.

Figure 2 is a sketch from under the **cableway** showing the U-shaped barge which is located at the point where the cables enter the water. The barge provides a convenient station for attaching vehicle to cableway, making adjustments, and starting tests. The test body is slid along the cables until submerged about 2 ft. Then pulling a **lanyard turns** on its instrumentation, which **starts the powerplant after** a few seconds.

Before each test, a set of runners on the Cable8 is towed by motorboat to the far end of the cableway. After the run, the motorboat tows the **runners** back to the launching barge and pulls the test vehicle with it.

The first test on the **cableway** was in August 1950, and the facility has been in almost constant use since then. Continuous improvements and refinements have brought about a gradual growth in the quantity and quality of the data obtained.

Instrumentation

All performance **instrumentation** is mounted inside the test vehicles, with a **14-channel** recording oscillograph for information **storage**. A typical test measures torque, **rotative speed**, Inlet flow-velocity profile to the propellers, **gas-flow** and propellant pressures, and **exhaust-gas** temperature.

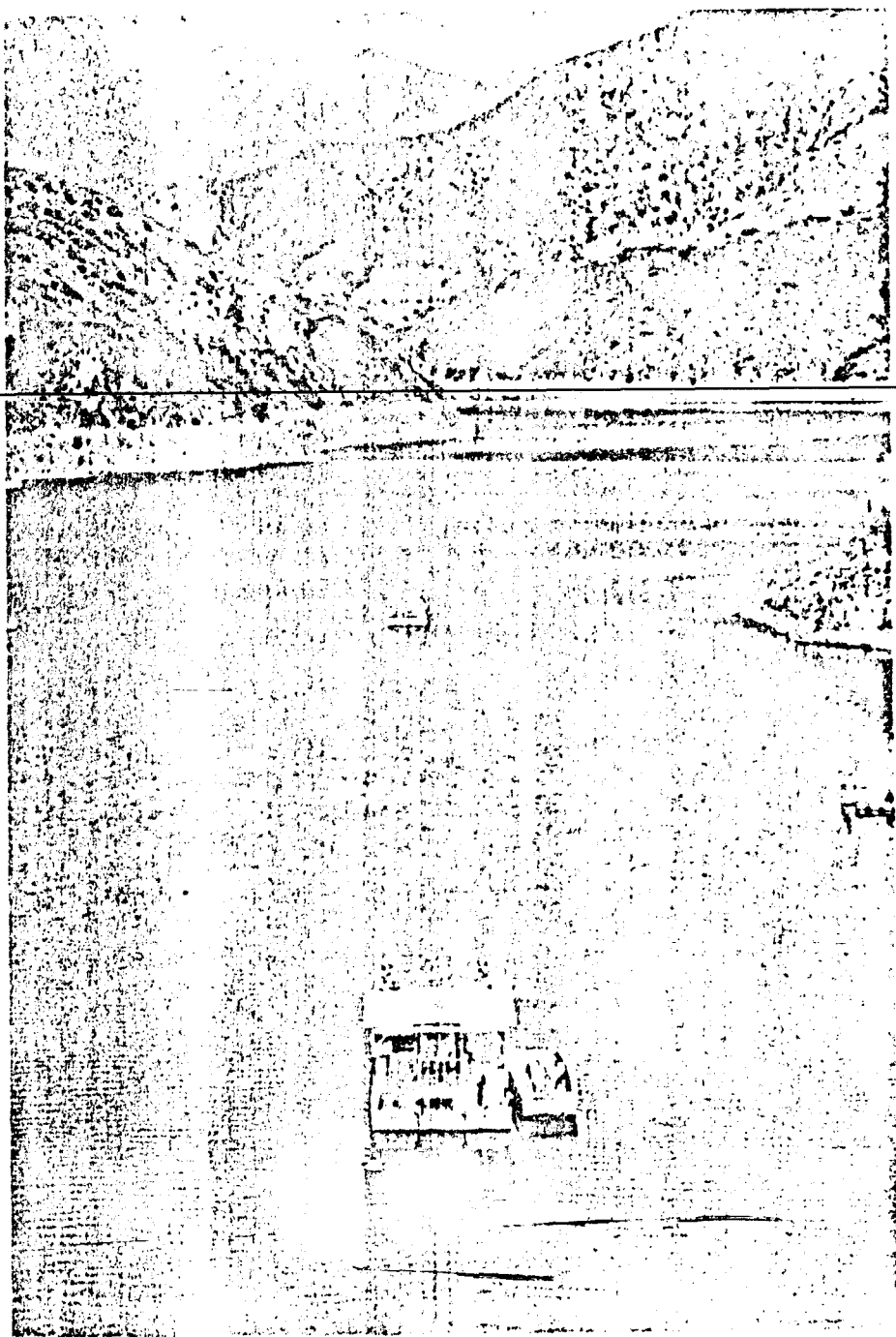


Fig. 1 View of Morris Dam **cableway** location. Launching barge in foreground.

To measure forward speed, one cable has been magnetized in spots accurately spaced 5 ft. apart. A **coil** in the torpedo support strut generates an electrical impulse as it **passes** these magnetized spots, from which forward velocity is computed using the time base of the **oscillograph**.

The **external** instrumentation is acoustic and photographic. Since radiated noise is often of considerable concern, a 60-kc narrow-beam-width hydrophone mounted on a buoyant framework can be clamped to the cableway, usually at 50-ft. depth, as shown in Fig. 3. The assembly is attached by a diver before each run. As the test vehicle passes under the framework, the output of the hydrophone is recorded on **magnetic tape**. After scanning is complete, struts attaching the test vehicle to the **cableway** release the clamps on the framework and the hydrophone floats to the surface. Since the forward velocity of the torpedo is known, the hydrophone output vs time can be interpreted as a function of axial length of the vehicle, **providing** charts as in Fig. 4. On quiet vehicles, a 60-kc tone may be placed near the nose of the test body to aid in the exact location of sources of noise. **Sources of 60-kc radiated** noise can be pinpointed to **within \pm 6 inches in axial position** on the test vehicle by this technique.

A broad-band, omnidirectional hydrophone is also provided, and, since the **range** geometry is known, distance corrections can be precisely established. Spectrum analyses as shown in Fig. 5 are usually made from this hydrophone output at the time the test vehicle passes under the narrow-band **hydrophone**. Radiated noise spectra obtained from the **cableway** closely resemble those from similar free-running vehicles.

Underwater **still** photography is also used. Figure 6 pictures a jet-propelled test vehicle at high speed. Also, motion pictures and automatic 4-by-5 still camera coverage shots of the surface wake are often made. Figure 7 is a wake photograph of a solid-propellant-driven test vehicle,

Design of Vehicle Attachment Struts

The design of the vehicle attachment struts, when testing certain powerplant components, can be fairly crude, since higher drag or reduced **forward** speed is not of **vital** concern. As shown in Fig. 8, the attachments can then be struts attached to **simple** girth **rings**, in order to use unmodified torpedo hardware. Such vehicles, checked in short runs on the cableway, can be tested later at sea with confidence in the reliability of **their powerplants**. However, when the

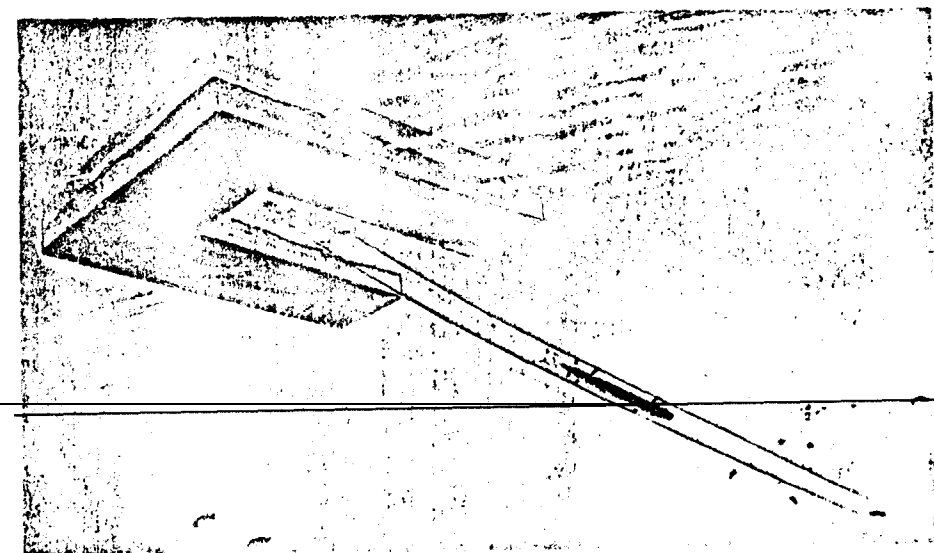


Fig. 2 Artist's sketch of **underwater view of cableway** and launching barge.

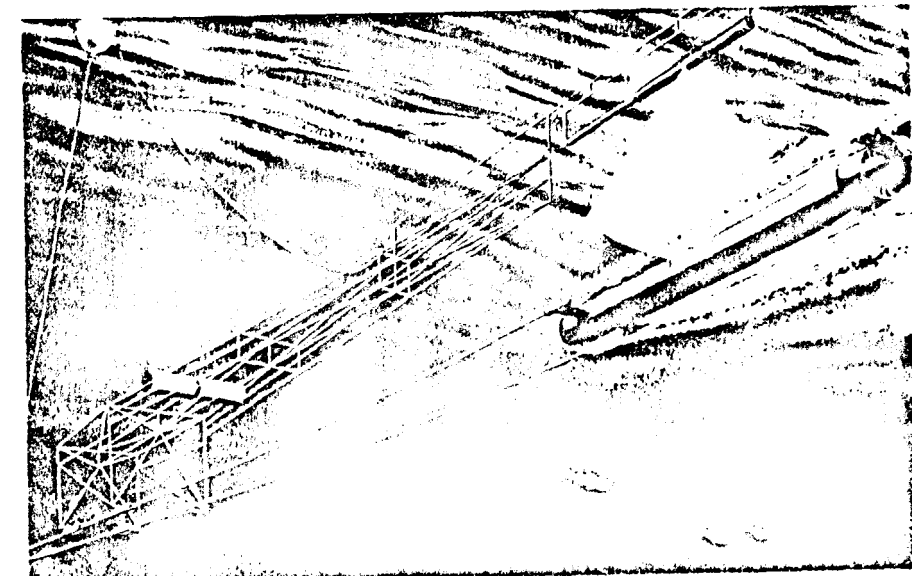


Fig. 3 Artist's sketch of scanning hydrophone installation on **cableway**.

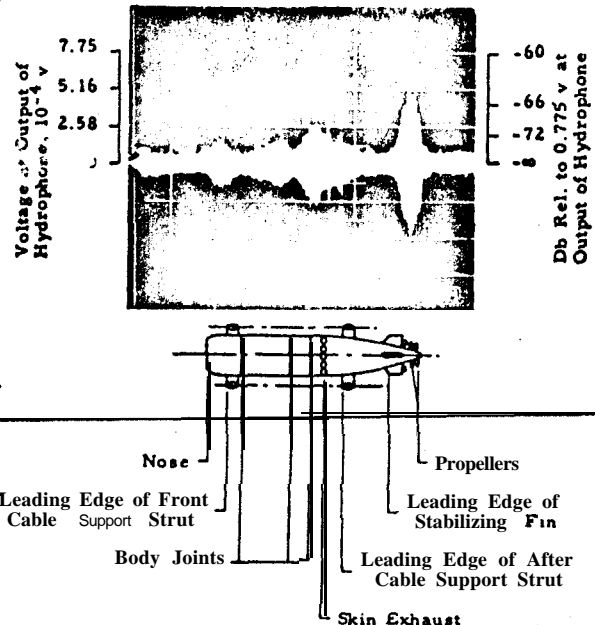


Fig. 4 Oscillogram from scanning hydrophone.

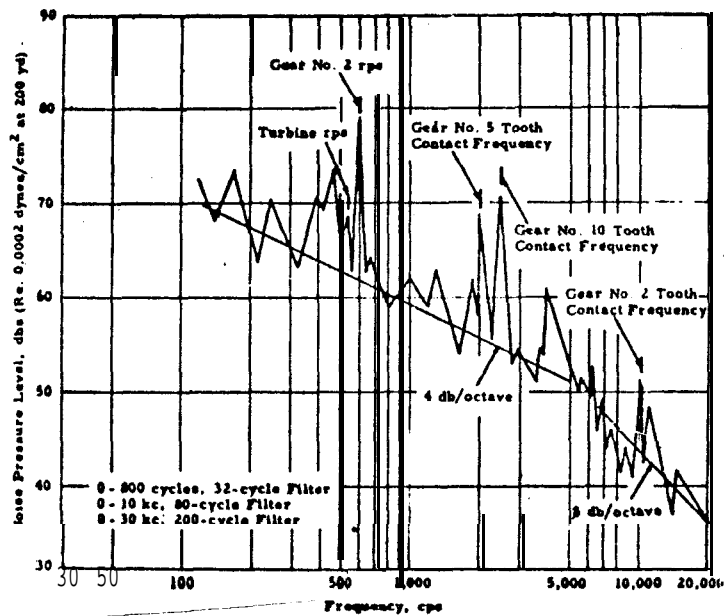


Fig. 5 Typical broad-band hydrophone result, with identification of frequency components.

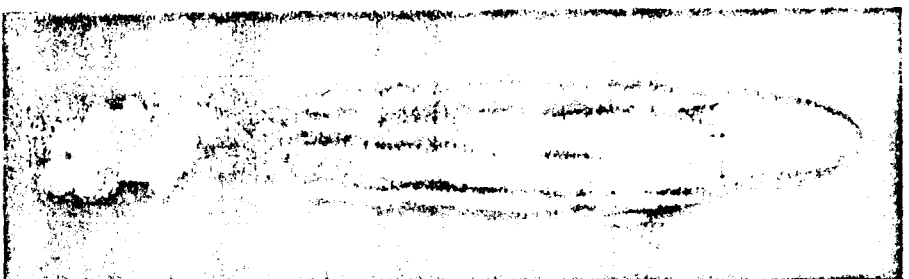


Fig. 6 Jet-propelled vehicle in underwater operation.

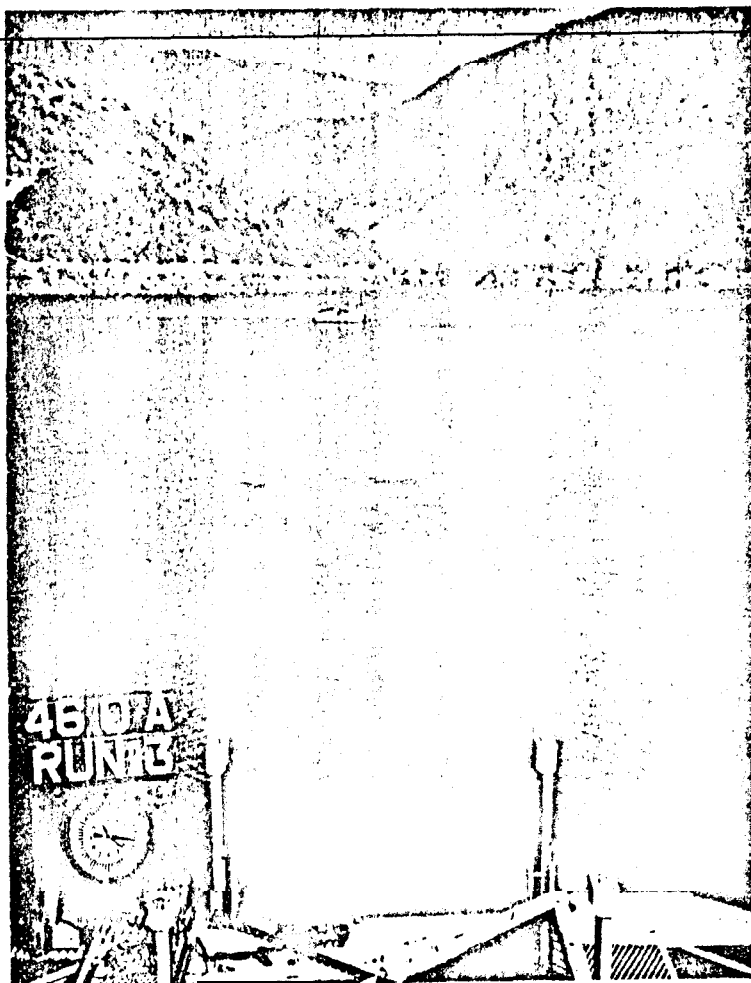


Fig. 7 Wake from a solid-propellant-driven experimental vehicle.

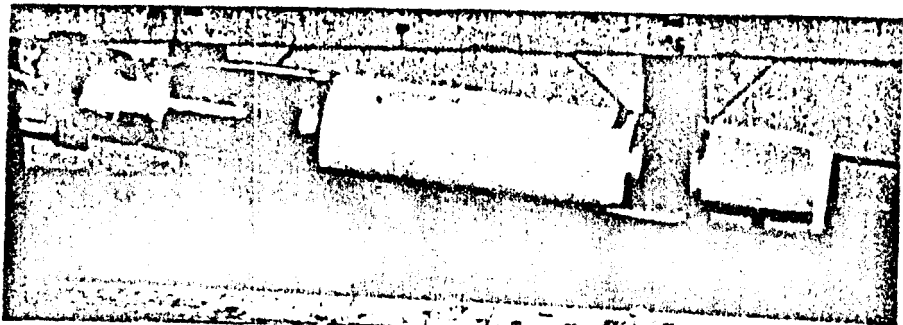


Fig. 8 Development-type vehicle supported on cableway by girth rings for short runs prior to sea testing.



Fig. 9 Experimental vehicle with extended rear strut to allow better noise scanning of ducted propeller.

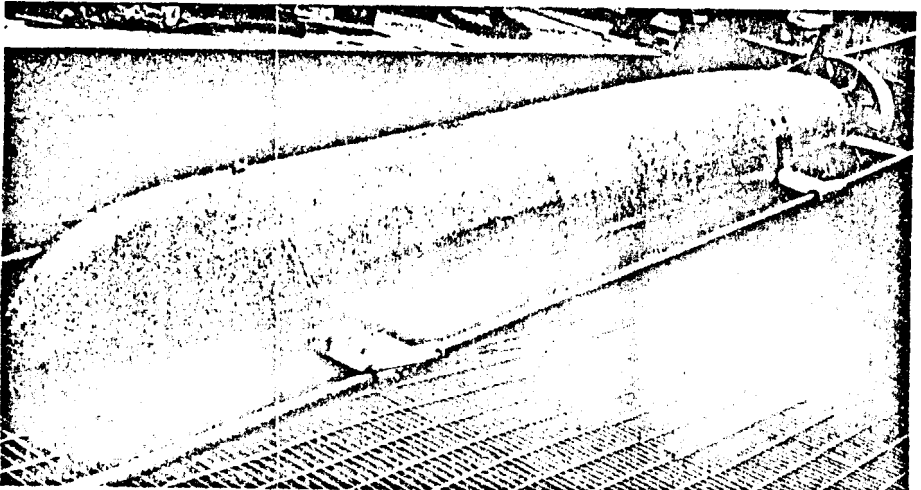


Fig. 10 Cableway test dynamometer with ducted propeller drive.

cableway is used to obtain research or design information, the support struts require careful attention.

Early in the history of the cableway, model studies and tests of support struts were made in the high-speed tunnel at the Hydrodynamics Laboratory of the California Institute of Technology. From them, attachment struts evolved with low drag, minimum strut-body interference effects, and good cavitation resistance. The drag of the present struts is considered to be primarily due to skin friction. In many cases, this can be compensated by partially removing, or eliminating, the torpedo stabilizing fins required when free running.

Mechanical friction drag of the shoes on the cable was a considerable problem in the early days.--Dater it was learned that the test vehicles should be essentially neutrally buoyant with centers of buoyancy and gravity coinciding closely, and that the moments of the shoes about the center of gravity should be equal. Loads on the shoes cause mechanical drag corresponding to a coefficient of friction of 0.1.

The cableway shoe is designed to allow a water film to form between the inside of the shoes and the cable, thus giving hydrodynamic lubrication. In addition, the cables are coated with water-resistant grease. Together with careful balancing of the forces on the shoes, mechanical friction drag on the cables is minimal. To support this conclusion, there has been no perceptible wear on the cables or shoes in a large number of test runs. Also, in deceleration tests in which a test body (less propeller) was boosted to a high speed by a rocket and then allowed to coast to a stop, no increase in drag coefficient over that expected from hydrodynamic drag could be determined. In practice, the vehicles are usually negatively buoyant by 15 to 40 lb. (the expendable fuel load), and the resulting friction drag of 1.5 to 4.0 lb. is ignored.

Occasionally, the location of the shoes is dictated by special requirements. For example, the arrangement of Fig. 9 was adopted to provide maximum acoustic scanning of a ducted propeller without interference from the support strut. Also, when radiated noise of a given component is of interest, it is desirable to place the support struts well away from it.

The Cableway Test Dynamometer

Of the many experimental vehicles used on the underwater. . .

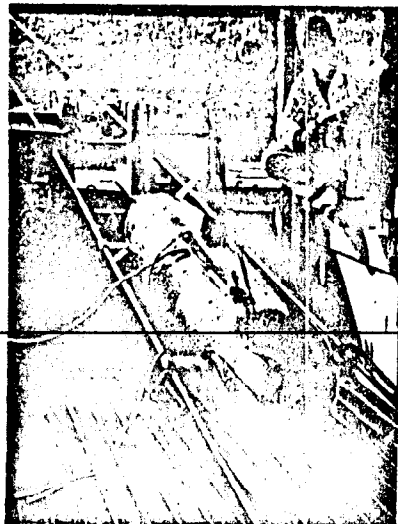


Fig. 11 Rerun check of cableway test dynamometer with ventilated, supercavitating propeller drive.

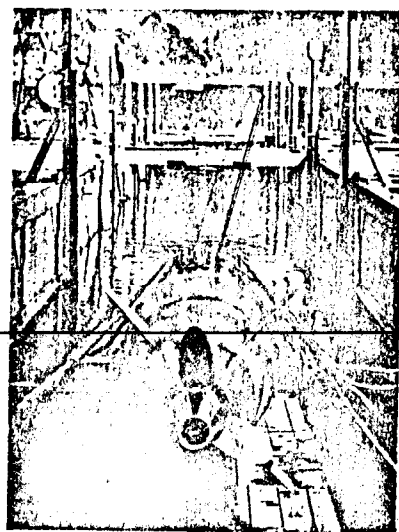


Fig. 12 Another view of dynamometer with ventilated propeller.

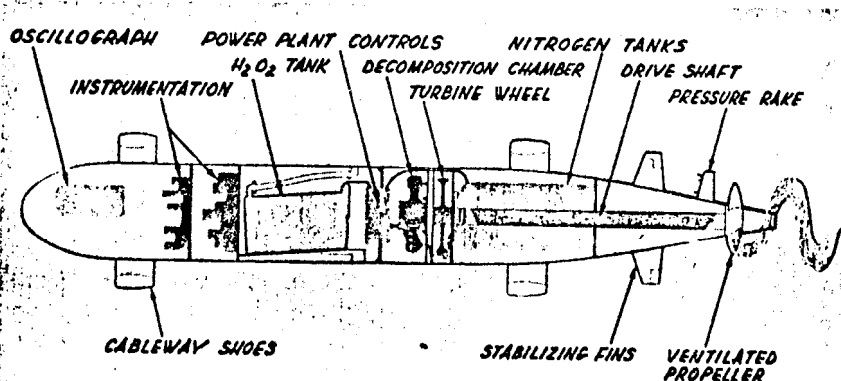


Fig. 13 Sketch of dynamometer components.

cableway, one has shown exceptional versatility for hydrodynamic work, and is now designated a "test dynamometer." It is shown with a pumpjet thrust producer in Fig. 10, and with a ventilated supercavitating propeller in Figs. 11 and 12.

The test dynamometer has a streamlined body, 15 in. in diameter and about 120 in. long with a displacement of about 600 lb. Four fins give stability and prevent rolling. The dynamometer is neutrally buoyant, except for the fuel load, and its centers of gravity and buoyancy coincide. As shown in Fig. 13, it is powered by decomposed 90% hydrogen peroxide, which drives a 12-in.-diam helical-flow turbine that is directly coupled to the thrust producer under test. Its exhaust-flows through the propeller shaft and is available at the hub for ventilation, if desired.

Its propellant tank holds 28 lb. of 90% hydrogen peroxide and is pressurized by nitrogen gas. The dynamometer's primary speed control is the pressure regulator in the nitrogen gas supply line, which is preset before each run. To start, the nitrogen and hydrogen peroxide valves are opened simultaneously. Hydrogen peroxide then flows into the decomposition chamber at a predetermined rate, and the resulting gases power the turbine. A wide range of power at various rotative speeds is available, with a maximum of about 350 hp at 7000 rpm.

Recent results with a supercavitating propeller, ventilated with exhaust gas from the dynamometer powerplant, demonstrate the utility of the underwater cableway. The three-bladed propeller, 11 in. in diameter, used the David Taylor Model Basin*modified Tulin blade sections, with two drilled passages on the suction face of each blade for ventilation. The dynamometer was operated at forward speeds up to 60 knots, with gas flows up to 50 ft³/min (stp) vented into the cavity region of the propeller. At the highest forward speed, the propeller rotative speed was 6600 rpm, and the dynamometer developed about 240 hp. Based on wind-tunnel body drag measurements, plus allowance for the "thrust deduction" effect, a propeller efficiency of about 75% was obtained. Figure 14 gives some results from a typical run.

These speeds and flow rates, typical of supercavitating ventilated propellers, already exceed the capabilities of most existing hydrodynamic facilities, and point up the usefulness of the underwater cableway in providing information on new devices.

*Presently Naval Ship Research and Development Center.

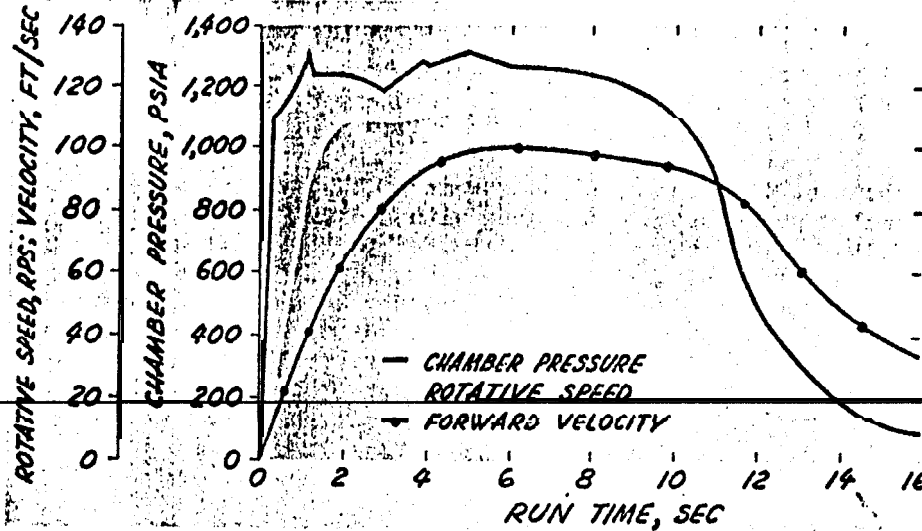


Fig. 14 Typical test results from ventilated propeller vehicle.

Conclusion

The underwater cableway, described here, is a versatile facility for testing torpedoes and torpedo components under conditions that simulate free-running, but without the hazard of loss of the missile or of the test data.

A TORPEDO TEST FACILITY SUSPENDED UNDER WATER

Eric D. Swanson* and James H. Green/

Naval Undersea Warfare Center, Pasadena, Calif.

Abstract

An inexpensive facility for testing an assembled torpedo under realistic sea conditions, but without danger of loss at sea, is described. The missile is suspended within a steel frame and lowered into a body of water to the desired depth. Arrangements are incorporated to simulate the environment of a running torpedo, and instruments are used to obtain operational parameters. A system of contrarotating disks is used to load the engine in a manner resembling propellers. Weights are added and a special fairing used to obtain a satisfactory sink rate for the facility.

Introduction

The development of a new torpedo propulsion system involves testing which begins with individual components and ends with free-running vehicles at sea. The assembled torpedo propulsion system should be evaluated in a realistic underwater environment but preferably without risk of loss at sea. Although pit testing can be thorough and realistic, subtle differences from an actual sea environment may hide problem areas. In addition, there are always parts or subsystems difficult to evaluate fully in this manner.

A static test facility to provide long-run time and deep-operating capabilities under realistic conditions, but without the risk of losing the vehicle at sea, is described. The facility 1) provides information on propulsion system functions not normally instrumented, 2) detects latent reliability problems by insuring the recovery of hardware, and 3) provides a means for realistically evaluating new propulsion components or subassemblies as they are introduced into the

* Mechanical Engineer, Turbomachinery Branch, Propulsion Division, Underwater Ordnance Department.

/ Head, Turbomachinery Branch, Propulsion Division, Underwater Ordnance Department.

system. As a result, it improves the *general* confidence level in propulsion system hardware before committing it to free sea runs.

Description of Facility

The Basic Frame Mount

The approach selected for the facility was simply to hang the torpedo on a soft suspension system inside a steel frame or cage and lower it into water to the desired test depth. The cage was portable so that it could be used in a tank, a lake, or at sea. It also could serve as a mounting platform for auxiliary equipment or instrumentation. Soft, low-frequency mounts isolated the higher frequency mechanical vibrations of the torpedo so that forces were not transmitted to the frame, and it could rest unsecured on the bottom or be suspended at the end of a single cable.

The frame was rectangular, 6 ft long by $4\frac{1}{2}$ ft square, and constructed of $\frac{1}{2}$ -in. x 3 -in. x $1\frac{1}{4}$ -in. angle iron. Attachments for springs were provided at the eight corners and the torpedo was fastened to the springs by clevises secured to a pair of steel clamp rings on the torpedo. The clamp rings were spaced so that the springs formed diagonals, 45° in the three orthogonal planes, between the corners of the frame and the torpedo, with similar natural frequencies of the suspended torpedo in all translational modes. Four longitudinal tie bars of $\frac{1}{2}$ -in. pipe were welded between the two clamp rings to maintain proper spacing and to support the axial spring tension. The clamp ring assembly was in clamshell halves for easy assembly and disassembly. Figure 1 shows the basic frame with a dummy torpedo suspended inside.

The soft suspension maintains the normal vibrational environment of a free-running torpedo. That is, the low-frequency mounts do not effectively transmit the relatively high-frequency power-plant vibrations that normally occur in a free run. For convenience, however, the suspension should be stiff enough to prevent bouncing during handling and to keep the torpedo from sagging under its weight while out of water. A natural spring-mount frequency of 2 cps was selected as an appropriate compromise, giving a combined spring constant of 230 lb/in. for the suspended torpedo or 80 lb/in. for an individual spring. After mounting the torpedo, each spring was stretched 2 inches by a takeup bolt to insure linear tension with movements up to 2 inches.

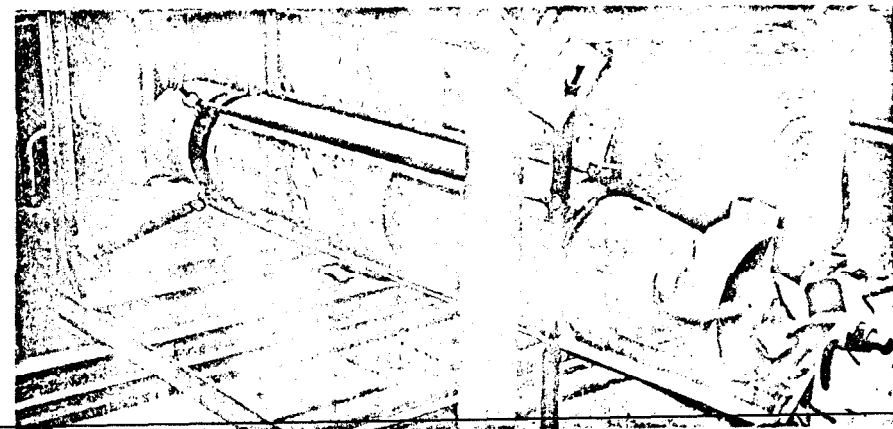


Fig. 1 Captive test facility; frame and spring suspension, without shock absorbers.

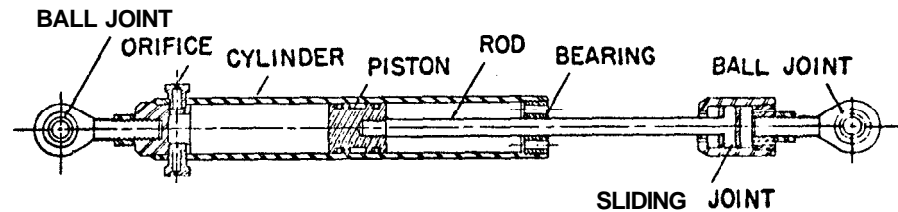


Fig. 2 Shock absorber, sectional view.

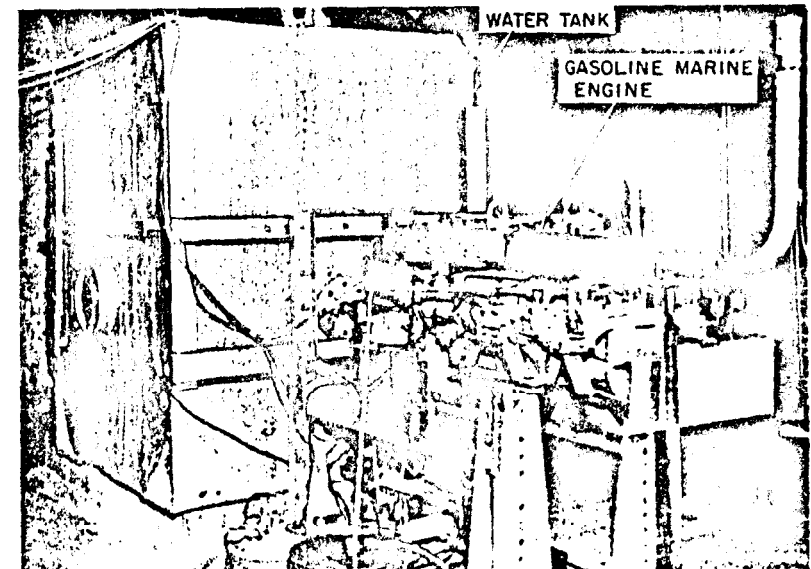


Fig. 3 Disk calibration facility from engine side.

In addition, eight shock absorbers, shown in Fig. 2, were mounted, one in parallel with each spring. The ambient water was the working fluid and, with fixed orifices, damping was proportional to the square of piston velocity. A sliding attachment allowed $1\frac{1}{2}$ in. of torpedo movement without moving the pistons. Maximum damping forces (i.e., at the maximum velocity point of an oscillation) were subcritical up to 2-in. oscillations and supercritical above (at 2 cps). These shock absorbers provided a safety factor in the event of unexpected low-frequency forces, such as wave action in the tank or bouncing at the end of a cable.

The Power Absorber

Since forward thrust of the torpedo propellers would be undesirable in the static facility; the propellers were replaced by contrarotating drag disks, one on each propeller shaft. The power absorbed by a rotating flat disk is described by the basic equation of Von Karman,¹

$$SHP = \frac{1}{2} \rho (C/550) \gamma^{1/5} R^{4.60} \omega^{2.8}$$

where ρ = density of water, slugs/ft³

C = experimental constant (determined by Von Karman from experimental flat plate data to be 0.146)

γ = kinematic viscosity of water, ft²/sec

R = disk radius, ft

ω = disk speed, radians/sec

With disks, shaft torque results from hydrodynamic skin-friction drag, and the power-to-rpm function is very nearly the cubic relationship of propellers.

Because absorbed shaft power varies with the 4.60 power of disk diameter and the exact value of the experimental constant C was uncertain, a means for calibrating the disks was necessary. A facility constructed for this purpose is shown in Fig. 3 and 4. It consisted of a 5-ft cube water tank in which the two disks were contrarotated by external drive sources. The disks used were of 1/2-in. aluminum plate, tapered to 1/4 in. at the periphery to machine our surface waviness. Disk hubs were machined, and hub and disk assemblies were balanced dynamically to propeller specifications. The drive-shaft rpm and torque were monitored, and various disk diameters and shaft rpm's were evaluated to verify the theoretical exponents of these functions. Disk spacing also

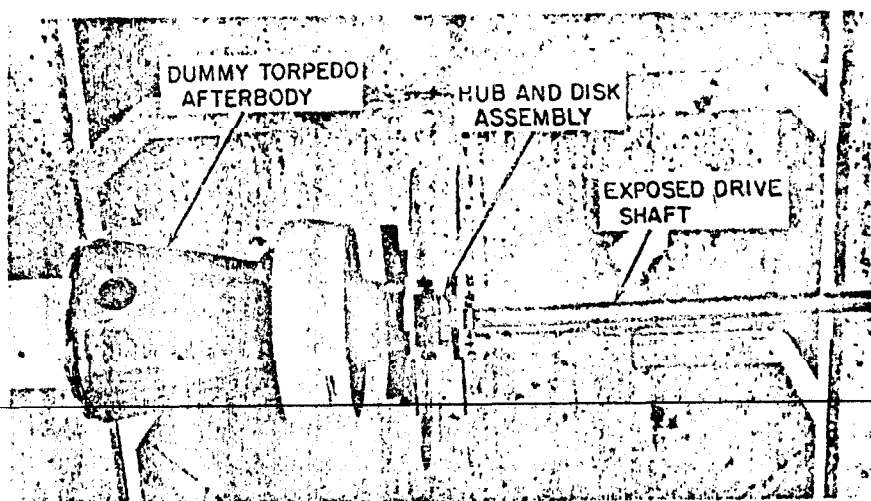


Fig. 4 Interior of calibration tank.

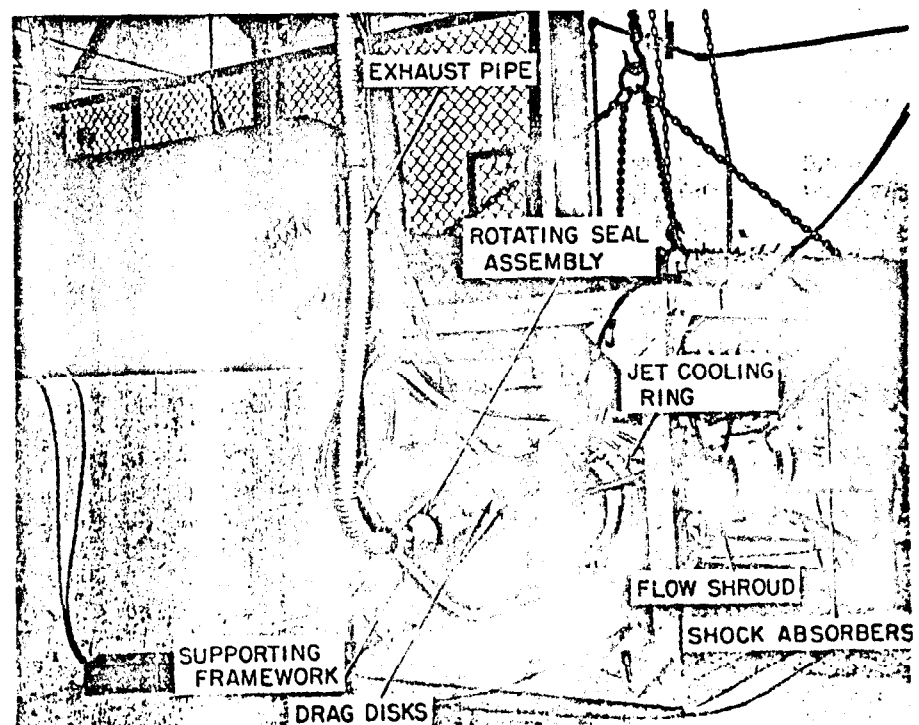


Fig. 5 Assembled test facility prior to tank run, rear view.

was varied to determine effects of contrarotation.* The experimental constant C was found to be 0.165 for the disks.

An operational aspect that was not duplicated by the disks was the inertia of the torpedo. With propellers, an rpm change is accompanied by a change in torpedo speed which is relatively gradual because of the inertia for the vehicle. But, when power is absorbed by low-mass rotating disks, speed changes were abrupt.

Special-Purpose Accessories

The frame, suspension, and drag disks comprise the basic captive-test facility. Additions to the basic test facility that were required for testing a specific torpedo are described below. Exhaust gases from this particular test torpedo discharged near the aft propeller hub. To prevent these gases from mixing with the water around the disks where they would affect drag, an exhaust pipe was installed, as shown in Fig. 5, and gases were ducted into it through a rotating bearing and seal arrangement. To support the tailpipe and prevent the seal from rotating, a framework of 3/4-in. tubing was welded to the after clamp ring. The gases from the pipe were normally discharged a few feet above the level of the drag disks but, during shallow-water tank testing, were ducted above the surface.

A cooling ring and shroud, visible in Fig. 5, were added just ahead of the after clamp ring, and circulated water forward over the shell and provided the cooling that normally results from the vehicle's forward motion. City water via a fire hose at a flow of about 80 gal/min was used or, for deep-water testing at sea, this water was provided by a battery-powered electric pump attached to the frame.

Instrumentation

In the shallow water tank, extensive instrumentation was used with an external 18-channel oscillograph as primary recorder. Internal data were transmitted through a cable. Backing gland in a dummy nose, as shown in Fig. 6. The nose cable also transmitted test commands to the torpedo. Seven external functions also were recorded, including digital rpm

* A disk spacing of 2 5/8 in. was used. With the disk diameters and speeds used, contrarotation did not affect absorbed power until the spacing was reduced to 1/2 in.

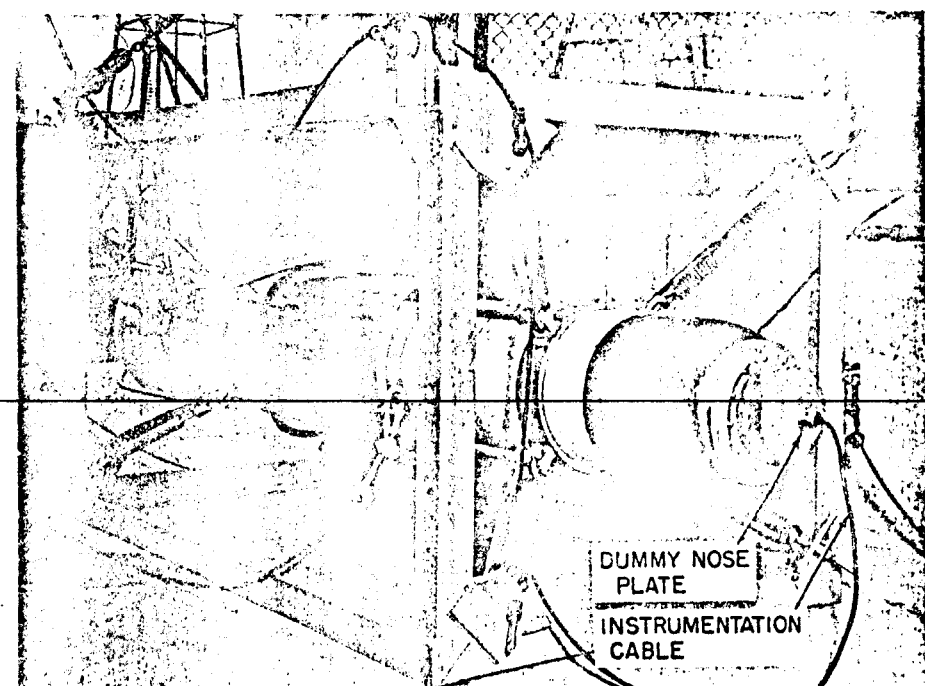


Fig. 6 Assembled test facility prior to tank run, front view.

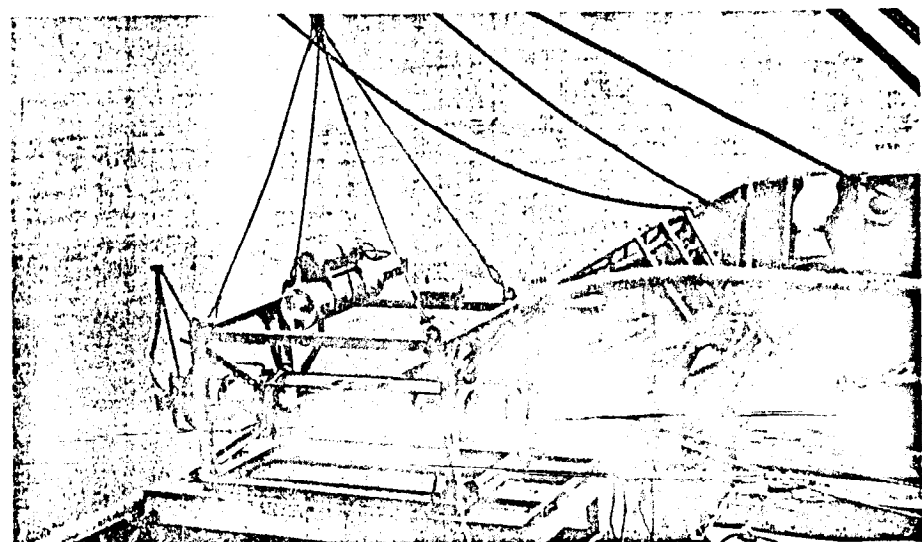


Fig. 7 Test facility prior to sea run.

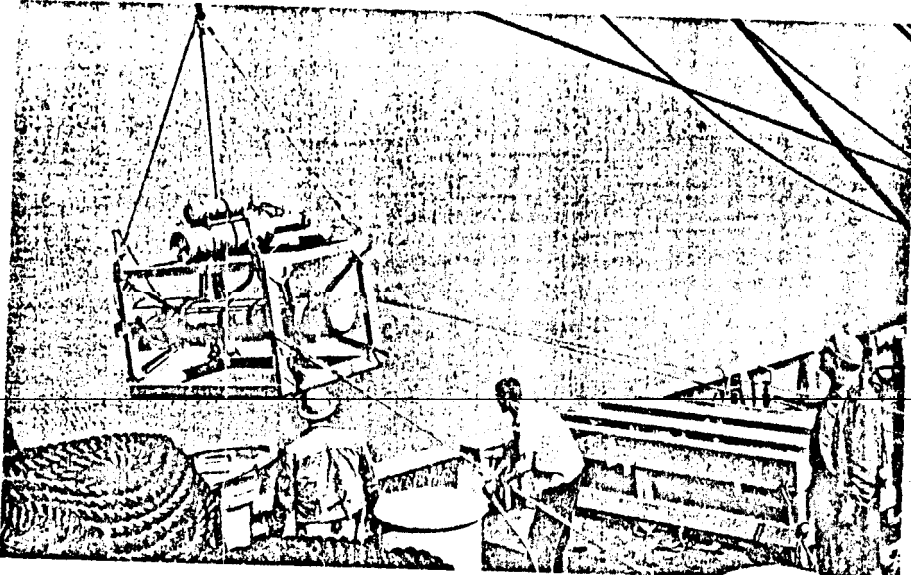


Fig. 8 Launching from USS GEAR.

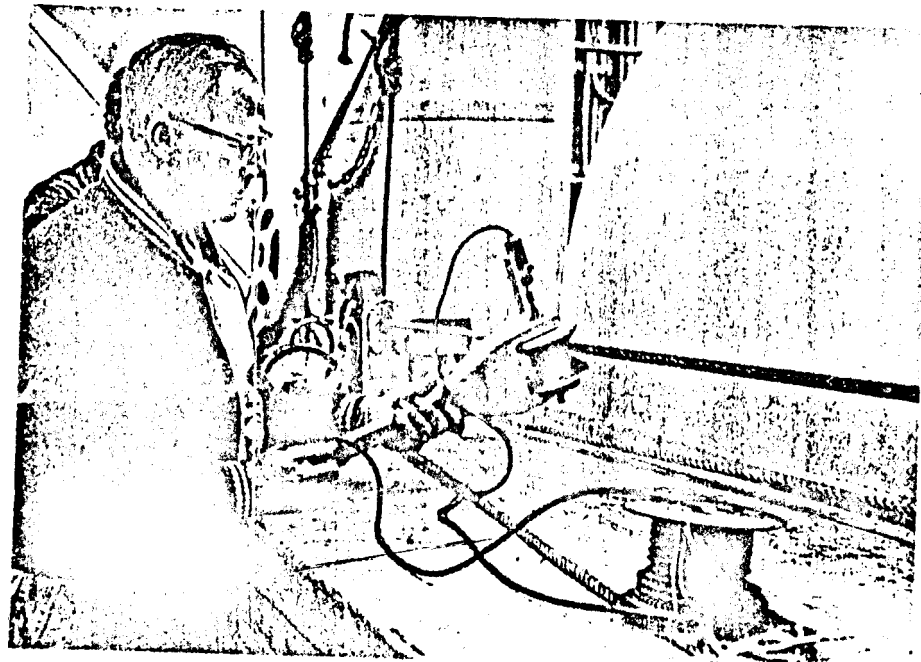


Fig. 9 Cable-speed indicator and, footage counter.

readings from both disks. A **visual** monitoring panel was used to **display** forward **and after** disk speed and important internal pressures and temperatures. During deep testing, **all** instrumented functions were recorded on an **oscillograph located** **within** the torpedo.

The Test Program

Tank Testing

To evaluate the captive test facility, tests were first conducted in a shallow **tank**. They proved that the spring mount did, in fact, provide a stable platform, that the **propulsion system components were performing normally, and th-** the drag disks properly loaded the **powerplant**.

Sea Testing

For the subsequent deep water tests, it was necessary to start the engine with the torpedo near the surface and lower to depth while running. Consequently, a high lowering rate was necessary if the torpedo was to spend a good portion of its available run time at test depth. Because the angle-iron frame was not streamlined, 1500 lb of additional weight was necessary to achieve the desired "**free-fall**" sink rate. Also, at least 300 lb of cable tension were estimated as necessary to provide adequate vertical stability, which brought the total additional weight to 1800 lb. To reduce these weights to more manageable values, the leading surfaces of the frame **were faired** with half-rounds on the bottom angles and wedges inside the top angles, and only 1350 lb of additional weight were then needed. Figure 7 shows the modified frame located on the afterdeck of the USS GEAR **from** which the deep tests were conducted. The **fairings** have been added and the lead weights are neatly packaged **inside** the angle-iron frames. **Instrumentation** showed that the **frame**, as modified, pitched + 20° at the necessary 8 fps sink rate, and roll and yaw were negligible.

Visible on top of the **frame** in Fig. 7 is the **external cooling** pump assembly **and** a pressure-actuated firing device for starting the torpedo at a **shallow** depth. The cooling ring flow shroud has been removed to allow **crossflow** cooling as the torpedo is lowered and **raised**. A sound recording boat can be seen in the **background**.

Figure 8 shows the procedure for putting the test assembly over the side of the ship. The cable payout was controlled by a brake at the winch cable drum. The operator controlled

brake tension while observing a cable speed monitoring device,
as shown in Fig. 9. A cable footage counter gave a constant reading of test depth. Cage and torpedo were hoisted to the surface immediately after a run.

Conclusions

The need for an inexpensive facility for testing torpedoes under realistic sea conditions has been met by a specially designed steel-frame apparatus in which the torpedo is suspended and then lowered into water. The suspension, consisting of springs and shock absorbers, decouples the missile from its mount so that the vibratory modes of the torpedo in a free-running condition are retained. Engine power is absorbed in a manner closely simulating a propeller by replacing the propellers with rotating disks. External cooling is simulated by flowing water over the missile body. A sink rate, rapid enough that operation at depth can continue for an interval long enough for an effective test, is achieved by fairing the frame and adding extra weights. The system has been tested in shallow and deep water and found to achieve all its design goals.

Reference

¹Von Karman, Th., "On laminar and turbulent friction," NACA TM 1092, Washington, D. C. (September 1946).

AN OPERATIONAL UNDERWATER THREE-DIMENSIONAL ACOUSTIC TRACKING SYSTEM

W. M. Sandstrom*

University of Washington, Seattle, Wash.

Abstract

An operational underwater three-dimensional acoustic tracking system, developed by the Applied Physics Laboratory, University of Washington, is described. Its basic physical elements are an acoustic-electronic unit in the tracked object, a shore or ship-based computer, one or more bottom-mounted acoustic transducer arrays, an electrical signal cable between arrays and computer, and a body of acoustically acceptable sea water. It is a pulse-type spherical system in which transit times of acoustic pulses traveling from tracked objects to the transducers are measured. A high-frequency system has been operational since May 1957 whose arrays can track objects at slant ranges of 1500 ft to a relative accuracy of +1 ft. The basic computation interval is about 2/3 sec. A low-frequency design, successfully tested in 1959 and installed for use, has a maximum slant range of 4500 ft and an ultimate accuracy of about +3 ft. Extrapolations to meet other conditions and requirements are discussed, particularly for deeper waters, for greater area coverage and for more sophisticated multiple tracking.

Introduction

The underwater three-dimensional tracking system, developed and built at the Applied Physics Laboratory (APL), University of Washington has been operational since early 1956. Although it began as an experimental installation of limited

Presented as Preprint 2597-62 at the ARS 17th Annual Meeting and Space Flight Exposition, Los Angeles, Calif., November 13-18, 1962. This work was supported by the Bureau of Naval Weapons, U.S. Navy, under Contracts Nord 12937 and Now 62-0579-d.

* Deputy Director, Applied Physics Laboratory, University of Washington.

capability, the first range obtained data on some 40 torpedo runs. With the addition of another, more extensive, range in May 1957, a period of continuing, rapid expansion of capabilities and utilization began, and many torpedoes, submarines, and surface vessels have since been tracked.

In 1958, the Naval Torpedo Station, Keyport, Wash. assumed responsibility for the existing range, and APL concentrated on extending the range principle to greater distances and deeper water. This resulted in temporary installation of an experimental low-frequency range in Alaskan waters in July 1959 and, later, a low-frequency array in California waters at San Clemente Island for the U.S. Naval Ordnance Test Station.

In 1961, at the request of the Bureau of Naval Weapons and the Commander of the Navy's Operational Test and Evaluation Force, APL studied means to provide a deep water three-dimensional tracking range for weapon evaluation and training by Fleet units on the east coast, which resulted in the range near St. Croix, U.S. Virgin Islands, in the spring of 1964. By mid-summer 1964, more than 70 torpedo runs had been tracked successfully on this range. All torpedoes currently in service can be tracked on it and work is underway on tracking new weapons, as ASROC and SUBROC.

Description of the General System

The three-dimensional tracking range (3-D range) is a system for determining the trajectory of suitably instrumented underwater and surface objects within an instrumented body of water. Its elements include an acoustic-electronic unit (synchronous clock and acoustic transducer) in the tracked object (tracked vessels are outfitted also with telemetering equipment and a clock synchronizer), a shore- or ship-based computer, a bottom mounted transducer array, and an electrical cable between the computer and the transducer array.

The transducer array defines a rectangular coordinate system to which measurements are referred. Positional information is obtained from the transit times of a pulsed acoustic signal from the tracked object to four independent hydrophones on the transducer array. The four time differences are entered into an electronic computer to calculate the three space coordinates.

The geometry is illustrated in Fig. 1. The four hydrophones, R_C , R_x , R_y , and R_z , are on four adjacent vertices of a

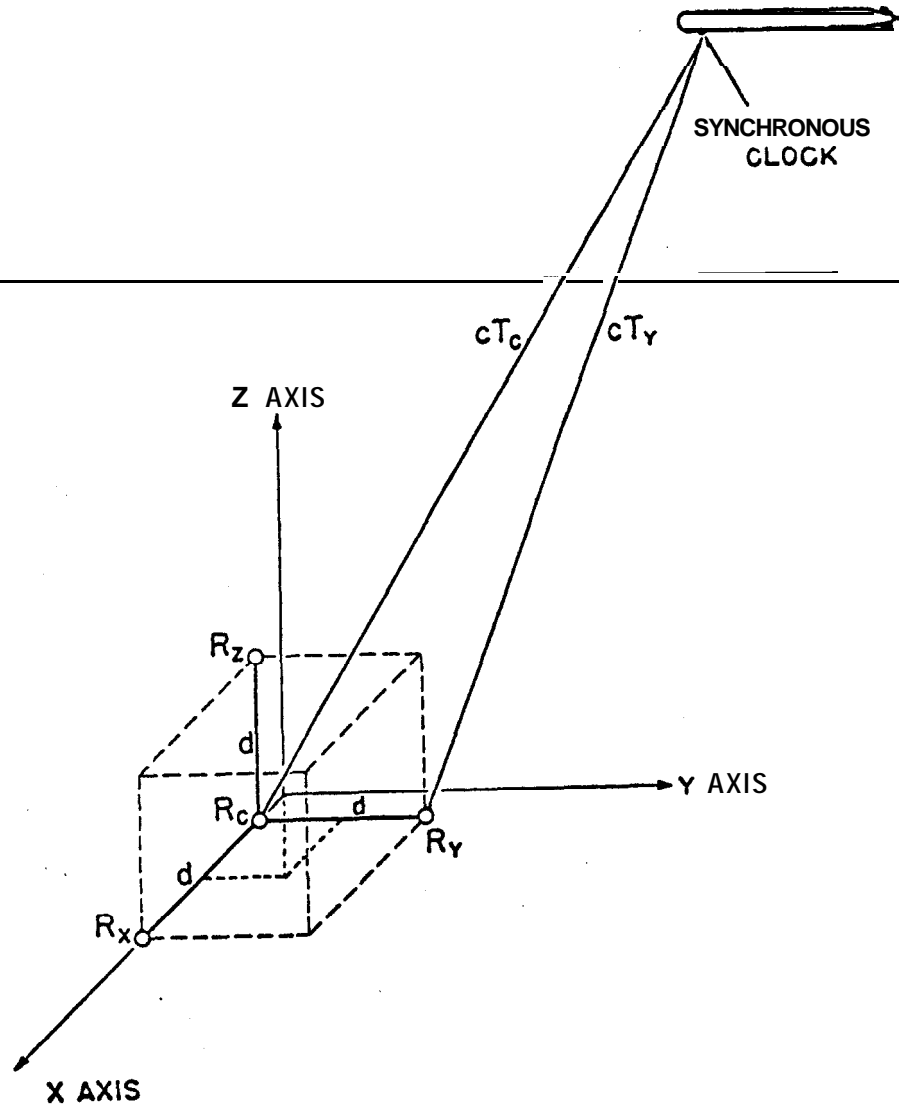


Fig. 1 Geometry for calculating positional coordinates.

cube, separated by a distance d . The origin of the coordinates is the center of the cube, with x , y , and z axes parallel to its edges. For transit times of the acoustic pulse from the tracked object to the center hydrophone (R_C), and the y hydrophone (R_y) of TC and T_y , respectively, and coordinates of the object, x , y , and z ,

$$T_C = \frac{1}{c} \left[\left(x + \frac{d}{2} \right)^2 + \left(y + \frac{d}{2} \right)^2 + \left(z + \frac{d}{2} \right)^2 \right]^{\frac{1}{2}} \quad (1)$$

and

$$T_y = \frac{1}{c} \left[\left(x + \frac{d}{2} \right)^2 + \left(y - \frac{d}{2} \right)^2 + \left(z + \frac{d}{2} \right)^2 \right]^{\frac{1}{2}} \quad (2)$$

where c is the velocity of sound. The difference between T_C^2 and T_y^2 is

$$T_C^2 - T_y^2 = \frac{1}{c^2} \left(y + \frac{d}{2} \right)^2 - \frac{1}{c^2} \left(y - \frac{d}{2} \right)^2 = \frac{2yd}{c^2} \quad (3)$$

Thus,

$$y = \left(c^2/2d \right) [T_C^2 - T_y^2] \quad (4)$$

Analogous expressions for the x and z coordinates are

$$x = \left(c^2/2d \right) [T_C^2 - T_x^2] \quad (5)$$

$$z = \left(c^2/2d \right) [T_C^2 - T_z^2] \quad (6)$$

It is essential to know the time when the tracked object emits an acoustic pulse, in order to measure transit time to the receiving hydrophones. This has been accomplished in three ways. The first was acoustic interrogation from a projector in the array to a transponder in the tracked object. This changes the scale factor in Eqs. (4-6) since the total transit time is the round trip, out and back. In addition, geometric corrections are required, depending on the relative magnitude of the transducer separation d and the range to the tracked unit R . The second method was transmission of a radio

pulse to a surface ship to trigger the acoustic pulse. The third technique, developed initially for submerged objects whose self-noise prevented acoustic interrogation, involves stable crystal-controlled clocks in the tracked unit and at the computer. Prior to a run, the two are synchronized by radio, so that the computer "knows" the time at which a pulse is emitted. This "synchronous clock" method is now used exclusively, because it is applicable to any object that has space for a clock and is electronically compatible with it.

At present, except at St. Croix, the computer utilizes primarily analog techniques to solve Eqs. (4-6), and coordinate data are presented in analog form as voltage outputs. ^f A linear-range generator with an output,

$$E_R = kt \quad (7)$$

where E_R is the output voltage, t is time, and k is constant, is started at the instant of interrogation ($t = 0$). This voltage goes to three identical x , y , and z analog integrators. Taking the y computation as an example, the y integrator is gated on at the time of the first return (TC or T_y) to begin integration of E_R , and is gated off at the second return. The voltage output of this unit, for the case of Fig. 1 for R_y excited first, is

$$E_y = k \int_{T_y}^{T_C} t dt = \frac{k}{2} (T_C^2 - T_y^2) \quad (8)$$

and is proportional to the y coordinate of Eq. (4). Calibration requires simple adjustment of the latter proportionality constant against time signals generated by a crystal-controlled oscillator whose frequency is chosen on the basis of the velocity of sound c and the transducer separation d of Eq. (4). The coordinate output voltage is read on analog plotters and recorded digitally for later analysis. The computer "knows" which hydrophone was last excited, and therefore assigns the proper sign to the coordinate data.

The preceding is applicable to both high-frequency and low-frequency systems, except at St. Croix where essentially the same computation is accomplished digitally. Since it is not feasible here-to detail the signal processing in a real design, and the procedures required for a useful operating tracking system based on these principles, the geometric and

^fThe St. Croix computer is an SDS 910 digital machine.

acoustic design parameters of the arrays of both the **high-frequency** and low-frequency 3-D ranges are given instead in Table 1, and typical hardware specifications for the **synchronous** clocks needed to instrument the tracked object are in Table 2.

Table 1. Specific design parameters for the high-frequency and low-frequency 3-D systems

Specific parameters	High-frequency range	Low-frequency range
Transducer separation d, ft	10	30
Slant range for good tracking, ft	1500	4500
Array receiving frequency, kc	250	72
Acoustic interrogating frequencies, kc	190; 330	none
Computation period, sec	0.661	1.32
Accuracy, ft	± 1	± 3

Table 2. Hardware specifications for synchronous clock

	High-frequency range	Low-frequency range
Total package weight, lb	6.4	11
Total volume, in. ³	247	291
Source level db vs 1 dyne/cm ²	95	95
@ 1 yd		
Transducer diameter, in.	1/2	1-3/8
Power requirements	39 w cont.; 1040 w for 500 msec	54 w cont.; 2000 w for 1.5 msec 80 amp pulse
Self-contained battery		
Package weight, lb	5-1/2	5-1/2

Fig. 2 illustrates the array of the low-frequency **system.** \neq

\neq The array was modified to accommodate greater depths at it', Croix.

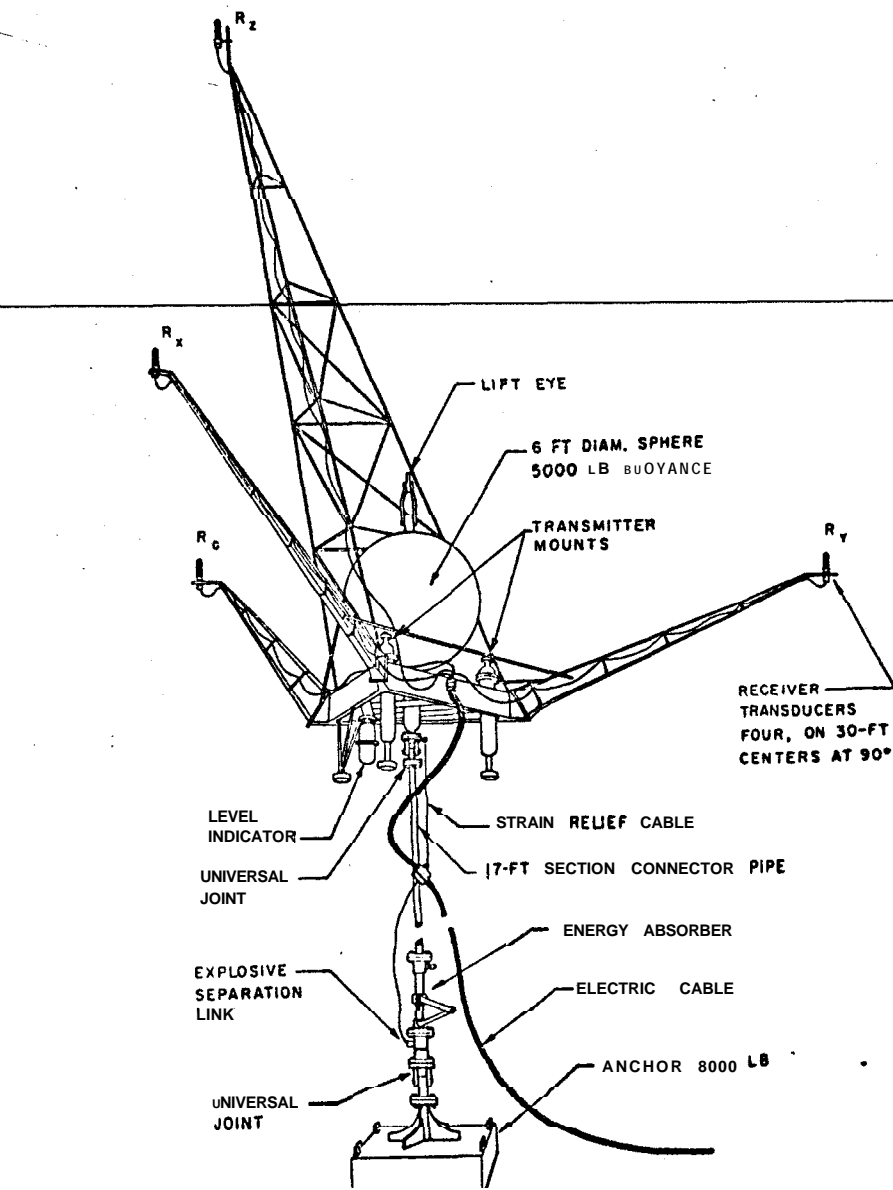


Fig. 2 The low-frequency array: transducer separation is 30 ft.

An inverted pendulum, established by a buoyant hollow steel sphere, assures that the plane of the hydrophones Rx, Ry, and RC tends toward horizontal. Universal joints in the connecting pipe between the sphere and its anchor allow self-leveling, but do not permit rotation about a vertical axis. A multi-conductor cable carries signals from each hydrophone and a level indicator to the computer. The hydrophones (and all transducers used in the 3-D system) are barium titanate hemispheres or spheres with a directivity index less than 3 db. For recovery, a shore command explodes a separation link and the sphere floats the array and cable to the surface.

The tracking accuracy of the systems is difficult to establish because, in addition to random or "jitter" errors in signal processing and in the computer itself, volume inhomogeneities in the water and man-made ambient acoustic noise levels are not constant but vary for different types of exercises. However, first-order corrections for sound velocity variations can be made, if the velocity distribution is known. Experience with the high-frequency system indicates that each position determination has a standard deviation of about 1 ft in normal, routine operations, and that positions obtained from simultaneous optic and acoustic tracking have a standard deviation of about 4 ft. Corresponding figures for the low-frequency system are about 3 and 5 ft, respectively.

Concerning the accuracy in synchronous clock operations, if AR is the maximum allowable error in range, c the velocity of sound, and T the time in seconds after synchronization, the relative stability required S is,

$$S = \Delta R / cT \quad (9)$$

This number can easily be held to about 10^{-6} in a torpedo-mounted clock, implying a maximum error of 3 ft in 10 min.

High-Frequency Operating Area

The high-frequency range area in Keyport, Wash. is geographically remote and sparsely populated with correspondingly low levels of man-made acoustical and electrical noises. The surrounding land masses offer protection from seasonal storms allowing year-round operation. Except for the upper 20 to 40 ft, the water is essentially isothermal and isosaline, averaging 9° C and 29 parts per thousand, respectively, with only small seasonal variations.

Fifteen high-frequency arrays are located on the bottom as shown by the circles in Fig. 3. The circles define the mean maximum range for good tracking and are 2000 ft in diameter. The array numbers are the distance in hundreds of yards from the zero range marker shown in the figure. Seven arrays are in a central cluster, which defines a continuous tracking volume about 1000 by 3000 yds. Cables from each array are brought to the computer building on the west side of the bay. Other physical facilities include Raydist for determining surface ship positions by radio and noise-measuring equipment designed and installed by the Ordnance Research Laboratory of Pennsylvania State University.

The arrangement at the computer building is shown in Fig. 4.

The computer, digital printers, and amplifiers are in the cabinet in the right background. Its controls permit selecting the output of any array for multiple tracking on time-sharing bases. The analog plot of the positional data, made by the x-y plotter in the right foreground, facilitates control of time sharing and the direction of the exercises on the range. Not shown in Fig. 4 are the radio equipment, recorders, underwater telephones, spotting glasses, and other paraphernalia needed.

Utilization of the High-Frequency Range

The original application of the 3-D range was for torpedo development and many weapons have been ranged. These include developmental runs, proofing runs, tactical data-runs to obtain fire control parameters, and hit shots against submarines. Many submarines and destroyers have also operated-on the high-frequency range, obtaining such ship and submarine radius of turn, tactical data as advance, reach, transfer, and stopping distance for various conditions.

An example of surface tracking is shown in Fig. 5, an actual, real time output of the plotter during a small-boat run over the range. Offsets in the track as it passes from one array into another occur at points marked 1 to 2, 3 to 7, and elsewhere. This rough plot was for the benefit of the range operator, and such discrepancies are acceptable. Accurate data are, of course, recorded on punch cards for later analysis. The plotter points are so close as to be unresolvable in this figure, since the boat moved very slowly. The width of the line is a measure of the plotter jitter. Note the sing points at the transition from array 2 to 3, where the boat was outside the tracking area of either. The sharp irregularity in the track above this shows maneuvers made by the

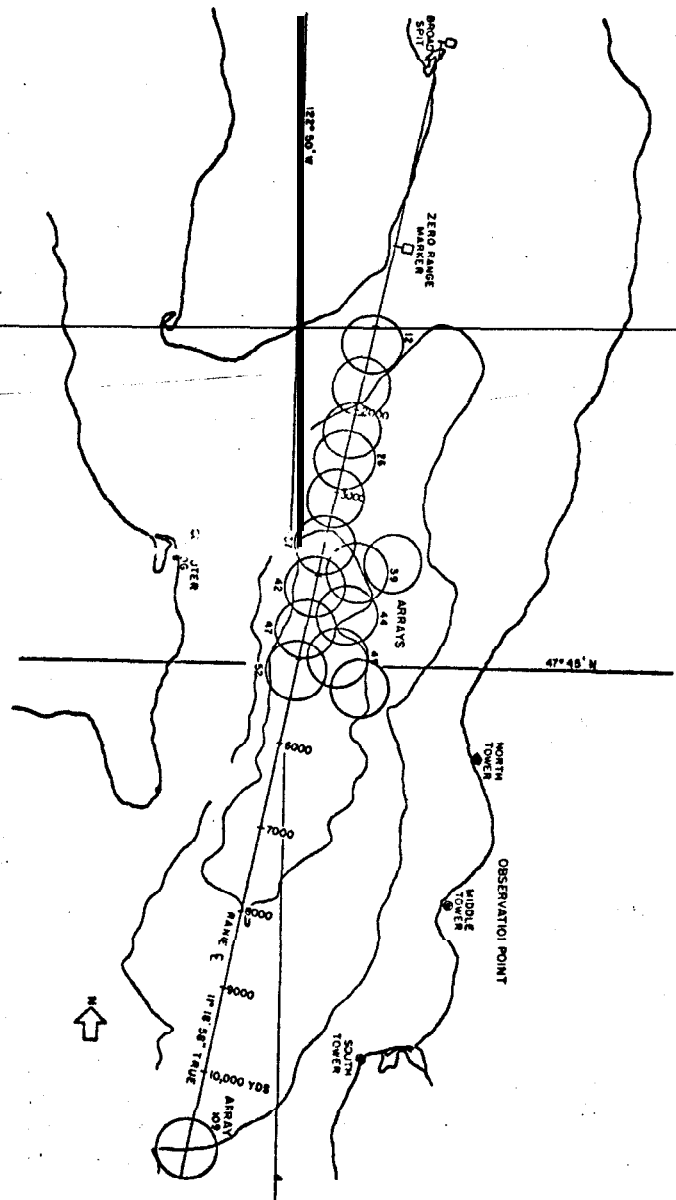


Fig. 3 The high-frequency array locations.



Fig. 4 The computer installation.

boat to avoid leaving the tracking area.

Utilization of the High-Frequency Range in Calibration

The use of the high-frequency range for calibrating ship equipment is another application now being exploited. In May 1959, an experiment was conducted to determine how well the range could measure range and bearing accuracy of the AN/SQS-4 sonar aboard the USS Brannon (DE 446). For this purpose, a transducer on one of the arrays was converted to a sonar target by connecting it to a transponder operating at the sonar frequency.

Brannon was stationed in several different areas to provide a spread in sonar range. The ship was stopped and allowed to drift. Its position was "fixed" by acoustic tracking when inside an array tracking area, and by triangulation from shore-based transits when outside. The actual range and true bearing to each "sonar target" array was obtained from this measurement and accurate knowledge of array positions. A transit on the bridge, aligned with the ship's center line, determined her heading by measuring relative bearings of a known shore marker. The actual relative bearing of each sonar target was obtained from ship's heading and position. In addition, the actual ship's heading was used to determine the accuracy of the gyrocompass.

The results obtained showed that the accuracy with which a ship's course, true sonar bearing and relative sonar bearing can be measured is, conservatively, $\pm 0.05^\circ$, and range ± 2 yd. This accuracy is greater than required, and it means that the standard deviations (σ) of the measurements are a measure of the "time-wise" stability and reading accuracy of the various equipments.

More recently, similar alignment and calibration checks were conducted aboard the destroyer John W. Thomason (DD 760), and the submarine Gudgeon (SS 567). The alignment axis for the latter's fire control is the mean axis of its forward torpedo tubes. The periscope is easily aligned with this axis while the ship is in dry dock and is generally taken as a secondary standard for alignment of other equipments. Consequently, in addition to checking Gudgeon's sonar and gyro alignment with respect to the ship's center line, alignment with respect to the periscope was measured.

In exercise with Gudgeon, her sonar transducer transmitting and receiving patterns were determined also. A transducer with a known position measured sonar output at a known range

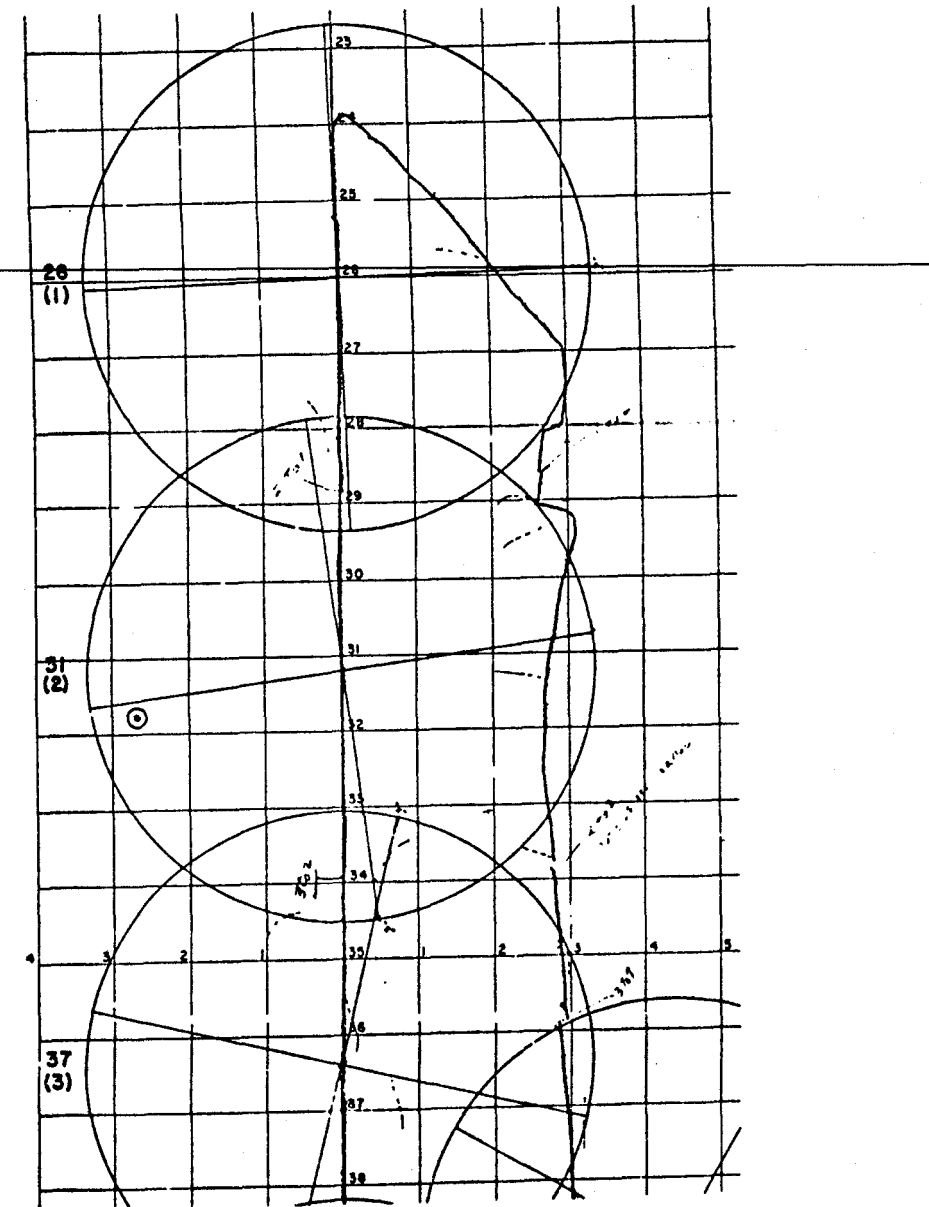


Fig. 5 3-D range plot of R-boat run, February 1962.

at varying beam positions while the ship swept through the beam pattern in azimuth. Similarly, the transducer was used as a known source for the receiving node of the sonar. The high-frequency range proved a simple and convenient means for determining such patterns on actual ship installations.

Operations with the Low-Frequency System

In July 1959, a two-week operation of the low-frequency range system in Alaskan waters was made as a joint effort of the Naval Torpedo Station, **Keyport**, Wash. and APL. Two ships were used: One carried the computer equipment; and one planted and recovered the array (Fig. 2) and cable and was the torpedo firing vessel. The performance of the equipment was very good, the range obtained exceeded design specification by 10%. In addition, the expedition successfully tracked nine torpedoes: one Mark 43 Mod 0, five Mark 39 Mod 1, and three Mark 37 Mod 0.

As further examples of the system's uses, Fig. 6, a direct tracing of an analog plot, shows the trajectory of a special drift bottle developed to investigate currents at tracking range sites. The transponderized drift bottle was trimmed to sink slowly (20 ft/min) while carried along with the current. On reaching bottom, it dropped a weight and rose again to repeat the process. In Fig. 6 the maximum currents are about 1/2 knot, the drops are about an hour long, and shear currents typical of turbulent water are clearly shown. The low-frequency hardware for the Alaskan tests was installed in March 1960 as the prototype element in an underwater tracking facility planned by the Naval Ordnance Test Station, Pasadena, Calif.

Future Plans

As described previously, the initial application of the 3-D range was to study torpedoes and this work continues. The recent utilization of the high-frequency range in calibration of shipboard equipment and in other diversified problems makes it clear that its instrumentation should be extended to utilize the full potentialities of the test area. Thus, present plans at NTS **Keyport** include installation of a second computer and an additional large, continuous tracking area south of the present range. This will allow separate, small exercises to be conducted simultaneously at both sites, while the combined areas will be available for larger problems.

This expanding use of this range area also makes apparent its limitations: in particular, it is too small. Thus, the

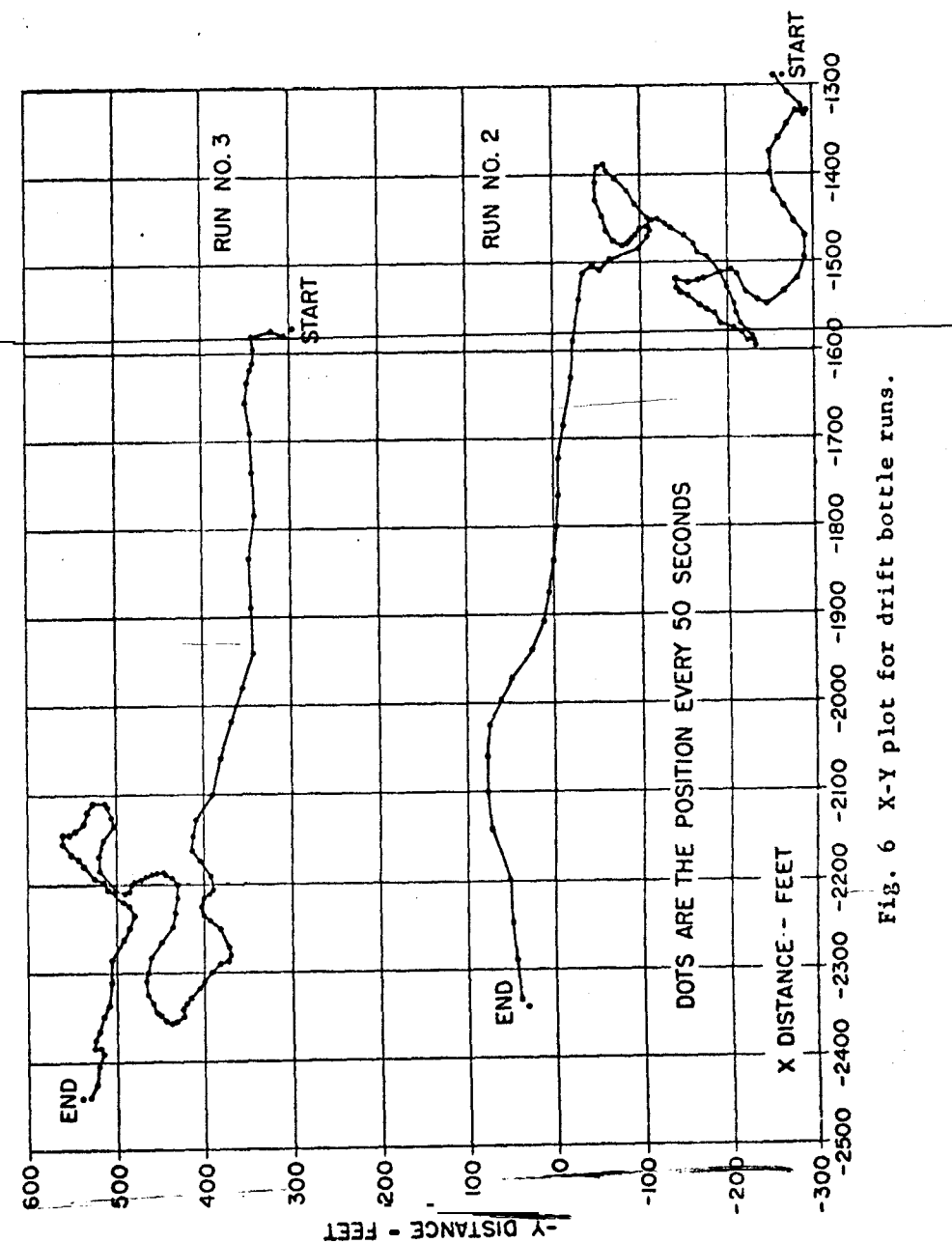


Fig. 6 X-Y plot for drift bottle runs.

larger and deeper St. Croix range, which is instrumented with the low-frequency system, is an important addition to the Navy's operation test and evaluation capability.

The basic methods employed in these two operating systems are not limited to the short ranges given in Table 1. One can, for example, trade accuracy for greater range by dropping frequency and taking into account the ambient and ship-noise power spectra. This was quantitatively shown in a recent study optimizing the relationship between parameters of the system, once array size and slant range are chosen, in which the low- and high-frequency systems described here represent but two data points on the optimum curve. It is anticipated that present and future needs for underwater tracking systems will result in further experimental verifications of this.

QUIETHIGH SPEED TRANSMISSION DRIVEFACILITY

Moe William Rosen*

U. S. Naval Ordnance Test Station, Pasadena, Calif.

Abstract

A facility to investigate transmission noises at the U. S. Naval Ordnance Test Station (NOTS) is described. Smooth, quiet operation of this driving machine at extreme speeds was attained, making it possible to measure and analyze the total noise radiation of transmissions at high speeds, and to compare noises of different transmissions.

Introduction

The NOTS transmission research program has two objectives: first, to design new machines that can run more quietly at high speeds than conventional transmissions without sacrifice of small size, high capacity, or efficiency, and second, to measure the intensity and characteristics of noises radiated by present high-speed, conventional transmissions. To conduct the necessary experiments, a special high-speed drive facility was designed and constructed.

Concept

To visualize the concept of the facility, imagine a transmission floating in midair, apart from any physical object, with a noiseless force turning its input shaft at very high speed and substantial power, and a noiseless body accepting and absorbing its output power. Then acoustic energy radiated from the transmission and measured at many points on a surrounding imaginary spherical surface, could be integrated to a total value and compared with that obtained with another transmission to determine their relative noise output. Figure 1 illustrates the concept.

*Also published as Naval Ordnance Report 6594, U. S. Naval Ordnance Test Station, China Lake, California.

*Senior Propulsion Research Engineer and Scientist, Propulsion Division.

General Arrangement

Figure 2 pictures the actual facility. The prime mover (a turbine) is in an adjoining concrete room. The walls and ceiling of the room are acoustically treated with a 2 in. thickness of glass wool making them sound absorbent. The shaft from the turbine is passed out of the turbine room through a 12-in. concrete wall to drive the test transmission. The latter transmits the power to its low-speed end, where it is absorbed by an electric dynamometer enclosed on a separate acoustically lined house. All machines are mounted on concrete and on rigid, steel bases. Each test transmission is isolated from its supports, the foundations, and the power shafting, so that these will not add to the radiated noises.

As shown in Fig. 3 the test area is out-of-door with two open sides, and two walled sides. The walls are covered with 3 in. of glass wool or with perforated metal acoustic panels filled with glass wool. Dense wool pads 2 in. thick, cover the horizontal surface and floors during tests. Thus the area itself is anechoic or "dead" to most sounds. During tests, activity in the area is stopped to minimize noise interference.

Prime Mover

The source of power is the steam turbine shown in Fig. 4. It is a single-stage impulse type with a rotor-tip diameter of 7 in., especially designed for quiet operation. Its blades (5/8 in. long and 1/2 in. wide) are integral with the disk metal. The rotor and shaft assembly are suspended by super-precision, "deep-groove", selected ball bearings, lubricated and cooled by jets of oil. The shaft (25-mm diam.) is unusually thick for such a small machine, to avoid torsional and transverse vibration, and critical frequencies. There are four De Laval nozzles, with about 500 psi, 500°F, steam entering their manifold. The steam is generated by a flash boiler and supplies the turbine through 200 feet of piping. Exhaust steam leaves through an 8-in. pipe and exits far enough away so that its noise is negligible.

The turbine is suspended as a dynamometer, its case rolling on its axis, so that its torque may be measured. The machine operates smoothly and quietly. It can develop 30 hp but is limited to 80 by the capacity of the boiler.

High-Speed Shaft

The shaft that carries the turbine power through the wall is considerably longer (39 in.) than conventional for the speeds

FACE OF MICROPHONE ROTATED
TO MANY POSITIONS ON IMAGINARY HEMI-
SPHERE.

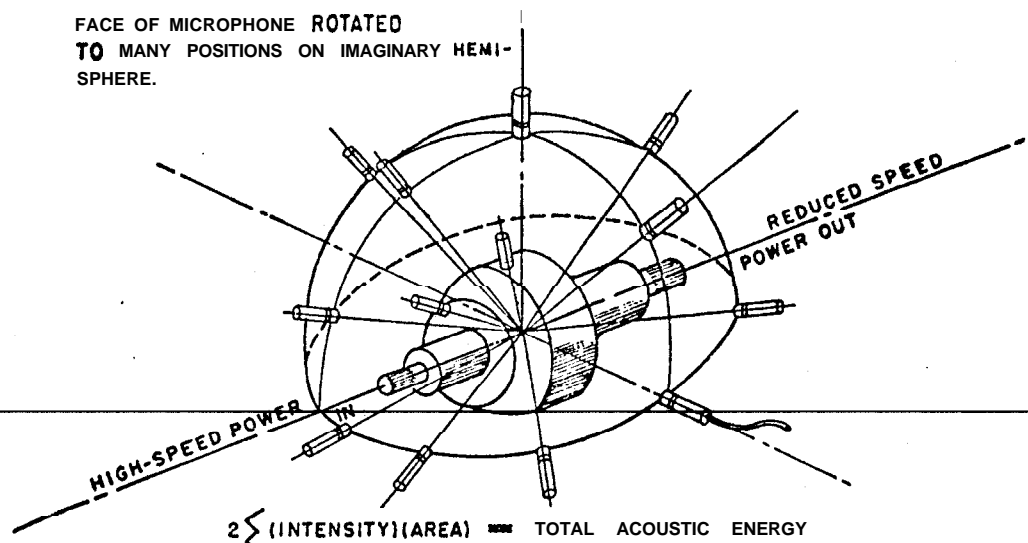


Fig. 1 Concept of quiet high speed transmission drive facility. Ideal hemispherical measurement of acoustical energy radiated by transmissions.

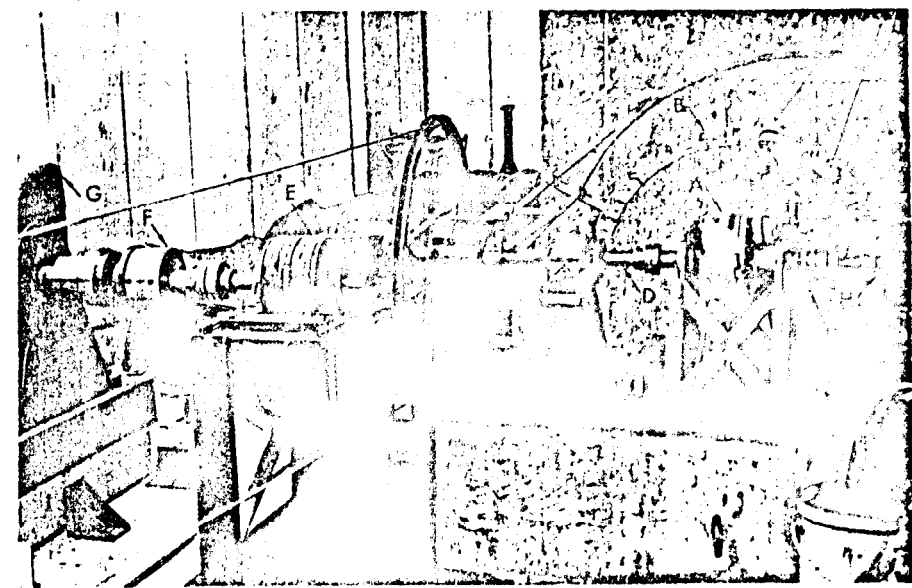


Fig. 2 Test area, showing (A) transmission, (B) microphone swinging arc support, (C) microphone isolated by soft sponge rubber, (D) output shafting, (E) secondary speed reducer with soundproof enclosure removed, (F) clutch, (G) dynamometer with soundproof hut removed, (H) high speed power input shaft coming from turbine room*

involved. Its four journals, **1.4375** in. diameter, are ground to align to each other within 0.0001 inches after heat treatment.

The four specially designed bearings which support the shaft **permit** operation to a theoretical critical vibrational speed of **58,500 rpm**, well above the actual **maximum** speed. These bearings are spherical, self-aligning, sleeve types, aligned to a straight line within **0.0002** in. using the shaft as guide. They are supported by a rigid steel tube, making a complete assembled unit with its own internal oil-distribution system. The oil grooves in the bearings (two annular, four axial) have "dams" to prevent hydrodynamic "oil whip", which could cause vibration at high speeds. Cooled oil is **pressure-fed into the grooves for several minutes before the shaft is permitted to rotate.**

Secondary Speed Reducer

Because the dynamometer speed is limited to about 4000 **rpm**, some of the **transmissions require** a secondary speed reducer. This is a **belt system**. Each belt is **2 5/8** in. wide, flat **on one side**, but with many small longitudinal V-shaped grooves on the working side which mate with circumferentially grooved pulleys. It is in a sound-proof **box** and cooled by refrigerated air. **It** operates smoothly and quietly while transmitting **70** hp at a belt speed of nearly 10,000 **ft/min.**

Clutch

An automatic overriding clutch of the slip-lock **roller** type is attached to the dynamometer shaft. It can carry torque in one direction, but not in the other. On two occasions the clutch prevented destructive damage by automatically **allowing** the heavy dynamometer **armature** to automatically "freewheel" when some bearings in the test transmission bound during high speed operation.

Dynamometer

The electric dynamometer absorbs power as a direct-current generator. Its field structure is suspended on ball bearings, **so** that direct and accurate **measurements may be made of** the torque and **power** input. Its normal capacity is **40** hp at **3,000** rpm, but it can be overloaded to **80** hp for **15** minutes at **4,100** **rpm.**

The dynamometer is vibration-isolated from its foundation, **and** is aligned by **screws in** the supports. -Enclosed **in its**

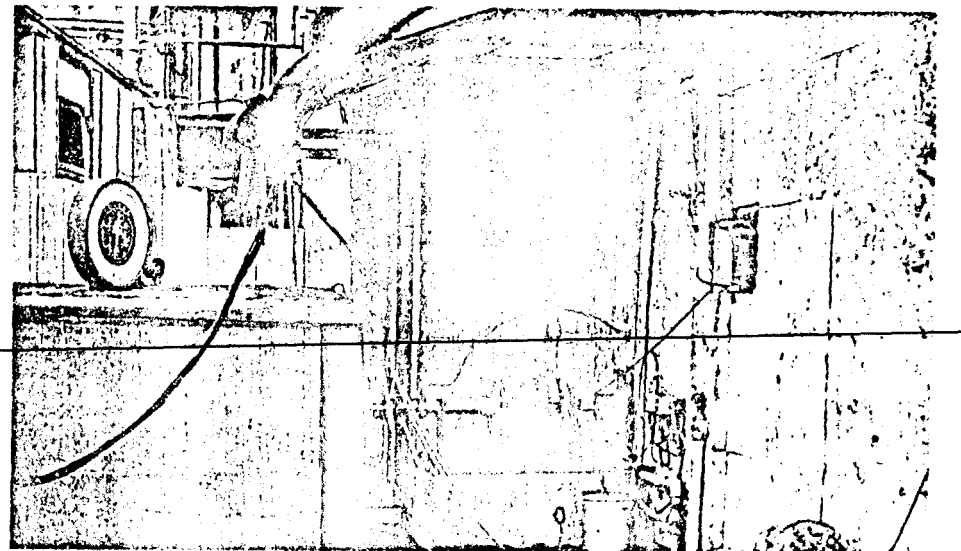


Fig. 3 Outdoor test area, dynamometer enclosed. Acoustically absorbent panels are on all walls **and** nearby floors. **Transmission** is a different one than in Fig. 2.

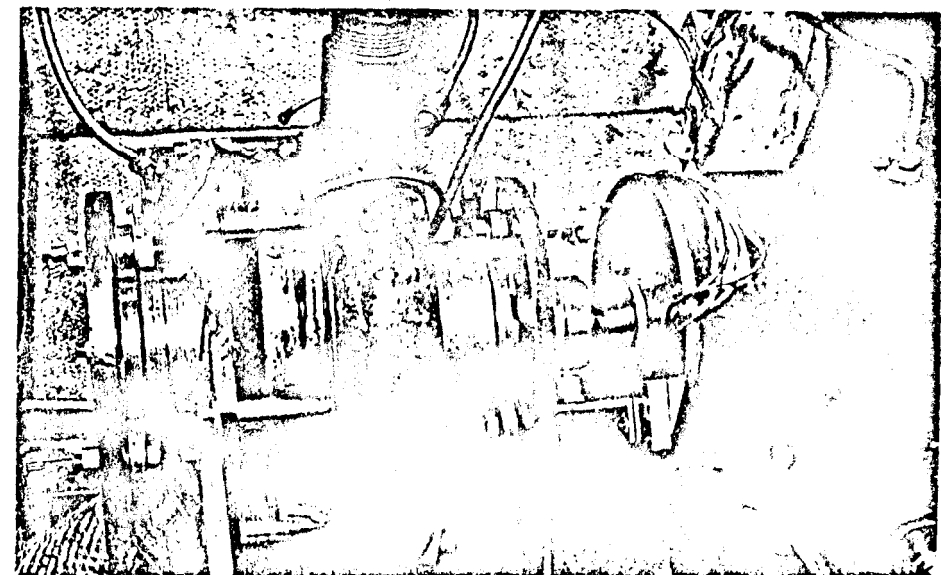


Fig. 4 Steam turbine drive (at left), **and** high speed shaft (right) in turbine room.

sound-muffling house, it can barely be heard when running at speeds up to **3,000 rpm**, and at 4,000 **rpm** only a low, subdued hum can be discerned.

Control of Speed and Power

The speed and power delivered by the turbine **are** adjusted manually by a steam valve, and the load absorbed by the dynamometer **is** controlled by varying field and **armature** voltage and current. Various combinations of speeds and powers are possible through simultaneous manipulations of these **controls**. When instruments show the desired readings, the machines are held steady while **acoustic** measurements are made.

An electric "eye" safety device, shown in Fig. 4, "watches" the **shaft** and automatically shuts off steam if speed rises above **35,000 rpm**. Otherwise, a failure or loss of load, with a heavy head of steam on the turbine would result in **an** acceleration which would lead to destruction *in two seconds or less*.

Speed and Torque Measurements

To measure turbine speed, a **beam** of light focused on the turbine coupling is reflected into a small photocell--the **same "eye"** also acts as the safety device (Fig. 4). **Half** of the coupling is painted **dull** black, so that the photocell sends out 1 impulse per revolution. Received by a frequency meter, this provides a direct reading of **rpm** to within **1%** accuracy. The speed of the dynamometer is measured by an automatic revolution counter as well as a direct-reading needle, and these give the **rpm** measurement to within **1/10** of **1%** accuracy. Turbine torque is registered *on a scale viewed via a porthole and mirror*. The torque input to the dynamometer is measured on a scale accurate to **1 part in 300**.

Noise Measurements

To measure transmission noises, a single **special condenser-type microphone**, capable of good response to 30 kc is placed on an apparatus that carries it through a **180°** arc on the surface of an **imaginary** hemisphere centered on the transmission (Fig. 2). The microphone is isolated by thick sponge from its supporting apparatus, which itself touches no operating machinery.

Observations- **are taken at 35** different points on the hemisphere while the machine is running a steady speed **and** power. Measurements are made of total noise intensity at each point. **Magnetic-tape** recordings at several points are used to analyze frequency **spectrums** to 30kc. Measurements of **separate** noise

intensities are integrated over the hemisphere, **and** doubled to give the total. acoustic energy radiated by the transmission at the particular speed and power.

This spherical integration differs from the conventional method in which a few isolated decibel (db) readings are taken 1 in. from the surface of the transmission at arbitrarily selected points. The spherical method **makes** a comparison of machine noises possible **and** gives a measure of their absolute radiation. Reliability has been verified by reruns, which repeat themselves with **only** an occasional variation of 1 db.

To make sure that the **measurements** were not colored by **noises from the driving facility, the turbine and the high-speed shaft** were operated both without and with 6 test transmission. Results obtained with the microphone at top dead center, **12 3/4** in. above the machinery **axis** (position **F**, Fig. 2) and without a transmission are shown **in** Table 1.

Table 1 Noise Output Without Transmission

Speed, rpm	Noise (db total intensity, relative to 0.0002 dyne/cm²)
3,300	68 to 72
5,500	68 to 72
10,000	72
15,000	72
20,000	72

Below 5,000 **rpm** no machinery noise could be detected in the earphones, with the microphone in the position described above. Above 5,000 **rpm** the turbine and shaft noises were present **as** a subdued hum; but even at 20,000 **rpm**, voices **35** ft. away from the microphone **were** clearly audible in the earphones.

When the facility **and** a transmission **were** operating together, in this case a spur-gear transmission of precision quality, the data **in** Table 2 were obtained.

Table 2 Noise Output With A Transmission

<u>Speed, rpm</u>	<u>Noise (db total. intensity, relative to 0.0002 dyne/cm²)</u>
2,500	89
5,000	94
10,000	100
15,000	103
20,000	108

Since transmission noises occupy the region of 85 to 130 db,
~~some 13 to 60 db above ambient noises, it can be seen that the~~
quiet high-speed transmission-drive facility, is a **powerful**
~~tool for investigating their noises.~~